

Supraglacial and englacial particle-ice interaction in dirty ice conditions

Katherine Frances Reeves

This thesis is submitted for the degree of Doctor of Philosophy at Lancaster
University, Lancaster Environment Centre

March 2022

Supraglacial and englacial particle-ice interaction in dirty ice conditions

Katherine Frances Reeves

This thesis is submitted for the degree of Doctor of Philosophy at Lancaster University, Lancaster Environment Centre, March 2022

Abstract

Particles can modify the thermodynamic behaviour of ice in response to insolation. Ice with surface particles is defined as 'debris-covered' or 'dirty' ice, depending on whether a continuous or discontinuous layer is present, respectively. The behaviour of dirty ice has not been extensively researched, although these ice conditions are common. Improving our understanding of discontinuous particle-ice interaction can aid forecasting of ice changes in a warming world.

Laboratory experiments were designed to address knowledge gaps in the behaviour of: (1) particle properties (thermal conductivity, albedo, density, and diameter) on influencing particle-ice interaction using control particles, such as plastics (e.g. polystyrene) and metals (e.g. brass and chrome steel); (2) volcanic particles (e.g. basaltic scoria and rhyolitic pumice) in dirty ice conditions; and (3) microplastic particles (e.g. polyethylene and polypropylene) in dirty ice conditions. Particle-ice interaction under analogue insolation (80 W LED) was studied in conditions analogous to the supraglacial and englacial environment, at scales ranging from individual particles to a scattering of particles, all with a diameter <12 mm. Experiments were conducted in a freezer (-6°C – +7°C) on optically transparent ice blocks (50-80 mm).

Results demonstrated that dirty ice conditions are significant for glacier ablation, with a range of particle-ice behaviours observed: (1) sinking particles created melt channels within ice; (2) floating particles created surface meltwater ponds with surface tension effects facilitating particle redistribution processes; (3) particles utilised pre-existing internal ice structures (e.g. vein networks) as ablation pathways; and (4) volcanic particle fragmentation. These were

controlled by the thermal state of ice, and particle properties. The englacial environment was additionally found to be significant for ablation. The laboratory behaviour of volcanic and microplastic particles compared well with behaviours estimated through systematic investigation of particle properties, suggesting that the fate of particles within ice can be mapped through assessment of particle properties.

Supraglacial and englacial particle-ice interaction in dirty ice conditions

Table of Contents

1. Introduction.....	1
1.1. The impacts of the cryosphere on life and society	1
1.1.1. Freshwater supply	1
1.1.2. Sea level rise	2
1.1.3. Ocean circulation	3
1.1.4. Natural hazards	3
1.1.5. Biological systems	3
1.2. Ablation of ice	4
1.2.1. Mechanisms of ablation	4
1.2.2. Energy balance.....	7
1.2.3. Albedo of snow and ice	7
1.3. Debris-covered and dirty ice	9
1.3.1. Properties of light absorbing particles	9
1.3.2. Common light absorbing particles	11
1.4. Aim	15
1.5. Objectives	15
2. A review of debris-covered and dirty ice science	17
2.1. Fieldwork approaches	17
2.1.1. Debris thickness	18
2.1.2. Particle thermal conductivity.....	22
2.1.3. Microplastics in the cryosphere	23
2.1.4. Summary of fieldwork studies.....	23
2.2. Laboratory approaches	25
2.2.1. Debris thickness	25
2.2.2. Diurnal cycles	26
2.2.3. Rainfall and particle permeability	27
2.2.4. Particle properties.....	28
2.2.5. Sublimation	30
2.2.6. Summary of laboratory studies.....	31
2.3. Modelling approaches	32
2.3.2. Modelling dirty ice conditions.....	34

2.3.3.	Common assumptions used in modelling of debris-covered and dirty ice	35
2.3.4.	Summary of modelling studies	36
2.4.	Justification of research plan	36
3.	Methods	39
3.1.	Method development	40
3.1.1.	Creation of optically transparent ice	40
3.1.2.	Creation of ice containing embedded particles	43
3.1.3.	Creation of opaque ice	44
3.1.4.	Artificial radiation source	44
3.2.	Experimental set-up.....	53
3.2.1.	Preventing sublimation	54
3.2.2.	Temperature measurements	55
3.2.3.	Placement of particles on the ice surface.....	57
3.2.4.	Time-lapse imagery	59
3.3.	Particles	59
3.3.1.	Particle properties (Chapter 4)	60
3.3.2.	Volcanic particles (Chapter 5)	60
3.3.3.	Microplastic particles (Chapter 6)	62
3.4.	Experimental process.....	62
3.5.	Data analysis	63
3.5.1.	Extraction of data from time-lapse images	63
3.5.2.	Calculation of particle velocity data	64
3.6.	Experimental implementation issues	67
3.6.1.	Unclear images.....	67
3.6.2.	Paint.....	67
3.7.	Thermal environment of ice in proximity to particles	68
4.	An experimental investigation of particle properties to determine the physical processes involved in particle-ice interaction.....	70
4.1.	Thermal conductivity.....	70
4.1.1.	P1: a thermally conductive chrome steel particle	71
4.1.2.	P3: a thermally conductive brass particle.....	78
4.1.3.	P8: two thermally conductive brass particles	88
4.1.4.	P48: a thermally conductive brass particle within opaque ice	94
4.1.5.	P49: a cooled thermally conductive brass particle	96
4.2.	Albedo	99
4.2.1.	P10: a high albedo chrome steel particle	100

4.2.2.	P11b: a comparison of a low albedo, intermediate albedo, and high albedo brass particle 102	
4.2.3.	P14: an intermediate albedo brass particle	113
4.3.	Density	117
4.3.1.	P18: an intermediate density Delrin® particle	118
4.3.2.	P22: a low density polypropylene particle	129
4.3.3.	P15: a low density polystyrene particle	132
4.3.4.	P17b: an embedded low density polystyrene particle	138
4.4.	Diameter	147
4.4.1.	P23b: a comparison of 6 mm and 8 mm brass and chrome steel particles	149
4.4.2.	P25b: a 12 mm brass particle	154
4.4.3.	P28: a 3 mm brass particle	158
4.4.4.	P29: a 1.5 mm brass particle	162
4.4.5.	P37: a comparison of 1.5 mm, 3 mm, 6 mm, and 12 mm brass particles	165
4.4.6.	P36: a 3x3 mm array of brass particles	172
4.5.	Conclusions	179
4.5.1.	Thermal conductivity	180
4.5.2.	Albedo	180
4.5.3.	Density	181
4.5.4.	Diameter	181
5.	An experimental investigation into the behaviour of volcanic particles within the cryosphere	183
5.1.	V1: a 6 mm cemented ash cluster	186
5.1.1.	Results and interpretation	187
5.1.2.	Melt pathway	187
5.1.3.	Basal meltwater pond	189
5.1.4.	Summary	190
5.2.	V2: a 12 mm cemented ash cluster	194
5.2.1.	Results and interpretation	195
5.2.2.	Melt pathway	196
5.2.3.	Surface meltwater pond	196
5.2.4.	Basal meltwater pond	197
5.2.5.	Summary	198
5.3.	V3: a 3 mm cemented ash cluster	199
5.3.1.	Results and interpretation	200
5.3.2.	Melt pathway	201
5.3.3.	Surface meltwater pond	201
5.3.4.	Basal meltwater pond	202

5.3.5.	Summary	202
5.4.	V9: a 6 mm basaltic-andesitic scoria particle	203
5.4.1.	Results and interpretation.....	203
5.4.2.	Melt pathway	204
5.4.3.	Surface meltwater pond.....	204
5.4.4.	Basal meltwater pond	205
5.4.5.	Summary	205
5.5.	V11: a 12 mm basaltic-andesitic scoria particle	207
5.5.1.	Results and interpretation.....	208
5.5.2.	Melt pathway	209
5.5.3.	Surface meltwater pond.....	210
5.5.4.	Basal meltwater pond	210
5.5.5.	Summary	210
5.6.	V15: a 3 mm basaltic-andesitic scoria particle	215
5.6.1.	Results and interpretation.....	216
5.6.2.	Melt pathway	217
5.6.3.	Surface meltwater pond.....	217
5.6.4.	Basal meltwater pond	218
5.6.5.	Summary	218
5.7.	V18: a 1.5 mm basaltic-andesitic scoria particle	220
5.7.1.	Results and interpretation.....	221
5.7.2.	Summary	223
5.8.	V25: a 6 mm rhyolitic pumice particle	228
5.8.1.	Results and interpretation.....	229
5.8.2.	Proximal surface meltwater pond	230
5.8.3.	Shallow surface meltwater pond	231
5.8.4.	Summary	231
5.9.	V27: a 12 mm rhyolitic pumice particle	232
5.9.1.	Results and interpretation.....	233
5.9.2.	Proximal surface meltwater pond	235
5.9.3.	Shallow surface meltwater pond	235
5.9.4.	Summary	235
5.10.	V26: a 3 mm rhyolitic pumice particle	236
5.10.1.	Results and interpretation.....	237
5.10.2.	Proximal surface meltwater pond	238
5.10.3.	Shallow surface meltwater pond	238
5.10.4.	Summary	239
5.11.	V28: a 1.5 mm rhyolitic pumice particle	240

5.11.1. Results and interpretation.....	240
5.11.2. Proximal surface meltwater pond	241
5.11.3. Shallow surface meltwater pond	241
5.11.4. Summary	241
5.12. V33: a scattering of basaltic-andesitic scoria particles	243
5.12.1. Results and interpretation.....	244
5.12.2. Melt pathway	247
5.12.3. Proximal surface meltwater pond	248
5.12.4. Shallow surface meltwater pond	249
5.12.5. Basal meltwater pond	250
5.12.6. Summary	251
5.13. V34: a scattering of basaltic-andesitic scoria particles within opaque ice	252
5.13.1. Results and interpretation.....	253
5.13.2. Melt pathway	254
5.13.3. Proximal surface meltwater pond	254
5.13.4. Shallow surface meltwater pond	255
5.13.5. Basal meltwater pond	256
5.13.6. Summary	257
5.14. Conclusions	257
5.14.1. Convection.....	258
5.14.2. Ice structure	258
5.14.3. Particle loss and fragmentation	258
6. An experimental investigation into the behaviour of microplastic particles within the cryosphere.....	260
6.1. Mp1: a small polyethylene surface particle	261
6.1.1. Results and interpretation.....	262
6.1.2. Surface meltwater.....	262
6.1.3. Summary	263
6.2. Mp8: a medium polyethylene surface particle	265
6.2.1. Results and interpretation.....	266
6.2.2. Surface meltwater.....	266
6.2.3. Summary	268
6.3. Mp2: a large polyethylene surface particle	268
6.3.1. Results and interpretation.....	269
6.3.2. Summary	270
6.4. Mp4: a large polypropylene surface particle	273
6.4.1. Results and interpretation.....	274

6.4.2.	Summary	275
6.5.	Mp6: embedded microplastic particles	282
6.5.1.	Results and interpretation.....	282
6.5.2.	Melt pathway	283
6.5.3.	Surface meltwater pond.....	284
6.5.4.	Basal meltwater pond	284
6.5.5.	Summary	285
6.6.	Mp15: a scattering of small surface microplastics	290
6.6.1.	Results and interpretation.....	291
6.6.2.	Melt pathway	292
6.6.3.	Proximal surface meltwater pond	293
6.6.4.	Shallow surface meltwater pond	293
6.6.5.	Basal meltwater pond	293
6.6.6.	Summary	294
6.7.	Mp17: a scattering of small surface microplastics upon opaque ice.....	296
6.7.1.	Results and interpretation.....	297
6.7.2.	Melt pathway	298
6.7.3.	Proximal surface meltwater pond	298
6.7.4.	Shallow surface meltwater pond	298
6.7.5.	Basal meltwater pond	299
6.7.6.	Summary	299
6.8.	Conclusions	300
7.	Discussion.....	302
7.1.	The melting processes	306
7.1.1.	Initialisation of particle-induced ice melt.....	306
7.1.2.	Melting in the supraglacial and englacial environment.....	307
7.1.3.	Thermal environment.....	310
7.2.	Other ablation processes.....	316
7.2.1.	Sublimation	316
7.2.2.	Evaporation	317
7.3.	Ice structure and hydrology	317
7.3.1.	Modifying the internal ice structure.....	318
7.3.2.	Particle-particle interaction	319
7.4.	Sorting mechanisms of particles within ice.....	319
7.4.1.	Sorting of dense particles	320
7.4.2.	Sorting of buoyant particles	323
7.5.	Redistribution processes on an ice surface	326

7.6.	Application to the natural environment.....	327
7.6.1.	Meteorite loss mechanisms	327
7.6.2.	Cryoconite holes	330
7.6.3.	Weathering crusts.....	333
7.6.4.	Microplastic particle contamination within ice.....	335
7.7.	Fragmentation of volcanic particles within ice.....	338
7.8.	Modelling dirty ice behaviour	342
7.9.	Future research.....	346
7.9.1.	Microplastic particle contamination in the cryosphere.....	346
7.9.2.	The behaviour of embedded particles	346
7.9.3.	Sublimation cooling offsetting melting processes.....	347
7.9.4.	Modelling dirty ice	347
8.	Conclusions.....	348
9.	Appendices	353
9.1.	Appendix 1: Summary of key light absorbing particles.	354
9.2.	Appendix 2: Supplementary table of reviewed published fieldwork studies. .	357
9.3.	Appendix 3: Supplementary table of reviewed published laboratory studies.	369
9.4.	Appendix 4: Supplementary table of reviewed published modelling studies.	373
9.5.	Appendix 5: Supplementary table of method development experiments to create optically transparent ice blocks.	386
9.6.	Appendix 6: Supplementary table of method development experiments to determine the appropriate artificial radiation source.	389
9.7.	Appendix 7: Example of workflow of a standard experimental procedure.....	393
9.8.	Appendix 8: Temperature data of experimental work conducted in Chapter 4. 394	
9.9.	Appendix 9: Key findings of experimental work investigating the role of particle thermal conductivity on particle-ice interaction.....	396
9.10.	Appendix 10: Key findings of experimental work investigating the role of particle albedo on particle-ice interaction.....	399
9.11.	Appendix 11. Key findings of experimental work investigating the role of particle density on particle-ice interaction.....	401
9.12.	Appendix 12: Summary of behaviour observed in experiment P21.	403
9.13.	Appendix 13: Key findings of experimental work investigating the role of particle diameter on particle-ice interaction.	405

9.14.	Appendix 14: Temperature data of experimental work conducted in Chapter 5.	410
9.15.	Appendix 15: Key findings of experimental work investigating volcanic particle-ice interaction.....	411
9.16.	Appendix 16: Temperature data of experimental work conducted in Chapter 6.	417
9.17.	Appendix 17: Key findings of experimental work investigating microplastic particle-ice interaction.....	418
9.18.	Appendix 18: A comparison of modelled and observed particle velocities. ...	421
9.19.	Appendix 19: Glossary of key terms.....	424
10.	References	426

List of Tables

Table 1.1. Primary classification of glacier types mentioned in this thesis. ¹ (Benn and Evans, 2014) and ² (NSIDC, 2020a).	1
Table 1.2. Summary of ice ablation processes, where LT = land-terminating, WT = water terminating, HA = high altitude, PR = polar regions, IS = ice sheet, and MG = mountain glaciers (Parish and Bromwich, 1987; Benn and Evans, 2014; Cuffey and Paterson, 2010; Marshall, 2011).	6
Table 1.3. Albedo range for snow and ice (Benn and Evans, 2014; Cuffey and Paterson, 2010).	8
Table 3.1. The particle properties of the synthetic materials used in experiments, and the ratio relative to water density (1000 kg m^{-3}) and ice thermal conductivity ($2.1 \text{ W m}^{-1} \text{ K}^{-1}$).	60
Table 3.2. Categorisation of particle properties.	60
Table 3.3. The particle properties of dry volcanic material used in experiments, and the ratio relative to water density (1000 kg m^{-3}) and ice thermal conductivity ($2.1 \text{ W m}^{-1} \text{ K}^{-1}$). ¹ Hobbs (2014) and ² Klug and Cashman (1996).	61
Table 3.4. Categorisation of dry volcanic particle properties.	61
Table 3.5. The particle properties of plastic material used in experiments, and the ratio relative to water density (1000 kg m^{-3}) and ice thermal conductivity ($2.1 \text{ W m}^{-1} \text{ K}^{-1}$). ¹ Patti and Acierno (2020).	62
Table 3.6. Categorisation of microplastic particle properties.	62
Table 4.1. A summary of experiments investigating the role of particle thermal conductivity in particle-induced ice melt, highlighting the types of particles used and associated thermal environments as defined in Chapter 3.	71
Table 4.2. Summary of key features observed in experiments P4, P5, P6, and P7.	85
Table 4.3. A summary of experiments investigating the role of particle albedo in particle-induced ice melt, highlighting the types of particles used and the associated thermal environments as defined in Chapter 3.	99
Table 4.4. Comparison of distance moved, particle velocity, and duration of particle movement for the LA, IA, and HA particles in experiments P12b and P13.	108
Table 4.5. A summary of the experiments investigating the role of particle density in particle-induced ice melt, organised by particle thermal conductivity. This indicates the type of particles used and associated thermal environments as defined in Chapter 3.	118
Table 4.6. Key features observed in repeat experiments P19, P20, and P21. *Relative to previous experiments involving thermally conductive and high density particles.	125
Table 4.7. The duration of the three melting and freezing cycles in the time-lapse images and the maximum dimensions of the surface meltwater ponds for experiment P15.	133
Table 4.8. A summary of the experiments that investigated the role of particle diameter in particle-induced ice melt, indicating the particle diameters, particle configurations and thermal environments as defined in Chapter 3.	148
Table 4.9. Behaviour of the P38, P39, P40, P42, and P43 particle arrays.	175

Table 5.1. (continued overleaf) A summary of experiments investigating the behaviour of volcanic particle-ice interaction, indicating the particle composition, diameter and associated thermal environments as defined in Chapter 3.	184
Table 5.2. Particle velocities associated with different particle configurations, where ‘cluster’ is referring to an accumulation of fine-grained volcanic particles.	246
Table 6.1. A summary of experiments investigating the behaviour of microplastic particle-ice interaction, indicating the particle composition, diameter and associated thermal environments as defined in Chapter 3.	260
Table 6.2. The variability of microplastic particle velocities in experiment Mp15 with associated code in Figure 6.27.	291
Table 6.3. The variability of microplastic particle velocities in experiment Mp16 with associated code in Figure 6.30.	294
Table 6.4. The variability of microplastic particle velocities in experiment Mp17 with associated code in Figure 6.34.	297
Table 7.1. Summary of key findings for properties investigated experimentally in Chapter 4.	303
Table 7.2. Summary of key processes associated with a combination of particle properties and the shift in behaviour from a surface particle to a submerged particle. ¹ Evatt et al. (2016), ² Labus and Labus (2018), and ³ Opeil et al. (2012).	309
Table 7.3. Comparison of modelled and observed particle velocity. Modelled particle velocities were calculated using the simple melt model described in Chapter 3.	343
Table 9.1. A summary of the key characteristics of ice surface particles that can influence ice ablation rates. *PCDs = pyroclastic density currents.	354
Table 9.2. Comparison of results from fieldwork experiments, where ¹ cited in Kirkbride and Dugmore, (2003) ² cited in Fujii (1977), ³ Kayastha et al (2000) and ⁴ cited in Fyffe et al. (2020). Climate classification is from Peel et al. (2007), where ^a : tropical, ^b : arid, ^c : temperate, ^d : cold, and ^e : polar.	357
Table 9.3. Comparison of results from laboratory experiments.	369
Table 9.4. Comparison of results from modelling experiments.	373
Table 9.5. A summary of method development experiments focusing on creating optically transparent ice blocks. These were placed in an upright freezer operating at temperatures between -10°C and -20°C.	386
Table 9.6. A summary of the method development experiments focusing on designing the experimental set-up and determining the artificial radiation source.	389
Table 9.7. Average temperature values for experimental work in Chapter 4.	394
Table 9.8. Key findings from the thermal conductivity series of experiments (e.g. P1-P9, P48-P49).	396
Table 9.9. Summary of key findings from the albedo series of experiments (e.g. P10-P14). ...	399
Table 9.10. Key findings from the density series of experiments (P15-P22).	401
Table 9.11. General behaviour observed in experiment P21(i)-P21(v).	403
Table 9.12. Key findings from the diameter series of experiments (P23b-P47)	405

Table 9.13. Average temperature values for experimental work in Chapter 5.	410
Table 9.14. Key findings from the volcanic particle series of experiments (V1-V34).	411
Table 9.15. Average temperature values for experimental work in Chapter 6.	417
Table 9.16. Key findings from the microplastic particle series of experiments (Mp1-Mp19), where PE is polyethylene and PP is polypropylene.	418

List of Figures

Figure 1.1. Diagram showing energy input for the solid-gas, solid-liquid, liquid-gas, and vice versa, phase changes of water. ¹ Whelan and Hodgson (1989), ² Cuffey and Paterson (2010)....	5
Figure 2.1. Stacked bar graph highlighting the variability of effective and critical thickness (cm) from reviewed field studies, separated into debris type.	19
Figure 2.2. The relationship between the mean daily ablation rate (cm day ⁻¹) and the thickness of debris cover (cm) at various locations. Smoothed curves from data points taken from (a) Mattson et al. (1993); (b) Khan (1989); (c) data points from Richardson and Brook (2010); (d) Loomis, 1970 and (e) Östrem (1959), reprinted from 'Ablation of debris-covered ice: some effects of the 25 September 2007 Mt Ruapehu eruption', Richardson, J. M., and Brook, M. S., Journal of the Royal Society of New Zealand, © copyright [2010], reprinted by permission of Informa UK Limited, trading as Taylor & Taylor & Francis Group, http://www.tandfonline.com	20
Figure 3.1. Diagrams showing (a) the stable thermal structure within water and (b) the maximum density anomaly reprinted from International Journal of Heat and Mass Transfer, vol. 49, Cawley, M. F., McGlynn, D., and Mooney, P. A., 'Measurement of the temperature of density maximum of water solutions using a convective flow technique', pg. 1764, Copyright (2006), with permission from Elsevier.	41
Figure 3.2. Cross-sectional diagram indicating the final experimental set-up for creating optically transparent ice, where (a) indicates initial placement into the freezer and (b) shows modification to the set-up once freezing had begun.	43
Figure 3.3. The wavelength (µm) and wavenumber (cm ⁻¹) of each region in the electromagnetic spectrum (adapted from Liou, 2002).	45
Figure 3.4. Solar irradiance (W m ⁻² µm ⁻¹) curve for the top of the atmosphere and Earth's surface with a solar zenith angle of 60° and a spectral resolution of 50 cm ⁻¹ . This indicates absorption and scattering regions (not including aerosol or cloud interaction). Absorption bands are highlighted in grey, whilst atmospheric windows are white regions under the curve (adapted from Liou, 2002). Reprinted from Introduction to Atmospheric Radiation (2 nd Ed), Liou, K. N., Absorption and Scattering of Solar Radiation in the Atmosphere, pg. 86, Copyright (2002), with permission from Elsevier.	46
Figure 3.5. Structure of a water molecule. Circles represent hydrogen and oxygen atoms, and black lines represent the covalent bonds between them. +/- symbols indicate electric charge.	46
Figure 3.6. Modes of vibrational (a-c) and rotational (d-f) movement of a liquid water molecule. Red and grey circles denote oxygen and hydrogen atoms respectively. Four modes are highlighted: (a) symmetrical stretching; (b) asymmetrical stretching; (c) bending; and (d-f) oscillating. Drawn by author with information taken from Liou (2002) and Maurellis and Tennyson (2003).	47
Figure 3.7. The infrared absorption spectrum for gaseous, solid, and liquid water (Chaplin, 2022).	48
Figure 3.8. Relative absorption of natural sunlight across the visible wavelengths, measured by a PG100N UPRtek handheld spectrometer held directly in the beam of illumination.	50

Figure 3.9. Relative absorption of a halogen bulb used in method development experiments, measured by a PG100N UPRtek handheld spectrometer held directly in the beam of illumination.	51
Figure 3.10. Relative absorption of the 80 W white LED radiation source used in laboratory experiments, measured by a PG100N UPRtek handheld spectrometer held directly in the beam of illumination.	52
Figure 3.11. Schematic diagram showing the final experimental set-up.....	53
Figure 3.12. Photograph of final experimental set-up.	54
Figure 3.13. Cross-sectional diagram indicating the positioning of the thermocouple when measuring proxy-ice temperatures.....	55
Figure 3.14. Continuous temperature data logger measurements of the proxy-ice temperature over a 22-hour period from experiment P49 (Chapter 4). The moving average was measured over 15 points (representing 5 minutes) and was used to elucidate the key cycles within the measurement period. (a) highlights the ‘short’ cycle, (b) indicates the ‘long’ cycle.	57
Figure 3.15. The experimental procedure.	63
Figure 3.16. Example of extraction of vertical distance moved by a particle.	64
Figure 3.17. Photograph of the silicon seal to reduce condensation effects.....	67
Figure 3.18. The definition of the thermal environments of the ice in proximity to the particles across the thermal range experienced in laboratory experiments.	69
Figure 3.19. Cross-sectional schematic indicating the observational criteria for determining the thermal environment in the proximity of a particle.	69
Figure 4.1. The thermal environment of particles in experiments investigating the role of particle thermal conductivity in particle-ice interaction. Experiment position has been derived from interpretation of observations, as described in Chapter 3, Section 3.7.	70
Figure 4.2. Cross-sectional diagram indicating the role of sublimation and surface cooling in preventing ice melt. Values of latent heat of sublimation taken from Cuffey and Paterson (2010).	72
Figure 4.3. Schematic cross-sectional view of the hypothesised particle-ice interaction in experiment P1b.	72
Figure 4.4. Cross-sectional diagram indicating the influence of a closed system on sublimation and deposition in experiment P1b.....	73
Figure 4.5. Vertical distance moved and velocity of an 8 mm chrome steel particle in experiment P1b.	74
Figure 4.6. Images showing the fluctuation in melt pathway morphology at two stages (5 and 14 hours) in experiment P1b. (a) observational line diagram, (b) photograph and (c) interpretation of the features.	76
Figure 4.7. Schematic cross-sectional view of the hypothesised particle-ice interaction in experiment P3.	79

Figure 4.8. Images showing lateral movement of the P3 particle when on the ice base within a drained melt pathway. (a) observational line diagram, (b) photograph and (c) interpretation of the features.	81
Figure 4.9. Cross-sectional photograph of the dome-shaped basal meltwater pond created by the P3 particle and the combined area of melt from the P2b and P3 particles.	83
Figure 4.10. Images showing the melt pathway development over six periods in experiment P6. (a) observational line diagram, (b) photograph and (c) interpretation of the features.	87
Figure 4.11. Schematic cross-sectional view of the hypothesised particle-ice interaction in experiment P8.	88
Figure 4.12. Graph showing the vertical distance moved by two 6 mm brass particles in experiment P8. Condensation on the freezer surface prevented continuous data extraction. ...	89
Figure 4.13. Images of teardrop melt pathway morphology and positive shift across the thermal range in experiment P8. (a) observational line diagram, (b) photograph and (c) interpretation of the features.	90
Figure 4.14. Images of basal meltwater pond and growing melt pathway. (a) observational line diagram, (b) photograph and (c) interpretation of the features.	91
Figure 4.15. Images indicating the shift from stable (warm) to stable (cool) in experiment P9, identified by open melt pathways and refreezing melt pathways, respectively. (a) observational line diagram, (b) photograph and (c) interpretation of the features.	93
Figure 4.16. Schematic cross-sectional view of the hypothesised particle-ice interaction in experiment P48.	94
Figure 4.17. Vertical distance moved and velocity of a 6 mm brass particle in experiment P48.	95
Figure 4.18. Plan-view photograph of the P48 open melt pathway at the ice surface.	95
Figure 4.19. Schematic cross-sectional view of the hypothesised particle-ice interaction in experiment P49.	97
Figure 4.20. Vertical distance moved and velocity of a 6 mm brass particle in experiment P49.	97
Figure 4.21. Images of the melt pathway and basal meltwater pond associated with the P49 particle. (a) observational line diagram, (b) photograph and (c) interpretation of the features. ...	98
Figure 4.22. The thermal environment of particles in experiments investigating the role of particle albedo in influencing particle-ice interaction. Experiment position has been derived from interpretation of observations, as described in Chapter 3, Section 3.7.	99
Figure 4.23. Schematic cross-sectional view of the hypothesised particle-ice interaction in experiment P10.	100
Figure 4.24. Vertical distance moved and velocity of the high albedo chrome steel particle in experiment P10.	101
Figure 4.25. Schematic cross-sectional view of the hypothesised particle-ice interaction in experiment P11b conducted on an unstable ice block.	103

Figure 4.26. The change in the ice surface level as the ice melted during experiment P11b, transitioning from a solid-water phase to a liquid-water phase.	104
Figure 4.27. Vertical distance moved by a low and intermediate albedo 6 mm brass particle and the ice surface lowering. The intermediate albedo particle does not start at '0 m' due to initial temperature differences between the particles and the ice resulting in immediate melting prior to time-lapse imaging. The low albedo particle started submerged within the ice because it was used in experiment P11a. Data could not be retrieved for the high albedo particle from the time-lapse images due to a restricted view of the top of the ice block.	106
Figure 4.28. Cross-sectional images of the low albedo (LA) and intermediate albedo (IA) melt pathways in experiment P11b. (a) observational line diagram, (b) photograph and (c) interpretation of the features.	107
Figure 4.29. Cross-sectional images of refreezing meltwater in experiment P12b. (a) observational line diagram, (b) photograph and (c) interpretation of the features.	110
Figure 4.30. Cross-sectional images of drainage of meltwater pathways in experiment P13 across three time frames. (a) observational line diagram, (b) photograph and (c) interpretation of the features.	112
Figure 4.31. Schematic cross-sectional view of the hypothesised particle-ice interaction in experiment P14.	113
Figure 4.32. Vertical distance moved and velocity of the intermediate albedo brass particle in experiment P14 (ii).	115
Figure 4.33. Cross-sectional images showing the refreezing of the IA melt pathway in experiment P14 (ii) across three time frames. (a) observational line diagram, (b) photograph and (c) interpretation of the features.	116
Figure 4.34. The thermal environment of particles in experiments investigating the role of particle density in influencing particle-ice interaction. Experiment position has been derived from interpretation of observations, as described in Chapter 3, Section 3.7.	118
Figure 4.35. Schematic cross-sectional view of the hypothesised particle-ice interaction in experiment P18.	119
Figure 4.36. Vertical distance moved and velocity of a Delrin® particle in experiment P18 from hour 12 to hour 24.	120
Figure 4.37. Cross-sectional images showing a narrowing of the top portion of the melt pathway and the presence of gas bubbles in experiment P18, with both indicating refreezing processes. (a) observational line diagram, (b) photograph and (c) interpretation of the features.	121
Figure 4.38. Cross-sectional images indicating the basal position of the Delrin® particle at the base of a melt pathway following a shift into the unstable thermal environment in experiment P18. (a) observational line diagram, (b) photograph and (c) interpretation of the features.	122
Figure 4.39. Comparison of the surface meltwater pond morphology development throughout a 20 hour period in experiment P19.	126

Figure 4.40. Cross-sectional images showing the change in water level in the drained melt pathway within a five-hour period in experiment P20. (a) observational line diagram, (b) photograph and (c) interpretation of the features.....	127
Figure 4.41. Vertical distance moved by the Delrin® particle over the five phases in experiment P21.....	128
Figure 4.42. Schematic cross-sectional view of the hypothesised particle-ice interaction in experiment P22.....	130
Figure 4.43. Plan-view photographs showing the evolution (a-i) of a surface meltwater pond in experiment P22.....	131
Figure 4.44. Schematic cross-sectional view of the hypothesised particle-ice interaction in experiment P15.....	132
Figure 4.45. Cross-sectional images of meltwater development (left) and refreezing (right) in P15 (i). (a) observational line diagram, (b) photograph and (c) interpretation of the features..	134
Figure 4.46. Cross-sectional images of meltwater development (left) and refreezing (right) in P15 (ii). (a) observational line diagram, (b) photograph and (c) interpretation of the features.	135
Figure 4.47. Plan-view photograph of the low density polystyrene particle on the ice surface at the end of experiment P15.....	136
Figure 4.48. Schematic cross-sectional view of the hypothesised particle-ice interaction in experiment P17b.....	138
Figure 4.49. Vertical distance moved and velocity of a polystyrene particle in experiment P17b to reach the ice surface.....	139
Figure 4.50. Cross-sectional images of the initial movement of the polystyrene particle and early development of a melt pathway in experiment P17b. (a) observational line diagram, (b) photograph and (c) interpretation of the features.....	140
Figure 4.51. Cross-sectional images indicating the development of the gas bubble beneath the polystyrene particle as it moved upwards through the ice in experiment P17b. (a) observational line diagram, (b) photograph and (c) interpretation of the features.....	141
Figure 4.52. Cross-sectional images highlighting the downwards movement of the particle after reaching the ice surface in experiment P17b. (a) observational line diagram, (b) photograph and (c) interpretation of the features.....	143
Figure 4.53. Cross-sectional images showing the development of an asymmetric melt pond in experiment P17b. (a) observational line diagram, (b) photograph and (c) interpretation of the features.....	145
Figure 4.54. The thermal environment of particles in experiments investigating the role of particle diameter in influencing particle-ice interaction. Experiment position has been derived from interpretation of observations, as described in Chapter 3, Section 3.7.....	148
Figure 4.55. Schematic cross-sectional view of the hypothesised particle-ice interaction in experiment P23b.....	150
Figure 4.56. Vertical distance moved by a 6 mm brass particle and 8 mm chrome steel particle in experiment P23b.....	151

Figure 4.57. Cross-sectional images of the drained melt pathways at the end of experiment P23b. (a) observational line diagram, (b) photograph and (c) interpretation of the features. ...	153
Figure 4.58. Schematic cross-sectional view of the hypothesised particle-ice interaction in experiment P25b.	155
Figure 4.59. Vertical distance moved and velocity of a 12 mm brass particle in experiment P25b.	155
Figure 4.60. Photographs of the basal meltwater ponds in experiments (a) P26b, (b) P31, and (c) P35.	158
Figure 4.61. Schematic cross-sectional view of the hypothesised particle-ice interaction in experiment P28.	159
Figure 4.62. Vertical distance moved and velocity of a 3 mm brass particle in experiment P28.	159
Figure 4.63. Cross-sectional images of the inclined melt pathway in experiment P28. (a) observational line diagram, (b) photograph and (c) interpretation of the features.	160
Figure 4.64. Cross-sectional images showing refreezing processes in experiment P45 following a negative shift across the thermal range. (a) observational line diagram, (b) photograph and (c) interpretation of the features.	162
Figure 4.65. Schematic cross-sectional view of the hypothesised particle-ice interaction in experiment P29.	163
Figure 4.66. Cross-sectional photograph of the basal meltwater experienced in experiment P46.	165
Figure 4.67. Plan-view photograph of the particle configuration on the ice surface in experiment P37.	166
Figure 4.68. Schematic cross-sectional view of the hypothesised particle-ice interaction in experiment P37.	166
Figure 4.69. Vertical distance moved by a 3 mm, 6 mm, and 12 mm brass particle in experiment P37.	167
Figure 4.70. Cross-sectional images of the melt pathways within the ice in experiment P37. (a) observational line diagram, (b) photograph and (c) interpretation of the features. Note that (b) was taken at an oblique angle from the opposite view of (a) and (c).	168
Figure 4.71. Cross-sectional images of the basal meltwater ponds in experiment P37. (a) observational line diagram, (b) photograph and (c) interpretation of the features. Note that (b) was taken at a 90° angle to (a) and (c) due to bubbles in the ice obscuring the view slightly. .	169
Figure 4.72. Cross-sectional images of the movement by the 3 mm, 6 mm, and 12 mm particles within the ice (left) and the 3 mm, 6 mm, and 12 mm on the ice base (right) in experiment P41. (a) observational line diagram, (b) photograph and (c) interpretation of the features.	171
Figure 4.73. Photograph of the surface configuration of the particle array in experiment P36.	173
Figure 4.74. Schematic cross-sectional view of the hypothesised particle-ice interaction in experiment P36.	173

Figure 4.75. Vertical distance moved and velocity of the 3x3 mm brass particle array in experiment P36. Data plotted up to hour 20, although the experiment was running for 120 hours. There was no discernible change between hour 20-120.	174
Figure 4.76. Plan-view photograph of initial movement of particles in experiment P43.	176
Figure 4.77. Vertical distance moved and velocity of the 16x3 mm brass particle array in experiment P43. Particle velocity was calculated from data from group 1. Although multiple particles were involved, the vertical distance moved was measured from the base of the same particle throughout the experiment to ensure consistency. The particles acted as a single group for most of the experiment and so it was assumed that the overall pattern of particle movement was applicable to all particles.....	177
Figure 4.78. Cross-sectional images of the clustering of the particles and refrozen melt pathway at the ice surface in experiment P43. (a) observational line diagram, (b) photograph and (c) interpretation of the features.	178
Figure 4.79. Cross-sectional images of the separation of the two groups of particle clusters in experiment P43. Photograph taken at a 90° angle to the time-lapse camera. (a) observational line diagram, (b) photograph and (c) interpretation of the features.	179
Figure 5.1. Associated thermal environment of particles in experiments investigating the behaviour of volcanic particle-ice interaction. Experiment position has been derived from interpretation of observations, as described in Chapter 3, Section 3.7.	184
Figure 5.2. Plan-view photograph of the 6 mm V1 cemented ash cluster.	186
Figure 5.3. Schematic cross-sectional view of the hypothesised particle-ice interaction in experiment V1.	186
Figure 5.4. Vertical distance moved and velocity of a 6 mm Eyjafjallajökull cemented ash cluster in experiment V1.....	187
Figure 5.5. Cross-sectional images indicating the morphology of the V1 melt pathway. (a) observational line diagram, (b) photograph and (c) interpretation of the features.....	188
Figure 5.6. Cross-sectional images showing the basal meltwater pond and melt pathway in experiment V1. (a) observational line diagram, (b) photograph and (c) interpretation of the features.	190
Figure 5.7. Cross-sectional images indicating the development of a melt pathway with an irregular morphology and a basal and surface meltwater pond in experiment V4. (a) observational line diagram, (b) photograph and (c) interpretation of the features.....	191
Figure 5.8. Cross-sectional images showing the initial disintegration of the V7 cluster. (a) observational line diagram, (b) photograph and (c) interpretation of the features.....	192
Figure 5.9. Cross-sectional images showing the progression of downwards movement by the disintegrated cemented ash clusters over two time frames in experiment V7. (a) observational line diagram, (b) photograph and (c) interpretation of the features.	193
Figure 5.10. Plan-view photograph of the 12 mm V2 cemented ash cluster.	194
Figure 5.11. Schematic cross-sectional view of hypothesised cemented ash-ice interaction in experiment V2.	195

Figure 5.12. Vertical distance moved and velocity of a 12 mm Eyjafjallajökull cemented ash cluster in experiment V2.....	195
Figure 5.13. Cross-sectional images of a basal and surface meltwater pond in experiment V2. (a) observational line diagram, (b) photograph and (c) interpretation of the features.	197
Figure 5.14. Plan-view photograph of refreezing in experiment V6a.	199
Figure 5.15. Plan-view photograph of the 3 mm V3 cemented ash cluster.	200
Figure 5.16. Schematic cross-sectional view of the hypothesised cemented ash-ice interaction in experiment V3.	200
Figure 5.17. Vertical distance moved and velocity of a 3 mm Eyjafjallajökull cemented ash cluster in experiment V3.....	201
Figure 5.18. Plan-view photograph of the 6 mm V9 scoria particle.	203
Figure 5.19. Schematic cross-sectional view of the hypothesised particle-ice interaction in experiment V9.	203
Figure 5.20. Vertical distance moved and velocity of a 6 mm scoria particle in experiment V9.	204
Figure 5.21. Cross-sectional photographs of refreezing melt pathway, surface meltwater pond, and the V9 particle submerged within a basal meltwater pond over a five hour period in experiment V9, where (a) is showing an open melt pathway, and (b) is showing a closed melt pathway.	205
Figure 5.22. Plan-view photograph of the 12 mm V11 scoria particle, also indicating fine-grained material that was lost from the particle surface.....	207
Figure 5.23. Schematic cross-sectional view of the hypothesised particle-ice interaction in experiment V11.	208
Figure 5.24. Vertical distance moved and velocity of a 12 mm scoria particle in experiment V11.	209
Figure 5.25. Cross-sectional images of a roughly spherical melt pathway observed in experiment V12. (a) observational line diagram, (b) photograph and (c) interpretation of the features.	212
Figure 5.26. Cross-sectional images showing the development of a drained melt pathway in experiment V12. (a) observational line diagram, (b) photograph and (c) interpretation of the features.	213
Figure 5.27. Photograph of multiple absorbing particles within the ice in experiment V24.....	214
Figure 5.28. Images of the multiple particles and melt pathways observed in experiment V24. (a) observational line diagram, (b) photograph and (c) interpretation of the features.	215
Figure 5.29. Plan-view photograph of the 3 mm V15 scoria particle.	216
Figure 5.30. Schematic cross-sectional view of the hypothesised particle-ice interaction in experiment V15.	216
Figure 5.31. Vertical distance moved and velocity of a 3 mm scoria particle in experiment V15.	217

Figure 5.32. Cross-sectional photograph of the basal and surface meltwater, joined by a refreezing melt pathway, in experiment V19.	220
Figure 5.33. Plan-view photograph of the 1.5 mm V18 scoria particle.	220
Figure 5.34. Schematic cross-sectional view of the hypothesised particle-ice interaction in experiment V18.	221
Figure 5.35. Cross-sectional images showing the fluctuation in the particle position in experiment V18. (a) observational line diagram, (b) photograph and (c) interpretation of the features.	222
Figure 5.36. Photograph of the early development of the surface meltwater pond in experiment V18.	223
Figure 5.37. Plan-view images of the early development of a surface meltwater pond in experiment V20 and the impact of lateral motion on meltwater morphology. (a) observational line diagram, (b) photograph and (c) interpretation of the features.	225
Figure 5.38. Cross-sectional diagram showing the suggested theory behind the process of periodic particle lowering.	226
Figure 5.39. Cross-sectional images of drained melt pathway formed in experiment V21. (a) observational line diagram, (b) photograph and (c) interpretation of the features.	227
Figure 5.40. Plan-view photograph of the 6 mm V25 pumice particle.	228
Figure 5.41. Schematic cross-sectional view of the hypothesised particle-ice interaction in experiment V25.	229
Figure 5.42. Cross-sectional images of the proximal surface meltwater pond and the melt pathway associated with a downwards moving smaller fragment of pumice in experiment V25. Convection systems are simplified. (a) observational line diagram, (b) photograph and (c) interpretation of the features.	230
Figure 5.43. Cross-sectional images of the proximal meltwater pond and a small fragment of pumice moving downwards through the ice in experiment V30. Convection systems are simplified. (a) observational line diagram, (b) photograph and (c) interpretation of the features.	232
Figure 5.44. Plan-view photograph of the 12 mm V27 pumice particle.	233
Figure 5.45. Schematic cross-sectional view of the hypothesised particle-ice interaction in experiment V27.	233
Figure 5.46. Cross-sectional photograph of pumice particle within a proximal surface meltwater pond and a downwards moving pumice fragment in experiment V27.	234
Figure 5.47. Plan-view photograph of the 3 mm V26 pumice particle.	237
Figure 5.48. Schematic cross-sectional view of the hypothesised particle-ice interaction in experiment V26.	237
Figure 5.49. Cross-sectional images indicating the proximal and shallow surface meltwater ponds in experiment V26. (a) observational line diagram, (b) photograph and (c) interpretation of the features.	238
Figure 5.50. Plan-view photograph of the 1.5 mm V28 pumice particle.	240

Figure 5.51. Schematic cross-sectional view of the hypothesised particle-ice interaction in experiment V28.	240
Figure 5.52. Plan-view photograph of proximal surface meltwater pond in experiment V32... ..	243
Figure 5.53. Plan-view photographs of the scoria particles used in experiment V33, where (a) is within a beaker and (b) is scattered on the ice surface.....	244
Figure 5.54. Schematic cross-sectional view of the hypothesised particle-ice interaction in experiment V33.	244
Figure 5.55. Cross-sectional images of the key features and behavioural modes associated with experiment V33. (a) observational line diagram, (b) photograph and (c) interpretation of the features. Note the presence of a basal meltwater pond, as demonstrated in Figures 5.58 and 5.61.....	245
Figure 5.56. Cross-sectional photograph indicating the seven particle configurations described in Table 5.2. Note that a high number of melt pathways has distorted the images in front of particles (c) and (d).	246
Figure 5.57. Cross-sectional photograph of the melt pathway system that developed within the ice.....	247
Figure 5.58. Cross-sectional images showing the multiple proximal surface meltwater ponds in experiment V33. (a) observational line diagram, (b) photograph and (c) interpretation of the features.	248
Figure 5.59. Plan-view photographs indicating the development of surface meltwater ponds over four time frames (a-d) in experiment V33.	249
Figure 5.60. Plan-view photograph of central area of melt that extended throughout the depth of the ice block in experiment V33.	250
Figure 5.61. Cross-sectional images of basal meltwater pond. (a) observational line diagram, (b) photograph and (c) interpretation of the features. Note that the photograph was taken at an angle, so 3D distortion of the image has occurred (a) and (c).....	251
Figure 5.62. Plan-view photographs of the scoria particles used in experiment V34, where (a) is within a beaker and (b) is scattered on the ice surface.....	252
Figure 5.63. Schematic cross-sectional view of the hypothesised particle-ice interaction in experiment V34.	253
Figure 5.64. Plan-view photograph of individual proximal surface meltwater ponds associated with floating particles and the scarred surface in experiment V34.....	255
Figure 5.65. Plan-view photographs showing the development of surface meltwater over nine time frames (a-i) in experiment V34.	256
Figure 6.1. Plan-view photograph of the 1 mm Mp1 polyethylene particle.	261
Figure 6.2. Schematic cross-sectional view of the hypothesised particle-ice interaction in experiment Mp1.....	262
Figure 6.3. Cross-sectional images showing the development of a surface melt pond in experiment Mp1. (a) observational line diagram, (b) photograph and (c) interpretation of the features.	263

Figure 6.4. Cross-sectional photograph of drained surface meltwater pond and the vein network in experiment Mp7.....	265
Figure 6.5. Plan-view photograph of the 1.5 mm Mp8 polyethylene particle.	265
Figure 6.6. Schematic cross-sectional view of the hypothesised particle-ice interaction in experiment Mp8.....	266
Figure 6.7. Images showing surface melting morphology in experiment Mp8, with a plan-view (left) and cross-sectional view (right). (a) observational line diagram, (b) photograph and (c) interpretation of the features.	267
Figure 6.8. Plan-view photograph of the 5 mm Mp2 microplastic particle.	269
Figure 6.9. Schematic cross-sectional view of the hypothesised particle-ice interaction in experiment Mp2.....	269
Figure 6.10. Cross-sectional images of elongated melt ponds in experiment Mp9 (left) and Mp14 (right). (a) observational line diagram, (b) photograph and (c) interpretation of the features.	272
Figure 6.11. Cross-sectional photographs comparing a partially drained meltwater pond and re-filled drained meltwater pond in experiment Mp9, with (a)-(b) denoting a three hour difference.	273
Figure 6.12. Schematic cross-sectional view of the hypothesised particle-ice interaction in experiment Mp4.....	274
Figure 6.13. Plan-view photographs of meltwater progression in experiment Mp4, with (a)-(c) denoting a 41 hour time difference.....	275
Figure 6.14. Cross-sectional images showing the development of a proximal surface meltwater pond over three time frames in experiment Mp5. (a) observational line diagram, (b) photograph and (c) interpretation of the features.	277
Figure 6.15. Cross-sectional photograph indicating melting associated with the advection of heat in experiment Mp5.....	278
Figure 6.16. Plan-view images of irregular melt surface in a full and partially drained meltwater pond in experiment Mp11. (a) observational line diagram, (b) photograph and (c) interpretation of the features.	279
Figure 6.17. Cross-sectional images showing the development of a new meltwater pond at the base of the drained meltwater pond in experiment Mp11. (a) observational line diagram, (b) photograph and (c) interpretation of the features.....	280
Figure 6.18. Cross-sectional photograph of icicles extruding from the Mp11 ice block.....	281
Figure 6.19. Schematic cross-sectional view of the hypothesised particle-ice interaction for experiment Mp6.....	282
Figure 6.20. Cross-sectional photograph of inclined melt pathway in experiment Mp6.....	284
Figure 6.21. Cross-sectional images of the basal and surface meltwater pond in experiment Mp6. (a) observational line diagram, (b) photograph and (c) interpretation of the features.	285
Figure 6.22. Cross-sectional photograph of meltwater surrounding an embedded microplastic particle in experiment Mp13.	287

Figure 6.23. Cross-sectional images of the melt pathway and proximal surface meltwater pond associated with the polypropylene particle in experiment Mp18, where left is indicating drainage immediately after reaching the surface, and right is showing the development of surface meltwater with lateral movement. (a) observational line diagram, (b) photograph and (c) interpretation of the features.	288
Figure 6.24. Cross-sectional photograph of polyethylene particles moving upwards through the ice in experiment Mp18.	289
Figure 6.25. Plan-view photograph of the small microplastic particles in experiment Mp15. ..	290
Figure 6.26. Schematic cross-sectional view of the hypothesised particle-ice interaction for experiment Mp15.....	290
Figure 6.27. Cross-sectional photograph indicating the four microplastic particles described in Table 6.2.	291
Figure 6.28. Cross-sectional images of the varied morphology of multiple melt pathways within the ice in experiment Mp15. (a) observational line diagram, (b) photograph and (c) interpretation of the features.	292
Figure 6.29. Cross-sectional images of the proximal surface meltwater pond in experiment Mp15.	293
Figure 6.30. Cross-sectional photograph indicating the five microplastic particles described in Table 6.3.	295
Figure 6.31. Cross-sectional photograph of melt pathway network within the ice in experiment Mp16.	296
Figure 6.32. Plan-view photograph of the small microplastic particles in experiment Mp17. ..	296
Figure 6.33. Schematic cross-sectional view of the hypothesised particle-ice interaction for experiment Mp17.....	297
Figure 6.34. Cross-sectional photograph indicating the five microplastic particles described in Table 6.4.	298
Figure 6.35. Plan-view photograph of the surface meltwater and scarred surface in experiment Mp19.	300
Figure 7.1. Hierarchy of the themes investigated in the experimental Chapters 4, 5, and 6. The ‘thermal conductivity’ theme was embedded throughout the thesis.	302
Figure 7.2. Flow diagram of some of the main the processes associated with particle-ice interaction for a particle initially placed on an ice surface, identified in experimental work.	304
Figure 7.3. The association between particle properties and a stable (warm) thermal environment, where HTC is ‘high thermal conductivity’ and LTC is ‘low thermal conductivity’. Conduction of heat away from the particle proximity through the ice is not considered in this figure as this does not prevent particle-induced ice melt in the particle proximity.	314
Figure 7.4. The association between particle properties and a stable (cool) thermal environment, where HTC is ‘high thermal conductivity’ and LTC is ‘low thermal conductivity’.	315

Figure 7.5. Summary diagram of sorting mechanisms of particles within ice, where: HD is high density, ID is intermediate density, and LD is low density. Spherical particles are depicted for simplicity.	320
Figure 7.6. Working hypothesis for heat transfer mechanisms of particles of different sizes, showing the difference in heat transfer between (a) surface particles and (b) embedded particles. Meltwater is not included in panel (b) for simplicity.	322
Figure 7.7. The process of re-emerging particles within the ice system, with 1-4 denoting progression through time. Spherical particle used for simplicity.	325
Figure 7.8. Cross-sectional comparison of cryoconite hole morphology described in (a) the literature (e.g. Fountain et al., 2004) and (b) in experimental work in this thesis. Individual particles are considered in (b) for simplicity, but features can be applied to a group of particles.	332
Figure 7.9. Plan view of the simplified evolution of surface meltwater in dirty ice conditions, informed by experimental work in Chapters 5 and 6, with 1-4 denoting progression through time.	334
Figure 7.10. Cross-sectional schematic diagram of the working hypothesis for pumice fragmentation within the ice system, with 1-4 denoting progression through time.	340
Figure 9.1. Comparison of modelled and observed particle velocities of metal particles. (a) low albedo 8 mm chrome steel, (b) high albedo 8 mm chrome steel, (c) low albedo 1.5 mm brass, (d) low albedo 3 mm brass, (e) low albedo 6 mm brass, (f) low albedo 12 mm brass, (g) intermediate albedo 6 mm brass, and (h) high albedo 6 mm brass particles. Data from Table 7.4, Chapter 7.	421
Figure 9.2. Comparison of modelled and observed particle velocities of plastic particles. (a) Delrin®, (b) polypropylene, (c) polyethylene, and (d) polystyrene. Data from Table 7.4, Chapter 7.	422
Figure 9.3. Comparison of modelled and observed particle velocities of volcanic particles. (a) 3 mm cemented ash cluster, (b) 6 mm cemented ash cluster, (c) 12 mm cemented ash cluster, (d) 3 mm scoria, (e) 6 mm scoria, and (f) 12 mm scoria particles. Data from Table 7.4, Chapter 7.	423

Acknowledgements

I'd like to express my deepest thanks to my supervisors, Dr. Jennie Gilbert, Dr. Stephen Lane, and Dr. Amber Leeson. Your wisdom and guidance throughout this process has been invaluable and inspiring to me. I would also like to thank my department, Lancaster Environment Centre, for being so accommodating and supportive when I resumed laboratory work during the Covid-19 pandemic.

The continuous support from my colleagues within Lancaster Environment Centre has been greatly appreciated for both my personal and professional development over the last four years. I will always feel bonded to those who have been alongside me on this journey.

I cannot begin to express my thanks to my parents, Andrew and Diane, brother, Adam, and sister, Emily, for their belief in me, encouragement and advice, and unquestionable willingness to help with data input and proof-reading. A special thanks to my partner, Dylan, who has supported me unconditionally and spent many a phone call listening to updates about this work. I find myself very lucky to have such an amazing and supportive family and partner, alongside our lovely little family dog, Annie, who sat next to me for most of the write-up of this work.

I declare that this thesis presented for the degree of Doctor of Philosophy has been composed entirely by myself and all major sources have acknowledged and cited. The work has not been submitted for any other degree or professional qualification.

1. Introduction

The cryosphere is used as an indicator of climate change due to the sensitivity of ice to climate fluctuations (Vincent et al., 2004; Racoviteanu et al., 2021). Although the cryosphere contains any component of nature that retains a frozen state of water (Vaughan et al., 2013), this study has a glacial focus. Glaciers are defined as flowing ice that has originated from an accumulation and compaction of snowfall (Cuffey and Paterson, 2010). These can be categorised according to size and location (Table 1.1).

Table 1.1. Primary classification of glacier types mentioned in this thesis. ¹(Benn and Evans, 2014) and ²(NSIDC, 2020a).

Type of glacier	Characterisation
Ice sheet	A > 50,000 km ² mass of ice that covers a landscape in which large-scale movement is independent of bed topography. ¹ Greenland and Antarctica are the only two ice sheets that currently exist on Earth.
Ice cap	A < 50,000 km ² mass of ice that covers the topography. ¹
Icefield	A < 50,000 km ² mass of ice (although typically smaller than an ice cap) in which the landscape peaks extrude from under the ice. ² The ice is usually comprised of many interconnecting glaciers that flow out in multiple directions. ¹
Outlet glacier	Channelled ice that moves from the interior of an ice sheet or ice cap. ¹
Mountain glacier	Glaciers that develop in mountainous regions (typically from an icefield). These are usually bound by topography, and flow into valleys. ²

1.1. The impacts of the cryosphere on life and society

Many communities are reliant on glaciers (Marzeion et al., 2014; Carenzo et al., 2016) due to glacial influence on hydrological cycles, sea level rise, ocean circulation, natural hazards, soil erosion, and biodiversity, amongst others (Lau et al., 2010). Therefore, it is critical to monitor glacier wastage to understand the past, predict future patterns, and implement appropriate mitigation for future changes (Dyurgerov and Meier, 2005).

1.1.1. Freshwater supply

Approximately 69% of global freshwater is stored in glaciers and ice sheets (Abram et al., 2019) and, consequently, many populations are reliant on glacial meltwater to supply rivers downstream (Kaser et al., 2010; Thayyen and Gergan, 2010). For example, the Himalayan glaciers provide water to approximately 800 million people in areas that are vulnerable to water

shortages. Therefore, glaciers can be viewed as a 'protection against drought' (Pritchard, 2019).

With a growing global population, and thus a growing demand for freshwater, the reliability of freshwater supply is vital (Schewe et al., 2014). However, with the shrinkage of glaciers it is expected that the volume of glacial runoff will decline following continued ice mass loss (Abram et al., 2019). Not only might this impact freshwater availability, but it may indirectly impact hydropower, crop yields and irrigation, and food security (Immerzeel et al., 2010).

1.1.2. Sea level rise

Contemporary contributors to a rising sea level involve cryosphere ice loss and thermal expansion of oceans. However, recent examination suggests that cryosphere contributions dominate (Oppenheimer et al., 2019). It has been suggested that melting of ice in Greenland and Antarctica has the potential to raise sea level by 6-7 m and 60 m, respectively (Van Den Broeke et al., 2008; Shukla et al., 2017). Other glaciers (outside of Antarctica and Greenland) have the potential to raise sea level by approximately 0.5 m (Oppenheimer et al., 2019).

The rate of ice melt and meltwater input to the oceans has accelerated in response to increases in global surface temperatures (Dyurgerov and Meier, 2005; Shukla et al., 2017; Allen et al., 2018; Golledge et al., 2019). This trend has been predicted to continue increasing (Church et al., 2013; Oppenheimer et al., 2019), with additional complexities likely to exacerbate this, e.g. marine ice sheet instability, and polar amplification processes (Beer et al., 2020).

Coastal areas are typically densely populated regions, and it is expected that the number of people living in low elevation regions (i.e. <10 m above sea level) will increase from 680 million to one billion by 2050 (Neumann et al., 2015; Shukla et al., 2017; IPCC, 2019). Therefore, many populations are exposed to the consequences of sea level rise. These include: an increased occurrence of rare extreme events (e.g. storm surges), permanent submergence of land,

damage to property, loss/change in coastal ecosystems, coastal erosion, changes to soil salinity, etc. (Oppenheimer et al., 2019).

1.1.3. Ocean circulation

Glaciers are an important contributor to freshwater exchange with the ocean, influencing ocean salinity, density stratification and circulation (Lehman and Keigwin, 1992; Dyurgerov and Meier, 2005; Abram et al., 2019). This can impact ocean ecosystems and circulation patterns on a local and global scale (Lehman and Keigwin, 1992). For example, climate variabilities in the Quaternary period have been correlated to changes in ocean circulation, triggered by the increased input of freshwater into oceans (Knutti et al., 2004). Therefore, many of these ocean circulation systems (e.g. Atlantic meridional overturning circulation) are recognised as tipping points in the Earth's climate system (Abram et al., 2019).

1.1.4. Natural hazards

The melting of glaciers and ice sheets can cause hazardous events (e.g. rockslides, floods, avalanches, etc.). These can be divided into two categories: (a) direct hazards occurring from the direct action of ice/snow, such as avalanches and glacial outburst floods; and (b) indirect hazards, i.e. those arising because of a glacial feature, such as rockslides or water resource issues (Richardson and Reynolds, 2000). Many of these glacial hazards (e.g. avalanches and flood events) are predicted to increase with a warming climate (Abram et al., 2019) and slope failure is now commonly observed in deglaciated mountain valleys (Cossart et al., 2008).

1.1.5. Biological systems

The cryosphere can influence biological systems, e.g. by changing ecosystems through forced migration of species, modifying the chemistry of lakes, and loss of habitat. As ecosystems are so interconnected (like many aspects of the Earth's system), one change in a population can trigger multiple adaptive responses within the ecosystem (Abram et al., 2019).

1.2. Ablation of ice

Glaciers cover approximately 10% of the current land surface (IPCC, 2019) and can be categorised as being in a state of negative or positive mass balance. A negative mass balance occurs when ablation (removal of ice) exceeds accumulation (an increase in ice volume) leading to glacier retreat. Conversely, a state of positive mass balance occurs when accumulation exceeds ablation, resulting in glacier growth (Benn and Evans, 2014). Global monitoring suggests that most glaciers (particularly mountain glaciers) are experiencing a negative mass balance across both hemispheres (e.g. Solomina et al., 2008; Vaughan et al., 2013) resulting in a global trend of glacial retreat (IPCC, 2019; Xie et al., 2020). Additionally, glaciers can be classified according to the thermal regime of the ice. This is within three categories: warm, polythermal, and cold thermal regimes, which are based on the internal ice temperature profile (Zhang et al., 2013). Warm (temperate) thermal regimes are when ice temperatures are fluctuating around pressure melting point (PMP), whilst cold (polar) thermal regimes are when internal temperatures are below PMP and so have no liquid water content. Polythermal refers to ice with a complex combination of these temperature states (Irvine-Fynne et al., 2011; Hambrey and Glasser, 2012).

1.2.1. Mechanisms of ablation

The context of this study is ice in an ablation environment. The three mechanisms for ablation are melting, sublimation and physical erosion (Table 1.2). However, this study will focus on ablation through melting and sublimation.

1.2.1.1. Melting, evaporation and runoff

Energy coupled into ice can raise ice temperatures to PMP (i.e. sensible heat) and cause melting (i.e. latent heat of fusion). Evaporation and runoff can then occur, although evaporation requires additional energy (i.e. the latent heat of vaporisation) to induce a phase change from liquid to gas. A combination of melting and runoff is the lowest-energy and dominant means of ice loss on most land-terminating glaciers, particularly in a temperate thermal regime.

1.2.1.2. Sublimation

Sublimation is the removal of ice directly into the gaseous phase (Stigter et al., 2018). Therefore, this 'skips' the melting and evaporation component of the phase change system (Figure 1.1), with the energy requirement for sublimation approximately equalling that required for both melting and evaporation. Sublimation is possible at all temperatures, dominating in cold and dry environments where melting cannot occur (Taberlet and Plihon, 2021).

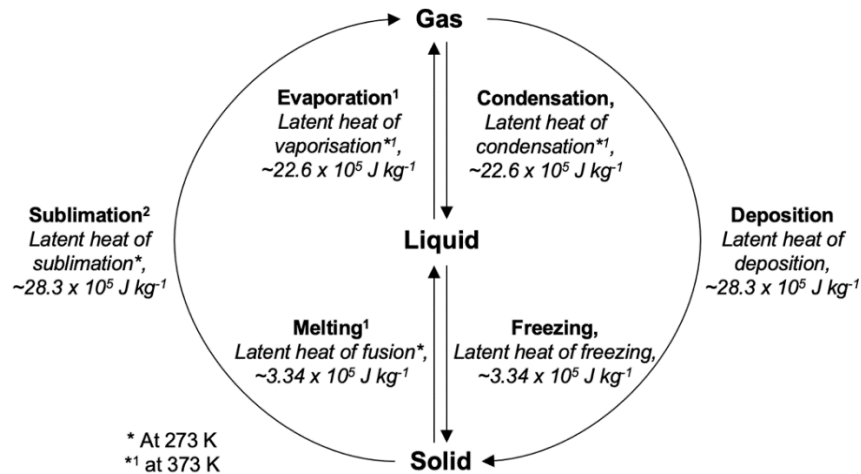


Figure 1.1. Diagram showing energy input for the solid-gas, solid-liquid, liquid-gas, and vice versa, phase changes of water. ¹Whelan and Hodgson (1989), ²Cuffey and Paterson (2010).

Table 1.2. Summary of ice ablation processes, where LT = land-terminating, WT = water terminating, HA = high altitude, PR = polar regions, IS = ice sheet, and MG = mountain glaciers (Parish and Bromwich, 1987; Benn and Evans, 2014; Cuffey and Paterson, 2010; Marshall, 2011).

Ablation mechanism		Process	Temperature dependent	Topography dependent	Optimal conditions	Energy requirements (J kg⁻¹)	Glacier type where this process is common	Associated thermal regime
Melting		Phase change from solid to liquid	Yes	No	Warm temperatures	Latent heat of fusion = 3.34×10^5	LT	Warm glaciers Polythermal glaciers
Sublimation		Phase change from solid to gas	No	No	Warm temperatures, dry air, strong winds	Latent heat of sublimation = 28.3×10^5	HA PR	Cold glaciers Polythermal glaciers
Physical erosion	Wind scour	Removal of snow by wind	No	Yes	Steep slopes	-	-	-
	Calving icebergs	Removal of ice by fracturing and collapse		No	Cold temperatures increasing the rigidity of the ice, allowing ice to fracture		IS WT	All thermal regimes
	Dry calving			MG			Cold glaciers	

1.2.2. Energy balance

Ice ablation is determined by the energy balance at the ice surface (equation 1.1) and occurs when the temperature of ice is at PMP (usually at 0°C):

$$S_{in} + S_{out} + L_{in} + L_{out} + Q_s + Q_L + G - Q = 0. \quad [1.1]$$

Where:

- S_{in} : incoming shortwave radiative flux,
- S_{out} : outgoing/reflected shortwave radiative flux,
- L_{in} : incoming longwave radiative flux,
- L_{out} : outgoing longwave radiative flux,
- Q_s : sensible heat flux,
- Q_L : latent heat flux,
- G : subsurface heat flux,
- Q : energy flux available for melt (Andreassen et al., 2008).

Therefore, the energy flux available for melt (Q) is defined as the sum of each of the components of shortwave and longwave radiation, and the remaining heat fluxes (i.e. $Q = S_{net} + L_{net} + Q_s + Q_L + G$). Shortwave radiation refers to all incoming solar radiation, whilst longwave radiation refers to re-radiated long wavelength energy, typically peaking at 11.3 μm (Prentice et al., 2012).

1.2.3. Albedo of snow and ice

The surface albedo, defined as a dimensionless measurement of surface reflectiveness (NSIDC, 2020b), influences solar radiation absorption. This dictates the extent of energy exchange at an ice surface and so has a crucial influence on the surface mass balance (Box et al., 2012). The albedo differs between substrates (e.g. snow/firn/ice), and with the snow/ice condition (Table 1.3).

Table 1.3. Albedo range for snow and ice (Benn and Evans, 2014; Cuffey and Paterson, 2010).

Surface type	Albedo range
Dry snow	0.80-0.97
Melting snow	0.66-0.88
Clean firn	0.43-0.69
Blue ice	0.60-0.65
Clean ice	0.34-0.51
Dirty ice	0.15-0.33
Debris-covered ice	0.10-0.15

Clean ice is transparent at the spectrum peak of solar radiation (i.e. visible light region) due to very weak absorption (see Chapter 3, Section 3.1.4 for an in-depth consideration of ice-solar radiation interaction). However, the presence of bubbles in ice can increase the albedo due to scattering of light. Additionally, impurities on/within ice provide a surface for radiation absorption, modifying the surface albedo (Hadley and Kirchstetter, 2012). The heat absorbed by particles can be transferred to the ice, leading to increased ice melt due to the presence of energy that would otherwise not be available (Reznichenko et al., 2010); this concept is the basis for this study.

Ice has a complex internal structure formed by veins at the triple junctions between ice grains. These can contain liquid water (Rempel, 2005), and are of particular importance when ice is close to melting as vein diameters widen with increasing temperature (Langham, 1974). Therefore, these can modify the thermodynamic behaviour of the ice and have been noted to act as conduits for material transport when the ice is near PMP (Nye, 1989).

Snow has a high number of internal interfaces and is one of the most reflective natural surfaces on Earth (Hadley and Kirchstetter, 2012). This results in a weak absorption of solar radiation because radiation is reflected away, apparent most at visible and near-ultraviolet wavelengths (Doherty et al., 2010). In the same way as ice, impurities on/within the snow can modify the surface albedo; this is particularly apparent in the regions of the spectrum where absorption is low, e.g. the visible region. Most glaciers have a combination of snow and ice surfaces (in addition to impurities and debris cover), and so experience a high spatial albedo variation. This can result in a high spatial variation in ice ablation.

1.3. Debris-covered and dirty ice

The presence of foreign particles (light absorbing particles, LAPs) can adjust the thermodynamic behaviour and optical properties of ice and snow, and is of particular importance when considering how glaciers respond to climate change (Nicholson and Benn, 2013; Carenzo et al., 2016; Dragosics et al., 2016). Glaciers with extensive cover of debris are termed 'debris-covered ice', whereas glaciers that are partially covered in debris are termed 'dirty ice' (Fyffe et al., 2020). Currently, 44% of glaciers >2 km² are debris-covered (Herreid and Pellicciotti, 2020), and the relative influence of debris-covered and dirty ice is predicted to increase with a global trend of retreating glaciers, in addition to an increase in mechanisms for particle presence on/within ice (Scherler et al., 2018; Herreid and Pellicciotti, 2020). This is due to increased atmospheric particle loading, which is directly correlated with particle deposition onto ice surfaces (Barrie, 1985), re-exposure of buried particles during ice melt, and instability of rock on valley sides as glaciers retreat (Reid and Brock, 2010; Reid et al., 2012; Zhen and Shiyin, 2012).

Surface particles can strongly influence ablation patterns because particles absorb electromagnetic radiation in the visible region (Benn et al., 2012). However, the amount of energy transferred into the ice is dependent on a variety of factors, including the thickness of the debris layer and the particle properties (Richardson and Brook, 2010).

1.3.1. Properties of light absorbing particles

This section will describe the physical properties of particles on/within ice that can absorb solar radiation (i.e. Light Absorbing Particles, LAPs). The properties and distribution of the particles ultimately determine the behaviour of particle-ice interaction and the influence on ice ablation.

1.3.1.1. Debris thickness

Ice ablation can be either hindered or enhanced depending on debris cover thickness (Juen et al., 2014). The threshold at which this behaviour shifts is known as the 'critical thickness', representing a scenario where the ablation rate

of debris-covered or dirty ice is equal to that of clean ice, i.e. the thickness of debris that has no influence on ice ablation (Kayastha et al., 2000). Ablation is enhanced below the critical thickness and hindered above it. The thickness at which maximum ablation occurs relative to clean ice is termed the 'effective thickness' (Brook and Paine, 2011).

Thick debris layers can insulate the underlying ice because the debris acts as a protective barrier to heat transfer (Juen et al., 2014), consequently reducing conduction of heat from solar radiation absorption to the underlying ice (Reid et al., 2012). Conversely, thin layers of debris, or a scattering of particles (i.e. dirty ice conditions), result in an increased absorption of solar radiation due to strong absorption by the particles in the visible range. This energy is transferred to the underlying ice and increases ablation rates. Therefore, dirty ice has a higher ablation rate than thick layers of debris-covered ice, and clean ice (Fyffe et al., 2020). Single particles on an ice surface can aggregate together to form a particle cluster (e.g. such as those in cryoconite holes, Section 1.3.2.4), further adding complexity to the ice ablation process in the presence of surface material. This study will focus on the behaviour of dirty ice.

1.3.1.2. Particle thermal conductivity

The presence of particles allows conduction of heat energy to the ice surface, although this will vary between particle type (Fyffe et al., 2020). Conduction of heat is predominantly controlled by the particle's thermal conductivity; particles with a low thermal conductivity will be inefficient conductors of heat to the underlying ice and will insulate the ice at a lower thickness than those with higher thermal conductivities (i.e. the critical thickness for thermally insulating particles would be lower than that for thermally conductive particles).

1.3.1.3. Particle albedo

The particle albedo influences particle-ice interaction as this dictates the extent of solar radiation that can be absorbed by the particle. Particles with a low albedo will absorb a greater amount of solar radiation compared to those with a

high albedo, and so can transfer a greater amount of energy to the underlying ice.

1.3.1.4. Particle density

The particle density determines whether a particle will be buoyant in meltwater generated (Hobbs, 2014), and if a particle can be redistributed across an ice surface by aeolian transport (Folco et al., 2002). This latter point is particularly important as wind may redistribute a continuous layer of debris into a dispersed scattering of particles, which may modify the ice response to the surface particles.

1.3.1.5. Particle diameter

A variety of grain sizes and particle morphologies are experienced within debris on an ice surface (Juen et al., 2013; Fyffe et al., 2020). The direct impact of particle diameter on the ability to melt ice is not yet fully understood; however, it is assumed that a larger particle would decrease ice ablation relative to a smaller particle. This is because of the known reduction of ablation with increasing debris thickness, and, in many instances, particle diameter has been used as a proxy for particle thickness (Fyffe et al., 2020). There are additional complexities associated with irregular particle morphology, meaning that a singular particle rarely has a uniform diameter.

1.3.2. Common light absorbing particles

Particles can be transported extensive distances from their source location to then settle on ice surfaces via wet or dry deposition, i.e. the removal of particles from the atmosphere through precipitation, or interaction of particles with the ice surface, respectively (Barrie, 1985). This can lead to a variety of surface particles in glacial environments (Doherty et al., 2013; Tedesco et al., 2016), which can modify the albedo of the ice system. However, the extent and behaviour of solar radiation absorption differs between particles (see supplementary Table 9.1 in Appendix 1). The most common types of LAPs that have relevance to this study are carbonaceous aerosols (e.g. containing

carbon) such as black carbon and brown carbon, dust particles, cryoconite, rock debris, volcanic particles, meteorites, and microplastic particles.

1.3.2.1. Black carbon

Black carbon (BC) particles are some of the most effective LAPs due to strong absorption of solar radiation, particularly at 0.4-0.7 μm in the visible wavelengths (Wang et al., 2014; Shen et al., 2017; Wu et al., 2020). This is responsible for the dark colour of BC particles. Therefore, a very small amount of BC can have a significant impact on ice bodies, e.g. concentrations of 10-100 parts per billion (ppb) can decrease the ice albedo by 1-5%. This has been observed in many instances, e.g. the darkening of Greenland (Tedesco et al., 2016). Additionally, 1 ng g^{-1} of BC has the same impact on albedo as 100 ng g^{-1} of dust (Section 1.3.2.3.) at a wavelength of 0.5 μm (Dumont et al., 2014).

1.3.2.2. Brown carbon

Brown carbon (BrC) has been considered a scattering (i.e. with reflective properties), rather than an absorbing particle, in many climate models (Wu et al., 2016). However, recent studies have demonstrated that the absorbing effect from BrC is greater than previously thought (Kirchstetter et al., 2004; Alexander et al., 2008; Doherty et al., 2010; Chung et al., 2012; Wu et al., 2020). For example, Doherty et al. (2010) found that BrC was responsible for approximately 40% of absorption in visible and UV wavelengths on the surface of Arctic snow. Globally, it has been noted that BrC particles are responsible for 20% of the total absorption by carbonaceous LAPs at visible wavelengths (Wu et al., 2020). Additionally, emerging research suggests that BrC is capable of absorbing in the mid- to long-visible region of the solar spectrum (Saleh, 2020).

1.3.2.3. Dust particles

Dust particles have a range of definitions within the literature (e.g. mineral particles, soil-derived particles, etc.), but are largely defined as particles with sizes of order micrometres. For the purpose of this thesis, the term 'dust' will be applied to only mineral-derived particles of this size (with feldspar and quartz dominating), and so non-mineral dust particles (e.g. black carbon particles) are

excluded from this category (Bowen and Vincent, 2021). Dust particles have varying compositions, reflecting their source conditions. This range of material can absorb across the electromagnetic spectrum (Dentener et al., 1996; Formenti, 2003), although predominantly in the visible region (Bergstrom et al., 2007; Mahowald et al., 2014). Although dust is not considered to have such a strong influence on albedo as other LAPs (e.g. BC), high concentrations of dust have been observed on the Greenland ice sheet, with values up to 500 ng g⁻¹ observed in Northern Greenland (Dumont et al., 2014). The small nature of dust particles facilitates aeolian transportation and deposition of particles, and so contamination on glacier surfaces is global (Mahowald et al., 2013; Du et al., 2017). Dust contamination on a glacier surface is a particular issue in the Himalayan region as Asia is a significant natural and anthropogenic dust source (Svensson et al., 2018).

1.3.2.4. Cryoconite

Glaciers can support life in the subglacial and supraglacial environments (Stibal et al., 2006; Anesio et al., 2017). Life on glaciers is typically in the form of microbial activity, which can be found in many environments, such as within ice vein networks, on the surface, within meltwater lakes, etc. (Anesio et al., 2017). When dust particles on a glacier surface aggregate together to form larger units, microenvironments that contain nutrients are created, allowing microorganisms to grow and reproduce (Zarsky et al., 2013; Schepanski, 2018). These sediment deposits, containing microbial activity that form on the ice surface, are called cryoconite deposits and can absorb solar radiation. This results in sediments melting the ice and, due to their dense nature, they move downwards to create a vertical cylindrical hole that is termed a cryoconite hole (Takeuchi et al., 2018). Therefore, cryoconite holes are features formed through differential melting of ice due to the presence of surface particles (Bagshaw et al., 2007).

1.3.2.5. Rock debris

This is a broad category that describes sedimentary, igneous, or metamorphic rock debris that is on a glacier surface. This differs from dust particles primarily due to larger particle sizes and non-aeolian transport mechanisms of

deposition. Instead, rock debris is typically entrained onto a glacier surface by several mechanisms, e.g. mass influx from valley sides, debris slumping, etc. This is typically associated with erosional processes, and consequently, the development of thick debris cover. Therefore, insulation effects are expected (Hewitt, 2005; Huo et al., 2021).

1.3.2.6. Volcanic material

Volcanic eruptions can impact glaciers in several ways, depending on the location of the ice, volcanic particle distribution, and eruption style and magnitude. The material deposited on a glacier could be from a variety of sources, for example: volcanic airfall, pyroclastic density currents, lahars, lava flows, edifice collapses, etc. The products of the different depositional processes are starkly different, resulting in a range of thermal and optical particle properties and varied deposit thicknesses. Therefore, both ablation and preservation effects may occur following deposition of volcanic material (Barr et al., 2018).

1.3.2.7. Meteorites

Ice sheets are high interest areas for meteorite collection due to processes that can result in the concentration of meteorites. For example, Antarctica is of particular interest to scientists interested in meteorites due to the large surface area and presence of meteorite stranding zones, in which upward flowing ice concentrates meteorites, through englacial transportation, on stable ice surfaces (Graham and Annexstad, 1989; Harvey, 2003; Evatt et al., 2016). Additionally, low weathering rates preserve the meteorites in the cold, dry climate (Folco et al., 2002). It has been discounted that the high numbers of meteorites found in these regions are from a single meteorite fall due to the variation in meteorite composition and type (Nagata, 1978). With relevance to this study, meteorites are capable of absorbing solar radiation and transferring heat into the ice to cause ice melt, in the same way as other LAPs.

1.3.2.8. Microplastics

The properties of microplastic particles (e.g. polymer types, shapes, sizes, colour, etc.) have ranges of values that lead to different potential behaviours within the environment. By definition, microplastic particles are < 5 mm in diameter; therefore, it is not surprising that recent research has demonstrated the capability of aeolian transport to deposit microplastics within the cryosphere in remote areas, e.g. high mountain regions (Allen et al., 2019; Ambrosini et al., 2019; Bergmann et al., 2019; Cabrera et al., 2020), the Arctic (Morgana et al., 2018; Kanhai et al., 2020; Stefánsson et al., 2021) and sediments in Antarctica (Munari et al., 2017). However, the behaviour of microplastic particles once within the cryosphere is not yet fully understood.

1.4. Aim

This research aims to investigate the influence of single particles and a scattering of particles on ice ablation.

1.5. Objectives

This study investigates particle-ice interaction by focussing on achieving the following objectives:

1. To monitor and take time-lapse images of the behaviour of particle-ice interaction in controlled experiment settings, to develop understanding of the role of particle properties (e.g. particle albedo, thermal conductivity, density, and diameter) in influencing particle-induced ice melt,
2. To monitor and take time-lapse images of the behaviour of volcanic material on and within ice in controlled experiment settings,
3. To monitor and take time-lapse images of the behaviour of microplastic particles on and within ice in controlled experiment settings,
4. To use these findings to hypothesise processes involved in dirty ice conditions,

5. To use these findings to hypothesise processes for volcanic and microplastic particles in naturally occurring cryospheric environments on Earth.

2. A review of debris-covered and dirty ice science

This chapter reviews research that has investigated debris-covered or dirty ice, as defined in Chapter 1. Literature was obtained via a key-term driven search strategy (i.e. utilising terms such as “debris-covered ice”, “dirty ice”, “supraglacial debris”, “ice ablation”, etc.), and collating references within key papers. The approaches taken in these studies included fieldwork techniques, laboratory experiments, modelling and remote sensing methods, or a combination of these. For ease of review, Chapter 2 is organised into fieldwork, laboratory, and modelling research approaches, with remote sensing methods omitted as they were outside the scope of this study. Research approaches are then further categorised into the common themes identified in the reviewed studies.

2.1. Fieldwork approaches

The presence of irregular melting, dirt cones and ‘glacier tables’ (i.e. ice pedestals overlain by rock) on ice systems initially raised the question if debris on an ice surface can modify the thermodynamic behaviour of ice (Swithinbank, 1950). These observations prompted fieldwork-based research into debris-covered and dirty ice, and one of the pioneering experimental studies conducted by Östrem (1959) identified multiple responses of ice to surface particles (e.g. enhanced versus reduced melting). This catalysed a series of field-based projects focussed on developing an understanding of the cause of these various responses (Table 9.2, Appendix 2). Results demonstrated high levels of variability, reflecting the degree of variability experienced within the natural system. This was observed between glaciers and between different points on the same glacier.

The purpose of field research has varied greatly; this has ranged from assessing the behaviour of debris characteristics (e.g. thickness, particle type, etc.) and the role on ice ablation (e.g. Östrem, 1959; Juen et al., 2013; Möller et al., 2018), to defining the spectral absorption of aerosols (Meloni et al., 2006) (Bergstrom et al., 2007) and ice (Askebjør et al., 1997) to aid understanding of aerosol and ice absorption of solar radiation. These studies have provided

background information on the behaviour of particle-ice interaction – useful as context-setting for future work and development of subsequent fieldwork and laboratory experiments. Fieldwork research has also gathered information to validate and develop modelling techniques (e.g. Brock et al., 2007; Brandt et al., 2011; Juen et al., 2014), and remote sensing techniques (e.g. Mihalcea et al., 2008), allowing future trends of ice behaviour to be predicted (e.g. Keegan et al., 2014) and observed. Many field experiments have investigated a ‘debris-covered ice’ system, rather than a dirty ice system. A range of particle types have been examined; for example, volcanic material (e.g. Brock et al., 2007), rock debris (e.g. Östrem, 1959), microplastics (e.g. Bergmann et al., 2019), and meteorites (e.g. Folco et al., 2002).

Fieldwork has been utilised to reconstruct long-term trends from measurements of particle concentrations from ice-cores, snow-pits, or glacial varves (e.g. Ram and Gayley, 1991; Takeuchi et al., 2011; Keegan et al., 2014; Du et al., 2017; Meyer et al., 2017; Muschitiello et al., 2017). These measurements can be used as a proxy for reconstruction of atmospheric particle concentrations such as black carbon, dust, etc. (Ming et al., 2008). The long-term climatic response of debris-covered glaciers has also been assessed through fieldwork observations (e.g. Sakai et al., 2002; Vincent et al., 2004; Boggild et al., 2010; Benn et al., 2012).

2.1.1. Debris thickness

A significant number of fieldwork studies investigated the role of debris thickness on ablation rates by measuring changes in ablation on natural and artificial plots of debris. These included a variety of particle characteristics and layer thicknesses and the deduction of effective and critical thicknesses (e.g. Östrem, 1959; Fujii, 1977; Driedger, 1981; Brock et al., 2007; Juen et al., 2013; Hobbs, 2014; Möller et al., 2018). The vertical surface lowering (relative to a fixed point) over a measurement period was typically measured using ablation stakes (Östrem, 1959; Mattson et al., 1993; Brook and Paine, 2011), vertical strings (Nakawo and Young, 1981), ropes (Bazhev, 1975), or a terrestrial laser scanner (Nield et al., 2013). These measurements generated values for critical and effective thicknesses of different debris in varying locations (Figure 2.1).

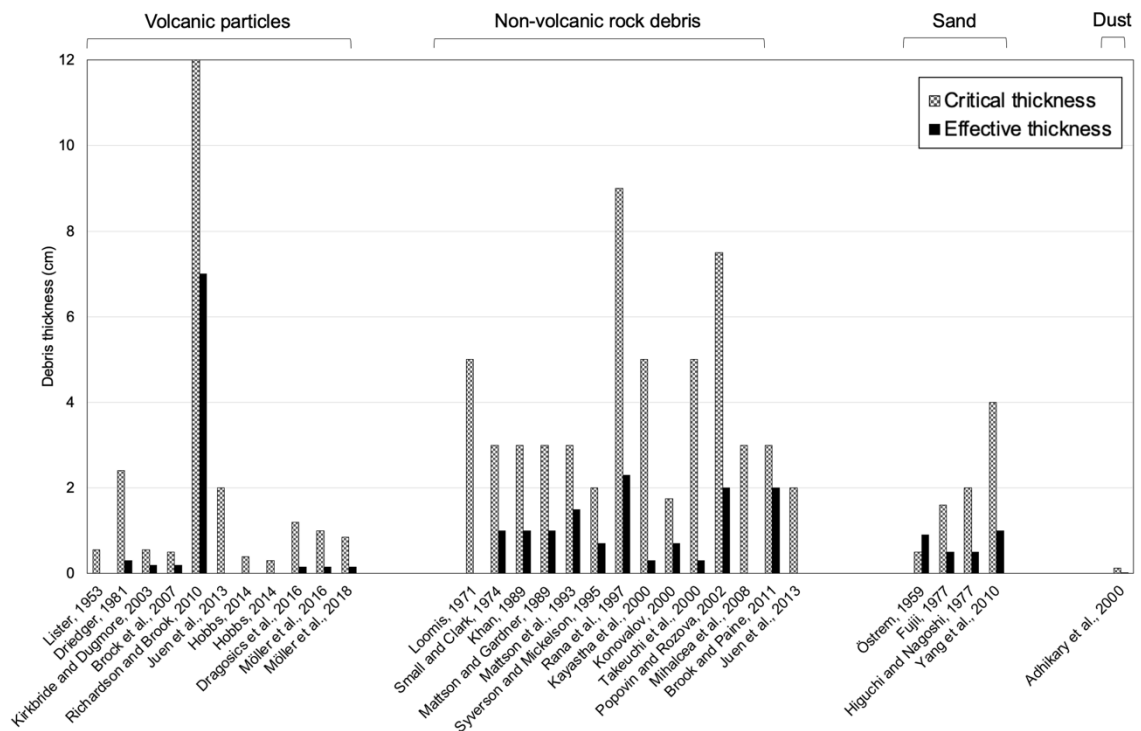


Figure 2.1. Stacked bar graph highlighting the variability of effective and critical thickness (cm) from reviewed field studies, separated into debris type.

Östrem (1959) pioneered the ablation monitoring technique and generated what is known as the ‘Östrem curve’. This method has subsequently been replicated in other studies at a variety of locations (Figure 2.2). All studies exhibited a similar shaped curve, where it was noted that ablation under thin layers of debris was enhanced, whilst ablation under thick layers of debris was hindered. The thickness of debris layers explored in the reviewed studies varied; generally, continuous layers were considered, with few studies studying dirty ice conditions (e.g. Fyffe et al., 2020). The broad category of debris investigated also differed, to include volcanic (e.g. Driedger, 1981; Kirkbride and Dugmore, 2003; Brock et al., 2007; Hobbs, 2014; Möller et al., 2018, etc.), and non-volcanic material. The non-volcanic rock debris was further categorised according to clast size, e.g. dust (Adhikary et al., 2000), sand (Fujii, 1977; Higuchi and Nagoshi, 1977; Nakawo and Young, 1981), and larger rock debris such as scree (Kayastha et al., 2000; Brook and Paine, 2011; Juen et al., 2013). These studies have highlighted that the effective thickness depended on debris properties (e.g. thermal conductivity, albedo, etc) and, therefore, debris type.

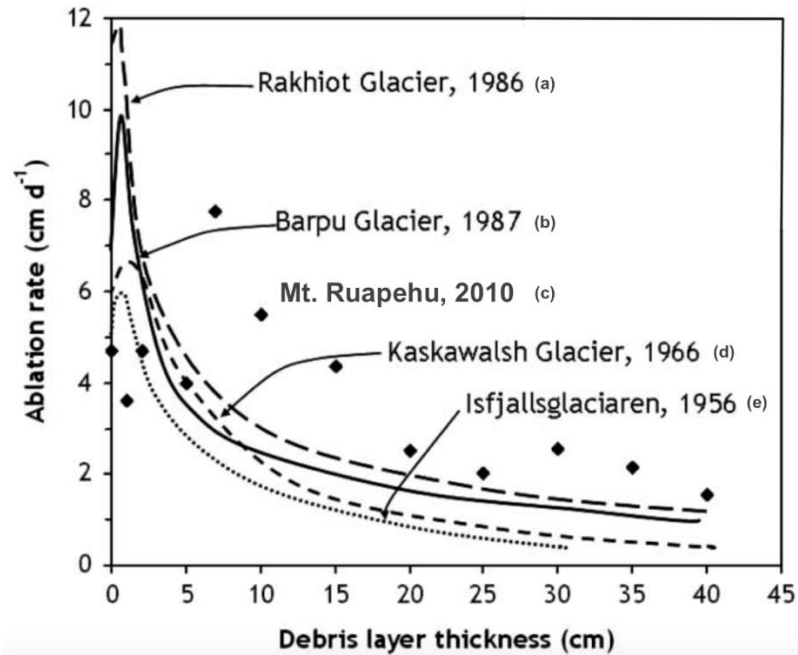


Figure 2.2. The relationship between the mean daily ablation rate (cm day^{-1}) and the thickness of debris cover (cm) at various locations. Smoothed curves from data points taken from (a) Mattson et al. (1993); (b) Khan (1989); (c) data points from Richardson and Brook (2010); (d) Loomis, 1970 and (e) Östrem (1959), reprinted from 'Ablation of debris-covered ice: some effects of the 25 September 2007 Mt Ruapehu eruption', Richardson, J. M., and Brook, M. S., *Journal of the Royal Society of New Zealand*, © copyright [2010], reprinted by permission of Informa UK Limited, trading as Taylor & Taylor & Francis Group, <http://www.tandfonline.com>.

Results from fieldwork experiments suggest that a balance exists between the increased absorption of solar (particularly, shortwave) radiation, facilitated by the presence of particles, and the conduction of heat through the particle layer (Driedger, 1981). Increased absorption of solar radiation would, theoretically, result in enhanced melting; however, if conduction of heat through a particle layer was inefficient, then melting would be reduced as the overlying layer would act as an insulator. These processes are determined by thermal conductivity and albedo of the particle layer, suggesting that these properties dominate control on particle-induced ablation (Kayastha et al., 2000). This balance results in the generation of effective and critical thicknesses. In the instances where ablation begins to decline, the conduction of heat through a debris layer is sufficiently slow to mitigate the initial effect of increased solar radiation absorption. Fieldwork results have demonstrated that the ablation rate decreases exponentially with increasing debris thickness above the critical thickness.

A common issue with many of these studies was that although a general curve of ablation was defined, the areas of maximum ablation, i.e. the effective thickness, typically had to be estimated (Östrem, 1959; Mattson et al., 1993). This was because this occurred under thin layers or, in some instances, when a continuous layer had not yet been established (Brock et al., 2007). This was not the focus of many studies, and meltwater erosion of the ice surface or redistribution of surface particles hindered measurement of thin layers in instances where it was considered (Hobbs, 2014; Fyffe et al., 2020). Although the reviewed literature provides an invaluable insight into the behaviour of debris with varying thicknesses of different debris type, it does not demonstrate the importance of single particle properties and may have inaccuracies associated with error and techniques used in the natural system when considering dirty ice conditions due to the area of maximum ablation being estimated in most cases.

The dynamic nature of glacier systems adds complexities and uncertainty to field measurements, as it is common for debris thicknesses to change during experimental periods (Khan, 1989). In some instances, storm events destroyed the experimental area prior to results being recorded (Hobbs, 2014). Additionally, many field experiments were restricted to short time periods (e.g. <17 days) with irregular monitoring. Möller et al. (2018) introduced an automated measurement system that enabled a continuous insight into the behaviour of tephra-ice interaction over longer timescales (e.g. throughout the entire ablation period). Additionally, a camera was utilised within the experimental set-up to capture the response of ice to a tephra layer, although this stopped working shortly after the measurement period began. However, the benefits of using such a system to enable regular measurements can be recognised despite technical failure in the field.

2.1.1.1. Fieldwork studies investigating the substrate underlying debris

A smaller number of field studies have investigated the role of the substrate underlying the debris in influencing surface particle behaviour. Results suggest that snow surfaces are more susceptible to ablation than an ice surface as full

insulation effects occur at higher debris thicknesses for snow than for ice (Hobbs, 2014). This was observed in a near-direct comparison between Möller et al. (2016) and Möller et al. (2018), where it was noted that tephra of the same thickness on a snow surface was not contributing to full insulation effects expected for ice. It has been proposed that the porous properties of snow/firn facilitated these findings, as meltwater produced on snow/firn penetrated through the porous layer, whilst that produced on ice remained on the surface (Bazhev, 1975; Hobbs, 2014). Therefore, evaporation of surface meltwater removed heat from the ice surface and reduced the amount of energy available for melt (Bazhev, 1975). Variability was observed within each theme of substrate, likely due to the particle properties.

2.1.2. Particle thermal conductivity

There has been limited fieldwork research into systematically assessing the effect of particle thermal conductivity on particle-ice relationships, despite the general agreement that debris-ice interaction is a balance between albedo and thermal conductivity processes. However, it is accepted that particles with a lower thermal conductivity readily insulate the underlying substrate at smaller thicknesses than particles with a high thermal conductivity. For example, Brock et al. (2007) found that volcanic particles provided more effective insulation than sedimentary rock debris for an equivalent thickness due to lower thermal conductivity values. However, this suggested that the thermal conductivity property became negligible when considering a discontinuous (i.e. dirty ice) or thin layers environment because ablation under these conditions was greatly enhanced relative to the debris-covered ice environment despite a low thermal conductivity. However, this effect has not been assessed with non-volcanic particles.

Fieldwork has also been in the form of campaigns searching for buried meteorites in Antarctica and Greenland (Delisle et al., 1993; Folco et al., 2002; Haack et al., 2007). The premise of this fieldwork is that thermally conductive iron-based meteorites can sink into the ice due to high meteorite-induced ice ablation rates and high meteorite densities. Fewer iron-based meteorites have been found in the field than expected; this has been suggested to be due to the

rate of downwards movement of meteorites exceeding that of upwelling ice and ablation of the ice surface, as described in Chapter 1 (Harvey, 2003; Evatt et al., 2016), representing a significant meteorite loss mechanism. Fieldwork has predominantly involved the search and collection of meteorites, although several field experiments have been conducted by Folco et al. (2002). The typical field procedure is through transect sampling once a region of meteorite concentration has been identified, e.g. using satellite imagery (Harvey, 2003), and so field techniques are typically coupled with remote sensing techniques (Folco et al., 2002).

2.1.3. Microplastics in the cryosphere

Fieldwork has facilitated the discovery of microplastic particles in remote regions (Bergmann et al., 2019). However, this is an emerging field of research and current studies have focused on quantifying the amount and types of microplastics found (Ambrosini et al., 2019). The direct effect of microplastic contamination is not yet fully understood. However, the annual waste production of microplastics is estimated to increase to 3.4 billion metric tonnes (from 0.38 billion metric tonnes in 2015) in the next 30 years (Obbard, 2018; Bergmann et al., 2019), and so the issue of microplastics as ice pollutants is expected to increase.

2.1.4. Summary of fieldwork studies

A review of the literature has demonstrated a comprehensive investigation into the effect of debris thickness on ice ablation using field techniques. This sets a general trend of increased ablation under thin, or discontinuous, layers of debris, and reduced ablation under thick, continuous layers. Despite this, the effective and critical thicknesses varied: a synthesis of results suggested that rock debris (e.g. produced from erosion/weathering processes) typically has effective and critical thicknesses at 1-2 cm and 3-4 cm, respectively, whilst dust and volcanic particles experienced this at thicknesses <0.3 cm and <2.5 cm, respectively. Values from Richardson and Brook (2010) have been excluded from the typical values for volcanic particles due to outlier values, although this reflects the large variability observed in results from studies focusing on

volcanic material (e.g. Figure 2.1). The range experienced within volcanic material was likely due to the wide range of particle properties and spatial distribution of particle thicknesses, in addition to external processes, for example, geothermal heat flow, as suggested by Richardson and Brook (2010). Although this variability has been investigated through the portfolio of published papers, most studies were restricted to a single type of volcanic horizon deposited from a specific volcanic eruption. A comprehensive, direct comparison of a variety of volcanic particles under the same meteorological conditions has not been conducted.

The literature is inclined towards research in glaciated regions with a highly evolved debris cover (e.g. usually associated with thick and continuous layers); however, this only represents approximately 12.9% of global debris-covered surface area (Herreid and Pellicciotti, 2020). There is a noted lack of observations of thin or discontinuous layers of particles, and associated uncertainty with our understanding (e.g. some work was destroyed or omitted due to particle distributions changing). Brock et al. (2007) stated that the effective and critical thickness values were observed prior to a continuous layer forming (i.e. in a dirty ice state). However, investigation into the behaviour of dirty ice was limited, evidencing a knowledge gap. Results from field studies have indicated that dirty ice conditions are those where ablation would be highest, and is most crucial when considering the effect of increased glacial mass loss (e.g. Fyffe et al., 2020). This state is also common in the natural system due to differences in clast size and reorganisation by meltwater (Fyffe et al., 2020). Adhikary et al. (2000) additionally recognised that glaciers classified as 'clean' still contained small surface particles (e.g. dust particles) that modified ablation patterns. This concept has become increasingly relevant with the discovery of microplastic particles within the cryosphere (Zhang et al., 2021). Therefore, understanding the behaviour of this common state of ice is crucial in understanding ice responses to climate change.

The thermal properties of a debris layer have been systematically considered in multiple field studies (Juen et al., 2013; Dragosics et al., 2016), although this is to a lesser extent than studies investigating debris thicknesses. It has been

accepted that the albedo and thermal conductivity of the debris are key controls on particle-induced ice melt (e.g. Kayastha et al., 2000), although additional complexities involved in factors that dictate the thermal properties of debris cannot be ignored. It is likely that an individual glacier will not only experience debris layers with differing thicknesses, but also debris with different lithologies and grain sizes. Indeed, Juen et al. (2013) demonstrated that the latter are likely contributors to ice melt (in addition to porosity and moisture content). Ultimately, there are many contributors to the thermal and optical properties of a surface particle. Although these have been discussed in fieldwork studies, there has been little work on systematically assessing the role of each property in influencing particle-induced ice melt.

2.2. Laboratory approaches

Variability in fieldwork results highlight the complexity of the natural world and the uncertainty associated with our understanding of processes involved in debris-covered and dirty ice. Laboratory experiments can enable investigation into the mechanisms involved under controlled conditions. However, there has been limited laboratory-based work in this research area (Reznichenko et al., 2010; Hadley and Kirchstetter, 2012; Hobbs, 2014; Dragosics et al., 2016; Evatt et al., 2016; Hénot et al., 2021; Taberlet and Plihon, 2021). In these studies, volcanic particles (Hobbs, 2014; Dragosics et al., 2016), synthetic particles (Hobbs, 2014), meteorites (Evatt et al., 2016), black carbon (Hadley and Kirchstetter, 2012), and analogous 'glacier tables' (Hénot et al., 2021) and 'zen stones' (Taberlet and Plihon, 2021) have been studied. While these have formed the basis of each study, additional themes were also assessed, for example, the impact of diurnal cycles, rainfall, particle permeability, thermal conductivity, density, etc. (Appendix 3). Primarily, the purpose of this published research was to isolate the physical processes from in-field conditions, to evaluate the mechanisms behind processes investigated.

2.2.1. Debris thickness

Reznichenko et al. (2010) and Dragosics et al. (2016) investigated the influence of surface particle thickness on ice ablation rates within the laboratory.

Dragosics et al. (2016) investigated volcanic particles, whilst Reznichenko et al. (2010) focused on sedimentary rock-avalanche debris and sand. These studies demonstrated the same trend as observed in the field, i.e. enhanced ablation under relatively thin layers and reduced ablation under relatively thick layers.

Reznichenko et al. (2010) and Dragosics et al. (2016) noted that variation in melt rates under different debris thicknesses was only apparent at the experiment start (e.g. initial ice melt was faster under thin layers) and that melt rates were comparable once a steady-state conduction was reached. These findings suggested that, under continuous radiation, thick debris cover (e.g. >5 cm) initially prevents ablation until an equilibrium is reached (approximately 60 hours into the experiment for a 13 cm layer, Reznichenko et al., 2010); after this, the thickness of debris did not appear to influence melting. However, it was noted that the total ablation was different between layer thicknesses due to the differences in melt onset (e.g. a greater surface lowering was associated with a 1 cm debris layer and bare ice relative to thicknesses > 5 cm).

Dragosics et al. (2016) conducted an outdoor study on the building roof to compared to controlled conditions and to allow natural solar input to be investigated. This used the same debris thicknesses as in laboratory experiments (e.g. negligible, 1 mm, 3 mm, and 9-13 mm with a grain size of 0.5 mm) but with the addition of volcanic ash with a grain size of 0.09 mm. These results noted that the overall behaviour of ice responding to volcanic material was the same for outdoor and indoor experiments (supplementary information in Appendix 3).

2.2.2. Diurnal cycles

The effect of diurnal radiation cycles on particle-induced ice melt was investigated by Reznichenko et al. (2010). This involved the placement of varying debris thicknesses on an ice surface and alternating exposure to radiation and a cooling environment (using a freezer) for equal time periods to simulate diurnal cycles. Results suggested that a steady-state conduction system could not be achieved in the thicker layers of debris (e.g. <5 cm); ice melt rates were lower relative to steady-state (i.e. continuous radiation)

conditions over the same duration. Results from these experiments demonstrated that debris-covered ice ablation rates can vary with the nature of diurnal cycling. This key finding was correlated with published values of critical thickness, and it was determined that a relationship existed between latitude and critical thicknesses in the Northern Hemisphere. This showed a decreasing critical thickness value with increasing latitude and elevation, suggested to be due to a decreasing amplitude of diurnal cycles (Reznichenko et al., 2010). Therefore, this suggested that debris-cover would have a greater effect on ablation in regions with strong diurnal cycles. It was noted that, although other complexities (e.g. debris type, meteorological conditions, surface roughness, etc.) may have also influenced the variability observed between field studies, the process of diurnal cycling cannot be ignored. This demonstrates the success of laboratory work in providing an insight into the complexities of processes that occur in particle-ice interaction.

2.2.3. Rainfall and particle permeability

The effect of rainfall was considered by Reznichenko et al. (2010) and was based on the principle that percolating water can alter the ice surface melt rate by modifying the heat flux within the debris layer through advection processes (Reznichenko et al., 2010). This work additionally considered the permeability of the debris layer as a flow route for rainwater and experiments were conducted within a diurnal cycle of radiation. Results demonstrated a higher melt rate with precipitation and permeable debris than in the experiments where precipitation was not considered (agreeing with conclusions from the Juen et al. (2013) and Möller et al. (2018) field experiments). However, debris with a low permeability did not demonstrate the same pattern; instead, the rate of advection of heat was low and so the additional effect of heat transfer by water was not observed. This was, in part, due to the diurnal cycling of radiation where saturating the dry debris took longer than the ablation period (12 hours). Refreezing processes were also observed within the debris during the cooling period (12 hours), contributing an additional 'barrier' to heat advection during the following ablation period (i.e. additional energy was required to melt the refrozen meltwater within the debris layer). The net effect of these processes resulted in no ablation occurring.

2.2.4. Particle properties

2.2.4.1. Particle thermal conductivity

Hobbs (2014) and Hénot et al. (2021) investigated the influence of particle thermal conductivity on ice ablation using single particles. Both studies directly compared particles with thermal conductivity values spanning two magnitudes (e.g. ball bearings and volcanic material in the Hobbs (2014) study, and plastics and volcanic material in the Hénot et al. (2021) study). These experiments suggested that thermal conductivity was the primary control on particle-induced ice ablation in a melting regime as thermally conductive particles were associated with higher melt rates.

Hénot et al. (2021) investigated the role of thermal conductivity in the formation of glacial tables: these are columns of ice underlying particles formed by differential ice melt rates. Single cylinders were used to simulate the formation of glacier tables and it was noted that the thermal conductivity of the cylinder heavily dictated the behaviour of glacial table formation. It was noted that melting of surrounding ice needed to exceed melting from surface particles for a glacial table to form, and this was not likely to occur when considering thermally conductive particles due to high ablation rates of ice underneath the particle (Hénot et al. (2021)).

Unlike the Hadley and Kirchstetter (2012), Hobbs (2014), Dragosics et al (2016) and Hénot et al. (2021) studies, Evatt et al. (2016) investigated embedded particles within ice. This was to represent meteorites in Antarctic ice and to investigate the difference between the amount of stony and iron meteorites found due to a noticeable lack of iron-based meteorites identified in fieldwork, such as Folco et al. (2002). The experiments were based on the premises that: (1) the thermal conductivities of meteorites dictate the behaviour of ice ablation; and (2) iron-based meteorites have a higher thermal conductivity than stony meteorites (Opeil et al., 2010). It was hypothesised by Evatt et al. (2016) that differences in meteorite thermal conductivities would enable iron-based meteorites to sink into the ice, whilst stony meteorites remain on the surface. Experimental work confirmed this hypothesis and demonstrated that the downwards movement of thermally conductive particles was sufficient to offset

upwelling processes that occur in the natural system, e.g. from glacial flow. Although this was a pioneering experiment that confirmed previous hypotheses of meteorite loss mechanisms, experimental work was limited to assessing the behaviour of only two particles (one stony and one iron-based meteorite) in four experiments. These experiments were limited to three-hour periods and insights were restricted to this time frame. It would be useful to systematically consider the thermal conductivity of particles in future experiments to develop these key findings.

2.2.4.2. Particle albedo

Hadley and Kirchstetter (2012) investigated the influence of black carbon and snow grain size on the albedo of snow. Investigation into the effect of snow grain growth was based on the principle that snow grains melt and fuse together with increasing amounts of absorbed solar radiation (e.g. due to the presence of black carbon particles), in turn, causing snow grains to grow much faster than in a 'normal' scenario. This is known to reduce the albedo of snow further as solar radiation can penetrate deeper (Flanner and Zender, 2006; Dang et al., 2015). Hadley and Kirchstetter (2012) isolated the effects of snow grain size and black carbon concentration from those resulting from complex, external factors (such as interactions of solar radiation with underlying surface, vegetation cover, etc.), as it was noted that black carbon influence is typically masked as a result. Results from this series of experiments demonstrated that black carbon reduces snow albedo; this was experienced to a greater extent in the visible wavelength region and within snow with larger snow grain sizes (described in detail in Appendix 3). The relationship between albedo and snow-grain sizes demonstrated the capability of a positive feedback that would be useful to consider in climate models. However, Hadley and Kirchstetter (2012) only considered snow albedo changes and did not assess the resulting melt rates.

Hobbs (2014) considered the role of albedo on ice ablation and utilised single particles to investigate the influence of particle albedo, removing additional processes that may interfere (e.g. particle-particle interaction). The melt rates of black and white ball bearings were compared: the particle with the lower albedo (i.e. black ball bearing) resulted in a higher rate of ablation and the shortest time

to initiate melting. This agreed with the fundamental theories suggested within the literature. However, Hobbs (2014) additionally demonstrated that the role of albedo was less than the role of thermal conductivity in influencing ablation. This was observed by increased ice ablation by a white ball bearing with a high thermal conductivity, relative to a black volcanic particle with a low thermal conductivity, despite a higher albedo. These experiments demonstrated that isolating particles from one-another was a useful technique when aiming to provide a deeper insight into the relative influence of specific particle properties.

2.2.4.3. Particle density

Hobbs (2014) hypothesised that particle density would have an influence on particle-induced ice ablation due to differences in heat transfer between a particle floating in meltwater and one in direct contact with ice. This demonstrated a possible correlation, where the particles with higher densities were associated with a greater volume of meltwater produced. However, it was suggested that this correlation was likely a result of higher thermal conductivity values that are typically associated with higher density particles. Additionally, it was noted that porous lower density particles floated in meltwater and became saturated with time, resulting in a density increase until the particles were no longer buoyant. These results were not from a systematic assessment of density, rather, a secondary result that was observed when investigating the behaviour of porous volcanic material.

2.2.5. Sublimation

Hobbs (2014) and Taberlet and Plihon (2021) investigated the influence of surface particles on sublimation and features that form from differential rates of ice sublimation, e.g. ice pedestals. Unlike Hénot et al. (2021), Hobbs (2014) and Taberlet and Plihon (2021) assessed the formation of ice pedestals from sublimation processes, rather than glacial table formation from melting processes. Hobbs (2014) investigated single and layers of particles, whilst Taberlet and Plihon (2021) assessed single metal plates to mimic zen stone formation (a stone balanced on an underlying ice pedestal).

Results from both studies demonstrated the ability of single particles to prevent sublimation processes underneath a particle to form ice pedestals. Experiments by Hobbs (2014) also indicated that layers of particles can inhibit sublimation, in addition to hindering melt (as demonstrated in Dragosics et al., 2016). It was noted, by both Hobbs (2014) and Taberlet and Plihon (2021), that thermal conductivity did not appear to have an impact on sublimation conditions. Taberlet and Plihon (2021) drew this conclusion due to minimal differences between the behaviour of ice pedestal formation associated with two different materials (copper and aluminium), despite a large increase of thermal conductivity of the copper compared to the aluminium. However, the metal disks used by Taberlet and Plihon (2021) were polished to increase the reflectivity of the material and to prevent absorption of infrared radiation. Therefore, the property of thermal conductivity was not investigated in full because the experiments removed additional complexities of particle-induced melting of the underlying ice, which are observed in the natural system.

2.2.6. Summary of laboratory studies

Laboratory experiments have facilitated insight into the behaviour of specific particle properties (e.g. layer thickness, thermal conductivity, and albedo), whilst removing complexities of the natural system. These have helped develop many hypotheses for processes observed in the natural environment; for example, Reznichenko et al. (2010) demonstrated the importance of permeability and diurnal cycles in particle-induced ice melt and correlated variability observed in the fieldwork with these findings, and Evatt et al. (2016) confirmed the processes associated with iron-meteorite loss. These laboratory experiments highlighted the complexity of processes within debris-covered and dirty ice systems and exposed the need for further work to identify and understand these processes. It is evident that the number of studies using laboratory approaches is limited compared to the number of fieldwork studies. Additionally, these typically tried to mimic solar radiation in a laboratory setting, ultimately leading to additional complexities from background ice melt. As Hadley and Kirchstetter (2012) identified, the effect of particle-ice interaction may be masked by background ice absorption of infrared radiation.

Although Hobbs (2014) conducted a detailed assessment of particle thermal conductivity and albedo, investigation into the influence of particle density on ice ablation was to a much lesser extent. Additionally, the particles investigated initially had a low density (allowing an insight into low density particle behaviour) but, due to the nature of the particle (e.g. high porosity), these became saturated with water and so the density increased with experiment duration. Although this is relevant to many natural particles (e.g. volcanic particles), it did not allow a systematic and comprehensive assessment of density in the same way as thermal conductivity and albedo was considered. As fieldwork studies have identified the presence of microplastics within ice systems, it is crucial to develop these findings by Hobbs (2014) to accurately describe how a non-porous low density particle may behave in ice. This applies to laboratory and fieldwork settings and is an evident gap in the literature.

Although secondary results demonstrate that finer grained particles are susceptible to redistribution processes on an ice surface (e.g. Dragosics et al., 2016), there has been no systematic laboratory investigation into the role of particle diameter on particle-induced ice ablation. Fieldwork by Juen et al. (2014) demonstrated the possibility of grain sizes having a control on ice ablation, and so it would be useful to consider particle diameter in a controlled setting to assess the role in influencing particle behaviour.

Finally, as indicated by both fieldwork and laboratory work, the impact of volcanic particles on ablation of ice varies greatly (Moller et al., 2018). However, there have been only a small number of controlled laboratory studies investigating the ablation constraints of ice in the presence of volcanic particles. This is predominantly restricted to an investigation of the supraglacial environment. There is, therefore, substantial scope for development of this work to further understanding of supraglacial and englacial volcanic material.

2.3. Modelling approaches

Modelling methods have been used to study debris-covered and dirty ice (Appendix 4) and can help predict future patterns of ice in response to a changing climate (e.g. Hall and Fagre, 2003; Benn et al., 2012; Tedesco et al.,

2016). The emphasis of modelling approaches in the literature is on clean or debris-covered ice (e.g. continuous layers of debris), with a focus on developing models to study thick debris layers (e.g. > 65 cm, Reid and Brock, 2010). These typically rely on simplified energy-balance equations (e.g. debris energy-balance models, DEB), or assumptions of melting through degree-day methods (i.e. temperature index) or enhanced temperature-index models. It is common for modelling methods to be used in conjunction with fieldwork studies for validation, or remote sensing applications to gather information, such as the debris surface temperature and the type of surface cover (e.g. Reid and Brock, 2020; Fyffe et al., 2014). This is of particular importance when considering inaccessible regions (Racoviteanu et al., 2021).

Pre-existing energy-balance models (EBM) of debris-covered ice assume decreasing ablation with increasing debris thickness, and rarely consider the maximum ablation (e.g. the effective thickness) observed under thin, or discontinuous, layers (i.e. the peak of the Östrem curve, Nicholson et al., 2021). This remains a difficult segment to accurately model as this is typically associated with a discontinuous layer of particles (Fyffe et al., 2020). For example, Möller et al. (2016) found that models had an increased accuracy with increased debris thickness. Although recent studies have begun to incorporate dirty ice state (Fyffe et al., 2014), comparisons with modelled outputs and field observations are limited and modelling ablation in dirty ice conditions remains in its infancy (Fyffe et al., 2020).

2.3.1.1. Energy balance equations

Many of the modelling approaches used to consider debris-covered and dirty ice are based on energy balance equations described by Nakawo and Young (1982). Although the extent of input parameters varies between approaches, these predominantly rely on information about particle properties.

As typical with DEB models, the ablation (a) for each ice/snow state at each modelled time step can be calculated from different sources of surface energy:

$$a = \frac{\Delta t}{\rho_w L_f} [(1 - \alpha_i) S \downarrow + L + H + LE + P] \quad [2.1]$$

Where Δt : model time step, ρ_w : water density, L_f : latent heat of fusion of water, α_i : albedo of clean/dirty ice or snow, $S \downarrow$: incoming shortwave radiation, L : net longwave radiation, H : sensible heat transfer, LE : latent heat transfer, and P : heat transfer due to precipitation (Reid and Brock, 2010; Fyffe et al., 2014). This is comparable to the equations used in Bozhinsky et al. (1986), Evatt et al. (2015) and Nicholson and Benn (2006):

At the top of the debris surface:

$$Q_D = Q_{SH} + Q_S + Q_L \quad [2.2a]$$

At the debris-ice interface:

$$Q_D = Q_F + Q_V \quad [2.2b]$$

These equations incorporate the following energy fluxes (Evatt et al., 2015):

- Shortwave energy flux (Q_S): incoming shortwave radiation (dependent on the albedo of the debris),
- Longwave energy flux (Q_L): re-emission of radiation from the debris (dependent on the thermal emissivity of the debris),
- Sensible heat flux (Q_{SH}): transfer of heat across the surface from the air into the debris layer (dependent on the temperature gradient within the debris),
- Heat flux due to evaporation at the ice surface (Q_V),
- Latent heat of fusion (Q_F),
- Heat flux within the debris layer (Q_D).

2.3.2. Modelling dirty ice conditions

The need to improve models based on DEB parameters to assess dirty ice was evident by their overestimation of melt when considering thick layers, and

underestimation of melt when considering thin layers, with errors highest when considering thin layers (Mattson et al., 1993). As many EBMs do not consider discontinuous layers, even when estimating ice melt beneath a thin layer (Nicholson and Benn, 2006), the typical modelling approach is not applicable when considering dirty ice ablation (Fyffe et al., 2020).

Fyffe et al. (2014) successfully used a combination of modelling techniques to assess the ablation over a glacier surface whilst taking into consideration differences in surface condition (i.e. debris-covered, dirty, and clean ice). This allowed models to run with higher accuracy in instances where debris cover was very thin (0.01 m) and likely very patchy; a reality that has not been considered in standard DEB models (e.g. Reid and Brock, 2010). This was based on the same fundamental energy balance equations (Section 2.3.1.1) and found that melt rate under debris was sensitive to modifications to the albedo and debris thermal conductivity input parameters. It was noted that the development focus for models that consider glaciers with different surface cover should be on better understanding and replicating ablation across the bare ice to the effective thickness region of the Östrem curve (Fyffe et al., 2014).

However, dirty ice conditions are associated with several complexities that are not considered in models. For example, the formation of 'weathering crusts', i.e. fragmented ice surfaces that form during ablation processes (Cooper et al., 2018), may lead to ice melt overestimation in modelled outputs (Brock et al., 2007), as it was observed that modelled melt closely matched field observations in conditions where high wind speeds removed the weathering crust. These features are commonly associated with dirty ice conditions, and so are a source of modelling error if not considered.

2.3.3. Common assumptions used in modelling of debris-covered and dirty ice

Common assumptions associated with modelling debris-covered or dirty ice systems are noted below:

- a continuous debris layer (this is most applicable to DEB models and, therefore, these models do not consider dirty ice conditions),

- heat conduction is the dominant heat transfer mechanism through the debris,
- a steady temperature profile within each calculation layer within the debris,
- snow/ice surfaces are at 0°C,
- debris properties are temporally and spatially constant throughout the modelled period,
- energy input from precipitation and condensation is neglected,
- meltwater leaves the debris immediately after being generated (without pooling) and has no impact on energy exchange processes (e.g. refreezing),
- conduction of heat within the ice is omitted.

2.3.4. Summary of modelling studies

Studies that model ablation under debris cover typically overlook ablation under thin or discontinuous layers (Nicholson et al., 2021), with only a small number of modelling approaches to investigate dirty ice published (e.g. Fyffe et al., 2014). However, fundamental models used in these studies are based on simplistic assumptions that, although allowing a general pattern to be modelled, greatly reduce the accuracy of model outputs. Additionally, the conditions represented by these assumptions are rarely observed in nature. Conducting a detailed investigation into the evolution of particle properties during particle-ice interaction should help inform input parameters in dirty ice modelling.

2.4. Justification of research plan

A review of the literature demonstrated that the laboratory approach for investigating debris-covered and dirty ice is heavily unexplored. However, this methodology is crucial in understanding the detail of the physical processes associated with dirty ice conditions and particle-ice interaction. Additionally, information gathered from experiments could feed forward into improving modelling of dirty ice.

One of the purposes of the literature review was to identify experimental areas for further investigation in the context of the broader literature. The three primary themes were as follows (as defined in Chapter 1):

1. The role of particle properties in influencing particle-ice interaction,
2. The behaviour of volcanic particles within ice,
3. The behaviour of microplastic particles within ice.

It is evident that fieldwork, modelling, and remote sensing approaches are weighted towards an investigation into evolved debris-covered ice, rather than dirty ice. This has led to the accumulation of uncertainties in models when considering dirty ice, and a lack of precision when determining the effective thickness of debris layers within the natural system. It would be useful to consider the ablation under dirty ice conditions in a controlled setting to further aid our understanding of these complex systems. This may provide understanding of how these areas on Earth will respond to future climate change.

Building on a knowledge gap identified by Juen et al. (2013), this thesis aims to provide an insight into the thermal properties of a variety of debris types. Conducting this in a laboratory environment has the benefit of reducing complexities involved. The success of using laboratory techniques has been demonstrated within this literature review, although there is substantial scope for further development due to the small number of these studies. Using automated techniques (e.g. time-lapse photography) such as in Möller et al. (2018) and Evatt et al. (2016) would enable a thorough insight into particle-ice interaction. Although Möller et al. (2018) benefited from using an automated method, results included complexities with conducting work in the natural system and only assessed the behaviour of volcanic particles. This was also a limitation of Evatt et al. (2016), where only meteorite particles were considered. It would be valuable to combine the benefits of laboratory experiments and automated techniques to build a comprehensive understanding of the behaviour of a variety of particle properties and types, to help inform future research. This is the first theme of this thesis work. Laboratory experiments will predominantly

involve single particles on or within an ice system, although an array of single particles and scattering of particles will also be investigated. This combination of particle configuration will allow an isolated assessment of particle-ice interaction, before building up to a representation of the natural system with a scattering of particles.

As identified by field studies, the thermal and optical properties of volcanic material vary considerably between glaciers, and across individual glaciers. The second theme of this study will investigate the behaviour of single volcanic particles and a scattering of volcanic particles, with the removal of additional complexities such as background ice melt. This will allow direct comparisons between results from this theme and the first theme of the thesis (i.e. particle properties) to help understand the dominant particle properties involved in volcanic particle-ice interaction. This will allow for the application of knowledge obtained from the particle properties theme to natural scenarios.

Finally, it is evident that there is a gap in knowledge as to how microplastic particles interact with ice. Multiple fieldwork campaigns have confirmed the presence of these particles in remote regions, and so it is crucial to gain an understanding of the behaviour of the particles once within the system. Therefore, the final theme of this study will investigate microplastic particle-ice interaction. This may inform the development of field studies and investigation of microplastic particles within the natural system. The combination of these three themes will enable the proposed experiments to provide insight into some features and processes observed in the natural system.

3. Methods

A review of the literature demonstrated a gap in knowledge of dirty ice and microplastic contamination in the cryosphere. In fact, it was noted that ice considered 'clean' is likely dirty in reality (e.g. Adhikary et al., 2000). Therefore, a series of laboratory experiments were conducted to investigate the role of particles on influencing ice ablation in conditions comparable to dirty ice. This addressed the lack of laboratory research techniques identified in the literature. Insights from Chapter 2 informed the basis for the experimental design conducted in this study (e.g. bubble-free ice, time-lapse imagery, infrared-free illumination, etc.). Initial experiments involved single particles in a series of control experiments to isolate particle-ice interaction and to explore fundamental particle properties (e.g. thermal conductivity, albedo, density, and diameter, Chapter 4). These techniques were developed to investigate a variety of surface particle distributions and an assessment of particle types (e.g. volcanic and microplastic particles, Chapters 5 and 6, respectively). Idealised 'optically transparent' (i.e. bubble-free) ice blocks were created, and particles were placed on the ice surface or embedded within the ice. These were illuminated with an 80 watt (W) white Light-Emitting Diode (LED), and time-lapse photography captured the ice response to particle-heating every five minutes. Rates of particle movement were deduced from time-lapse images and calculated by measuring the distance moved relative to a fixed point. In addition, in-person visual observations were made, and standard photography carried out.

The experiments were not an analogue system because real particles were used on the surface of real ice. However, some differences to the natural system (i.e. optically transparent ice, infrared-free illumination, and absence of diurnal cycles) were applied to reduce complexities and to allow fundamental properties to be isolated and examined in detail. Although many variables were broadly controlled (e.g. particle properties, illumination), the accuracy of control required for some variables exceeded what was possible in the laboratory environment (e.g. ice temperatures). However, these serendipitous experiments provided insight into many processes that may have otherwise not been found

in a fully controlled system and allowed a wide range of behaviours to be observed.

3.1. Method development

This section describes the development of the experimental approach: both the characteristics of the ice used (i.e. optically transparent or opaque) and the type of artificial radiation source were investigated through a literature review and series of control experiments (Appendix 5 and 6). The control experiments were carried out in a chest freezer, and the full experimental setup is described and illustrated in Section 3.2.

3.1.1. Creation of optically transparent ice

Optically transparent ice blocks were used in most experiments to allow particle-ice interaction to be investigated in a less complex setting than the natural system. This isolated particle behaviours from external complexities and allowed the role of particle properties in influencing particle-ice interaction to be assessed. Additionally, the use of optically transparent ice enabled cross-sectional time-lapse photography to capture the response of the ice and particles to a radiation source without any obstructions (e.g. bubbles) that would have otherwise reduced image quality (Section 3.2.3).

Liquid water has a unique thermodynamic behaviour in how the density responds to falling temperatures (Tanaka, 1998). It follows the general rule of thermal contraction, whereby the density increases with decreasing temperature, but this reaches its maximum value at a temperature of 4°C (Tanaka et al., 2001; Meng et al., 2015; Okajima et al., 2018). At temperatures below this, density decreases with decreasing temperatures: this concept is known as the ‘maximum density anomaly’. Consequently, water typically forms a frozen top layer in natural systems due to cold water rising, causing top-down freezing (Figure 3.1). However, this natural way of freezing traps air bubbles from the atmosphere within ice. Therefore, natural ice typically contains impurities and bubbles causing the ice to become opaque as light is refracted,

reflected, and scattered at interfaces where refractive index changes (Carte, 1961).

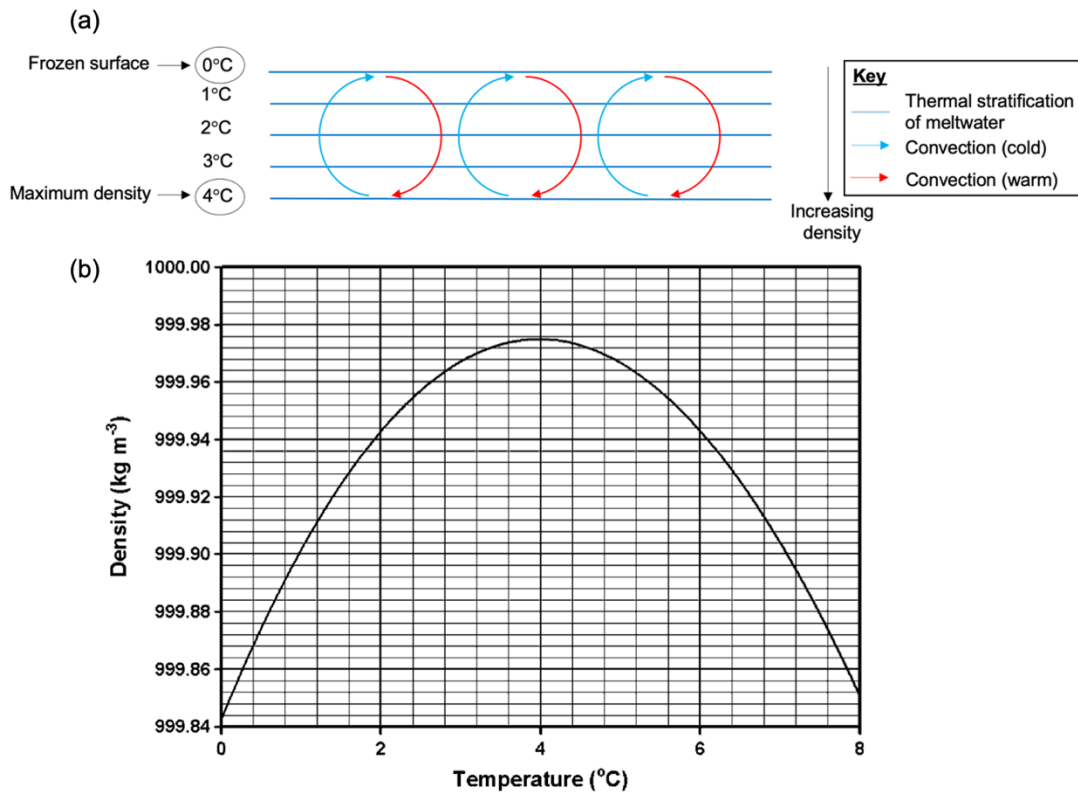


Figure 3.1. Diagrams showing (a) the stable thermal structure within water and (b) the maximum density anomaly reprinted from *International Journal of Heat and Mass Transfer*, vol. 49, Cawley, M. F., McGlynn, D., and Mooney, P. A., ‘Measurement of the temperature of density maximum of water solutions using a convective flow technique’, pg. 1764, Copyright (2006), with permission from Elsevier.

A series of method development experiments were conducted to consider the appropriate technique to create optically transparent ice (experiments M1-M16, Appendix 5). Containers used in initial method development experiments were cylindrical with a diameter and depth of approximately 215 mm and 95 mm, respectively. However, these produced optically distorted cross-sectional images when viewed perpendicular to the cylinder axis and so were replaced with cuboid containers that measured 200x200x100 mm (Figure 3.2). The containers were placed in an upright freezer operating at temperatures between -10°C and -20°C and left for a 7-10-day period (and so was a time-consuming process). Minor modifications throughout the freezing period were made to increase the freezing speed once sufficient ice had formed, such as placing a gap in the roof insulation (Figure 3.2b).

A variety of techniques were utilised in the method development experiments (Table 9.5, Appendix 5). These demonstrated that three approaches were best used in combination: the use of side insulation to engineer a lateral thermal gradient and encourage freezing in a horizontal direction, top insulation to limit top-down cooling, and a magnetic stirrer to, (1) disrupt the thermal stratification and prevent top-down freezing, (2) provide warmth in the region of the stirrer to limit freezing, and (3) prevent gas bubbles settling on the water-ice interface and being incorporated into the vein network within the ice. Deionised water was used in the method development experiments to reduce the number of impurities within the water, although this was later modified to tap water after comparisons confirmed no significant differences between deionised or tap water ice. The experiments indicated that foam insulation was most efficient as top insulation (compared to wool or bubble wrap) as it created ice with minimal air bubbles (aside from in the proximity of the magnetic stirrer). Bubble wrap was sufficient as side insulation and was placed on one side of the container to encourage impurities and trapped gases to concentrate at one end of the ice block. This was placed on the side containing the magnetic stirrer so that this region froze last, allowing the magnetic stirrer to be in use for much of the freezing process.

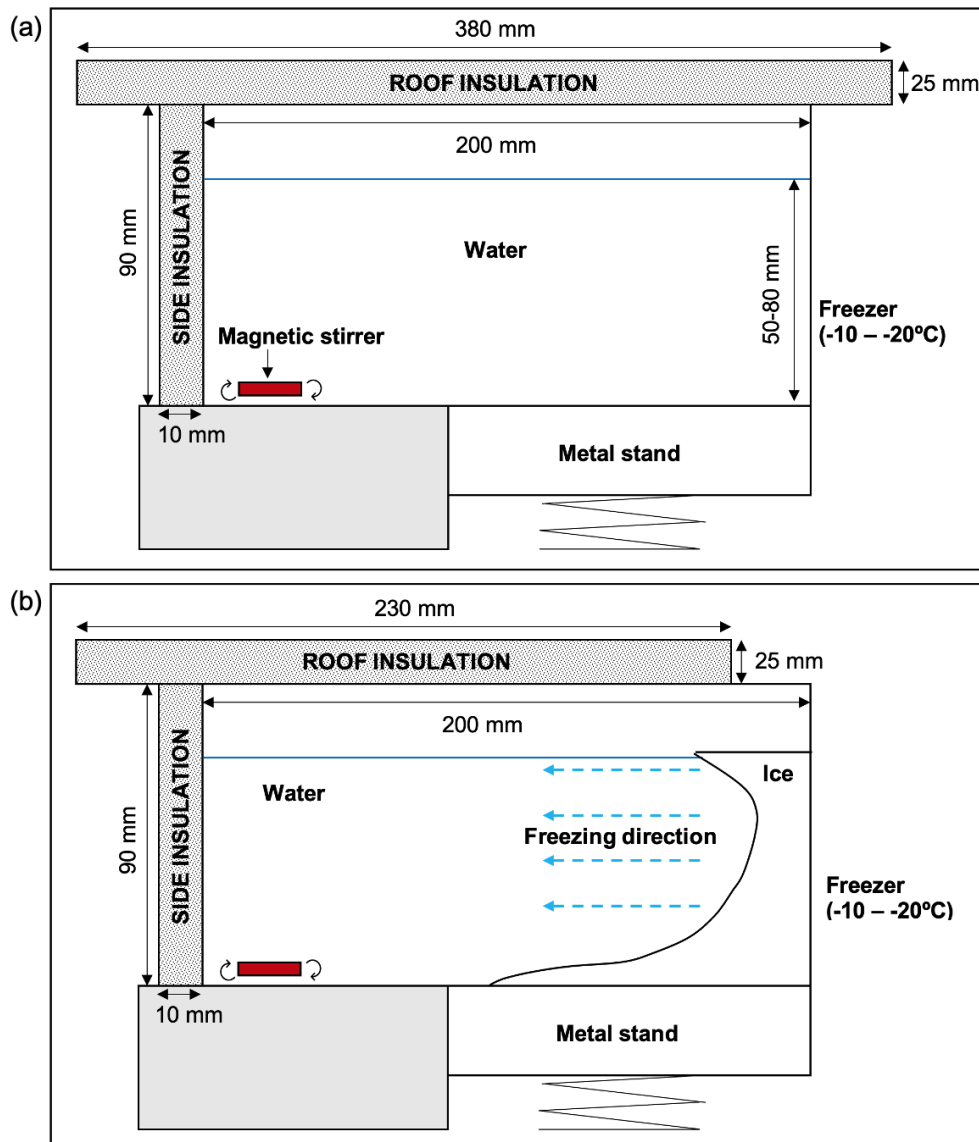


Figure 3.2. Cross-sectional diagram indicating the final experimental set-up for creating optically transparent ice, where (a) indicates initial placement into the freezer and (b) shows modification to the set-up once freezing had begun.

3.1.2. Creation of ice containing embedded particles

Optically transparent ice blocks containing embedded particles were required for five experiments in Chapters 4 and 5 (P17a, P17b, Mp6, M13, and M18). Particles used in these experiments had a lower density than water; therefore, to ensure that these froze within the ice (rather than at the ice surface), the freezing process was split into two stages. Both stages utilised the same techniques of a magnetic stirrer with side and top insulation, within an upright freezer. The first stage involved pouring a depth of approximately 25 mm of tap water into a cuboid container that contained the particles that were to be

embedded. A magnetic stirrer was used as standard procedure to disrupt the thermal stratification, but this was on a low setting (i.e. a stir setting of four-five out of a maximum setting of ten) to disrupt the smaller volume of water. Therefore, the particles were frozen into the top surface of this small volume of water. When this was nearly fully frozen (except for around the magnetic stirrer), additional water was poured into the container to fill to the appropriate level (i.e. 50-80 mm depth); this marked the start of the second stage of freezing. Water was cooled to near freezing point prior to pouring so that it did not melt the ice. The remainder of the freezing process followed the same steps as for creating optically transparent ice.

3.1.3. Creation of opaque ice

Opaque (i.e. bubble-rich) ice blocks were used in three experiments (P48, Mp17, Mp19) as a control. These were created by placing a cuboid container filled with tap water in an upright freezer operating at temperatures between -10 and -20°C with no control of freezing and the water left unstirred. This created an opaque ice block with a fractured surface. Bubbles concentrated in the centre of the ice block, with an optically transparent perimeter (except for vertical trails of air bubbles). These were inferred to be bubbles trapped in the vein network of the ice.

3.1.4. Artificial radiation source

A crucial step in the experimental design process was the selection of a suitable artificial radiation source. This was first assessed through determining the electromagnetic spectrum of solar radiation and understanding how the absorption spectrum of water differs between each state.

3.1.4.1. Solar radiation spectrum

Solar radiation transfers heat to the Earth and is emitted in the form of electromagnetic energy (Cuffey and Paterson, 2010). This is across 0.2-4 μm wavelengths (Figure 3.3) and covers the ultraviolet, visible, and infrared regions (Benn and Evans, 2014; Tawfik et al., 2018). However, approximately half of the

energy is concentrated in the visible band at wavelengths of 0.4-0.7 μm (Cubash et al., 2013).

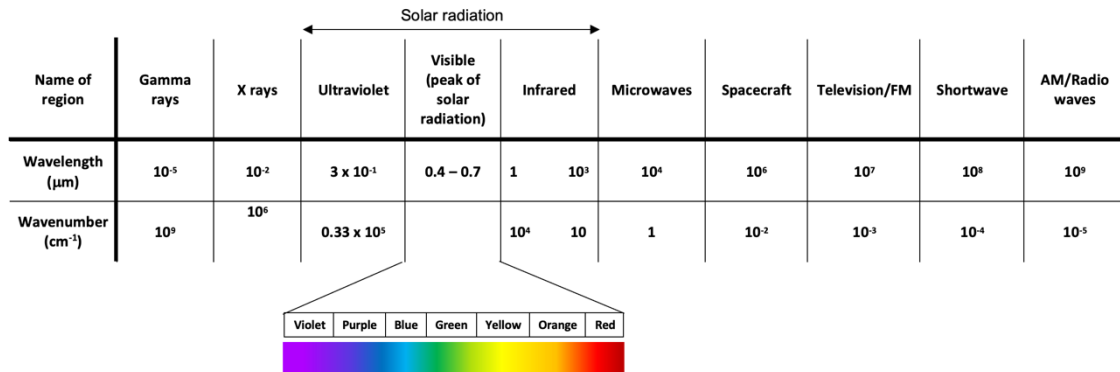


Figure 3.3. The wavelength (μm) and wavenumber (cm^{-1}) of each region in the electromagnetic spectrum (adapted from Liou, 2002).

Solar radiation can be absorbed and reflected/scattered by molecules and clouds in Earth’s atmosphere before it reaches the Earth’s surface (Prentice et al., 2012), resulting in a depletion of radiation (Iqbal, 1983). Scattering processes are independent of wavelength, whilst absorption is selective. Areas in which electromagnetic radiation is absorbed by the atmosphere are termed ‘absorption bands’, whilst areas that are transparent to radiation are known as ‘atmospheric windows’ (Trenberth, 2014). Atmospheric windows and absorption bands for H_2O , CO_2 , O_2 and O_3 are highlighted in Figure 3.4. There is a wide range of water vapour absorption bands (due to the complex molecular structure of water), consequently resulting in a strong contribution to the greenhouse effect.

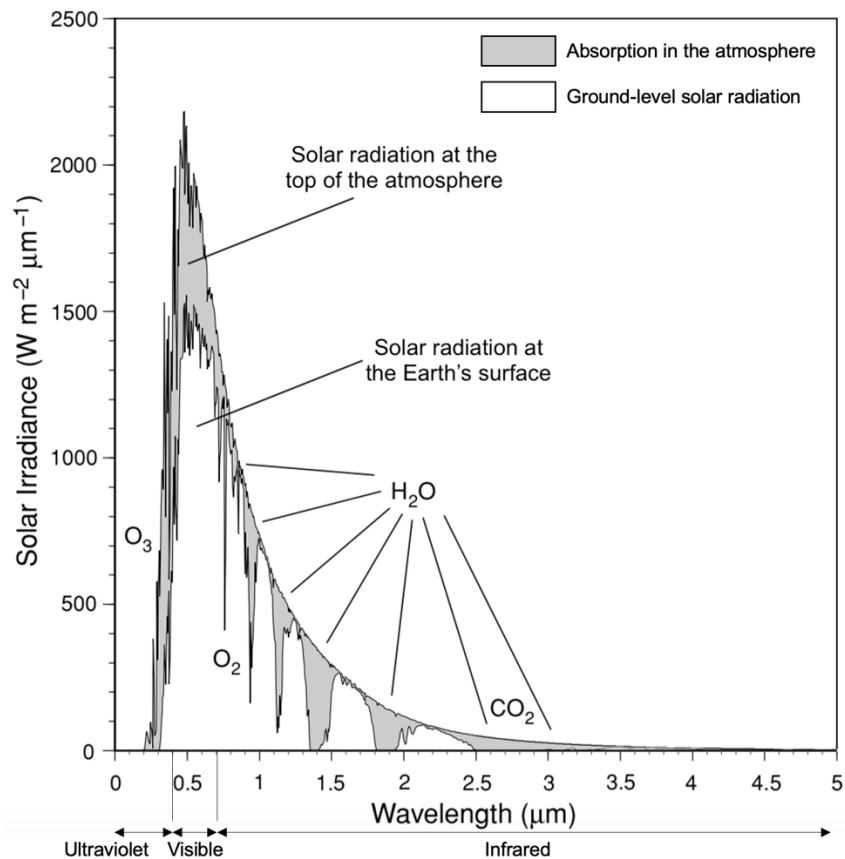


Figure 3.4. Solar irradiance ($\text{W m}^{-2} \mu\text{m}^{-1}$) curve for the top of the atmosphere and Earth's surface with a solar zenith angle of 60° and a spectral resolution of 50 cm^{-1} . This indicates absorption and scattering regions (not including aerosol or cloud interaction). Absorption bands are highlighted in grey, whilst atmospheric windows are white regions under the curve (adapted from Liou, 2002). Reprinted from Introduction to Atmospheric Radiation (2nd Ed), Liou, K. N., Absorption and Scattering of Solar Radiation in the Atmosphere, pg. 86, Copyright (2002), with permission from Elsevier.

3.1.4.2. Water absorption spectra

Unlike many other tri-atomic molecules (e.g. CO_2), water molecules exhibit a bent, triangular structure (Figure 3.5, Liou et al., 2002; Maurellis and Tennyson, 2003; Finney, 2015). This feature adds complexity to the mechanisms by which water molecules absorb and re-emit electromagnetic energy.

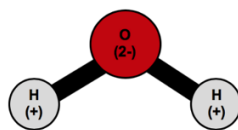


Figure 3.5. Structure of a water molecule. Circles represent hydrogen and oxygen atoms, and black lines represent the covalent bonds between them. +/- symbols indicate electric charge.

A water molecule has three vibrational modes and three rotational modes and can either rotate or vibrate in a 'stretch' or 'bend' movement (Figure 3.6, Liou, 2002). These modes enable energy changes to occur, and the unique structure of the molecule allows for extensive movement. This results in absorption of electromagnetic radiation over a broad range of wavelengths (from ultraviolet to far infrared). Unlike molecules with linear structures, such as carbon dioxide (CO₂), water can additionally stretch in an asymmetric manner, adding further complexity to the absorbance spectrum.

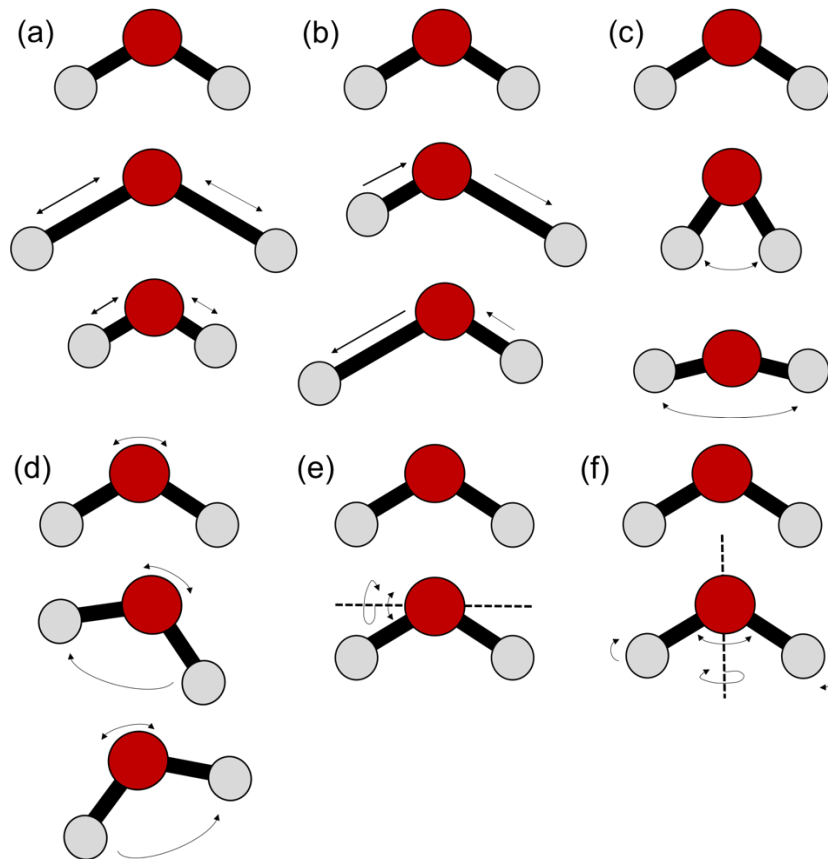


Figure 3.6. Modes of vibrational (a-c) and rotational (d-f) movement of a liquid water molecule. Red and grey circles denote oxygen and hydrogen atoms respectively. Four modes are highlighted: (a) symmetrical stretching; (b) asymmetrical stretching; (c) bending; and (d-f) oscillating. Drawn by author with information taken from Liou (2002) and Maurellis and Tennyson (2003).

Water on Earth exists naturally in three different states: gas (water vapour), solid (ice), and liquid (water). As such, the wavelengths of solar radiation absorbed by water will depend on the state (Figure 3.7).

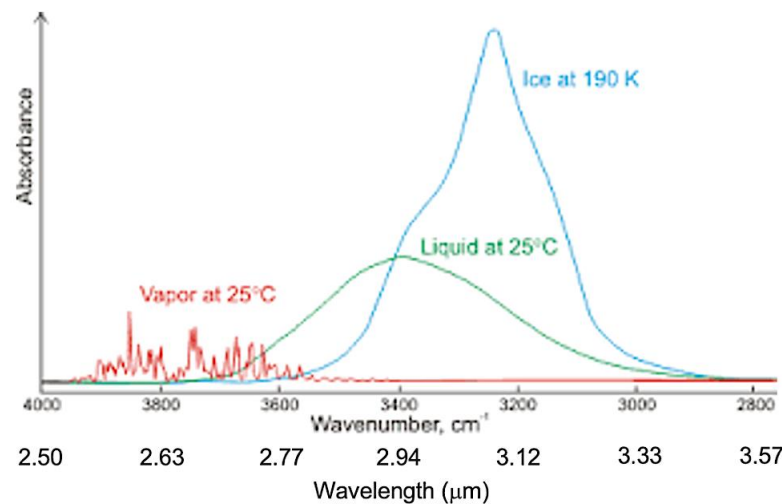


Figure 3.7. The infrared absorption spectrum for gaseous, solid, and liquid water (Chaplin, 2022).

(a) Gaseous water (water vapour)

Water vapour is a greenhouse gas (Schneider et al., 2010) and the largest absorber of solar radiation in the Earth’s atmosphere (Myhre et al., 2013; Tennyson et al., 2014). These molecules absorb approximately 70% of incoming solar energy, with the strongest absorption bands in the infrared region (Maurellis and Tennyson, 2003). The vibrational modes (i.e. Figure 3.5 a-c) are responsible for absorption in the near- and mid-infrared regions, whilst the rotational modes (i.e. Figure 3.5 d-f) are responsible for absorption in the far-infrared and microwave regions (Liou, 2002).

(b) Solid water (ice)

The absorption spectrum of optically transparent ice has been well-documented (Eisenberg and Kauzmann, 1969; Askebjerg et al., 1997; He and Price, 1998; Warren, 1982; Warren et al., 2006; Warren and Brandt, 2008). Although there are small discrepancies between published values in the visible region of the spectrum, the overall trends are as follows:

- Strong absorption in the ultraviolet region (<1.7 μm).

- Weak absorption in the visible region. Minimum values have been estimated between 0.3-0.5 μm , with suggested values of 0.47 μm (Grenfell and Perovich, 1981), 0.39 μm (Warren et al., 2006), 0.39-0.47 μm (Warren, 1982; Warren and Brandt, 2008), 0.41-0.45 μm (He and Price, 1998), and 0.3-0.4 μm (Askebjør et al., 1997).
- Moderate absorption in the near-infrared (1-3 μm). This increases exponentially from the minimum at approximately 0.4 μm to a peak at 3.1 μm (Askebjør et al., 1997). The strong absorption at 3.1 μm is thought to be a result of the O-H stretching mode (Eisenberg and Kauzmann, 1969; Askebjør et al., 1997).
- Strong absorption in the infrared region (3-150 μm). Rotational absorption is responsible for this.
- Weak absorption in the microwave region (>1 cm).

(c) Liquid water (water)

Liquid and solid water have a comparable absorption spectrum (Warren et al., 2006), where absorption is strong in the infrared region (although shifted to slightly lower wavelengths compared to solid), and weak in the visible region (Eisenberg and Kauzmann, 1969). Infrared absorption is particularly prominent at the 2.8, 4.7, 6.1, 14.2 and 51.8 μm wavelengths. The minimum absorption is also in the visible region near the ultraviolet boundary (Warren et al., 2006). The wavelength of this absorption minimum is debated; Warren et al. (2006) suggested a wavelength of 0.39 μm whilst Pope and Fry (1997) have suggested a wavelength of 0.42 μm .

3.1.4.3. Determining the artificial radiation source

Although there are many types of illumination, in practice, no source can perfectly replicate the range of wavelengths of the ground-level solar spectrum. The Sun acts as a blackbody radiator at a temperature of 5777 K (calculated from the Stefan-Boltzmann equation, Iqbal, 1983; Tawfik et al., 2018), and few light sources can reach these higher colour temperatures. Ground level radiation is at its highest intensity ($\sim 1500 \text{ W m}^{-2} \mu\text{m}^{-1}$) in the visible wavelengths

(Figure 3.4 and Figure 3.8), although there is still a noticeable amount of energy in the near-infrared region. Therefore, to replicate natural ground-level solar radiation, there are several requirements: (1) illumination would need to be heated to 5777 K and exhibit a blackbody pattern; (2) filtering of the near-infrared region would be required to mimic the wavelength bands that are absorbed by water vapour and other atmospheric gases; and (3) illumination would have to cover 0.3-2.5 μm wavelengths, extending over three electromagnetic regions. Combining these three requirements is difficult. Therefore, to isolate the behaviour of particle-ice interaction to allow a detailed assessment of the micro-processes involved, it was decided to utilise the visible wavelengths of the solar spectra in experiments. These correlate with the peak of ground-level solar radiation and do not interact with optically transparent ice (Grenfell and Perovich, 1981; Warren et al., 2006).

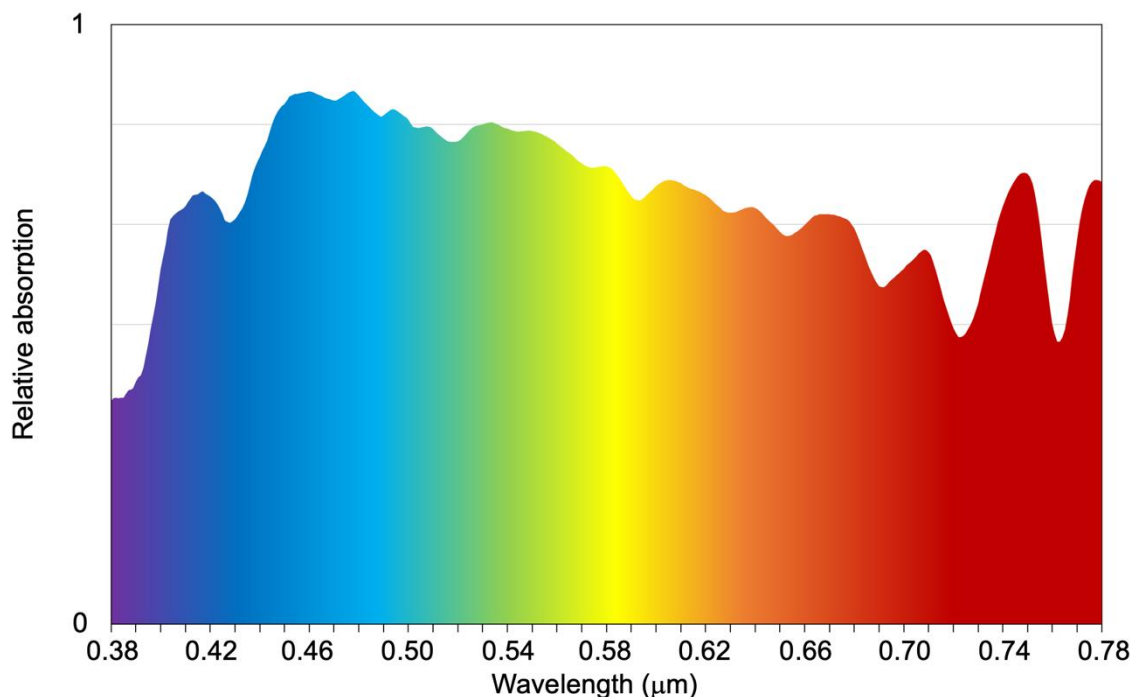


Figure 3.8. Relative absorption of natural sunlight across the visible wavelengths, measured by a PG100N UPRtek handheld spectrometer held directly in the beam of illumination.

In the initial stages of method development, (i.e. experiments M17-M27, Appendix 6), a Philips halogen bulb was investigated. This was used in combination with a water filter to remove infrared radiation (as water vapour does in the atmosphere). Control experiments demonstrated that the entire ice block melted without the use of a water filter due to radiation-ice interaction (Figure 3.9). However, subsequent experiments experienced bulk ice melt even

with use of the water filter as ice-radiation interaction was not entirely removed (likely from the water filter warming with continued infrared radiation absorption and re-radiating energy into melting ice). Additionally, there was limited particle-ice interaction when an 8 mm chrome steel particle was placed on the ice surface (experiment M24). Interpretation of the results suggested that the halogen bulb illumination may not have been interacting sufficiently with the particle (due to a low power density) to initiate particle-induced ice melt. Consequently, alternative radiation sources were investigated.

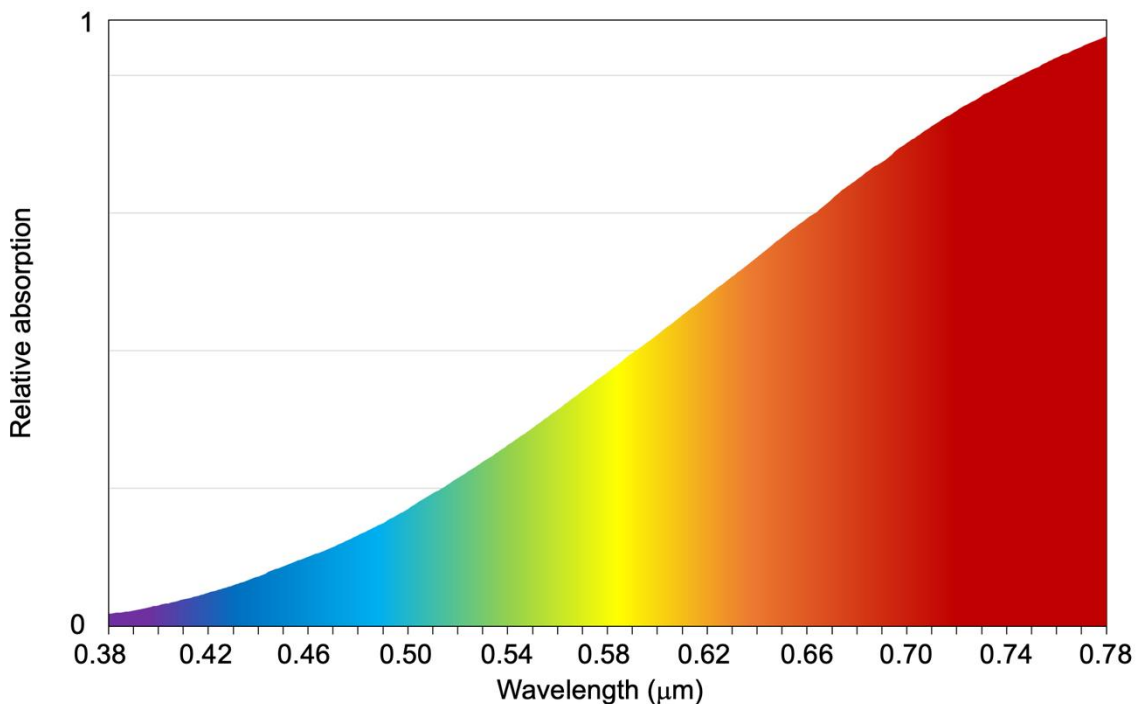


Figure 3.9. Relative absorption of a halogen bulb used in method development experiments, measured by a PG100N UPRtek handheld spectrometer held directly in the beam of illumination.

The use of a water filter to remove excess infrared radiation from the halogen bulb resulted in predominantly visible radiation interacting with the particle (although this was missing radiation in the blue wavelength range, and it had a low power density). A complicated set-up was required to generate an appropriate radiation spectrum (i.e. predominantly visible radiation) using the halogen bulb, and so the use of a Light-Emitting Diode (LED) was investigated. This would supply radiation across the entire visible wavelengths with a higher power density than the halogen bulb and without the need for a water filter to remove infrared radiation. Experiments M29-M31 with a LED successfully

demonstrated that particle-induced ice melt could occur without independent ice melt.

Method development experiments demonstrated that an 80-watt white LED was the most suitable source of radiation. This matched peak wavelength bands emitted from solar energy (i.e. the visible wavelengths, Figure 3.10) and did not interact with the optically transparent ice. Therefore, the illumination spectrum had a different distribution to the natural system but allowed isolation of the particle heating effect by interacting with the particle and being unable to interact with the ice (as the spectrum was within the transmission window for ice). The LED was additionally combined with an equinox Gobo projector to generate a focused light beam approximately 1 m from the ice block. This produced a power density approaching typical solar values (32,000 to 98,000 lux): the LED specification states 8000 lux at 2 m, and so the illumination for the experiments was estimated at approximately 32,000 lux, and the power density at approximately 300 W m^{-2} , comparable to natural sunlight (NASA, 2009).

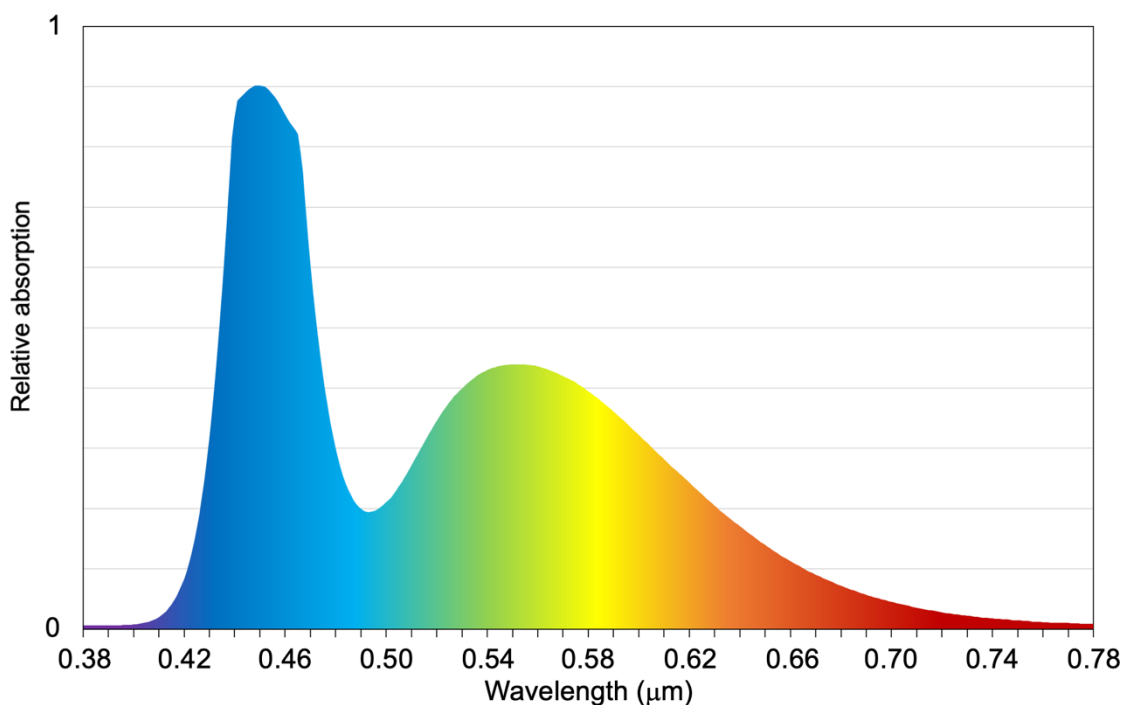


Figure 3.10. Relative absorption of the 80 W white LED radiation source used in laboratory experiments, measured by a PG100N UPRtek handheld spectrometer held directly in the beam of illumination.

The method development experiments met the following key design criteria:

- Optically transparent ice would be created to reduce ice-radiation interaction and to allow cross-sectional imaging through the ice as a method of data collection,
- The chosen illumination would not be absorbed by the optically transparent ice or water to cause direct heating but would be absorbed by the particles.

3.2. Experimental set-up

Experiments were conducted within a closed chest freezer operating at temperatures between -6 and $+7^{\circ}\text{C}$ (although typically within the -2 to $+1^{\circ}\text{C}$ temperature range), using ice blocks approximately $200 \times 200 \times 50\text{--}80$ mm in size (Figure 3.11, Figure 3.12). A variety of particle distributions were used (e.g. single particles, direct comparison of single particles, particle arrays, scattering of particles, and embedded particles).

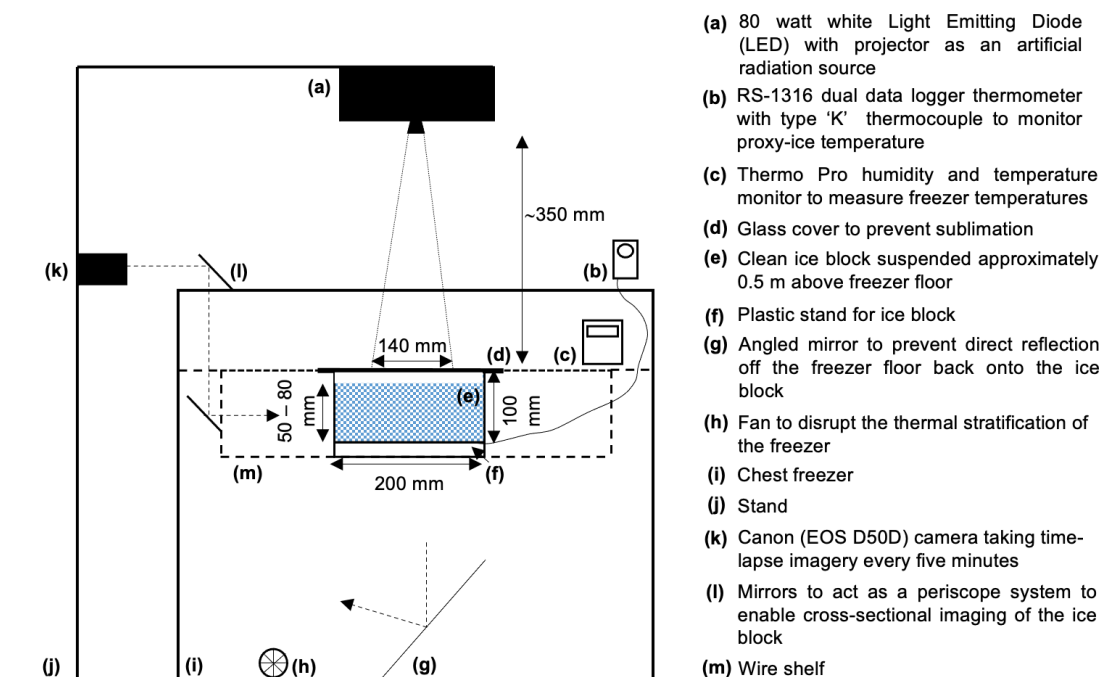


Figure 3.11. Schematic diagram showing the final experimental set-up.

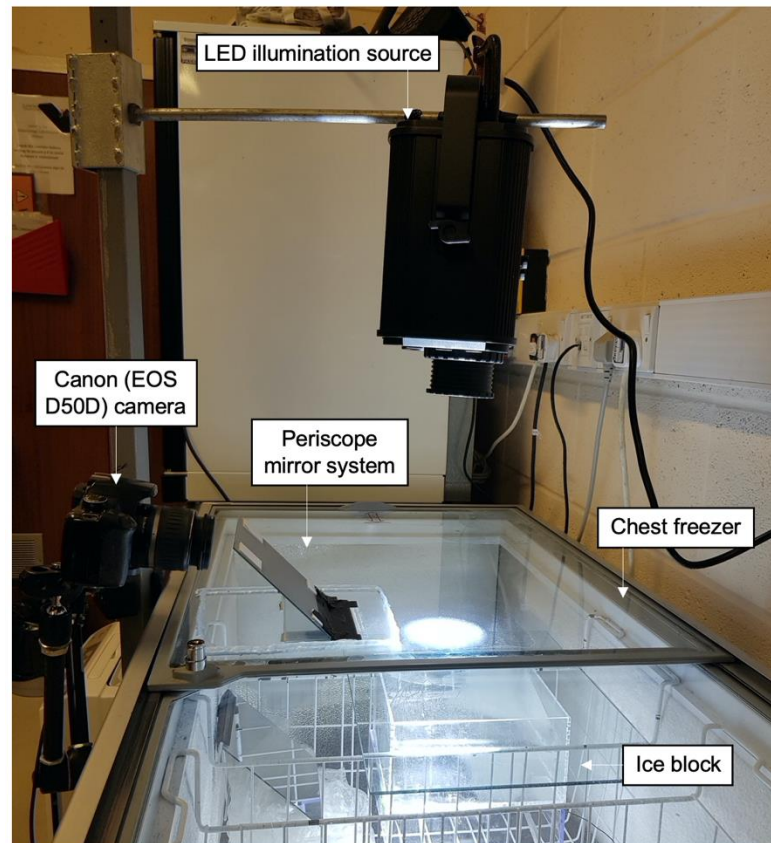


Figure 3.12. Photograph of final experimental set-up.

3.2.1. Preventing sublimation

Early experiments in the method development phase (i.e. M24-M26) suggested that sublimation cooling could lower the ice surface temperature relative to the rest of the ice, consequently restricting the effects of heat coupling from the particle into the underlying ice. This was sufficient to stabilize ice above an ambient environmental temperature of 0°C and to ‘armour’ the ice surface against melting. This was observed through the formation of ice pedestals under surface particles as the particle prevented water molecules directly underneath escaping from the ice surface (i.e. experiment M24). Consequently, a glass cover was placed over the ice container to simulate a high humidity environment and to minimise water molecule escape and the sublimation cooling effect. This left a gap of approximately 50 mm between the cover and ice surface.

3.2.2. Temperature measurements

To monitor the temperature of the experimental system, temperature data were recorded manually from a ThermoPro indoor humidity and temperature monitor (model number: TP-55) within the freezer, and an RS Pro data logger thermometer (RS-1316) and thermocouple (type K) at the base of the ice (between the base of the container and the top of the plastic stand that supported the ice, Figure 3.13). These two approaches were used to determine the approximate temperature of the freezer and a proxy temperature of the ice block, respectively. This was used in combination with an observational system described in Section 3.7 to provide an assessment of the thermal environment of the ice. Of particular interest was the thermal environment of the ice near the particle.

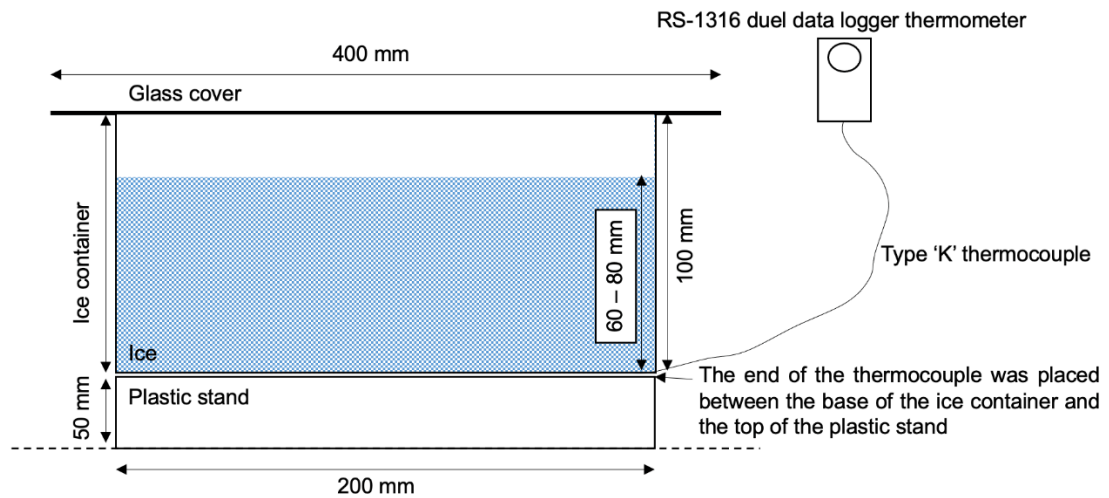


Figure 3.13. Cross-sectional diagram indicating the positioning of the thermocouple when measuring proxy-ice temperatures.

The ThermoPro temperature monitor had a temperature resolution and accuracy of 0.1°C and $\pm 1^{\circ}\text{C}$, respectively, and a relative humidity resolution and accuracy of 1% and $\pm 2-3\%$, respectively. The monitor updated measurements every ten seconds, and so all data were representative of the freezer at the given time of measurement. Relative humidity measurements were also noted from the monitor, although analysis focused on temperature data because an artificial high humidity environment was created directly above the ice in most experiments (Section 3.2.4).

The RS Pro data logger thermometer had a resolution and accuracy of 0.1°C and $\pm 0.05\% + 0.5^{\circ}\text{C}$, respectively. Measurements were taken at random points in the early experiments but taken systematically at approximately 30-minute intervals (when possible) in later experiments. The thermocouple was used as a proxy for ice temperature due to inaccuracy of data if placed within the ice itself (e.g. exposure to radiation resulting in incorrect values). This would have also created an additional object that may have interfered with the particles (e.g. re-emission of radiation from the thermocouple itself) if embedded within the ice. There were additional logistical difficulties in embedding the thermocouple into the ice due to the complex method of creating optically transparent ice.

Continuous logging of temperature was also taken over a single 22-hour period to assess the freezer temperature cycle. This was measured using the RS Pro data logger thermometer and measurements were taken at intervals of 20 seconds (Figure 3.14). This confirmed that freezer temperatures behaved in a cyclic nature, with two ongoing cycles. The first cycle operated on a relatively short timescale of approximately 30 minutes, where a total of 63 cycles occurred over the 22-hour period (averaging at 2-3 per hour). This involved a change in temperature of approximately $0.1\text{-}0.15^{\circ}\text{C}$ and likely correlated with operation of the freezer pump. The second cycle operated over a relatively long timescale of 4.5-6 hours, where a total of four cycles occurred over the 22-hour period. Both cycles were identified in the temperature data regardless of data manipulation techniques (e.g. data were averaged over every 1 minute, every 5 minutes and every ten minutes), although the cause of these cycles was not fully understood.

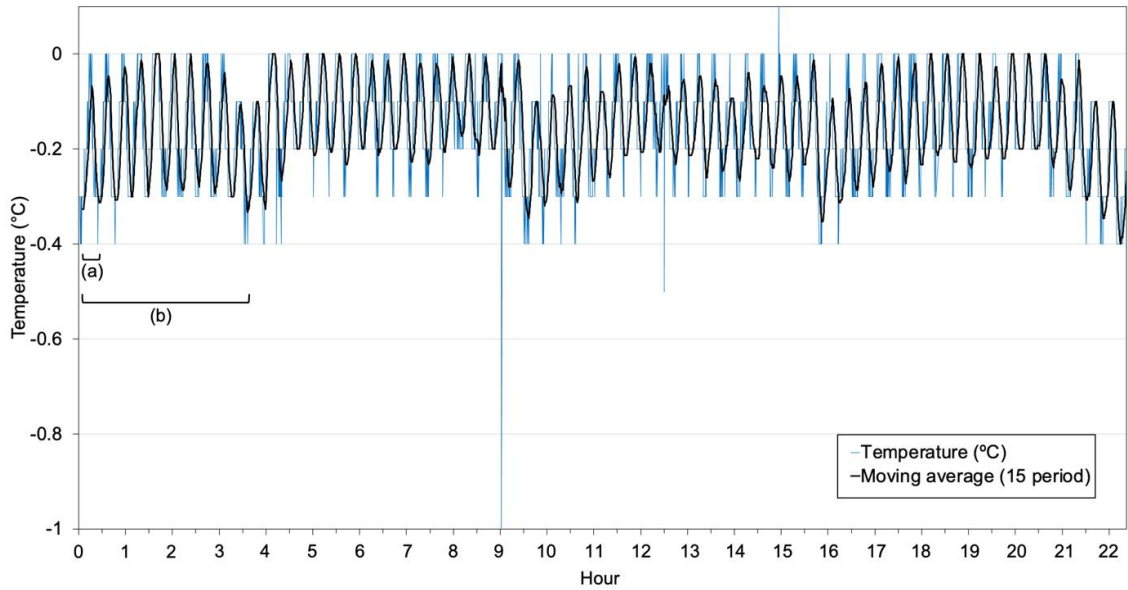


Figure 3.14. Continuous temperature data logger measurements of the proxy-ice temperature over a 22-hour period from experiment P49 (Chapter 4). The moving average was measured over 15 points (representing 5 minutes) and was used to elucidate the key cycles within the measurement period. (a) highlights the 'short' cycle, (b) indicates the 'long' cycle.

3.2.3. Placement of particles on the ice surface

Particles were placed on the ice surface in the centre of the radiation beam (approximately 79 cm^2). The area chosen for each experiment was limited to a specific sector of the ice to permit multiple uses of an individual block (each used for approximately four experiments). Particle placement differed depending on the planned distribution of particles. The standard approach was placement at room temperature and in the centre focus of the radiation beam.

3.2.3.1. Single particles

To ensure the particle was placed in the centre of radiation, a white piece of paper with a 10 mm hole in the centre was used to define the area of radiation and to cast a shadow on the central focus point. This central point was marked as an indentation on the ice surface using a metal screwdriver, and particles were placed on the central mark at room temperature to prevent rolling on the ice surface and away from the centre focus of the radiation. There was one exception to this (experiment P49) where the particle was pre-cooled prior placement.

3.2.3.2. Multiple single particles

Multiple single particles were used to directly compare results from individual particles, but to avoid particle-particle interaction. Placement depended on the particle diameter and thermal conductivity as this related to the thermal sphere of influence of each particle (and so informed the separation distance).

Experiments of this type typically investigated thermally conductive particles, and so a minimum of one particle diameter (from edge-to-edge) was measured between particles. This was to prevent particles (or the hydrological systems created by the particles) interacting with one another, although this was not always achieved. Close placement near the centre of the radiation beam (marked on the ice surface) ensured equal distribution of radiation with a high-power density.

3.2.3.3. Array of particles

Particle arrays were used in experiments that investigated the behaviour of a group of particles. These experiments are presented in Chapter 4 and investigated the role of particle diameter on particle-ice interaction (i.e. experiments P36, P38, P39, P40, P42, P43). Multiple array formations were used (e.g. triangle, square, and diamond) although 'diamond' was preferred as it allowed particles to experience an equal distribution of a high-power density radiation and to be imaged clearly in time-lapse images with limited particle overlap. Array configurations varied with 3x3 mm, 5x3 mm, 4x3 mm, 9x3 mm, and 16x3 mm particle arrays investigated. These were placed in a flat formation, so the vertical dimension of the array was the same diameter as the individual particle (i.e. 3 mm) prior to clustering. The centre focus of radiation was marked on the ice surface and particles were placed around this in the same way as single particles (Section 3.2.2.1).

3.2.3.4. Scattering of particles

This involved a random distribution of particles on the ice surface and was utilised most in the 'microplastics' experiments (i.e. Mp15-17, and Mp19 in Chapter 6), and two volcanic particle experiments in Chapter 5 (i.e. V33, V34). Particles were typically a small (<2 mm) size and so a sieve was used to scatter

the particles randomly on the ice surface. Any larger particles investigated in this configuration (e.g. 2-3 mm) were placed on the ice surface by hand. The central focus of radiation was marked as an indentation on the ice surface prior to particle scattering to ensure that all particles were in the beam focus. However, it was acknowledged that particles may not all experience an equal power-density of the radiation due to random scattering.

3.2.3.5. Embedded particles

Particle placement of embedded particles was not directly controlled as this relied on the freezing behaviour of the ice. However, to ensure that the embedded particle was at the centre of radiation, a piece of paper with a 10 mm hole in the centre was used to identify the central focus of radiation. The position of the ice and radiation source were adjusted to place the particle under this point.

3.2.4. Time-lapse imagery

Time-lapse images were taken through a periscope system every five minutes using a Canon (EOS 50D) camera to capture the response of embedded particles and ice to radiation (Figure 3.11). This allowed calculation of particle velocities and was used in combination with in-person observations and photography.

3.3. Particles

Synthetic and natural particles were used in laboratory experiments to investigate three themes: particle properties, volcanic particles, and microplastic particles. The relevant physical properties and their magnitudes that most influence ice ablation were determined from the literature, and the albedo was calculated with reference to a known albedo (e.g. white paper) by measuring the relative reflectance of each particle in a photograph taken in the same conditions using ImageJ. The documented density values of the particles were compared with test experiments where the particles behaviour in a beaker of water at 0°C was noted. The observed behaviours (i.e. sinking or floating)

confirmed the relative density of particles cited in the literature and Table 3.2, Table 3.4, and Table 3.6.

3.3.1. Particle properties (Chapter 4)

Five synthetic materials were chosen to investigate the properties of particle thermal conductivity, albedo, density, and diameter (Table 3.1). Aside from experiments that investigated the role of particle albedo, all particles were painted black with matte Black 2.0™ paint to minimise the particle albedo, increase the time efficiency of experiments, and provide calibration. Each property was further categorised for clarification (Table 3.2).

Table 3.1. The particle properties of the synthetic materials used in experiments, and the ratio relative to water density (1000 kg m^{-3}) and ice thermal conductivity ($2.1 \text{ W m}^{-1} \text{ K}^{-1}$).

Particle	Thermal conductivity ($\text{W m}^{-1} \text{ K}^{-1}$)/ratio	Density (kg m^{-3})/ratio	Diameter (mm)	Albedo	
Chrome steel	30-60/21.4	7000-8000/7.5	8	0.57	
Brass	~ 100/47.6	8000/8	6	Black	0.12
				Unpainted	0.50
				White	0.60
Polyoxymethylene (delrin®)	0.37/0.18	1400/1.4	6	0.12	
Polypropylene	0.1-0.22/0.097	890-920/0.9	5	0.12	
Polystyrene	0.03/0.01	960-1050/1	8	0.12	

Table 3.2. Categorisation of particle properties.

Particle property	Category					
	Low		Intermediate		High	
	Criteria	Particle	Criteria	Particle	Criteria	Particle
Thermal conductivity	Lower than ice	Polystyrene	-	-	Higher than ice	Chrome steel, brass
Albedo	Absorbing surface (e.g. <0.2)	Matte black particles	Partially reflective surface (e.g. 0.2-0.5)	Unpainted particles	Predominant reflective surface (e.g. >0.5)	Unpainted chrome steel, white particles
Density	Lower than water	Polypropylene, polystyrene	Higher than water, but close to the boundary	Delrin®	Higher than water	Chrome steel, brass

3.3.2. Volcanic particles (Chapter 5)

Three types of volcanic particles were used in experiments in Chapter 5 (Table 3.3, Table 3.4). These initially involved cemented ash clusters from the 2010

Eyjafjallajökull, Iceland, summit eruption (trachyandesitic in composition, 58-60% SiO₂). Disintegration of clusters was observed and, whilst providing serendipitous observations, were not suitable for use when assessing the behaviour of single particles. Therefore, pumice from the May 18 (1980) Plinian pumice fall eruption at Mount St. Helens, USA, and scoria from Volcán Sollipulli, Chile, were used in subsequent experiments. The Mount St. Helens pumice was used as intermediate albedo (IA) volcanic material. This was highly vesicular, light in colour and rhyolitic in composition (James, 1998). The Chile scoria was used as low albedo (LA) volcanic material. This was dark in colour and basaltic-andesitic in composition (Hobbs, 2014). The particle diameters varied between experiments but were similar to those used in the ‘diameter’ subsection in Chapter 4 (i.e. 1.5 mm, 3 mm, 6 mm, and 12 mm) to allow comparisons. Particles <1 mm in diameter were used when multiple particles in a scattering configuration were investigated (as described in Section 3.2.3.4).

Table 3.3. The particle properties of dry volcanic material used in experiments, and the ratio relative to water density (1000 kg m⁻³) and ice thermal conductivity (2.1 W m⁻¹ K⁻¹). ¹Hobbs (2014) and ²Klug and Cashman (1996).

Particle	Thermal conductivity (W m ⁻¹ K ⁻¹)/ratio	Density (kg m ⁻³)/ratio	Diameter (mm)	Estimated porosity (%)	Albedo
Eyjafjallajökull cemented ash	0.3 ¹	2500/2.5	Varied	-	0.29
Mount St. Helens pumice	0.1 ¹	700-1200/0.95	Varied	60-80 ²	0.38
Volcán Sollipulli scoria	0.2 ¹	1954/1.9 ¹	Varied	73 ¹	0.14

Table 3.4. Categorisation of dry volcanic particle properties.

Particle property	Category					
	Low		Intermediate		High	
	Criteria	Particle	Criteria	Particle	Criteria	Particle
Thermal conductivity	Lower than ice	Eyjafjallajökull ash clusters	-	-	-	-
Albedo	Absorbing surface	Eyjafjallajökull ash clusters, Volcán Sollipulli scoria	Partially reflective surface	Mount St. Helens pumice	-	-
Density	Lower than water	Dry Mount St. Helens pumice	-	-	Higher than water	Volcán Sollipulli scoria, wet Mount St. Helens pumice

3.3.3. Microplastic particles (Chapter 6)

Polypropylene and polyethylene particles were used to investigate the behaviour of microplastic particles with ice (Table 3.5, Table 3.6). These had varied morphologies, e.g. spherical polypropylene particles, and polyethylene particles with irregular morphologies. All particles had a low albedo to increase the efficiency of particle-ice interaction, and any particles that were not previously black were painted with matte Black 2.0™ paint. The plastics used were split into three categories for ease of comparison: ‘small’ plastics (<1 mm), ‘medium’ plastics (1-4 mm) and ‘large’ plastics (>4 mm). These fit within the overarching category of ‘microplastics’ as they were smaller than 5 mm in diameter (Evangelidou et al., 2020).

Table 3.5. The particle properties of plastic material used in experiments, and the ratio relative to water density (1000 kg m^{-3}) and ice thermal conductivity ($2.1 \text{ W m}^{-1} \text{ K}^{-1}$).¹Patti and Acierno (2020).

Particle	Thermal conductivity ($\text{W m}^{-1} \text{ K}^{-1}$)/ratio	Density (kg m^{-3})/ratio	Diameter (mm)	Albedo
Polypropylene	0.1-0.22/0.07 ¹	890-920/0.9	5	0.12
Polyethylene	0.33/0.16	910-940/0.9	Varied, although < 5	0.18

Table 3.6. Categorisation of microplastic particle properties.

Particle property	Category					
	Low		Intermediate		High	
	Criteria	Particle	Criteria	Particle	Criteria	Particle
Thermal conductivity	Lower than ice	Polypropylene, polyethylene	-	-	-	-
Albedo	Absorbing surface	Polypropylene, polyethylene	-	-	-	-
Density	Lower than water	Polypropylene	Close to the boundary of water	Polyethylene	-	-

3.4. Experimental process

An experimental checklist was used to ensure consistency between experiments (Appendix 7). This comprised a list of guidelines and noted proxy ice temperature, freezer temperature and relative humidity at the beginning of experiments (Figure 3.15), with subsequent readings taken throughout.

Experiments ended following no changes for approximately 24 hours as standard experimental practice, unless time constraints prevented this.

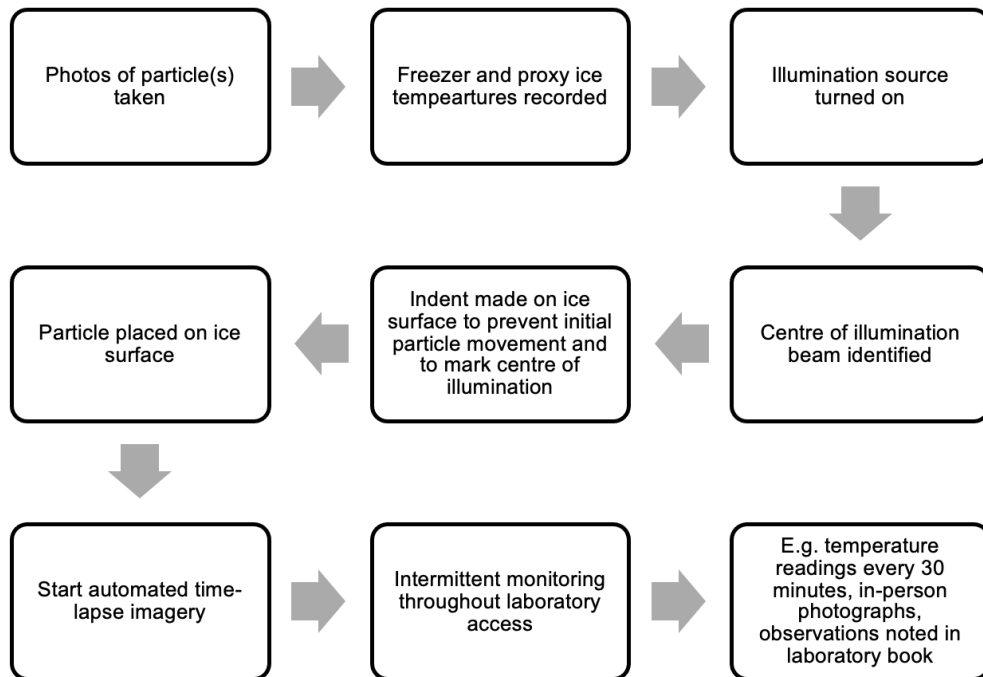


Figure 3.15. The experimental procedure.

3.5. Data analysis

3.5.1. Extraction of data from time-lapse images

Qualitative and quantitative data were extracted from time-lapse images. Automated photography occurred every five minutes to allow assessment of particle movement through the ice. This, in combination with in-person observations, noted key features that formed due to particle-ice interaction (e.g. melt pathway morphology, drainage events, formation of basal meltwater ponds, etc.). A typical experiment generated 800-1000 images, and these were analysed in chronological order. The particle movement within each image was measured relative to a fixed point (this varied from experiment to experiment) to allow calculation of the distance moved by a particle. Measurements were taken from the particle base to the ice surface (Figure 3.16) and had a precision to 1 mm. Scaling of the images was determined from the known particle width and was applied to the distance moved measured in the image, to convert to distance moved in the laboratory. Analysis predominantly focused on vertical distance moved, although lateral deviations were also considered.

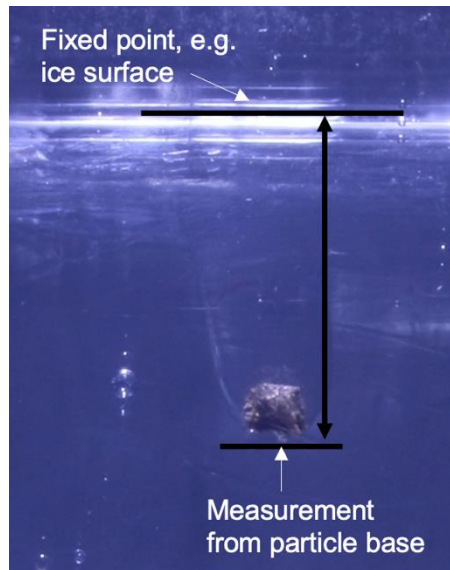


Figure 3.16. Example of extraction of vertical distance moved by a particle.

Photographs of the processes observed were a key tool for interpretation of experimental results. These are documented throughout the thesis and have a standard format with the number of hours from experiment start, time and date, and a scale bar included for clarity.

3.5.2. Calculation of particle velocity data

Calculation of the particle velocity through the ice was a key contribution for interpreting results as it was used as a proxy for ice melt rate. Four variations of particle velocity were calculated to aid interpretation: (1) from a conceptual melt model (theoretical data based on particle properties), (2) the overall velocity from time-lapse images (manipulated data from observations), (3) the incremental velocity from time-lapse images (observed data), and (4) the 'smoothed' moving average velocity from the incremental velocity (manipulated data from observations).

3.5.2.1. Particle velocity from conceptual melt model

A conceptual model of ice melt was created to inform the hypothesis of many experiments and predict the velocity of a moving particle through the ice (equation 3.4). This included the following assumptions:

1. The ice was at pressure melting point (PMP).
2. All heat that coupled into the particle was coupled into the ice to cause ice melt.
3. There was no ice-radiation interaction.

The model involved an input power density (L_{pd} [watts m^{-2}]), assumed to have no ice interaction as optically transparent ice does not absorb wavelengths within the visible spectrum. Adding a particle into the system required consideration of an absorption surface; this was the area that was perpendicular to the direction of light (i.e. the projected area of the particle, A_p [m^2]). The amount of power that could be absorbed into the particle would depend on the particle albedo (α). Therefore, energy that could be absorbed into ice would be equal to $1-\alpha$. The power that could be coupled into a given particle (W_p [watts]) is defined as:

$$W_p = L_{pd}A_p(1 - \alpha) \quad [3.1]$$

It was assumed that all heat absorbed by the particle would be coupled into the ice. This would result in ice melt and would allow the particle to move downwards through the ice ($\frac{dx}{dt}$), if sufficiently dense. This would allow calculation of the volume melt rate of ice ($m^3 s^{-1}$, equation 3.2):

$$\text{volume melt rate of ice} = \frac{dx}{dt} A_p \quad [3.2]$$

Considering the latent heat of fusion ($L_f J m^{-3}$) gives:

$$W_p = L_f \frac{dx}{dt} A_p \quad [3.3]$$

Combining equations 3.1 and 3.3 suggested that the particle diameter would not have an impact on particle-induced ice melt rate, and that the particle-ice interaction would only be dependent on the radiation power input and particle albedo.

$$\frac{dx}{dt} = \frac{L_{pd}(1-\alpha)}{L_f} \quad [3.4]$$

Where: $\frac{dx}{dt}$ = particle velocity (m s^{-1}), L_{pd} = lamp power density ($\sim 300 \text{ W m}^{-2}$), α = albedo of particle, L_f = latent heat of fusion of ice ($3.06 \times 10^8 \text{ J m}^{-3}$). When $\alpha = 0$ (black particle) the predicted particle melting velocity is approximately $1 \mu\text{m s}^{-1}$.

3.5.2.2. Particle velocity from time-lapse images

To calculate an overall mean particle velocity, the total distance of particle movement was divided by movement duration. However, this did not consider velocity variations during particle movement. Therefore, this was used in combination with other velocity calculations to aid interpretation of processes.

Point-by-point velocity (termed ‘incremental velocity’) was calculated at each timestep using the standard velocity equation. Particle velocity values were plotted for each particle to visually investigate how the velocity of a particle varied with time and to allow comparisons between particles. The velocity data were then smoothed to reduce noise from the dataset (from a lack of precision in the extraction of distance-moved data described in Section 3.5.1). This was termed the ‘smoothed velocity’ and was reached by calculating a moving average over a standard of 18 data points, although this differed in experiments with uncharacteristically small or large datasets, i.e. 30 data points were used in experiments P10 and P15 (Chapter 4). The data were then plotted onto a summary graph to enable trends to be identified. Therefore, graphs did not include the final nine (or 15, in the case of experiments P10 and P15) smoothed velocity values due to ‘zero’ data points.

3.6. Experimental implementation issues

3.6.1. Unclear images

3.6.1.1. Bubbles

In many instances, gas bubbles within the ice restricted the view of particles in the time-lapse images and prevented extraction of 'distance moved' data. Bubbles were particularly prevalent near the ice surface and impacted the view of the smallest particles to a greatest extent. This issue further demonstrated the need for optically transparent ice.

3.6.1.2. Condensation

Condensation of water vapour onto the chest freezer glass surface obscured the view in the periscope system in several experiments and typically covered the entire frame of images. To reduce this issue, a silicon seal was created and a film of liquid water was placed within the seal to allow imaging through the water (Figure 3.17). This did not appear to produce any optical distortion effects in the time-lapse images.

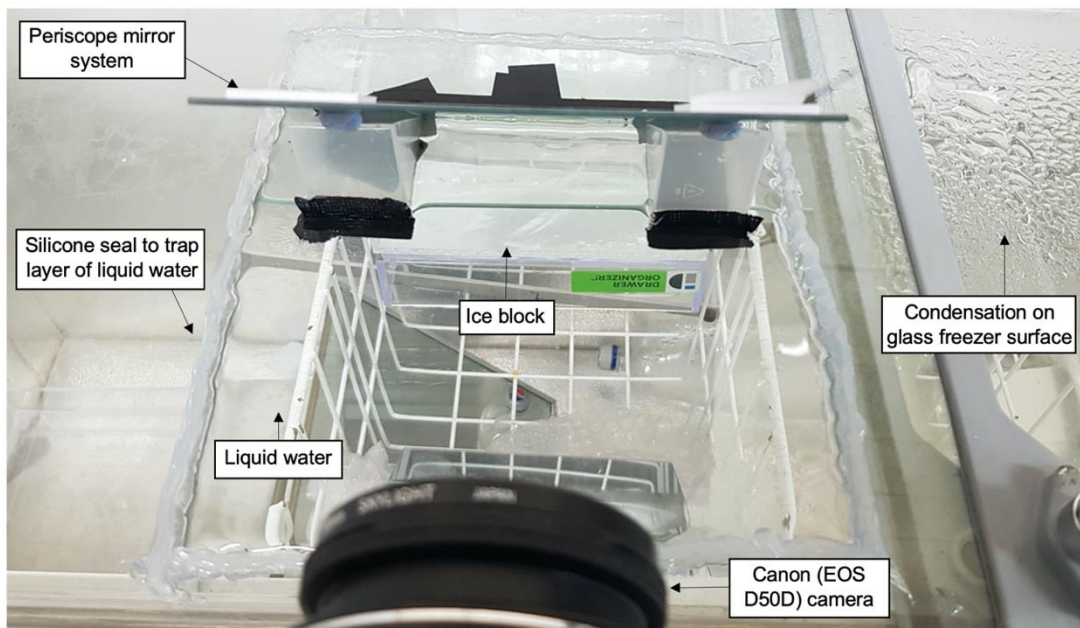


Figure 3.17. Photograph of the silicon seal to reduce condensation effects.

3.6.2. Paint

Paint leaked off particles into meltwater when particles were not painted with sufficient drying time prior to the experiment start. Although this was useful in indicating drainage patterns and meltwater movement, it may have influenced

the behaviour of particles by modifying the particle albedo. Additionally, it was noted that there were issues with guaranteeing that all particles were painted with the same thickness of paint to ensure that the thermal conductivity values were not affected. This was a particular issue with the smaller particles (e.g. 1.5 mm) due to difficulties in handling the small sizes.

3.7. Thermal environment of ice in proximity to particles

The thermal environment of the ice close to particles emerged as a crucial component of the experimental design. The ice was defined as being within one of two environments: unstable, where illuminated ice melted independently of particle-ice interaction, or stable, where ice remained indefinitely in a solid state. Many experiments demonstrated the sensitivity of particles to the thermal environment and so, for ease of experimental set-up and discussion, four thermal environments were defined and investigated across a thermal range (Figure 3.18). These were not categorised with definitive boundaries, except for in the cases of 'unstable' and 'stable (cold)'. Instead, the thermal environment was identified across a range of behaviours (termed the 'thermal range' hereinafter). These environments dictated the extent of ice that was pushed into the 'unstable' state by particle-ice interaction.

The thermal environments were described where a 'positive shift' indicated ice temperatures moving closer to an 'unstable' environment, whilst a 'negative shift' indicated temperatures moving towards the stable (cold) end state. The ideal thermal environment for particles was when the ice was stable as a solid and all heat transfer coupled into melting, i.e. exactly at PMP as this was a common assumption used in modelling techniques. However, this was not feasible for most experiments as ice block creation was a resource-expensive process and conducting experiments at PMP would destroy each ice block after a single experiment. Therefore, many experiments were conducted within the stable (warm) or stable (cool) areas of the thermal range of the ice to enable particle-induced ice melt without total ice block destruction. The understanding of the various thermal environments developed as experiments progressed; however, these are defined here for clarity.

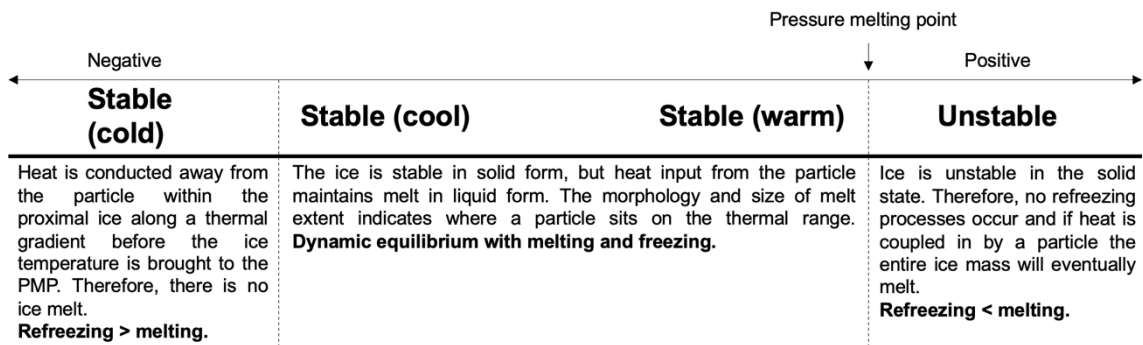


Figure 3.18. The definition of the thermal environments of the ice in proximity to the particles across the thermal range experienced in laboratory experiments.

Determining the thermal environment was largely dependent on observations of the ice (Figure 3.19). Observations were used in conjunction with temperature data to: (1) interpret the outcomes of the experiments; and (2) inform whether modification of the freezer temperature was required during an experiment. If the latter was the case, then the environment was categorised as ‘variable’. This category would also apply to an experiment where a natural shift across the thermal range was observed.

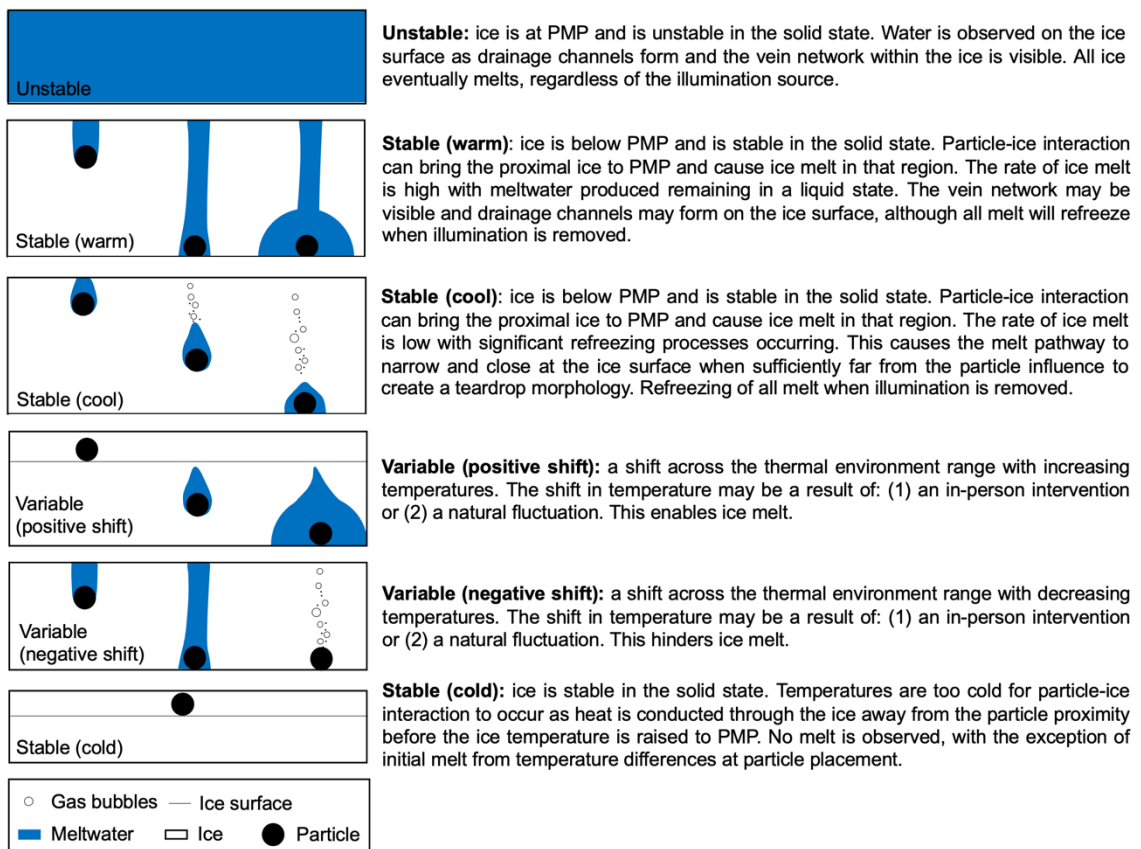


Figure 3.19. Cross-sectional schematic indicating the observational criteria for determining the thermal environment in the proximity of a particle.

4. An experimental investigation of particle properties to determine the physical processes involved in particle-ice interaction

This suite of 49 experiments assessed the role of particle thermal conductivity, albedo, density, and diameter on influencing the behaviour of particle-ice interaction. Experiments predominantly involved single particles illuminated by a light emitting diode (LED) radiation source, although 11 experiments assessed a direct comparison between particles and six experiments assessed an array of particles (as described in Chapter 3). Experiment results are described in a systematic and individual manner, in chronological order of experiment code. Repeat experiments are described as a synthesis of findings to allow comparisons to be drawn. The average freezer and proxy ice temperatures for each experiment are recorded in Table 9.7, Appendix 8.

4.1. Thermal conductivity

Experiments P1b-P9 and P48-P49 investigated the behaviour of thermally conductive chrome steel and brass particles within ice (Figure 4.1, Table 4,1). All particles had a low albedo and diameters in the range 6-8 mm.

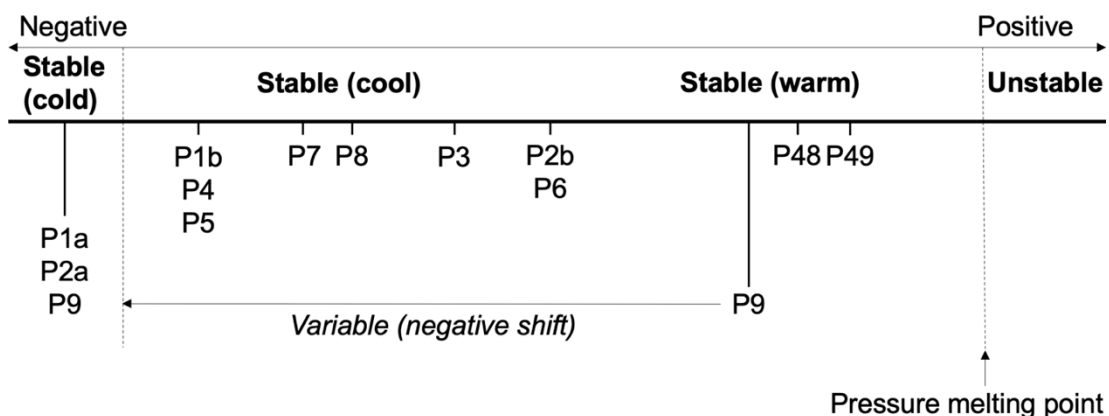


Figure 4.1. The thermal environment of particles in experiments investigating the role of particle thermal conductivity in particle-ice interaction. Experiment position has been derived from interpretation of observations, as described in Chapter 3, Section 3.7.

Table 4.1. A summary of experiments investigating the role of particle thermal conductivity in particle-induced ice melt, highlighting the types of particles used and associated thermal environments as defined in Chapter 3.

Experiment	Particle type	Thermal environment
P1a	8 mm chrome steel	Stable (cold)
P1b	8 mm chrome steel	Stable (cool)
P2a	8 mm chrome steel	Stable (cold)
P2b	8 mm chrome steel	Stable (warm)
P3	6 mm brass	Stable (cool)
P4	6 mm brass	Stable (cool)
P5	6 mm brass	Stable (cool)
P6	6 mm brass	Stable (warm)
P7	6 mm brass	Stable (warm)
P8	2 x 6 mm brass	Variable: stable (cool) to stable (warm)
P9	2 x 6 mm brass	Variable: stable (warm) to stable (cold)
P48	6 mm brass	Stable (warm)
P49	6 mm brass	Stable (warm)

4.1.1. P1: a thermally conductive chrome steel particle

Experiment P1 assessed particle-ice interaction involving a thermally conductive chrome steel particle with a high density, low albedo, and 8 mm diameter. This was separated into two experiments, P1a and P1b, due to external factors influencing particle-ice interaction.

P1a began as an open system with ice exposed to freezer conditions (e.g. the freezer relative humidity). Aside from the initial 20 minutes of the experiment, there was limited particle-ice interaction. It was observed that the particle sat on a 'peak' of higher topography approximately 48 hours after surface placement. This was indicative of a sublimation environment, where water molecules were removed from the solid ice surface directly to the vapour phase, resulting in a surface lowering. This process used latent heat to convert mass from the solid phase to the vapour phase, removing heat from the system and cooling the ice surface (Figure 4.2).

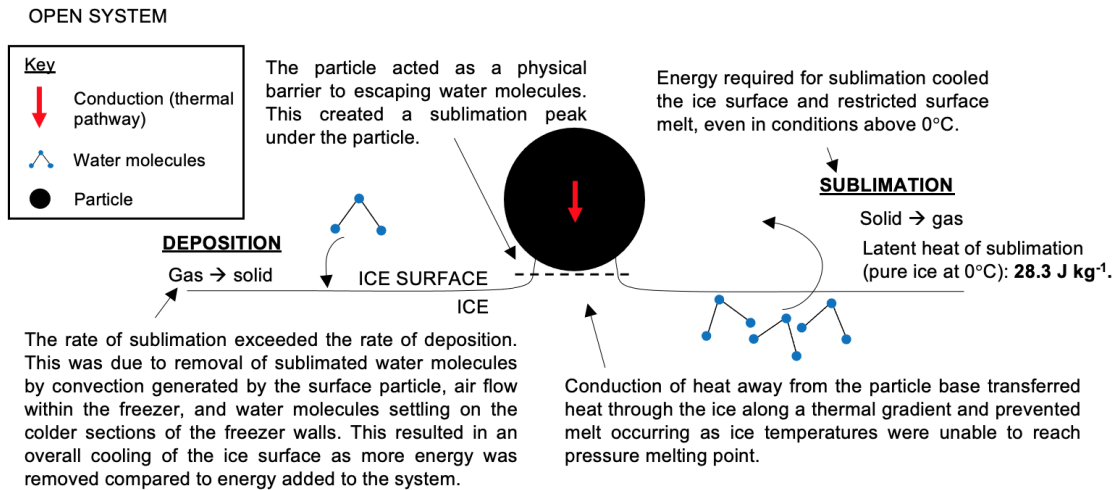


Figure 4.2. Cross-sectional diagram indicating the role of sublimation and surface cooling in preventing ice melt. Values of latent heat of sublimation taken from Cuffey and Paterson (2010).

A glass cover was placed over the container to offset sublimation cooling processes, marking the start of experiment P1b. The hypothesis for experiment P1b is shown in Figure 4.3.

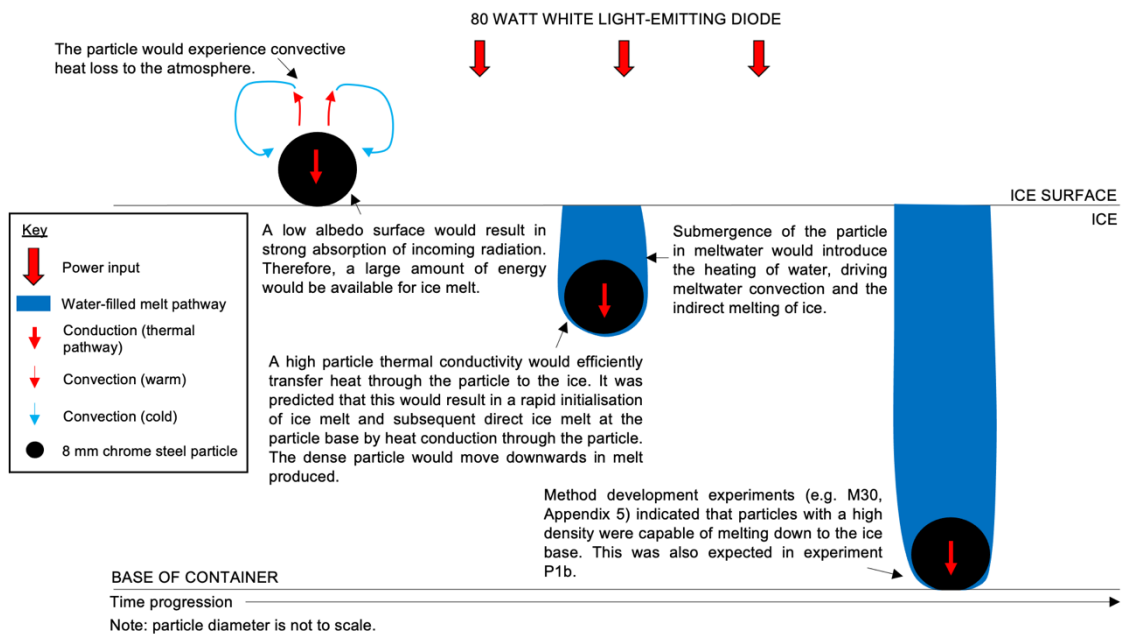


Figure 4.3. Schematic cross-sectional view of the hypothesised particle-ice interaction in experiment P1b.

4.1.1.1. Results and interpretation

P1a showed that sublimation cooling could hinder particle-ice interaction. Therefore, experiment P1b operated within a closed system to induce an increased relative humidity environment (Figure 4.4). This trapped sublimated

water molecules within the local area, causing deposition back onto the ice surface.

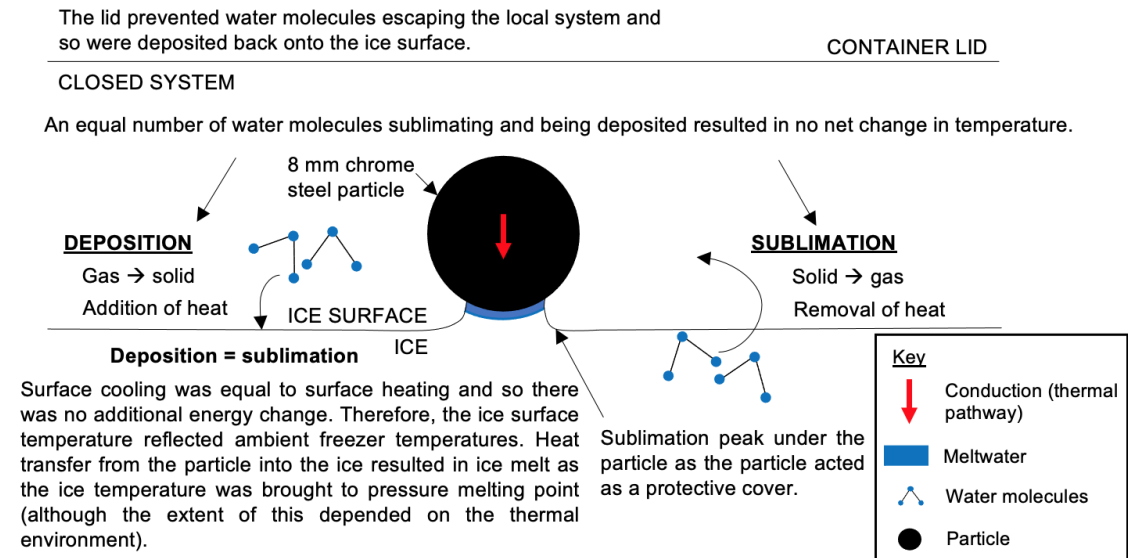


Figure 4.4. Cross-sectional diagram indicating the influence of a closed system on sublimation and deposition in experiment P1b.

Offsetting sublimation processes allowed the particle to directly transfer heat into the underlying ice to raise the temperature to PMP, causing ice melt. This confirmed the interpretations that sublimation cooling prevented ice melt in experiment P1a as particle-induced ice melt was initiated approximately ten minutes after the cover was placed on the ice container in experiment P1b. Following this, downwards movement of the particle in meltwater was observed, resulting in particle descent to reach the ice base within 23 hours (Figure 4.5). This supported the hypothesis and was a result of the high particle density (relative to meltwater). A full particle submergence was observed within two hours, interpreted to remove heat loss mechanisms to the atmosphere and to drive convection in the melt pathway. All energy absorbed was available to melt the ice, resulting in ice melt and downwards movement to the base at a mean particle velocity of $7.19 \times 10^{-7} \text{ m s}^{-1}$. An initial high velocity (e.g. $5.0 \times 10^{-6} \text{ m s}^{-1}$ measured for the first data point) suggested that initial movement was associated with the effects of temperature differences between particle and ice as it was placed on the ice surface at room temperature.

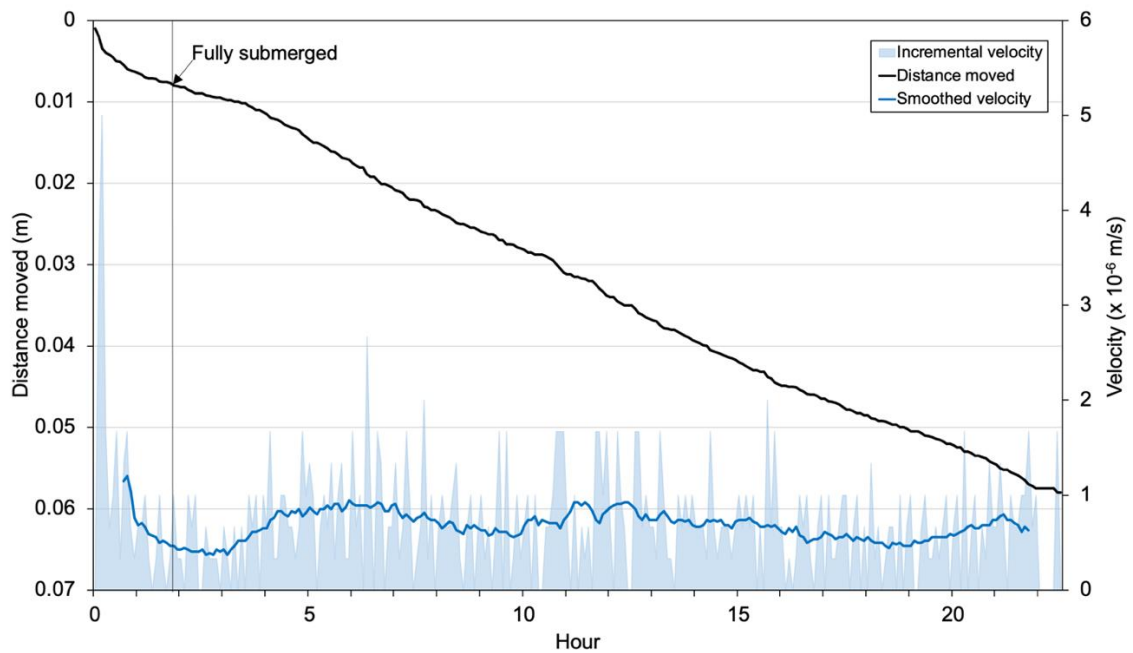


Figure 4.5. Vertical distance moved and velocity of an 8 mm chrome steel particle in experiment P1b.

4.1.1.2. Melt pathway

Once the particle was embedded within the ice, meltwater with a teardrop morphology developed directly above the particle (representing the melt pathway, Figure 4.6) and followed particle movement. The meltwater formed as heat was conducted through the particle to the ice at the particle base, causing ice melt. This process represents the direct heat transfer pathway, controlled by the particle thermal conductivity. The high density of the particle allowed the particle to move downwards into meltwater produced, causing the particle to sit at the base of the meltwater. In addition to this direct heat transfer mechanism, the warm meltwater moved downwards around the particle to the particle base (meltwater convection) and continued to contribute to ice melt (due to the inverse density-temperature relationship of water below 4°C, described in Chapter 3). This represents the indirect heat transfer pathway. Therefore, two heat transfer mechanisms controlled the rate of ice melt, and both were in the vicinity of the melt pathway base. The downwards movement of warm water (and upwards movement of cold water) created the teardrop morphology; the colder water (although still above zero degrees) at the top was close to freezing temperatures and so began to refreeze away from the particle sphere of influence (i.e. the immediate region of ice melt, in the form of both direct and

indirect heating mechanisms). The development of a teardrop morphology of meltwater suggested that the ice was in a stable (cool) thermal environment, whereby ice melt was a result of particle-ice interaction only and an entire closure of the melt pathway was observed (Section 3.7, Chapter 3).

Steady changes in the melt pathway size and morphology were observed throughout the experiment. The melt pathway reduced in height over a two-hour period to extend a maximum height of 2 mm above the particle. This decreasing volume meltwater was associated with a change in the angle of particle movement (from an almost vertical trajectory to an angled trajectory). The modification to trajectory orientation may have been controlled by the ice structure (e.g. the vein network). Changes in the meltwater extent and orientation of particle movement were suggested to be due to two processes: (1) subtle temperature changes encouraging a higher refreezing rate, and (2) meltwater entering the vein network allowing the particle to follow the vein trajectory. These observations suggested that, although within a stable (cool) thermal environment, it was likely that the P1b particle was close to the stable (cold) boundary.

The melt pathway increased in size to form another teardrop melt pathway as the particle continued to move downwards through the ice, likely reflecting subtle changes in temperature (Figure 4.6).

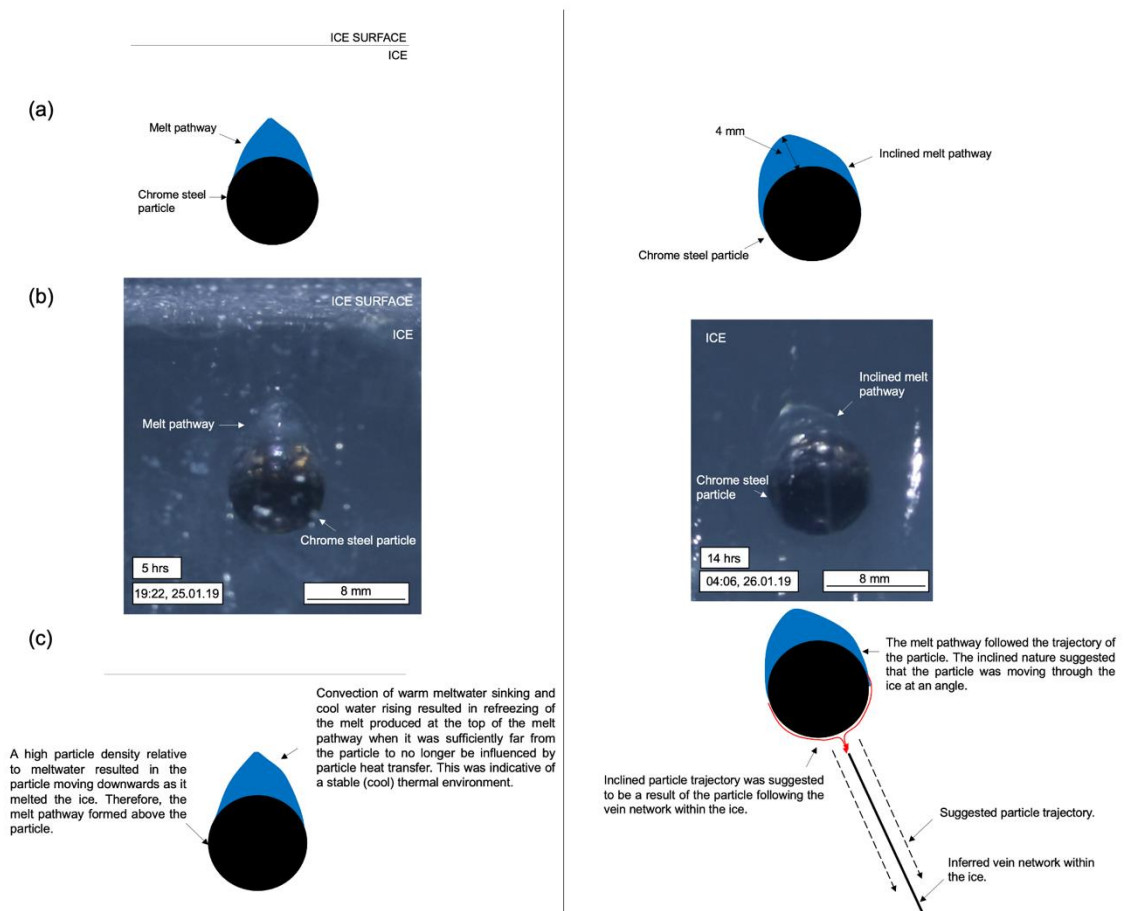


Figure 4.6. Images showing the fluctuation in melt pathway morphology at two stages (5 and 14 hours) in experiment P1b. (a) observational line diagram, (b) photograph and (c) interpretation of the features.

4.1.1.3. Basal meltwater pond

The particle could no longer melt downwards when reaching the ice base and so heat transfer remained in the local environment. This created a basal meltwater pond that facilitated lateral particle movement that continued to melt the basal ice. Lateral movement was suggested to be due to a combination of heterogeneous convection systems within the basal meltwater pond, and freezer vibrations pushing the particle along the ice base as it was perfectly spherical with a smooth surface (i.e. low friction). Particle heat transfer was able to melt ice approximately 2 mm away from the particle top; this was likely because of heating by conduction at the particle base and convection moving warm water to the container base. Therefore, expansion of basal meltwater was predominantly horizontal with little vertical expansion, with a maximum width of approximately 17 mm. This indicated that the sphere of influence of a conductive and high-density particle was small and on the sub-10 mm scale in a

stable (cool) thermal environment as heating was predominantly at the particle base.

4.1.1.4. Summary

Surface cooling from sublimation processes hindered particle-ice interaction in experiment P1a. However, a glass cover prevented sublimation in experiment P1b, and the particle was able to efficiently melt the ice. The particle moved downwards to the ice base with a mean particle velocity of $7.19 \times 10^{-7} \text{ m s}^{-1}$ (agreeing with the hypothesised outcome). However, refreezing processes and interaction with the vein network modified the morphology of the melt pathway and created an inclined particle trajectory. A closed melt pathway was indicative of a stable (cool) thermal environment. Additionally, a basal meltwater pond with a dome-shaped morphology formed when the particle remained at the ice base. It appeared as if this had a heating influence of approximately 2 mm from the particle top, suggesting a small sphere of influence for a high density and thermally conductive particle in a cool environment. It would be useful to assess this in repeat experiments and to inform understanding of the influence of the vein network on sinking particles.

Experiment P2 was separated into two experiments in the same way as experiment P1 (i.e. P2a and P2b); however, cold temperatures (e.g. a minimum of -5.9°C , Table 9.7, Appendix 8) prevented particle-ice interaction in experiment P2a, rather than sublimation cooling as observed in experiment P1a. Experiment P2b followed from experiment P2a after a freezer temperature adjustment. Condensation on the freezer surface obscured time-lapse images and so results relied on in-person observations. As such, the particle velocity could not be accurately calculated. However, experiment P2b confirmed key results from experiment P1b: namely, that a particle with a high thermal conductivity and high density could melt the ice sufficiently to melt downwards to the ice base. In the case of P2b this occurred within 21 hours. However, the melt pathway morphology differed due to drainage events of meltwater (likely into the vein network), and refreezing/redeposition processes, ultimately dependent on the ice temperature and particle thermal environment. This resulted in the formation of a narrow (approximately 2-3 mm wide) drained melt

pathway that extended towards the ice surface, contrasting to the teardrop morphology observed in experiment P1b. However, although this was open at the ice surface, refreezing or vapour deposition processes occurred as the melt pathway diameter was smaller than the particle diameter. However, the unclear time-lapse images could not determine if narrowing processes occurred prior to, or after, drainage, and so it could not be determined whether refreezing or deposition processes were occurring. Similar to experiment P1b, the melt pathway was inclined suggesting particle intersection with the vein network. Additionally, a larger basal meltwater pond than expected developed (although precise measurements could not be made), demonstrating the capability of a thermally conductive particle with a high density to generate a significant volume of meltwater even away from the direct heating zone. This contrasted with results from experiment P1b, although this was likely a result of differences in the thermal environment as the P2b particle experienced a stable (warm) thermal environment. Repeat experiments to determine particle velocities and assess the meltwater extent and possible drainage events in detail would be useful.

4.1.2. P3: a thermally conductive brass particle

Experiment P3 investigated the behaviour of a 6 mm black brass particle within ice, placed on the same ice block as that used in P2b. The particle had a high thermal conductivity, high density, and low albedo. The hypothesis for experiment P3 is shown in Figure 4.7.

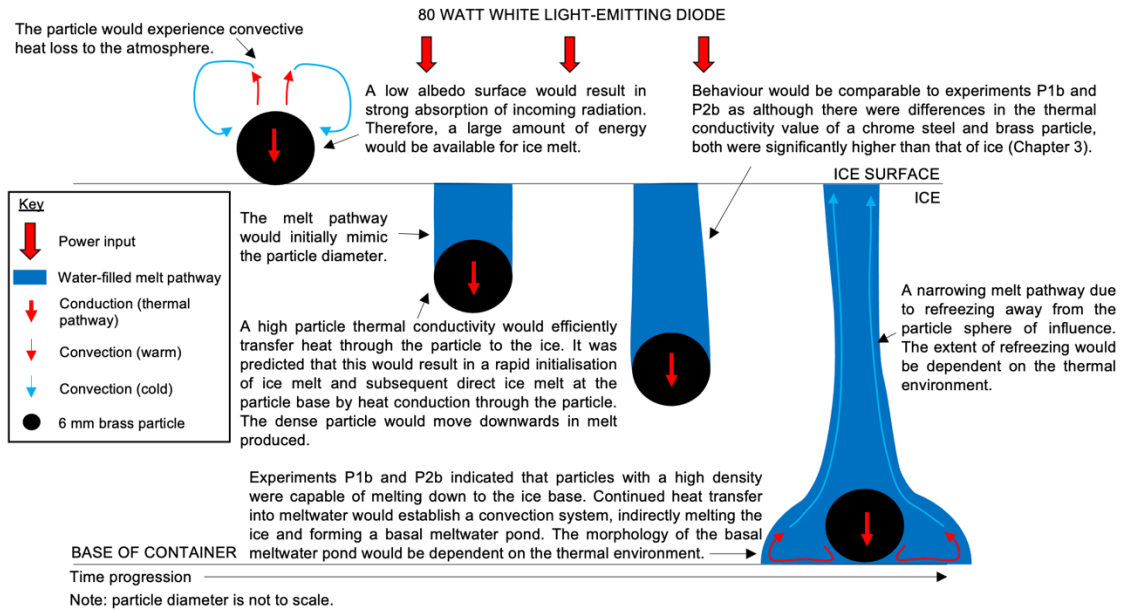


Figure 4.7. Schematic cross-sectional view of the hypothesised particle-ice interaction in experiment P3.

4.1.2.1. Results and interpretation

Exposure issues with the time-lapse camera limited time-lapse image quality and so results relied on in-person observations. The P3 particle immediately transferred heat into the ice to increase the ice temperature to PMP, causing ice melt. This resulted in a downwards particle movement in meltwater with a mean particle velocity of $2.35 \times 10^{-6} \text{ m s}^{-1}$ to reach the ice base within eight hours.

4.1.2.2. Melt pathway

The melt pathway width initially approximated the particle diameter (approximately 6 mm); this was indicative of conduction-driven ice melt as increased convection-driven ice melt would likely result in a widened melt pathway. Additionally, the presence of a strongly reflective region above the particle was identified approximately five hours after the experiment start. This was interpreted as gas space due to large differences in refractive indices between gas and water (i.e. 1.30 and 1.00, respectively) and was indicative of draining meltwater. This continued to drain as the particle moved downwards through the ice to create a gas-filled channel within the ice. Similar to experiment P2b, the melt pathway narrowed at the top to a minimum of approximately 2 mm. In-person observations noted that this narrowed prior to drainage, suggesting refreezing conditions. Although the melt pathway

remained open at the ice surface, this was due to drainage processes removing meltwater and preventing full refreezing of the melt pathway. Therefore, it was deduced that the P3 particle experienced a stable (cool) thermal environment.

A similar drainage process was also observed in experiment P2b, conducted on the same ice block. Therefore, it was interpreted that the drainage process relied on the internal structure of the ice block (e.g. the vein network) and the possibility of spaces for the water to drain into (e.g. between the ice block and container, or from a leak in the plastic container).

4.1.2.3. Basal meltwater pond

The P3 particle melted the basal ice and moved laterally within the ice. However, movement was not within meltwater; instead, the particle melted ice through direct heat transfer between the particle and the ice with minimal meltwater (likely a result of active drainage processes). This created a gas-filled channel along the ice base (in addition to the gas-filled melt pathway extending vertically through the ice, Figure 4.8).

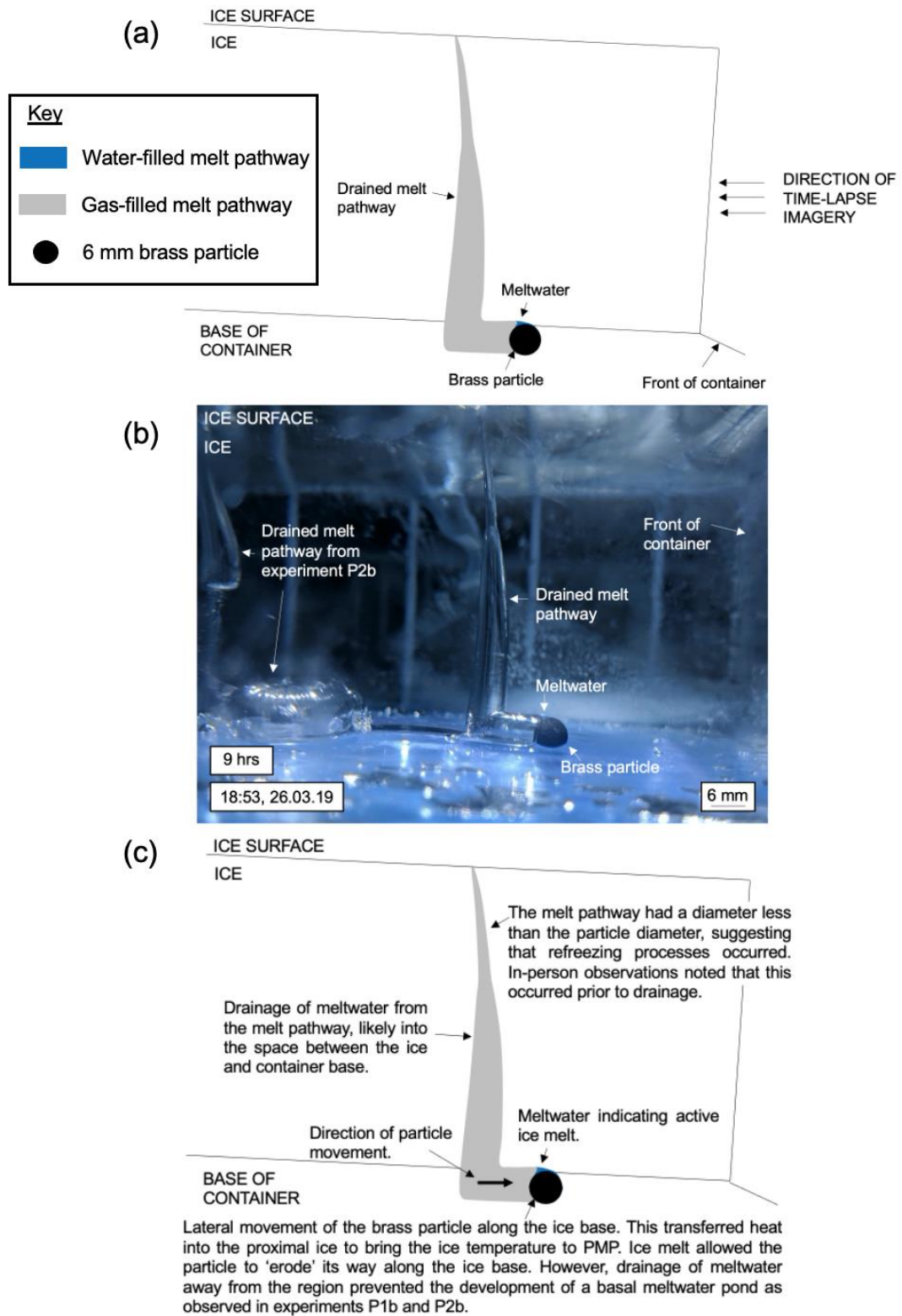


Figure 4.8. Images showing lateral movement of the P3 particle when on the ice base within a drained melt pathway. (a) observational line diagram, (b) photograph and (c) interpretation of the features.

The particle remained stationary for approximately eight hours after reaching the ice base. Heat transfer from the stationary particle created a basal meltwater pond that had a width and height of approximately 10 mm and 8 mm, respectively. This was dome-shaped in morphology and had similar dimensions to the basal meltwater pond in experiment P1b, suggesting this morphology was typical of a thermally conductive particle within a stable (cool) thermal environment.

The P2b particle was also on the ice base from the previous experiment and absorbed incoming radiation. Consequently, the P2b particle transferred heat into the surrounding ice to create a basal meltwater pond whilst the P3 particle was descending through the ice. P2b particle movement within the basal meltwater pond caused lateral ice melt (a process also observed in experiment P1b). The P2b basal meltwater pond eventually combined with melt from the P3 particle to form a larger volume of basal melt (approximately 120 mm in width and 12 mm in height), topped by the P2b and P3 open melt pathways. This resulted in meltwater filling the gas-filled melt pathway previously made by lateral movement of the P3 particle along the ice base. The connected basal meltwater pond was larger than that seen in experiments P1b and P2b and was likely a result of combined heating effects from two particles (Figure 4.9). This demonstrated the capability of multiple particles to form a hydrological connection.

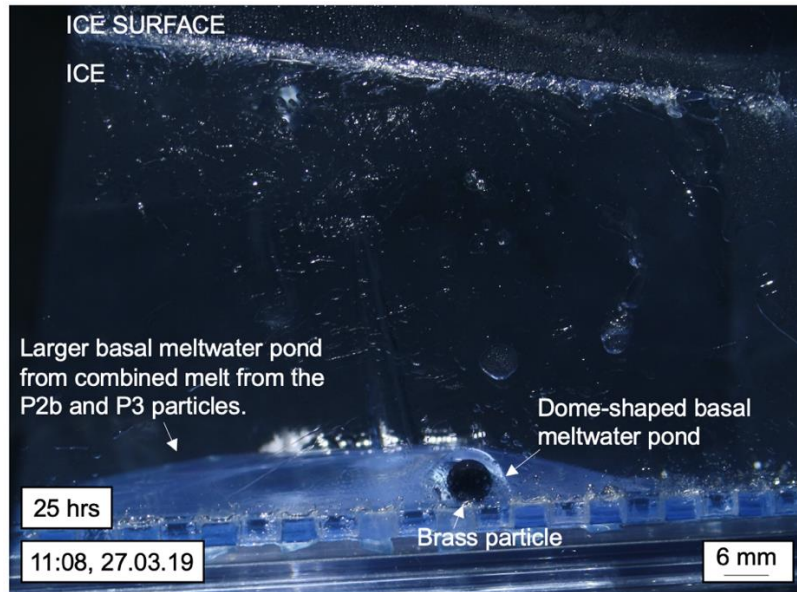


Figure 4.9. Cross-sectional photograph of the dome-shaped basal meltwater pond created by the P3 particle and the combined area of melt from the P2b and P3 particles.

To confirm that the presence of meltwater was a result of particle-ice interaction, the illumination was turned off and the experimental system was left for 24 hours. Observations demonstrated that all meltwater had refrozen in this period, confirming that meltwater generated was through melting of ice from particle heat transfer and that the ice was in a stable solid state.

4.1.2.4. Summary

Results from experiment P3 compared well with the hypothesised outcomes (i.e. downwards movement of the particle to reach the ice base and create a basal meltwater pond with a refreezing melt pathway). This experiment also provided an insight into the hydrological connections that form between particles, resulting in a greater extent of ice melt. This aided the method development process and showed the need to shield particles from previous experiments from illumination in future experiments when single particles were investigated. Additionally, experiment P3 provided insights into drainage events, confirming that these events were likely controlled by the ice structure itself.

This experiment type was repeated a further four times (experiments P4, P5, P6, and P7) to confirm findings. These demonstrated a variability in results, likely representing the complexities associated with particle-ice interaction and

the importance of thermal environment as a control on particle behaviour (Table 4.2). Other complexities were also present, e.g. P4 exhibited a staggered progression of ice melt, whilst experiments P6 and P7 experienced significant drainage events that modified the internal structure of the ice systems. Experiment P5 demonstrated steady downwards movement with refreezing events. It was noted that refreezing of the melt pathway created gas bubbles within the ice along the particle trajectory, indicating the 'fossil' melt pathway and modifying the optical properties of the ice.

Table 4.2. Summary of key features observed in experiments P4, P5, P6, and P7.

Experiment	Duration of downwards movement (hours)	Particle velocity (m s ⁻¹)	Melt pathway morphology	Basal meltwater pond		Thermal environment
				Width (mm)	Height (mm)	
P4	68-140	-	Teardrop. Photographs unclear due to camera focusing issues.	8	9	Stable (cool)
P5	17	1.03 x 10 ⁻⁶	Teardrop, along an inclined trajectory (lateral movement by approximately 3 mm).	8	8	Stable (cool). Equilibrium system established with ice (i.e. a stable volume of meltwater).
P6	12	1.87 x 10 ⁻⁶	Open at ice surface and partially drained when particle reached the ice base.	75	10	Stable (warm)
P7	18	1.32 x 10 ⁻⁶	Closed at ice surface and partially drained. Photographs unclear due to high number of bubbles within ice.	16 (total of 90 if considering accumulation of drained meltwater).	8	Stable (cool)

The staggered motion in experiment P4 was likely a result of the particle nearing the boundary of the stable (cold) thermal environment. Subtle differences in the temperature caused an environment shift (e.g. from stable (cool) to stable (cold), and vice versa), causing a shift in motion or static behaviour. Observations indicated that stalled phases were longer than particle movement phases (e.g. an average of 14 hours compared to 3 hours). There did not appear to be any correlation with diurnal cycles as movement phases were observed in both day and night periods.

Experiment P6 provided an insight into drainage and melt initialisation processes. This demonstrated fluctuations in particle velocity where the velocity was slower than $1 \times 10^{-6} \text{ m s}^{-1}$ for the first 2.5 hours of the experiment and increased throughout the experiment. The slower particle velocity during the first 2.5 hours was associated with the top surface of the particle being exposed at the ice surface. The particle velocity increased after the particle moved to a depth below 6 mm into the ice (and, therefore, was fully submerged). This was interpreted to be a result of removing heat loss mechanisms to the atmosphere, allowing all absorbed energy to be available for transfer to the ice.

Experiments P6 and P7 demonstrated the complex nature of drainage events. Downwards movement of the P6 particle to reach the ice base coincided with the development of a strongly reflective region within the time-lapse images. It was interpreted that this was from strong differences in refractive indices of ice and gas caused by a gas-filled melt pathway. The evolution from water-filled to a gas-filled pathway was due to drainage events, facilitated by the P6 particle melting the basal ice and providing a pathway for drainage to spaces between ice and container. Drainage in experiment P7 differed as drainage occurred during particle descent, prior to the particle melting a drainage route at the base. This could suggest that drainage of meltwater in this case was through the vein network within the ice. Ultimately, P6 and P7 indicated that the drainage events were complex as multiple processes were observed (Figure 4.10).

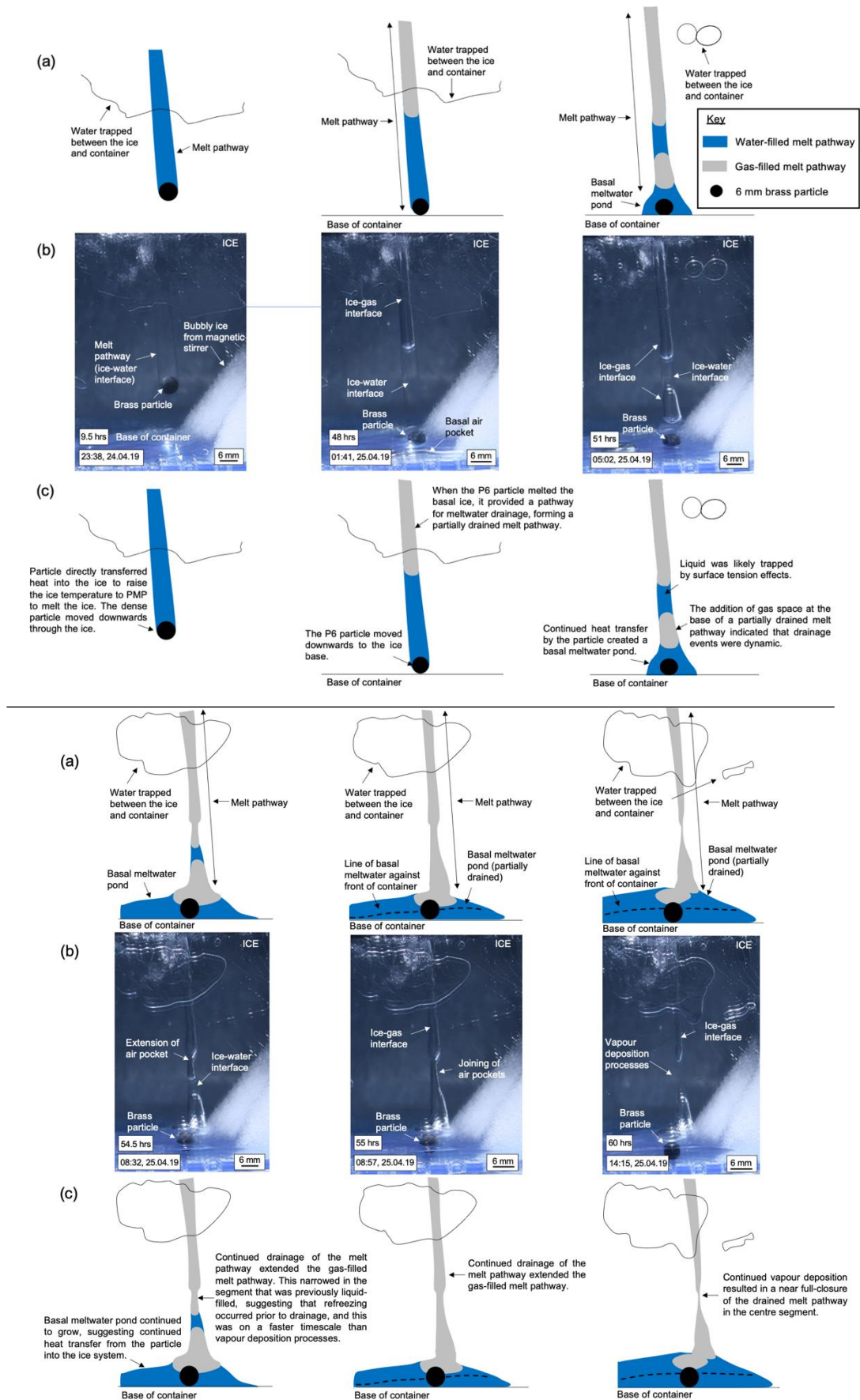


Figure 4.10. Images showing the melt pathway development over six periods in experiment P6. (a) observational line diagram, (b) photograph and (c) interpretation of the features.

4.1.3. P8: two thermally conductive brass particles

Experiment P8 directly compared behaviours of two (described below as particle 1 and particle 2) 6 mm brass particles. Previous experiments indicated the importance of ice structure in influencing particle-ice behaviour, and so experiment P8 was conducted to assess how the background ice structure may influence the behaviour of identical particles within the same ice system. These were placed on the ice surface sufficiently far apart to prevent particle-particle interaction but with an equal focus of illumination. The hypothesis for experiment P8 is shown in Figure 4.11.

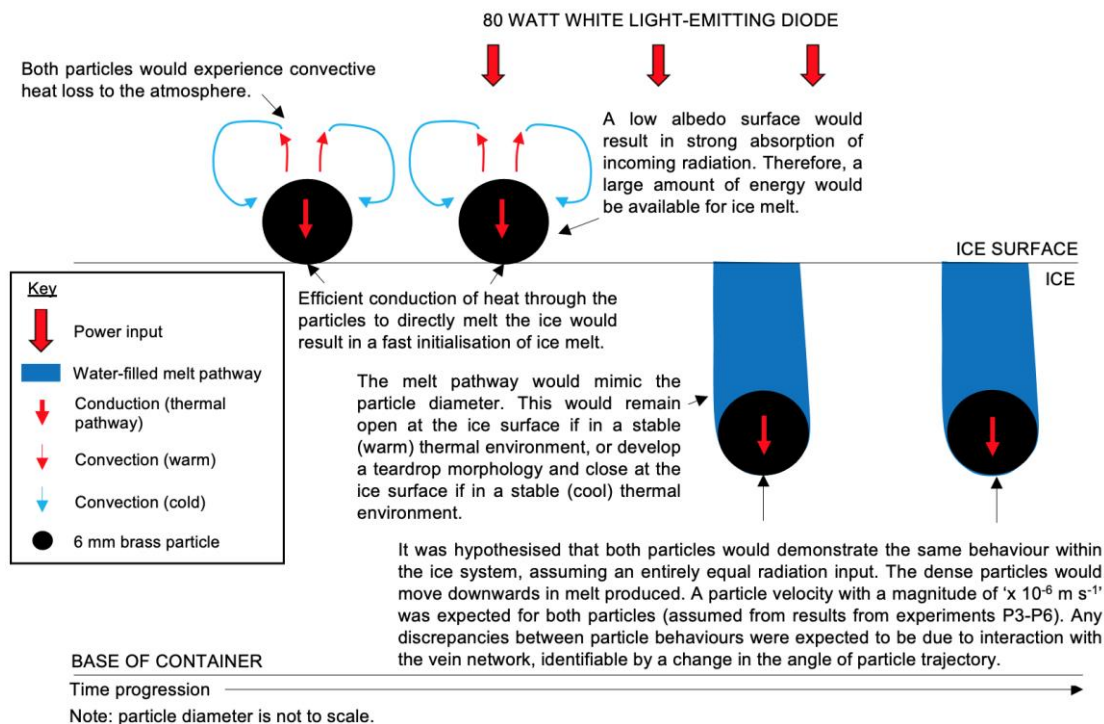


Figure 4.11. Schematic cross-sectional view of the hypothesised particle-ice interaction in experiment P8.

4.1.3.1. Results and interpretation

Condensation on the freezer surface prevented clear time-lapse images in hour 6-27 (with an exception from hour 23-25). Therefore, the detail of downwards particle movement relied on in-person observations. This indicated that the particles immediately melted the ice after surface placement and became fully submerged within meltwater within 1.5 hours (Figure 4.12). Although it was hypothesised that both particles would melt the ice at an equal rate, differences between their particle-ice interactions were observed. Similar initial patterns were observed until the particle 2 velocity increased relative to particle 1 after

hour five. This was a result of particle 1 remaining stationary near the ice surface for approximately three hours. Additionally, it was noted that both particles experienced lateral movement within the ice (e.g. particle 1 moved approximately 7 mm, whilst particle 2 moved approximately 3 mm). This suggested that the particles intercepted the vein network within the ice.

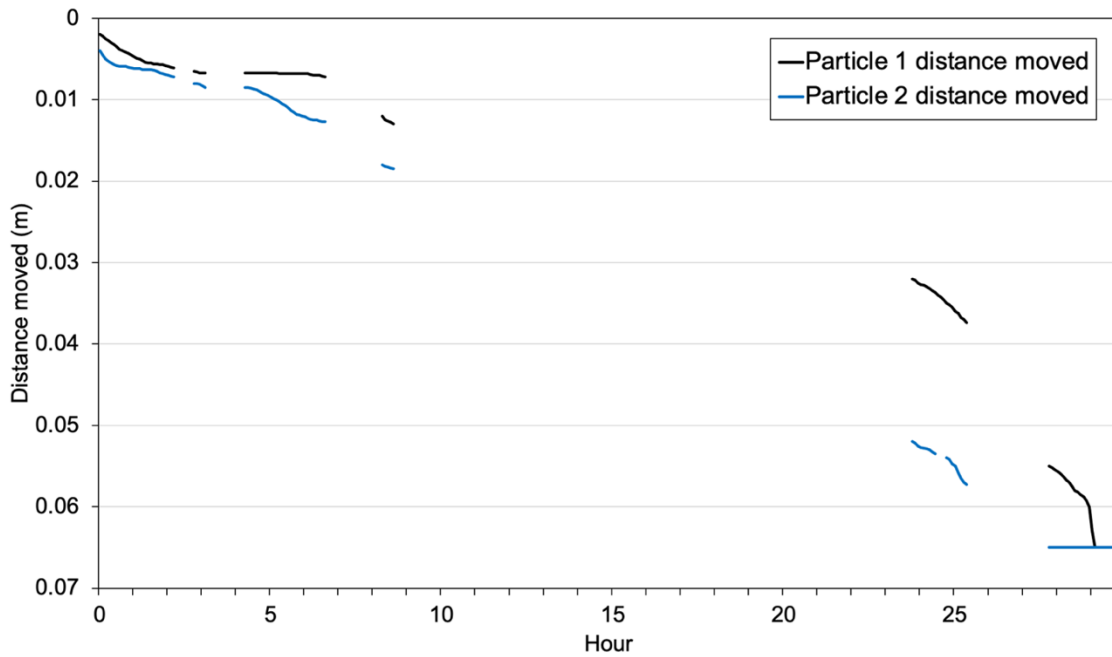


Figure 4.12. Graph showing the vertical distance moved by two 6 mm brass particles in experiment P8. Condensation on the freezer surface prevented continuous data extraction.

4.1.3.2. Melt pathway

Both melt pathways started to refreeze within three hours, creating a melt pathway with a teardrop morphology. This suggested that both particles experienced a stable (cool) thermal environment, and allowed for the development of bubbles within the ice indicating the ‘fossil’ melt pathway near the ice surface. However, a change in the particle 1 melt pathway morphology was noted after hour 25, indicative of a positive shift along the thermal range into a stable (warm) environment (Figure 4.13). This may have facilitated a higher particle 1 velocity in the last hour of the experiment.

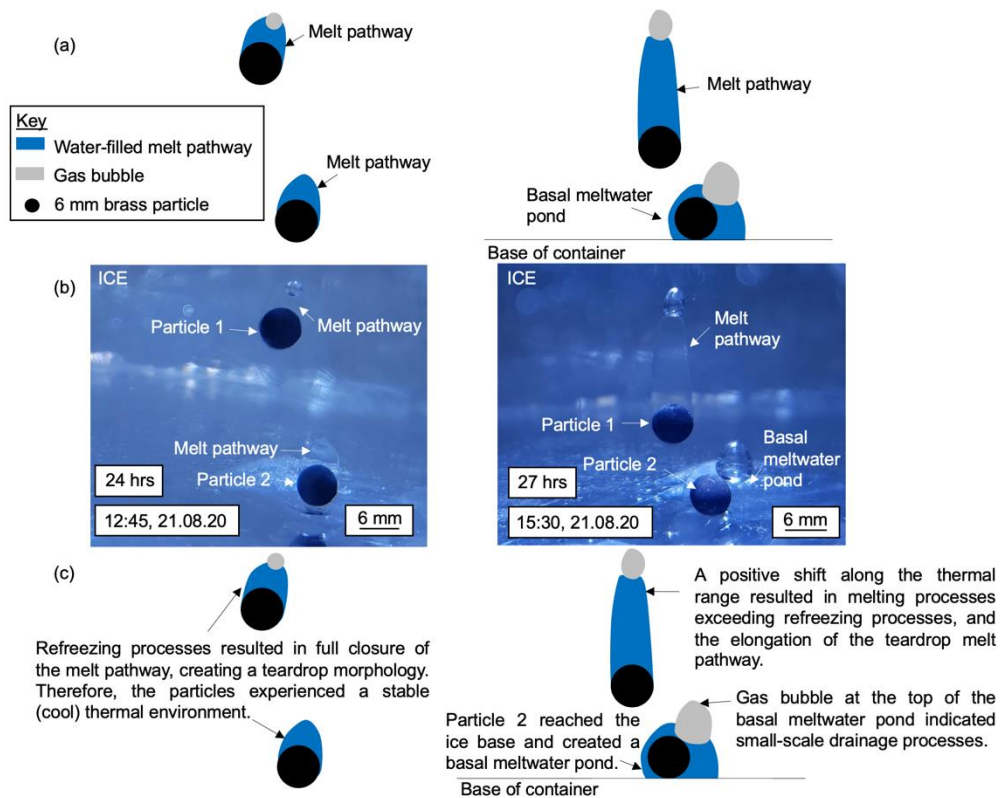


Figure 4.13. Images of teardrop melt pathway morphology and positive shift across the thermal range in experiment P8. (a) observational line diagram, (b) photograph and (c) interpretation of the features.

4.1.3.3. Basal meltwater pond

Particle 2 created a hemispherical basal meltwater pond (similar in morphology to previous experiments with particles in the stable (cool) thermal environment, e.g. P4 and P5) as particle 1 continued to move downwards through the ice (Figure 4.14). This allowed particle 1 to drop downwards by 5 mm into meltwater to reach the ice base.

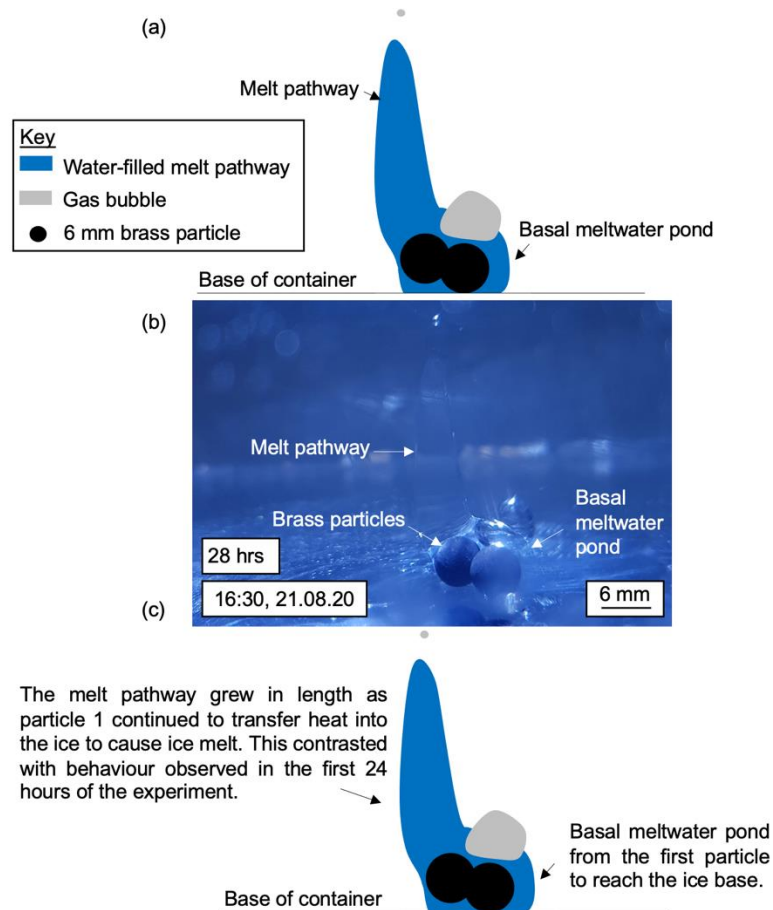


Figure 4.14. Images of basal meltwater pond and growing melt pathway. (a) observational line diagram, (b) photograph and (c) interpretation of the features.

4.1.3.4. Summary

Results from experiment P8 indicated a difference between the downwards movement of the two particles, despite being of the same composition and exhibiting the same fundamental behaviours (e.g. sinking in meltwater). Unclear time-lapse images prevented thorough assessment of particle movement, but broad insights demonstrated that both particles moved laterally as they descended through the ice. This was indicative of the particles utilising the vein network within the ice. However, the difference between particle results was attributed to particle 1 stalling at the ice surface (almost fully submerged) for three hours. It is likely that the particles were experiencing a thermal environment close to the stable (cold) boundary in the first 25 hours of the experiment. The particles were especially sensitive to subtle changes in temperature in this region of the thermal range. Particle sensitives to subtle shifts along the thermal environment range will be investigated in future experiments.

Experiment P9 was conducted as a repeat of experiment P8 due to unexpected results. Similar to experiment P8, the particles experienced a variable thermal environment. However, this was a negative shift from a stable (warm) thermal environment into a stable (cold) thermal environment and occurred when particle 2 was on the ice base and particle 1 was approximately 5 mm above the ice base. The shift across the thermal range was identified by the change from melt pathways that extended upwards to the ice surface with no indication of refreezing processes, to entirely refrozen melt pathways and the absence of meltwater surrounding the particles; this also caused particle 1 to stall within the ice prior to reaching the base (Figure 4.15). However, despite this shift in thermal environment, it was evident that there was a difference between the behaviour of the two particles. This was particularly clear after the first two hours where, prior to this, both particles moved downwards with relatively equal particle velocities. However, after this, particle 2 moved downwards through the ice at a higher particle velocity than particle 1. The increase in particle 2 velocity relative to particle 1 was associated with an inclined melt pathway (with a total lateral movement of approximately 9 mm), suggesting that particle 2 intercepted the vein network within the ice. This may have facilitated a higher particle velocity as the vein network would be more active in the stable (warm) thermal environment.

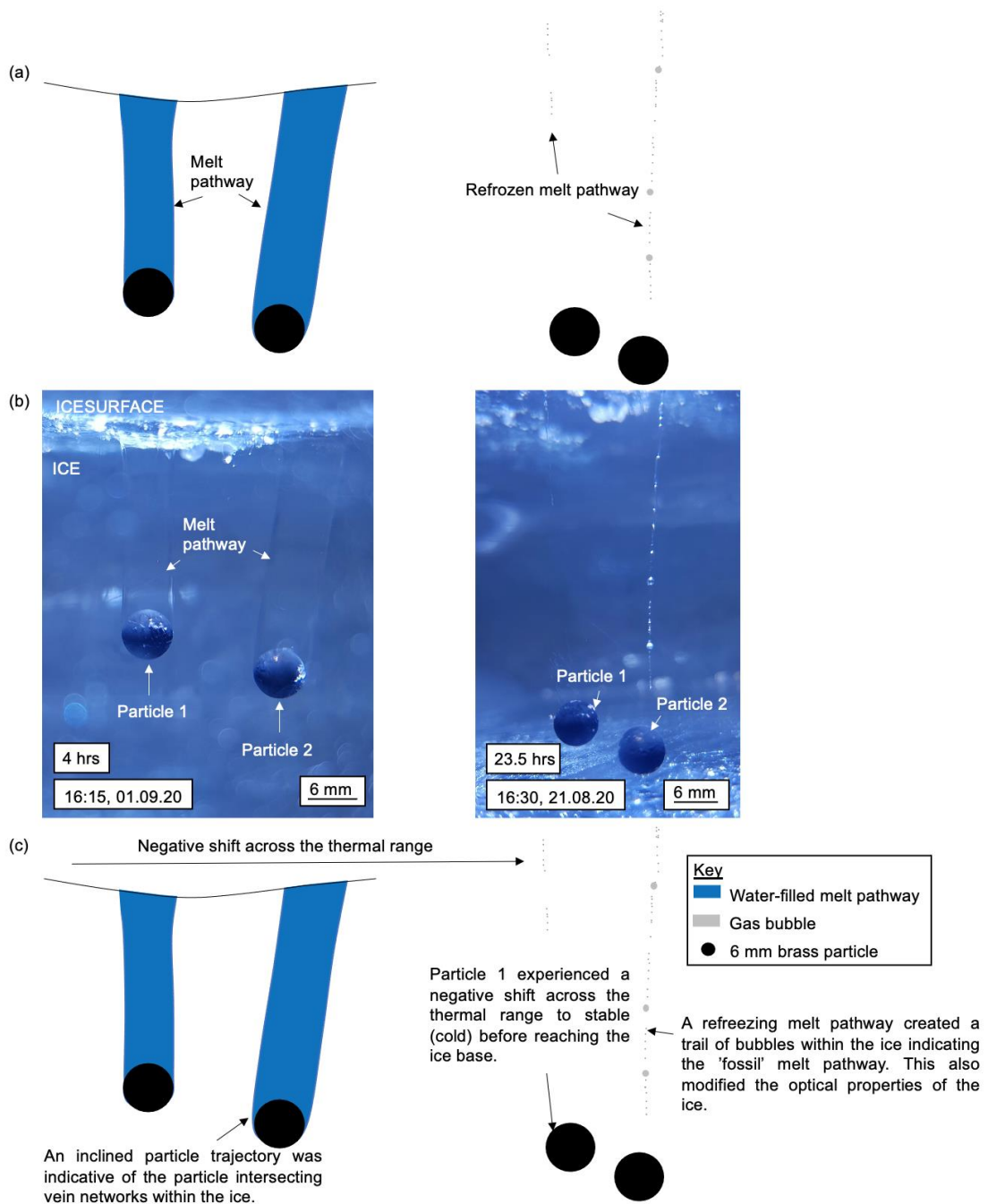


Figure 4.15. Images indicating the shift from stable (warm) to stable (cool) in experiment P9, identified by open melt pathways and refreezing melt pathways, respectively. (a) observational line diagram, (b) photograph and (c) interpretation of the features.

Experiments P8 and P9 suggested that the particle thermal environment may be a key control on particle-induced ice melt. There were differences between the two particle velocities in both experiments that were suggested to be due to stalled particle movement in experiment P8 (likely due to the position on the thermal range), and the internal structure of the ice (identified by an angled trajectory associated with a faster particle) in experiment P9. The angled

trajectory has been identified in previous experiments as a feature of particles utilising veins within ice to facilitate downwards movement. However, this may not have facilitated faster particle movement in experiment P8 as the ice was cooler and the vein network was likely less prominent.

4.1.4. P48: a thermally conductive brass particle within opaque ice

This experiment was conducted as a control experiment where a 6 mm brass particle was placed on the ice surface of an opaque (i.e. bubble-rich) ice block. This was to assess if the presence of bubbles within ice had an influence on particle-ice interaction. The hypothesis for experiment P48 is shown in Figure 4.16.

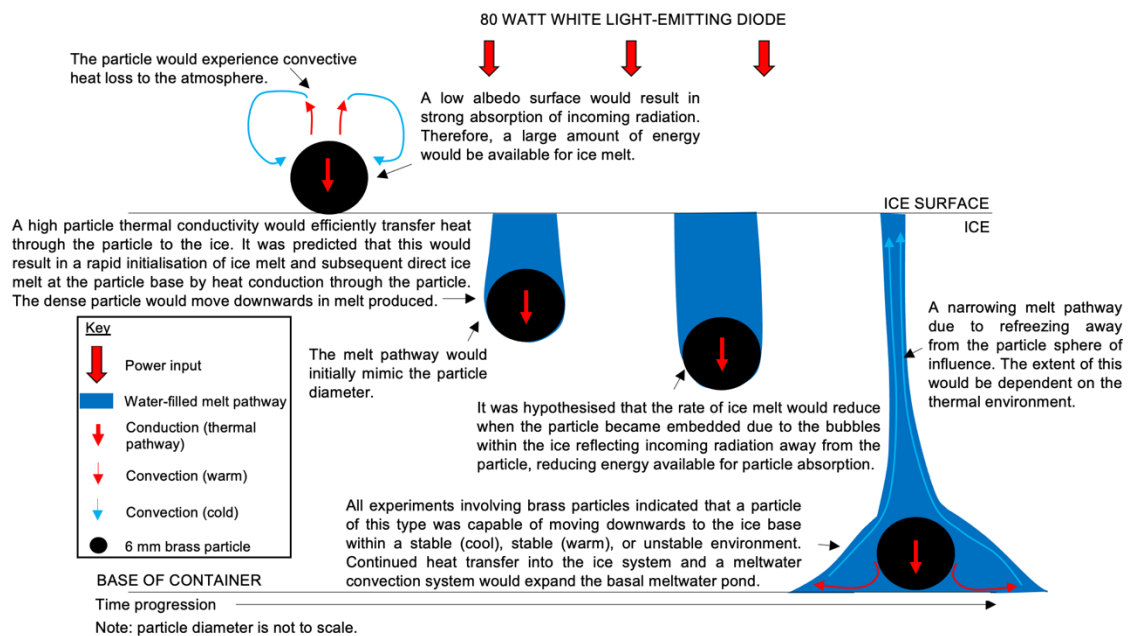


Figure 4.16. Schematic cross-sectional view of the hypothesised particle-ice interaction in experiment P48.

4.1.4.1. Results and interpretation

Initialisation of particle-ice interaction was similar to previous experiments, where an immediate downwards movement of the particle was observed. This caused downwards particle movement with a velocity of $1.75 \times 10^{-6} \text{ m s}^{-1}$ to reach the ice base within nine hours (Figure 4.17). However, the velocity appeared to decrease momentarily as the particle became fully submerged, although it is important to note the difficulties of obtaining values of particle movement from imaging opaque ice.

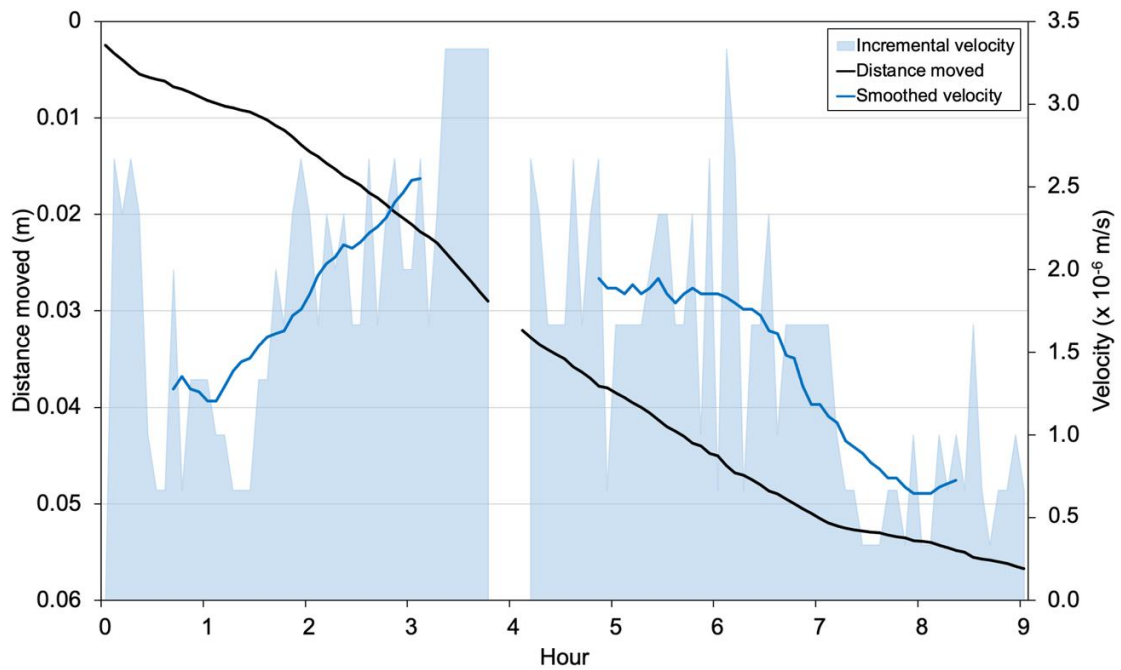


Figure 4.17. Vertical distance moved and velocity of a 6 mm brass particle in experiment P48.

4.1.4.2. Melt pathway

The melt pathway had a similar width to the particle diameter (i.e. approximately 6 mm) and was open at the ice surface throughout the experiment (Figure 4.18). Therefore, no refreezing was observed, and it was deduced that the P48 particle experienced a stable (warm) thermal environment. Bubbles within the ice limited the clarity of time-lapse images and so detailed analysis of the melt pathway could not be conducted.

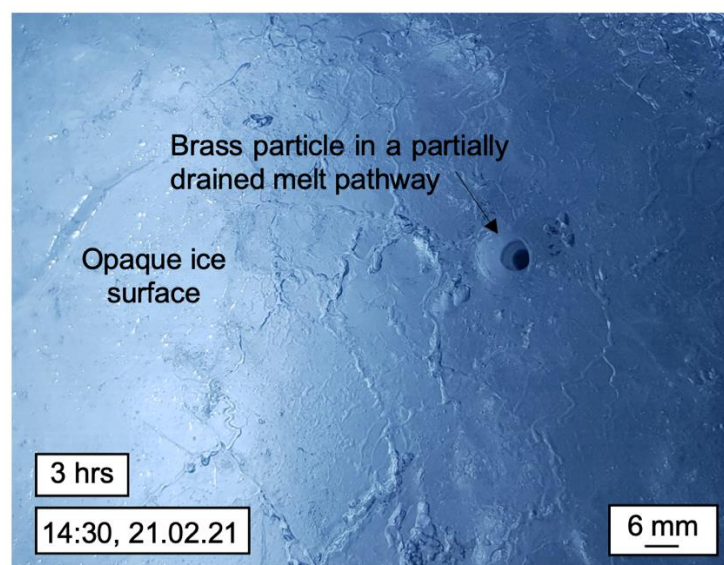


Figure 4.18. Plan-view photograph of the P48 open melt pathway at the ice surface.

4.1.4.3. Basal meltwater pond

The P48 particle continued to transfer heat into melting the ice when on the ice base to create a basal meltwater pond (width and height of approximately 25 mm and 8 mm, respectively). Lateral particle movement by approximately 21 mm was observed, indicating heat transfer between the particle and basal ice. This suggested that the particle was able to absorb incoming radiation, despite being overlain by opaque ice with a high number of interfaces. In addition to the basal meltwater pond formed by the P48 particle, there was a shallow (approximately 3 mm) basal meltwater pond that extended across the entire base of the ice block. This formed prior to the particle reaching the ice base by meltwater draining through the ice, likely facilitated by many gas spaces within the ice.

4.1.4.4. Summary

A particle velocity of $1.75 \times 10^{-6} \text{ m s}^{-1}$ was comparable with many of the experiments in this experimental series, and similar features were observed (e.g. a melt pathway with the same width as the particle diameter and development of a basal meltwater pond). Therefore, results suggested that the influence of opaque ice on particle-induced ice melt was relatively low.

4.1.5. P49: a cooled thermally conductive brass particle

Experiment P49 was conducted as a control experiment to assess the behaviour of a cooled particle when placed on the ice surface. This differed from previous experiments where particles were at room temperature during placement, as the P49 particle was placed within the chest freezer (operating at temperatures -0.2 to 0.0°C) approximately three hours prior to surface placement. The removal of the effect from initial heating by a room temperature particle allowed the initialisation of melting to be assessed. The hypothesis for experiment P49 is shown in Figure 4.19.

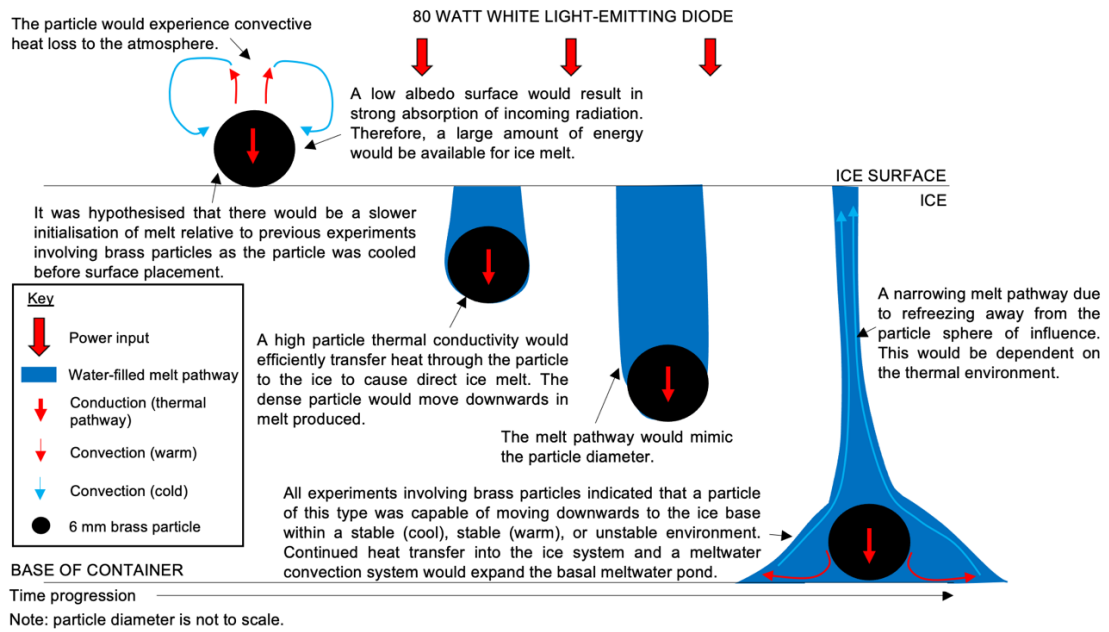


Figure 4.19. Schematic cross-sectional view of the hypothesised particle-ice interaction in experiment P49.

4.1.5.1. Results and interpretation

The P49 particle moved downwards into the ice immediately and was fully submerged approximately 40 minutes after surface placement. The particle moved with a velocity of $2.07 \times 10^{-6} \text{ m s}^{-1}$ to reach the ice base within 6.5 hours (Figure 4.20). Therefore, there did not appear to be any lag associated with particle placement when the particle was cold.

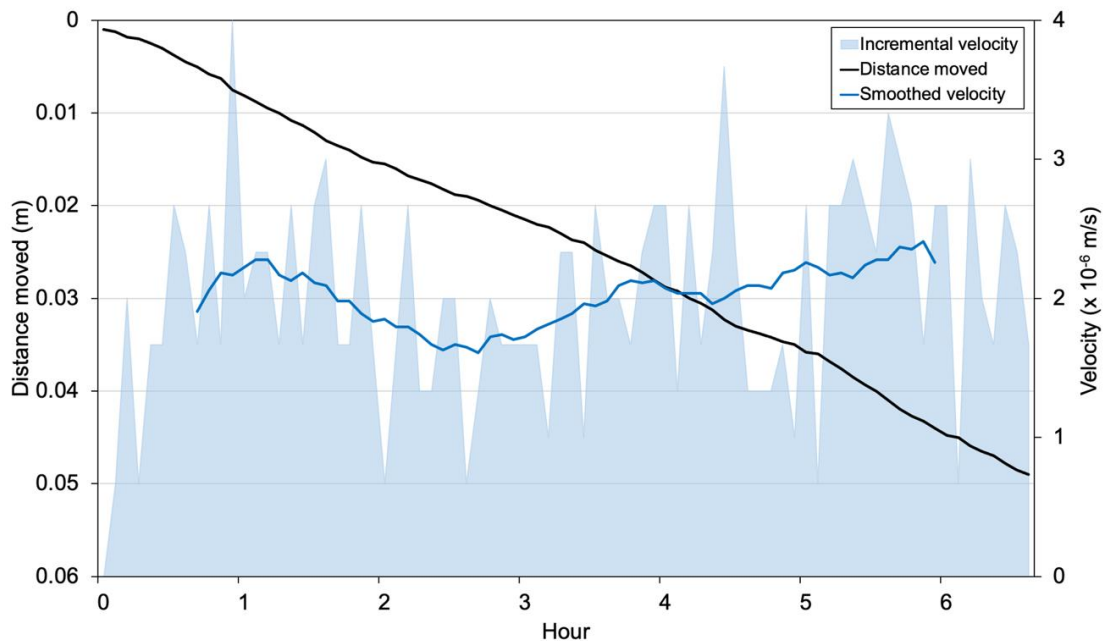


Figure 4.20. Vertical distance moved and velocity of a 6 mm brass particle in experiment P49.

4.1.5.2. Melt pathway

As in all previous experiments, the melt pathway had a similar width to the particle diameter. Fluctuations in water level within the melt pathway occurred throughout the experiment, representing a balance between drainage and particle-induced ice melt.

4.1.5.3. Basal meltwater pond

The particle continued to melt the ice after reaching the ice base to create a basal meltwater pond (Figure 4.21). This had a similar morphology to that observed in experiment P6, although the basal meltwater pond in experiment P49 was entirely water-filled.

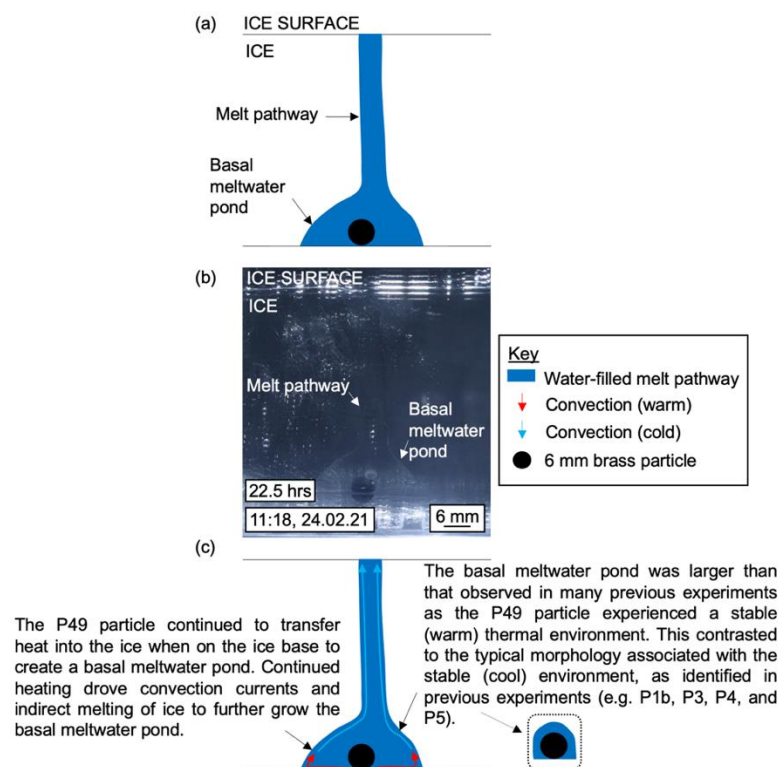


Figure 4.21. Images of the melt pathway and basal meltwater pond associated with the P49 particle. (a) observational line diagram, (b) photograph and (c) interpretation of the features.

4.1.5.4. Summary

This experiment provided an insight into the initialisation of particle-induced ice melt and determined that there was a negligible difference between a cooled particle and a particle placed on at room temperature. This exhibited many of the same features as observed in other experiments with particles within the

stable (warm) thermal environment (e.g. an open melt pathway, drainage events, and the development of a basal meltwater pond).

4.2. Albedo

This set of experiments investigated the role of particle albedo on particle-ice interaction (Figure 4.22, Table 4.3). Low albedo (LA), intermediate albedo (IA) and high albedo (HA) particles were assessed. These were matte black, unpainted, and white, respectively. All particles were 6 mm in diameter and brass spheres to allow the property of albedo to be investigated in isolation, except for experiment P10 where an 8 mm chrome steel, HA unpainted, particle was used.

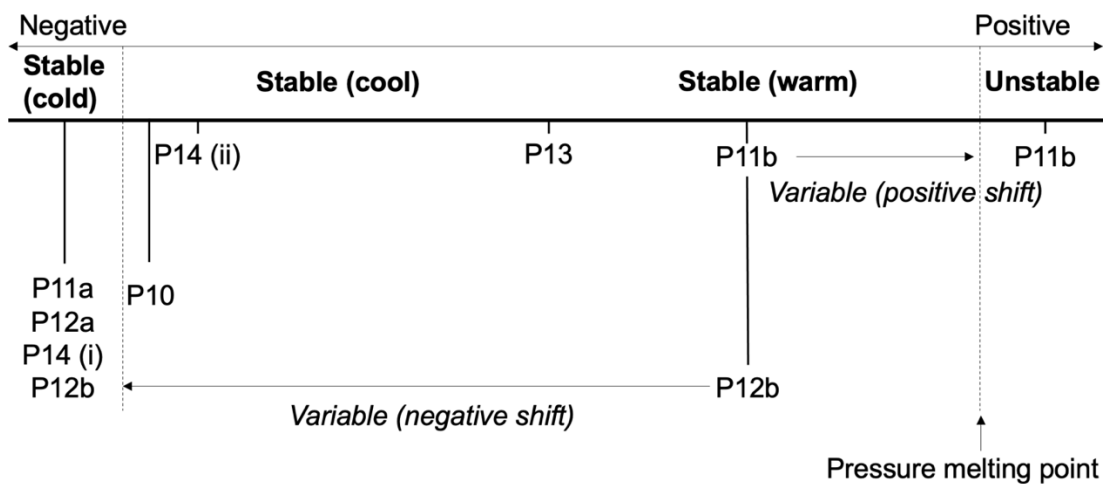


Figure 4.22. The thermal environment of particles in experiments investigating the role of particle albedo in influencing particle-ice interaction. Experiment position has been derived from interpretation of observations, as described in Chapter 3, Section 3.7.

Table 4.3. A summary of experiments investigating the role of particle albedo in particle-induced ice melt, highlighting the types of particles used and the associated thermal environments as defined in Chapter 3.

Experiment	Particle type	Thermal environment
P10	8 mm chrome steel (HA)	Stable (cool)
P11a	6 mm brass (LA)	Stable (cold)
P11b	3 x 6 mm brass (LA, IA, and HA)	Variable: stable (warm) to unstable
P12a		Stable (cold)
P12b	3 x 6 mm brass (LA, IA, and HA)	Variable: stable (warm) to stable (cold)
P13	3 x 6 mm brass (LA, IA, and HA)	Stable (warm)
P14	6 mm brass (IA)	Variable: stable (cold) in P14 (i) and stable (cool) in P14 (ii)

4.2.1. P10: a high albedo chrome steel particle

Experiment P10 assessed the behaviour of a high albedo (0.57) 8 mm chrome steel particle when placed on an ice surface. The hypothesis for experiment P10 is shown in Figure 4.23.

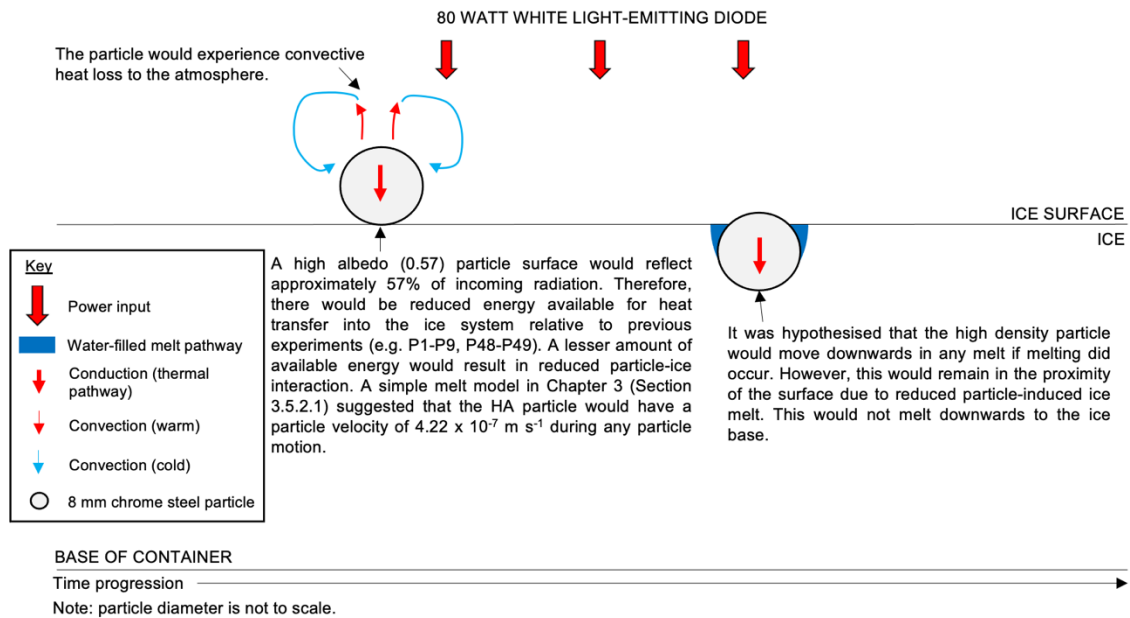


Figure 4.23. Schematic cross-sectional view of the hypothesised particle-ice interaction in experiment P10.

4.2.1.1. Results and interpretation

The time-lapse images indicated that the particle melted the ice to move downwards to a depth of approximately 13 mm over a 43-hour period with a mean velocity of $8.46 \times 10^{-8} \text{ m s}^{-1}$ (Figure 4.24). After this period, no movement was observed for the remainder of the experiment (23 hours). Initial melting from temperature differences between the particle and the ice contributed to approximately 2 mm of particle movement, and all subsequent melting was attributed to heat transfer between particle and ice. However, the particle remained stationary at a depth of ~2 mm for approximately six hours before active ice melt began, likely representing the initialisation of particle-induced ice melt as the particle-ice system thermally equilibrated.

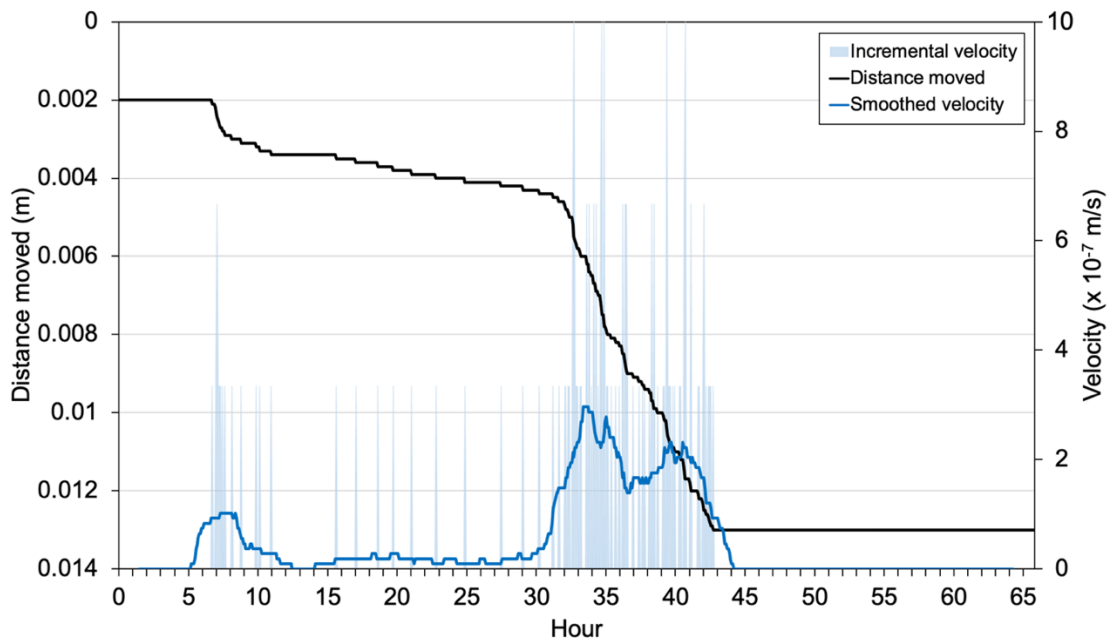


Figure 4.24. Vertical distance moved and velocity of the high albedo chrome steel particle in experiment P10.

Analysis of time-lapse images indicated that the particle moved downwards through the ice in a staggered manner, where alternating periods of stationary behaviour and active melt were observed. This behaviour was like that observed in experiment P4, although there appeared to be a reduced difference between the duration of each phase (e.g. active melt lasted approximately 6 hours on average, whilst stationary behaviour lasted approximately 9 hours on average).

4.2.1.2. Melt pathway

A small volume of meltwater was present during experiment P10, although this was only associated with periods of active melt (i.e. particle movement). Downwards particle movement and sustained ice melt during active melt phases created a melt pathway with a teardrop morphology, indicative of a stable (cool) thermal environment. The absence of meltwater during stationary phases was suggestive of a stable (cold) thermal environment. Therefore, the particle bordered the stable (cold) and stable (cool) thermal environment. This was likely the cause of the lower particle velocity observed than that hypothesised from the simple melt model, as this did not consider deviations from the PMP. Similar to interpretation in experiment P4, this could suggest that

the staggered behaviour was a result of subtle changes in the thermal environment. As the absorbing surface had a high albedo, less energy would be available for heat exchange with the ice system due to a high reflection of incoming radiation. Therefore, a lower rate of energy would be transferred into the ice; this would be insufficient to raise the ice temperature to PMP before conduction of energy from the region through the ice along a temperature gradient. However, subtle changes in the ice temperature would allow temperatures to be raised to PMP in some instances (i.e. in the 'active melt' phases).

4.2.1.3. Summary

Experiment P10 demonstrated that a particle with an albedo greater than 0.5 was capable of transferring sufficient energy into the ice to cause ice melt. However, there were several contrasts with the hypothesised outcome: (1) a lower particle velocity of $8.46 \times 10^{-8} \text{ m s}^{-1}$ was observed, and (2) the particle moved downwards in a staggered manner. These were suggested to be due to the particle bordering the stable (cool) and stable (cold) region of the thermal range. Direct comparisons of particles with different albedos will be assessed in subsequent experiments.

4.2.2. P11b: a comparison of a low albedo, intermediate albedo, and high albedo brass particle

Experiment P11b progressed from experiment P11a, where a low albedo (LA, 0.12) brass particle experienced a stable (cold) thermal environment, consequently limiting particle-ice interaction (aside from initial movement from temperature differences). It was deduced that cold freezer temperatures (and the need for the freezer to be defrosted) were responsible for the stable (cold) thermal environment, rather than particle properties hindering ice melt. The freezer was turned off, and an intermediate albedo (IA, 0.50) and high albedo (HA, 0.60) brass particles were placed on the same ice block as that used in P11a; this marked the start of experiment P11b.

Experiment P11b directly assessed the role of particle albedo on influencing ice-melt on a melting ice block (i.e. one at PMP and unstable in the solid state). The IA and HA particles were placed close to one another (with an 8 mm distance between each particle) to allow the same radiation input. However, the LA particle was already submerged in the ice at the start of P11b due to 15 mm of movement in experiment P11a. As identified in previous experiments (e.g. P1, P2, P3, etc.), particles of this type have a small sphere of influence (typically one particle diameter), and so could be placed at this distance without incurring measurable particle-particle interaction (i.e. thermal or physical) or hydrological connections forming during downwards movement. The hypothesis for experiment P11b is shown in Figure 4.25.

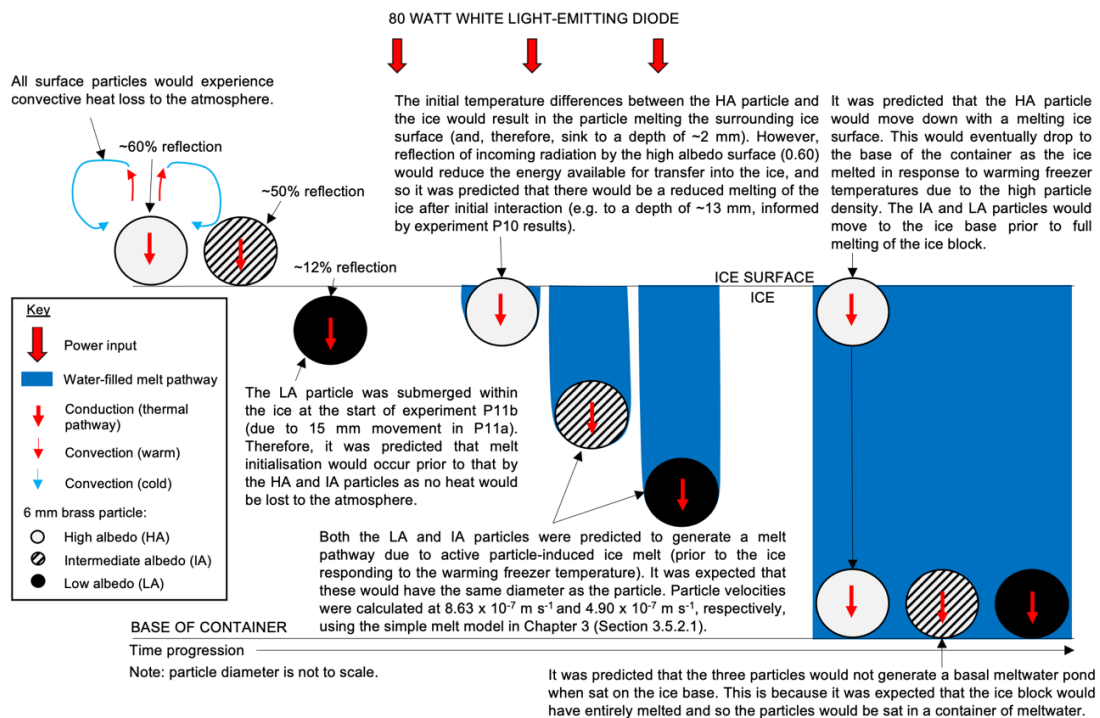


Figure 4.25. Schematic cross-sectional view of the hypothesised particle-ice interaction in experiment P11b conducted on an unstable ice block.

4.2.2.1. Ice surface lowering

The ice surface remained stable in the first hour of the experiment, representing the lag time before the ice responded to the increasing freezer temperatures (Figure 4.26). Following this, a 2 mm and 5 mm surface lowering was observed during LA and IA particle movement, respectively, and a total lowering by 14 mm was observed throughout the experiment. This suggested that independent

ice melt in response to warming temperatures occurred during particle movement. Therefore, it was deduced that the particles and ice were in an unstable thermal environment for much of the experiment. However, the presence of an undulating surface during LA and IA particle movement confirmed a solid ice surface during particle descent; if this had melted, then it would be expected that the surface would be level. It is important to note that the containers were not fully waterproof (due to the water expanding as it froze and putting strain on the edges of the container). Therefore, some surface lowering may have been a result of water loss from the container. However, the ice had melted in its entirety by the end of the experiment (e.g. 26 hours).

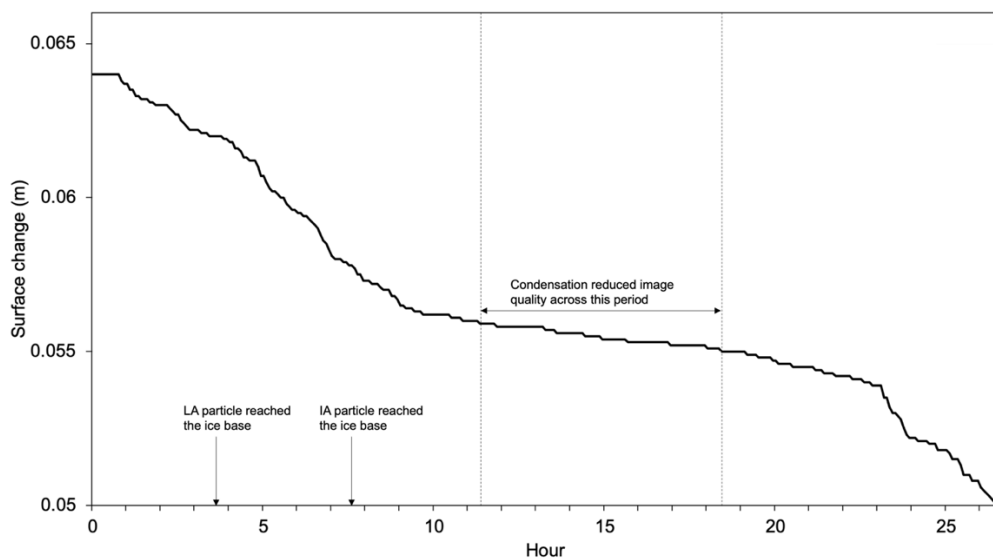


Figure 4.26. The change in the ice surface level as the ice melted during experiment P111b, transitioning from a solid-water phase to a liquid-water phase.

4.2.2.2. Results and interpretation

The LA and IA particles immediately melted the ice and moved downwards to reach the ice base within four and eight hours, respectively (Figure 4.27). Average particle velocities were calculated at $3.63 \times 10^{-6} \text{ m s}^{-1}$ and $2.32 \times 10^{-6} \text{ m s}^{-1}$, respectively. The smoothed velocity indicated that the LA particle movement was split into two main phases: an increasing velocity until approximately hour two (from $2.69 \times 10^{-6} \text{ m s}^{-1}$ to $4.07 \times 10^{-6} \text{ m s}^{-1}$), and a second phase where the velocity plateaued at approximately $3.90 \times 10^{-6} \text{ m s}^{-1}$. The first phase may reflect the particle coming into equilibrium with the ice system. Additionally, the IA particle velocity was consistently slower than the LA particle, indicating differences in heat transfer behaviour for LA and IA particles.

This compared well with the hypothesis that the partially reflective IA particle surface would not absorb as much incoming radiation as the LA particle. However, the IA particle velocity is much higher than that calculated from the simple melt model (and this is the case for both particles). This is likely due to the complexities that were not considered in the simple melt model, e.g. the interaction with the ice structure.

Analysis of the incremental velocity suggested that the initial velocity of the IA particle was lower than that of the LA particle in the first hour of the experiment (i.e. $1.92 \times 10^{-6} \text{ m s}^{-1}$ compared to $2.31 \times 10^{-6} \text{ m s}^{-1}$, respectively). This was likely a result of convective heat loss to the atmosphere experienced by the IA particle, whereas all heat absorbed by the LA particle would have transferred into the ice as it began submerged by 15 mm in the ice following from experiment P11a. It is expected that these differences in initial particle velocity would have been even greater if both particles experienced the same conditions as it was likely that surface placement of the IA particle at room temperature influenced the initial movement of the IA particle. However, these findings provided a useful insight into the process of surface versus embedded particle initialisation of melt.

The HA particle remained at the ice surface until ice melted independently in response to increasing temperatures and moved to the container base when full melting had occurred. Therefore, all three particles were at the container base within 26 hours (i.e. by the end of the recorded time-lapse imagery period). The time at which the HA particle reached the ice base could not be identified due to unclear images, although behaviour in the first 19 hours of the experiment showed minimal movement from particle-induced melt. Therefore, it was proposed that the HA particle moved with the surface lowering from melting ice and dropped into meltwater produced to the base of the container.

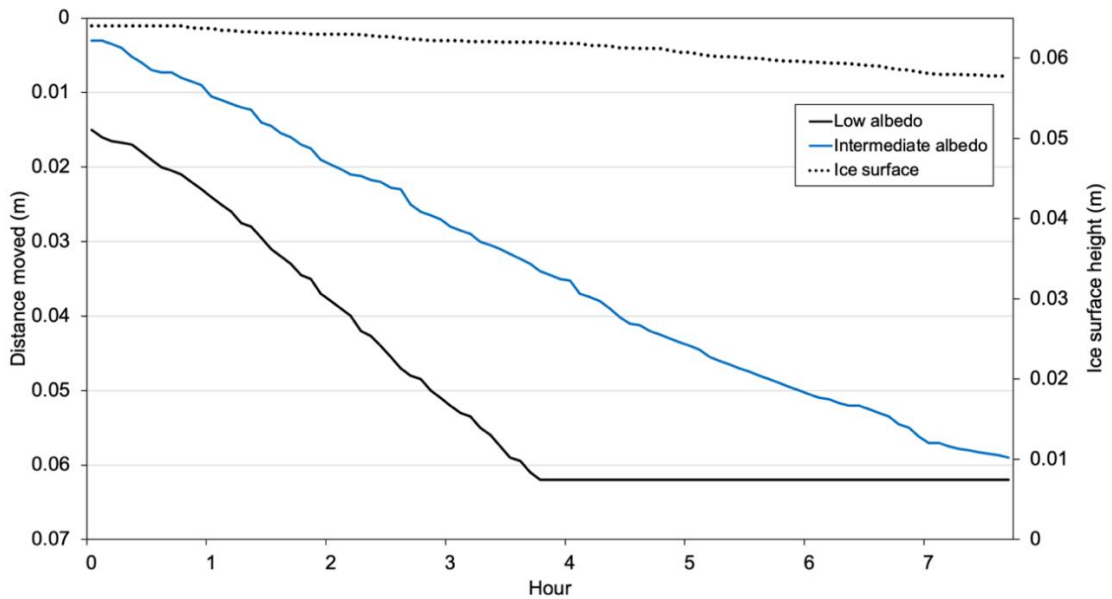


Figure 4.27. Vertical distance moved by a low and intermediate albedo 6 mm brass particle and the ice surface lowering. The intermediate albedo particle does not start at '0 m' due to initial temperature differences between the particles and the ice resulting in immediate melting prior to time-lapse imaging. The low albedo particle started submerged within the ice because it was used in experiment P11a. Data could not be retrieved for the high albedo particle from the time-lapse images due to a restricted view of the top of the ice block.

4.2.2.3. Melt pathway

The LA and IA particle melt pathways were visible for the first two hours of the experiment (Figure 4.28). However, melt was obscured by condensation as freezer temperatures increased, although intermittent removal of condensation revealed that the LA melt pathway extended upwards to the LA starting position for the duration of particle movement (suggesting that the ice had not melted in its entirety during LA particle movement). This suggested that the particle was melting the ice through particle-induced melt, agreeing with the hypothesis.

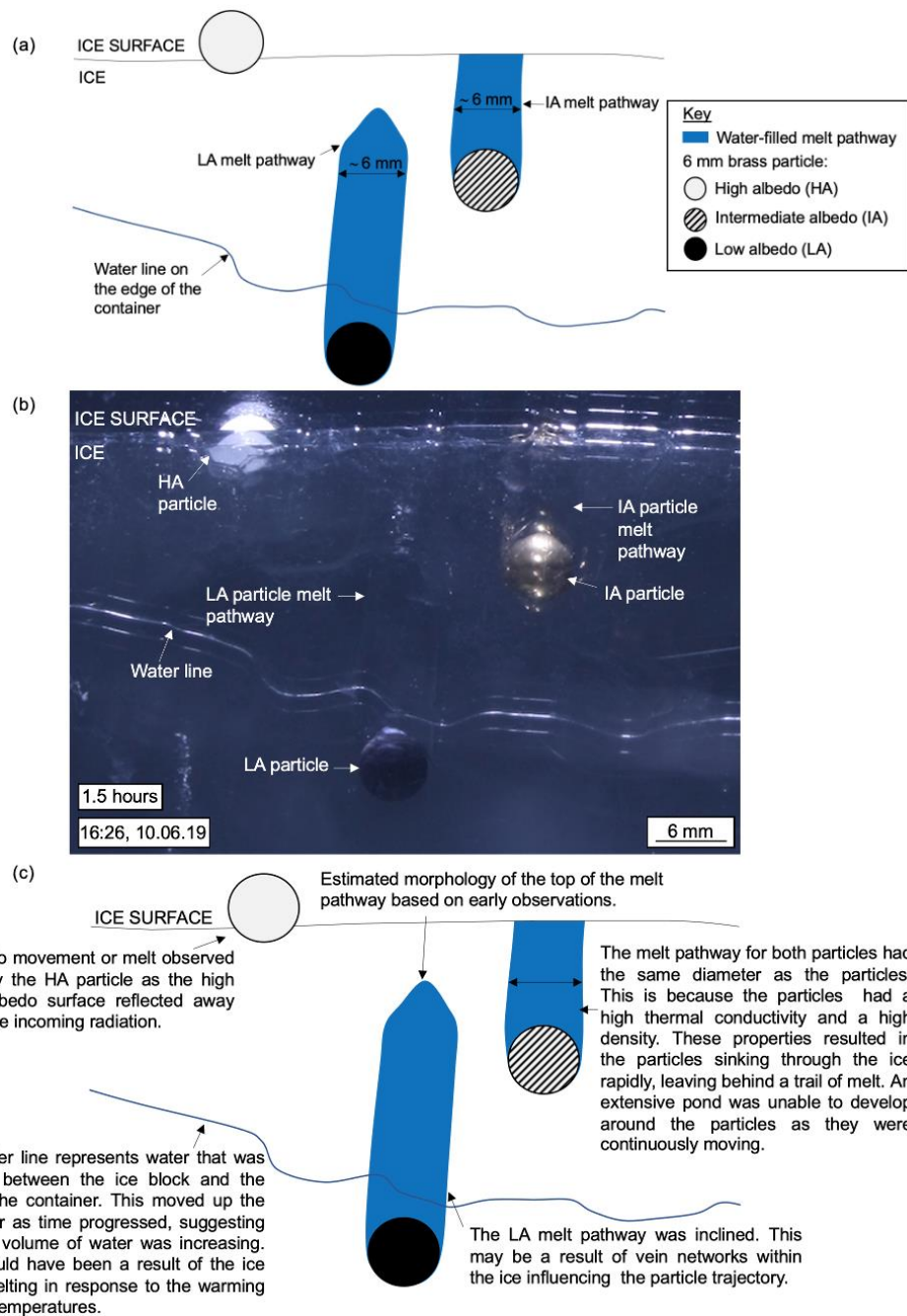


Figure 4.28. Cross-sectional images of the low albedo (LA) and intermediate albedo (IA) melt pathways in experiment P11b. (a) observational line diagram, (b) photograph and (c) interpretation of the features.

4.2.2.4. Summary

This experiment demonstrated how particles behaved in ice in a variable thermal environment, with a positive shift from a stable (warm) to an unstable environment. Results indicated that particle behaviour differed depending on the particle's albedo and compared well with the hypothesis that the HA particle would be incapable of moving downwards to the ice base from particle-induced

ice melt alone. Ultimately, bulk melting of ice dictated the positioning of the particles, as the HA particle eventually dropped to the container base when the ice melted (combined interpretation from this experiment and P10 suggested that it is likely that this would have otherwise remained near the ice surface). The presence of melt pathways created by the LA and IA particles suggested that particle-induced ice melt occurred prior to full independent ice melt. However, both had higher particle velocities than predicted by the simple melt model. It would be useful to compare the behaviour of different particle albedos in stable thermal environments.

Experiments P12b and P13 were conducted as repeat experiments and used the same particles as in experiment P11b. P12b followed on from experiment P12a, in which the HA, IA, and LA particles experienced a stable (cold) thermal environment and limited particle ice interaction. Experiments P12b and P13 were within a stable ice system, although the thermal environment between experiments (e.g. a variable thermal environment in experiment P12b, with a negative shift across the range from stable (warm) to stable (cold) from in-person intervention, and a stable (warm) thermal environment in experiment P13). However, particle movement in experiment P12b corresponded with particles experiencing a stable (warm) thermal environment, and so particle velocities compared well with experiment P13 (Table 4.4).

Table 4.4. Comparison of distance moved, particle velocity, and duration of particle movement for the LA, IA, and HA particles in experiments P12b and P13.

Experiment		Distance moved (mm)	Particle velocity (m s ⁻¹)	Duration of particle movement	
P12b	LA	64 (ice base)	2.29 x 10 ⁻⁶	7 hours, 45 minutes	
	IA	64 (ice base)	1.94 x 10 ⁻⁶	9 hours, 10 minutes	
	HA	44	2.39 x 10 ⁻⁷	51 hours	
P13	LA	74 (ice base)	1.68 x 10 ⁻⁶	12 hours, 15 minutes	
	IA	Phase one	65.5	1.46 x 10 ⁻⁶	12 hours, 30 minutes
		Phase two	0	0	40 hours, 55 minutes
		Phase three	8.5	4.72 x 10 ⁻⁶	30 minutes
		Overall	74 (ice base)	3.81 x 10 ⁻⁷	53 hours, 55 minutes
HA	Exposed at ice surface	-	-		

The meltwater created in experiments P12b and P13 exhibited comparable morphologies, with melt pathways open at the ice surface during particle movement. Similar to previous experiments involving thermally conductive particles, the pathways had a width that did not exceed the particle diameter, indicating a conduction-driven melt process. Modification to melt systems because of particle-particle interaction was also observed in both experiments, where combination of two basal meltwater ponds (created by the LA and IA particles) occurred in experiment P12b and drainage of meltwater into neighbouring melt pathways occurred within experiment P13.

The combination of basal melt in experiment P12b to form a large basal melt pond was a result of the LA and IA ponds linking approximately three hours after both particles reached the ice base. This grew from continuous heat transfer driving meltwater convection and IA particle lateral movement on the ice base. However, in-person modification of freezer temperatures resulted in a negative shift across the thermal range into a stable (cold) environment, causing all melt to refreeze (Figure 4.29).

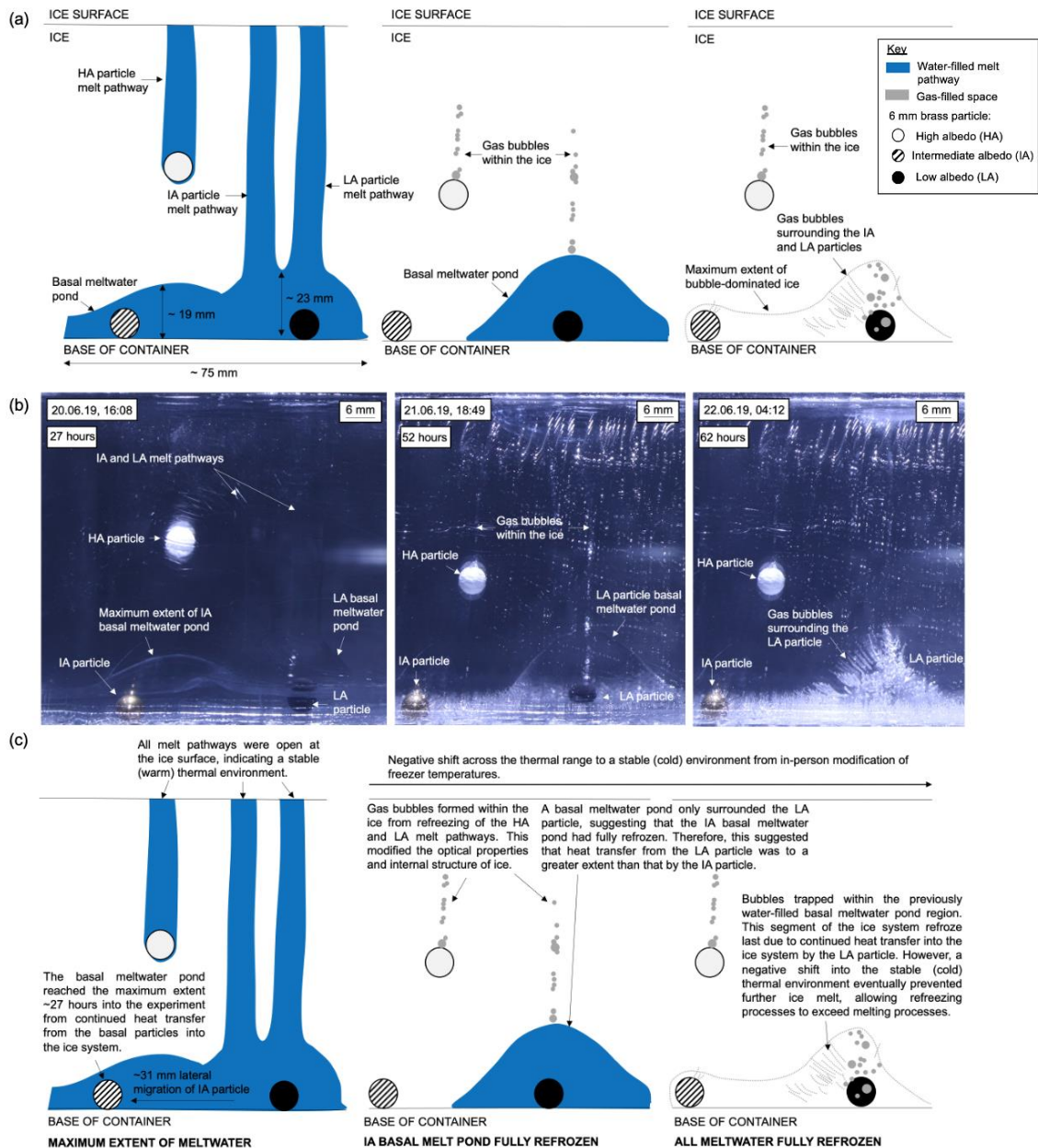


Figure 4.29. Cross-sectional images of refreezing meltwater in experiment P12b. (a) observational line diagram, (b) photograph and (c) interpretation of the features.

In contrast with experiment P11b and P12b, experiment P13 demonstrated complexities associated with drainage processes, resulting in two phases of IA particle movement. In phase one, the LA and IA particles moved downwards through the ice with particle velocities of $1.68 \times 10^{-6} \text{ m s}^{-1}$ and $1.46 \times 10^{-6} \text{ m s}^{-1}$, respectively, comparing with results from experiment P12b (data from IA phase one in Table 4.4). However, the IA particle remained stationary at 0 m s^{-1} for approximately 41 hours (phase two in Table 4.4) when the LA particle reached the ice base. This stalled behaviour coincided with drainage of water from the

IA melt pathway into the LA melt pathway (Figure 4.30), indicating a hydrological connection between the two particles that was likely caused by the IA particle moving laterally by 6 mm during descent. The development of a LA basal meltwater pond allowed the stalled IA particle to drop into the meltwater to reach the ice base (phase three in Table 4.4). The staggered IA particle movement resulted in an overall IA particle velocity of $3.81 \times 10^{-7} \text{ m s}^{-1}$: an order of magnitude lower than the LA particle.

The stalled behaviour of the IA particle was not observed in experiments where particles were unable to interact with one another (e.g. experiment P12b), suggesting that advection of heat with meltwater moving into the LA meltwater pond reduced particle movement, rather than the particle properties itself (an assessment of an IA particle with no particle interaction is described in experiment P14). This interpretation was confirmed by the growth of a basal meltwater pond around the IA particle when on the ice base, demonstrating active particle-induced ice melt. This could suggest that ice hydrology at the scale of the particle can override the influence of the physical properties of the particles.

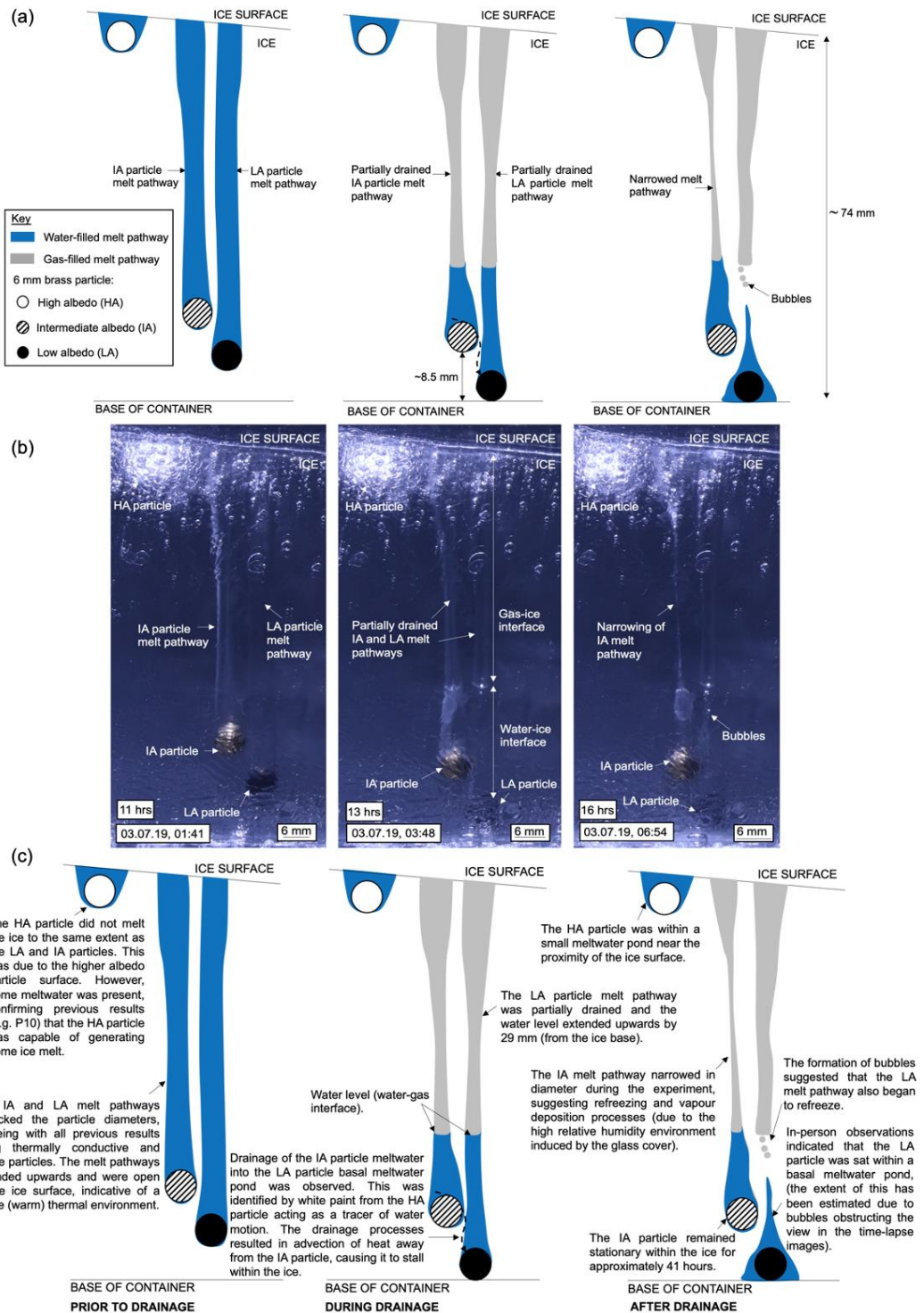


Figure 4.30. Cross-sectional images of drainage of meltwater pathways in experiment P13 across three time frames. (a) observational line diagram, (b) photograph and (c) interpretation of the features.

The HA particles showed contrasting behaviours in experiments P12b and P13 as particle movement was to a depth of 44 mm and 10 mm, respectively. It was deduced that the cause of this was differing thermal environments: particles in experiment P13 experienced a cooler thermal environment relative to

experiment P12b, although still within a stable (warm) environment. Additionally, drainage processes from the HA particle melt pathway into the IA particle melt pathway would have advected heat away from the particle system, in the same way as that observed by the IA particle.

4.2.3. P14: an intermediate albedo brass particle

Experiment P14 assessed the behaviour of an IA particle without any particle-particle interaction (as seen in P13b). The particle was the same type as in previous experiments (i.e. spherical, brass and 6 mm in diameter) and was placed on the ice surface at room temperature. The hypothesis for experiment P14 is shown in Figure 4.31.

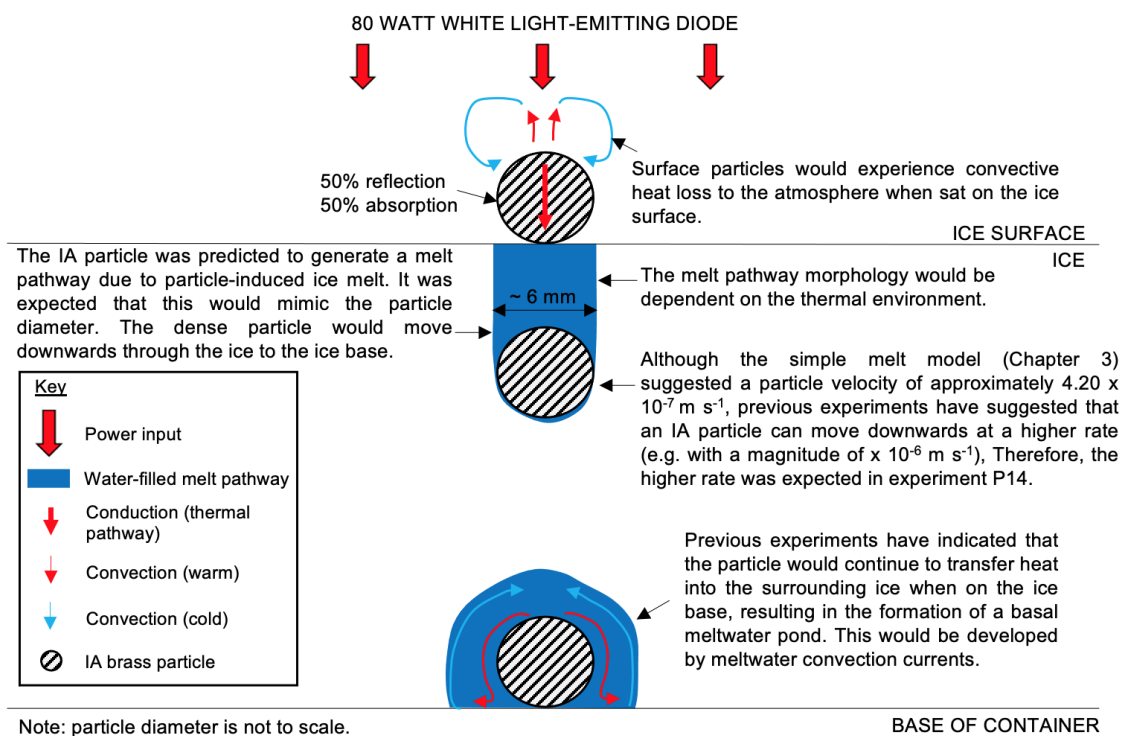


Figure 4.31. Schematic cross-sectional view of the hypothesised particle-ice interaction in experiment P14.

4.2.3.1. Results and interpretation

Two behavioural phases were identified in this experiment: the P14 (i) demonstrated limited particle movement aside from initial melting from temperature differences between the particle and ice (lasting 70 hours), whereas P14 (ii) indicated active melting and subsequent sinking of the IA particle to the ice base (within an eight-hour period).

4.2.3.1.1 P14 (i)

The IA particle initially moved downwards into the ice by approximately 3 mm, due to temperature differences between the particle and ice from surface placement causing ice melt. However, the particle remained stationary for 70 hours and did not appear to interact with the ice. Prior to the experiment, the ice block was within the freezer without a glass cover. This will have allowed sublimation and, consequently, sublimation cooling of the ice surface (e.g. similar to that observed in experiment P1a). It was acknowledged that this may have prevented initial ice melt. However, this would have been expected to diminish as the surface sublimation cooling effect stopped when the cover was placed over the container at the experiment start (due to an increase in relative humidity, as discussed in experiment P1a). Therefore, as the IA particle was on the ice surface 70 hours after initial particle placement, it was discounted that sublimation cooling prevented particle-ice interaction. Instead, this could suggest that partial absorption of incoming radiation, in addition to convective heat loss to the atmosphere, resulted in insufficient heat transfer into the ice preventing the ice temperature to be raised to PMP. It was inferred that the surface particle in P14 (i) experienced a stable (cold) thermal environment at these ice temperatures. This resulted in the particle remaining at the ice surface and refreezing of most meltwater produced from initial particle placement; this marked the end of P14 (i).

4.2.3.1.2 P14 (ii)

To assess if there was any meltwater present on the ice surface, the particle and surrounding area was physically examined and, on contact, the particle rotated (this was an artifact of in-person intervention). This allowed the absorbing top surface of the particle to come into direct contact with the underlying ice. It was noted that this resulted in the particle moving downwards into the ice to become fully submerged in meltwater; this marks hour '0' on Figure 4.32 and the start of P14 (ii). It was likely that this was a result of the previous top particle surface interacting with the ice, allowing the warm absorbing surface to directly melt the ice. This caused continued ice melt and downwards movement, likely exacerbated by full submergence of the particle. This removed heat loss to the atmosphere and allowed all absorbed heat to

transfer into the surrounding meltwater to drive meltwater convection, further driving ice melt. Consequently, the IA particle melted the ice at a steady rate and moved downwards to the ice base within eight hours, with a mean particle velocity of $2.36 \times 10^{-6} \text{ m s}^{-1}$. This highlights the change in heat transfer mechanisms between surface and embedded particles.

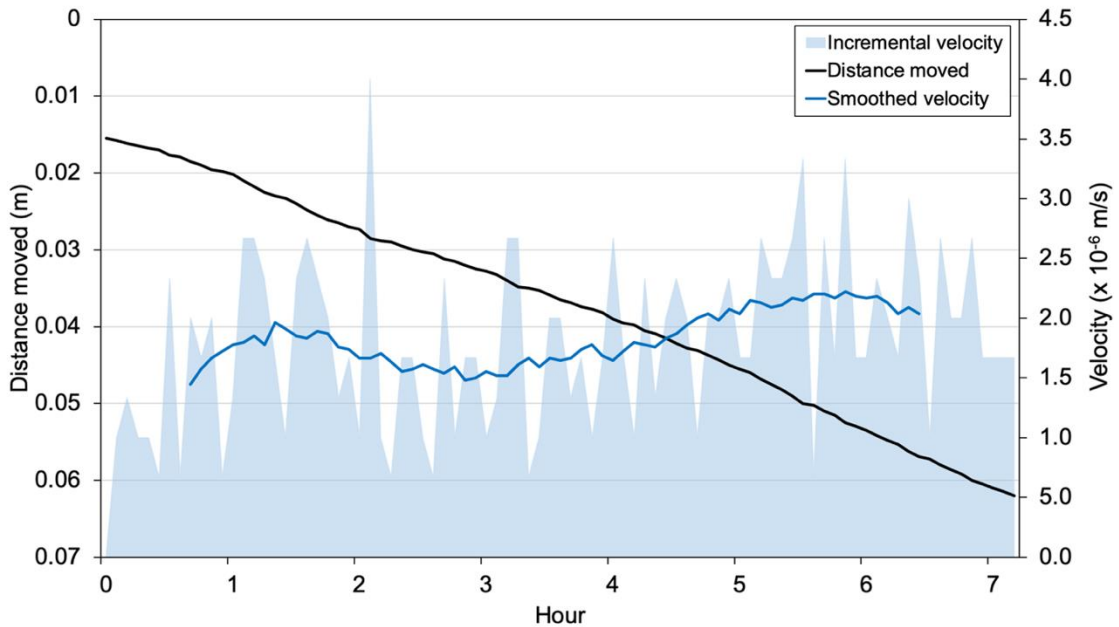


Figure 4.32. Vertical distance moved and velocity of the intermediate albedo brass particle in experiment P14 (ii).

4.2.3.2. Melt pathway

The P14 particle melt pathway had a similar width to the particle diameter but was limited to a length of approximately 25 mm due to refreezing processes (Figure 4.33). This suggested that the P14 particle experienced a stable (cool) thermal environment.

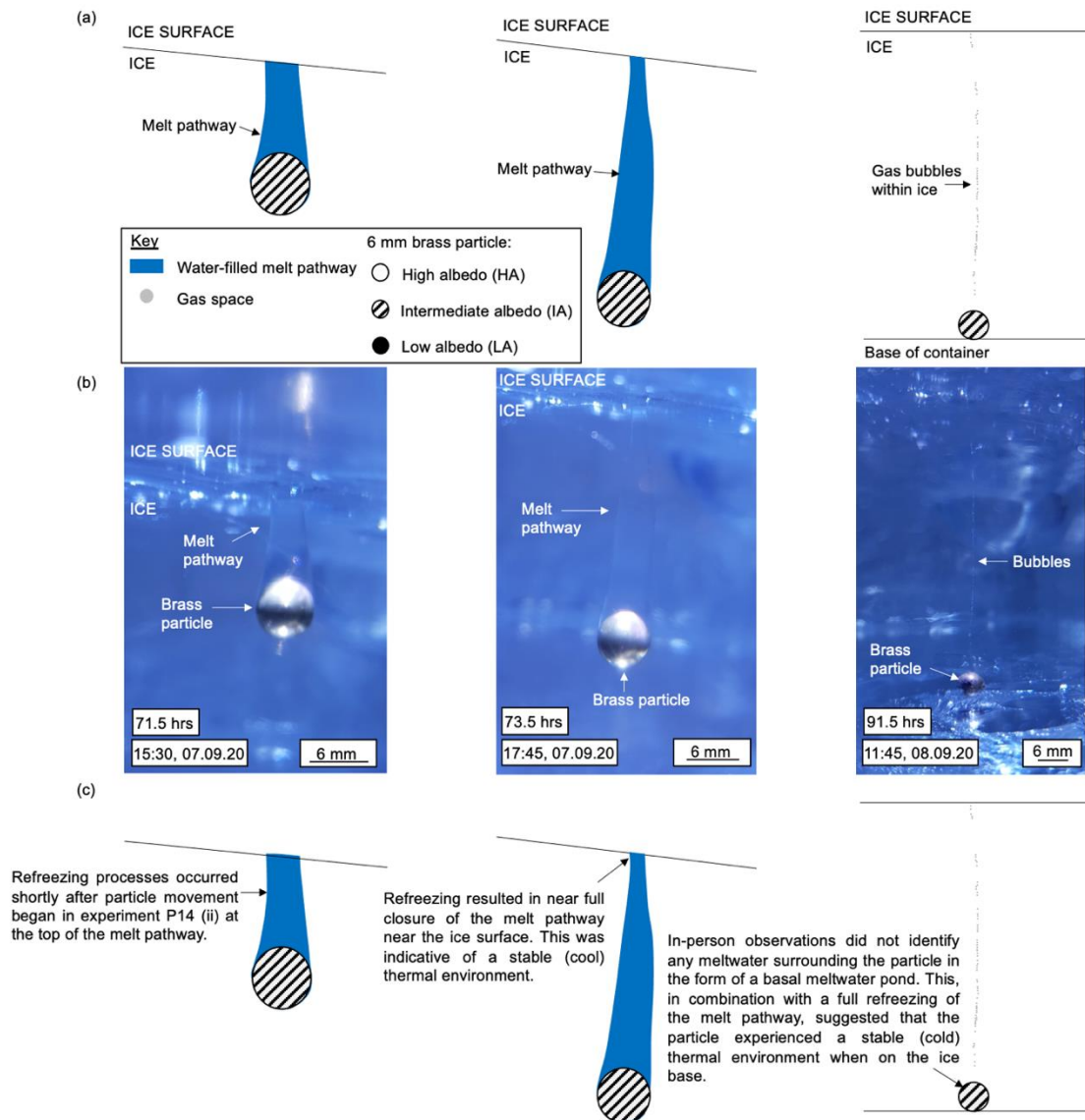


Figure 4.33. Cross-sectional images showing the refreezing of the IA melt pathway in experiment P14 (ii) across three time frames. (a) observational line diagram, (b) photograph and (c) interpretation of the features.

4.2.3.3. Basal meltwater pond

Condensation on the freezer surface prevented observation of the behaviour of the particle after reaching the ice base in time-lapse images. However, in-person observations indicated that a basal meltwater pond was not present. This, in combination with a refreezing melt pathway and a lag in particle movement in the first phase of the experiment, confirmed the interpretation that the particle experienced a stable (cool) thermal environment during particle movement, and a stable (cold) thermal environment when on the ice surface and ice base.

4.2.3.4. Summary

This experiment was split into two phases, whereby limited particle-ice interaction was observed for 70 hours until a physical disturbance to the particle resulted in active ice melt for eight hours. The active phase of the experiment, i.e. P14 (ii), showed the IA particle moving through the ice at a particle velocity of $2.40 \times 10^{-6} \text{ m s}^{-1}$, in line with values from previous experiments. Results from this experiment particularly highlighted differences in heat transfer mechanisms between a surface and embedded particle.

The contrast between the stalled P14 (i) surface particle, and the moving P14 (ii) embedded particle, indicated that the particle experienced differences in thermal environment when on the ice surface versus when embedded within the ice, i.e. stable (cold) and stable (cool), respectively. When on the ice surface, all heat absorbed by the particle (already limited by an IA surface) was not transferred into the ice due to convective heat loss to the atmosphere. Therefore, the rate of energy transferred into the ice did not equal the rate of heat conduction away from the region, and was not sufficient to raise ice temperatures to PMP. However, an artificial disturbance that rotated the particle triggered ice melt; once embedded within the ice, all heat absorbed was coupled into the ice. This was sufficient to bring ice temperatures to PMP and cause ice melt and downwards particle movement. As identified in experiment P12b, the behaviour of particle-induced ice melt is very sensitive. In this instance, this was limited by convective heat loss to the environment when placed on the ice surface. This was likely exacerbated by the partly reflective surface of the IA particle reducing absorption of incoming radiation.

4.3. Density

A set of eight experiments investigated the behaviour of a particle with a low density (defined as lower than water, e.g. polystyrene and polypropylene with a density of $960\text{-}1050 \text{ kg m}^{-3}$ and $890\text{-}920 \text{ kg m}^{-3}$, respectively) or intermediate density (defined as higher but close to the density of water, e.g. Delrin® with a density of 1400 kg m^{-3}), with the aim of improving understanding of floating and submerged particle-interaction with ice (Figure 4.34, Table 4.5). Particles had low albedo and diameters in the range 5-8 mm. Experiments have been written

up in order of higher thermal conductivity to lower thermal conductivity, although all particles had a lower thermal conductivity than ice. This approach was chosen as it progresses from the assessment of thermally conductive particles in all previous experiments (e.g. P1b-P14b).

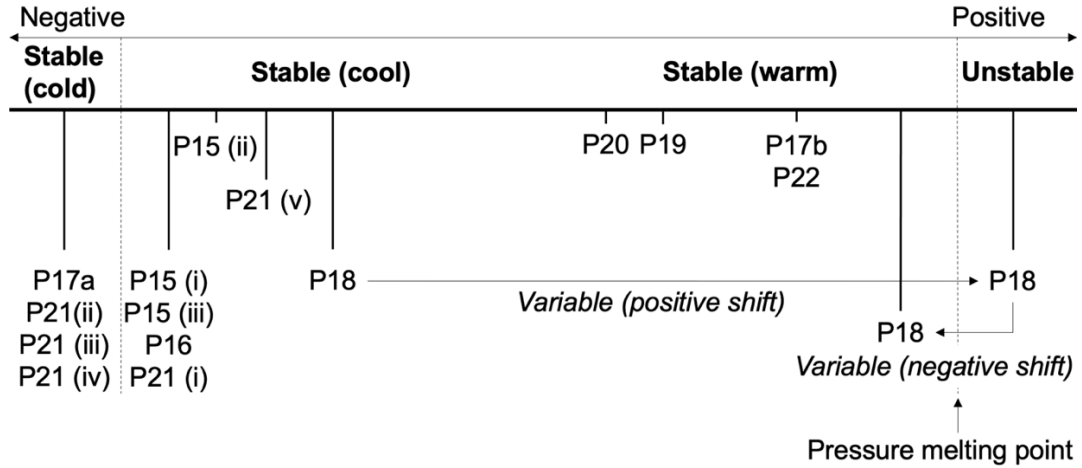


Figure 4.34. The thermal environment of particles in experiments investigating the role of particle density in influencing particle-ice interaction. Experiment position has been derived from interpretation of observations, as described in Chapter 3, Section 3.7.

Table 4.5. A summary of the experiments investigating the role of particle density in particle-induced ice melt, organised by particle thermal conductivity. This indicates the type of particles used and associated thermal environments as defined in Chapter 3.

Experiment	Particle type	Thermal environment
P18	6 mm polyoxymethylene (Delrin®)	Variable: stable (cool) to stable (warm)
P19	6 mm polyoxymethylene (Delrin®)	Stable (warm)
P20	6 mm polyoxymethylene (Delrin®)	Stable (warm)
P21	6 mm polyoxymethylene (Delrin®)	Variable: stable (cold) in P21 (ii), (iii), and (iv) to stable (cool) in P21 (i) and (v)
P22	5 mm polypropylene	Stable (warm)
P15	8 mm polystyrene	Stable (cool)
P16	8 mm polystyrene	Stable (cool)
P17a	8 mm polystyrene	Stable (cold)
P17b	8 mm polystyrene	Stable (warm)

4.3.1. P18: an intermediate density Delrin® particle

Experiment P18 investigated the behaviour of a Delrin® particle when placed on an ice surface. The particle had an intermediate density relative to water, a low albedo, low thermal conductivity relative to ice, and was 6 mm in diameter (Chapter 3, Section 3.3.1). The hypothesis for experiment P18 is shown in Figure 4.35.

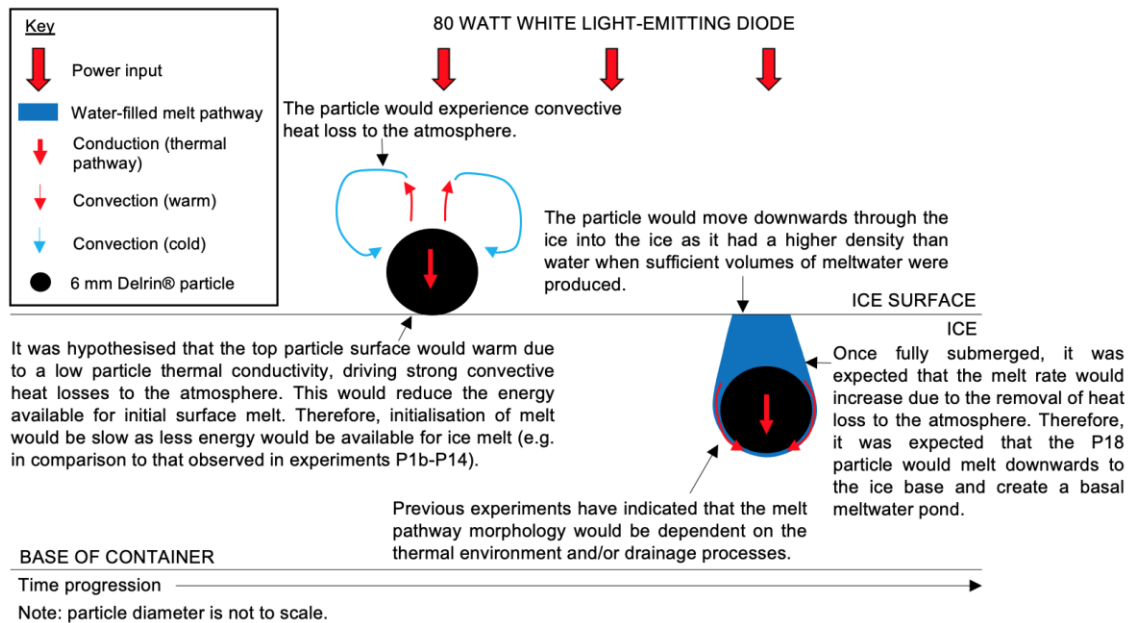


Figure 4.35. Schematic cross-sectional view of the hypothesised particle-ice interaction in experiment P18.

4.3.1.1. Results and interpretation

Analysis of time-lapse images indicated that the particle did not melt the ice during the first hour of the experiment, supporting the hypothesis that initialisation of ice melt would be slow due to a low thermal conductivity. However, freezer vibrations dislodged the periscope system and prevented time-lapse imaging of particle behaviour between 2-12, and 24-120 hours of the experiment. Therefore, initialisation of ice melt could not be identified in time-lapse images, and particle velocity information was restricted to a 12-hour period (Figure 4.36). The particle moved downwards through the ice during this period with a mean particle velocity of $2.06 \times 10^{-7} \text{ m s}^{-1}$. There appeared to be little to no movement 21.5 hours after the experiment start and the particle reached a maximum depth of approximately 15 mm. The particle remained stationary for a period of 2.5 hours, suggesting refreezing processes exceeded melting processes, and then moved upwards within the ice by approximately 3 mm (and so remained at a depth of approximately 13 mm). This, in combination with in-person observations showing the presence of gas bubbles below the melt pathway, confirmed that refreezing was occurring. However, further analysis of this behaviour could not be conducted due to a power cut moving the ice into an unstable state. This resulted in the particle moving to the ice base.

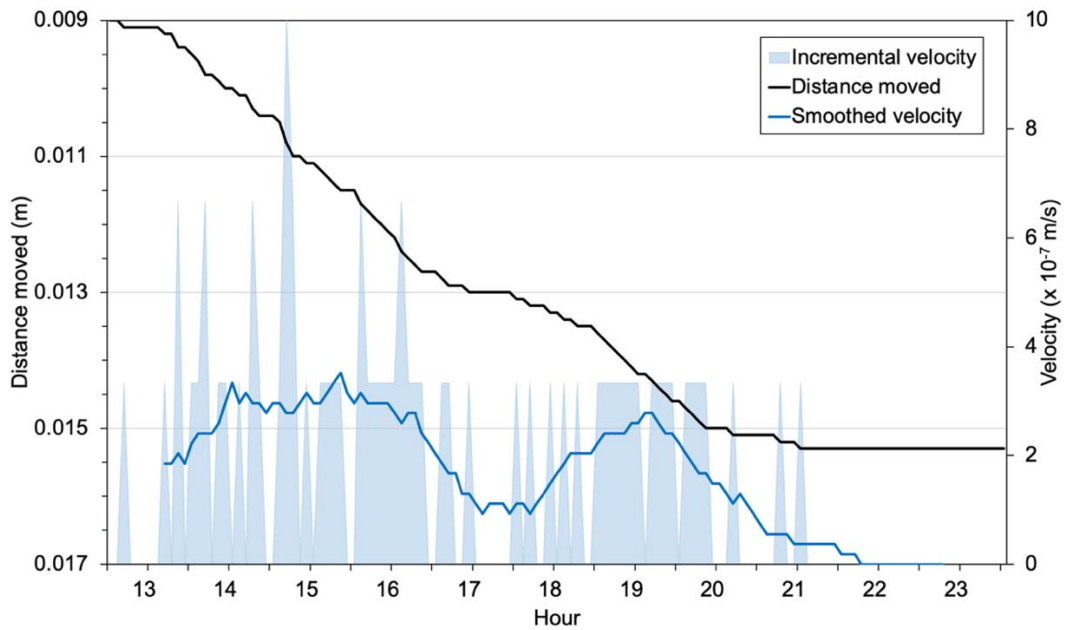


Figure 4.36. Vertical distance moved and velocity of a Delrin® particle in experiment P18 from hour 12 to hour 24.

4.3.1.2. Melt pathway

A surface meltwater pond developed and the intermediate density (i.e. higher than the density of water but close to the boundary) resulted in the particle sinking into the meltwater until fully submerged. Although the start of the experiment was not documented by time-lapse imaging, in-person observations indicated that ice melt occurred quickly, e.g. a widening of approximately 3 mm was observed over two hours. The melt pathway differed from that observed in experiments P1b-P14 as it had a width of approximately 13 mm (approximately double the particle diameter).

The reduction in meltwater extent by refreezing processes to push the particle upwards would have been feasible due to the small density difference between the water and particle. Therefore, the upwards force from the liquid-solid state change exceeded the downwards force from density differences. This caused upwards movement of the particle within meltwater, rather than the particle becoming embedded in surrounding ice (as seen with particles with a high density, e.g. brass). The presence of bubbles observed at the base of a refreezing melt pathway (Figure 4.37) suggested that the particle experienced a stable (cool) thermal environment. However, a power cut occurred 96 hours into the experiment, and this increased the freezer temperature to a maximum of

11.1 °C whilst illumination ceased. This event temporarily shifted the ice into an unstable state, and so the thermal environment for the entire experiment was defined as ‘variable’.

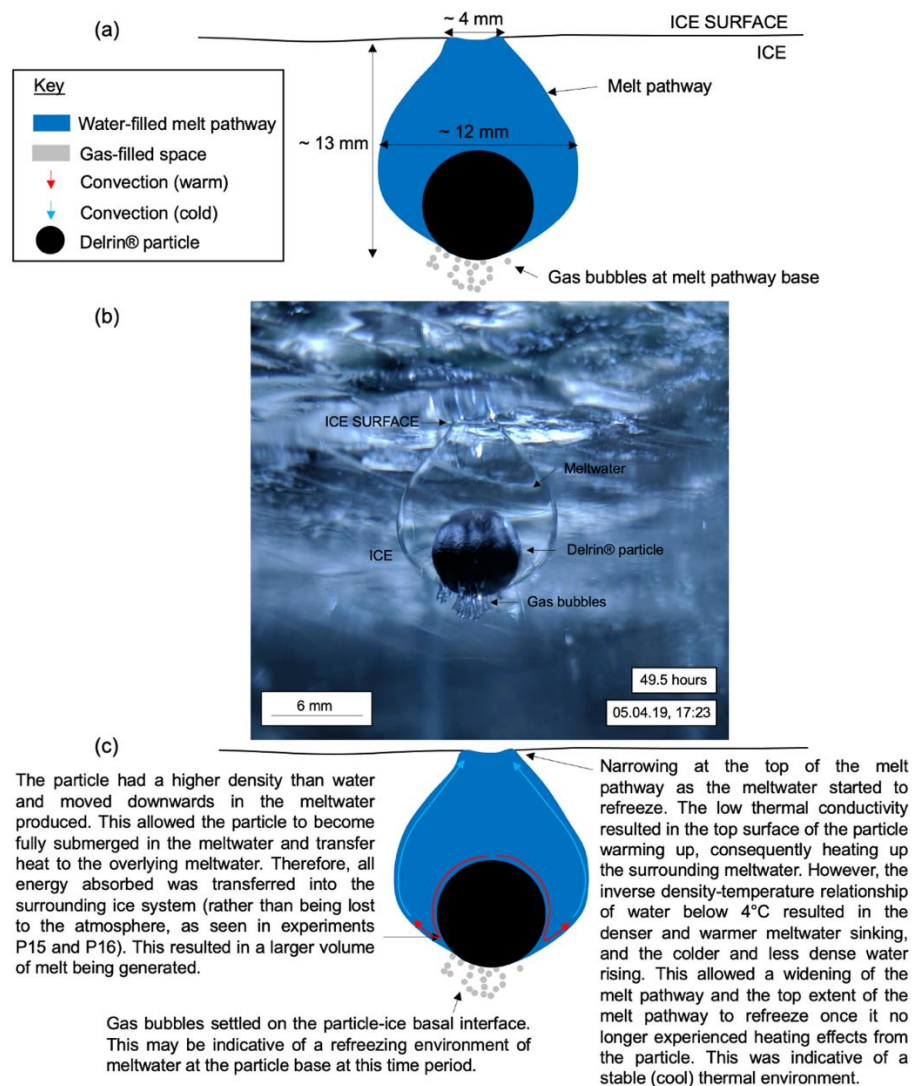


Figure 4.37. Cross-sectional images showing a narrowing of the top portion of the melt pathway and the presence of gas bubbles in experiment P18, with both indicating refreezing processes. (a) observational line diagram, (b) photograph and (c) interpretation of the features.

A shift into an unstable thermal environment allowed the Delrin® particle to move downwards to the ice base within a period of no in-person observations or time-lapse imagery. However, 24 hours following the power cut (and consequently, approximately 120 hours into the experiment), it was noted that the particle sat at the ice base with a vertical melt pathway extending towards the ice surface (Figure 4.38). Therefore, the temporary shift into an unstable state did not cause the ice to melt in its entirety; rather, the increasing temperature of the ice allowed continued melt in the proximity of the particle

and offset refreezing processes that had been previously occurring whilst the particle was within a stable (cool) thermal environment. This facilitated downwards movement of the Delrin® particle to the ice base. This sequence of events was deduced due to the preservation of an open melt pathway within the ice (which would otherwise have been destroyed by full melting), and the expectation that refreezing features (e.g. an increase in ice opacity due to trapped air bubbles) would be present if the ice had melted entirely and refroze; this was not the case.

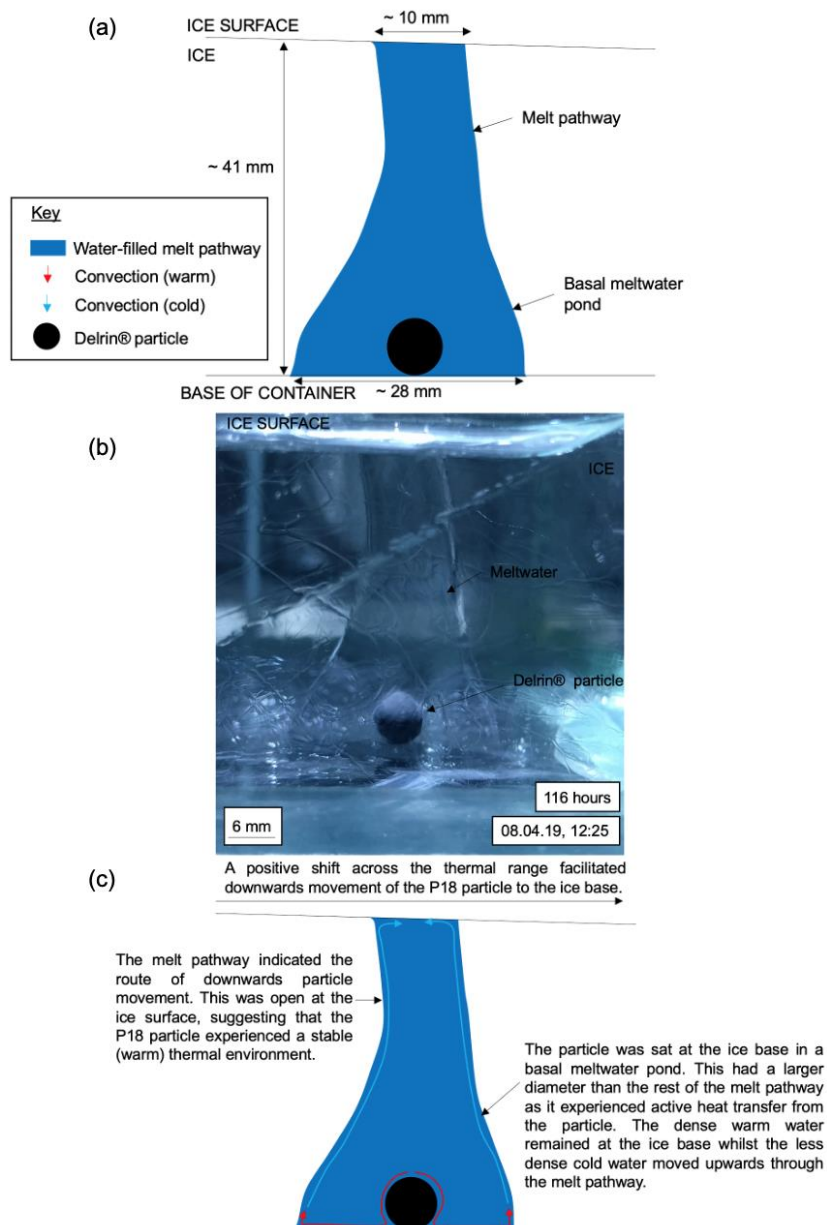


Figure 4.38. Cross-sectional images indicating the basal position of the Delrin® particle at the base of a melt pathway following a shift into the unstable thermal environment in experiment P18. (a) observational line diagram, (b) photograph and (c) interpretation of the features.

4.3.1.3. Summary

The Delrin® particle had a higher density than water, and so the particle moved downwards to create a melt pathway. The low thermal conductivity property of the particle enabled efficient heat transfer between the warm top surface of the particle and the overlying meltwater, driving strong convection systems that widened the melt pathway past the particle diameter. Therefore, ice melt was predominantly convection-driven, in contrast to previous experiments (identified by differences in melt pathway width e.g. P1b-P14, P48-P49). Additionally, a lack of particle-ice interaction was noted in the first hour of the experiment, supporting the hypothesis that a lower thermal conductivity would slow the rate of initial ice melt. However, a dislodgment of the experimental set-up restricted the view in time-lapse images and so this behaviour could not be analysed further. The observed processes confirmed that the particle thermal conductivity was a dominant melt-influencing property.

External factors temporarily shifted the experiment across the thermal range into an unstable environment, resulting in a subsequent shift in particle behaviour. Although this demonstrated that the temperature of the ice ultimately dictates the behaviour of particle-ice interaction, it would be useful to assess the behaviour of particles within a stable environment for the duration of the experiment. Additionally, issues with time-lapse imagery prevented detailed analysis of particle behaviour. Therefore, this experiment was repeated in experiments P19, P20, and P21.

Results from experiments P19, P20, and P21 contrasted with one another, indicating a range of behaviours associated with a particle of this type (Table 4.6). Experiments P20 and P21 showed downwards movement of the Delrin® particle (with velocities of $6.44 \times 10^{-7} \text{ m s}^{-1}$, and $1.89 \times 10^{-7} \text{ m s}^{-1}$, respectively), comparing well with experiment P18. However, the P19 particle floated in meltwater, creating an elongated surface meltwater pond. The contrast in behaviour observed by the P19 particle was suggested to be due to surface tension effects, where the strong intermolecular forces (e.g. hydrogen bonding) between the water molecules at the surface of the meltwater pond held the intermediate density particle at the ice surface. This was facilitated by the close

density value of Delrin® to that of water, suggested as this process had not been observed with particles with a greater density, such as metal particles used in P1b-P14.

Table 4.6. Key features observed in repeat experiments P19, P20, and P21. *Relative to previous experiments involving thermally conductive and high density particles.

Experiment	Particle velocity (m s⁻¹)	Initialisation of melting*	Particle behaviour	Type of meltwater produced	Melt morphology	Thermal environment
P19	4.72 x 10 ⁻⁷ during first five hours (i.e. prior to floating behaviour).	Slow, floating behaviour initiated at 3.5 hours	Floating	Surface meltwater pond	Width of 43 mm x 22 mm and depth of 24 mm.	Stable (warm)
P20	6.44 x 10 ⁻⁷	Could not be identified due to unclear time-lapse images.	Downwards movement to ice base	Melt pathway and basal meltwater pond. Partial drainage of melt pathway when particle reached ice base.	Melt pathway had a width of approximately 15 mm. The basal meltwater pond had a width of 126 mm and height of 15 mm.	Stable (warm)
P21	1.89 x 10 ⁻⁷	Complex. Slow initial movement (initiated at 4.5 hours). Fully submerged within 124 hours.	Downwards movement to ice base, staggered behaviour	Melt pathway and basal meltwater pond	Melt pathway morphology fluctuated throughout experiment. Maximum width of melt pathway was approximately 20 mm.	Stable (cool)

Despite the floating behaviour of the P19 particle, the surface meltwater pond increased in depth and width throughout the experiment. Heat was likely transferred from the proximity of the particle to the pond base by the sinking action of the warmer (and, therefore, denser) meltwater. Therefore, this represented the effect of indirect melting from heating by meltwater convection and demonstrated the ability of a floating particle with a low thermal conductivity to efficiently melt the ice. It is likely that the exposure of the top particle surface to the atmosphere for the experiment duration also facilitated convective heat losses from the top particle surface to the nearby ice. It was noted that the morphology of the surface meltwater pond was dependent on lateral movement by the floating P19 particle (e.g. an initially circular meltwater pond developed into an elongated meltwater pond, Figure 4.39). Refreezing of all meltwater after the illumination was turned off confirmed that the ice was stable in a solid state and the P19 particle experienced a stable (warm) thermal environment.

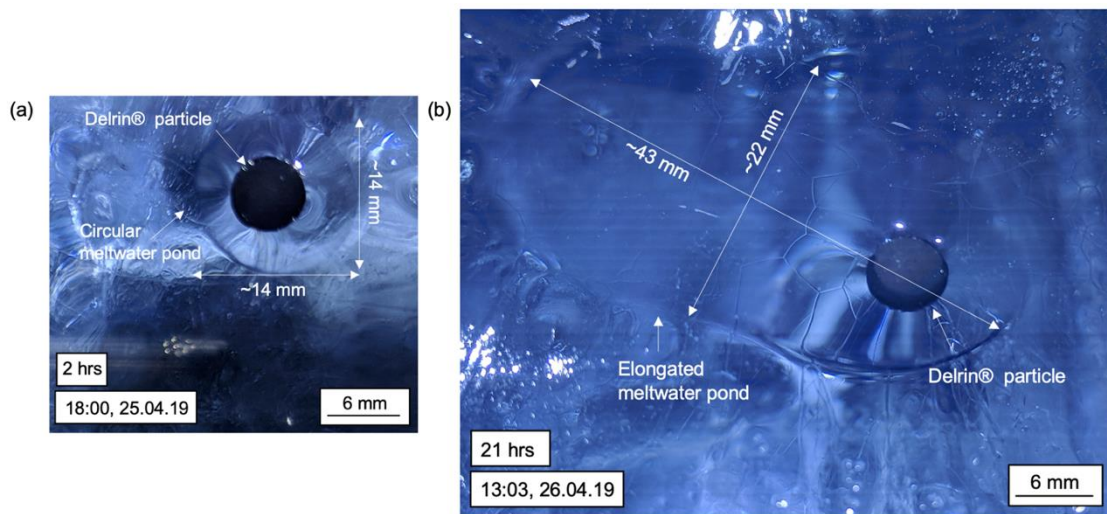


Figure 4.39. Comparison of the surface meltwater pond morphology development throughout a 20 hour period in experiment P19.

The downwards movement of the Delrin® particles in experiments P20 and P21 created melt pathways with a diameter approximately double the particle diameter, agreeing with experiment P18 results. However, experiment P20 additionally provided insights into the behaviour of drainage events, where the drainage of meltwater from particle-ice interaction resulted in the advection of heat to the ice base to create a basal meltwater pond before the P20 particle reached the ice base (Figure 4.40).

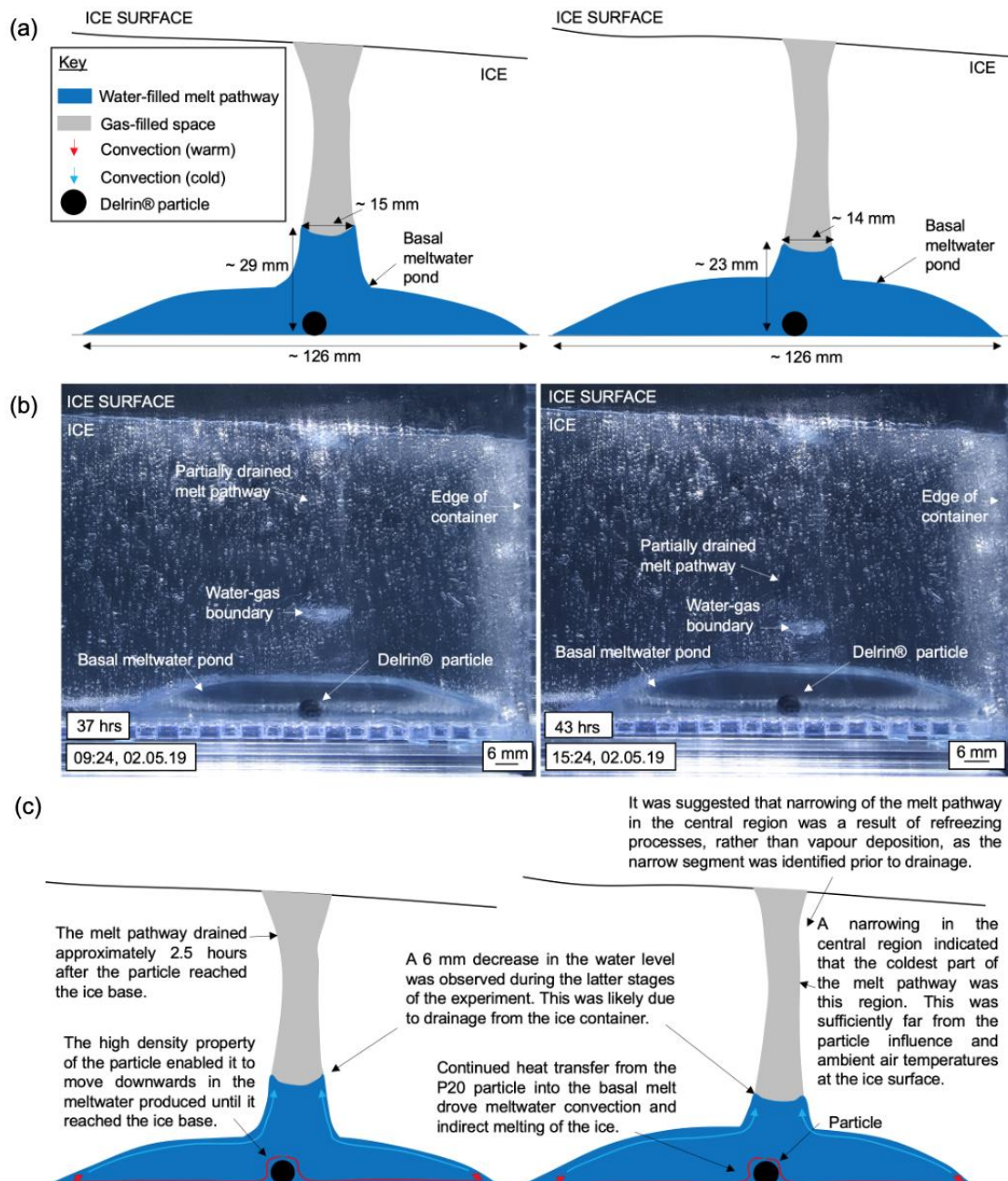


Figure 4.40. Cross-sectional images showing the change in water level in the drained melt pathway within a five-hour period in experiment P20. (a) observational line diagram, (b) photograph and (c) interpretation of the features.

Experiment P21 indicated the role of particle rotation and thermal environment on influencing particle-ice interaction and saw varying behaviours throughout the experiment. This was split into five phases (P21 (i)-(v), Figure 4.41 and Appendix 12) due to the expiry of the time-lapse camera battery. Periods between each phase ranged between 20 and 123 hours. The experiment lasted for approximately 529 hours (22 days). The final phase (P21 (v)) was the most

crucial in understanding active particle-ice interaction and downwards movement of a particle with a low thermal conductivity, whilst the first phases provided an insight into drainage events and thermal environment limitations due to limited downwards movement.

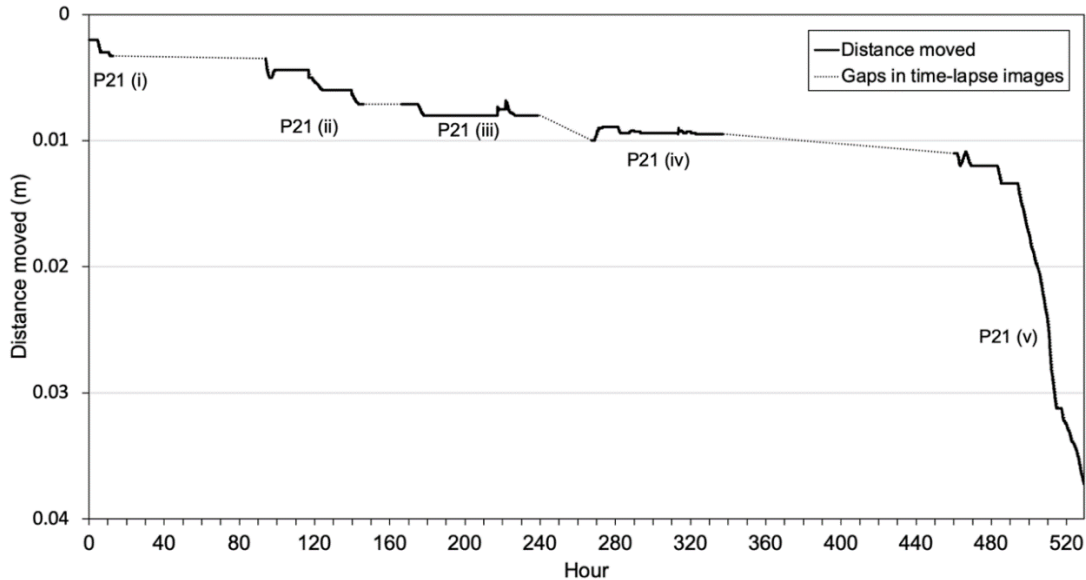


Figure 4.41. Vertical distance moved by the Delrin® particle over the five phases in experiment P21.

The staggered behaviour of the Delrin® particle in experiment P21 was likely a result of a combination of factors. Firstly, the particle bordered a stable (cold) and stable (cool) thermal environment for much of the experiment (identified by limited ice melt in phases (i-iv) and refreezing of the melt pathway in phase (v)). Similar to phase P14 (i) in experiment P14, the exposure of the top particle surface to the atmosphere in phases P21 (i-iv) reduced the heat available for ice melt, meaning that the ice temperature was rarely brought to PMP. Additionally, drainage events removed meltwater from the system, also removing a key driver of ice melt (i.e. meltwater convection) as direct ice melt was limited by a low particle thermal conductivity. This suggested that indirect melting through meltwater convection has a dominant role in particle-induced ice melt in the case of thermally insulating particles.

Phase P21 (v) saw downwards particle movement with a particle velocity of $1.89 \times 10^{-7} \text{ m s}^{-1}$, possibly a result of the particle becoming fully submerged and the removal of heat loss to the atmosphere. However, substantial movement was only triggered at hour 494, and this appeared to be associated with a

rotational movement of the particle (observed in the time-lapse images). This resulted in the absorbing hot top surface contacting the underlying ice, driving ice melt in the immediate period following particle rotation. This may have surpassed a threshold at which enough meltwater had been generated in the immediate area to drive sufficient meltwater convection processes to continue driving ice melt. It was, therefore, interpreted that the rotational movement acted as a trigger to start this feedback process. This may not have been seen in previous phases due to the exposure of the top surface to the atmosphere and subtle temperature fluctuations. Although it would be expected that an increased movement could be associated with freezer response to increased ambient temperatures during the day, it appeared as if stationary phases were associated with day periods, whilst downwards movement was initiated at night.

To conclude, the downwards movement of the Delrin® particle in experiments P18, P20, and P21 indicated that the fundamental behaviour of a particle of this type was to sink in the meltwater produced. These experiments provided useful insights into the behaviour of an intermediate density particle, with P20 building knowledge of drainage events and P21 developing the nature of staggered particle movement and developing theory from experiment P14 about initialisation of ice melt. Additionally, experiment P19 demonstrated that surface tension processes could influence particle behaviour when a particle density is close to that of water.

4.3.2. P22: a low density polypropylene particle

This experiment investigated the behaviour of polypropylene particle interaction with ice. The particle had a low density, low thermal conductivity, low albedo, and a diameter of 5 mm. The hypothesis for experiment P22 is shown in Figure 4.42.

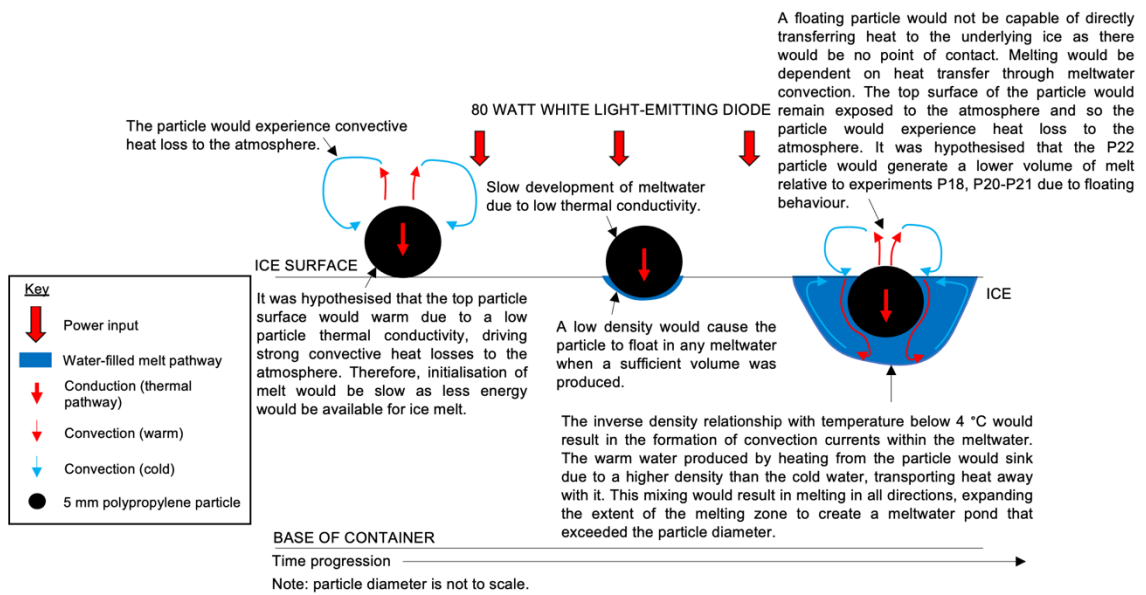


Figure 4.42. Schematic cross-sectional view of the hypothesised particle-ice interaction in experiment P22.

4.3.2.1. Results and interpretation

Clarity in time-lapse images was poor and so the extent of meltwater could not be determined, although key periods of movement were identified. Results relied predominantly on in-person observations and photographs. The production of meltwater from heat transfer from the P22 particle into the ice caused downwards movement of the particle during the first two hours of the experiment with a particle velocity of $8.18 \times 10^{-7} \text{ m s}^{-1}$. Downwards movement ended when floating behaviour occurred (agreeing with the hypothesised outcome). This was observed through lateral movement of the particle by approximately 4 mm. It was noted that the top surface of the P22 particle was exposed to the atmosphere throughout the experiment.

Linear features surrounded the particle within the first ten minutes of the experiment. These extended radially from the particle and were interpreted to have formed by convective heat transfer from the warm top particle surface to heat the air and the nearby ice, bringing the ice to PMP to cause ice melt and form meltwater. The linear features grew to a maximum length of 5 mm and radiated from the outer extent of a developing meltwater pond (Figure 4.43) and combined to form a single meltwater pond within 24 hours. This had a circular and relatively symmetrical morphology in the first 48 hours of the experiment,

and the particle floated in the centre. However, lateral particle movement evolved the pond morphology from circular to elongate. A deepening of the surface meltwater pond was observed throughout the experiment (i.e. 13 mm at 24 hours, 16 mm at 48 hours and 20 mm at 120 hours). The maximum pond dimensions were measured at approximately 48 mm in width and 20 mm in depth.

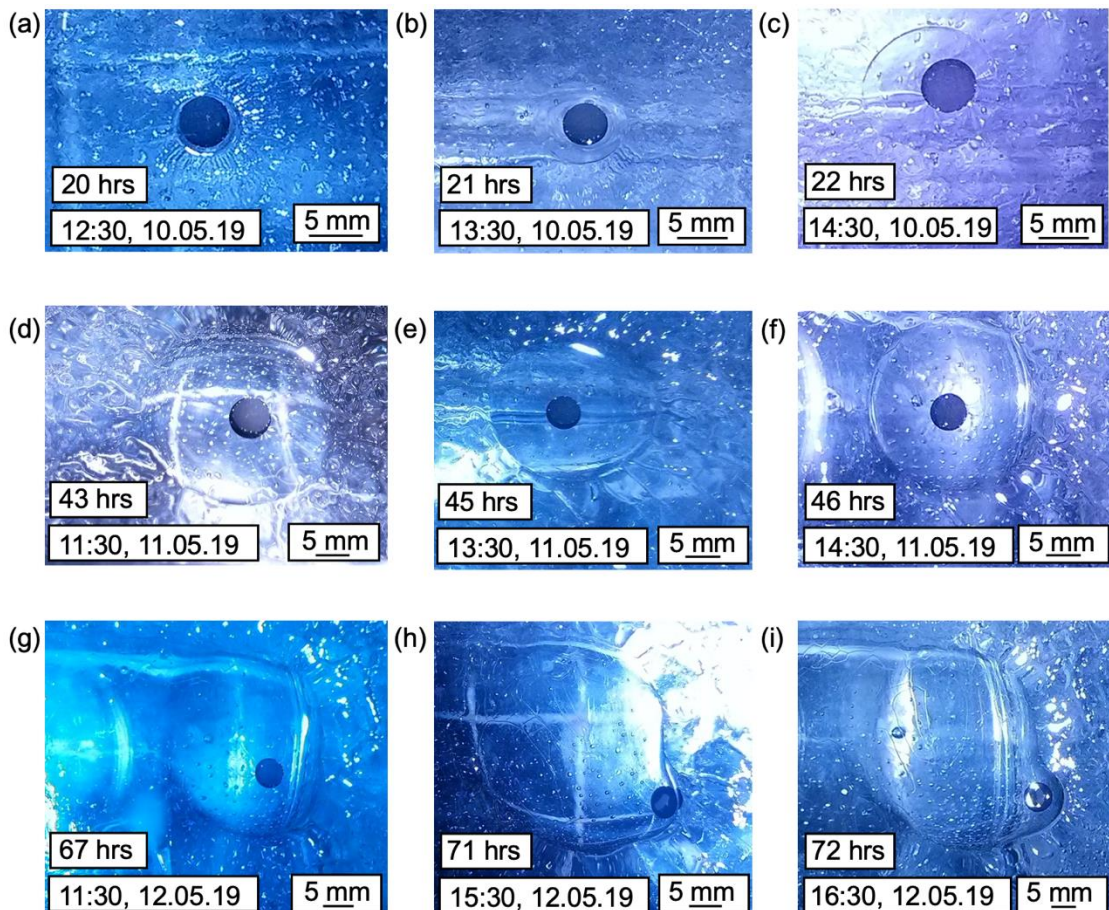


Figure 4.43. Plan-view photographs showing the evolution (a-i) of a surface meltwater pond in experiment P22.

4.3.2.2. Summary

Experiment P22 demonstrated the ability of a low density particle to maintain a stable surface meltwater pond and actively transfer heat into the ice to cause ice melt. This, and the floating behaviour, compared well with the hypothesised outcome, although the suggested slow initialisation and limited ice melt was not observed. This indicated that heat transfer from the particle to the ice exceeded: (1) convective heat loss to the atmosphere, and (2) conduction of heat away from the particle proximity through the ice (i.e. two mechanisms that encouraged refreezing processes). Therefore, this could suggest that the P22

particle experienced a stable (warm) environment, as previous experiments indicated the sensitivity of surface particles to cooler temperatures (e.g. it is harder for surface particles to ‘offset’ refreezing mechanisms in cooler environments due to convective heat loss to the atmosphere).

4.3.3. P15: a low density polystyrene particle

Experiment P15 investigated the behaviour of a polystyrene particle within an ice system. The particle had a low density relative to water (and lower than the polypropylene particle in experiment P22), low albedo, low thermal conductivity relative to ice, and a diameter of 8 mm. The experiment lasted approximately 146 hours (although time-lapse imagery only captured the first 68 hours). The P15 particle was placed on the surface of the same ice block used in the P1b and P10 experiments, although it was offset from the particles to avoid particle-particle interaction. The hypothesis for experiment P15 is shown in Figure 4.44.

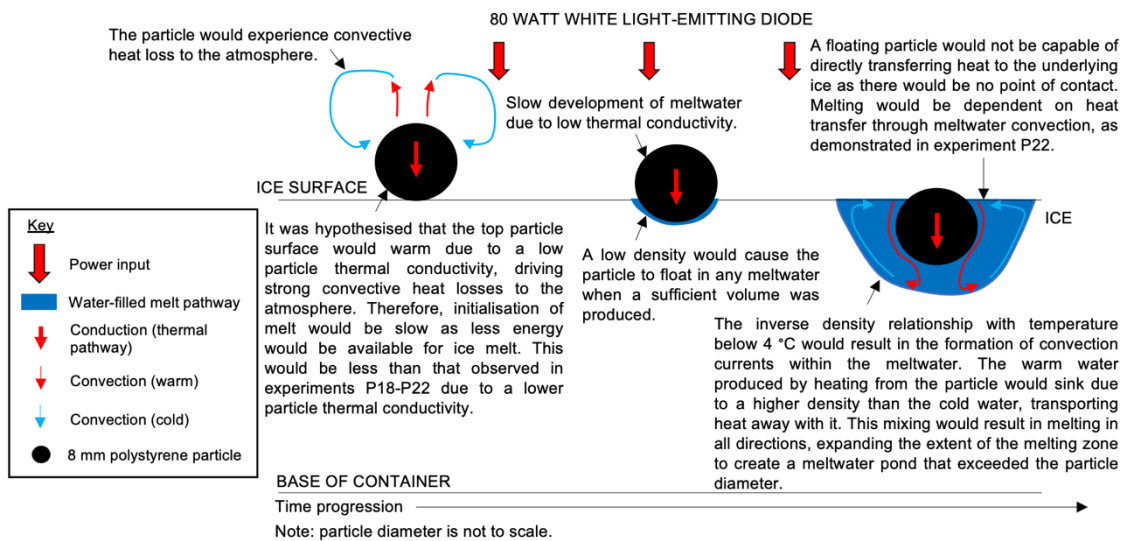


Figure 4.44. Schematic cross-sectional view of the hypothesised particle-ice interaction in experiment P15.

4.3.3.1. Results and interpretation

Initial melting from temperature differences between the P15 particle and ice was observed, although the particle remained near the ice surface with limited melting for the experiment duration. Melting occurred in a cyclic nature of melting and refreezing, and this did not appear to be correlated with the day phase of diurnal cycles as melting phases often occurred during night. An active

melt stage, refreezing melt stage, and subsequent stationary behaviour within a stable ice system was defined as one cycle. Three of these cycles were observed: P15 (i), (ii), and (iii), typically occurring with an active melt stage spanning 5-20 hours and a refreezing stage lasting 0.5-9 hours. The particle floated in meltwater when a sufficient volume had been produced, although this was restricted to a seven hour period in P15 (ii). Lateral movement of approximately 2 mm was also observed throughout the experiment.

4.3.3.2. Meltwater development

Three cycles of meltwater production were identified (Table 4.7). In all cases, meltwater growth initially began in a horizontal direction before a vertical direction, although an increasing depth of the meltwater away from the particle base (i.e. producing a floating particle) was only observed in P15 (ii).

Table 4.7. The duration of the three melting and freezing cycles in the time-lapse images and the maximum dimensions of the surface meltwater ponds for experiment P15.

Cycle	Duration of cycle (hours)	Melting (hours)	Refreezing (hours)	No apparent melting/refreezing (hours)	Meltwater diameter (mm)	Meltwater depth (mm)
P15 (i)	9	5	0.5	3.5	11	5
P15 (ii)	24	13	11	-	15	8
P15 (iii)	34.5	27	1	6	10	7

4.3.3.2.1 P15 (i)

Melting began immediately after particle placement. The meltwater had a maximum diameter of approximately 11 mm when including the particle diameter, and did not develop vertically from the particle base, indicating that the particle was not floating during this period (Figure 4.45). Therefore, the density property had little influence on particle-ice interaction at this stage. The absence of meltwater at the particle base suggested that direct heat transfer through the particle was not sufficient to cause ice melt in this region, likely a result of the low thermal conductivity of the particle, agreeing with the hypothesis.

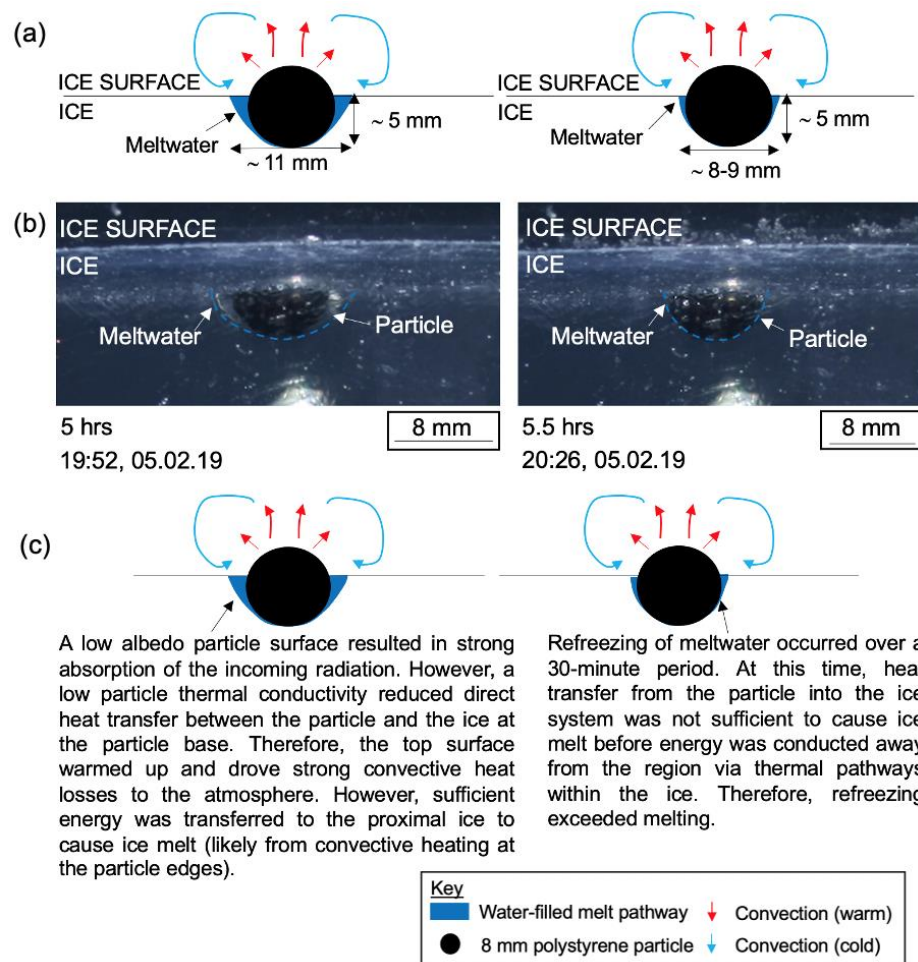


Figure 4.45. Cross-sectional images of meltwater development (left) and refreezing (right) in P15 (i). (a) observational line diagram, (b) photograph and (c) interpretation of the features.

4.3.3.2.2 P15 (ii)

P15 (ii) experienced the most active meltwater development, where a vertical and horizontal extension of the meltwater was observed (Figure 4.46). The meltwater pond initially had the same morphology as that observed in P15 (i) until a deepening was observed approximately 6.5 hours after melting resumed. Once meltwater was established at the edges of the particle, a convection system developed, encouraging further melting of the ice and a deepening of meltwater. Lateral particle movement was identified, indicating floating behaviour. Therefore, the particle density had an influence on the behaviour of particle-ice interaction in P15 (ii). Refreezing started 13 hours after melting began and meltwater had refrozen within approximately 11 hours. There was no obvious link with natural diurnal cycling (e.g. the freezer responding to ambient warming during the day) despite the 24 hour length of the melting/refreezing

cycle; in fact, the largest volume of meltwater was associated with night. Therefore, the longer timescale of refreezing when compared to P15 (i) was likely a result of subtle temperature differences within the ice system as previous experiments have indicated the sensitivity of particle-induced ice melt to temperature.

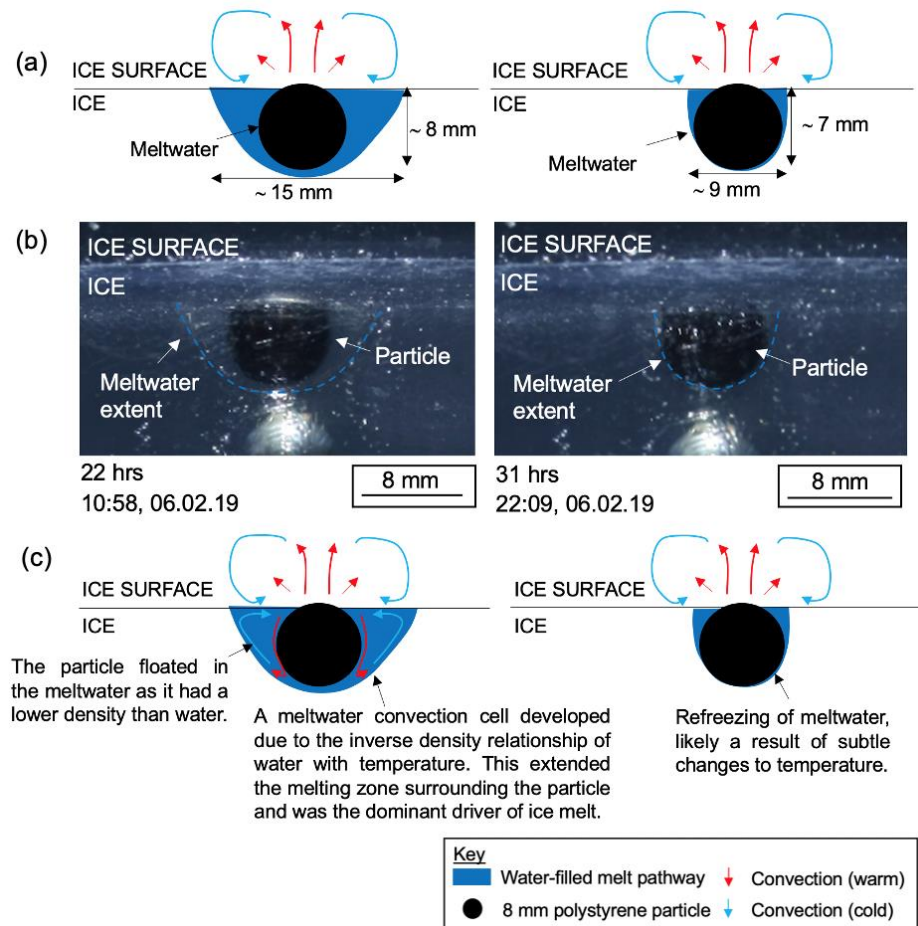


Figure 4.46. Cross-sectional images of meltwater development (left) and refreezing (right) in P15 (ii). (a) observational line diagram, (b) photograph and (c) interpretation of the features.

4.3.3.2.3 P15 (iii)

P15 (iii) experienced the smallest change in meltwater volume as the meltwater pond had a maximum diameter of approximately 10 mm. Meltwater was not observed beneath the particle, and so floating could not occur. Therefore, the particle density did not influence the behaviour of particle-ice interaction. Refreezing began approximately 27 hours into P15 (iii) and lasted approximately one hour. It could not be determined whether the meltwater extent continued to fluctuate to the end of the experiment as changes were too minor to be identified on the time-lapse images. In-person observations showed

a 10-mm-diameter meltwater pond at the end of the experiment (Figure 4.47), and this had remained in this state for approximately 72 hours. This could suggest that an equilibrium had been established between melting and refreezing processes. The presence of meltwater suggested that particle-induced ice melt was possible and it was deduced that the particle experienced a stable (cool) thermal environment. However, the lower volume of meltwater observed than in the previous two cycles suggested that this was cooler than in P15 (i) and (ii) and was likely on the boundary between the stable (cold) and stable (cool) thermal environment.

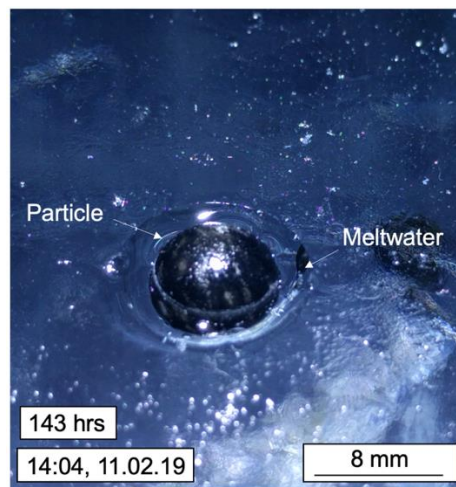


Figure 4.47. Plan-view photograph of the low density polystyrene particle on the ice surface at the end of experiment P15.

The melting/freezing cycling suggested that heat transfer from the particle to the ice was insufficient to maintain a stable meltwater pond for much of this experiment. It was suggested that a low particle thermal conductivity caused a hot particle top surface due to continued absorption of illumination and an inefficient thermal pathway, consequently increasing convective heat loss to the atmosphere. Although this process likely facilitated small volumes of melting at the particle edges, a stable (cool) thermal environment limited the extent of melt. This could suggest that subtle changes in freezer temperatures were responsible for fluctuations in melting and refreezing cycles. Although the particle density had little effect on this experiment due to limited floating, it may have prevented a ‘trigger’ event (e.g. as seen in experiment P21). For example, if the P15 particle had a high density, it would have likely become fully submerged within the ice during P15 (ii). This may have exacerbated ice melt

due to the removal of heat loss to the atmosphere and demonstrates the importance of both the thermal conductivity and density property of a surface particle. Therefore, this could suggest that particles with a relatively low thermal conductivity and density may be more sensitive to temperature changes within the environment, as this behaviour had not been observed to the same extent in the suite of experiments investigating thermally conductive particles. This will be investigated in future experiments.

4.3.3.3. Removal of artificial humid environment

Collection of the time-lapse images ended when no changes were observed for approximately 24 hours (approximately 68 hours after the experiment start), as per experimental practice. However, the experiment continued running without the use of automated measurements for an additional 48 hours to ensure that all activity had stopped (thus lasting 116 hours). The cover was removed from the container to reduce the relative humidity and further assess the behaviour of the sublimation cooling and evaporation processes. Observations indicated that the particle was sitting in an empty hollow 168 hours after the cover was removed, suggesting that the meltwater had evaporated. This demonstrated that the evaporation rate was higher than the melting rate as the particle was still capable of transferring energy into the ice from the illumination. When the cover was placed back on the container, the P15 particle melted the ice to generate meltwater. This indicated that the external evaporation processes could override the particle-ice interaction.

4.3.3.4. Summary

Melting was limited in experiment P15 compared to experiments P1b- P14 and P18-P22. A low thermal conductivity prevented efficient conduction of heat through the particle and, therefore, limited direct particle-induced ice melt. Continued absorption of incoming radiation warmed the top surface of the particle and increased the convective heat loss to the atmosphere. Although this enabled some lateral development of meltwater, it prevented the particle from directly melting the ice. Meltwater rarely exceeded the particle depth,

prohibiting (1) floating of the P15 particle and (2) establishment of meltwater convection systems surrounding the lower half of the particle.

It was likely that the cycles of melting and refreezing were controlled by a combination of the physical properties of the particle reducing the capability of inducing ice melt, and subtle shifts across the thermal range. It was deduced that the P15 particle experienced a stable (cool) thermal environment, although this was bordering the stable (cold) boundary. It would be useful to heat a surface particle from an oblique angle (e.g. P16, Table 9.9, Appendix 10) and an embedded particle (e.g. P17b) to further evaluate the role of heat loss to the ambient atmosphere.

4.3.4. P17b: an embedded low density polystyrene particle

This experiment was conducted to assess the behaviour of an 8 mm low density polystyrene particle that was initially embedded within ice. Experiment P17b progressed from experiment P17a after a temperature modification, as the P17a particle experienced a stable (cold) thermal environment and, therefore, limited particle-ice interaction. The hypothesis for experiment P17b is shown in Figure 4.48.

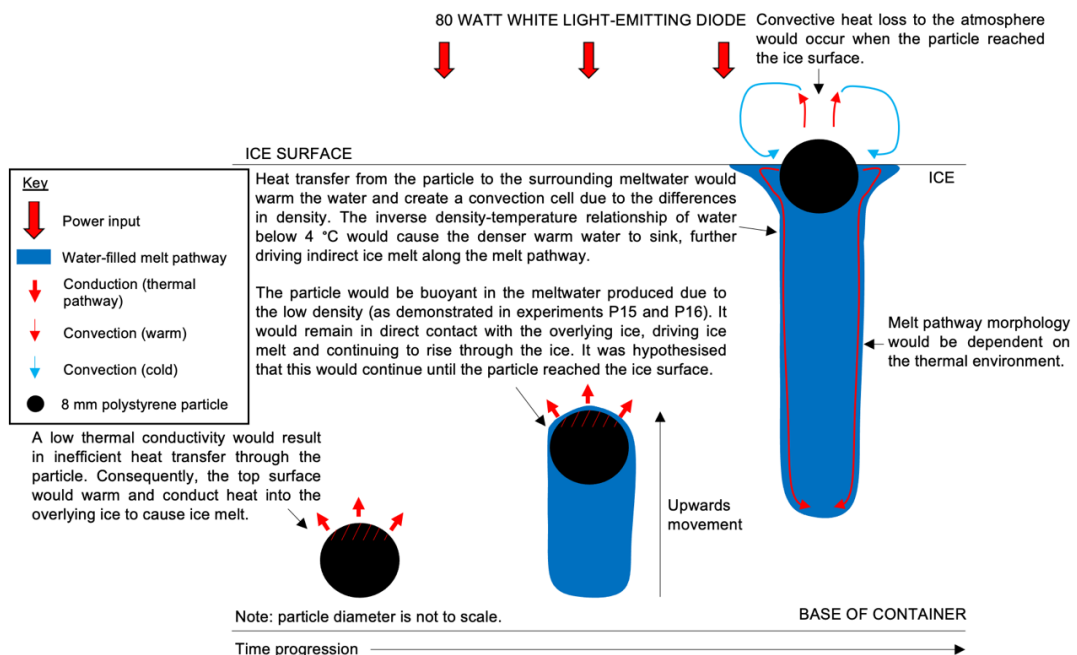


Figure 4.48. Schematic cross-sectional view of the hypothesised particle-ice interaction in experiment P17b.

4.3.4.1. Results and interpretation

The particle was initially embedded approximately 10 mm above the container base and started to melt the ice within 30 minutes. This moved upwards to the ice surface with a particle velocity of $2.20 \times 10^{-6} \text{ m s}^{-1}$ (Figure 4.49) within approximately 8.5 hours.

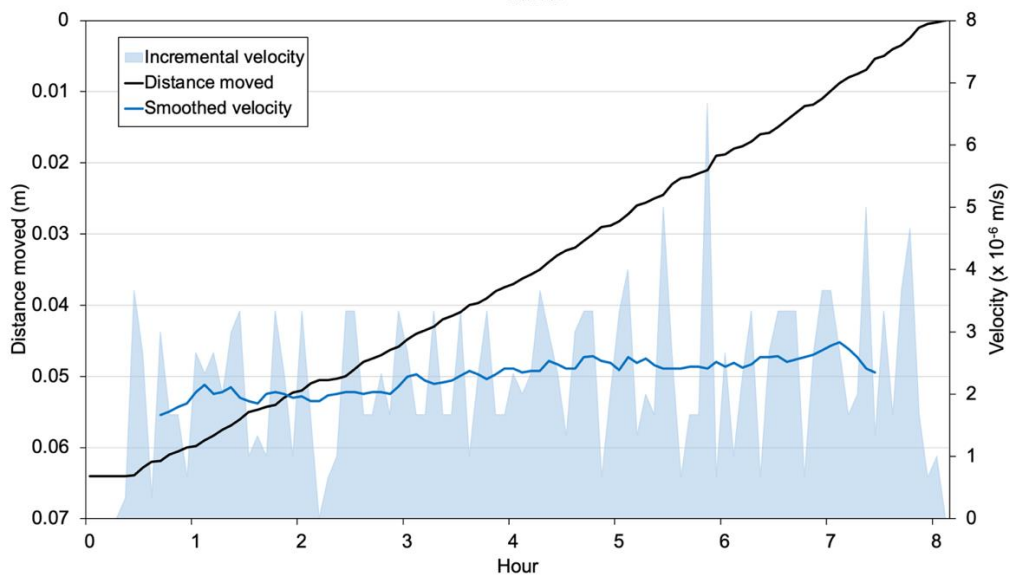


Figure 4.49. Vertical distance moved and velocity of a polystyrene particle in experiment P17b to reach the ice surface.

4.3.4.2. Melt pathway

The production of meltwater facilitated an upward movement of the P17b particle due to its low density. Initial meltwater was observed approximately 0.5-1 mm from the top surface of the particle, indicating that ice melt was caused by interaction with this surface. This supported the hypothesis and was a result of top surface warming from continued particle absorption of incoming radiation, enabling direct heat transfer to the overlying ice to bring the proximal ice to PMP (Figure 4.50). A gas bubble was attached to the particle base (identified as it followed particle movement) and container base in the initial phases of gas bubble development.

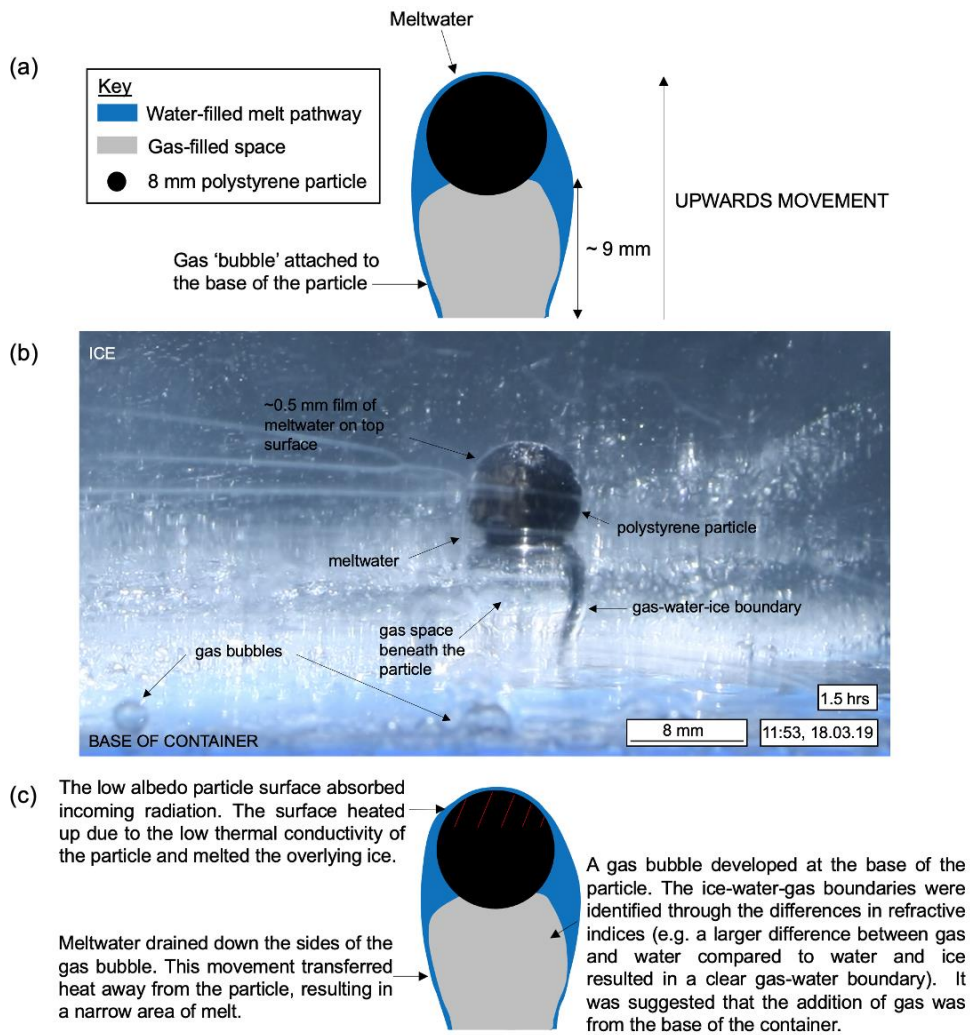


Figure 4.50. Cross-sectional images of the initial movement of the polystyrene particle and early development of a melt pathway in experiment P17b. (a) observational line diagram, (b) photograph and (c) interpretation of the features.

The gas bubble increased in length as it moved with the particle to the ice surface. This reached a state of equilibrium approximately four hours into the experiment (when it was no longer touching the base of the ice container) and remained a constant width and length of approximately 8 mm (matching the particle diameter) and 28 mm, respectively, as it moved through the ice. This suggested that addition of gas was likely from between the ice and container base. The gas bubble was contained within a melt pathway that extended to the original particle position, although both were inclined due to the angled trajectory of particle movement (Figure 4.51). This became more prominent as the particle rose through the ice, likely a result of the particle utilising veins within ice.

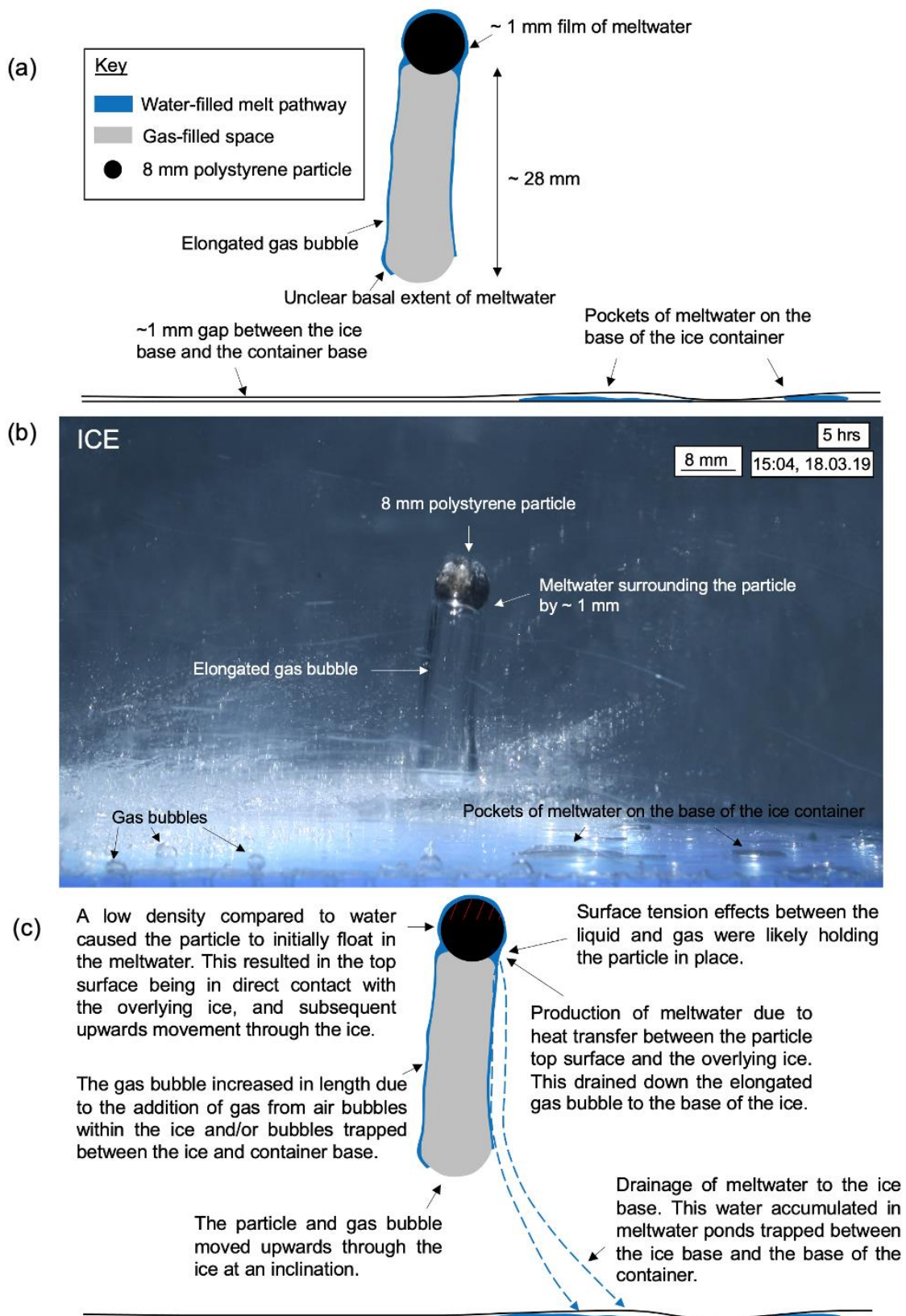


Figure 4.51. Cross-sectional images indicating the development of the gas bubble beneath the polystyrene particle as it moved upwards through the ice in experiment P17b. (a) observational line diagram, (b) photograph and (c) interpretation of the features.

4.3.4.3. Movement of the particle within the gas bubble

The particle remained at the top of the gas bubble as it rose through the ice, suggested to be held in place through surface tension forces between meltwater at the boundary of the particle-ice-gas interface. However, the particle fell through the gas bubble into the underlying melt pathway once the particle reached the ice surface (Figure 4.52), resulting in a decreasing length of the gas bubble as this was filled with meltwater from continued ice melt. It was noted that the particle moved laterally to 'detach' itself from the base of the gas region, now connected to the air above the ice, and continued to move upwards through the ice to extend the melt pathway width. The gas region was filled with meltwater within 14 hours (and, therefore, six hours after the particle dropped from the surface) to create a water-filled melt pathway that extended to the original particle position.

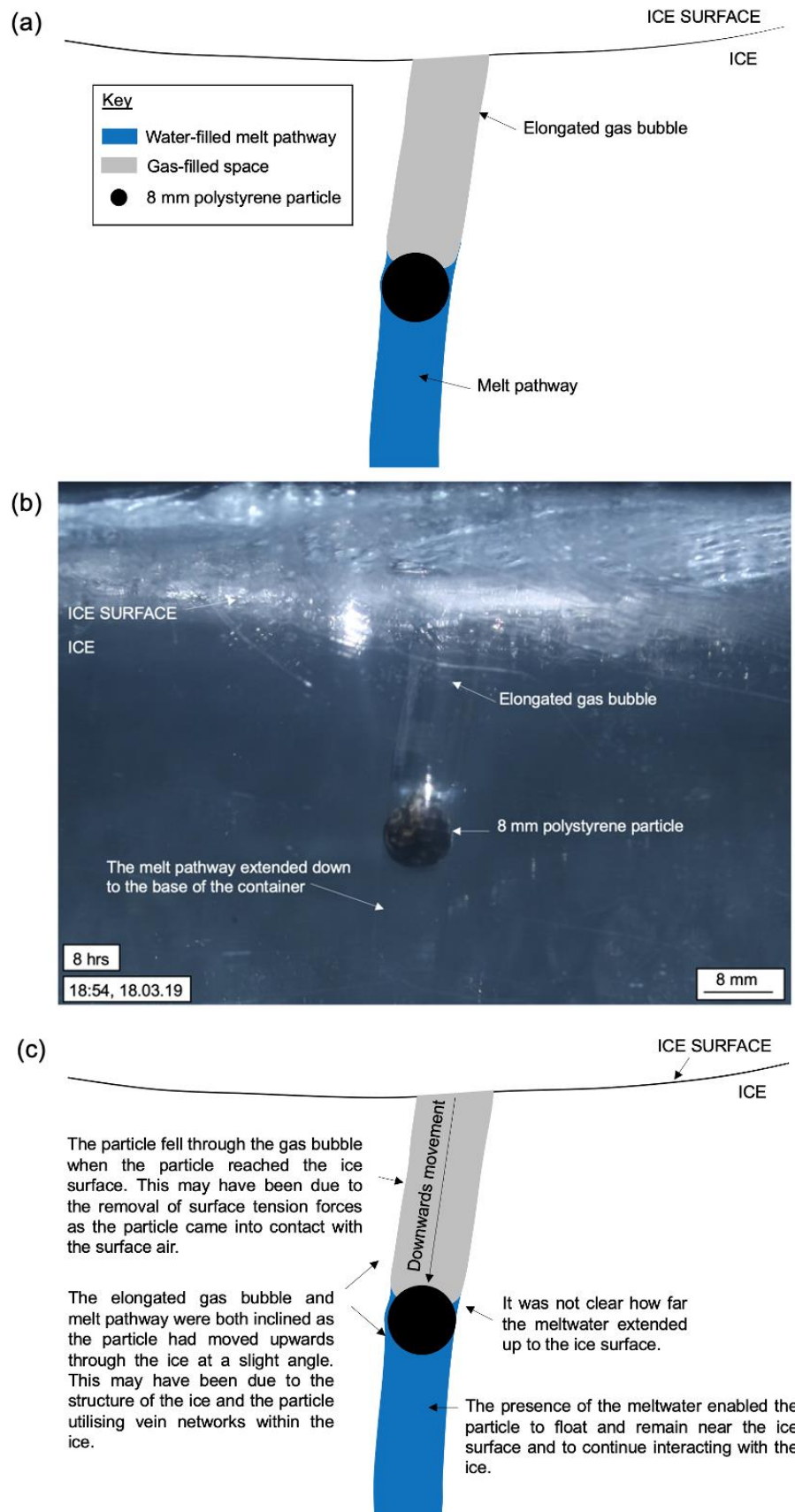


Figure 4.52. Cross-sectional images highlighting the downwards movement of the particle after reaching the ice surface in experiment P17b. (a) observational line diagram, (b) photograph and (c) interpretation of the features.

4.3.4.4. Surface meltwater pond

The particle created a surface meltwater pond that was connected to the top of the melt pathway (Figure 4.53). Refreezing processes were not observed, indicating that the P17b particle experienced a stable (warm) thermal environment. The particle was not exposed at the meltwater surface and settled at the neutral point of buoyancy due to the close density value to water (960-1050 kg m⁻³, Chapter 3). Therefore, all heat absorbed by the particle was fully transferred into the ice rather than experiencing heat loss to the atmosphere.

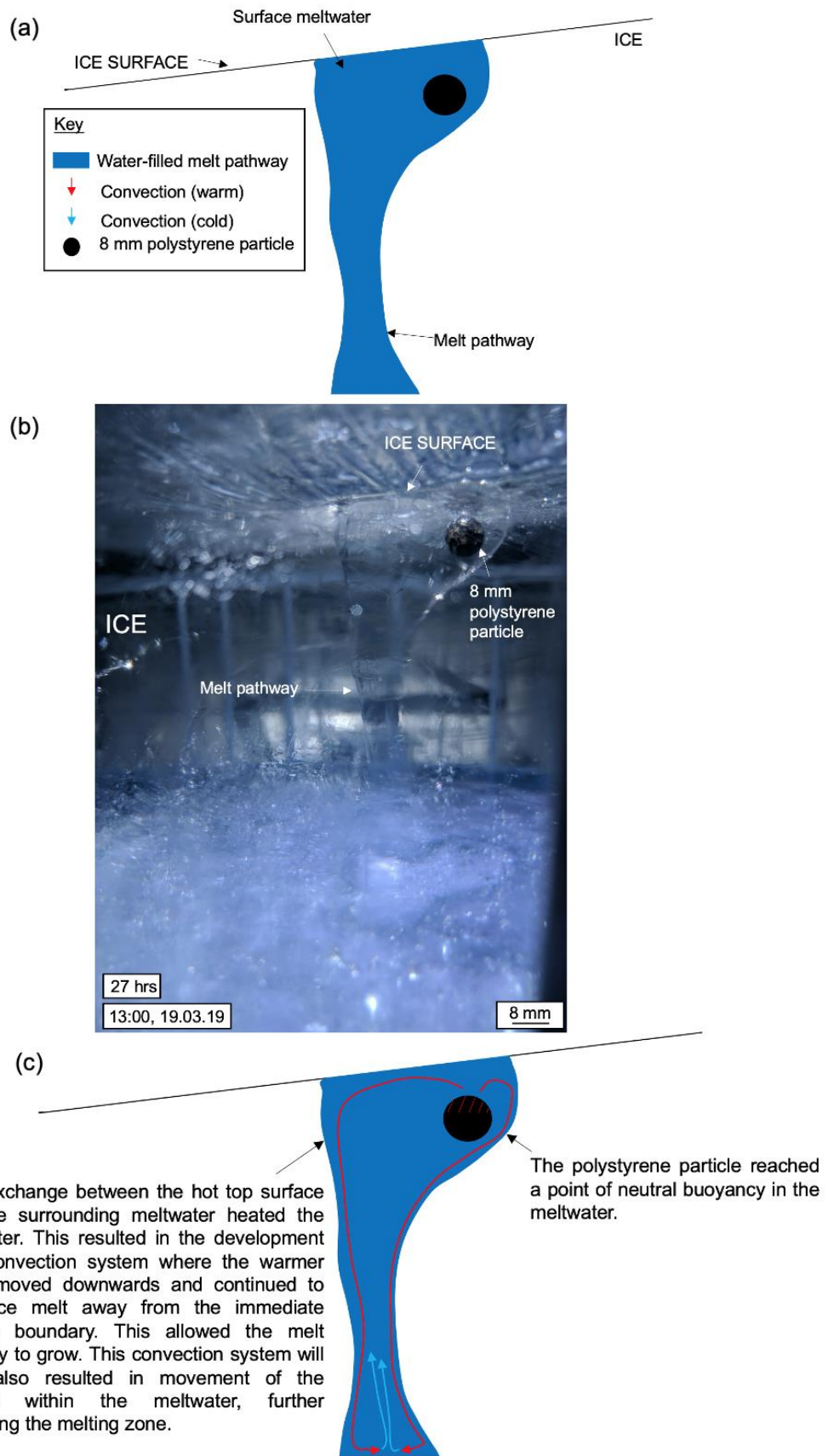


Figure 4.53. Cross-sectional images showing the development of an asymmetric melt pond in experiment P17b. (a) observational line diagram, (b) photograph and (c) interpretation of the features.

4.3.4.5. Basal meltwater pond

A basal meltwater pond developed during particle ascent. It was interpreted that the gas bubble within the melt pathway facilitated drainage of meltwater to the ice base in the early phases of particle-induced ice melt, allowing advection of heat through the system. This likely drained into a gap between the ice and container (the interpreted source of the gas bubble). Evidence for this was identified six hours into the experiment through the formation of air pockets and a layer of water at the base of the container, suggesting that the ice base was not in direct contact with the container base and consequently allowed a space for the meltwater to drain into. Continuous melting, drainage of meltwater, and expansion of the meltwater through a convection system resulted in the growth of a basal meltwater pond to reach a maximum width and height of approximately 180 mm and 20 mm, respectively. This indicated that heat transfer from the floating particle was sufficient to maintain both a surface and basal meltwater pond and indicating the importance of meltwater convection in enhancing a particle's sphere of influence.

4.3.4.6. Summary

These results highlighted that low density particles could re-emerge at the ice surface if exposed to incoming radiation; this concept helped inform the experimental design of experiments carried out in the 'microplastics' theme (Chapter 6). Particle movement was at a velocity of $2.20 \times 10^{-6} \text{ m s}^{-1}$, comparing well with values from experiments involving thermally conductive and high density particles with a low albedo (e.g. P1-P9) in a stable (warm) thermal environment. Two heat transfer mechanisms were demonstrated as the main contributors to ice melt: direct conduction of heat from the top surface of the particle to the overlying ice/water and indirect meltwater convection, supporting the hypothesis. Possible advection of heat through drainage processes and meltwater convection enabled melting of ice away from the direct sphere of influence of the P17b particle.

Differences in heat transfer mechanisms between a submerged particle and a surface particle were highlighted when comparing the behaviour of the P17b particle with the behaviour of particles in experiments P15-P16, and P18-P22.

The P17b particle was initially embedded within the ice, and so it was able to directly heat the overlying ice/water, whilst the particles from experiment P15, P16, and P18 experienced convective heat loss to the atmosphere as the top surface remained exposed to the atmosphere. More ice melt was associated with experiment P17b, suggesting that a low density and a thermally insulating particle has a higher capability of melting ice if embedded within the ice. However, it is likely that the observed differences in ice melt were also partially due to subtle differences in the thermal environment as in experiment P15, agreeing with the emerging theme that the movement of particles is sensitive to subtle changes in temperature.

4.4. Diameter

The P23b-P47 experiments investigated the role of particle diameter in influencing particle-ice interaction. These investigated: (1) single particles; (2) multiple single particles as a single experiment; and (3) particle arrays (Figure 4.54, Table 4.8). Most particles were brass, although chrome steel was also assessed in two experiments, and had a low albedo, high thermal conductivity, and high density. Particle diameters were in the size range 1.5-12 mm. Experiments are described according to experimental code and particle diameter, with repeat experiments clustered for ease of comparison.

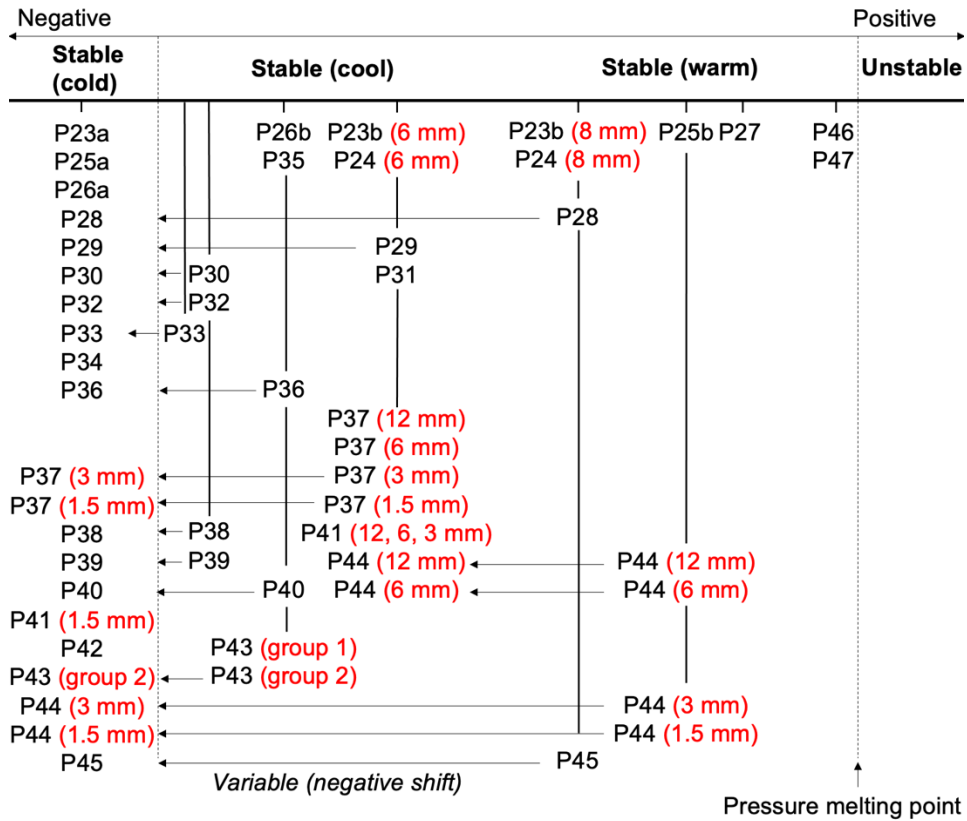


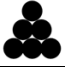

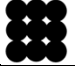
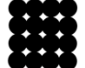


Figure 4.54. The thermal environment of particles in experiments investigating the role of particle diameter in influencing particle-ice interaction. Experiment position has been derived from interpretation of observations, as described in Chapter 3, Section 3.7.

Table 4.8. A summary of the experiments that investigated the role of particle diameter in particle-induced ice melt, indicating the particle diameters, particle configurations and thermal environments as defined in Chapter 3.

Experiment	Particle diameter (mm)	Particle configuration	Thermal environment
P23a	6, 8	Comparison of multiple single particles	Stable (cold)
P23b	6, 8	Comparison of multiple single particles	8 mm: stable (warm) 6 mm: stable (cool)
P24	6, 8	Comparison of multiple single particles	8 mm: stable (warm) 6 mm: stable (cool)
P25a	12	Single particle	Stable (cold)
P25b	12	Single particle	Stable (warm)
P26a	12	Single particle	Stable (cold)
P26b	12	Single particle	Stable (cool)
P27	12	Single particle	Stable (warm)
P28	3	Single particle	Variable: stable (warm) to stable (cold)
P29	1.5	Single particle	Variable: stable (cool) to stable (cold)
P30	1.5	Single particle	Variable: stable (cool) to stable (cold)
P31	12	Single particle	Stable (cool)
P32	1.5	Single particle	Variable: stable (cool) to stable (cold)
P33	1.5	Single particle	Variable: stable (cool) to stable (cold)

Experiment	Particle diameter (mm)	Particle configuration	Thermal environment
P34	3	Single particle	Stable (cold)
P35	12	Single particle	Stable (cool)
P36	3 x 3 array	1 x 2 triangle particle array (3) 	Variable: stable (cool) to stable (cold)
P37	1.5, 3, 6, 12	Comparison of multiple single particles	6 mm, 12 mm: stable (cool) 1.5 mm, 3 mm: variable: stable (cool) to stable (cold)
P38	3 x 3 array	1 x 2 triangle particle array (3) 	Variable: stable (cool) to stable (cold)
P39	5 x 3 array	3 x 2 triangle particle array (5) 	Variable: stable (cool) to stable (cold)
P40	4 x 3 array	2 x 2 square particle array (4) 	Variable: stable (cool) to stable (cold)
P41	1.5, 3, 6, 12	Comparison of multiple single particles	3 mm, 6 mm, 12 mm: stable (cool) 1.5 mm: stable (cold)
P42	9 x 3	3 x 3 square particle array (9) 	Variable: stable (cool) to stable (cold)
P43	16 x 3	4 x 4 square particle array (16) 	Group 1: stable (cool) Group 2: variable, stable (cool) to stable (cold)
P44	1.5, 3, 6, 12	Comparison of multiple single particles	6 mm, 12 mm: variable: stable (warm) to stable (cool) 1.5 mm, 3 mm: variable: stable (warm) to stable (cold)
P45	3	Single particle	Variable: stable (warm) to stable (cold)
P46	1.5	Single particle	Stable (warm)
P47	1.5, 3, 6, 12	Comparison of multiple single particles	Stable (warm)

4.4.1. P23b: a comparison of 6 mm and 8 mm brass and chrome steel particles

Experiment P23b directly compared the behaviour of a 6 mm brass particle with an 8 mm chrome steel particle. Although this experiment was conducted to assess the role of particle diameter on influencing particle-ice interaction, this also considered small differences in particle thermal conductivity. Therefore, this was a useful study of the differences in results between experiments P1b-P2 and experiments P3-P9 in the ‘thermal conductivity’ experimental series.

Experiment P23b led on from experiment P23a following a freezer temperature adjustment, as particle P23a experienced a stable (cold) thermal environment and limited particle-ice interaction. Therefore, both particles were fully embedded within the ice at the experiment start. The hypothesis for experiment P23b is shown in Figure 4.55.

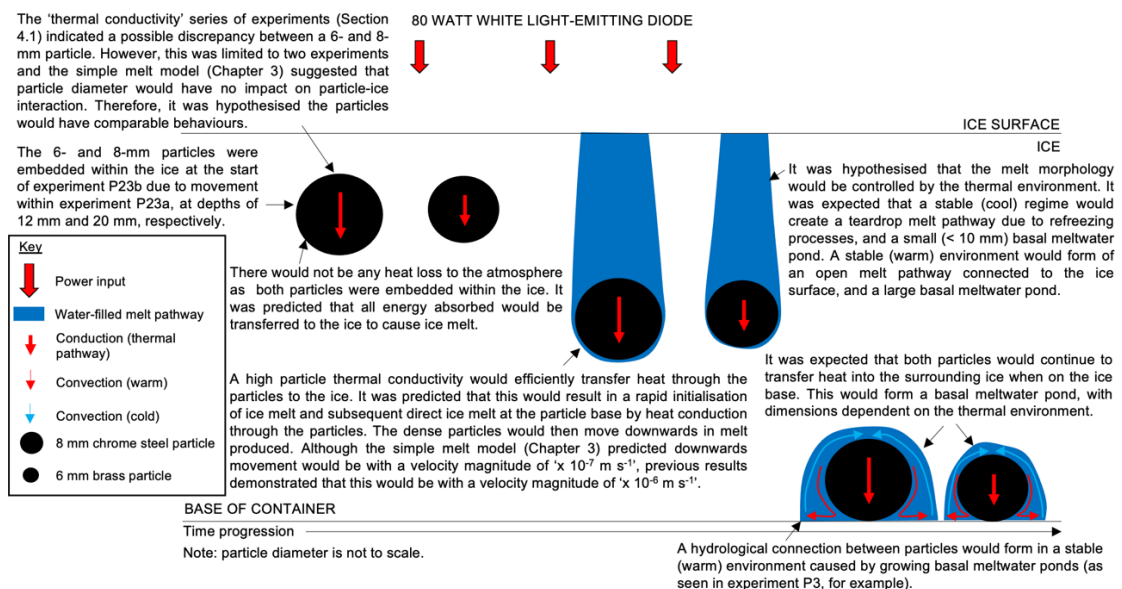


Figure 4.55. Schematic cross-sectional view of the hypothesised particle-ice interaction in experiment P23b.

4.4.1.1. Results and interpretation

The particles melted the ice immediately and moved downwards through the ice. Similar behaviours were noted until approximately four hours, when the 6 mm particle increased in velocity (Figure 4.56) and the particle velocities for the 6 mm and 8 mm particles were $1.69 \times 10^{-6} \text{ m s}^{-1}$ and $1.41 \times 10^{-6} \text{ m s}^{-1}$, respectively. This resulted in the 6 mm particle reaching the ice base approximately 2.5 hours prior to the 8 mm particle. Both particles experienced a velocity increase in the first three (6 mm) and five (8 mm) hours (defined as the 'adjustment period') before stabilising for the remainder of the experiment, likely a result of the particle-ice system reaching a thermal equilibrium. The end of the adjustment period for the 8 mm particle was associated with a shift in behaviour between the two particles, possibly suggesting that the 'equilibrium' rate of particle-ice heat transfer was more efficient for the 6 mm particle than for the 8 mm particle (as identified by the higher particle velocity).

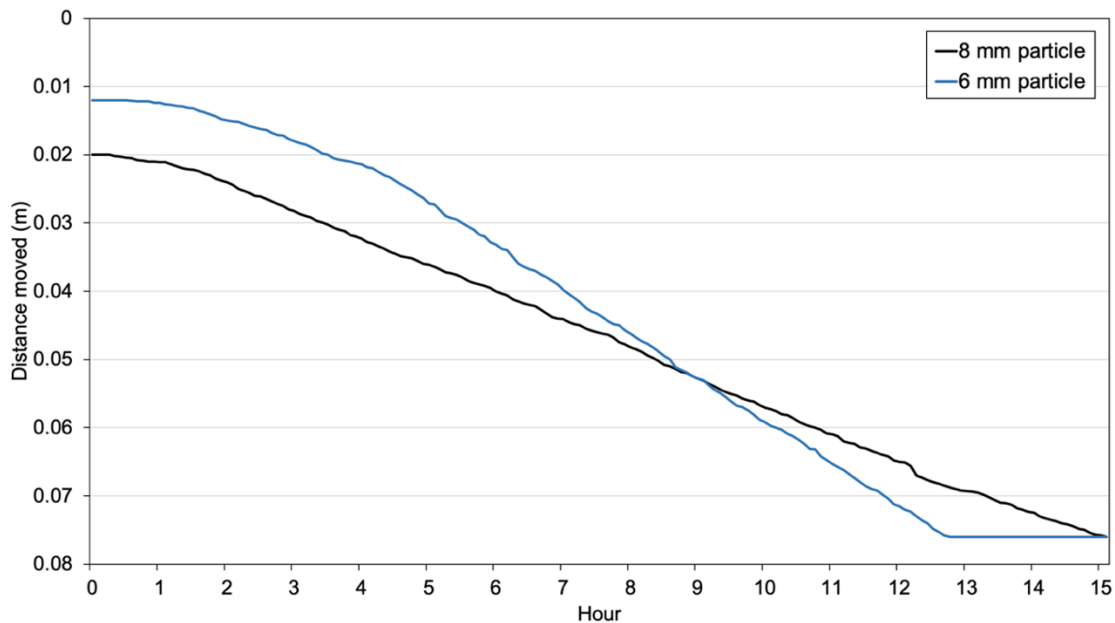


Figure 4.56. Vertical distance moved by a 6 mm brass particle and 8 mm chrome steel particle in experiment P23b.

4.4.1.2. Melt pathway

The melt pathways had a width similar to the particle diameters, with the maximum diameter closest to the particle. Refreezing of meltwater occurred away from the particle heating influence during the experiment, identified by a narrowing of melt pathway diameter. This resulted in closure at the top of the 6 mm particle melt pathway (with an approximate pathway length of 35 mm remaining liquid-filled), suggesting a stable (cool) thermal environment. However, the 8 mm particle melt pathway remained open at the ice surface throughout, although the top extent had narrowed by approximately 1 mm. If refreezing rates were equal, the 8 mm melt pathway should have experienced a narrowing to a diameter of 2 mm (reflecting the 6 mm diameter refreezing observed in the 6 mm melt pathway). As this was not observed, it was deduced that the difference between melt pathway morphologies was unlikely to be due to the different volume of meltwater, and another factor must have been involved.

The differences in particle velocities and melt pathway morphologies were likely a result of two features: (1) the 8 mm particle had a longer thermal pathway due to a bigger particle diameter, and (2) the 8 mm chrome steel particle had a lower thermal conductivity than the 6 mm brass particle (Chapter 3). Both

features would have resulted in the 8 mm particle top surface warming up to a greater extent than the 6 mm particle, to drive stronger convection in the 8 mm particle melt pathway relative to the 6 mm particle melt pathway. Heat from meltwater convection would be used for either (1) indirect ice melt or (2) maintaining water in the liquid form (both would be more difficult in a stable (cool) environment, as identified in this experiment). Therefore, much of the convection energy was used to prevent refreezing in the case of the 8 mm particle in this thermal environment, and so energy was not going into driving indirect ice melt. This differed from the behaviour of the 6 mm particle, whereby a shorter thermal pathway and higher thermal conductivity induced a weaker convection system, resulting in refreezing of the melt pathway. Therefore, much of the convection system established could indirectly drive melting rather than maintaining water in liquid form. Ultimately, this saw the 8 mm particle experience less refreezing in the melt pathway, but also less melting through convection-driven processes, whilst the 6 mm particle experienced more refreezing in the melt pathway, but also more melting through convection-driven processes (identified by a higher particle velocity, used as a proxy for particle-induced ice melt). Although both particles were also experiencing conduction-driven ice melt at the particle base, the subtleties with complex allocation of energy transfer by convection systems in a stable (cool) thermal environment was responsible for the difference between the two particles. However, it was noted that this effect would be diminished with warming temperatures.

4.4.1.3. Basal meltwater pond

The particles reaching the ice base caused the melt pathways to drain, creating a gas-filled pathway (Figure 4.57). However, both particles continued to melt the proximal ice when on the ice base, to create small (<10 mm diameter) hemispherical basal meltwater ponds. Additionally, observations showed that the 6 mm and 8 mm particles moved laterally by approximately 60 mm and 8 mm, respectively. The 8 mm particle did not move across the ice base to the same extent as the 6 mm particle and so did not create a channel; instead, it remained in a partially drained hemispherical basal meltwater pond near the base of the melt pathway.

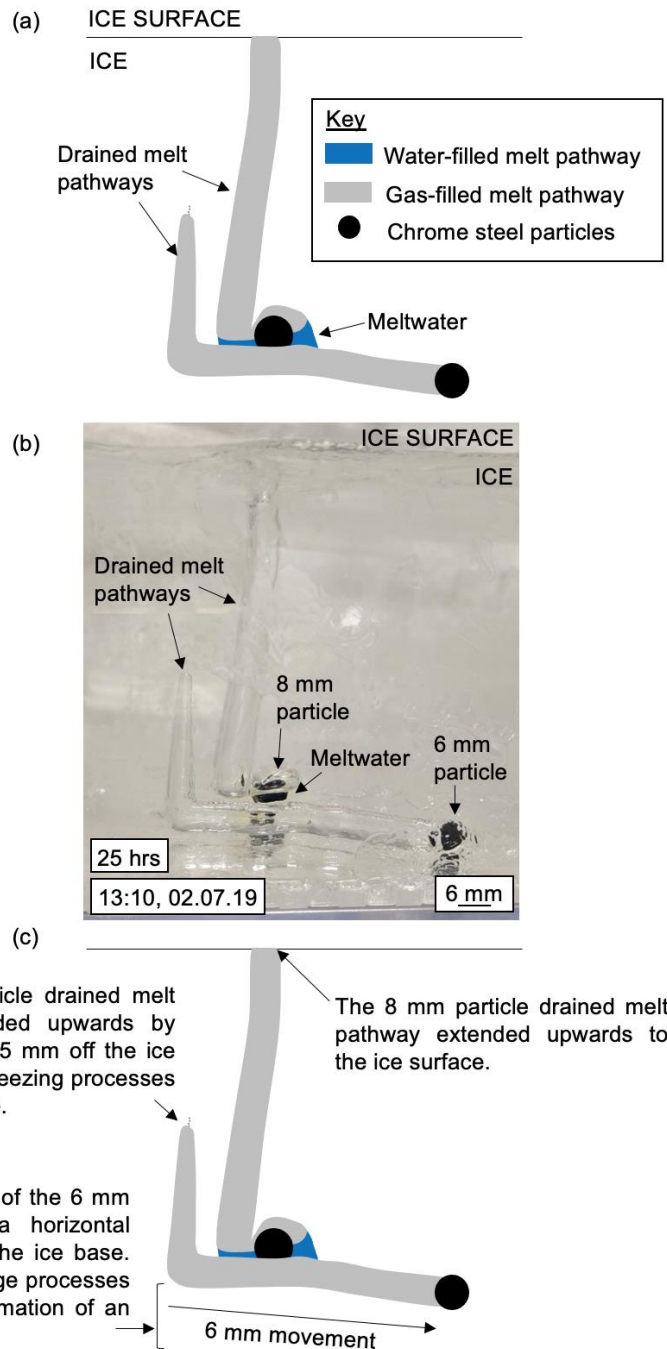


Figure 4.57. Cross-sectional images of the drained melt pathways at the end of experiment P23b. (a) observational line diagram, (b) photograph and (c) interpretation of the features.

4.4.1.4. Summary

The 6 mm and 8 mm particles moved downwards through the ice at particle velocities of $1.69 \times 10^{-6} \text{ m s}^{-1}$ and $1.41 \times 10^{-6} \text{ m s}^{-1}$, respectively. This velocity difference equated to a 2.5 hour difference in the time taken for particles to reach the ice base, and may suggest that particle diameter can influence particle-ice interaction. Subtleties with energy distribution by meltwater convection, indicated by differences between the melt pathway morphologies

(e.g. a closed 6 mm particle pathway and open 8 mm melt pathway), may have been a consequence of the differing particle properties, which also contributed to the inconsistencies in particle-ice behaviour due to the difference balance between heat transfer directed at maintaining liquid water or indirectly melting the ice.

Results from a repeat experiment (P24) compared well with P23b results, where the 6 mm particle had a higher particle velocity than the 8 mm particle ($2.96 \times 10^{-6} \text{ m s}^{-1}$ compared to $1.01 \times 10^{-6} \text{ m s}^{-1}$, respectively), despite a refreezing melt pathway. Although the difference in thermal conductivity between the two materials was considered minimal in the hypothesis, this likely had an influence on behaviour due to subtle differences in heat transfer mechanisms from a warmer top particles surface. Therefore, it would be useful for future experiments to isolate the role of particle diameter by using same material. Subsequent experiments investigated low albedo brass particles with differing diameters (e.g. 1.5 mm, 3 mm, 6 mm, and 12 mm).

4.4.2. P25b: a 12 mm brass particle

Experiment P25b assessed the behaviour of a 12 mm brass particle-ice interaction. This progressed from experiment P25a after an adjustment of freezer temperatures, and so the particle was at a depth of approximately 8 mm at the experiment start. The hypothesis for experiment P25b is shown in Figure 4.58.

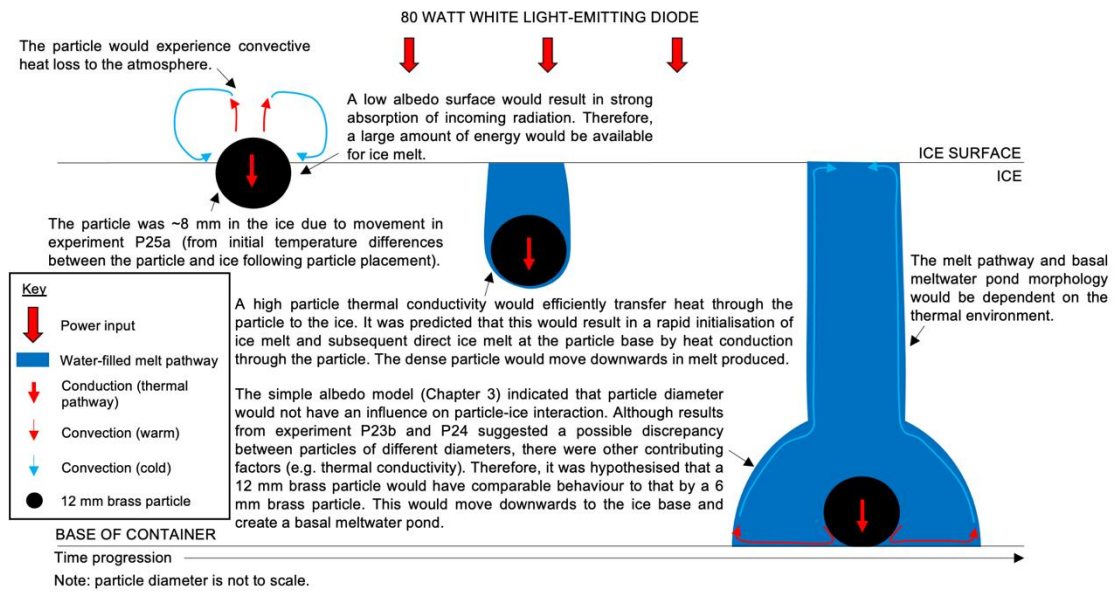


Figure 4.58. Schematic cross-sectional view of the hypothesised particle-ice interaction in experiment P25b.

4.4.2.1. Results and interpretation

The 12 mm particle moved downwards with a particle velocity of $1.32 \times 10^{-6} \text{ m s}^{-1}$ to reach the ice base within approximately 12 hours (Figure 4.59). This followed a vertical trajectory through the ice with approximately 1 mm of lateral movement.

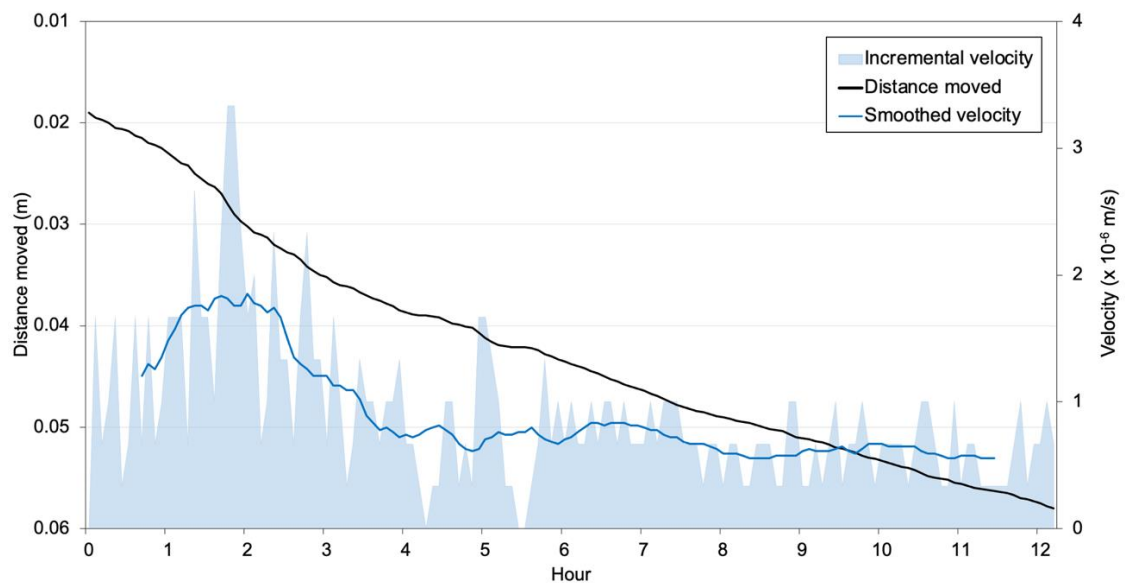


Figure 4.59. Vertical distance moved and velocity of a 12 mm brass particle in experiment P25b.

4.4.2.2. Melt pathway

The 12 mm particle moved downwards to create a melt pathway that extended upwards towards the initial position of the particle and had a width of approximately 12 mm. An area with a strong reflective boundary developed approximately four hours after particle movement began, shown by in-person observations as a gas space above the particle and suggested that partial drainage of the melt pathway occurred. It was inferred that these drainage events were possible due to the thermal state of the ice as the experiment was operating at warm temperatures and so it was likely that the vein network within the ice was liquid-filled. Drainage of water from the vein network into a drainage space (e.g. between ice and container) facilitated further drainage of meltwater from the melt pathway into the vein network and drainage space.

4.4.2.3. Basal meltwater pond

The particle continued to transfer heat to cause ice melt when at the ice base and created a basal meltwater pond. Lateral movement of the particle (from freezer vibrations or asymmetrical heating during meltwater convection) extended the basal meltwater pond (e.g. a maximum width and height of approximately 32 mm and 16 mm, respectively) and this was connected to a partially drained melt pathway.

The radiation source was turned off and the ice block monitored to confirm if meltwater produced was a result of particle-ice interaction or if the ice was in an unstable environment. This showed the refreezing of all meltwater, suggesting that melt was caused by heat transfer between the particle and ice. This confirmed that the particle experienced a stable (warm) thermal environment.

4.4.2.4. Summary

Experiment P25b provided initial insights into the behaviour of a 12 mm thermally conductive particle and agree with results from experiments in the 'thermal conductivity' series, with the particle velocity within the range for 6 mm particles (i.e. $1.32 \times 10^{-6} \text{ m s}^{-1}$). Drainage events (inferred to occur because of the presence of liquid-filled veins) did not appear to have an impact on the melt rate of the particle. The downwards movement of the 12 mm particle to the ice

base following a freezer temperature adjustment in the P25b experiment also demonstrated that the lack of movement in the P25a experiment was caused by the ice being in a stable (cold) thermal environment.

Five repeat experiments were conducted (experiment P26a, P26b, P27, P31 and P35). Experiment P26a demonstrated contrasting results from experiment P25b, where the P26a particle experienced a stable (cold) thermal environment and particle-ice interaction was not observed. However, experiments P26b, P27, P31, and P35 indicated the same behaviour as P25b, i.e. heat transfer into the ice to cause ice melt and subsequent downwards movement to the ice base. However, these exhibited thermal environment-controlled features: experiment P27 was conducted within a stable (warm) thermal environment (and so had an open melt pathway, drainage events, and a relatively high particle velocity of $3.10 \times 10^{-6} \text{ m s}^{-1}$), whilst P26b, P31 and P35 were conducted within a stable (cool) thermal environment (and so had melt pathways with a teardrop morphology and a relatively low particle velocity of $7.05 \times 10^{-7} \text{ m s}^{-1}$, $1.12 \times 10^{-6} \text{ m s}^{-1}$ and $8.73 \times 10^{-7} \text{ m s}^{-1}$, respectively). This allowed the calculation of a mean 12 mm brass particle velocity of $1.36 \times 10^{-6} \text{ m s}^{-1}$; this was higher than the modelled velocity (calculated from the simple melt model in Chapter 3, i.e. $8.63 \times 10^{-7} \text{ m s}^{-1}$), and lower than the mean for 6 mm brass particles (i.e. $1.84 \times 10^{-6} \text{ m s}^{-1}$).

The extent of basal meltwater by a 12 mm particle experiencing a stable (cool) thermal environment was consistent with results from experiments operating in a stable (cool) thermal environment with 6-8 mm thermally conductive particles (e.g. P1b, P3, P5, P8, etc.) as these had a hemispherical morphology and extended approximately 2 mm above the particle (Figure 4.60). These experiments confirmed previous findings that demonstrated the relative importance of thermal environment on controlling particle-induced ice melt.

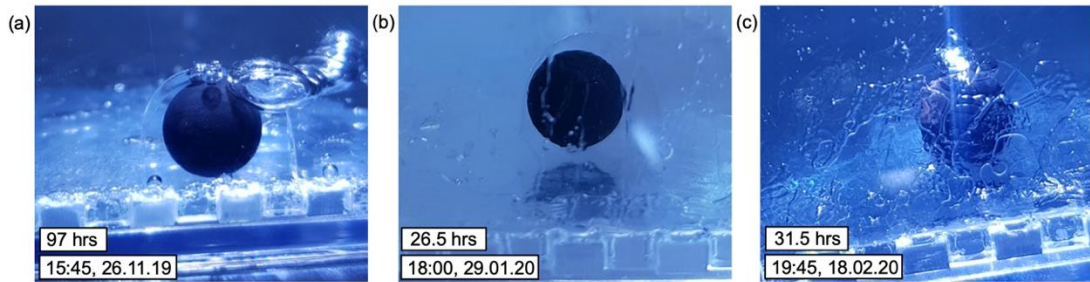


Figure 4.60. Photographs of the basal meltwater ponds in experiments (a) P26b, (b) P31, and (c) P35.

The refreezing melt pathways retained consistent dimensions throughout particle movement (approximately 4 mm above particle P26b, approximately 11 mm above particle P31, and approximately 7 mm above particle P35) and did not exceed a width greater than the particle diameter. This suggested that dynamic equilibrium between heat transfer from the particle and the ice was established in these experiments, and confirmed previous interpretations that a high thermal conductivity was associated with a narrow melt pathway.

4.4.3. P28: a 3 mm brass particle

Previous experiments had suggested that there may be a possible difference between behaviours of particles with different diameters. Therefore, experiment P28 was conducted to assess the behaviour of a smaller particle than previously used. This investigated a single 3 mm black brass particle placed on the ice surface. The hypothesis for experiment P28 is shown in Figure 4.61.

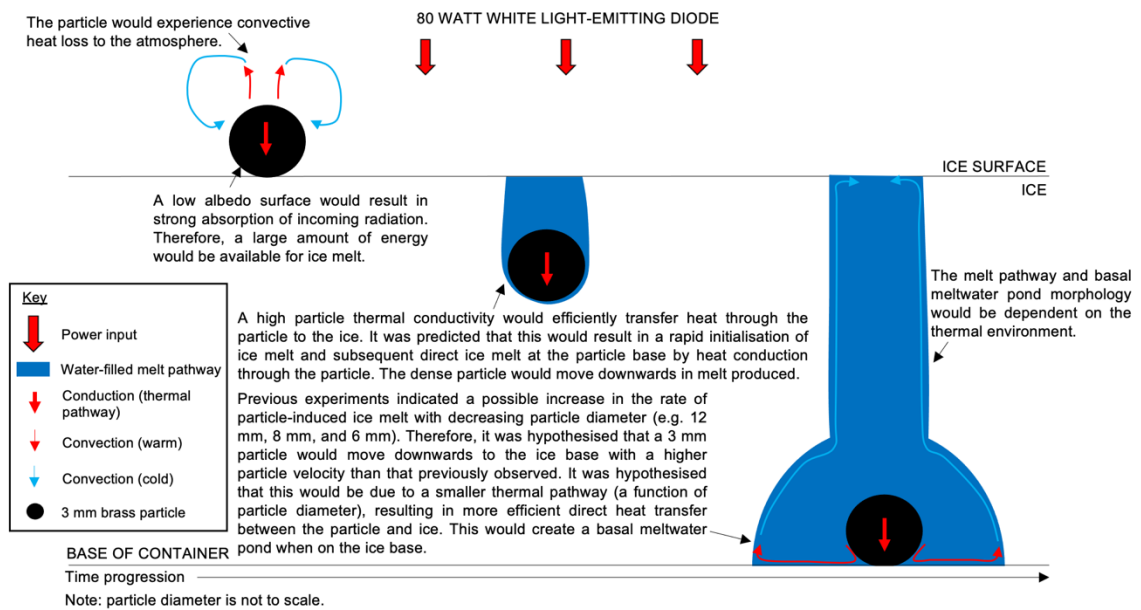


Figure 4.61. Schematic cross-sectional view of the hypothesised particle-ice interaction in experiment P28.

4.4.3.1. Results and interpretation

The 3 mm particle moved downwards to a maximum depth of 46 mm with a mean particle velocity of $1.26 \times 10^{-6} \text{ m s}^{-1}$. Movement was within the first 11 hours, until the particle remained stationary for the remainder of the experiment (approximately 43.5 hours, Figure 4.62). It was interpreted that downwards movement was caused by active particle-ice interaction, rather than exclusively the initial temperature differences of the particle and ice immediately after surface placement, due to the prolonged time of movement.

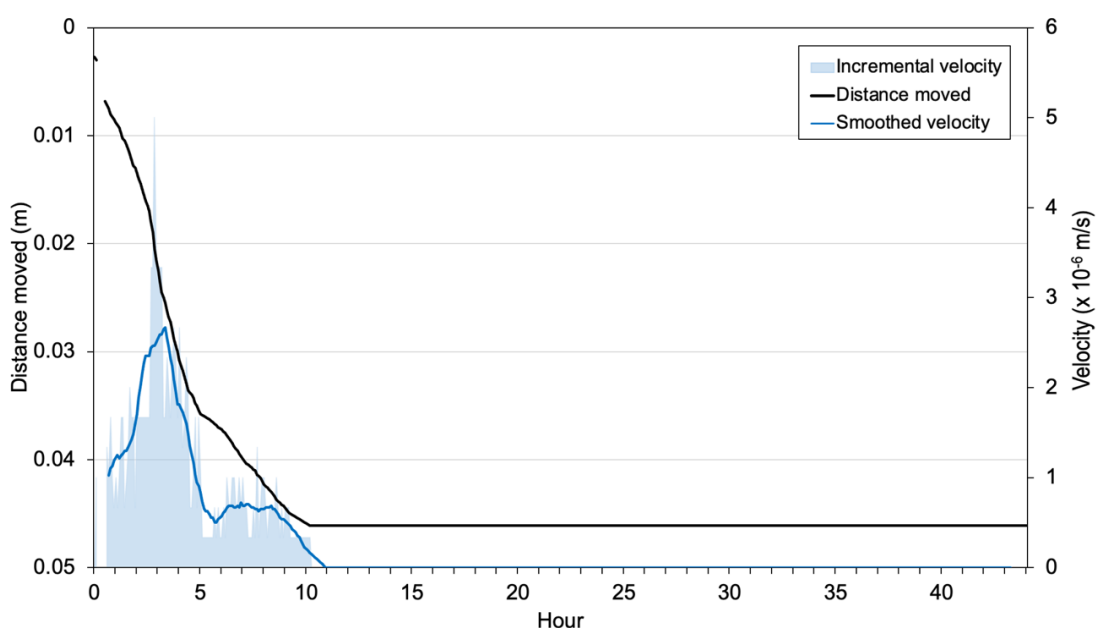


Figure 4.62. Vertical distance moved and velocity of a 3 mm brass particle in experiment P28.

4.4.3.2. Melt pathway

In the first six hours of the experiment, the particle created an inclined melt pathway that extended to the ice surface and had a width similar to the particle diameter (Figure 4.63). However, refreezing occurred, identified by a narrowing of the central segment of the melt pathway and consequent reduction in pathway length to create a teardrop melt pathway approximately 2 mm above the particle. The change in melt pathway morphology demonstrates the dynamic nature of the internal hydrological systems within ice. It was proposed that the thermal environment experienced by the 3 mm particle shifted from a stable (warm) environment to a stable (cold) environment, consequently stalling the particle within the ice system. At this point, heat transfer from the particle to the ice was not sufficient to cause ice melt and maintain a liquid-filled melt pathway. The stalled 3 mm particle will be investigated in subsequent experiments.

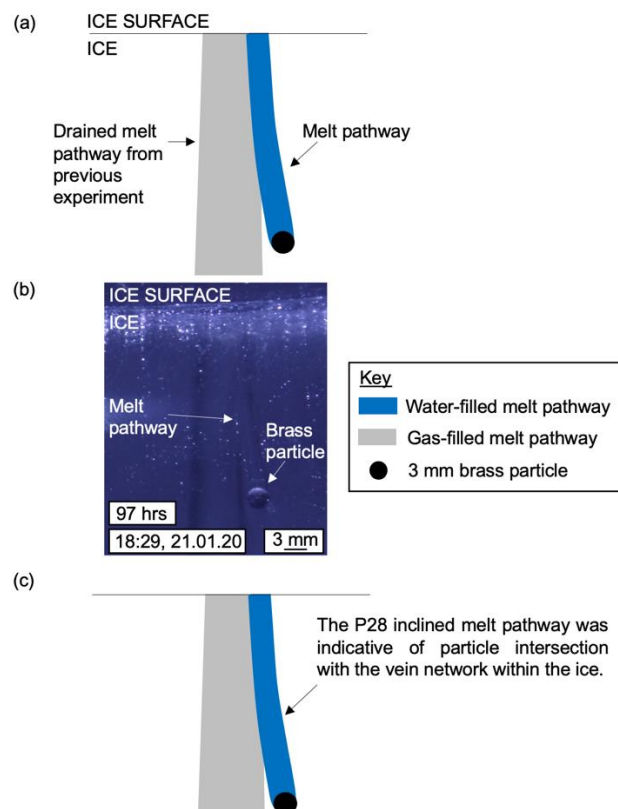


Figure 4.63. Cross-sectional images of the inclined melt pathway in experiment P28. (a) observational line diagram, (b) photograph and (c) interpretation of the features.

4.4.3.3. Summary

Experiment P28 demonstrated that a 3 mm particle could not melt the ice to move to a depth >46 mm. This did not support the hypothesised outcome, where it was expected that the 3 mm particle would melt to the ice base with a higher particle velocity than the 6 mm, 8 mm, and 12 mm particles. However, a negative shift across the thermal range (identified by a change in melt pathway morphology) occurred during this experiment, and so it could not be ruled out that 3 mm particle-ice interaction ceased due to a shift into a stable (cold) environment.

To confirm interpretation of experiment P28, investigation into a 3 mm particle was repeated in two further experiments (P34 and P45). Both demonstrated that a 3 mm particle was unable to sufficiently melt the ice to move downwards to the ice base. Experiment P34 was conducted within a stable (cold) environment, where the particle moved downwards to a depth of approximately 3.4 mm over a 45 minute period. This relatively short period suggested that movement was a result of initial temperature differences between the particle and ice. Conversely, the P45 particle initially experienced a stable (warm) thermal environment, allowing a 13 mm downwards movement with a particle velocity of $5.04 \times 10^{-7} \text{ m s}^{-1}$ over a seven hour period. However, similar to experiments P28 and P32, the P45 particle then stalled within the ice, suggesting a negative shift to the stable (cold) environment once the particle was embedded (Figure 4.64). Two control experiments using different particle diameters (e.g. 12 mm in P31 and P35) confirmed that the freezer system was in an environment that allowed particle-induced ice melt for experiments P28 and P34. This confirmed that these findings were a result of the particle diameter and suggested that the thermal environment may be diameter-dependent (e.g. it appeared as if smaller particles experienced stable (cold) thermal environments at warmer temperatures than larger particles). It would be useful to assess the behaviour of a smaller particle to determine if the same finding also applies.

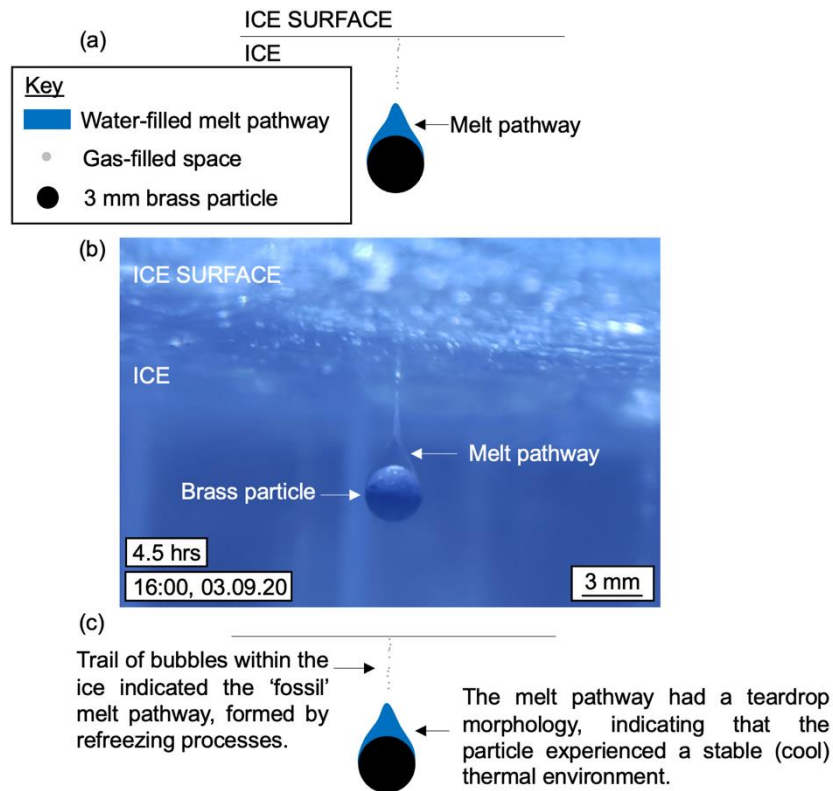


Figure 4.64. Cross-sectional images showing refreezing processes in experiment P45 following a negative shift across the thermal range. (a) observational line diagram, (b) photograph and (c) interpretation of the features.

4.4.4. P29: a 1.5 mm brass particle

Results from experiments P28, P34 and P45 (3 mm particle) demonstrated a stalling behaviour once the particle became embedded within ice. The behaviour of a 1.5 mm particle was investigated to further assess this finding. This would confirm whether particles with a diameter less than 6 mm experienced reduced particle motion. The hypothesis for experiment P29 is shown in Figure 4.65.

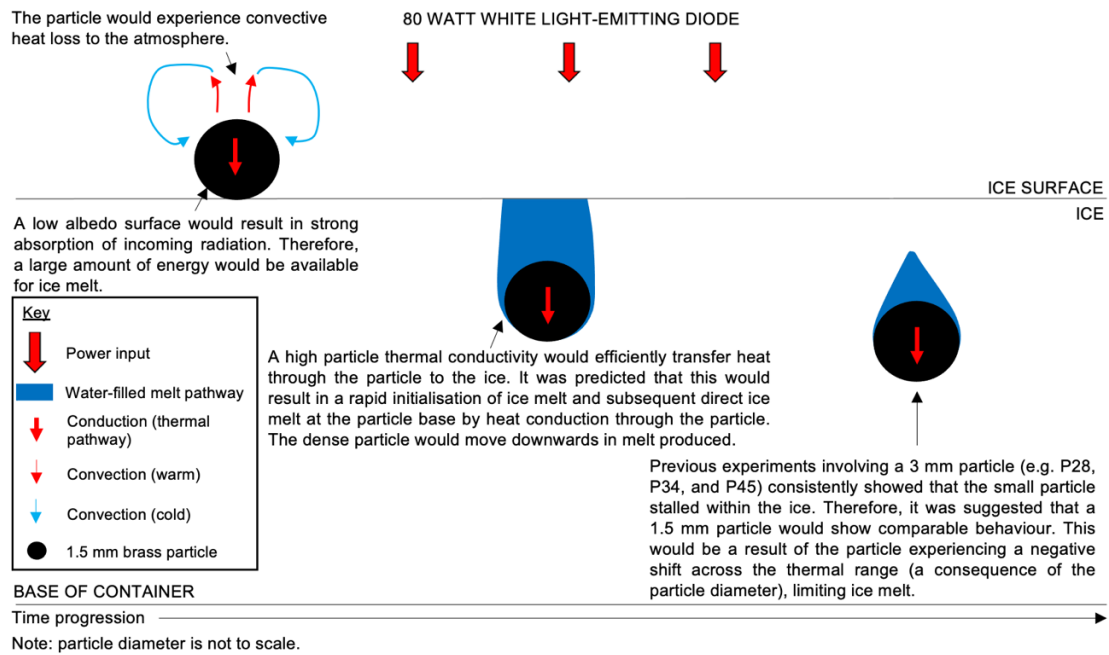


Figure 4.65. Schematic cross-sectional view of the hypothesised particle-ice interaction in experiment P29.

4.4.4.1. Results and interpretation

The particle moved downwards through the ice with a particle velocity of $1.59 \times 10^{-7} \text{ m s}^{-1}$ to a depth of 19 mm within 33 hours. This could not be plotted in graphical format due to unclear time-lapse images. It was interpreted that downwards movement was caused by active particle-ice interaction, rather than exclusively the initial temperature difference of the particle and ice immediately after surface placement, due to the prolonged time of movement. In-person observations noted that the 1.5 mm particle moved with a refreezing melt pathway, suggesting that the experiment was conducted within the stable (cool) thermal environment. The stalled behaviour suggested a negative shift across the thermal range to a stable (cold) environment.

4.4.4.2. Summary

Experiment P29 demonstrated that a 1.5 mm particle, like a 3 mm particle, was unable to sufficiently melt the ice to reach the ice base. The particle velocity was also reduced ($1.59 \times 10^{-7} \text{ m s}^{-1}$) compared to previous experiments. A control experiment (experiment P31) confirmed that the freezer temperatures were in an environment where particle-ice interaction was possible for a 12 mm particle. Therefore, a logical interpretation would be that the limited particle-

induced ice melt in experiment P29 was due to the particle diameter. These findings reinforce the interpretation that the thermal environment was diameter-dependent.

Subsequently, an investigation into 1.5 mm particle-ice interaction was repeated four times in experiments P30, P32, P33 and P46. Experiments P30, P32, and P33 exhibited similar results to P29 as there was limited particle movement to depths of approximately 5 mm, 4 mm, and 1 mm, respectively. Experiment P32 was conducted on a more transparent ice block (to assess the possibility that bubbles hindered 1.5 mm particle-induced ice melt) and confirmed that reduced particle-ice interaction was still observed even without the presence of bubbles. Experiment P33 investigated an unpainted particle to investigate if the thickness of the black paint may have reduced the thermal conductivity of the particle. This confirmed that reduced particle-ice interaction was still observed even without a paint layer. As previous experiments involving unpainted brass particles (IA) demonstrated their capability of efficient ice melting (e.g. P11b, P12b, etc.), this concluded that the black paint thickness was not controlling this observed behaviour. P31 established that the ice was in a thermal environment where particle-ice interaction could occur, and so results from P29, P30, P32 and P33 were confirmed as being caused by the particle diameter.

P46 contrasted with all other experiments of this type as the particle was able to melt downwards to the ice base; however, this also showed bulk melting of the ice and it was inferred that these results were due to the ice proximity to the unstable environment (Figure 4.66). At PMP, all heat transferred from the 1.5 mm particle was coupled into melting. These findings suggest that, although ultimately controlled by the thermal environment, the heat transfer distribution from smaller particles (e.g. < 3 mm) differs from larger particles (e.g. > 6 mm), consequently reducing the ice melting rate. Additionally, this may indicate that the boundaries between stable (cold) and stable (cool) for smaller particles (e.g. 1.5 mm and 3 mm) may be at higher temperatures than for larger particles (e.g. 6 mm and 12 mm). Therefore, the thermal environment boundaries are diameter dependent. A similar finding was also observed in the 'density' series of experiments, and so it can be deduced that the thermal environment is

overall dependent on particle properties. A direct comparison of all particles of each diameter would be useful to assess the behaviour within the same thermal and hydrological system.

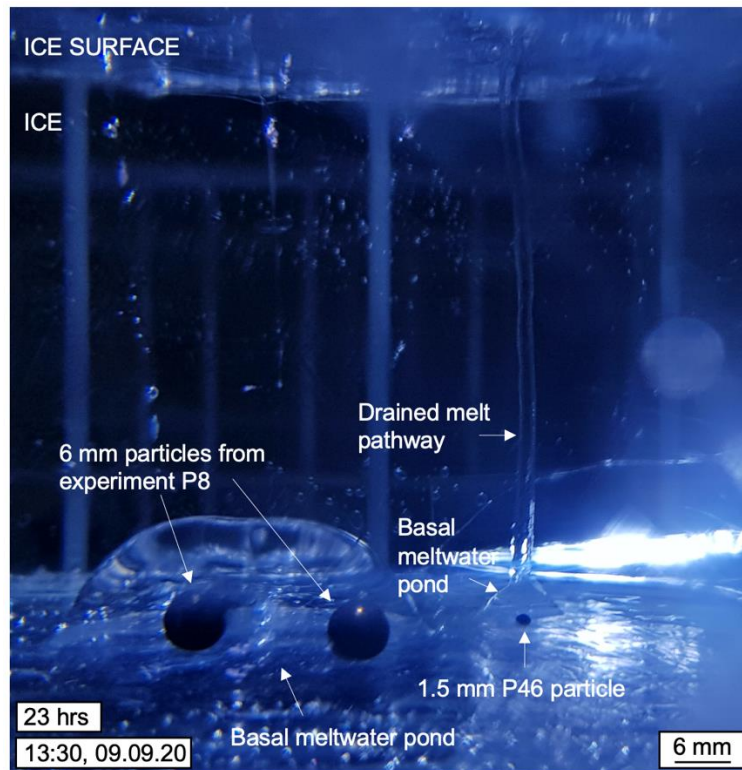


Figure 4.66. Cross-sectional photograph of the basal meltwater experienced in experiment P46.

4.4.5. P37: a comparison of 1.5 mm, 3 mm, 6 mm, and 12 mm brass particles

Experiment P37 directly compared the behaviour of four black brass particles with the same physical properties, excluding diameter, on an ice surface. This comparison involved particles diameters used in previous single-particle experiments (e.g. 1.5 mm, 3 mm, 6 mm, and 12 mm), and allowed observations within similar thermal and hydrological systems. Particles were placed in a square array on the ice surface with a minimum distance of 7 mm between particles to avoid particle-particle interaction (Figure 4.67). The hypothesis for experiment P37 is shown in Figure 4.68.

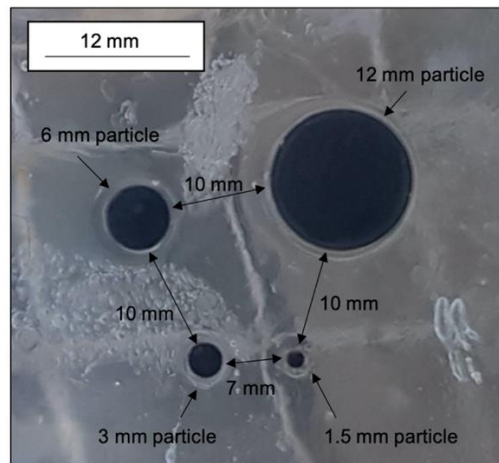


Figure 4.67. Plan-view photograph of the particle configuration on the ice surface in experiment P37.

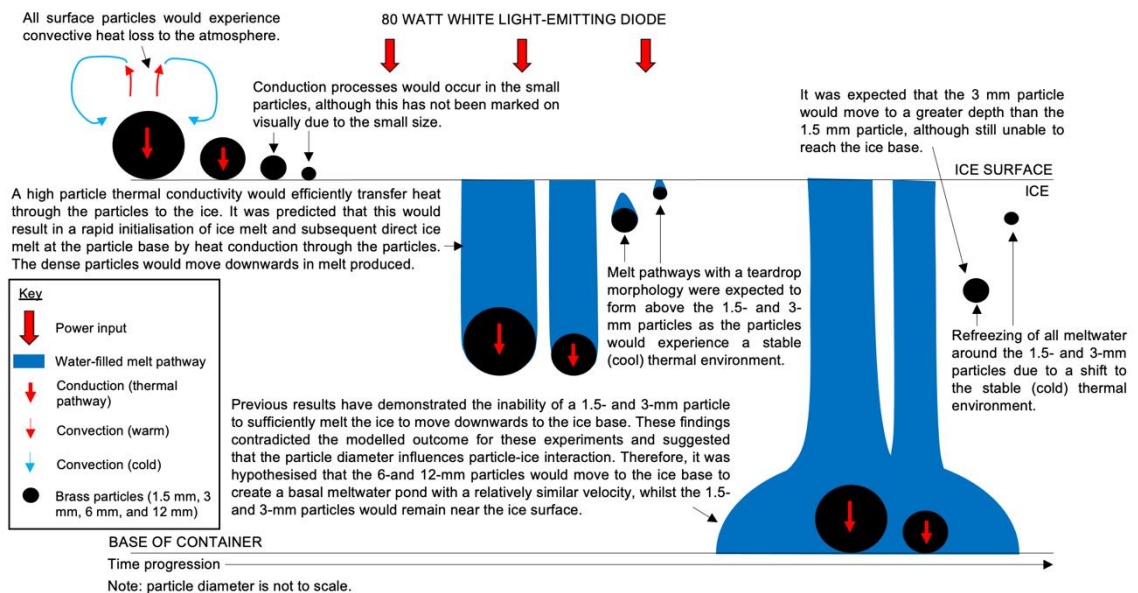


Figure 4.68. Schematic cross-sectional view of the hypothesised particle-ice interaction in experiment P37.

4.4.5.1. Results and interpretation

All particles melted the ice immediately after surface placement and, consequently, moved downwards into the ice immediately. The 12 mm and 6 mm particles had a similar particle velocity during the initial stages of the experiment (i.e. $1.13 \times 10^{-6} \text{ m s}^{-1}$ and $1.07 \times 10^{-6} \text{ m s}^{-1}$, respectively), although the 6 mm particle velocity increased relative to the 12 mm particle after six hours. The relative increase resulted in the 6 mm particle reaching the ice base three hours faster than the 12 mm particle, despite the 12 mm particle initially having a slightly higher velocity. The 1.5 mm and 3 mm particles did not melt the ice

sufficiently to reach the base of the ice; the 3 mm particle ceased moving at a depth of approximately 26 mm, whilst the 1.5 mm particle stalled at a depth of approximately 3 mm. Overall, the average particle velocities were calculated at $9.03 \times 10^{-7} \text{ m s}^{-1}$, $1.06 \times 10^{-6} \text{ m s}^{-1}$, and $4.15 \times 10^{-7} \text{ m s}^{-1}$ for the 12 mm, 6 mm, and 3 mm particles, respectively (Figure 4.69). Data for the 1.5 mm particle movement were not collected due to a restricted view in the time-lapse images.

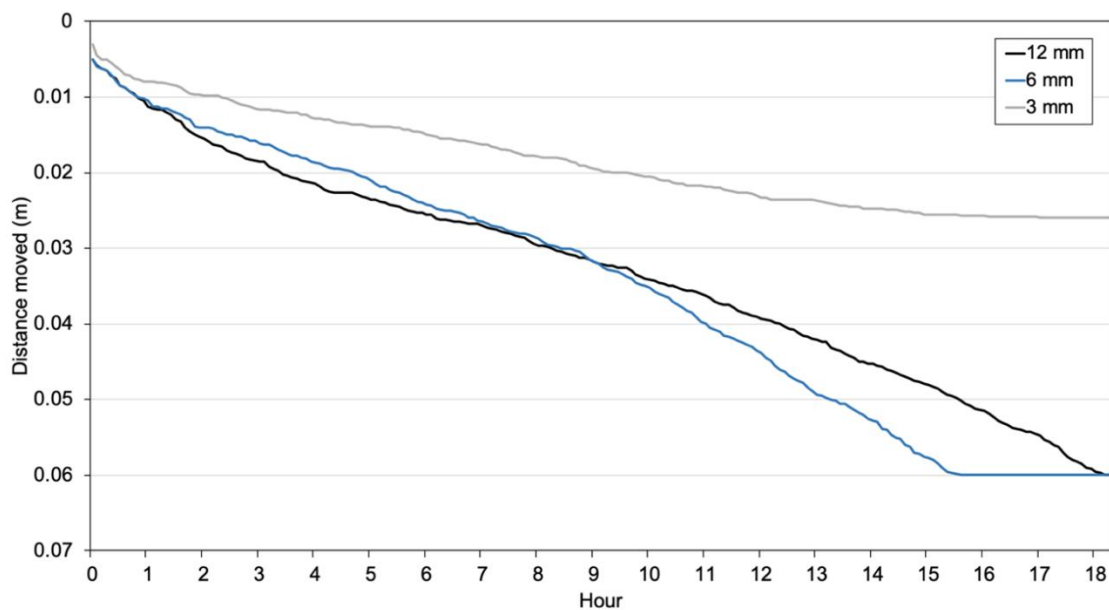


Figure 4.69. Vertical distance moved by a 3 mm, 6 mm, and 12 mm brass particle in experiment P37.

4.4.5.2. Melt pathway

The 3 mm, 6 mm, and 12 mm particles generated melt pathways that had a width of the respective particle diameters, whereas melt associated with the 1.5 mm particle had refrozen within the first five hours of the experiment. All melt pathways refroze during the experiment, although these were at different rates due to the differing diameters of the pathways. For example, the 12 mm particle melt pathway remained open to the ice surface for a minimum of five hours; at this point, all other melt pathways had completely refrozen at the surface (Figure 4.70). This demonstrated similar results to experiments P23b and P24, where the larger particle sustained an open melt pathway for a longer period than smaller particles. However, unlike experiment P23b, maintaining a melt pathway in a liquid form did not hinder the indirect component of melting through convection. This could be due to a higher thermal conductivity associated with a 12 mm brass particle, and subtle differences in the thermal

state of the ice. Experiments have demonstrated thus far that subtle changes in heat transfer mechanisms can significantly alter the behaviour of a particle.

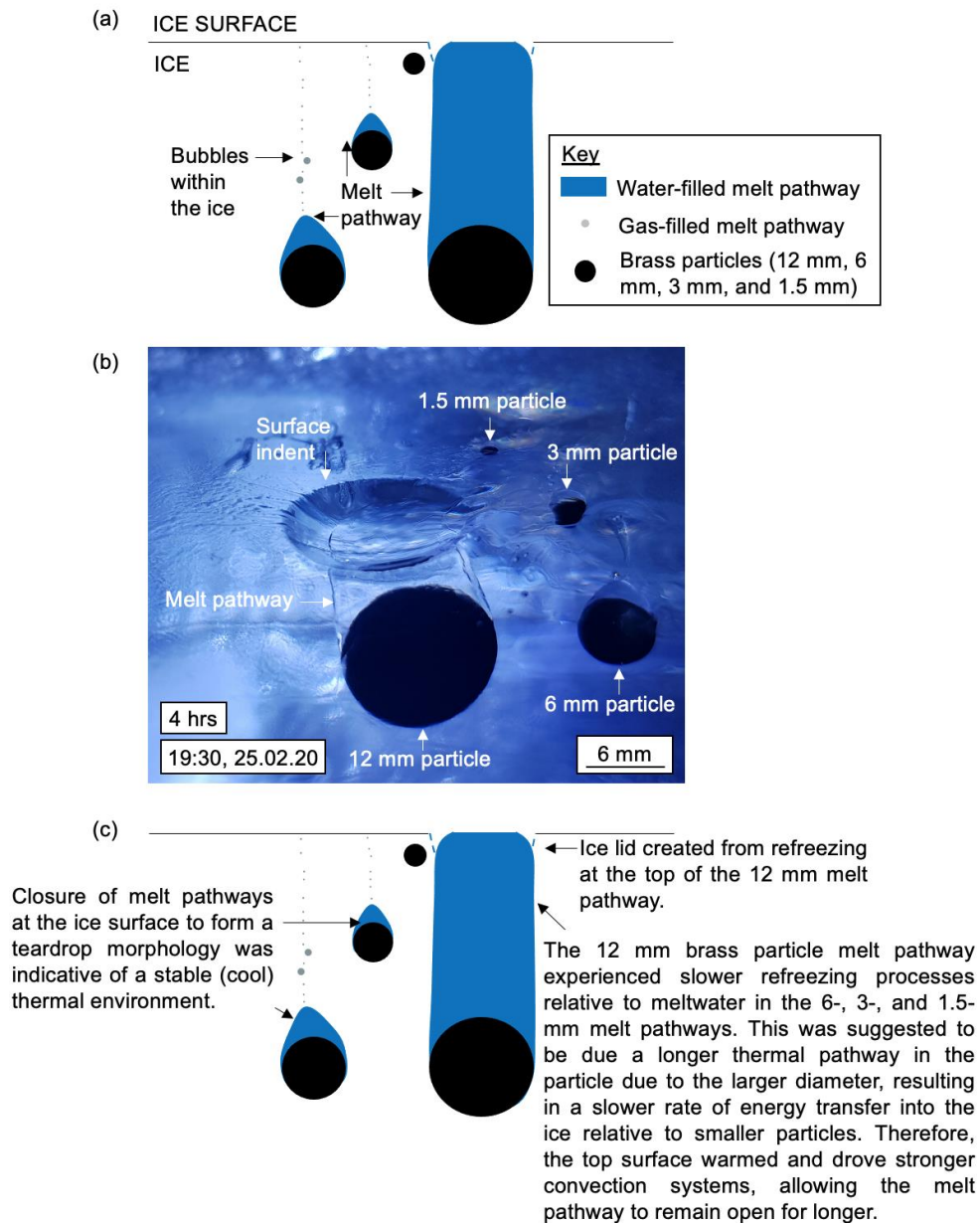


Figure 4.70. Cross-sectional images of the melt pathways within the ice in experiment P37. (a) observational line diagram, (b) photograph and (c) interpretation of the features. Note that (b) was taken at an oblique angle from the opposite view of (a) and (c).

4.4.5.3. Basal meltwater pond

Particles continued to transfer heat into melting the ice when at the ice base to create basal meltwater ponds (Figure 4.71). However, refreezing of melt pathways, in addition to the relatively small size of the basal meltwater ponds, suggested that the 6 mm and 12 mm particles experienced a stable (cool)

thermal environment for the experiment duration, whilst the 1.5 mm and 3 mm particles experienced a negative shift from stable (cool) to stable (cold).

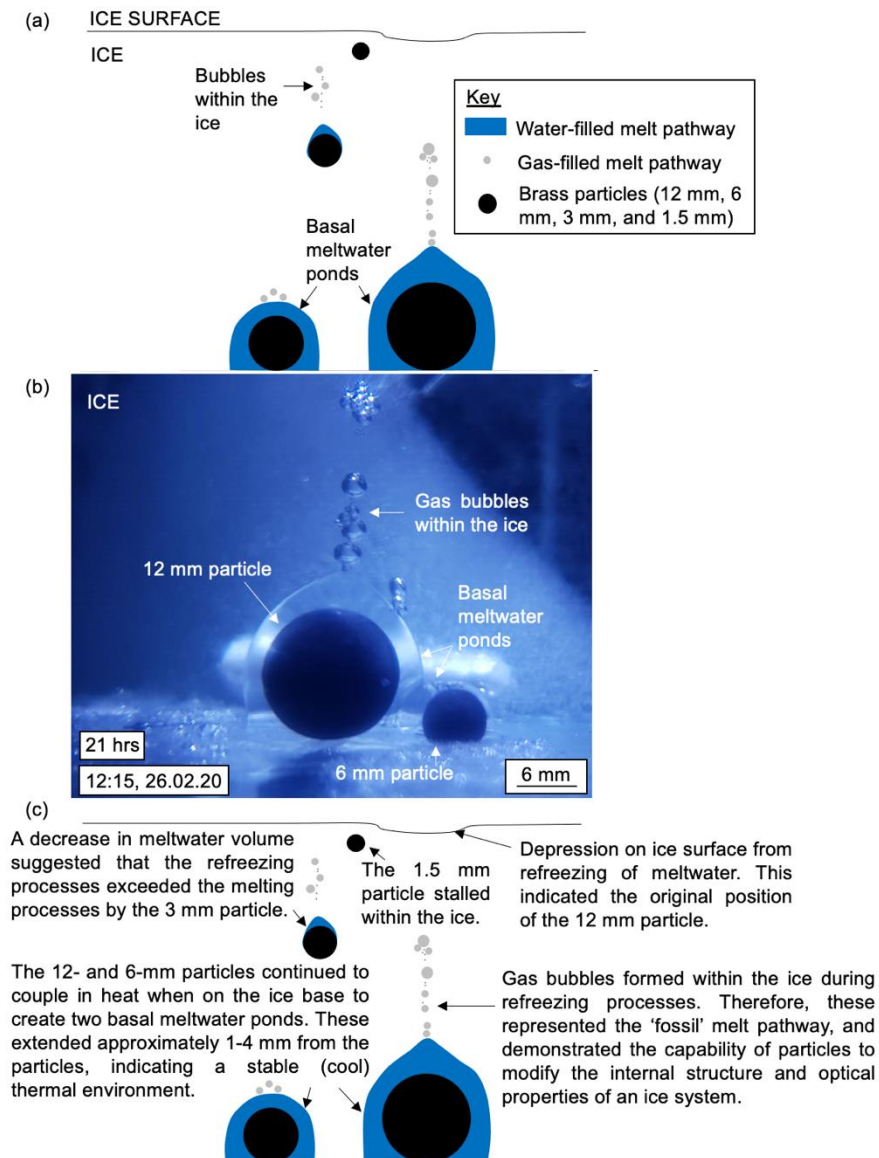


Figure 4.71. Cross-sectional images of the basal meltwater ponds in experiment P37. (a) observational line diagram, (b) photograph and (c) interpretation of the features. Note that (b) was taken at a 90° angle to (a) and (c) due to bubbles in the ice obscuring the view slightly.

4.4.5.4. Summary

This experiment indicated that the smallest particles (e.g. 1.5 mm) become trapped at the ice surface, the middle-sized particles (e.g. 3 mm) stall when embedded within ice, and the largest particles (e.g. 6 mm and 12 mm) melt the ice sufficiently to move downwards to the ice base. Results supported the hypothesised outcome and confirmed interpretation from previous experiments that smaller particles have a heat transfer distribution that causes substantially

reduced ice melt relative to the larger particles. The working hypothesis and implications of this will be discussed in Chapter 7. Results also concluded that the smaller particles were more sensitive to temperature, and the boundary of stable (cold) and stable (cool) may be operating at higher temperatures relative to that of the larger particles.

This experiment was repeated in three instances in experiments P41, P44, and P47), although the results were contrasting. Experiment P41 showed that the 3 mm, 6 mm, and 12 mm particles moved down to the ice base whilst the 1.5 mm stalled at a depth of approximately 3 mm. It was observed that the 3 mm, 6 mm, and 12 mm particles moved downwards through the ice within the same melt pathway, and so it was inferred that a hydrological connection between these particles enabled the 3 mm particle to be 'dragged' to the ice base (Figure 4.72). Therefore, direct comparisons between P41 and other experiments of this type were difficult. It was concluded that the 6 mm and 12 mm particles were operating within a stable (cool) environment (identified by a refreezing melt pathway), whilst the 1.5 mm particle was unable to melt the ice over a sustained period and was likely in the stable (cold) environment. The thermal environment of the 3 mm particle could not be deduced as this was masked by features from the 6 mm and 12 mm particle-ice interaction.

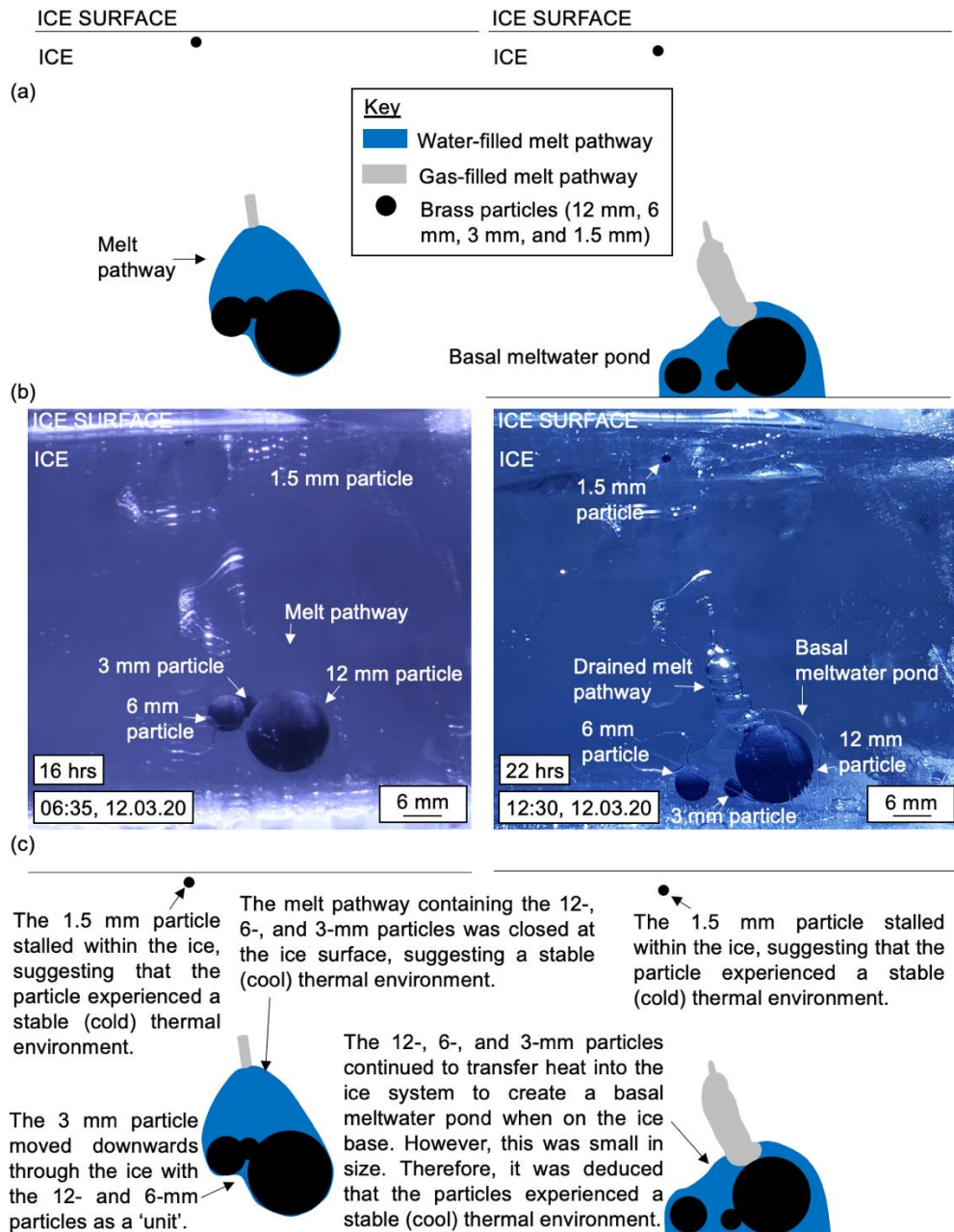


Figure 4.72. Cross-sectional images of the movement by the 3 mm, 6 mm, and 12 mm particles within the ice (left) and the 3 mm, 6 mm, and 12 mm on the ice base (right) in experiment P41. (a) observational line diagram, (b) photograph and (c) interpretation of the features.

The results of experiments P44 and P47 contrasted with those of experiments P37 and P41 as all particles moved downwards to the ice base. Experiment P44 showed that particles were within a stable (warm) environment in the first half of the experiment (identified by melt pathways extending upwards to the ice surface with no refreezing processes observed). However, a staggered negative shift across the thermal range was observed, where the thermal environment experienced by the 1.5 mm, 3 mm, 6 mm, and 12 mm particles

evolved into a stable (cool) environment 4 hours, 6.5 hours, 10.5 hours, and 10.5 hours into the experiment, respectively. The 1.5 mm and 3 mm particles then further shifted into a stable (cold) environment when sat on the ice base (identified by a complete refreezing of meltwater). The 6 mm and 12 mm particles remained within a stable (cool) environment for the remainder of the experiment. This confirmed previous interpretations that the thermal environment is diameter dependent and provided an insight into the behaviours of particles when shifting across multiple thermal environments.

Unlike P44, experiment P47 bordered a stable (warm) and unstable environment, as particle melt pathways remained open at the ice surface and bulk melting of the ice was observed (e.g. drainage channels forming on the ice surface). Therefore, it was assumed that the ice was close to PMP, and that most, if not all, heat transferred from each particle was coupled into melting the ice. This explains the differences in results between experiment P47 and experiments involving 3 mm and 1.5 mm particles.

Although experiments P37, P41, P44, and P47 exhibited slightly different results, these spanned a range of thermal environments, demonstrating a positive shift across the range from experiment P37 to P47. This highlighted the complexities associated with particle-induced ice melt and the thermal range, but also demonstrated the overarching finding that the stable (cold) environment is experienced by smaller particles (e.g. < 3 mm) at higher temperatures when compared to larger particles (e.g. > 3 mm).

4.4.6. P36: a 3x3 mm array of brass particles

The following series of experiments investigated an array of 3 mm brass particles to study the point at which single particles began acting as a singular, larger unit. Experiment P36 investigated a 3x3 mm triangular particle array. All particles were placed directly next to one another and so the horizontal dimensions were approximately 6-7 mm (Figure 4.73). The hypothesis for experiment P36 is shown in Figure 4.74.

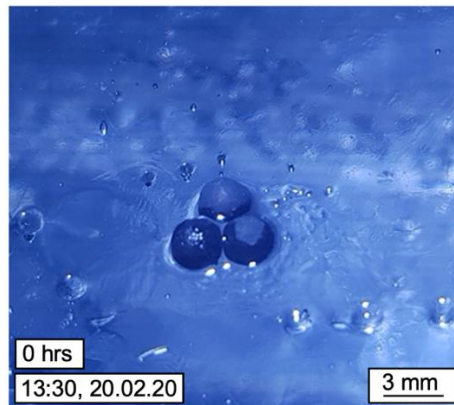


Figure 4.73. Photograph of the surface configuration of the particle array in experiment P36.

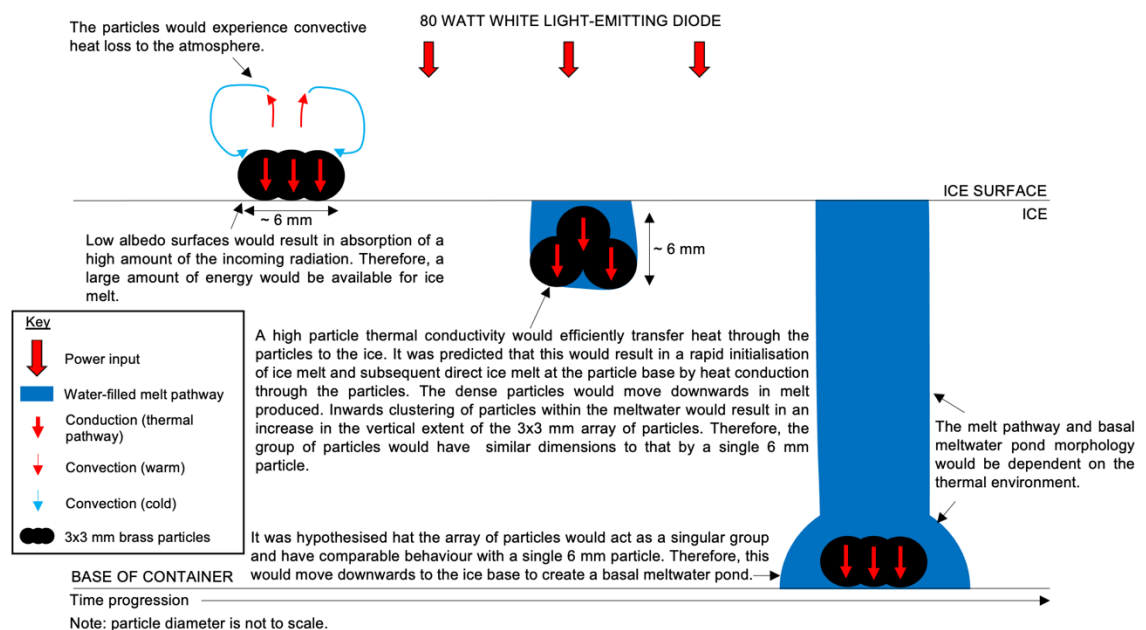


Figure 4.74. Schematic cross-sectional view of the hypothesised particle-ice interaction in experiment P36.

4.4.6.1. Results and interpretation

The particles immediately transferred heat into the ice to cause ice melt after surface placement. These moved downwards in the melt produced over approximately 18 hours before movement ceased at a depth of 6 mm. Downwards motion was with a mean particle velocity of $9.16 \times 10^{-8} \text{ m s}^{-1}$ (Figure 4.75), which was significantly lower than that measured in previous experiments. The velocity remained relatively constant (at approximately $3.3 \times 10^{-7} \text{ m s}^{-1}$) until hour 1.5 when the velocity began to fluctuate, eventually resulting in a prolonged stationary period (e.g. hours 6-16). Small-scale changes to the particle velocity from hour 1.5 appeared 'stepped' due to visual estimates with a 0.1 mm level of precision and the five-minute interval between

observations; this indicates that the particle movements were <0.1 mm in these instances and were minimal.

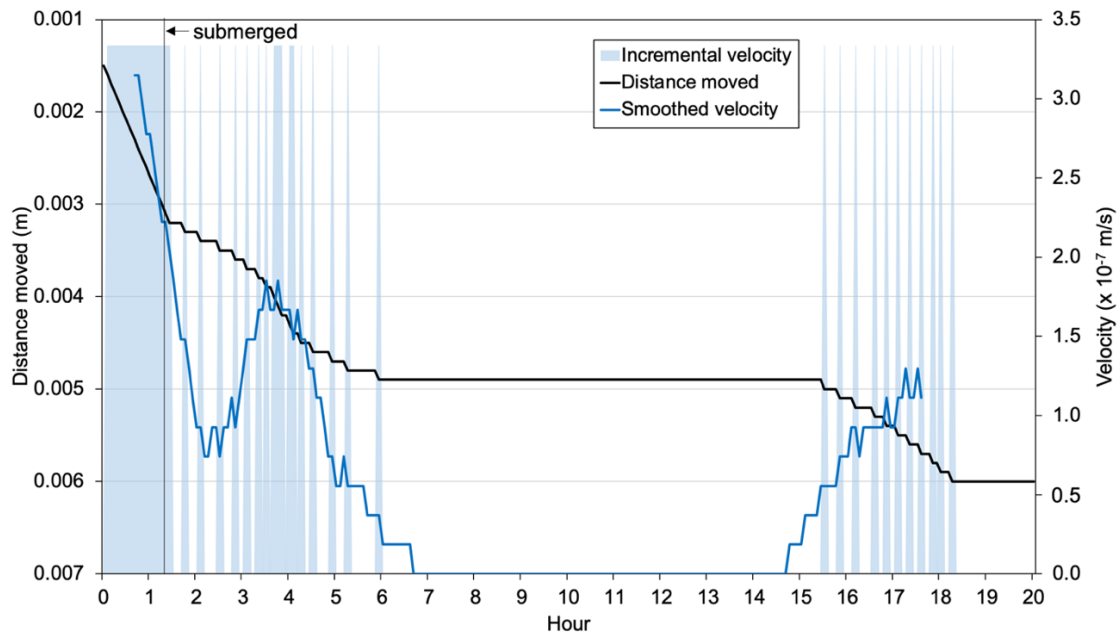


Figure 4.75. Vertical distance moved and velocity of the 3x3 mm brass particle array in experiment P36. Data plotted up to hour 20, although the experiment was running for 120 hours. There was no discernible change between hour 20-120.

4.4.6.2. Melt pathway

The three particles immediately created a small (<1 mm) meltwater pond that enabled downwards movement into the ice. By approximately 1.5 hours into the experiment, all particles were fully submerged and had created a single melt pathway that did not extend past the particle array diameter; this demonstrated that although multiple particles were involved, the same fundamental behaviour of meltwater generation was observed. Additionally, it was noted that the change in particle velocity was observed after the particles had become fully submerged. This indicated that the difference between heat transfer mechanisms by surface particles compared to embedded particles was a likely driver in modifying the behaviour of particle-ice interaction. This suggests that the thermal environment diameter-dependency is applicable once a particle has become embedded within the ice. All meltwater had refrozen by hour 18, associated with no further downwards movement of the particle group, indicating a shift into a stable (cold) thermal environment.

4.4.6.3. Summary

Experiment P36 demonstrated that a 3x3 mm particle array did not act as a larger unit and exhibited the same behaviour as a widespread distribution of single 3 mm particles as downwards movement ceased at a depth of approximately 6 mm. These results did not support the hypothesised outcome, where it was expected that the three particles would act as a group and exhibit similar behaviours as that by a thermally conductive 6 mm particle.

A variety of particle arrays were investigated in subsequent experiments (P38, P39, P40, P42, and P43, Table 4.9). There did not appear to be a notable difference between the particle movement of a 9x3 mm array of particles compared to a 3x3 mm array of particles (e.g. P38-P42) as the larger configuration moved to the same depth as a 3x3 mm particle array over the same period. This further confirms interpretation that the particles were acting as single units.

Table 4.9. Behaviour of the P38, P39, P40, P42, and P43 particle arrays.

Experiment	Particle array configuration	Distance moved (mm)	Duration of movement (hours)	Behaviour
P38	3x3 mm	13.3	4	Stalled
P39	5x3 mm	10.5	1.4	Stalled
P40	4x3 mm	13	4	Stalled
P42	9x3 mm	5	21.5	Stalled
P43	16x3 mm	48.5	22.5	Group 1 moved to ice base
		40.2	12.5	Group 2 stalled

Experiment P41 (directly comparing particles of all diameters, see Section 6.4) was conducted following experiment P40 to also determine whether the ice temperature was in an environment that allowed particle-induced ice melt. The results from this experiment showed that freezer temperatures allowed particle-induced ice melt and the larger particles could move downwards to the ice base. Previous conclusions demonstrating that the thermal environment was diameter dependent also applied to this experiment, and reinforced interpretation that particles in experiments P36-P40 were not acting as a larger unit, as this would have seen them moving downwards to the ice base as in the same way as the 6 mm and 12 mm particles in experiment P41.

Experiment P43 contrasted with all experiments of this type as the original array of particles separated into two groups (group 1 and group 2), and group 1 melted the ice sufficiently to move to the ice base. Initial movement into the ice was in the same configuration as the surface placement and as individual particles (Figure 4.76).

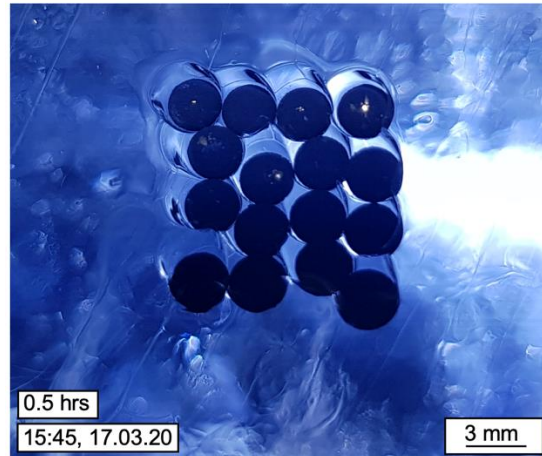


Figure 4.76. Plan-view photograph of initial movement of particles in experiment P43.

The particles clustered together in the vertical dimensions approximately 2 hours after the experiment start (e.g. Figure 4.78). These moved to a depth of approximately 40.2 mm with a mean particle velocity of $8.93 \times 10^{-7} \text{ m s}^{-1}$ and remained stationary for approximately seven hours (Figure 4.77). The particle array then split into two discrete groups: group 1 (approximately ten particles) continued to move to the ice base, whilst group 2 (approximately six particles) remained stalled within the ice. This second stage of movement by group 1 was with a mean velocity of $7.48 \times 10^{-7} \text{ m s}^{-1}$ (i.e. similar to the first stage of movement) to reach the ice base approximately 22.5 hours after the experiment start. The basal cluster of particles remained on the ice base and continued to actively transfer heat into the ice whilst group 2 remained stalled in the ice. The overall mean particle velocity calculated for group 1 (accounting for both active particle movement and stalled periods) was $5.92 \times 10^{-7} \text{ m s}^{-1}$.

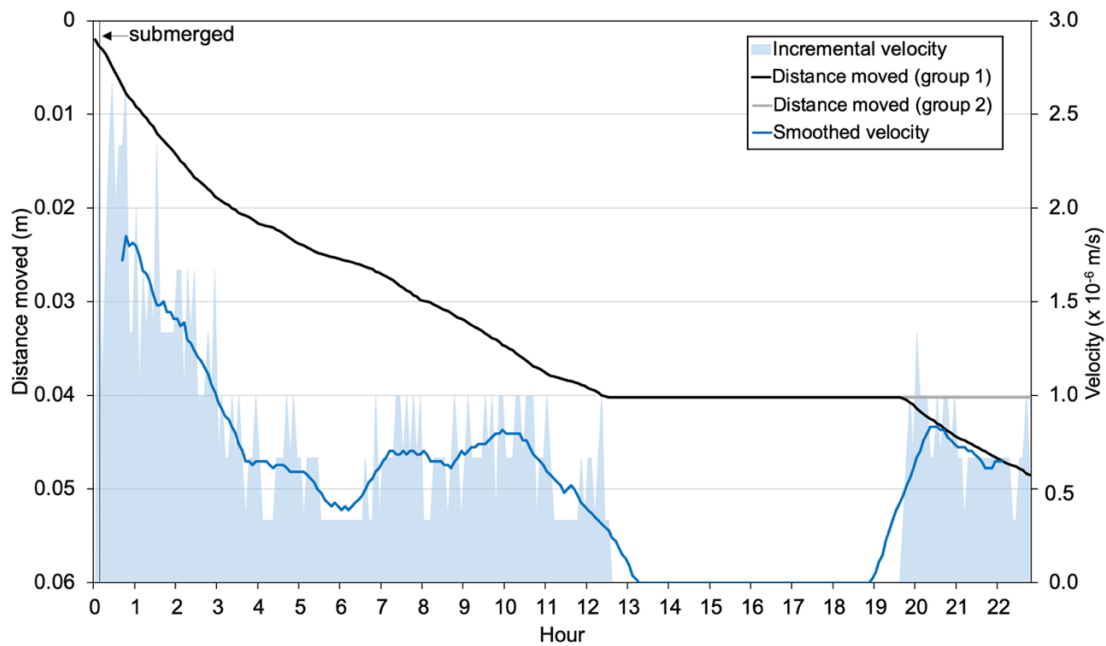


Figure 4.77. Vertical distance moved and velocity of the 16x3 mm brass particle array in experiment P43. Particle velocity was calculated from data from group 1. Although multiple particles were involved, the vertical distance moved was measured from the base of the same particle throughout the experiment to ensure consistency. The particles acted as a single group for most of the experiment and so it was assumed that the overall pattern of particle movement was applicable to all particles.

It was deduced that group 1 was sufficiently large to be within a stable (cool) environment, where the particles clustered together to act as a single, larger unit, enabling them to melt ice in conditions where their individual sizes would otherwise not allow. This was comprised of a minimum of 10 particles (precise numbers could not be identified due to clarity issues in the images). However, group 2 experienced a negative shift across the thermal range from a stable (cool) to a stable (cold) environment once the original particle array split.

The melt pathway width did not exceed the particle array dimensions, indicating a stable (cool) thermal environment. Refreezing processes were observed by hour four (identified by a narrowing less than the particle array diameter), until closure at the ice surface at hour six (Figure 4.78 and 4.79).

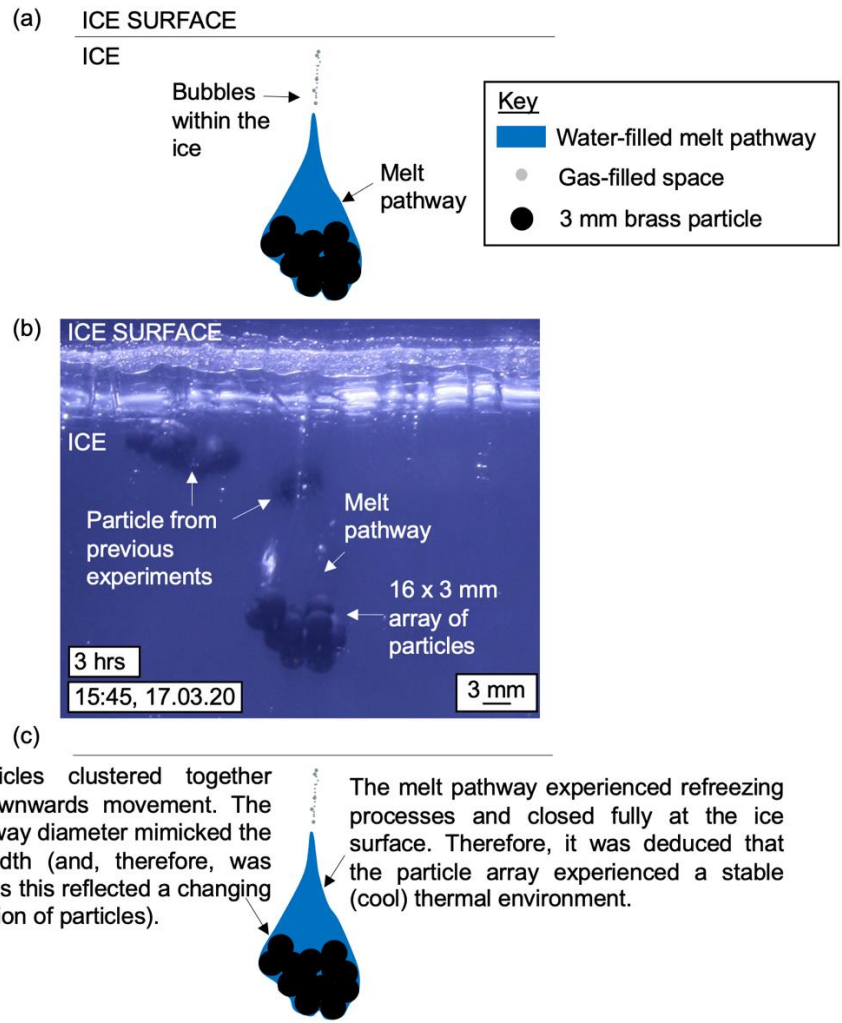


Figure 4.78. Cross-sectional images of the clustering of the particles and refrozen melt pathway at the ice surface in experiment P43. (a) observational line diagram, (b) photograph and (c) interpretation of the features.

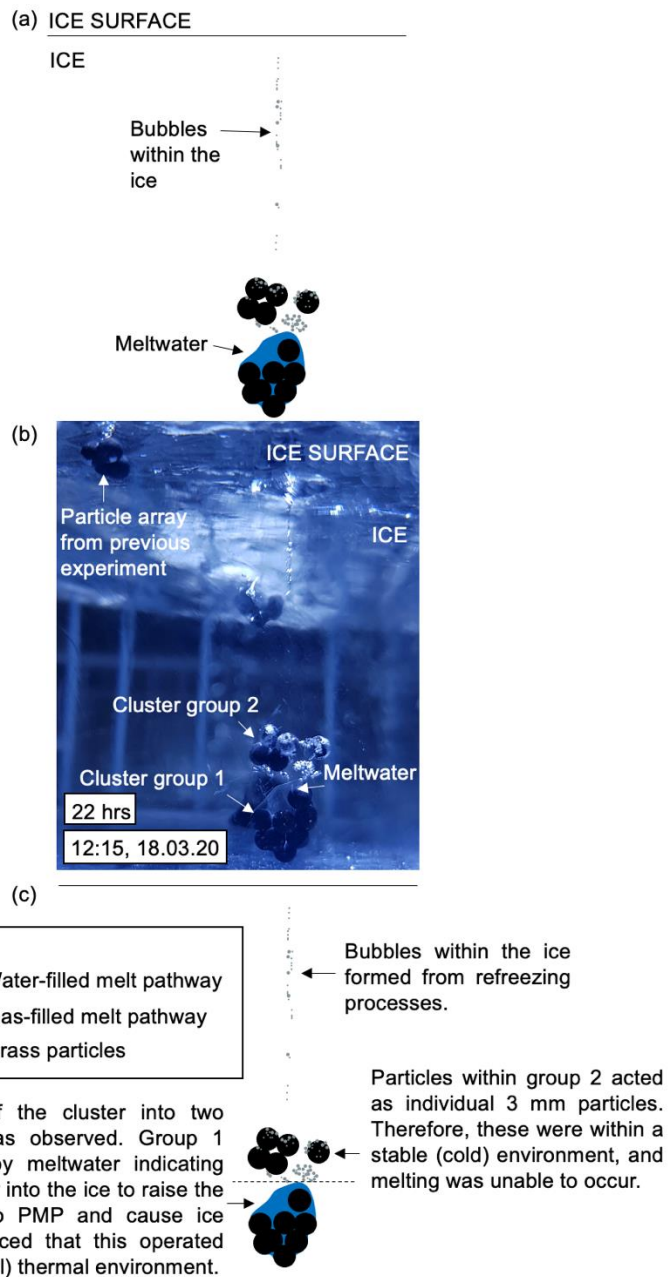


Figure 4.79. Cross-sectional images of the separation of the two groups of particle clusters in experiment P43. Photograph taken at a 90° angle to the time-lapse camera. (a) observational line diagram, (b) photograph and (c) interpretation of the features.

4.5. Conclusions

Chapter 4 provided a unique insight into how particle properties can influence particle behaviour within an ice system. This also aided understanding of many subtleties associated with particle-induced ice melt. For example, the difference in relative importance between heat transfer mechanisms of a surface and embedded particle, the way in which particle properties (related to diameter and albedo) can result in sorting of particles within ice, and how the properties of a

particle can increase the particle sensitivity to external factors, such as thermal environment and surface tension.

4.5.1. Thermal conductivity

The particle thermal conductivity had a key control on the initialisation of melt and dictated the dominant type of heat transfer mechanism involved. For example, direct melting by heat conduction through the particle versus indirect melting driven by convection currents in meltwater. Typically, particles with a lower thermal conductivity were associated with stronger convection-driven indirect melting (as identified by melt pathway's exceeding the particle diameter).

Differences in behaviour between a particle on the ice surface and a particle embedded in the ice was noted. These two configurations experienced different heat transfer mechanisms, with the removal of convective heat losses from a particle absorbing surface to the atmosphere once it became submerged in meltwater, predominantly controlled by the particle thermal conductivity. For example, a particle with a relatively low thermal conductivity would experience stronger convective heat loss from the top particle surface due to less efficient conduction of energy through the particle, leading to a warming top surface. This was particularly crucial when the particle was experiencing other melt-limiting properties, e.g. partial reflection from the top surface of a particle with an intermediate or high albedo (as observed in experiment P14), or a long thermal pathway reducing the rate of conduction to the ice.

4.5.2. Albedo

The particle albedo dictated the rate of particle-induced ice melt by determining the absorption of energy. For example, a low albedo particle had a higher particle velocity (used as a proxy for the rate of ice melt) than a high albedo particle due to a higher rate of energy transfer into the ice as the low albedo surface absorbed a greater proportion of incoming energy. However, the particle velocities for the low and intermediate albedos were comparable with an average magnitude of $\times 10^{-6} \text{ m s}^{-1}$. Experiments also suggested that high

albedo particles could transfer energy into the ice, despite a predominantly reflective particle surface. Therefore, it was deduced that unless a particle was a perfect reflector (i.e. it had an albedo of 1), it could generate some melt; this was more achievable with ice at temperatures close to PMP (i.e. a stable (warm) thermal environment). Initialisation of melt could lead to more extensive indirect melting driven by meltwater convection (as discussed above), possibly allowing for the amplification of melting processes once past the melt initialisation stage. Results also demonstrated that the effect of particle albedo could be attenuated by other factors (e.g. ice microstructure and small-scale ice hydrology, as observed in experiment P13).

4.5.3. Density

The particle density did not appear to directly impact the capability of a particle to melt the ice (although, a low density is typically associated with a low thermal conductivity in nature which, in of itself, is a key control on ice melt). Instead, this dictated the fundamental behaviour of the particle (i.e. if it would sink or float). Particles with a higher density than water typically sank in the meltwater produced and moved to the ice base, whilst particles with a density lower than water became buoyant when sufficient meltwater was produced. Additionally, a particle with an intermediate density (i.e. close to that of water) was susceptible to retention at the water surface by surface tension effects, and therefore, experienced both behavioural modes. Finally, relatively low density particles embedded within ice could melt the ice to move upwards to reach the ice surface (e.g. as observed in experiment P17b). It is important to note that the role of particle density did not have an impact until sufficient meltwater had been produced to initiate either buoyant or non-buoyant behaviour; this property is not considered in the melt initialisation process. Ultimately, the density of a particle dictated if a particle became submerged or remained at the ice surface; this is crucial in determining the extent of particle-induced melting.

4.5.4. Diameter

Surprisingly, the particle diameter had an influence on the behaviour of particle-ice interaction. This did not support the simplified melt model described in

Chapter 3 (Section 3.5.2.1) and reflected the complexity of processes associated with particle-ice interaction on an individual particle scale. Experiments investigating widely dispersed single particles indicated that larger particles (e.g. > 6 mm) transferred heat into melting the ice sufficiently to move downwards to the ice base, whereas the smaller particles (e.g. < 3 mm) could not, unless within a thermal environment close to PMP. However, the difference in particle behaviour appeared to be strongest after full submergence of the particle (and was associated with the removal of convective heat losses to the atmosphere). This noted that smaller particles experienced stable (cold) thermal environments at higher temperatures than larger particles; for example, a particle smaller than 3 mm would be within a stable (cold) environment (and so unable to melt the ice), whilst a particle larger than 6 mm would be within a stable (cool) or (warm) environment (and so able to melt the ice) at the same temperature. This suggested that the thermal environment in the proximity of the particle had a diameter dependency in the case of thermally conductive particles (discussed in detail in Chapter 7). This indicated that particles have a sensitivity to temperature that varies with diameter. Experiments investigating particle arrays provided insights into the particle clustering within a melt pathway and associated behavioural changes when clusters of particles split from one another.

5. An experimental investigation into the behaviour of volcanic particles within the cryosphere

The V1-V34 experimental series in Chapter 5 investigated the behaviour of volcanic particles on the ice surface and moving through the ice system (Table 5.1, Figure 5.1). As Chapter 4 demonstrated that particle impact on ice depended on particle properties, experiments in Chapter 5 were designed so that the albedo, density, and diameter of volcanic material differed between experiments to better understand the role of these properties. Single particles, a cluster of particles, and a scattering of particles were investigated, with particle diameters approximately in the range 1.5-12 mm (allowing comparisons with control experiments described in Chapter 4). Particle diameters described in Chapter 5 are approximate values due to the irregular surface morphologies, although particles were roughly spherical. Clusters of cemented ash particles (hereafter referred to as cemented ash clusters) of trachyandesitic composition, and single particles of basaltic-andesitic scoria and rhyolitic pumice were used. Experiments are described according to particle composition, diameter (6 mm, 12 mm, 3 mm, and 1.5 mm) and the nature of experimental progression, in chronological order of experiment code. Repeat experiments are grouped for ease of comparison. Surface meltwater is described by the horizontal extent on the ice surface (i.e. width and length), and depth within the ice. This is further split into two features: a proximal meltwater pond (i.e. the deeper zone of meltwater near a particle), and a shallow surface meltwater pond (i.e. a larger extent of shallow melt on the ice surface). The average freezer and proxy ice temperatures for each experiment are recorded in Table 9.13, Appendix 14.

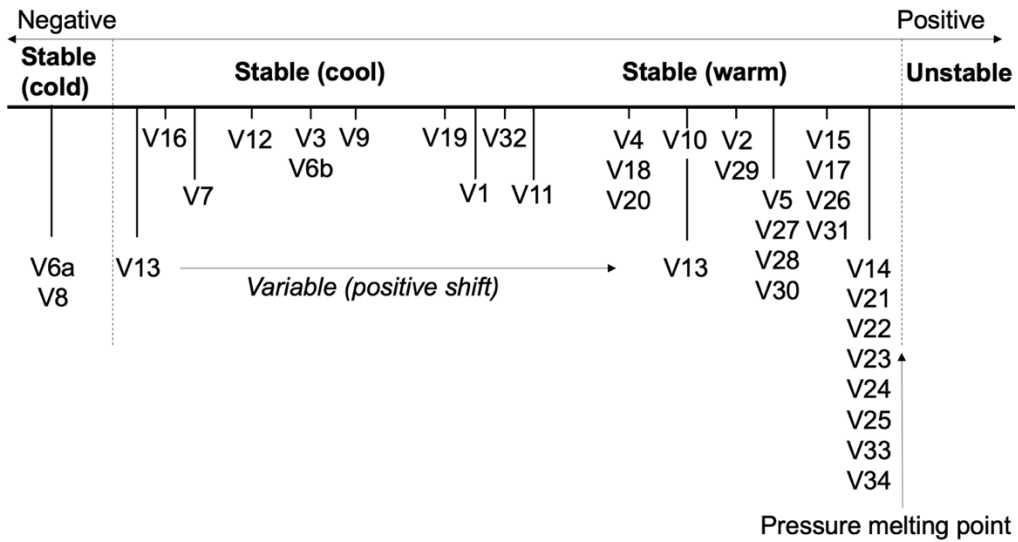


Figure 5.1. Associated thermal environment of particles in experiments investigating the behaviour of volcanic particle-ice interaction. Experiment position has been derived from interpretation of observations, as described in Chapter 3, Section 3.7.

Table 5.1. (continued overleaf) A summary of experiments investigating the behaviour of volcanic particle-ice interaction, indicating the particle composition, diameter and associated thermal environments as defined in Chapter 3.

Experiment	Particle composition	Particle diameter (mm)	Thermal environment
V1	Trachyandesitic cemented ash (Eyjafjallajökull, Iceland)	6	Stable (warm)
V2	Trachyandesitic cemented ash (Eyjafjallajökull, Iceland)	12	Stable (warm)
V3	Trachyandesitic cemented ash (Eyjafjallajökull, Iceland)	3	Stable (cool)
V4	Trachyandesitic cemented ash (Eyjafjallajökull, Iceland)	6	Stable (warm)
V5	Trachyandesitic cemented ash (Eyjafjallajökull, Iceland)	12	Stable (warm)
V6b	Trachyandesitic cemented ash (Eyjafjallajökull, Iceland)	12	Stable (cool)
V7	Trachyandesitic cemented ash (Eyjafjallajökull, Iceland)	6	Stable (cool)
V9	Basaltic-andesitic scoria (Volcán Sollipulli, Chile)	6	Stable (cool)
V10	Basaltic-andesitic scoria (Volcán Sollipulli, Chile)	6	Stable (warm)
V11	Basaltic-andesitic scoria (Volcán Sollipulli, Chile)	12	Stable (warm)
V12	Basaltic-andesitic scoria (Volcán Sollipulli, Chile)	12	Stable (cool)
V13	Basaltic-andesitic scoria (Volcán Sollipulli, Chile)	6	Variable
V14	Basaltic-andesitic scoria (Volcán Sollipulli, Chile)	6	Stable (warm)
V15	Basaltic-andesitic scoria (Volcán Sollipulli, Chile)	3	Stable (warm)

Experiment	Particle composition	Particle diameter (mm)	Thermal environment
V16	Basaltic-andesitic scoria (Volcán Sollipulli, Chile)	3	Stable (cool)
V17	Basaltic-andesitic scoria (Volcán Sollipulli, Chile)	3	Stable (warm)
V18	Basaltic-andesitic scoria (Volcán Sollipulli, Chile)	1.5	Stable (warm)
V19	Basaltic-andesitic scoria (Volcán Sollipulli, Chile)	3	Stable (cool)
V20	Basaltic-andesitic scoria (Volcán Sollipulli, Chile)	1.5	Stable (warm)
V21	Basaltic-andesitic scoria (Volcán Sollipulli, Chile)	1.5	Stable (warm)
V22	Basaltic-andesitic scoria (Volcán Sollipulli, Chile)	6	Stable (warm)
V23	Basaltic-andesitic scoria (Volcán Sollipulli, Chile)	12	Stable (warm)
V24	Basaltic-andesitic scoria (Volcán Sollipulli, Chile)	12	Stable (warm)
V25	Rhyolitic pumice (Mount St. Helens, USA)	6	Stable (warm)
V26	Rhyolitic pumice (Mount St. Helens, USA)	3	Stable (warm)
V27	Rhyolitic pumice (Mount St. Helens, USA)	12	Stable (warm)
V28	Rhyolitic pumice (Mount St. Helens, USA)	1.5	Stable (warm)
V29	Rhyolitic pumice (Mount St. Helens, USA)	3	Stable (warm)
V30	Rhyolitic pumice (Mount St. Helens, USA)	6	Stable (warm)
V31	Rhyolitic pumice (Mount St. Helens, USA)	12	Stable (warm)
V32	Rhyolitic pumice (Mount St. Helens, USA)	1.5	Stable (warm)
V33	Basaltic-andesitic scoria (Volcán Sollipulli, Chile)	Scattering	Stable (warm)
V34	Basaltic-andesitic scoria (Volcán Sollipulli, Chile)	Scattering	Stable (warm)

5.1. V1: a 6 mm cemented ash cluster

This experiment was conducted to assess the role of relatively low albedo (Chapter 3, Section 3.3.2) Eyjafjallajökull cemented ash clusters on influencing ice ablation when placed on an ice surface. The cemented cluster was approximately 6 mm in diameter (6x7 mm) and roughly spherical (Figure 5.2). The hypothesis for experiment V1 is shown in Figure 5.3.



Figure 5.2. Plan-view photograph of the 6 mm V1 cemented ash cluster.

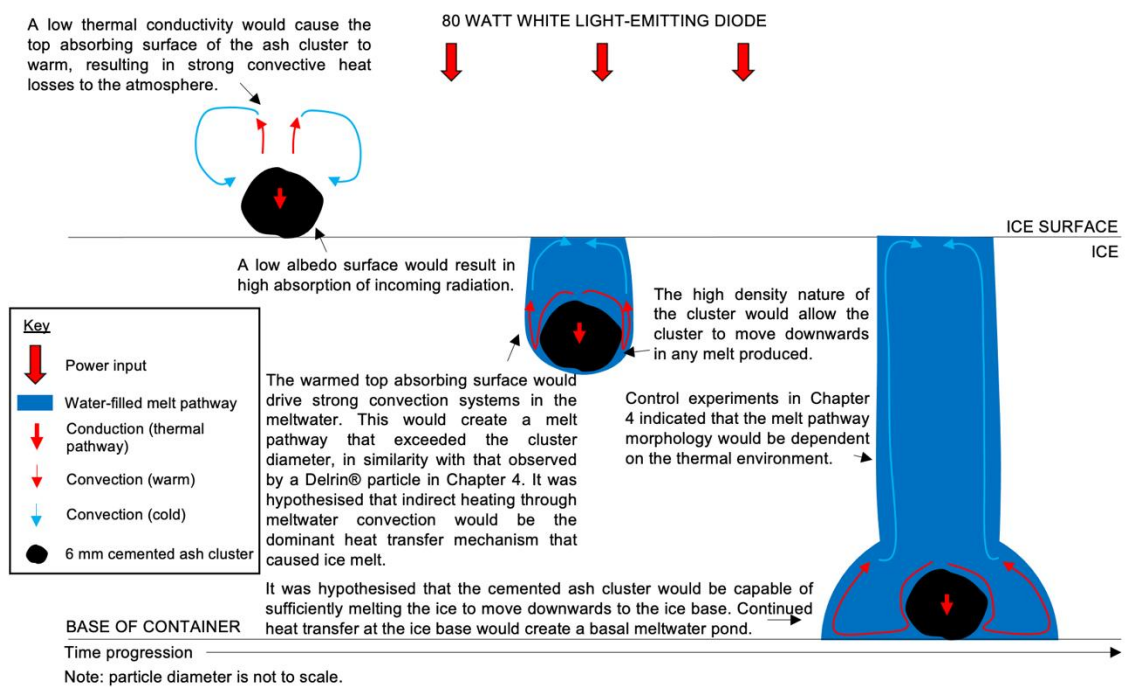


Figure 5.3. Schematic cross-sectional view of the hypothesised particle-ice interaction in experiment V1.

5.1.1. Results and interpretation

The cemented ash cluster immediately transferred heat to melt ice after surface placement (Figure 5.4). The dense nature (2500 kg m^{-3} , Chapter 3) of the cluster relative to water caused downwards movement in meltwater produced with a mean particle velocity of $1.13 \times 10^{-6} \text{ m s}^{-1}$ to reach the ice base within 16 hours. A shift in orientation of the cemented ash cluster was observed during downwards movement approximately 13 hours into the experiment, associated with an increase in the smoothed velocity. Partial rotation of the cluster possibly facilitated a short-term increase in particle velocity because a rotation would place the absorbing top surface in contact with another area of ice/meltwater to encourage fast ice melt.

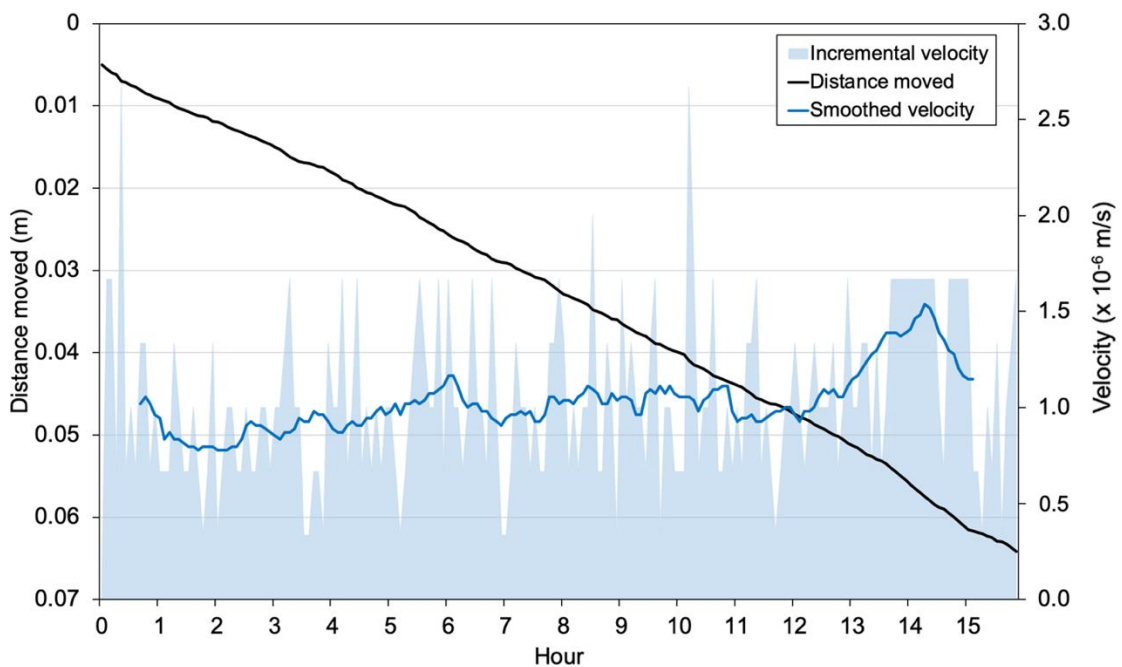


Figure 5.4. Vertical distance moved and velocity of a 6 mm Eyjafjallajökull cemented ash cluster in experiment V1.

5.1.2. Melt pathway

In contrast to results using highly conductive particles (e.g. brass and chrome steel), the cemented ash cluster created a melt pathway that had a width of approximately double the cluster diameter with a rounded base (Figure 5.5). This was likely due to a strong convection system attributed to a low particle thermal conductivity, as described when considering low density particles in Chapter 4. A rounded melt pathway base larger than the diameter of the cluster reinforced interpretation of strong convection systems within the meltwater.

Observations indicated that the cluster experienced a stable (warm) environment as refreezing processes were slow and the melt pathway remained open at the ice surface. Floating fine-grained material, likely lost mechanically from the particle surface when placed on the ice surface, was present at the top of the melt pathway, and contributed to ice melt at the ice surface. It was interpreted that the small particle sizes allowed surface tension effects to retain particles at the ice surface (as observed in experiment P19, Chapter 4).

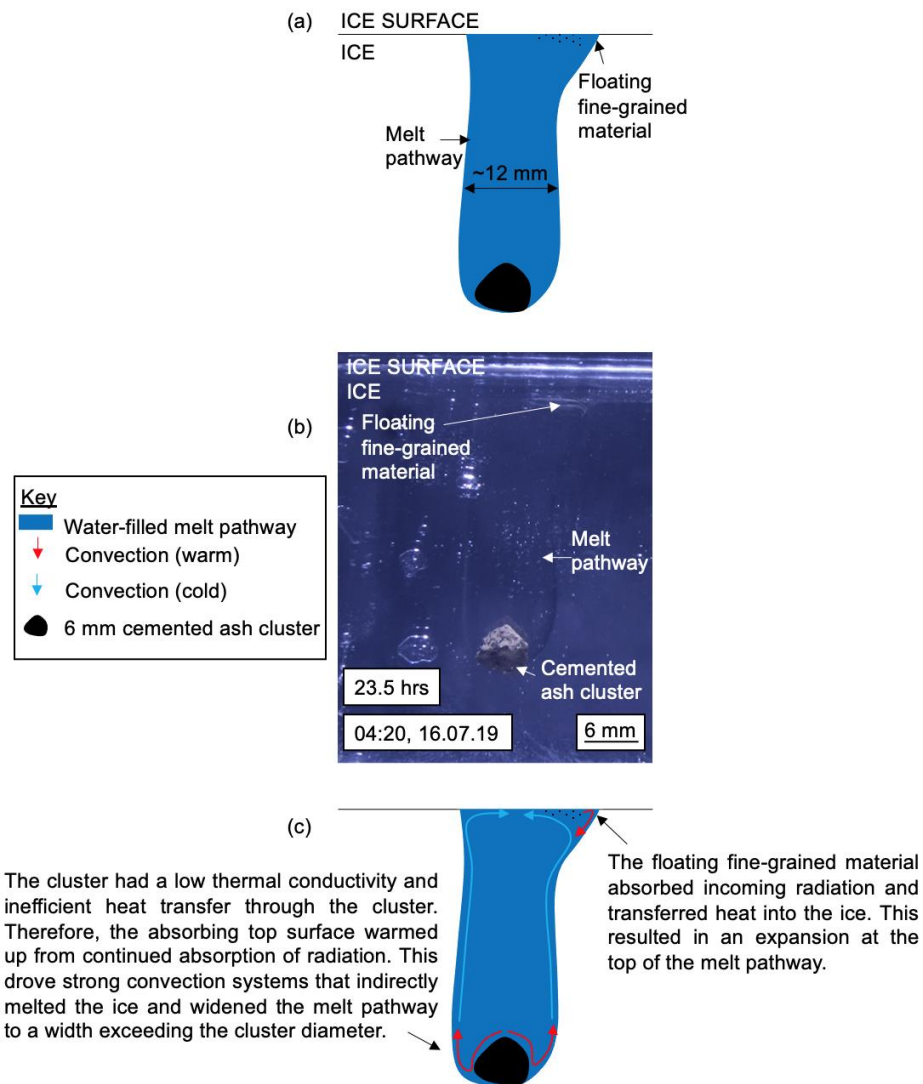


Figure 5.5. Cross-sectional images indicating the morphology of the V1 melt pathway. (a) observational line diagram, (b) photograph and (c) interpretation of the features.

Refreezing of meltwater started within the central segment of the melt pathway, and only occurred when the cluster was on the ice base. The morphology of the refreezing process appeared similar to results from experiments using control particles in Chapter 4 and suggested that the central segment of the melt

pathway was the coldest. This region was sufficiently far from: (1) direct heat transfer from the cemented ash cluster, (2) heating from convection systems, and (3) heat transfer from warmer ambient air temperatures above the ice, and so refreezing processes could occur. Refreezing processes did not occur near the cemented ash cluster itself, suggesting that the cluster had a vertical volume of influence that reached approximately 10 mm (measured from the top extent of the cluster). The central segment of the melt pathway was fully frozen by hour 44.

5.1.3. Basal meltwater pond

The V1 cluster continued to transfer heat into the basal ice to form a basal meltwater pond. This reached a maximum diameter of 43 mm and height of 18 mm (Figure 5.6). This was approximately hemispherical in shape and was connected to the refreezing melt pathway. In contrast to many of the synthetic particle experiments, there was no apparent lateral movement of the V1 cluster when on the ice base, likely due to the difference in morphology (e.g. an irregular sphere compared to a perfect sphere). Therefore, the morphology and dimensions of the basal meltwater pond likely represented the sphere of heat influence, from direct heat transfer from the volcanic material itself, and strong convection systems within the meltwater.

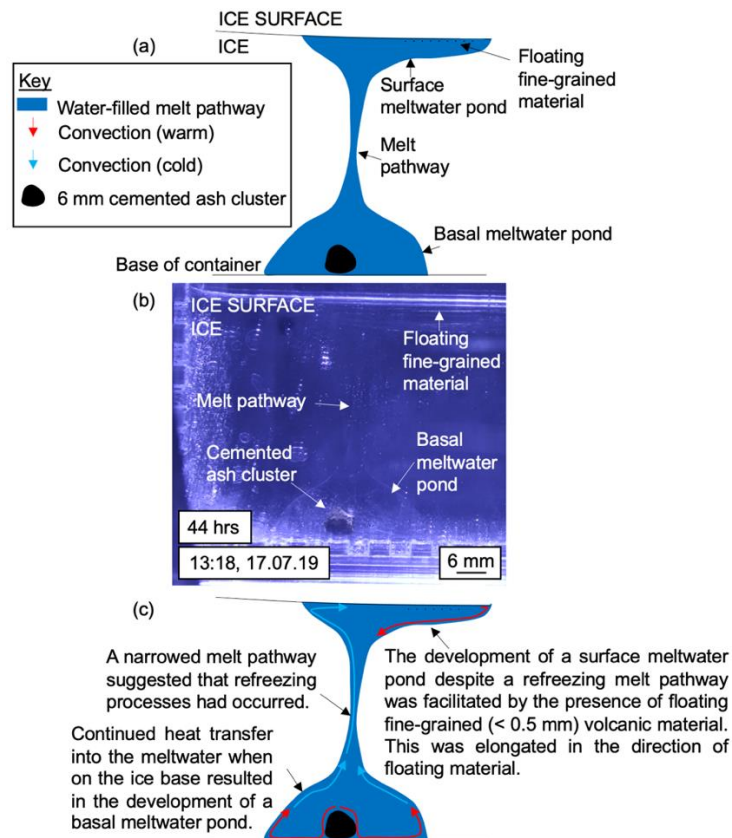


Figure 5.6. Cross-sectional images showing the basal meltwater pond and melt pathway in experiment V1. (a) observational line diagram, (b) photograph and (c) interpretation of the features.

5.1.4. Summary

Key characteristics of cemented ash-ice interaction were similar to those observed within experiments presented in Chapter 4 (e.g. downwards movement, creation of a melt pathway and a basal meltwater pond, refreezing processes, etc.), although some components differed (e.g. the melt pathway extended past the particle diameter).

This experiment was repeated in a further two experiments (V4 and V7). V4 compared well with results from experiment V1 as the V4 cemented ash cluster melted the ice and moved to the ice base with a mean particle velocity of $2.71 \times 10^{-6} \text{ m s}^{-1}$. This created a melt pathway approximately double the diameter of the cluster, a basal meltwater pond, and a surface meltwater pond (Figure 5.7). Similar to V1, the V4 cluster rotated within the melt pathway during downwards movement, although the V4 cluster maintained an open melt pathway with minimal refreezing.

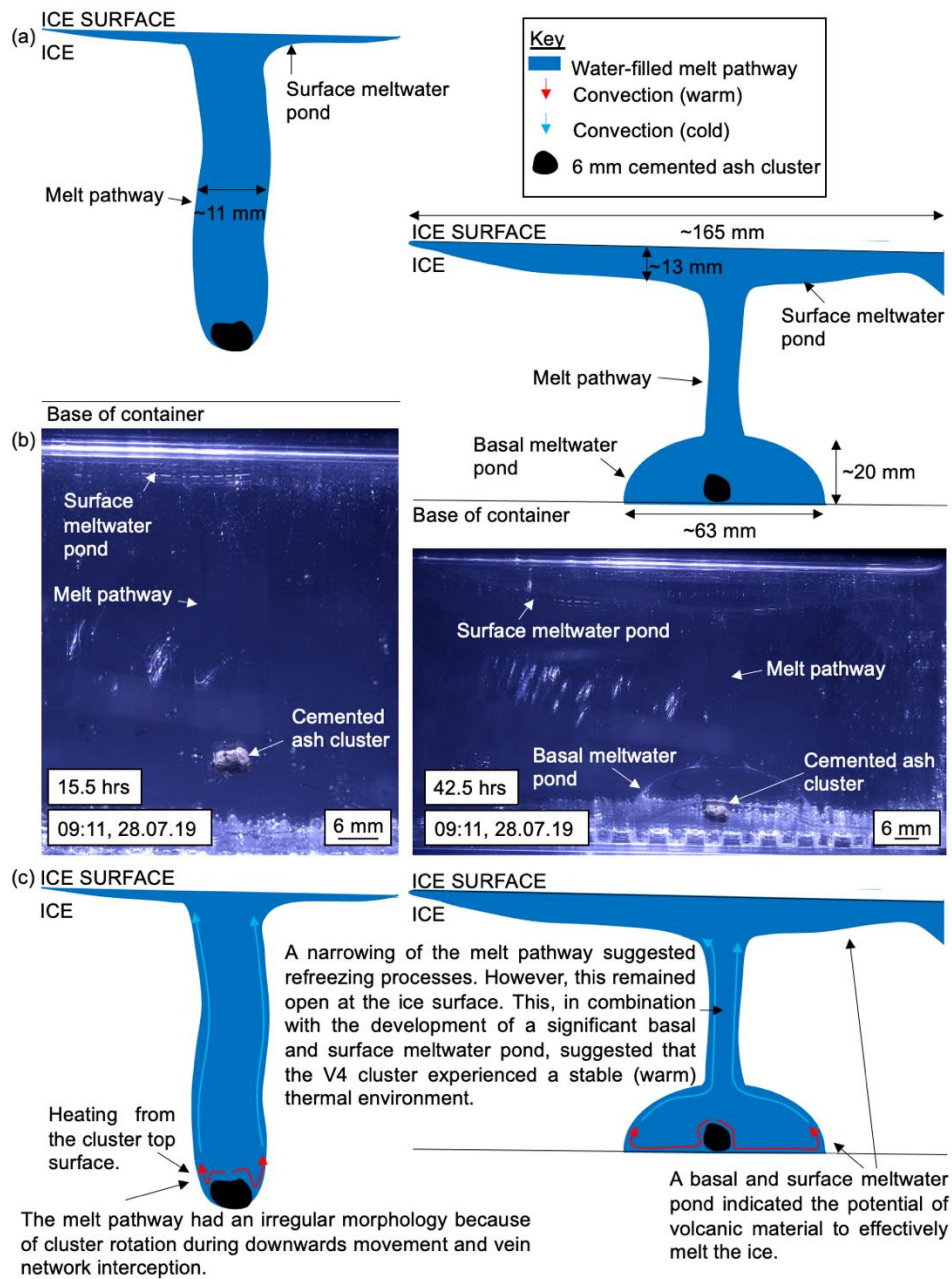


Figure 5.7. Cross-sectional images indicating the development of a melt pathway with an irregular morphology and a basal and surface meltwater pond in experiment V4. (a) observational line diagram, (b) photograph and (c) interpretation of the features.

Unlike V1 and V4, the cluster in experiment V7 disintegrated into smaller particle clusters, and did not represent the behaviour of a single 6 mm cluster. Disintegration occurred approximately 38 hours into the experiment; prior to this, cemented ash cluster-induced ice melt was relatively low and downwards movement was restricted to approximately 11 mm. It was likely that the cluster

became fully water-saturated within this period, and experienced refreezing processes due to a cold thermal environment. This could suggest that disintegration was a result of freeze-thaw processes arising from refreezing meltwater that had percolated through the cluster at the cluster base (Figure 5.8). The cluster split into two discrete groups that were well established by 74 hours into the experiment (37 hours after initial cluster disintegration). This split may have occurred earlier, but expiry of the time-lapse camera battery resulted in a ten-hour gap in the time-lapse images.

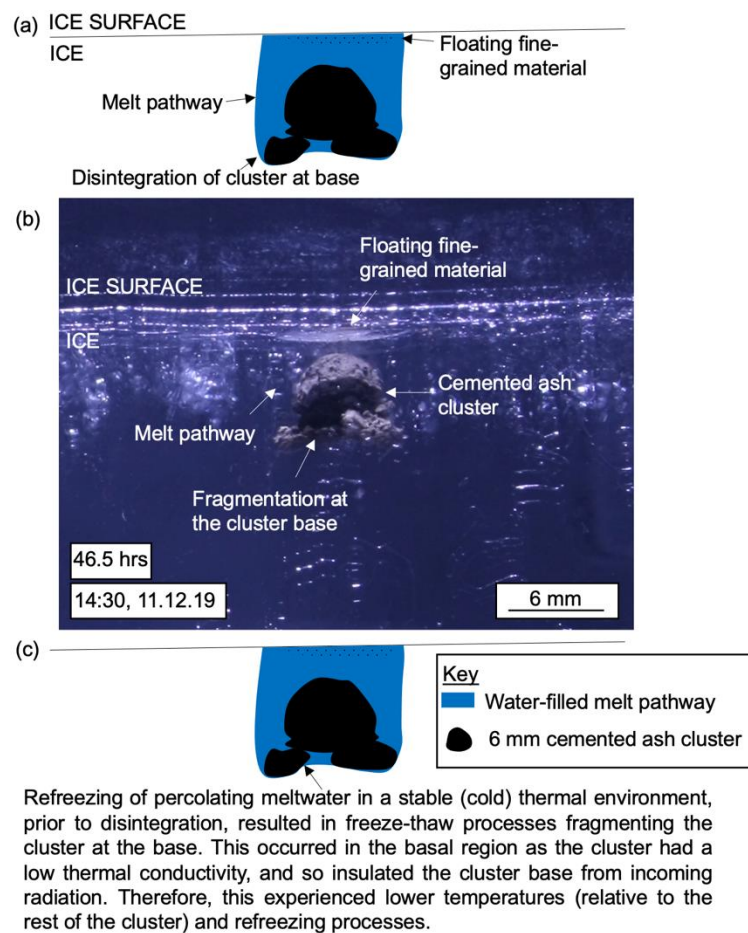


Figure 5.8. Cross-sectional images showing the initial disintegration of the V7 cluster. (a) observational line diagram, (b) photograph and (c) interpretation of the features.

The ice melt rate increased after the V7 cluster disintegration, and the clusters moved downwards through the ice as two units (Figure 5.9). Differential ice melt was observed, dependent on cluster size: the smaller cluster (approximately 3 mm thickness) moved downwards through the ice with a higher mean particle velocity of $2.01 \times 10^{-7} \text{ m s}^{-1}$, compared to $1.92 \times 10^{-7} \text{ m s}^{-1}$ for the larger cluster

(with a thickness of approximately 6 mm). Post-disintegration velocities (i.e. calculated after separation of each cluster group) were $6.92 \times 10^{-7} \text{ m s}^{-1}$, and $5.87 \times 10^{-7} \text{ m s}^{-1}$ for each cluster group, respectively. The increase in particle velocities after cluster disintegration may be due to the input of a greater particle absorbing surface area and, therefore, a greater heat transfer rate from the cluster to the ice. This would also drive stronger convection systems, previously identified as a key driver of ice melt.

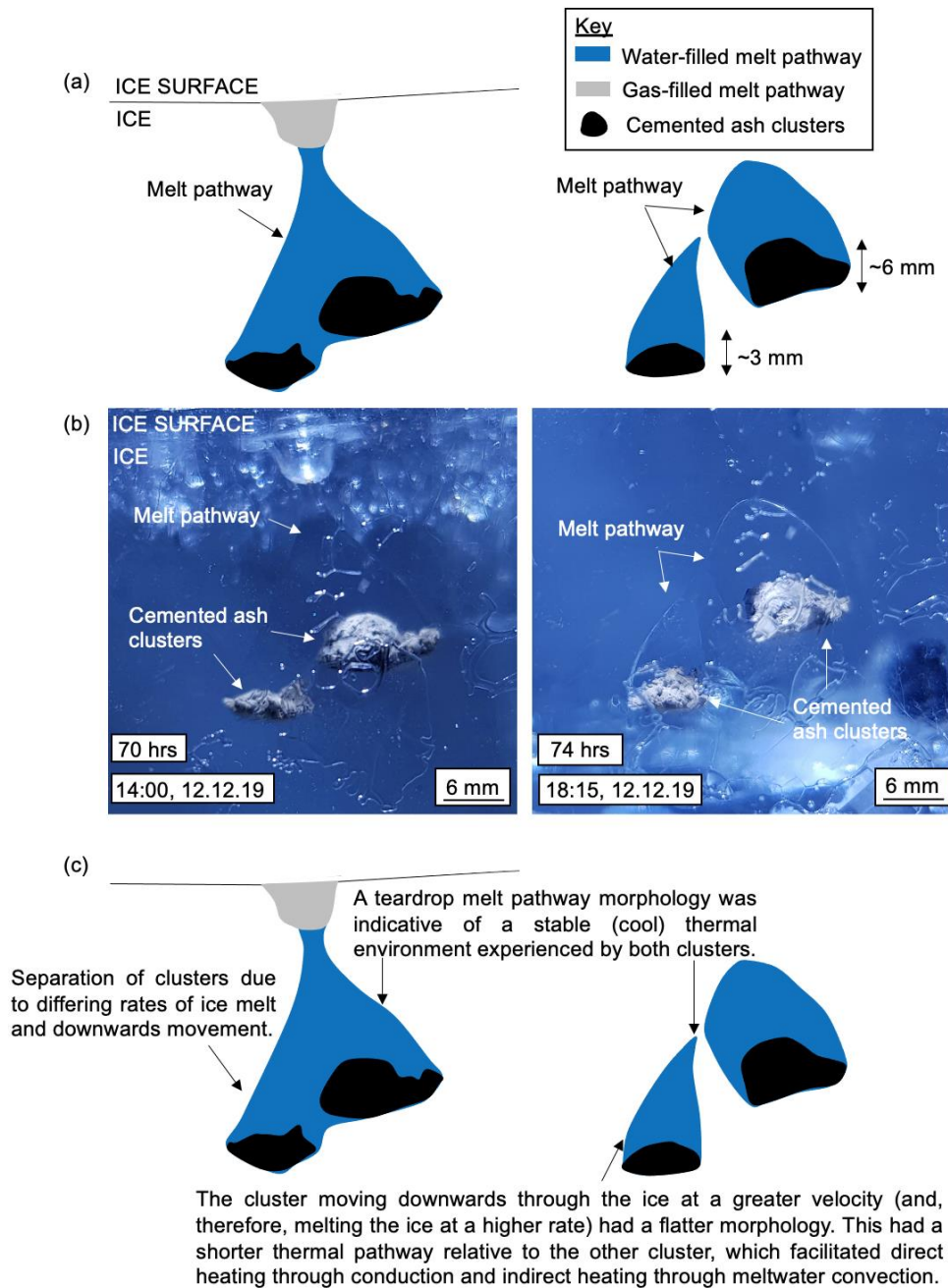


Figure 5.9. Cross-sectional images showing the progression of downwards movement by the disintegrated cemented ash clusters over two time frames in experiment V7. (a) observational line diagram, (b) photograph and (c) interpretation of the features.

Refreezing processes modified the cluster position within the ice in several instances. For example, an upwards movement of approximately 2 mm was observed whilst the V7 cluster was acting as a single 6 mm cemented ash cluster; this was associated with a refreezing of meltwater ‘pushing’ the cluster upwards in the ice and lasted approximately six hours. This was also observed after disintegration, where smaller clusters of volcanic material had moved downwards away from the initial V7 cluster, but refreezing processes pushed the clusters back upwards to the V7 cluster position. Additionally, refreezing processes occurred during downwards cluster movement, creating teardrop melt pathway morphologies. Therefore, it was interpreted that both clusters of ash particles were in a stable (cool) thermal environment. The lower particle velocities compared to previous experiments using 6 mm cemented ash clusters were likely associated with the clusters experiencing a cooler thermal environment, and complexities associated with the disintegration process.

5.2. V2: a 12 mm cemented ash cluster

Experiment V2 investigated the behaviour of a 12 mm Eyjafjallajökull cemented ash cluster. This was approximately 12x11 mm in size (Figure 5.10). The hypothesis for experiment V2 is shown in Figure 5.11.



Figure 5.10. Plan-view photograph of the 12 mm V2 cemented ash cluster.

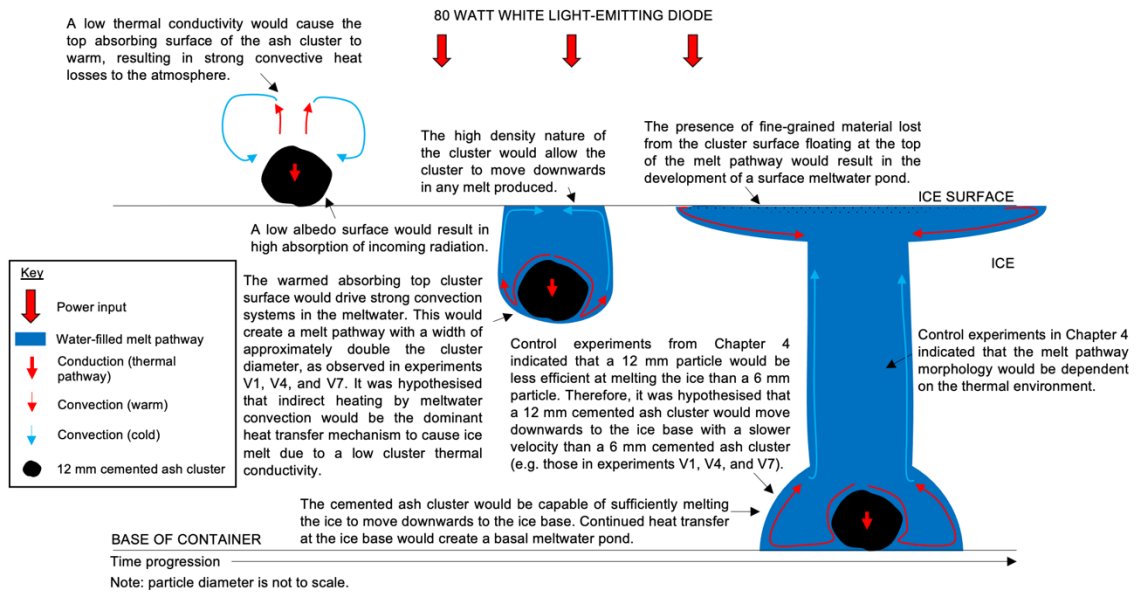


Figure 5.11. Schematic cross-sectional view of hypothesised cemented ash-ice interaction in experiment V2.

5.2.1. Results and interpretation

Ice melt occurred immediately after cemented ash cluster placement, causing downwards movement through the ice to reach the ice base within 23 hours (Figure 5.12). The cluster moved with a mean velocity of $7.57 \times 10^{-7} \text{ m s}^{-1}$.

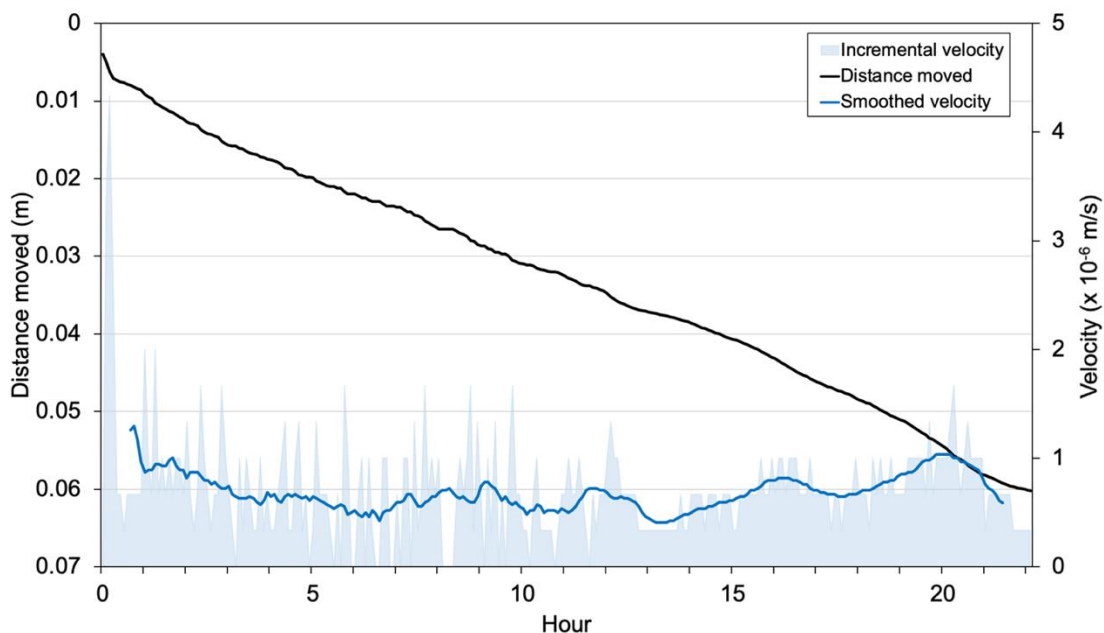


Figure 5.12. Vertical distance moved and velocity of a 12 mm Eyjafjallajökull cemented ash cluster in experiment V2.

5.2.2. Melt pathway

Comparable to experiments involving 6 mm cemented ash clusters (V1, V4, and V7), the V2 melt pathway was approximately double the cluster diameter (e.g. 26 mm). This strongly supported the hypothesis. The melt pathway was inclined with an observed 6 mm lateral movement by the V2 cluster, likely caused by the cluster intercepting vein structures within ice. Although irregular heating from the irregular surface morphology was also suggested as a mechanism for inclined downwards movement, previous experiments involving perfectly spherical particles also demonstrated an inclined melt pathway, suggesting that particle trajectory is controlled by the ice structure (alongside gravity).

There was no apparent refreezing of the melt pathway, suggesting that the cemented ash cluster was within a stable (warm) environment. Despite significant ice melt, it was determined that the V2 cluster experienced a stable (warm) rather than unstable environment because the cemented ash cluster at the ice base from experiment V1 (since disintegrated) was under the illumination also; this was initially embedded within solid ice at the start of experiment V2, suggesting that the ice was in a stable state. After the illumination was turned on, the disintegrated V1 cluster resumed melting the ice and created a basal meltwater pond. Although unintentional, the presence of the V1 cluster under the illumination acted as a control and demonstrated the ice was in a stable state where, if heat transfer from the volcanic material was removed, it would remain solid.

5.2.3. Surface meltwater pond

A scattering of fine-grained (<0.1 mm) volcanic particles were observed on the ice surface; these melted the ice with floating and sinking behaviours noted. It was inferred that the particles were introduced onto the ice surface from the V2 cluster surface during surface placement. Additionally, it was possible that particles were removed from the V2 cluster into the water column of the melt pathway. The melt pathways for the downwards moving fine-grained ash particles could not be identified in the time-lapse images due to their small sizes, although in-person observations noted that these created individual micro-melt pathways and contributed to internal ice melt. Some particles

remained floating in a surface meltwater pond and contributed to ice melt at the surface. This provided an initial insight into the behaviour of a scattering of volcanic material (later explored in experiments V33 and V34) and the fine grained particles were a probable contributor to the increased volume of ice melt with experiment V2 (compared to other experiments with particles in the stable (warm) thermal environment).

5.2.4. Basal meltwater pond

The V2 cluster continued to melt basal ice to create a basal meltwater pond (Figure 5.13). The basal meltwater pond grew until it combined with another growing basal meltwater pond (produced by the disintegrated V1 cluster) approximately five hours after the V2 cluster reached the ice base (and 27 hours after the experiment start).

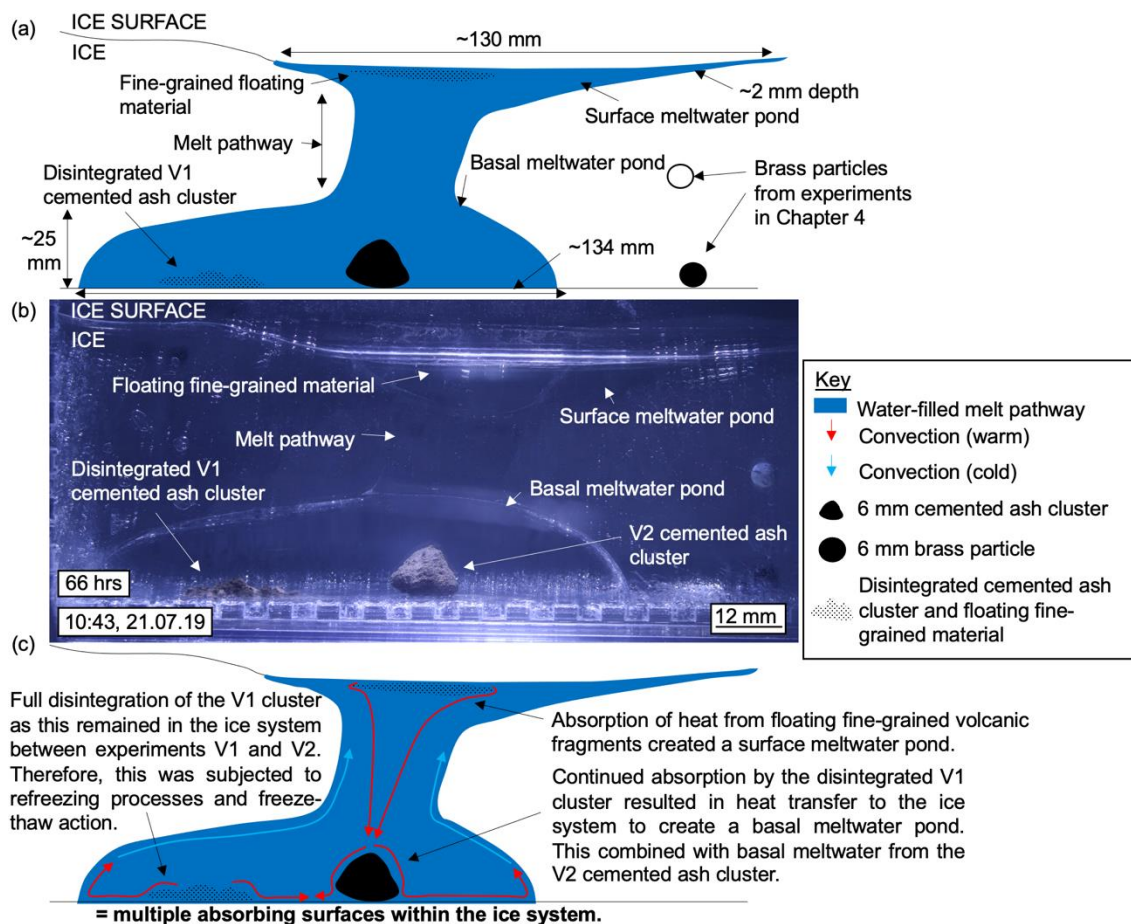


Figure 5.13. Cross-sectional images of a basal and surface meltwater pond in experiment V2. (a) observational line diagram, (b) photograph and (c) interpretation of the features.

5.2.5. Summary

Experiment V2 results confirmed the hypothesis that a 12 mm cemented ash cluster would melt downwards to the ice base. This was at a lower velocity than for the 6 mm clusters, suggesting a similar pattern to that observed in the 'diameter' series of experiments (i.e. a 6 mm particle is most efficient at inducing ice melt). Additionally, results showed that a scattering of fine-grained volcanic material (on the surface and within the melt pathway) resulted in an increased volume of meltwater produced in multiple regions (on the ice base and ice surface). Therefore, experiment V2 provided an insight into the complexities of ice interaction with numerous volcanic particles with a range of sizes – a likely representation of volcanic material within the natural system. This was repeated in experiments V5 and V6 to confirm findings.

Results from experiment V5 were comparable to those of V2 and demonstrated downwards movement with a velocity of $9.06 \times 10^{-7} \text{ m s}^{-1}$. Additionally, basal and surface meltwater ponds were created with widths of 104 mm and 210 mm, and depths of 26 mm and 15 mm, respectively. Significant ice melt and no signs of refreezing indicated that the V5 cluster was within a stable (warm) environment.

Contrastingly, experiment V6 did not show a similar behaviour to V2 and V5. This, instead, was split into two experiments (e.g. V6a and V6b). The cemented ash cluster remained within the ice with little particle-ice interaction for approximately 145 hours in experiment V6a. Therefore, experiment V6b followed on from an increase in freezer temperatures. Results from experiment V6b closely compared with experiment V7, where a disintegration of the 12 mm cluster was observed four hours after the experiment start, followed by subsequent downwards movement to the ice base within approximately 36 hours. The nature of the disintegration reinforced interpretation from experiment V7 that freeze-thaw processes from refreezing meltwater within the cluster caused the disintegration of the cemented ash cluster, as the V6b cluster experienced multiple refreezing events during experiment V6a (Figure 5.14).

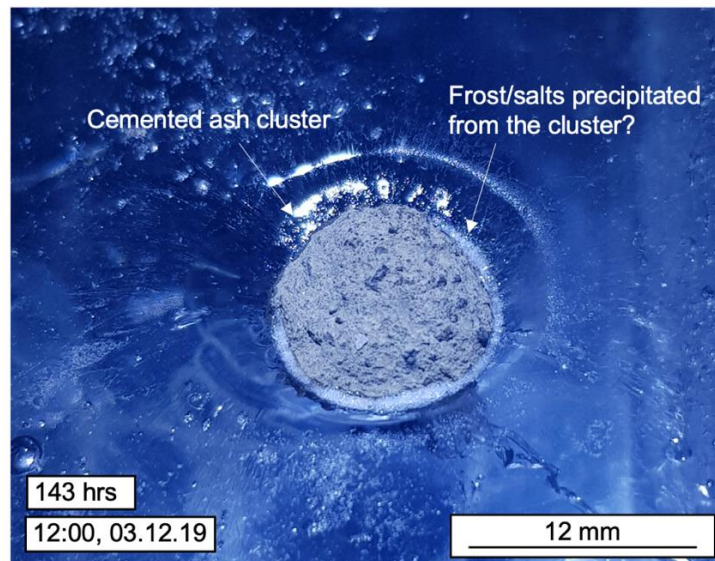


Figure 5.14. Plan-view photograph of refreezing in experiment V6a.

The disintegrated clusters moved downwards as a single unit until approximately 27.5 hours, when the smaller disintegrated clusters (approximately 6 mm) moved laterally away from the group to form two discrete groupings. This showed that the smaller cluster of finer-grained (<0.1 mm) disintegrated volcanic material moved downwards through the ice at a higher rate than the initial, since fragmented, V6b cluster (i.e. an overall mean particle velocity of approximately $5.21 \times 10^{-7} \text{ m s}^{-1}$ compared to $4.46 \times 10^{-7} \text{ m s}^{-1}$, respectively). This compared well with behaviour observed in experiment V7. The melt pathway fully refroze in the central segment, suggesting that the V6b cluster experienced a stable (cool) thermal environment.

Despite the contrast in behaviour from disintegration of volcanic material, experiment V2, V5, and V6b indicated that a 12 mm cemented ash cluster induced a lower rate of ice melt (a mean velocity of $7.03 \times 10^{-7} \text{ m s}^{-1}$) compared to a 6 mm cluster (a mean velocity of $1.40 \times 10^{-6} \text{ m s}^{-1}$). This appeared to follow the findings from the diameter series of experiments and suggested that particle diameter has an influence on particle-induced ice melt.

5.3. V3: a 3 mm cemented ash cluster

To further explore the role of particle diameter on volcanic particle-ice interaction, the behaviour of a 3 mm Eyjafjallajökull cemented ash cluster was

assessed in experiment V3. This was approximately 3x2.5 mm in size (Figure 5.15). The hypothesis for experiment V3 is shown in Figure 5.16.



Figure 5.15. Plan-view photograph of the 3 mm V3 cemented ash cluster.

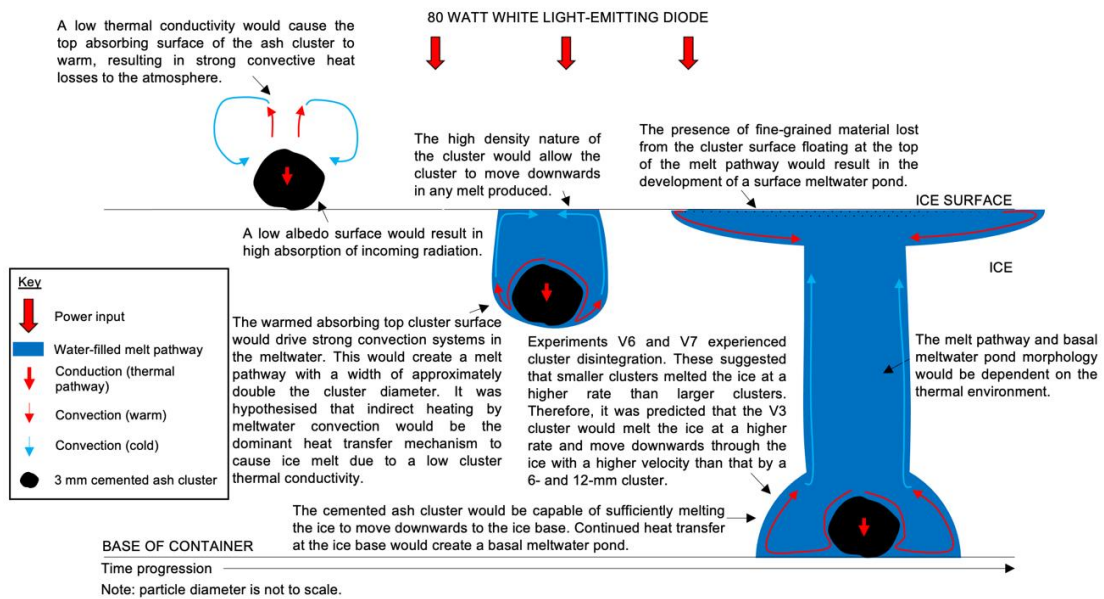


Figure 5.16. Schematic cross-sectional view of the hypothesised cemented ash-ice interaction in experiment V3.

5.3.1. Results and interpretation

The V3 cluster melted the ice surface immediately, resulting in the immediate downwards movement through the ice with a mean particle velocity of $1.01 \times 10^{-6} \text{ m s}^{-1}$ (Figure 5.17). This resulted in the V3 cluster reaching the ice base within 23 hours of the experiment start.

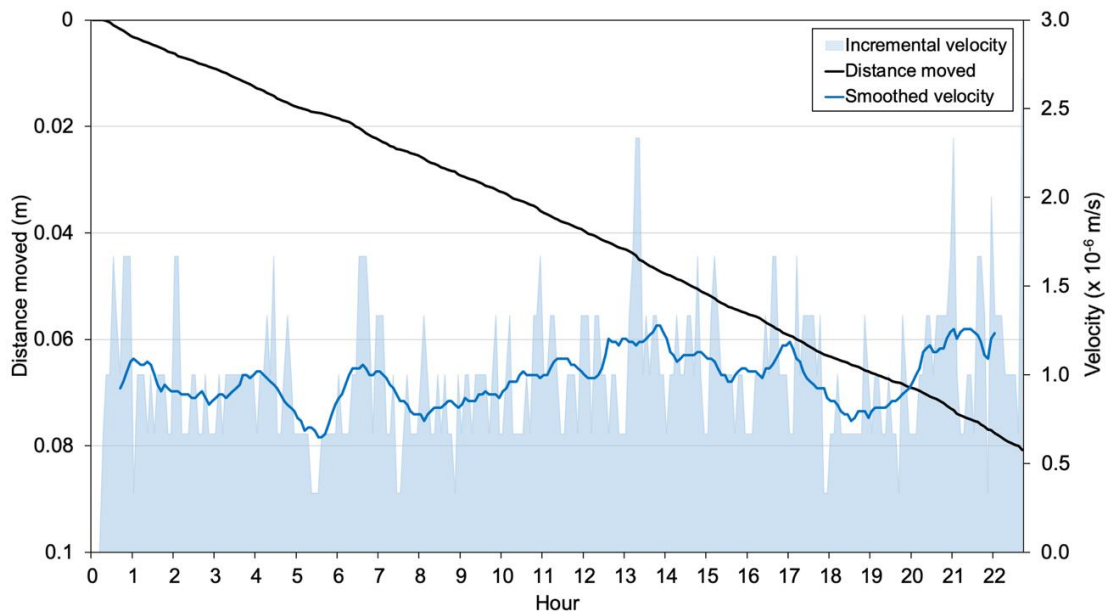


Figure 5.17. Vertical distance moved and velocity of a 3 mm Eyjafjallajökull cemented ash cluster in experiment V3.

5.3.2. Melt pathway

The melt pathway was approximately 7 mm wide, confirming the interpretation that volcanic particles generate a melt pathway that exceeds the cluster diameter (contrasting with results of thermally conductive particles in Chapter 4). Refreezing started approximately 14 hours after cluster placement and was fully closed at the ice surface at hour 17. This created a melt pathway with a teardrop morphology with a length of approximately 30 mm during cluster movement. Therefore, it was interpreted that the V3 cluster was in a stable (cool) thermal environment.

5.3.3. Surface meltwater pond

A surface meltwater pond developed despite the melt pathway fully refreezing. This was dish-shaped in morphology and had a width of approximately 150 mm and a maximum depth of approximately 9 mm (averaging at 3 mm). Although this segment of the ice did not receive heat transfer from the V3 cluster, the presence of a scattering of floating fine-grained (<0.1 mm) particles that had been removed from the V3 cemented ash cluster was observed (in the same way as in previous experiments involving cemented ash clusters). These small particles enabled heat transfer at the ice surface and caused ice melt to create a surface meltwater pond. This supports interpretation in previous experiments

(e.g. V4 and V2) that the development of a surface meltwater pond was likely due to the presence of surface particles, rather than the ice being in an unstable state.

5.3.4. Basal meltwater pond

The V3 cluster continued to transfer heat into the basal ice to create a basal meltwater pond. This was approximately 10 mm in width and 7 mm in height, smaller than those observed in previous experiments and agreeing with the interpretation that the cluster experienced a stable (cool) environment.

5.3.5. Summary

The 3 mm cemented ash cluster supported the hypothesis that the thermally insulating cluster could sufficiently melt ice to move downwards to the ice base. Downwards movement was comparable with 6 mm clusters (i.e. $\times 10^{-6} \text{ m s}^{-1}$), contrasting with the finding that the reduced ice melt was associated with smaller particles in Chapter 4. Therefore, the findings of a diameter-dependency of the thermal environment and rate of ice melt may not be applicable to thermally insulating particles. However, this could not be stated with confidence at this stage due to the limited number of experiments conducted; this will be assessed in subsequent experimental work.

Complexities associated with disintegration of clusters may be more comparable to the particle arrays (e.g. experiments assessing particle diameter, Chapter 4), rather than single particles. Although results from experiments V1-V7 unintentionally provided an insight into the behaviour of a group of volcanic particles, the nature of these clusters added complexities into the series of experiments and added uncertainty to results. The purpose of experimental work in Chapter 5 was to systematically assess volcanic material with specific properties and so it was determined that single particles, rather than cemented clusters, would be used in the subsequent volcanic particle investigation to allow a more focussed assessment. Therefore, there were no repeat experiments assessing a 3 mm cemented ash cluster.

5.4. V9: a 6 mm basaltic-andesitic scoria particle

Basaltic-andesitic scoria particles from Volcán Sollipulli (Chile) were used to assess the influence of a low albedo volcanic particle on ice ablation. The V9 particle had a relatively low albedo, high density, low thermal conductivity (relative to ice), and a diameter of approximately 6 mm (Figure 5.18). The hypothesis for experiment V9 is shown in Figure 5.19.



Figure 5.18. Plan-view photograph of the 6 mm V9 scoria particle.

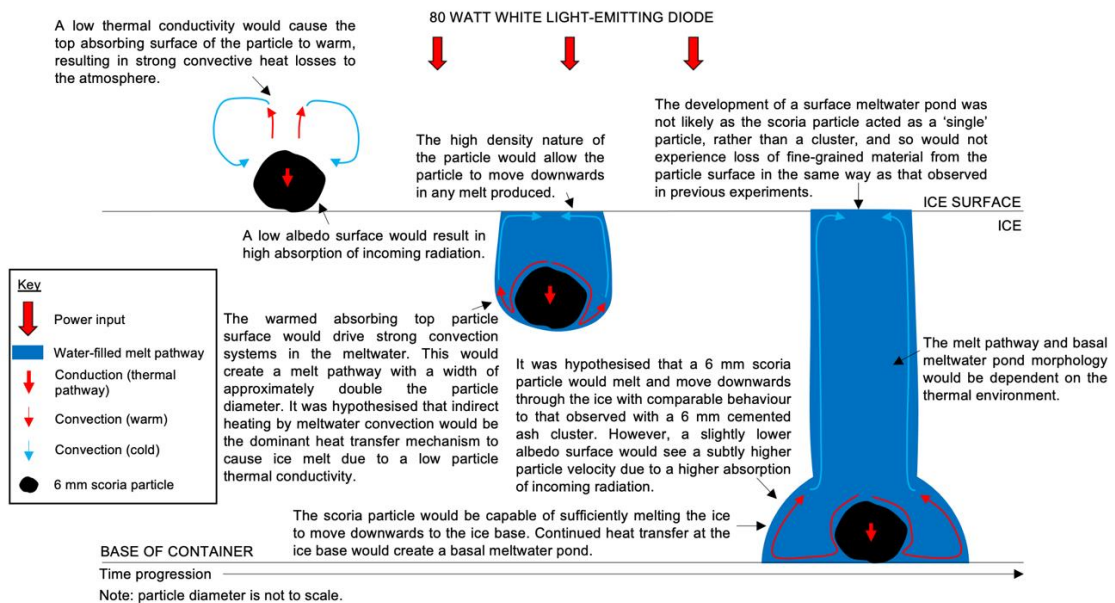


Figure 5.19. Schematic cross-sectional view of the hypothesised particle-ice interaction in experiment V9.

5.4.1. Results and interpretation

The particle immediately transferred heat into melting the ice after surface placement, causing downwards movement of the dense scoria particle through the ice. However, condensation on the freezer glass surface prevented clear time-lapse images after hour 7. After this, results relied on in-person observations. The

mean particle velocity prior to this was calculated at $6.70 \times 10^{-7} \text{ m s}^{-1}$ (Figure 5.20).

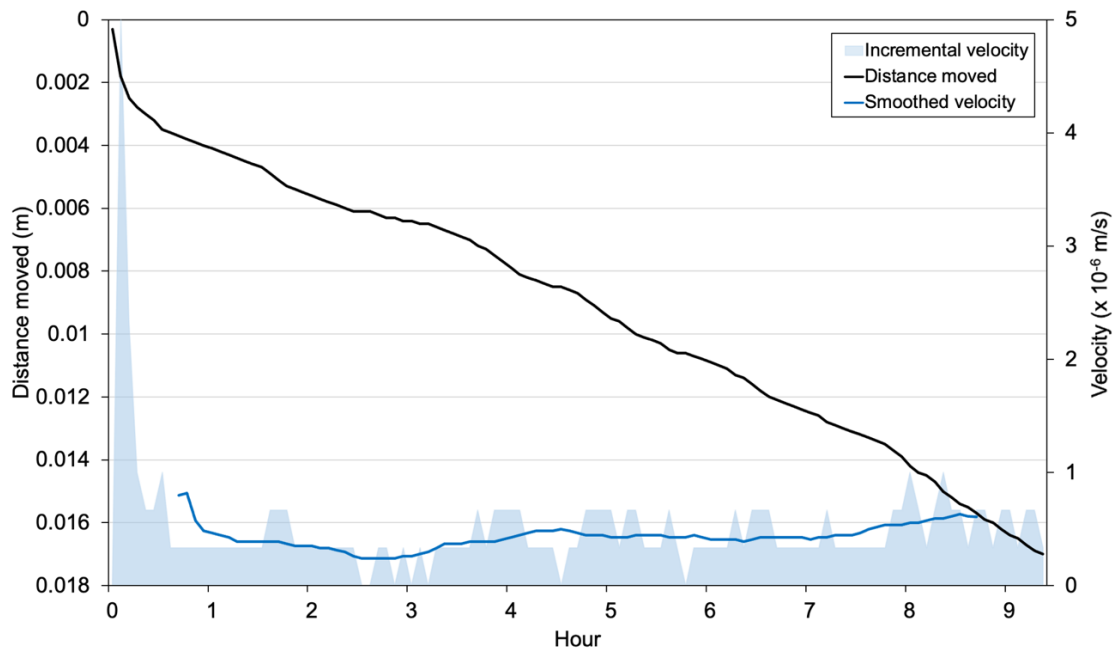


Figure 5.20. Vertical distance moved and velocity of a 6 mm scoria particle in experiment V9.

5.4.2. Melt pathway

Similar to the cemented ash clusters, the V9 scoria particle created a melt pathway that had a diameter approximately double the particle (i.e. approximately 14 mm). Condensation obscuring the view in time-lapse images prevented detailed analysis of the melt pathway, although in-person observations revealed that this experienced refreezing processes. Similar to experiment V1, this refroze fully in the central segment of the melt pathway. Refreezing of meltwater when sufficiently far from the particle sphere of influence suggested that the particle was within a stable (cool) thermal environment.

5.4.3. Surface meltwater pond

A surface meltwater pond developed despite a refreezing melt pathway. This was observed in previous experiments (e.g. V3, V4, etc.), and was likely due to the presence of fine-grained ($<0.1 \text{ mm}$) scoria particles that were unable to sink due to surface tension effects transferring heat into melting the ice surface. The presence of these particles was confirmed by in-person observations and demonstrated that intact volcanic material was capable of shedding finer-

grained fragments to the ice system in the same way as cemented ash clusters, contrasting with the hypothesis.

5.4.4. Basal meltwater pond

In-person observations demonstrated that the particle continued to transfer heat into the base of the ice to create a basal meltwater pond (Figure 5.21). This had a width and height of approximately 60 mm and 28 mm, respectively. All meltwater refroze after the illumination was turned off, indicating that the ice was in a stable environment and all meltwater was a result of particle-induced ice melt.

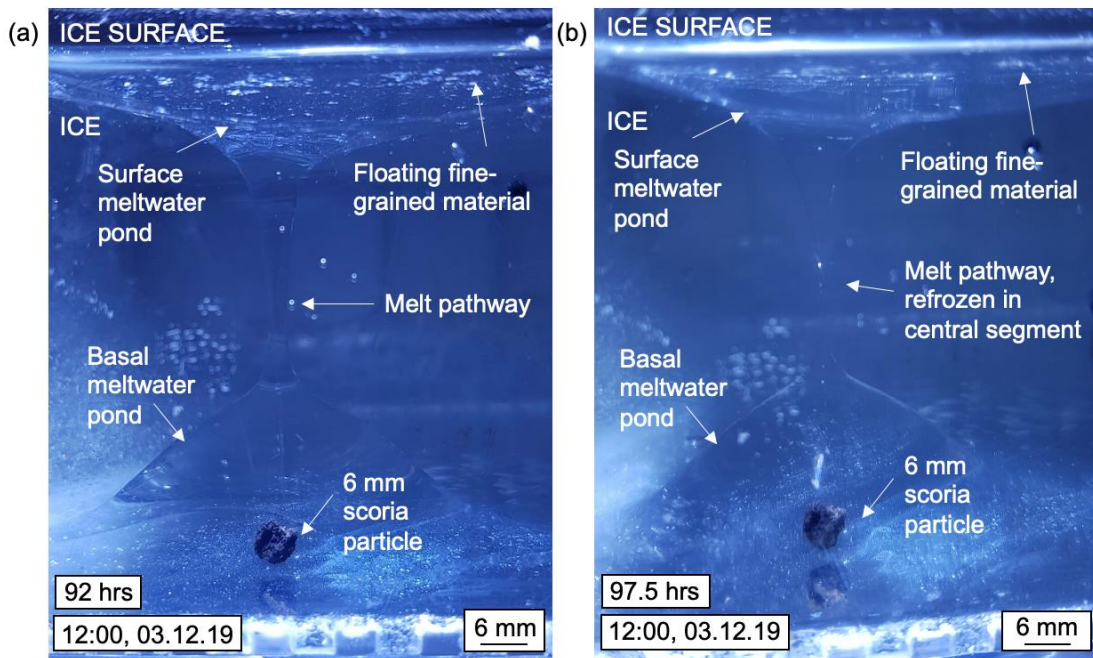


Figure 5.21. Cross-sectional photographs of refreezing melt pathway, surface meltwater pond, and the V9 particle submerged within a basal meltwater pond over a five hour period in experiment V9, where (a) is showing an open melt pathway, and (b) is showing a closed melt pathway.

5.4.5. Summary

Results from experiment V9 demonstrated similar key features to results from the 6 mm cemented ash clusters, for example: (1) a melt pathway extending past the margin of the particle, (2) a surface meltwater pond due to the presence of fine-grained volcanic material floating in meltwater, and (3) a basal meltwater pond as the particle melted the basal ice.

This experiment was repeated a further four times (V10, V13, V14, and V22), showing downwards movement of particles to the ice base with mean velocities of $8.71 \times 10^{-7} \text{ m s}^{-1}$, $4.15 \times 10^{-7} \text{ m s}^{-1}$, $9.15 \times 10^{-7} \text{ m s}^{-1}$, and $1.06 \times 10^{-6} \text{ m s}^{-1}$, respectively. The thermal environment experienced by the particle differed from experiment to experiment, causing the variation of mean particle velocities. However, these experiments allowed the calculation of a mean particle velocity of $7.86 \times 10^{-7} \text{ m s}^{-1}$ for the 6 mm scoria particles; this compared relatively well with the modelled particle velocity calculated using the simple melt model in Chapter 3 (i.e. $8.43 \times 10^{-7} \text{ m s}^{-1}$). Similar features were observed in repeat experiments: (1) melt pathways with a diameter of approximately double the particle diameter (i.e. approximately 15 mm) and (2) surface meltwater ponds developed in all instances from heat transfer by floating fine-grained material (e.g. 150 x 80 mm width, and 5 mm depth in experiment V10). However, results from experiments V13, V14, and V22 demonstrated some additional variability.

In contrast to experiments V9 and V10, experiment V13 was conducted within a variable thermal environment. An initial downwards movement was observed until the particle stalled at a depth of approximately 10 mm for a period of approximately 19 hours, with refreezing processes observed (e.g. a reduction in melt width by approximately 2 mm). Despite this, the V13 particle maintained a meltwater pond that surrounded the particle throughout the stalled period. However, this was limited in size and only extended approximately 1 mm from the particle extent. This suggested that all heat that was transferred into ice was maintaining the small meltwater pond in a liquid form. The particle was unable to further melt the ice to create a larger meltwater pond, or move downwards in the ice, as the ice was conducting heat away sufficiently fast to prevent further ice melt. This suggested that the V13 particle had reached an equilibrium within a stable (cool) thermal environment. This was not a stable (cold) thermal environment, as the presence of meltwater was indicative of active particle-ice interaction. An in-person modification of the freezer temperature increased the ambient temperatures and the V13 particle was able to sufficiently melt downwards to the ice base. Therefore, the particle experienced a positive shift across the thermal range to allow ice melt. In this environment, the V13 particle

created a melt pathway with the same morphology as that observed in experiment V9 and V10.

Experiments V14 and V22 were conducted further along the thermal range in a stable (warm) thermal environment (Figure 5.1), identified by a significant volume of meltwater and drainage channels on the ice surface. The presence of fine-grained volcanic particles floating in surface meltwater was interpreted as an important contributor to the higher volume of meltwater in both V14 and V22 (as seen in experiments V9, V10, and V13). In both instances, it was deduced that the ice was not unstable as the meltwater started to refreeze when the illumination was turned off (and, therefore, when heat transfer from the V14/V22 particles and fine-grained surface particles to the ice was removed). This indicated that meltwater was a result of particle-ice interaction rather than an unstable ice system. However, the ice refroze over a long period (i.e. approximately 24 hours in both instances), suggesting that the particles were experiencing a stable (warm) environment, close to the unstable boundary, in both experiments. This allowed both the V14 and V22 particles to move downwards with a higher mean particle velocity than the V9, V10, and V13 particles, despite being the same composition with the same properties.

5.5. V11: a 12 mm basaltic-andesitic scoria particle

V11 investigated the behaviour of a 12 mm scoria particle placed on the ice surface (Figure 5.22). The hypothesis for experiment V11 is shown in Figure 5.23.



Figure 5.22. Plan-view photograph of the 12 mm V11 scoria particle, also indicating fine-grained material that was lost from the particle surface.

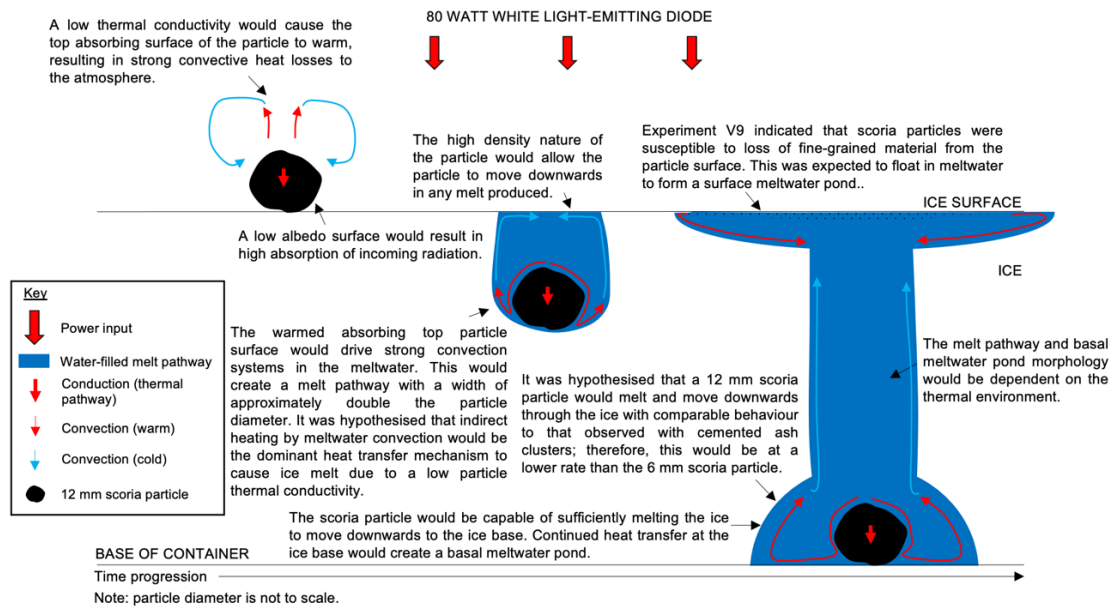


Figure 5.23. Schematic cross-sectional view of the hypothesised particle-ice interaction in experiment V11.

5.5.1. Results and interpretation

The V11 particle melted the ice and moved downwards with a particle velocity of $5.77 \times 10^{-7} \text{ m s}^{-1}$ to reached the ice base within 29 hours (Figure 5.24). It was noted that a smaller fragment (approximately 1 mm in diameter) was present below the particle after hour 11. This was not directly below as the smaller fragment was also illuminated, facilitating downwards movement of the 1 mm particle until movement of the V11 particle resulted in the smaller fragment no longer receiving illumination. This demonstrated the capability of the scoria particles to shed fragments on the mm-scale, and that these smaller particles could move downwards through the ice.

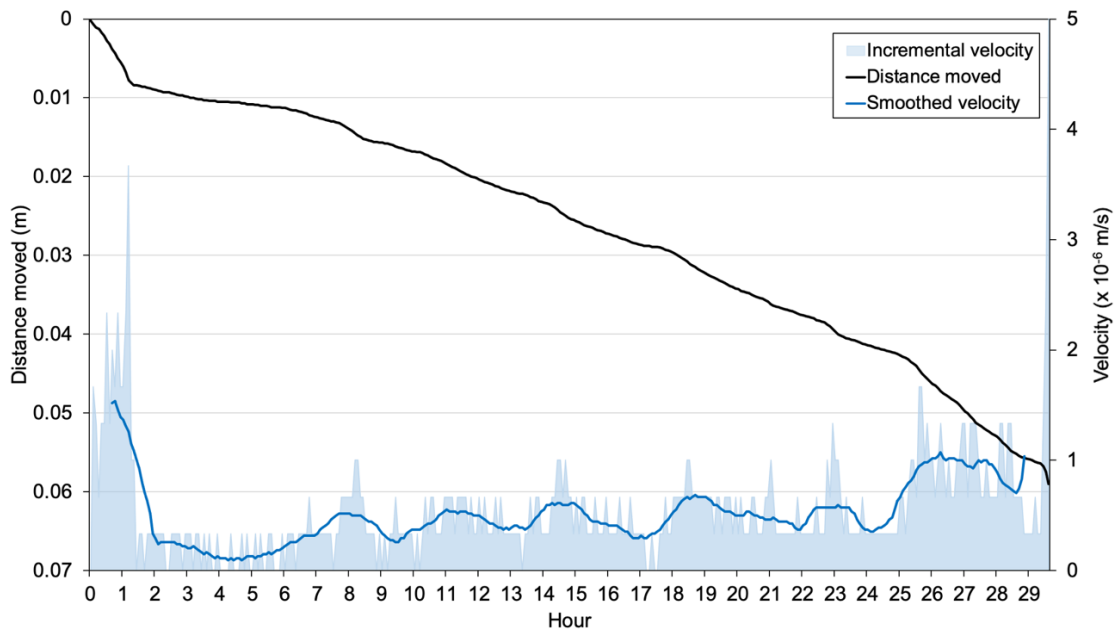


Figure 5.24. Vertical distance moved and velocity of a 12 mm scoria particle in experiment V11.

5.5.2. Melt pathway

The melt pathway had a width approximately double the particle diameter (approximately 25 mm) and was thus comparable with results from previous volcanic particle experiments. It was rounded and extended from the particle at the base of the melt pathway, suggesting that the particle was efficiently driving convection within the melt pathway. This interpretation was based on the process of warm meltwater extending the area of melt past the conduction-driven direct melting (typically represented by a narrow melt pathway and base, frequently observed with metal particles in Chapter 4) at the base of the melt pathway. This could suggest that the convection system, in addition to the presence of smaller fragments of the particle within the melt pathway, contributed to the width of the melt pathway. Whilst the melt pathway was open at the surface throughout particle movement, it began refreezing after the particle reached the ice base. This refreezing process was commonly observed with the volcanic material. However, the melt pathway did not fully refreeze, and measured approximately 20 mm in width at the end of the experiment. These processes indicated that the V11 particle experienced a stable (warm) thermal environment as the melt pathway remained open throughout the experiment.

5.5.3. Surface meltwater pond

Similar to previous experiments involving volcanic material, the development of a surface meltwater pond was observed throughout the experiment. This reached maximum dimensions of 60x50 mm in width, and 1-2 mm in depth. This was likely due to the loss of fine-grained volcanic particles from the scoria particle providing additional absorbing surfaces into the ice system.

5.5.4. Basal meltwater pond

A basal meltwater pond developed throughout the experiment during downwards particle movement from a particle in a previous experiment. This allowed the particle to drop down into the basal melt (e.g. over the last 2 mm of particle movement). Once on the ice base, the V11 particle created a basal meltwater pond that reached a maximum dimension of approximately 50 mm wide and 25 mm high.

5.5.5. Summary

Experiment V11 demonstrated many of the common features observed within the volcanic experimental series: for example, effective convection in meltwater widening the melt pathway to approximately double the particle diameter; the development of a basal meltwater pond; the development of a surface meltwater pond; and refreezing processes within the melt pathway when sufficiently far from the particle. Although a downwards particle velocity of $6.26 \times 10^{-7} \text{ m s}^{-1}$ was lower than the average value of $8.17 \times 10^{-7} \text{ m s}^{-1}$ for the 6 mm scoria particles, it fits within the range of velocities.

This experiment was repeated three times to confirm observations and particle velocities (V12, V23, and V24). These generally compared well with one another; an exception to this was experiment V12 due to drainage events and slower particle movement as the particle experienced a stable (cool) thermal environment (e.g. $1.68 \times 10^{-7} \text{ m s}^{-1}$). Experiments V23 and V24 were comparable with particle velocities of $1.06 \times 10^{-6} \text{ m s}^{-1}$ and $1.52 \times 10^{-6} \text{ m s}^{-1}$, respectively; this was likely due to the V23 and V24 particles operating within a stable (warm) thermal environment, as no refreezing processes were observed.

All repeat experiments developed a surface meltwater pond due to the presence of surface fine-grained scoria particles (although experiment V12 lost surface meltwater due to drainage events). These results, in combination with experiment V11, suggested a mean particle velocity of $1.21 \times 10^{-6} \text{ m s}^{-1}$ for 12 mm scoria particles; this was a higher value than the 6 mm mean particle velocity, suggesting possible differences between the behaviour of volcanic particle with different diameters. However, it is important to consider the differing thermal environments experienced by the particles in these experiments, and, therefore, that experiments may not be directly comparable. The calculated 12 mm mean particle velocity was also higher than the modelled calculation using the simple melt model in Chapter 3.

Experiment V12 provided an insight into the influence of particle velocity on melt pathway morphology and into the behaviour of drainage events. A slower particle velocity and refreezing melt pathway suggested that, unlike experiments V23 and V24, the V12 particle was in a stable (cool) thermal environment. This was closer to the stable (cold) boundary than in experiment V11, identified by a greater volume of refreezing and lower rate of particle movement. These processes, in combination with an efficient convection system, resulted in the melt pathway becoming almost spherical (Figure 5.25). This contrasted with long, wide pathways with vertical walls seen in previous experiments, and indicated the role of particle velocity in influencing the morphology of meltwater produced.

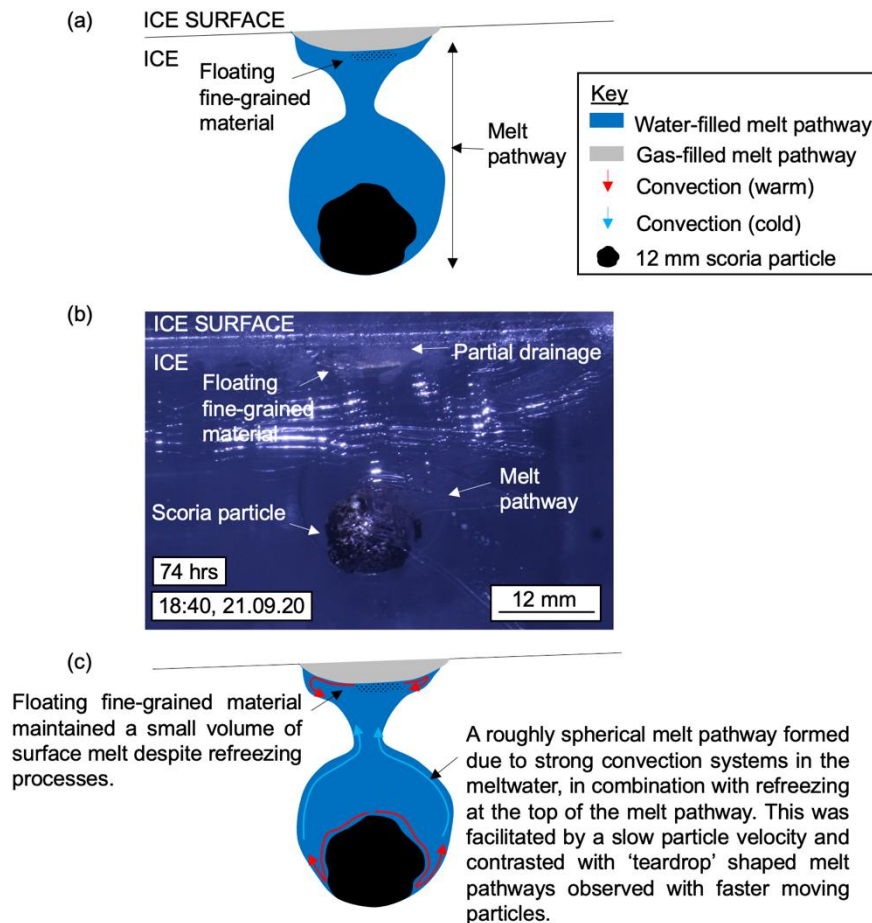


Figure 5.25. Cross-sectional images of a roughly spherical melt pathway observed in experiment V12. (a) observational line diagram, (b) photograph and (c) interpretation of the features.

As the particle velocity increased during the experiment, the melt pathway extended to a teardrop morphology. This further confirmed the role of particle velocity in influencing the morphology of a melt pathway (i.e. a slower particle would create a circular area of melt, whilst a faster moving particle would create an elongated teardrop melt pathway).

A partial drainage event occurred approximately 96.5 hours into the experiment (Figure 5.26). However, the water level within the partially drained melt pathway rose after the initial event by approximately 2 mm. This suggested that particle-induced ice melt was still occurring, or drainage from surface melt created from the fine-grained surface particles had also occurred. The latter was probable, as observations noted a hollow on the ice surface and subsequent removal of water from the ice surface. The gas space above the particle reflected incoming

radiation (observed by a bright spot in the image and the particle being much darker in colour), likely also contributing to the end of particle movement as less energy would be absorbed by the particle.

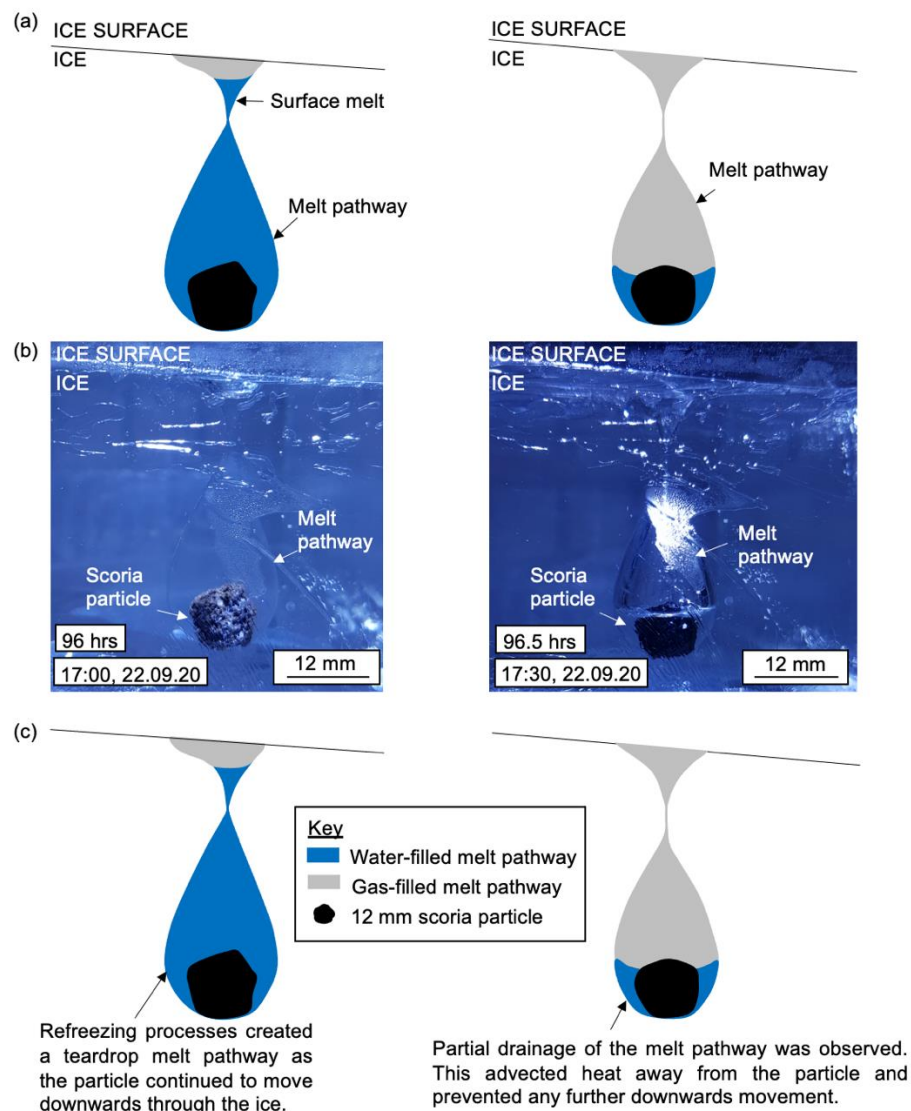


Figure 5.26. Cross-sectional images showing the development of a drained melt pathway in experiment V12. (a) observational line diagram, (b) photograph and (c) interpretation of the features.

Experiment V24 showed the addition of multiple downwards moving absorbing particles into the ice system (Figure 5.27). This was noted by the presence of a smaller (e.g. approximately 2 mm x 0.5 mm) particle beneath the particle that moved downwards to the ice base within 10.5 hours and with a particle velocity of $6.46 \times 10^{-7} \text{ m s}^{-1}$.

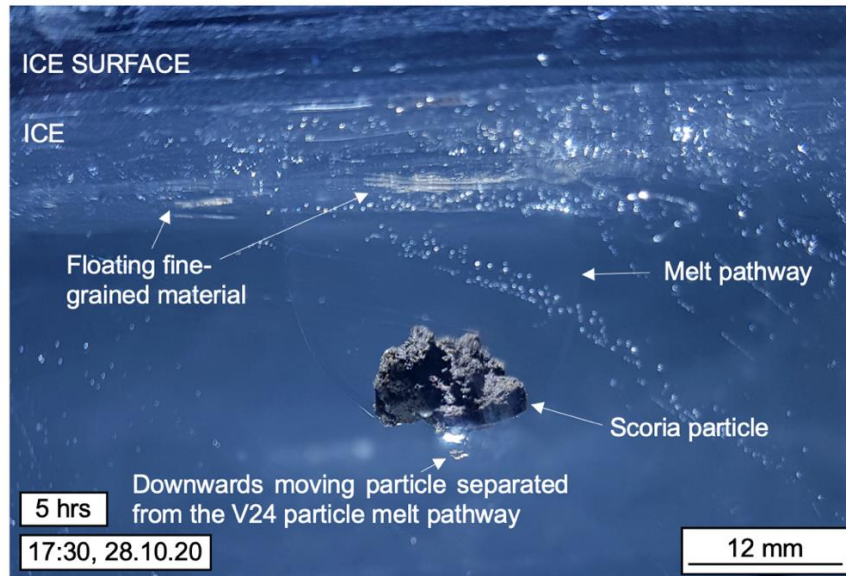


Figure 5.27. Photograph of multiple absorbing particles within the ice in experiment V24.

The multiple downwards moving absorbing particles within the ice was first noted approximately 2.5 hours after the experiment start. This created an individual melt pathway during descent through the ice (Figure 5.28). This was subsequently noted a second time with a particle approximately 0.5 mm in diameter. However, it could not be determined if these were clusters of fine-grained material that was introduced into the ice system beneath the particle (and, therefore, did not experience surface tension retaining the particles at the ice surface), or solid fragments of the scoria particle broken off due to freeze-thaw action (as discussed with the cemented ash clusters, e.g. experiment V6 and V7). This will be investigated in subsequent experiments.

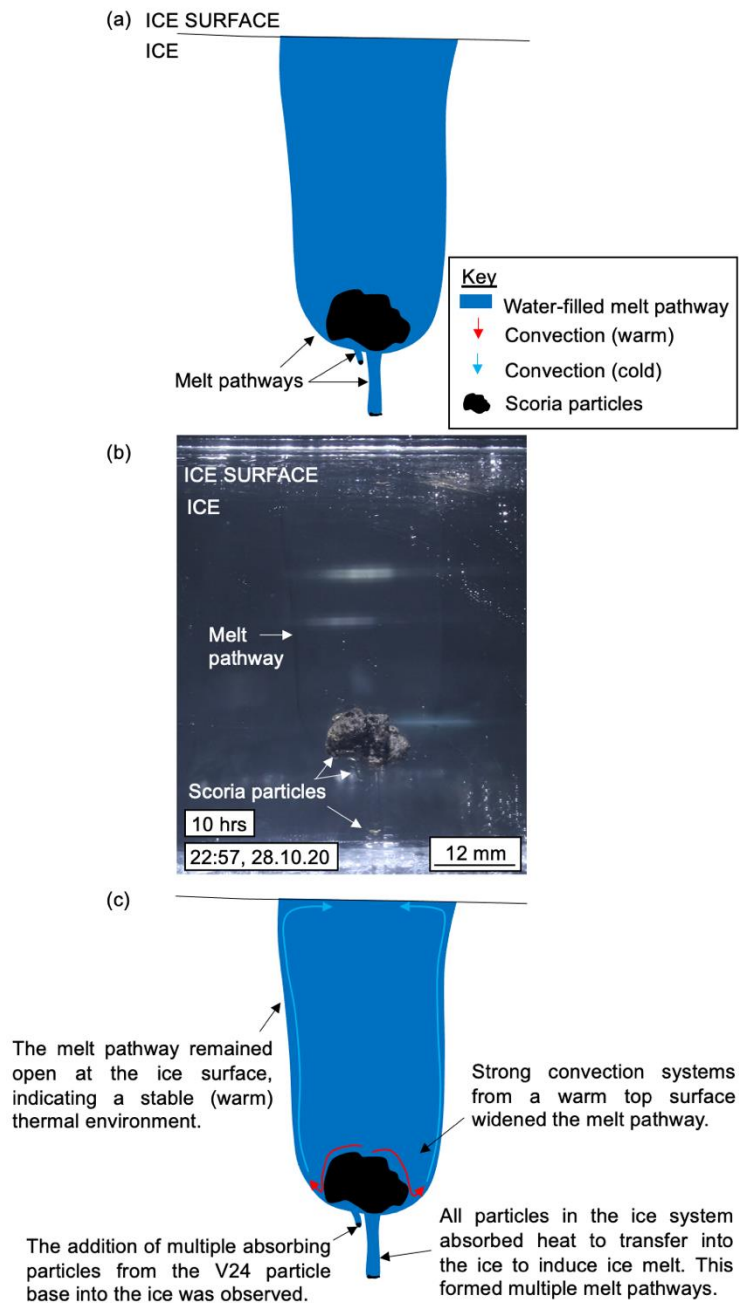


Figure 5.28. Images of the multiple particles and melt pathways observed in experiment V24. (a) observational line diagram, (b) photograph and (c) interpretation of the features.

5.6. V15: a 3 mm basaltic-andesitic scoria particle

To further assess the role of particle diameter on volcanic particle-ice interaction, a 3 mm scoria particle was investigated (Figure 5.29). This had the same composition as the 6 mm and 12 mm particles (e.g. V9 onwards), and so, the particle properties were comparable. The hypothesis for experiment V15 is shown in Figure 5.30.

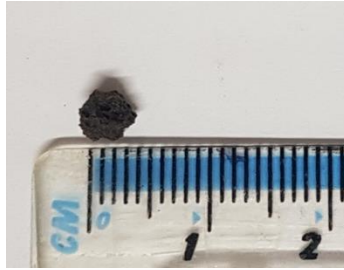


Figure 5.29. Plan-view photograph of the 3 mm V15 scoria particle.

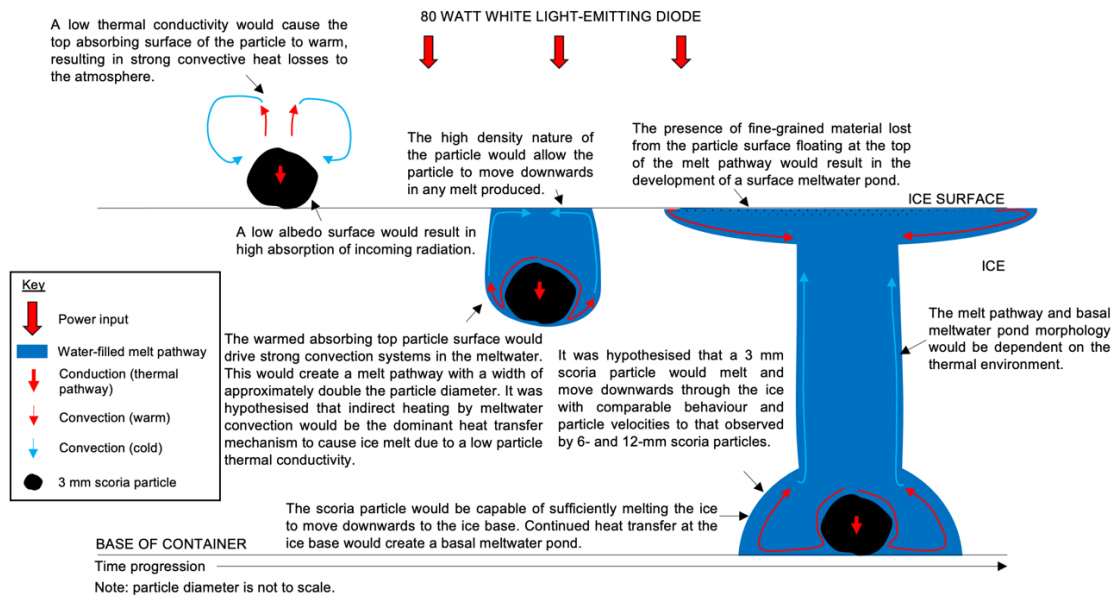


Figure 5.30. Schematic cross-sectional view of the hypothesised particle-ice interaction in experiment V15.

5.6.1. Results and interpretation

An immediate downwards movement was observed by the 3 mm particle. This moved through the ice with a particle velocity of $1.01 \times 10^{-6} \text{ m s}^{-1}$ and reached the base of the ice within 18 hours (Figure 5.31). The particle dropped into a basal meltwater pond created by a previous particle (V12) that was approximately 4 mm in height; this facilitated a high velocity at the end of particle movement that was not indicative of the rate of 3 mm particle-induced ice melt.

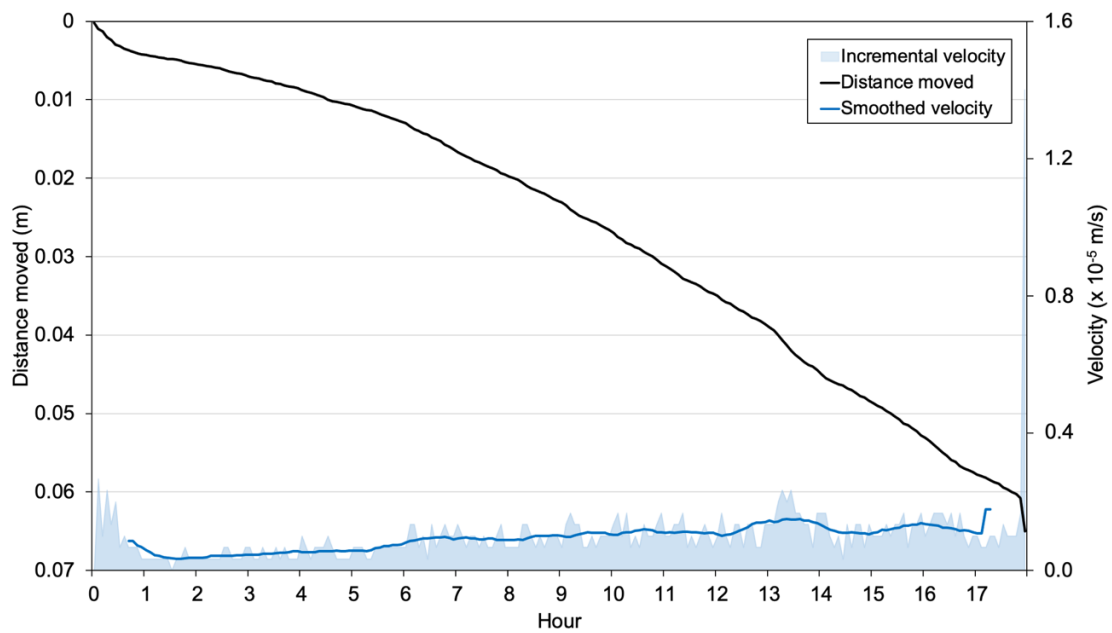


Figure 5.31. Vertical distance moved and velocity of a 3 mm scoria particle in experiment V15.

5.6.2. Melt pathway

The 3 mm particle created a melt pathway that extended from the particle and was approximately 8 mm in width. This width was maintained throughout the duration of the experiment, and so it was deduced that the particle was within a stable (warm) thermal environment due to the lack of refreezing processes and a sustained open melt pathway. The melt pathway morphology was comparable to those from larger scoria particles within a stable (warm) thermal environment.

5.6.3. Surface meltwater pond

Similar to results from previous experiments involving volcanic material, a surface meltwater pond developed during experiment V15, caused by heat transfer from floating fine-grained surface material. The meltwater pond was extensive and had a horizontal extent of approximately 170x120 mm, and an average depth of approximately 7 mm. The illumination was turned off at the experiment end and the meltwater monitored to confirm that the ice was stable; full refreezing of meltwater indicated that the V15 particle experienced a stable (warm) thermal environment.

5.6.4. Basal meltwater pond

The particle created a basal meltwater pond once at the ice base. This reached a maximum width of 147 mm and height of 10 mm. As the horizontal extent of the V15 basal meltwater was large, meltwater interacted with particles from previous experiments that were not under the illumination source (e.g. V12). Therefore, convection systems within the basal meltwater pond extended the pond to form hydrological connections with other particles. Although a small volume of meltwater was already present on the ice base from a previous experiment (facilitating the rapid velocity at the end of V15 particle movement), much of the water in the basal meltwater pond was a result of V15 particle-induced ice melt. This was identified by enlargement of the basal meltwater pond once the V15 particle reached the ice base.

5.6.5. Summary

Experiment V15 was largely consistent with the behaviours observed by the 6 mm and 12 mm scoria particles. However, results suggested a higher rate of movement of a 3 mm particle (e.g. $1.01 \times 10^{-6} \text{ m s}^{-1}$) compared to a 6 mm or 12 mm particle, although confirmation is needed with repeat experiments. Aside from a higher particle velocity, the same key features were observed. This additionally indicated that a 3 mm scoria particle in a stable (warm) environment, could generate an extensive volume of melt, as demonstrated by the large basal and surface meltwater ponds.

Three experimental repeats (V16, V17, and V19) were conducted to confirm the behaviour observed in experiment V15. Results matched well with one another, although technical issues in experiment V16 prevented a full documentation of the experiment. All experiments created a surface and basal meltwater pond, and a meltwater pathway that had a width extending past the particle margins (even in instances of refreezing). Particle velocities were calculated as $6.30 \times 10^{-7} \text{ m s}^{-1}$ in V16 (although issues with the illumination source were noted), $1.20 \times 10^{-6} \text{ m s}^{-1}$ in V17, and $1.31 \times 10^{-6} \text{ m s}^{-1}$ in V19. Therefore, the mean particle velocity for a 3 mm scoria particle was calculated at $1.04 \times 10^{-6} \text{ m s}^{-1}$; this was faster than mean values for the 6 mm and 12 mm scoria particles, confirming

initial findings from experiments investigating cemented ash clusters. Additionally, this was faster than the modelled velocity (i.e. $8.43 \times 10^{-7} \text{ m s}^{-1}$).

V16 demonstrated a slower particle velocity relative to other experiments of this type. Although a freezer temperature decrease after V15 may have shifted the V16 particle into a stable (cool)/stable (cold) thermal environment, it was noted that illumination in experiment V16 stopped functioning, with a decrease in illumination prior to this. An identical replacement illumination source was used in experiment V17 with no freezer temperature adjustment, and this showed a higher velocity of the 3 mm particle within this experiment, comparing well with other experiments of this type. Therefore, the lower rate of movement in V16 was attributed to illumination issues. The lower illumination output in experiment V16 caused a lower heat absorption by the particle and, therefore, a lower heat transfer rate into the ice. This caused refreezing and the development of a teardrop melt pathway with a similar morphology to that observed in the initial stages of experiment V12, as the low rate of downwards particle movement created an almost spherical melt pathway. This confirmed the interpretation that the morphology of a melt pathway is also dictated by the particle velocity. This has only been observed in the volcanic series of experiments (i.e. those with a relatively low thermal conductivity and high density).

Experiments V17 and V19 were comparable with rapid particle movement and the development of extensive surface and basal meltwater ponds. However, these also demonstrated contrasting behaviour, as experiment V17 experienced cyclic drainage events and experiment V19 experienced refreezing processes. It was interpreted that the V17 particle was within a stable (warm) thermal environment whilst the V19 particle was within a stable (cool) thermal environment (although close to the stable (warm) boundary due to very slow refreezing processes and high particle velocities). Refreezing events in experiment V19 occurred when the particle reached the ice base and began in the central segment of the melt pathway (agreeing with the general behaviour observed by volcanic material). It was likely that this was due to strong convection within the melt pathway preventing refreezing until convection systems drove the development of a basal meltwater pond (Figure 5.32).

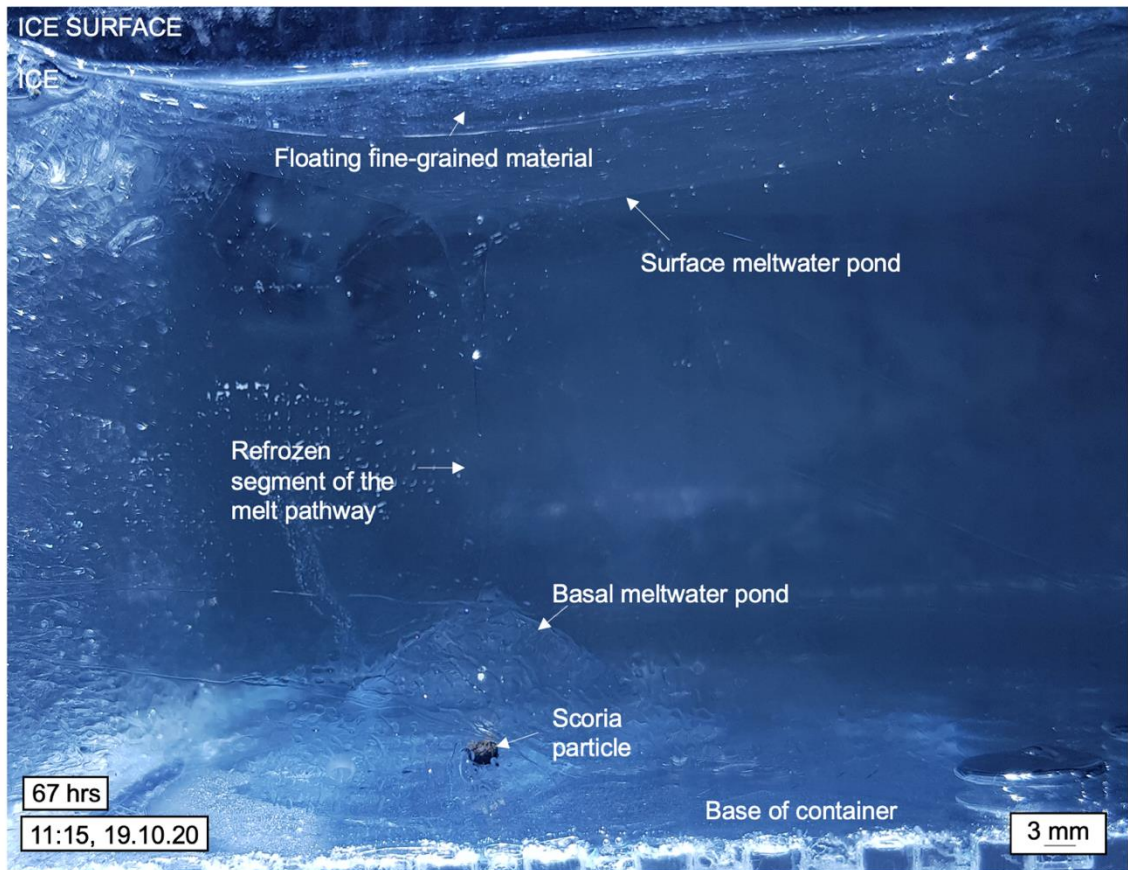


Figure 5.32. Cross-sectional photograph of the basal and surface meltwater, joined by a refreezing melt pathway, in experiment V19.

5.7. V18: a 1.5 mm basaltic-andesitic scoria particle

A 1.5 mm scoria particle was investigated to further assess the role of particle diameter on the behaviour of volcanic material (Figure 5.33). This particle diameter had not been considered in previous volcanic experiments (e.g. cemented ash clusters). The hypothesis for experiment V18 is shown in Figure 5.34.

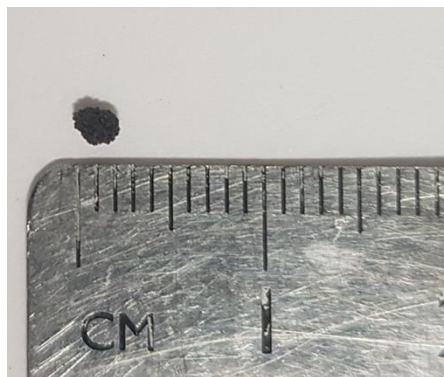


Figure 5.33. Plan-view photograph of the 1.5 mm V18 scoria particle.

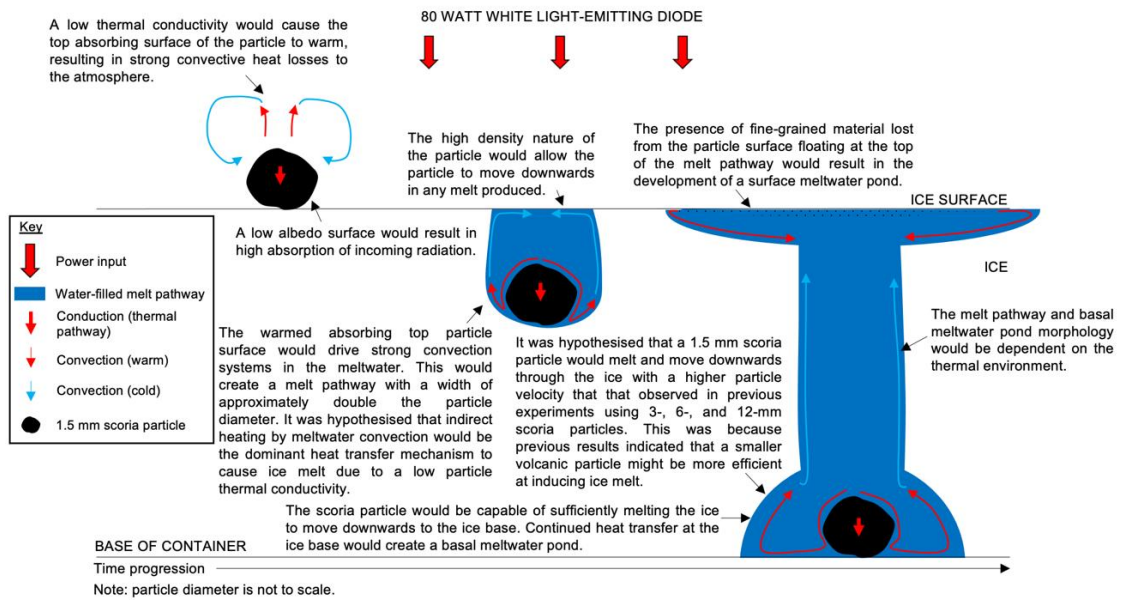


Figure 5.34. Schematic cross-sectional view of the hypothesised particle-ice interaction in experiment V18.

5.7.1. Results and interpretation

In contrast to previous experiments, the 1.5 mm scoria particle did not move downwards through the ice. Instead, the V18 particle floated in meltwater, resulting in a fluctuation in the particles vertical position in the ice (to a maximum depth of approximately 7 mm) as the particle was retained at a fluctuating meltwater surface level with periodic drainage events (Figure 5.35). However, fluctuations of meltwater level stabilised after nine hours, and the particle floated in meltwater at the original ice surface for the remainder of the experiment.

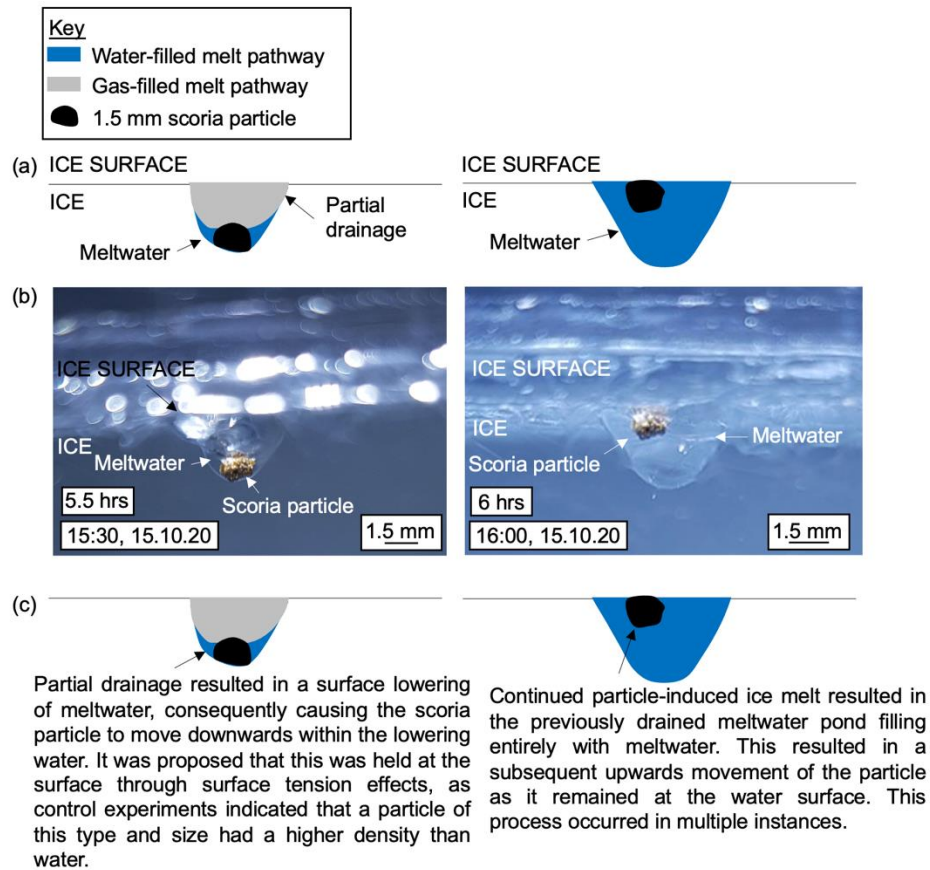


Figure 5.35. Cross-sectional images showing the fluctuation in the particle position in experiment V18. (a) observational line diagram, (b) photograph and (c) interpretation of the features.

The initial surface meltwater pond was elongated in morphology. It was observed that the early development of the surface meltwater pond aligned with the orientation of drainage channels on the ice surface (Figure 5.36). Thus, this could suggest that the surface pond geometry was caused by ice preferentially melting along ‘weaker’ regions of ice, i.e. those already containing meltwater, for example, the vein network or drainage channels on the ice surface.

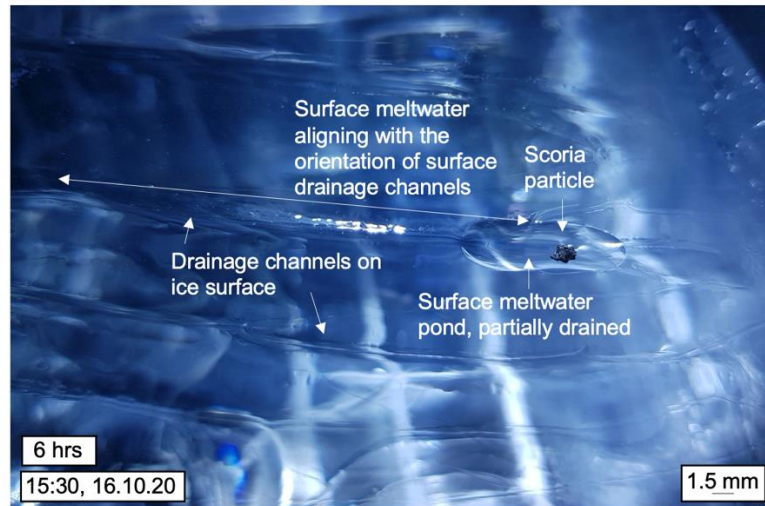


Figure 5.36. Photograph of the early development of the surface meltwater pond in experiment V18.

Floating particles (controlled by surface tension effects) created an extensive surface meltwater pond with an approximate length of 175 mm, width of 80 mm, and mean depth of 5 mm. This extended downwards to a maximum depth of approximately 7 mm (reflecting the initial downwards movement of the particle in the first nine hours). The particle moved laterally across the ice surface during the experiment as it floated in the surface meltwater pond. This appeared circular in motion (and this was also seen in the movement of the smaller fragments of scoria floating in the surface meltwater pond). Surface motion was likely caused by convection within the meltwater and enabled the development of an extensive area of melt. No refreezing processes were evident, and it was deduced that the V18 particle experienced a stable (warm) thermal environment.

5.7.2. Summary

The behaviour observed in experiment V18 did not support the hypothesised behaviour of downwards movement. Instead, the 1.5 mm particle floated in meltwater produced. This was interpreted to be a result of surface tension effects, rather than a low density, as control experiments demonstrated that a 1.5 mm scoria particle had a higher density than water. It would be useful to assess if the floating behaviour is observed in repeat experiments. Therefore, a further two experiments were conducted (V20 and V21). Although these both demonstrated the floating behaviour of a 1.5 mm particle, all three experiments

contrasted with each other, demonstrating the number of complex processes involved in volcanic particle-ice interaction.

Experiment V20 did not experience a lowering of the particle within the ice; instead, this floated in a surface meltwater pond throughout the experiment (after enough melt was produced). However, this showed comparable behaviour to experiment V18, where an elongated meltwater pond developed in the initial phases of the experiment. Lateral motion was observed to a greater extent in experiment V20 compared to experiment V18, causing the early development of an irregular shaped surface meltwater pond (Figure 5.37). This eventually evolved into a large region of surface melt (spanning a length of 150 mm and width of 110 mm, with an average depth of 2 mm). The maximum depth of meltwater was 7 mm, directly below the particle. Lateral movement of the V20 particle to an area of ice no longer under illumination approximately 7 hours into the experiment occurred. The presence of fine-grained fragments floating in surface meltwater pond maintained the meltwater in liquid form during this time as these remained under the focus of illumination. Although the result of experimental artefacts, this demonstrated the capability of fine-grained material in contributing to ice melt, despite the focal particle (e.g. V20) being unintentionally removed from the influence of illumination.

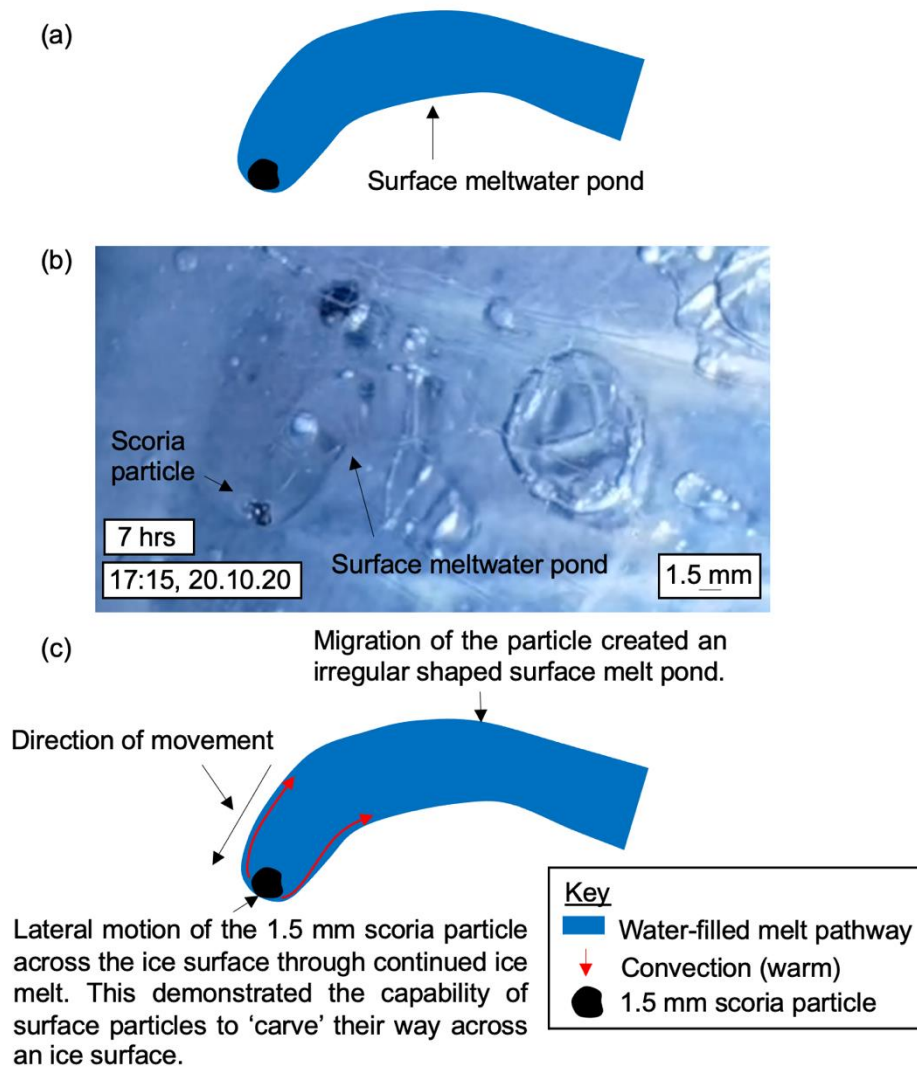


Figure 5.37. Plan-view images of the early development of a surface meltwater pond in experiment V20 and the impact of lateral motion on meltwater morphology. (a) observational line diagram, (b) photograph and (c) interpretation of the features.

In the same way as experiment V18, Experiment V21 experienced a fluctuation of particle depth. However, this was to a much greater extent than experiment V18 as an overall downwards particle movement by approximately 42 mm was observed (Figure 5.38).

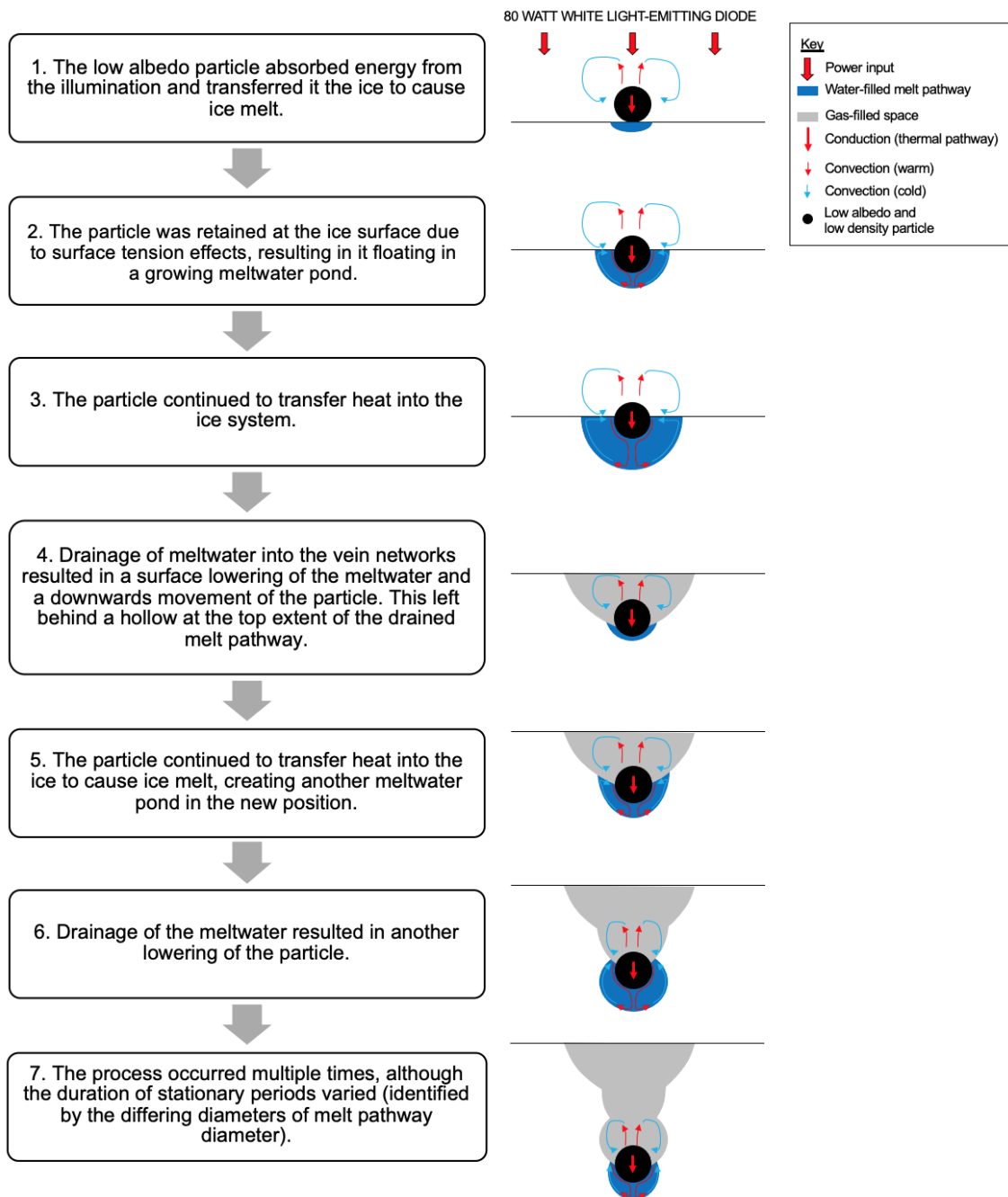


Figure 5.38. Cross-sectional diagram showing the suggested theory behind the process of periodic particle lowering.

Drainage events modified the internal ice structure and created a drained melt pathway (Figure 5.39). This had the same morphology to the meltwater and convection system previously created by the 1.5 mm particle. The vein network within the ice itself were also visible by-eye, suggesting that the ice was bordering the stable/unstable boundary. Additionally, previous experiments (Chapter 4) demonstrated that hydrological connections with the vein network formed more readily in warmer temperatures.

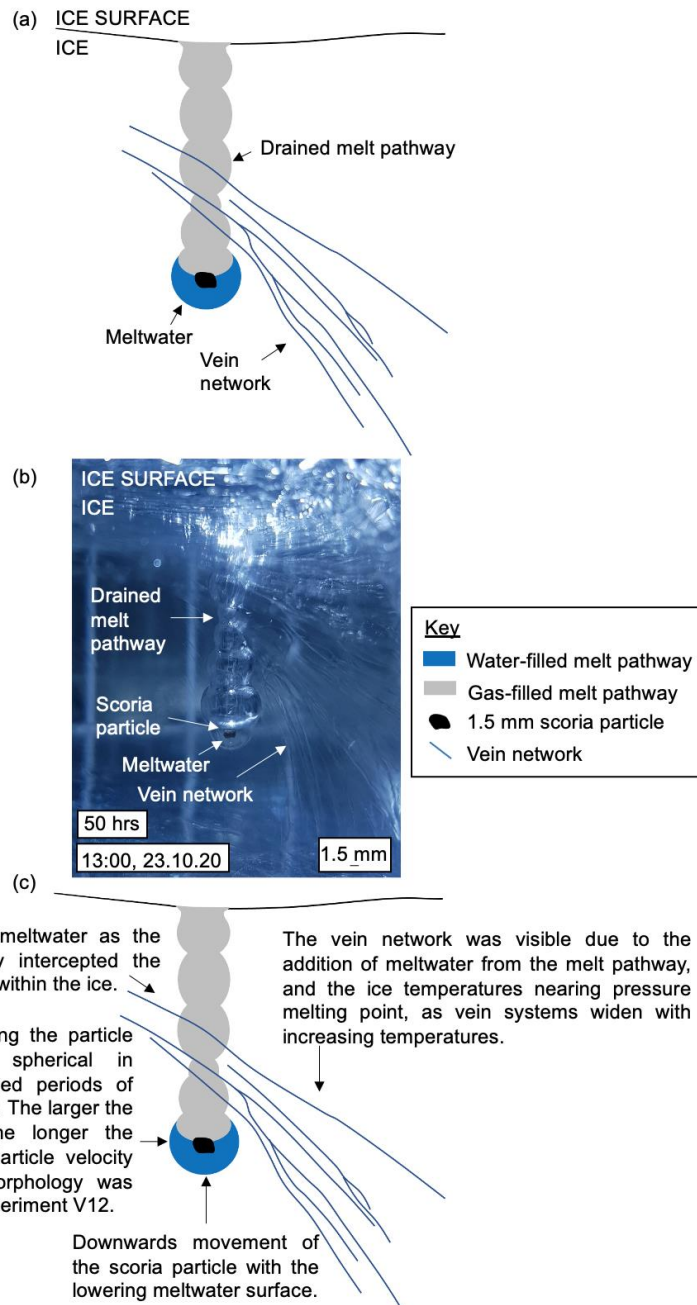


Figure 5.39. Cross-sectional images of drained melt pathway formed in experiment V21. (a) observational line diagram, (b) photograph and (c) interpretation of the features.

The floating behaviour of the 1.5 mm particles indicated that surface tension effects can dominate with a small particle with small density differences between the particle and water. Although the particle velocity (used as a proxy for ice melting rate) could not be calculated for a 1.5 mm particle, extensive areas of surface melt demonstrated that a particle of this size could efficiently melt the ice. These results contrasted with the behaviour observed with the synthetic material, where a thermally conductive 1.5 mm particle ‘stalled’ within the ice system once fully submerged.

This series of experiments demonstrated the complexities associated with small, volcanic particles and the role of surface tension in preventing downwards movement, retaining particles at the surface when they otherwise would have become embedded within the ice. This experiment broadened the features associated with particle-induced ice melt, to include a large volume of surface melt, and a complex morphology of a drained melt pathway.

5.8. V25: a 6 mm rhyolitic pumice particle

To assess the role of particle albedo and density on volcanic particle-ice interaction, the following series of experiments investigated the behaviour of rhyolitic pumice particles from Mount St. Helens (USA). These had an intermediate albedo and a high porosity (Chapter 3). To allow direct comparison, the same diameters as that assessed using the low albedo scoria particles were used. Experiment V25 investigated the behaviour of a 6 mm rhyolitic pumice particle (Figure 5.40). The hypothesis for experiment V25 is shown in Figure 5.41.



Figure 5.40. Plan-view photograph of the 6 mm V25 pumice particle.

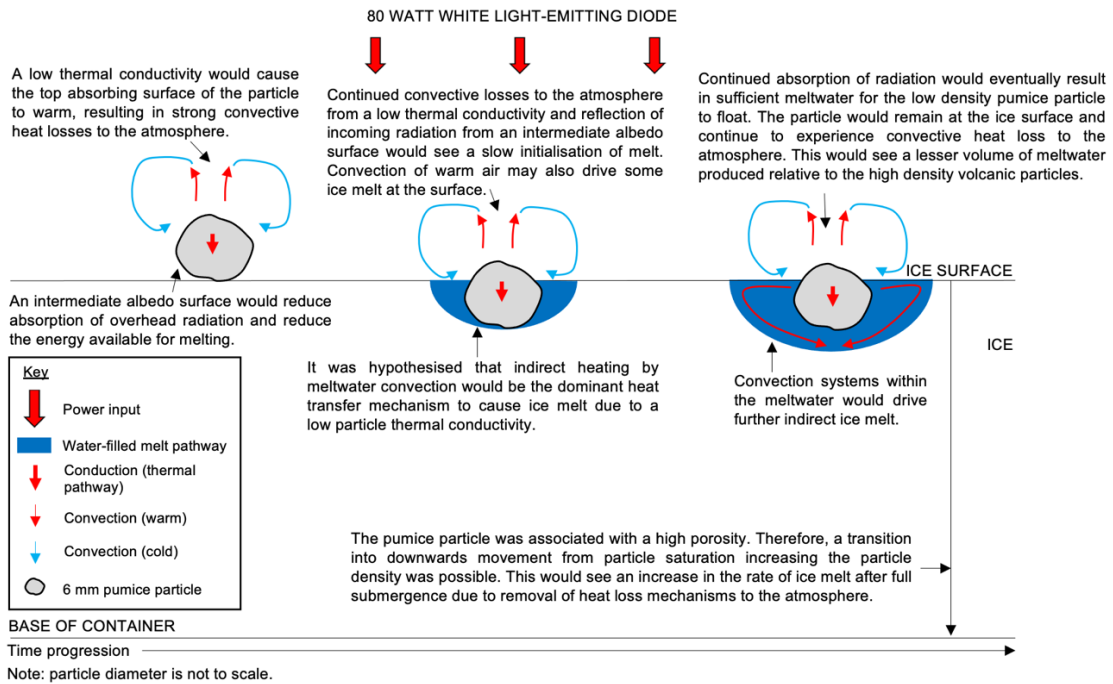


Figure 5.41. Schematic cross-sectional view of the hypothesised particle-ice interaction in experiment V25.

5.8.1. Results and interpretation

The 6 mm pumice particle floated in meltwater produced, contrasting to behaviours of a 6 mm scoria particle. This was due to the higher porosity (and, therefore, lower density) of the V25 pumice particle. However, this generated a large volume of melt, comparable to that generated by low albedo particles, in the form of a shallow surface meltwater pond and deep area of meltwater below the particle (hereafter referred to as the ‘proximal surface meltwater pond’).

An unexpected feature observed in experiment V25 was the presence of a small pumice fragment (approximately 0.5-1 mm) broken from the 6 mm particle. In-person observations confirmed that the fragment was from the V25 particle. This was first observed approximately 6.5 hours into the experiment after the V25 particle started to float in meltwater, and it was noted that this moved downwards through the ice with a particle velocity of $7.66 \times 10^{-7} \text{ m s}^{-1}$ to reach the ice base. This created a small-scale melt pathway within the ice (Figure 5.42). The downwards movement of the smaller fragment did not follow the hypothesised outcome of the pumice particle floating in meltwater. The mechanism for downwards movement was unclear; it could not be determined if the melt pathway was draining as the particle and melt pathway were small and

so detail could not be extracted from time-lapse images. However, there were no other drainage processes observed during particle descent.

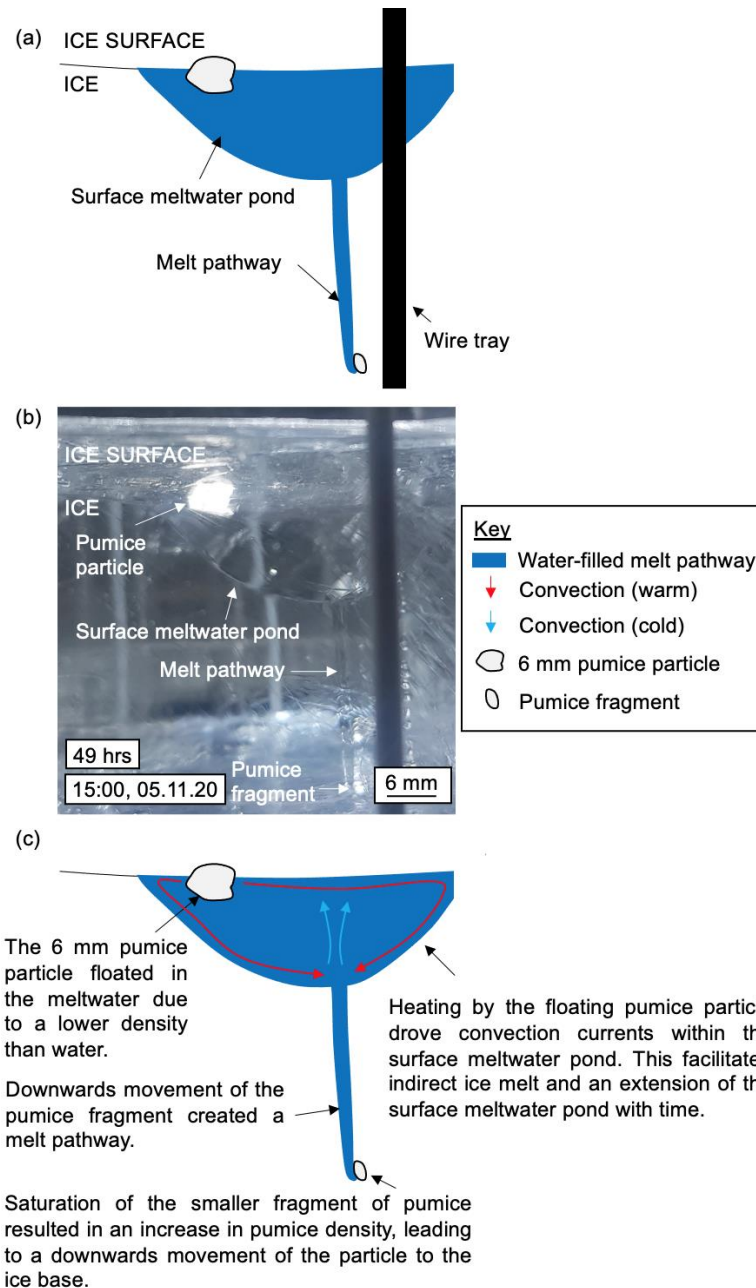


Figure 5.42. Cross-sectional images of the proximal surface meltwater pond and the melt pathway associated with a downwards moving smaller fragment of pumice in experiment V25. Convection systems are simplified. (a) observational line diagram, (b) photograph and (c) interpretation of the features.

5.8.2. Proximal surface meltwater pond

The proximal surface meltwater pond had a width of approximately 42 mm and a depth of approximately 25 mm. This represented the particle's sphere of influence, likely extended by indirect convection melting and confirmed the

importance of meltwater convection in ice melt. Lateral particle movement extended the proximal surface meltwater pond; growing ceased when particle movement stopped. The implication was that, at this stage, the meltwater had reached an equilibrium with the particle heat transfer. No refreezing processes of melt were observed and so it was deduced that the V25 particle experienced a stable (warm) thermal environment.

5.8.3. Shallow surface meltwater pond

In the same way as in previous experiments involving volcanic material, fine-grained (<0.1 mm) particles were observed floating in the meltwater. These created a shallow surface meltwater pond with a horizontal extent of approximately 135x105 mm. The pond had a depth of approximately 1 mm at the furthest extent, and an average depth of approximately 5-6 mm. It was deduced that the scattering of fine-grained surface particles were responsible for the shallow surface meltwater pond, whilst the larger V25 particle was responsible for the deeper proximal meltwater pond.

5.8.4. Summary

Experiment V25 indicated that a pumice particle exhibited a different behaviour to cemented ash clusters and scoria particles (aside from the 1.5 mm scoria particles). This was due to a high porosity and low density, suggesting that the porosity and density of particles are a key control on the behaviour of particle-ice interaction. A large volume of meltwater was produced despite an intermediate albedo and low thermal conductivity, contradicting initial predictions of the behaviour of a particle of this type. Results also indicated further complexities associated with fragmentation of volcanic material, and this will be investigated in detail in further experiments.

To confirm the behaviour of a pumice particle, this experiment was repeated in experiment V30. These results were largely consistent with one another, as the 6 mm pumice particle efficiently melted the ice and floated in meltwater produced. The floating V30 particle created a proximal surface meltwater pond with a width and depth of approximately 27 mm and 13 mm, respectively, whilst

floating fine-grained particles created a shallow surface meltwater pond approximately 130x70 mm wide, and an average depth of 1-2 mm. Interestingly, a small pumice fragment with a hemispherical morphology was observed in experiment V30 in the same way as V25, first observed approximately 8.5 hours into the experiment (Figure 5.43). This had a similar size (approximately 0.5-1 mm) and morphology and moved downwards through the ice with a mean particle velocity of $2.35 \times 10^{-7} \text{ m s}^{-1}$, confirming the behaviour of the pumice fragment in experiment V25. Time-lapse imagery ended before this reached the ice base. Pumice fragmentation was likely a result of similar processes observed during experiment V6b and V7, where freeze-thaw of percolating meltwater within pumice pore spaces fractured the V25/V30 particles to create smaller pumice fragments.

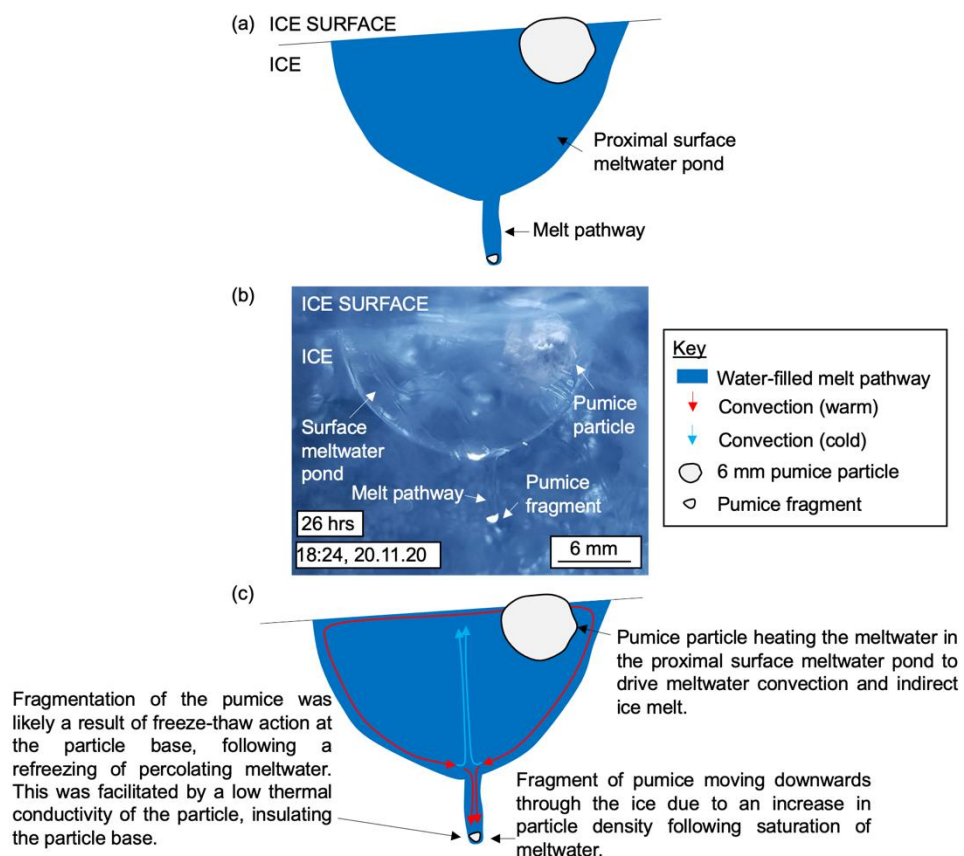


Figure 5.43. Cross-sectional images of the proximal meltwater pond and a small fragment of pumice moving downwards through the ice in experiment V30. Convection systems are simplified. (a) observational line diagram, (b) photograph and (c) interpretation of the features.

5.9. V27: a 12 mm rhyolitic pumice particle

A 12 mm rhyolitic pumice particle was investigated in experiment V27 to assess the role of particle diameter on influencing the behaviour of a low density and

intermediate albedo volcanic particle (Figure 5.44). The hypothesis for experiment V27 is shown in Figure 5.45.



Figure 5.44. Plan-view photograph of the 12 mm V27 pumice particle.

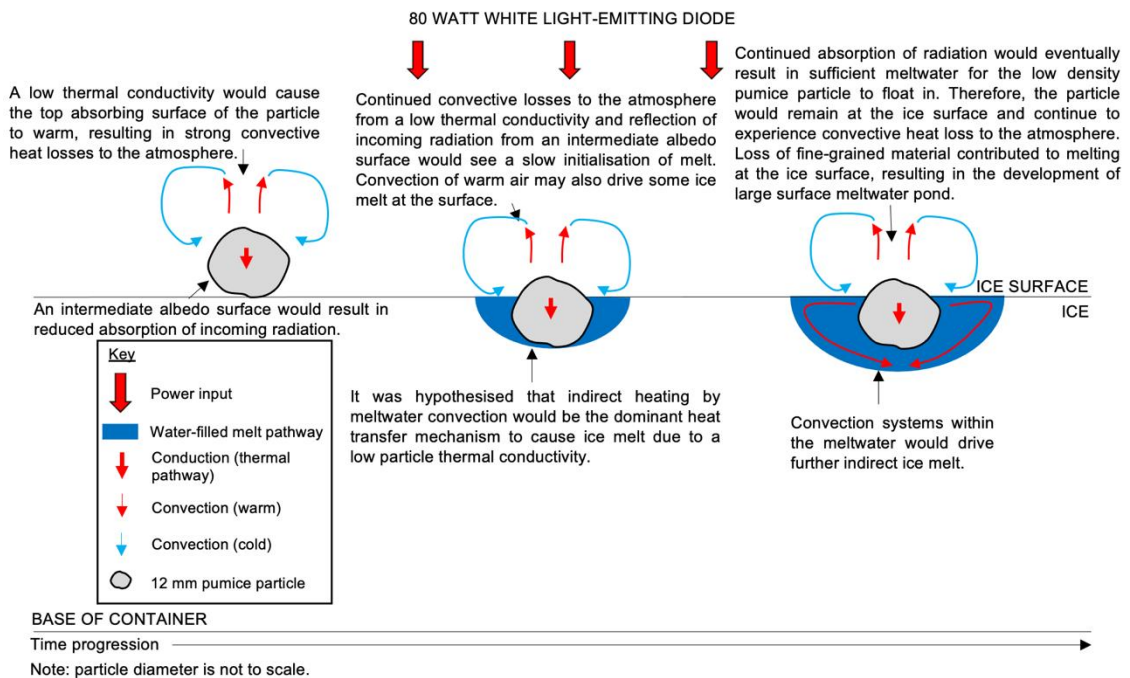


Figure 5.45. Schematic cross-sectional view of the hypothesised particle-ice interaction in experiment V27.

5.9.1. Results and interpretation

Heat transfer from particle to ice caused ice melt immediately after particle placement, causing an observed downwards movement of the V27 particle until it reached its point of buoyancy and started to float. This was approximately six hours into the experiment and was identified by the meltwater extent exceeding the particle base, and a rotation of the particle as it began floating. The particle floated in meltwater throughout the experiment to create a proximal and shallow surface meltwater pond, in the same way as V25 and V30.

Two pumice fragments (approximately 1x2 mm, and <0.5 mm) were observed in the same way as experiments V25 and V30 (Figure 5.46). This suggested that the fragmentation of a pumice particle and subsequent downwards movement of a pumice fragment was a common process associated with pumice-ice interaction. This additionally demonstrated the ability of pumices to experience multiple fragmentation events. Fragments were first observed approximately 8.5 hours into the experiment at the base of the proximal meltwater pond. Continued downwards movement of the 2 mm and <0.5 mm pumice fragments with particle velocities of $6.52 \times 10^{-7} \text{ m s}^{-1}$ and $5.55 \times 10^{-7} \text{ m s}^{-1}$, respectively, formed two melt pathways within the ice. Downwards movement periodically eased when the larger pumice particle (12 mm) moved within the surface meltwater pond to shield the fragments from illumination. Downwards movement resumed when the 12 mm particle moved laterally and re-exposed the pumice fragments to illumination.

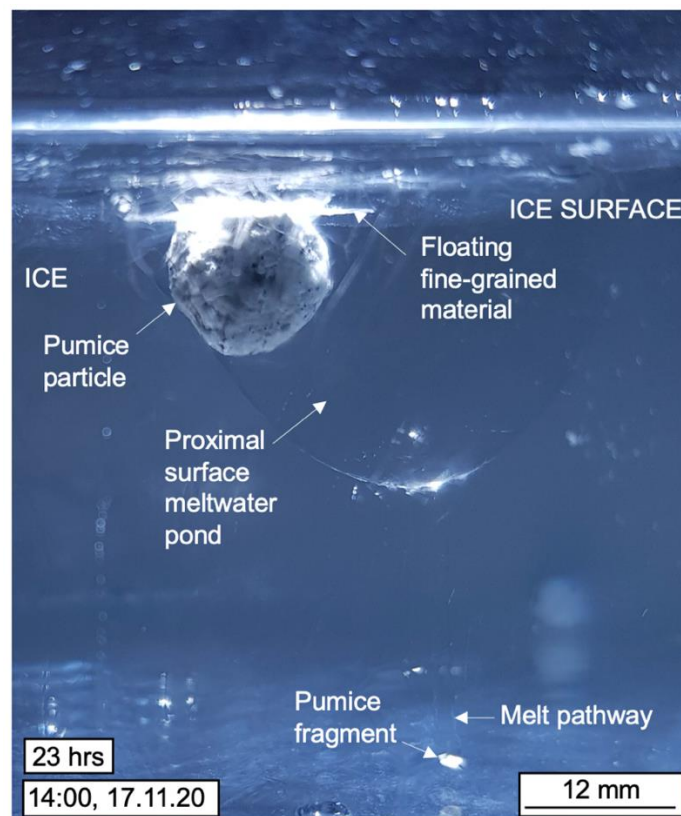


Figure 5.46. Cross-sectional photograph of pumice particle within a proximal surface meltwater pond and a downwards moving pumice fragment in experiment V27.

5.9.2. Proximal surface meltwater pond

Similar to previous experiments involving pumice, a proximal surface meltwater pond developed. This had a maximum width of approximately 45 mm and a maximum depth of 29 mm. The pond reached greater depths than that observed by a 6 mm particle (i.e. 25 mm and 15 mm in experiments V25 and V30, respectively), likely due to the larger diameter of the 12 mm particle. The width of the proximal meltwater pond was also larger than that created by a 6 mm particle (i.e. 42 mm and 27 mm in experiments V25 and V30, respectively). It was determined that lateral movement of the particle was a key control on the pond width, although particle diameter likely had a role in the same way as controlling pond depth.

5.9.3. Shallow surface meltwater pond

Fine-grained (<0.1 mm) particles were observed floating in the surface meltwater. This, in addition to heat transfer from the 12 mm V27 particle, created a shallow meltwater pond that extended across the ice surface. This was approximately 130x120 mm wide and 1.5 mm in depth, and was predominantly maintained by the fine-grained floating particles. Additionally, melt was observed at the front of the ice block due to a surface ice gradient and spanned the near entirety of the ice block (approximately 195 mm), with a depth of approximately 2 mm.

Although a similar size, the 0.5 mm pumice fragment described in Section 5.8.2 demonstrated contrasting behaviour to the floating fine-grained particles lost from the particle surface. The saturation of the particles fragmenting from the larger pumice at the particle base was likely responsible for the increase in density and subsequent downwards movement. Although it is likely that the floating fine-grained particles experienced this process also, surface tension effects at the water surface prevented downwards movement of these particles.

5.9.4. Summary

Overall, these results demonstrated that a 12 mm pumice particle exhibited a similar behaviour to a 6 mm pumice particle. A deeper proximal meltwater pond

was associated with a 12 mm particle due to its larger size and, therefore, its larger sphere of influence.

Results from a repeat experiment (V31) were consistent with this behaviour. Initiation of floating behaviour occurred later in the experiment (i.e. at 9.5 hours compared to 6 hours in V27), but progression of the experiment remained the same (with a proximal surface pond that had maximum dimensions of 50 mm width and 35 mm depth, in addition to a shallower (1 mm) surface meltwater pond that extended 95x80 mm horizontally across the ice block). This confirmed a key interpretation, i.e. that the larger (6 mm and 12 mm) particles created a deeper (proximal) meltwater pond, whilst the scattering of finer (<0.1 mm) material created a shallow meltwater pond with a greater horizontal extent. Additionally, it appeared that the larger (12 mm) particle created a deeper and greater extent of a proximal meltwater pond compared to the smaller (6 mm) particle.

In the same way as all other pumice experiments, two small fragments (approximately 2x1 mm, and 1x1 mm) separated from the main melt region and moved downwards through the ice. Despite the varying diameters, the small pumice fragments exhibited the same behaviour, where a downwards movement to reach the ice base was observed. The larger fragment moved downwards with a mean particle velocity of $5.69 \times 10^{-7} \text{ m s}^{-1}$, whilst the smaller fragment moved downwards with a lower mean particle velocity of $4.13 \times 10^{-7} \text{ m s}^{-1}$ and did not move to the ice base prior to the experiment ending (although movement was continuous throughout).

5.10. V26: a 3 mm rhyolitic pumice particle

V26 investigated the behaviour of a 3 mm pumice particle with an intermediate albedo (Figure 5.47). The hypothesis for experiment V26 is shown in Figure 5.48.

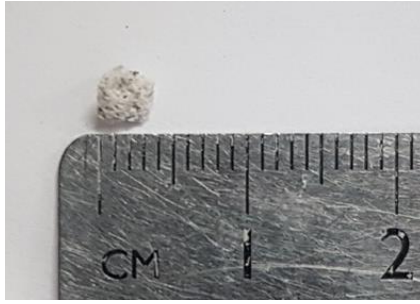


Figure 5.47. Plan-view photograph of the 3 mm V26 pumice particle.

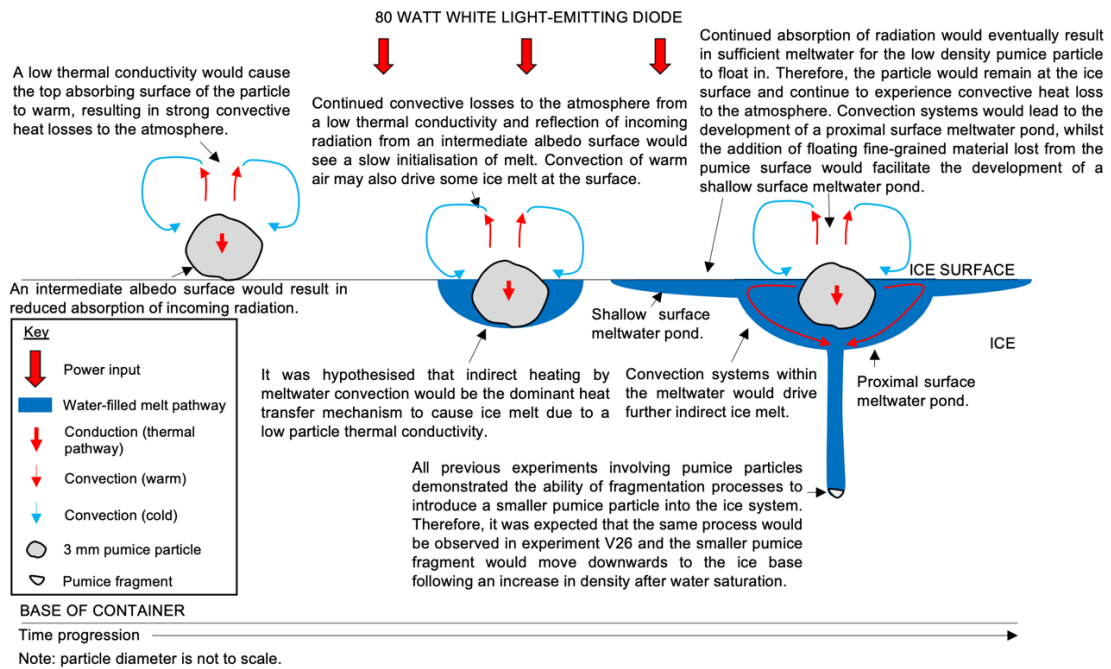


Figure 5.48. Schematic cross-sectional view of the hypothesised particle-ice interaction in experiment V26.

5.10.1. Results and interpretation

The 3 mm V26 pumice particle floated in meltwater produced, first identified after five hours, and confirmed the hypothesised outcome. Extensive particle rotation was observed within the meltwater pond throughout the first seven hours of the experiment. Despite this, the particle predominantly remained in the same location within the surface meltwater throughout the experiment.

Similar to all experiments involving pumice particles, a 0.5 mm pumice fragment moved downwards to the ice base with a mean particle velocity of $3.94 \times 10^{-7} \text{ m s}^{-1}$. This was first observed at the base of the surface melt pond approximately 15 hours into the experiment. Downwards movement was along an inclined trajectory, indicating vein network interception.

5.10.2. Proximal surface meltwater pond

The proximal meltwater pond reached a maximum width of approximately 23 mm and depth of 15 mm. This was smaller than previous experiments involving 6- and 12-mm particles, confirming previous findings that a smaller particle had a smaller sphere of influence relative to a larger (e.g. 12 mm) particle (although this was proportional to the particle size). No refreezing processes were observed and so it was deduced that the V26 particle was within a stable (warm) thermal environment.

5.10.3. Shallow surface meltwater pond

A shallow (approximately 6 mm), horizontally extensive (e.g. approximately 150x110 mm) meltwater pond was identified. This behaviour closely matched other pumices and was likely facilitated by the presence of fine-grained (<0.1 mm) material (Figure 5.49).

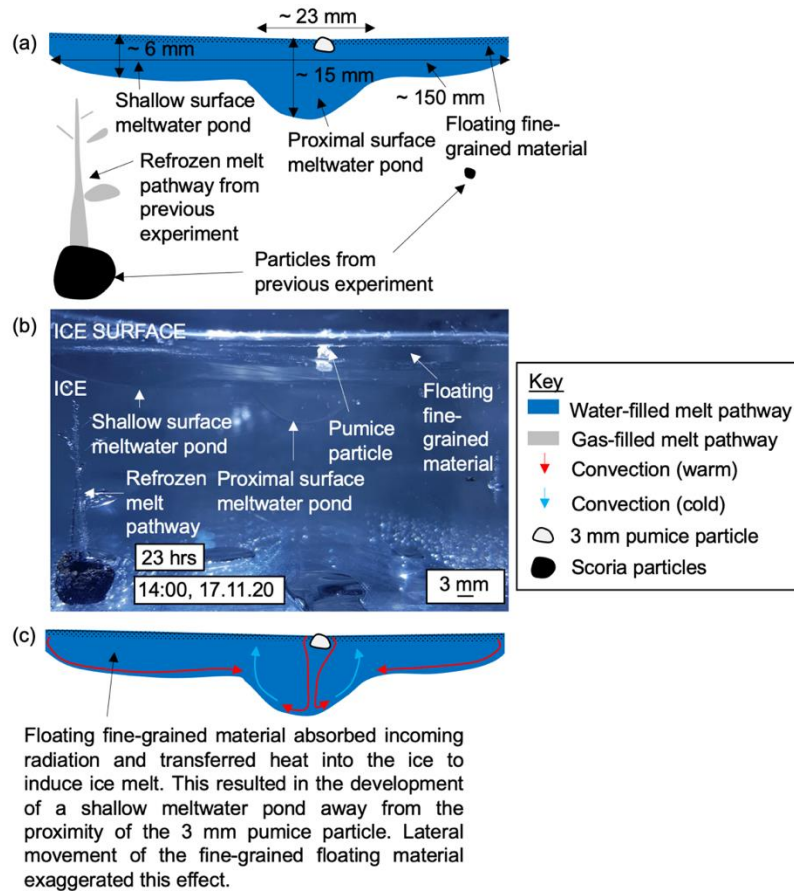


Figure 5.49. Cross-sectional images indicating the proximal and shallow surface meltwater ponds in experiment V26. (a) observational line diagram, (b) photograph and (c) interpretation of the features.

5.10.4. Summary

Experiment V26 followed the same pattern of behaviour as that proposed in the hypothesis and observed in previous results. This also reinforced previous findings that a pumice particle sphere of influence is dependent on the particle size as a smaller volume of melt was created in the proximal pond relative to 6 mm and 12 mm pumice particles. However, the shallow surface pond was deeper than expected (e.g. 6 mm rather than 1-2 mm). This may have been due to slightly warmer temperatures than that experienced in previous experiments as Chapter 4 demonstrated the sensitivity of particle-ice interaction to subtle changes in temperatures, or a larger number of surface particles associated with extensive lateral movement.

Results from a repeat experiment (V29) compared well with results from V26. Dimensions of the proximal surface meltwater pond were comparable, with a maximum width and depth measured at 20 mm and 11 mm, respectively. However, the V29 particle did not create a large shallow surface meltwater pond as observed in previous experiments. Instead, a hollow within the ice created in a previous experiment filled entirely with water. Therefore, it was possible that surface melt that exceeded the proximal meltwater pond region drained along topographic gradients into the hollow, preventing the creation of a large shallow pond as in previous experiments. However, once this was entirely water-filled, surface meltwater extended outwards from the hollow to create a shallow surface meltwater pond with a width and depth of approximately 65x80 mm and 1 mm, respectively. Therefore, the development and morphology of the shallow meltwater pond differed from previous experiments. This demonstrates how the surface morphology of the ice surface can control the development of surface meltwater ponds.

Similar to all previous pumice experiments, a smaller fragment (approximately 0.5 mm) with a hemispherical morphology separated from the main pumice particle and melted downwards through the ice. The particle velocity ($4.29 \times 10^{-7} \text{ m s}^{-1}$) of the smaller fragment was comparable to experiment V26 ($3.94 \times 10^{-7} \text{ m s}^{-1}$).

5.11. V28: a 1.5 mm rhyolitic pumice particle

Experiment V28 investigated a 1.5 mm pumice particle to assess the behaviour of small intermediate albedo volcanic particles within an ice system (Figure 5.50). The hypothesis for experiment V28 is shown in Figure 5.51.



Figure 5.50. Plan-view photograph of the 1.5 mm V28 pumice particle.

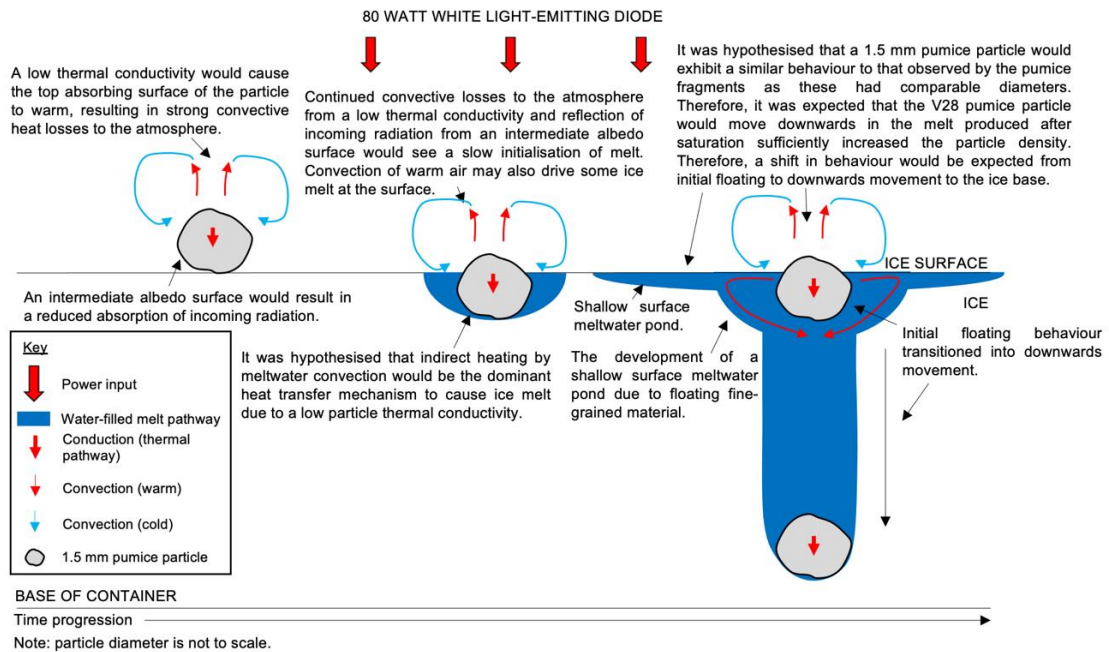


Figure 5.51. Schematic cross-sectional view of the hypothesised particle-ice interaction in experiment V28.

5.11.1. Results and interpretation

The particle appeared to immediately move around on the ice surface, indicating the presence of surface meltwater immediately after particle placement. This was confirmed by in-person observations. A floating behaviour was retained throughout the experiment, contrasting with the hypothesised behaviour. This could suggest that the pumice particle was held at the meltwater surface by surface tension effects, in the same way as the fine-

grained material in previous experiments. Unlike all other pumice experiments, experiment V28 did not show pumice fragmentation. However, this is not to say this did not occur; rather, it was not visible in the time-lapse images.

5.11.2. Proximal surface meltwater pond

The angle of time-lapse imagery prevented determination of the presence of a proximal surface meltwater pond. Therefore, results from this experiment were limited and relied predominantly on in-person observations and photographs. These noted that the 1.5 mm pumice particle did not create a proximal meltwater pond. Lateral movement of the V28 particle across the surface meltwater pond resulted in the particle moving to an area that did not receive illumination (in the same way as observed in experiment V20). This may have prevented the development of a proximal meltwater pond.

5.11.3. Shallow surface meltwater pond

An extensive surface meltwater pond was created with a width of approximately 95 mm, and a depth of approximately 3 mm. This contained the floating V28 particle and fine-grained (<0.1 mm) particles. However, lateral movement of the V28 particle to a region of no-illumination occurred six hours into the experiment, and the particle did not move into a region of illumination for the remainder of the experiment (i.e. 19 hours). However, surface meltwater was maintained during this period suggesting that the fine-grained particles were actively transferring sufficient heat into the ice and confirmed previous interpretations that fine-grained particles were responsible for the shallow surface meltwater pond. It was deduced that the V28 particle was within a stable (warm) thermal environment.

5.11.4. Summary

Results from the V28 experiment did not support the hypothesised outcome, where it was expected the 1.5 mm pumice particle would melt downwards through the ice. In fact, the particle demonstrated buoyant behaviour, consistent with results from previous experiments. However, although this generated a large volume of melt, a proximal deeper meltwater pond was not observed. This

contrasted with previous results, although it was determined that this was due to the particle moving out of the illumination focus, rather than the particle's behaviour.

This was repeated in experiment V32, confirming that a 1.5 mm pumice particle placed on the ice surface would float in meltwater, rather than sinking downwards through the ice as predicted in the hypothesis. Floating behaviour was first observed approximately 11 hours after the experiment start. This behaviour demonstrated the effect of surface tension in retaining a particle at the meltwater surface, despite a small size and likely full saturation of the V32 particle. Fragmentation of the pumice was also observed, where two < 0.5 mm fragments moved down through the ice; these were first identified in the time-lapse images approximately 11.5 hours into the experiment.

Unlike in experiment V28, a proximal surface meltwater pond developed in experiment V32. This grew to a maximum width and depth of 3 mm and 4 mm, respectively, and confirmed findings that smaller floating particles were associated with smaller proximal meltwater ponds. The volume of surface meltwater in experiment V32 also contrasted with experiment V28 and was limited to the proximal surface meltwater pond (Figure 5.52). This was suggested to be due to limited migration of the V32 particle across the meltwater surface, in addition to a drainage event occurring approximately 20 hours into the experiment. This draining resulted in a 4 mm lowering of the particle, similar to behaviour observed experiment V21.

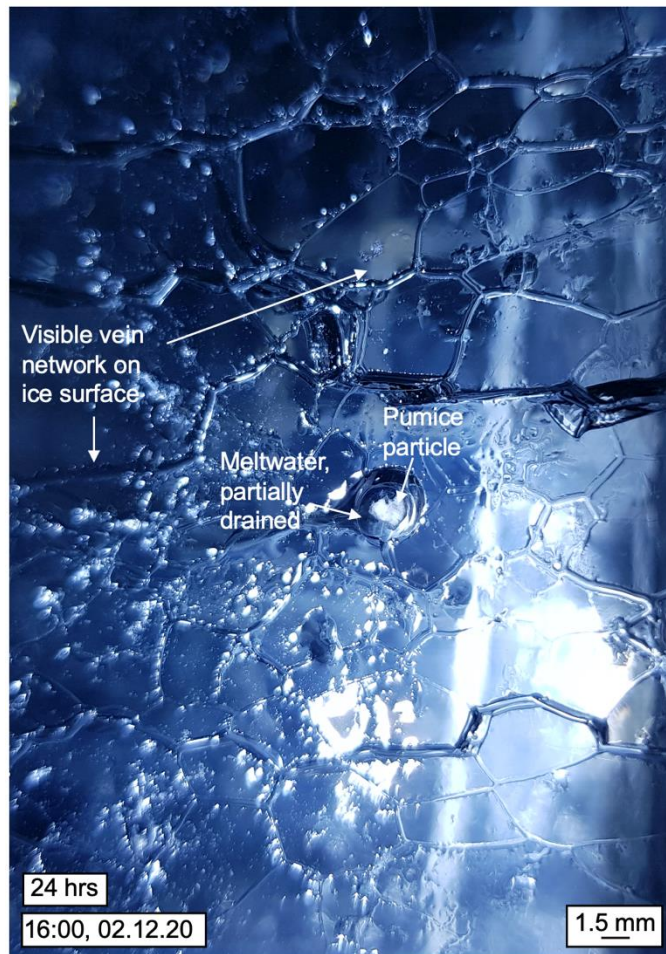


Figure 5.52. Plan-view photograph of proximal surface meltwater pond in experiment V32.

5.12. V33: a scattering of basaltic-andesitic scoria particles

This experiment assessed the behaviour of a 0.5 g scattering of surface volcanic particles (equivalent to the weight of a single 12 mm particle of the same composition). Particle diameters ranged from <1-3 mm (Figure 5.53). This experiment also considered particle-particle interaction, which has had limited focus in previous experiments. Basaltic-andesitic scoria particles were chosen for time-efficiency as these demonstrated the most efficient heat transfer. Smaller particles were sieved onto the ice surface using a 1 mm sieve, whilst particles with a diameter exceeding 1 mm were placed on the surface by hand. The hypothesis for experiment V33 is shown in Figure 5.54.

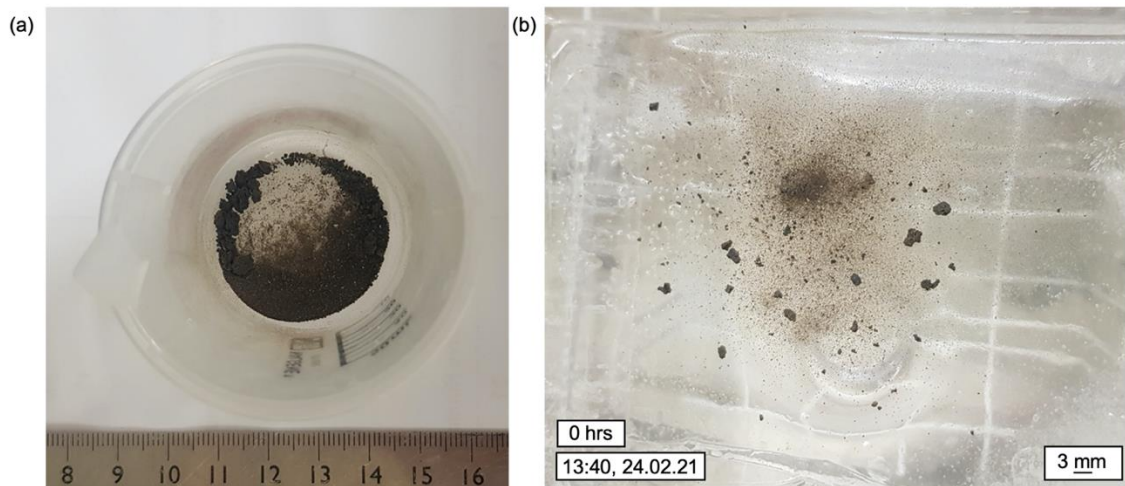


Figure 5.53. Plan-view photographs of the scoria particles used in experiment V33, where (a) is within a beaker and (b) is scattered on the ice surface.

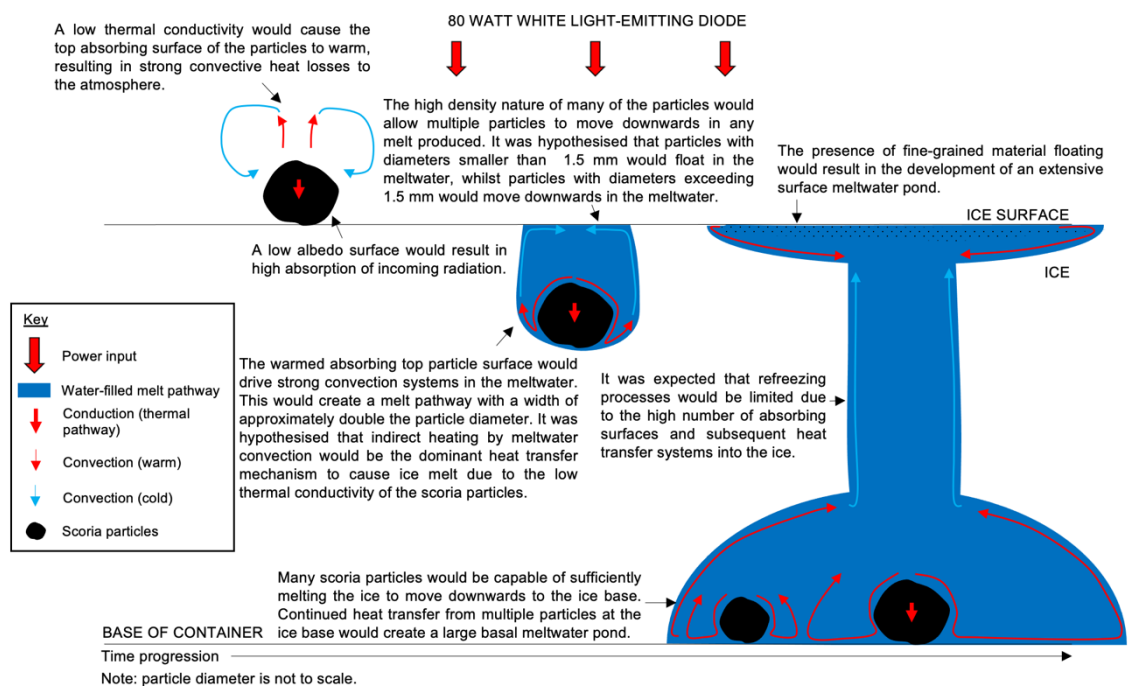


Figure 5.54. Schematic cross-sectional view of the hypothesised particle-ice interaction in experiment V33.

5.12.1. Results and interpretation

As expected, there were a variety of behaviours observed (Figure 5.55). These fell into the following categories:

- (1) Downwards movement as individual particles,
- (2) Downwards movement as particle groups,
- (3) Particles floating in the surface meltwater pond,
- (4) Particles settling on the meltwater pond base at the water-ice interface.

Each of these behaviour modes had been observed in previous experiments, aside from particles settling on the base of the meltwater pond at the water-ice interface. These four behaviours resulted in the formation of many melt pathways within the ice, an extensive region of surface melt with multiple proximal surface meltwater ponds (as defined as a deeper pond near a cluster of particles), and a basal meltwater pond.

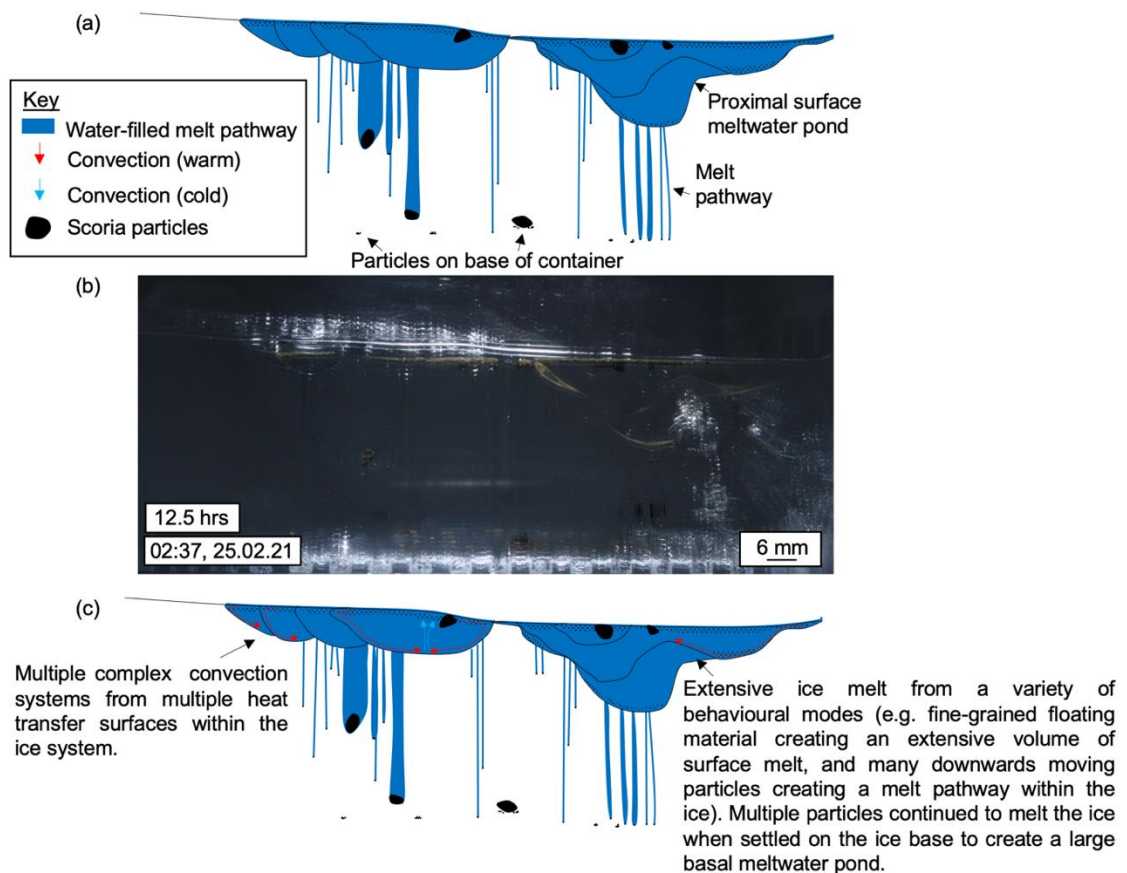


Figure 5.55. Cross-sectional images of the key features and behavioural modes associated with experiment V33. (a) observational line diagram, (b) photograph and (c) interpretation of the features. Note the presence of a basal meltwater pond, as demonstrated in Figures 5.58 and 5.61.

Surface ice melted immediately, resulting in a significant change to the ice system within the first hour. This saw initiation of all behavioural modes, and an approximately 10 mm surface lowering of the ice surface. This was interpreted to be a result of the high rate of ice melt. In many instances, particles clustered together to form particle groups: the larger particles formed clusters that moved downwards through the ice as a unit (similar to the particle array series of experiments in Chapter 4 and cemented ash clusters, e.g. V1-V7 in Chapter 5), whilst the smaller particles (e.g. <1 mm) clustered to form a layering of finer

particles either floating on the surface meltwater pond or remaining at the proximal meltwater pond base. Individual particle movement was also observed. This diverse behaviour of particles resulted in a variety of particle velocities that melted downwards through the ice (Table 5.2, Figure 5.56). In-person observations and time-lapse images indicated that clusters of varying diameters containing fine-grained (e.g. <0.1 mm) material moved downwards through the ice at higher particle velocities than large (e.g. >1 mm) individual particles. This was likely due to the flat morphology of the particle clusters relative to individual particles (also observed in experiments V6b and V7).

Table 5.2. Particle velocities associated with different particle configurations, where ‘cluster’ is referring to an accumulation of fine-grained volcanic particles.

Particle configuration	Code and approximate size (mm)	Particle velocity (m s ⁻¹)	Average (m s ⁻¹)
Single particle	a, 0.1 x 0.1	1.16 x 10 ⁻⁶	1.25 x 10 ⁻⁶
	b, 0.3 x 1	1.86 x 10 ⁻⁶	
	c, 3 x 3.5	1.16 x 10 ⁻⁶	
	d, 2.5 x 4	7.94 x 10 ⁻⁷	
Cluster of particles (<0.1 mm)	e, 1 x 10	1.96 x 10 ⁻⁶	1.61 x 10 ⁻⁶
	f, 0.5 x 4	1.49 x 10 ⁻⁶	
	g, 0.5 x 4.5	1.37 x 10 ⁻⁶	

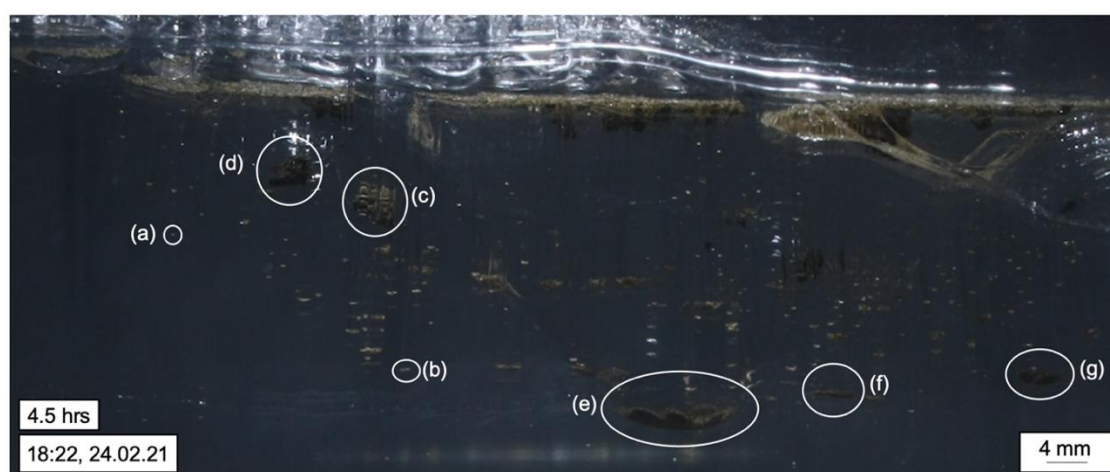


Figure 5.56. Cross-sectional photograph indicating the seven particle configurations described in Table 5.2. Note that a high number of melt pathways has distorted the images in front of particles (c) and (d).

5.12.2. Melt pathway

Larger particles (>1 mm) melted downwards through the ice as single particles, whilst a cluster of fine-grained material accumulated to move down through the ice as a unit. A similar process was observed in experiments V6b and V7, although the mechanism of clustering differed: for example, fine-grained scoria particles clustered while on the ice surface due to surface tension effects of the meltwater in experiment V33, whilst experiments V6b and V7 initiated with cemented ash clusters that disintegrated to form smaller clusters. Therefore, many melt pathways (too numerous to determine from the images) formed within the ice (Figure 5.57). Many of these were similar sizes to the clusters of particles; however, the pathways were much wider in instances where there was a large accumulation of fine-grained material. For example, cluster 'e' on Figure 5.54 created a melt pathway from the base of the surface meltwater pond; therefore, when this reached the ice base, the surface and base were connected by a wide area of melt (approximately 50 mm across). Many melt pathways were vertical in orientation, although the clustered particles formed a concave upward morphology at the melt pathway base. All melt pathways remained open at the ice surface, with no refreezing processes observed. This suggested that the particles were within a stable (warm) thermal environment. No drainage processes were observed.

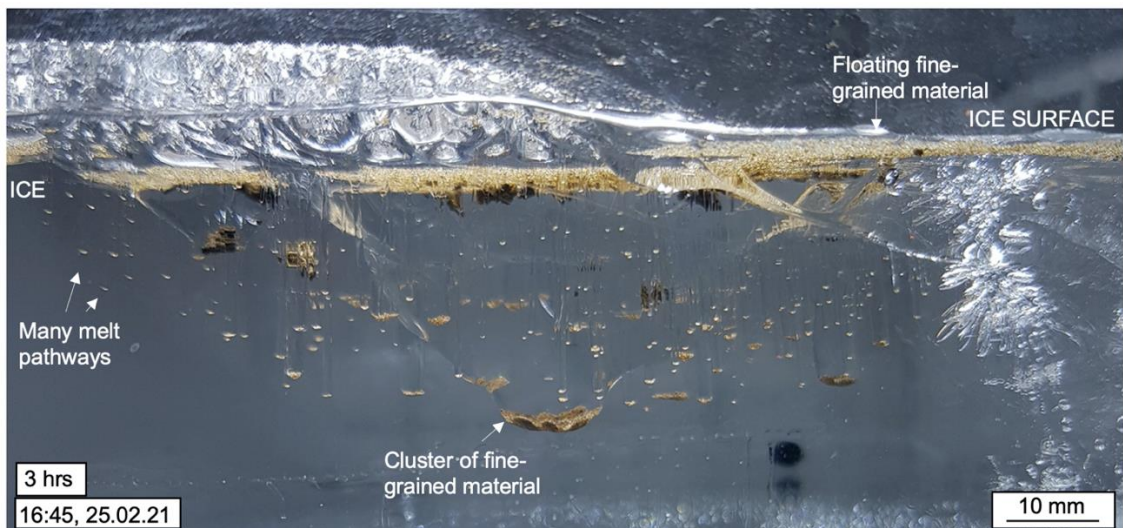


Figure 5.57. Cross-sectional photograph of the melt pathway system that developed within the ice.

5.12.3. Proximal surface meltwater pond

Multiple proximal surface meltwater ponds developed during experiment V33 (Figure 5.58). These varied in dimensions (i.e. 12-80 mm wide and 5-24 mm deep, measured at the end of the experiment). All surface meltwater ponds developed immediately and reached an ‘equilibrium’ within approximately 14 hours (identified by a stable pond system with no further growth). The combination of individual ponds formed a larger meltwater pond; therefore, the number of proximal meltwater ponds decreased throughout the experiment (i.e. from >10 to approximately five). The largest of the ponds (i.e. 80 mm wide and 24 mm deep) was associated with a settling of scattered fine-grained material on the base of the pond, in addition to multiple large (approximately 3 mm) particles. The presence of fine-grained material on the base of the surface pond at the water-ice interface contributed to heat transfer processes and ice melt and was likely responsible for the larger pond dimensions relative to previous experiments.

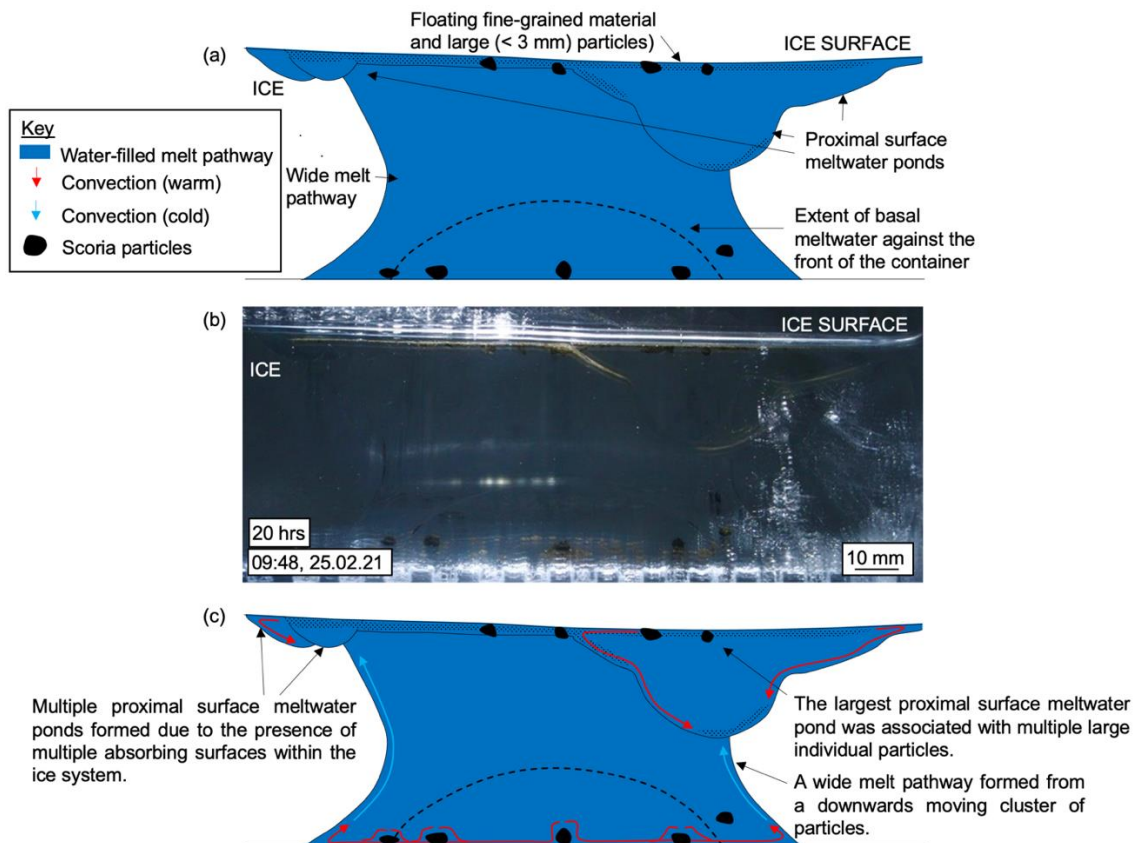


Figure 5.58. Cross-sectional images showing the multiple proximal surface meltwater ponds in experiment V33. (a) observational line diagram, (b) photograph and (c) interpretation of the features.

5.12.4. Shallow surface meltwater pond

Initial ice melting created a 'scarred' ice surface, where fine-grained particles clustered to form accumulated areas of melt (Figure 5.59). Many of these combined to create larger regions of surface melt throughout the experiment. 'Micro' melt ponds also formed in instances where individual fine-grained particles remained isolated from the main melting region, contributing to a rough and irregular ice surface. Additionally, it was noted that some fine-grained material drained along surface gradients of the ice block to accumulate at the edge of the ice block in areas of low topography. This demonstrated the ease of redistribution of fine-grained floating material (e.g. reliant on gradient effects with no wind processes involved).

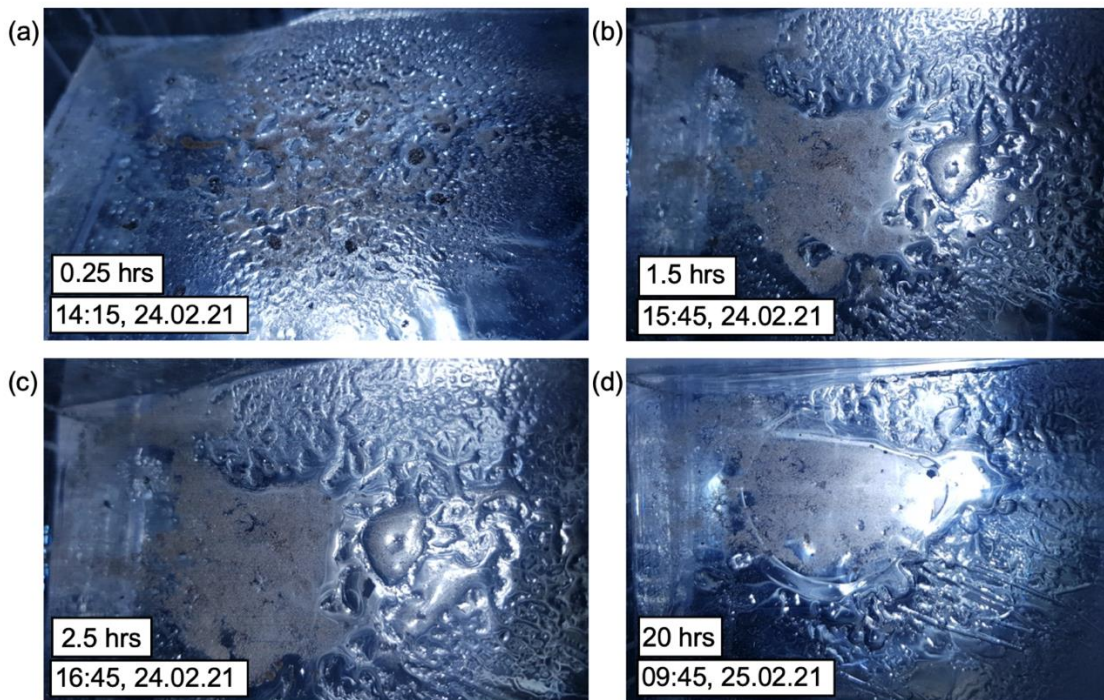


Figure 5.59. Plan-view photographs indicating the development of surface meltwater ponds over four time frames (a-d) in experiment V33.

Accumulation of surface melt and the development of large melt pathways and a large basal meltwater pond created a central region of melt that extended throughout the entire depth of the ice block (Figure 5.60). This was roughly circular in plan-view with a width of approximately 60-95 mm.

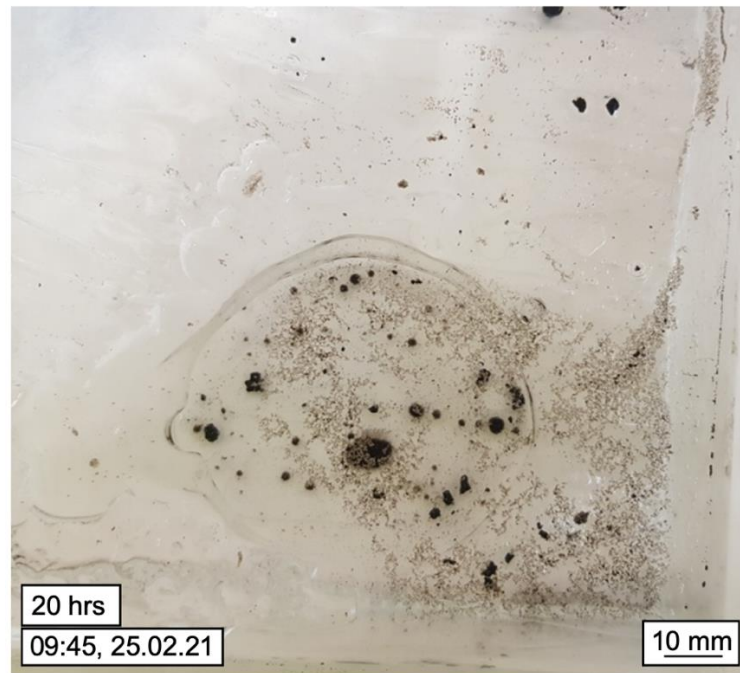


Figure 5.60. Plan-view photograph of central area of melt that extended throughout the depth of the ice block in experiment V33.

5.12.5. Basal meltwater pond

Many particles moved downwards to the ice base to create a large basal meltwater pond that facilitated rapid downwards movement of sinking particles (Figure 5.61). This grew throughout the experiment and so did not reach an equilibrium with the ice within the 20-hour time-frame. Maximum dimension were measured at approximately 75 mm wide and 18 mm high, measured at the front of the ice block. The development of a surface meltwater pond and large melt pathway meant that much of this basal meltwater pond was connected to the surface.

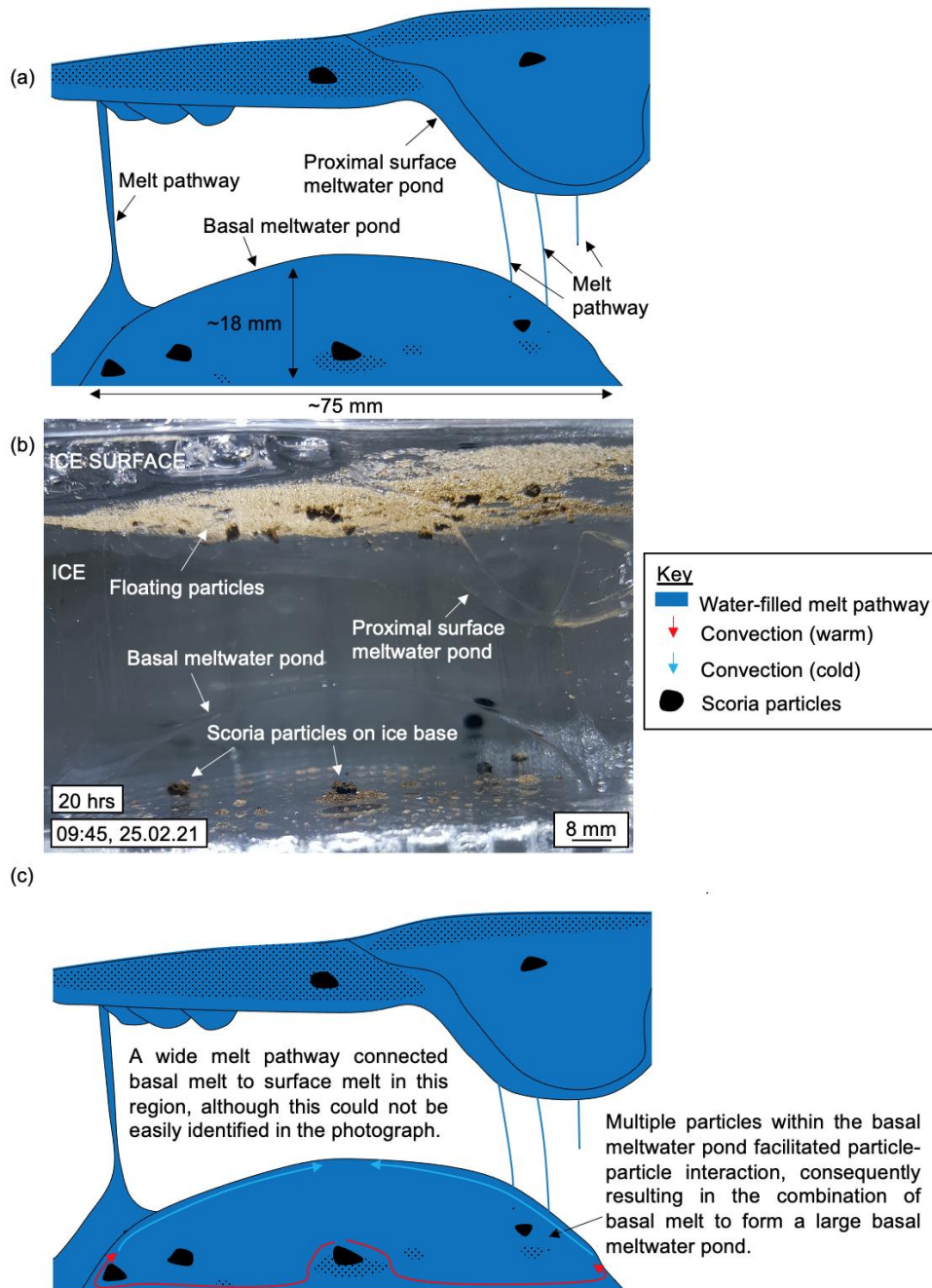


Figure 5.61. Cross-sectional images of basal meltwater pond. (a) observational line diagram, (b) photograph and (c) interpretation of the features. Note that the photograph was taken at an angle, so 3D distortion of the image has occurred (a) and (c).

5.12.6. Summary

Experiment V33 provided an insight into the behaviour of multiple volcanic particles within an ice system in a stable (warm) thermal environment. This demonstrated a mixed range of behaviours and tied together behaviours observed throughout the experimental series (i.e. V1-V32). This demonstrated the likelihood of a variety of behaviours occurring within a natural system. Many

features observed in experiment V33 had also been observed in previous experiments (e.g. a melt pathway connected to the ice surface and a basal meltwater pond). Although all particles demonstrated the capability of melting the ice, results suggested that clusters of fine-grained (<1 mm) material were the most efficient particles at inducing ice melt. In the case of single particles, the fine-grained material (<1 mm) experienced the higher particle velocities relative to the larger, single (approximately 3 mm) particles.

5.13. V34: a scattering of basaltic-andesitic scoria particles within opaque ice

Similar to experiment V33, this experiment assessed the behaviour of a 0.5 g scattering of volcanic material on an ice surface (Figure 5.62). This was conducted on an opaque ice block to also assess the influence of bubbles on particle-ice interaction. The hypothesis for experiment V34 is shown in Figure 5.63.

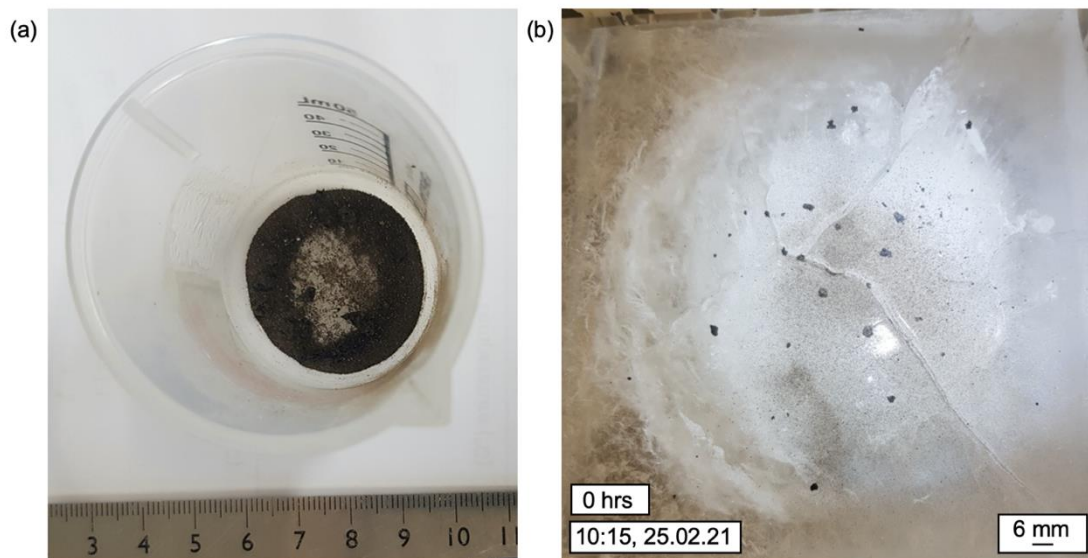


Figure 5.62. Plan-view photographs of the scoria particles used in experiment V34, where (a) is within a beaker and (b) is scattered on the ice surface.

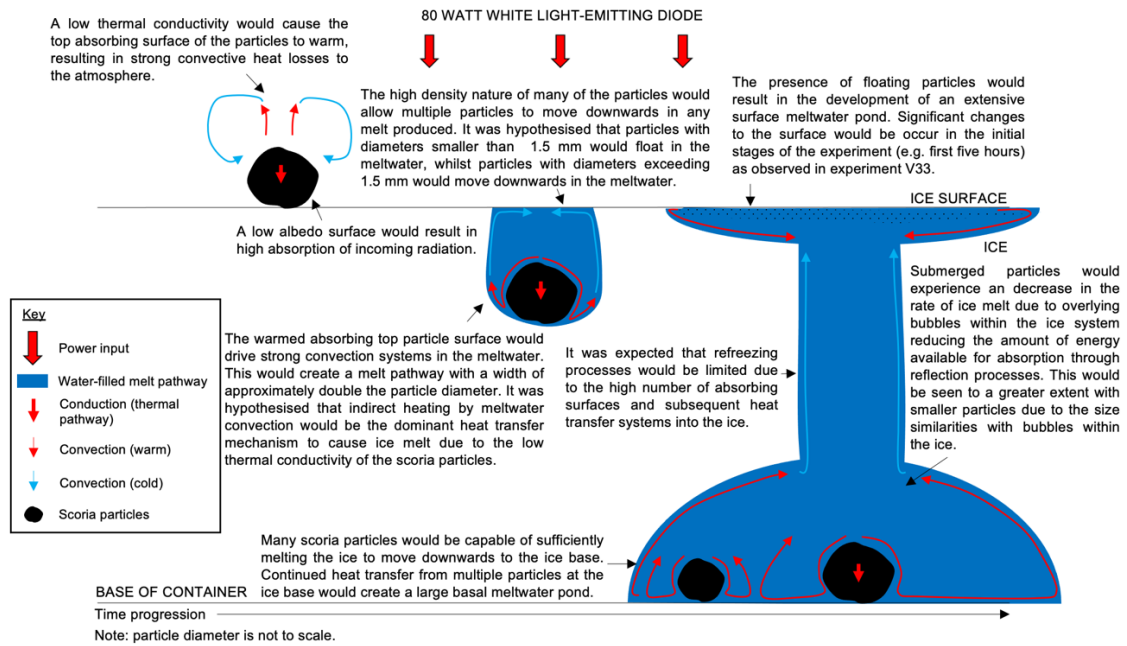


Figure 5.63. Schematic cross-sectional view of the hypothesised particle-ice interaction in experiment V34.

5.13.1. Results and interpretation

Using opaque ice led to issues with time-lapse image clarity (hence, the justification of using optically transparent ice in experimental design). General patterns could be identified in time-lapse images (e.g. downwards movement of particles, drainage events, etc.), although results predominantly relied on in-person observations and photography. All observations demonstrated widespread ice melt immediately after particle placement.

A range of behaviours was observed (consistent with results from experiment V33): for example, downwards moving particles to create multiple melt pathways within the ice, floating fine-grained (<0.1 mm) particles in a cluster and accumulated area of melt, single floating fine-grained particles creating micro-scale melt ponds, and floating single large (>1 mm) particles. However, it could not be determined if a scattering of fine-grained particles settled on the surface pond base at the water-ice interface in the same way as experiment V33 due to the presence of bubbles obscuring the cross-sectional view. Many particles moved downwards to reach the ice base; these were of all sizes and suggested that the presence of bubbles within the ice did not prevent downwards motion. The configuration of the first particles to reach the ice base

was a cluster of fine-grained particles (agreeing with results from experiment V33) and occurred within nine hours. This moved downwards to the ice base with a particle velocity of $2.38 \times 10^{-6} \text{ m s}^{-1}$ (higher than the highest velocity in experiment V33). Additional particle velocities could not be calculated due to image clarity issues.

5.13.2. Melt pathway

Downwards movement of many particles created multiple melt pathways within the ice in the same way as in experiment V33. Particles ranged from single large (3 mm) particles and clusters of fine-grained particles. It was evident that the clusters of fine-grained material were most efficient at melting downwards through the ice. Many melt pathways exhibited drainage features (identified by a gas bubble and meniscus indicating the gas/water interface), possibly facilitated by bubbles within the ice (although it was also noted that the container holding the ice was leaking).

5.13.3. Proximal surface meltwater pond

The presence of proximal surface meltwater ponds could not be identified in time-lapse images due to clarity issues. However, in-person observations noted the development of multiple proximal meltwater ponds in regions away from the central area of melt (described below). These were typically associated with a large (>1 mm) floating particle and floating fine-grained (<1 mm) particles (Figure 5.64).

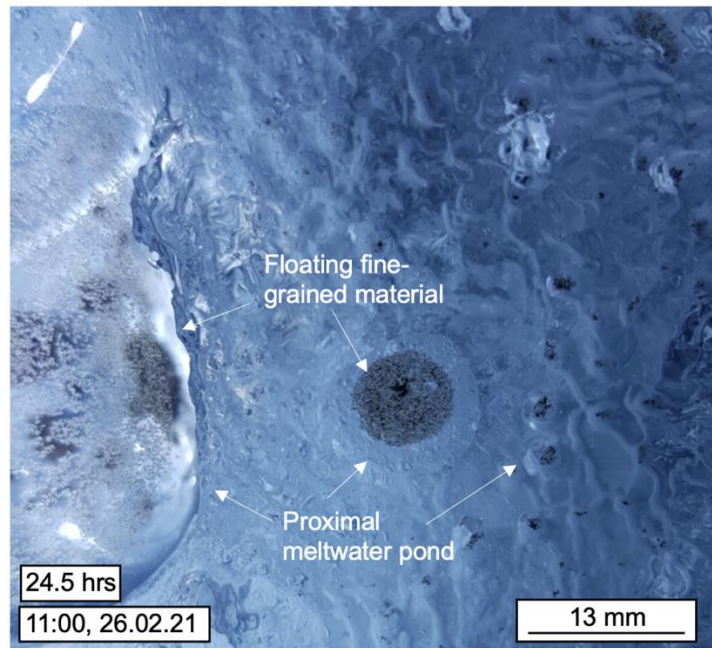


Figure 5.64. Plan-view photograph of individual proximal surface meltwater ponds associated with floating particles and the scarred surface in experiment V34.

Similar to experiment V33, wide melt pathways and a basal meltwater pond caused the central region of melt to extend down the entirety of the ice block. In-person observations showed a similar structure as observed in experiment V33, with a width of approximately 70x60 mm. A cluster of fine-grained particles at the base of the ice were responsible for the downwards extent of the melt.

5.13.4. Shallow surface meltwater pond

The development of surface meltwater occurred on the same timescale and produced the same features as observed in experiment V33. The surface meltwater produced a ‘scarred’ ice surface with areas of accumulated melt, ‘micro’ surface melt ponds, central areas of melt, and redistribution of surface particles across surface gradients. The similarity in ice surface texture in both experiments indicated that bubbles within the ice had little influence on the surface meltwater development. In experiment V34 the most substantial changes occurred within the first three hours of the experiment (Figure 5.65), where small regions of melt accumulated to create a central surface meltwater pond. These utilised already-present weaknesses within the ice (e.g. fractures on the ice surface) as areas of accumulation. However, a drainage event four

hours into the experiment lowered the central area of surface meltwater (Figure 5.65e), and resulted in a concentration of floating particles in a hollow on the ice surface, although these remained floating in the meltwater. The presence of fine-grained particles in the regions away from the central area of melt created small surface melt ponds.

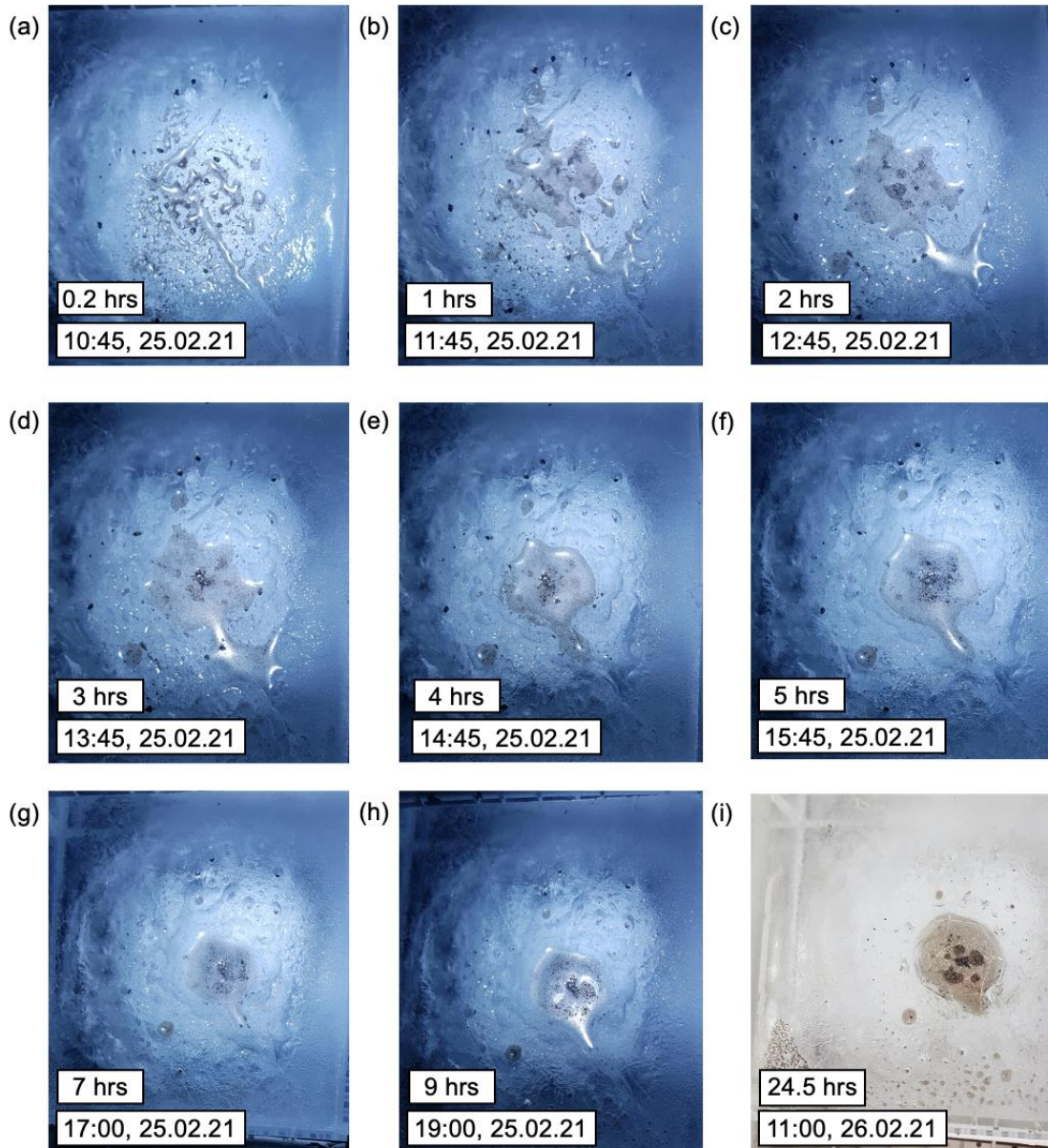


Figure 5.65. Plan-view photographs showing the development of surface meltwater over nine time frames (a-i) in experiment V34.

5.13.5. Basal meltwater pond

The presence of a basal meltwater pond could not be confirmed by time-lapse images due to clarity issues. However, in-person observations noted that surface meltwater extended downwards to the ice base. Therefore, it can be

interpreted that downwards moving particles created a basal meltwater pond which combined with many of melt pathways within the ice to create the central area of melt. Results from experiment V33 informed this interpretation as many of the processes involved in experiment V34 occurred in a similar manner to experiment V33.

5.13.6. Summary

Many processes observed with an optically transparent ice system (i.e. in experiment V33) also occurred with an opaque ice system (experiment V34). Although this could not be imaged in the same detail as in previous experiments, in-person observations noted the presence of a variety of behavioural modes. These created similar features to those observed in previous experiments (e.g. surface meltwater, melt pathways within ice, a basal meltwater pond). However, drainage events occurred within this experiment, allowing the development of hollows on the ice surface. Many of the downwards moving particles were within a partially drained melt pathway, and the central surface meltwater pond experienced a surface lowering that concentrated fine-grained floating particles in the central segment of the ice block. The widespread drainage event was likely due to the nature of the bubbly ice, with plenty of air space for water to drain into. However, it was also noted that water was leaking from the plastic container, contributing to the drainage of water within the ice.

5.14. Conclusions

Experimental work in Chapter 5 demonstrated that volcanic particles can effectively melt ice, despite having traditionally viewed 'melt-limiting properties' (e.g. a low thermal conductivity, high albedo in the case of pumice particles, etc.). Results (1) provided an insight into the relationship between thermally insulating particles and meltwater convection, (2) further developed interpretation from Chapter 4 on the role of the ice structure on influencing particle-ice interaction, and (3) demonstrated the possibility of particle fragmentation and/or loss of fine-grained material from a particle surface and the impact of these two processes on particle-ice interaction.

5.14.1. Convection

Volcanic particles were associated with a melt pathway that exceeded the particle diameter. This was typically double the particle diameter and was indicative of strong convection systems within the melt pathway. It is likely that this was driven by a warmed particle top surface (associated with a low thermal conductivity). This process resulted in a near-spherical melt pathway morphology in the case of slow moving particles (e.g. experiment V12).

These findings were consistent with results from experiments using thermally insulating control particles (e.g. Delrin®) and contrasted with results from experiments using thermally conductive control particles (e.g. metal particles) in Chapter 4. Ultimately, this demonstrated two key points: (1) the larger extent of melting associated with volcanic particles through meltwater convection, and (2) meltwater convection was the dominant heat transfer mechanism during volcanic particle-ice interaction.

5.14.2. Ice structure

Results of Chapter 5 confirmed those of Chapter 4, in which the vein network influenced the angle of downwards particle trajectory and rate of particle movement. Experimental work in Chapter 5 developed these findings and indicated that the vein network also controlled the melt pathway morphology, predominantly through facilitating drainage events (e.g. as observed in experiment V21). This additionally allowed melt-limiting processes to occur sometimes; for example, advection of heat away from the particle-ice interaction via draining meltwater (as observed in experiment V12).

5.14.3. Particle loss and fragmentation

The loss of fine-grained material from a particle surface was observed in almost all experiments involving volcanic material. These fine-grained particles floated in meltwater and remained at the ice surface whilst, in some cases, the original particle moved downwards through the ice. The fine-grained material acted as absorbers of incoming radiation in the same way as the single particle and

transferred energy into the ice, increasing the volume of melt. Therefore, this process facilitated multiple focal points of ice melt and allowed for the development of a surface meltwater pond away from the proximity of the original particle. It was likely that the fine-grained material was also introduced into the melt pathway column of meltwater, encouraging a widening of this region.

Interestingly, experimental work also indicated the likelihood of particle fragmentation once within the ice system. This differed from that described above; instead, it was observed that particles fragmented at the particle base. This was the case for all material investigated in this experimental series, although this occurred most with the pumice particles (e.g. experiments V25-V32). This was likely a result of the high porosity associated with the pumice particles, facilitating a pathway for percolating meltwater and saturation of the particle. Freeze-thaw mechanisms were suggested as the responsible process for particle fragmentation, reinforced by refreezing processes observed when analysing the disintegration of cemented ash clusters. Working hypotheses for this are discussed in detail in Chapter 7.

6. An experimental investigation into the behaviour of microplastic particles within the cryosphere

Microplastic particles are accumulating within the cryosphere (Zhang et al., 2021) and so understanding the behaviour of these particles on and within ice is important. This microplastics study investigated surface and embedded single particles and a scattering of surface particles (Mp1-Mp19). Polypropylene and polyethylene particles were used, and these had low relative albedo and thermal conductivity (Chapter 3). Polypropylene had a low density (i.e. floating behaviour) and polyethylene had an intermediate density, where test experiments showed mixed behaviours of floating and sinking particles within a beaker of water at 0°C. Three categories based on particle diameter were investigated: (1) large: 4-5 mm, (2) medium: 1-4 mm, and (3) small: <1 mm. Experiments were described individually according to these diameter categories for ease of discussion, in chronological order of experiment code, and repeat experiments were subsequently grouped to allow comparisons to be drawn. Surface meltwater is described by the horizontal extent on the ice surface (i.e. width and length), and depth within the ice. This is further split into two features: a proximal meltwater pond (i.e. the deeper zone of meltwater near a particle), and a shallow surface meltwater pond (i.e. a larger extent of shallow melt on the ice surface). The thermal environment was difficult to distinguish in many experiments in Chapter 6 as particles typically remained stationary and so has not been included as rigorously during the interpretation of processes. The average freezer and proxy ice temperatures for each experiment are recorded in Appendix 16.

Table 6.1. A summary of experiments investigating the behaviour of microplastic particle-ice interaction, indicating the particle composition, diameter and associated thermal environments as defined in Chapter 3.

Experiment code	Particle composition	Placement	Diameter and category (mm)
Mp1	Polyethylene	Single, surface	<1 (small)
Mp2	Polyethylene	Single, surface	5 (large)
Mp3	Polypropylene	Single, surface	5 (large)
Mp4	Polypropylene	Single, surface	5 (large)
Mp5	Polypropylene	Single, surface	5 (large)
Mp6	Polyethylene	Multiple, embedded	4-5 (large)
Mp7	Polyethylene	Single, surface	<1 (small)

Experiment code	Particle composition	Placement	Diameter and category (mm)
Mp8	Polyethylene	Single, surface	1.5 (medium)
Mp9	Polyethylene	Single, surface	5 (large)
Mp10	Polyethylene	Single, surface	<1 (small)
Mp11	Polypropylene	Single, surface	5 (large)
Mp12	Polyethylene	Single, surface	1.5 (medium)
Mp13	Polyethylene	Multiple, embedded	1-4 (medium)
Mp14	Polyethylene	Single, surface	4.5 (large)
Mp15	Polyethylene	Scattering, surface	<1 (small)
Mp16	Polyethylene	Scattering, surface	<0.5 (small)
Mp17	Polyethylene	Scattering, surface	<1 (small)
Mp18	Polyethylene and polypropylene	Multiple, embedded	1-5 (medium and large)
Mp19	Polyethylene	Scattering, surface	<1 (small)

6.1. Mp1: a small polyethylene surface particle

Mp1 investigated a 'small' 1 mm microplastic particle to assess the behaviour of microplastic particle-ice interaction. This was roughly spherical and black in colour (Figure 6.1), with an intermediate density (i.e. close to the value of water, Chapter 3). The hypothesis for experiment Mp1 is shown in Figure 6.2.



Figure 6.1. Plan-view photograph of the 1 mm Mp1 polyethylene particle.

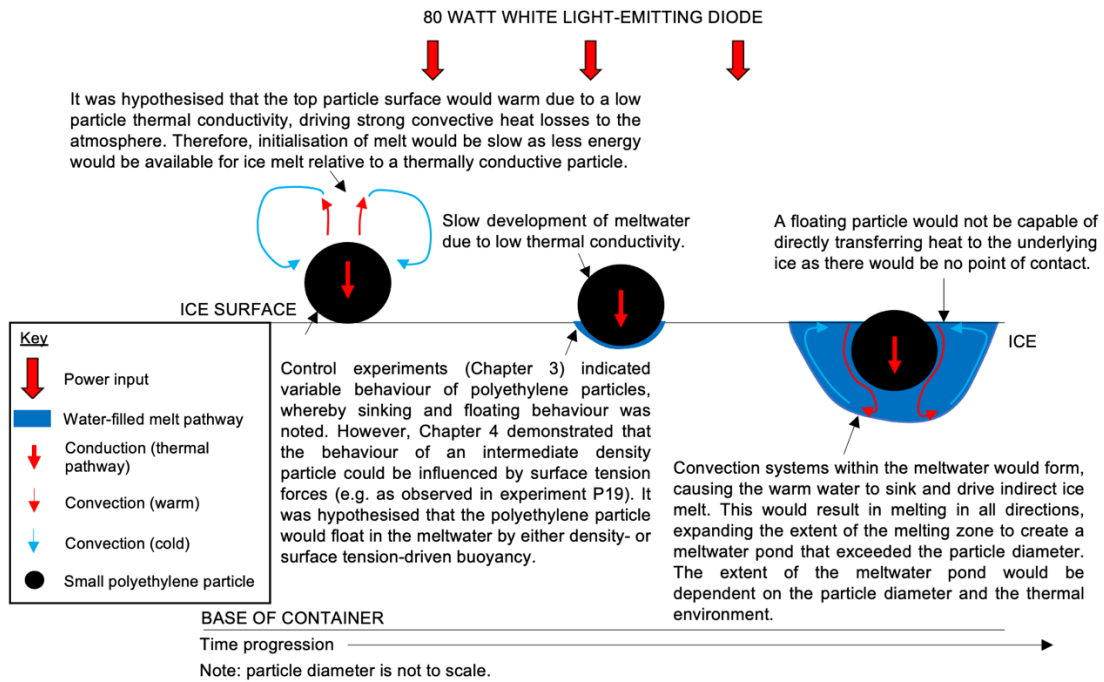


Figure 6.2. Schematic cross-sectional view of the hypothesised particle-ice interaction in experiment Mp1.

6.1.1. Results and interpretation

The Mp1 particle melted the ice after surface placement and floated when sufficient meltwater had been produced, agreeing with the hypothesised outcome. Floating behaviour was identified by the meltwater pond extending from the particle base within the first hour of the experiment. This resulted in lateral particle movement by approximately 5 mm as it floated in the surface meltwater pond. It was determined that the Mp1 particle experienced a stable (warm) thermal environment, although it was likely that this was close to the stable (cool) thermal environment as ice melt was observed throughout the experiment with no refreezing processes noted, although melt extent was limited relative to results from the density series of experiments (Chapter 4). The limited meltwater was determined to be a combination of a slightly cooler stable (warm) thermal environment, and drainage events.

6.1.2. Surface meltwater

Initial ice melt created a circular meltwater pond, although lateral particle movement elongated the surface meltwater during the first nine hours. This was caused by the particle being ‘pinned’ to the pond edge, likely a result of surface tension effects. There were no signs of refreezing in the region remote from the

particle. The surface meltwater evolved into an almost symmetrical area of melt when lateral movement of the particle ceased (Figure 6.3, although the extent of meltwater was limited compared to results from previous experiments (e.g. the density series in Chapter 4). The cause of limited meltwater will be investigated in future experiments (e.g. possible drainage into the vein network).

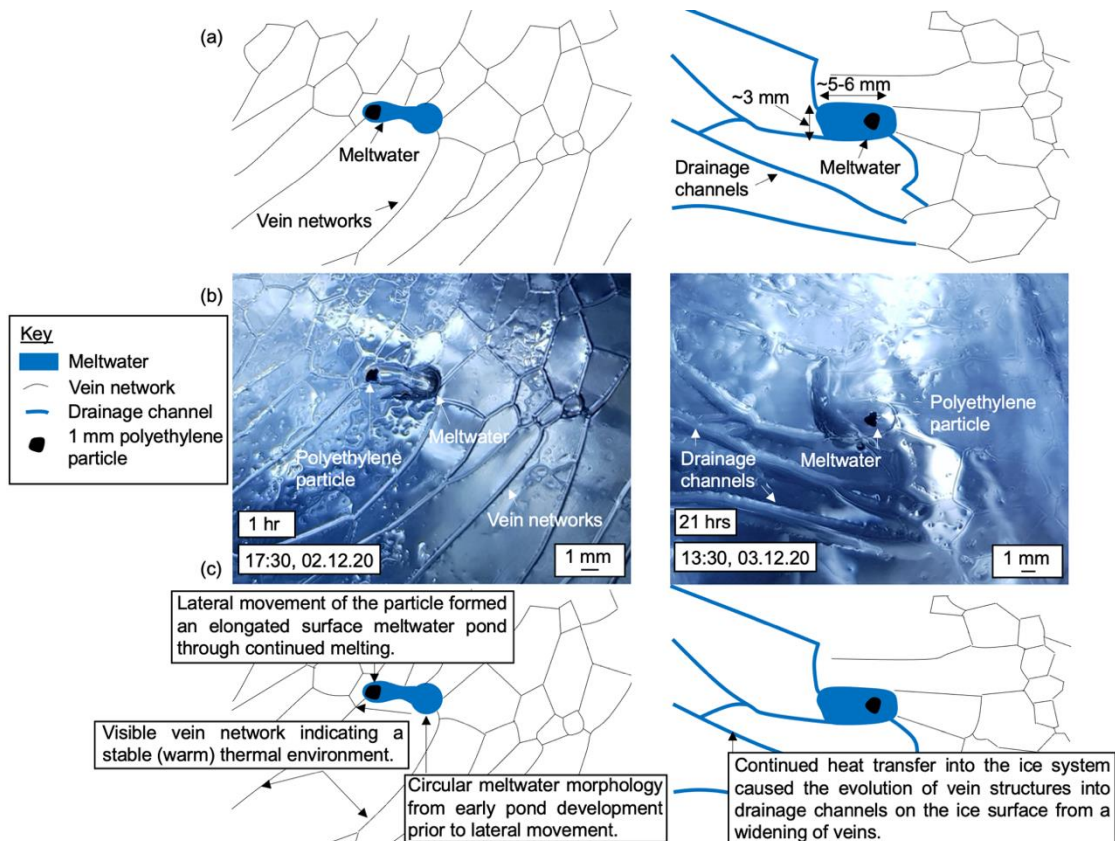


Figure 6.3. Cross-sectional images showing the development of a surface melt pond in experiment Mp1. (a) observational line diagram, (b) photograph and (c) interpretation of the features.

6.1.3. Summary

Experiment Mp1 was consistent with results from many of the low density experiments in Chapter 4, where the particle was buoyant in meltwater produced. Despite a low thermal conductivity, efficient heat transfer (due to a low albedo surface and short thermal pathway) resulted in particle-induced ice melt throughout the entire experiment. This formed a circular meltwater pond initially, although migration of the particle on the ice surface created an elongated pond and demonstrated the capability of low density particles in

modifying the morphology of surface melt by redistribution processes. Melt was restricted to the immediate proximity to the particle (approximately 1 mm from the particle extent), suggesting that this was the sphere of influence in this thermal environment.

Mp7 and Mp10 nominally duplicate Mp1 and both showed that a small polyethylene particle floated in the meltwater produced, although the extent of melt differed between each experiment. The melt extent in experiment Mp7 compared well with that observed in Mp1 (e.g. <5 mm), although this was likely due to extensive drainage processes. Results in experiment Mp10 contrasted with both Mp1 and Mp7 as the particle created an extensive meltwater pond (approximately 160 mm width, extending inwards by 60 mm with a depth of 1-2 mm). Extensive drainage processes and surface meltwater observed in experiments Mp7 and Mp10 were indicative of the ice being at, or very close to, PMP.

Drainage in experiment Mp7 was to a much greater extent than in experiment Mp1 and resulted in a downwards movement of the Mp7 particle to a depth of approximately 9 mm (compared to approximately 1 mm in experiment Mp1). This was a result of the particle moving with the periodically lowering meltwater surface (e.g. similar to that observed in experiment V21) during drainage events. This supported previous results from control experiments in Chapter 4 that drainage events were intermittent. In contrast with experiment V21, there was a period of upward movement of the meltwater pond (and, therefore, particle). It was identified in these instances, particle-induced ice melt exceeded the rate of meltwater drainage.

The diameter of the drained melt pathway varied with depth, where larger widths (e.g. approximately 5 mm) represented longer periods of stationary behaviour allowing the particle to melt the proximal ice and widen the melt pathway, whilst smaller widths (e.g. approximately 3 mm) represented shorter time periods of stationary behaviour (this was consistent with results from experiment V21). It was deduced that the ice was at PMP in experiment Mp7

due to the fragmentation of the ice surface from the wide, water-filled vein network (Figure 6.4). This likely facilitated the extensive drainage processes.

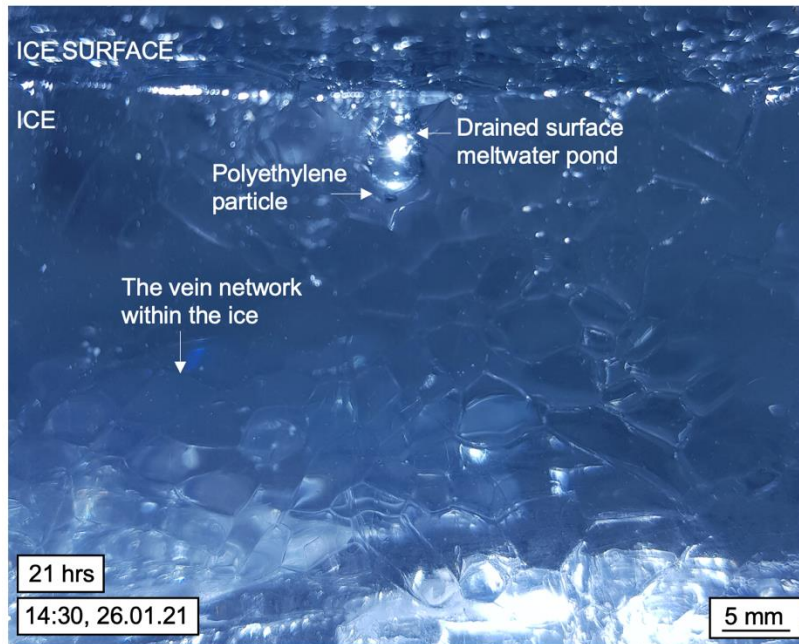


Figure 6.4. Cross-sectional photograph of drained surface meltwater pond and the vein network in experiment Mp7.

6.2. Mp8: a medium polyethylene surface particle

Experiment Mp8 investigated a medium-sized (approximately 1.5 mm) microplastic (Figure 6.5). Therefore, this considered the role of particle diameter on microplastic-ice interaction. The hypothesis for experiment Mp8 is shown in Figure 6.6.

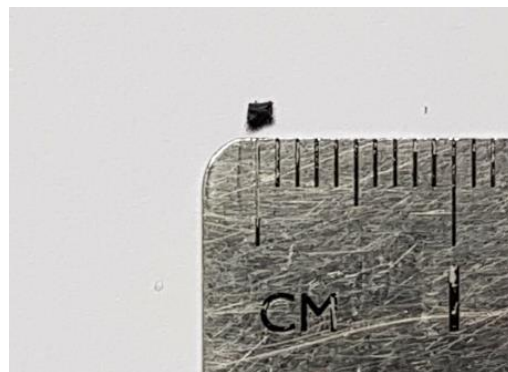


Figure 6.5. Plan-view photograph of the 1.5 mm Mp8 polyethylene particle.

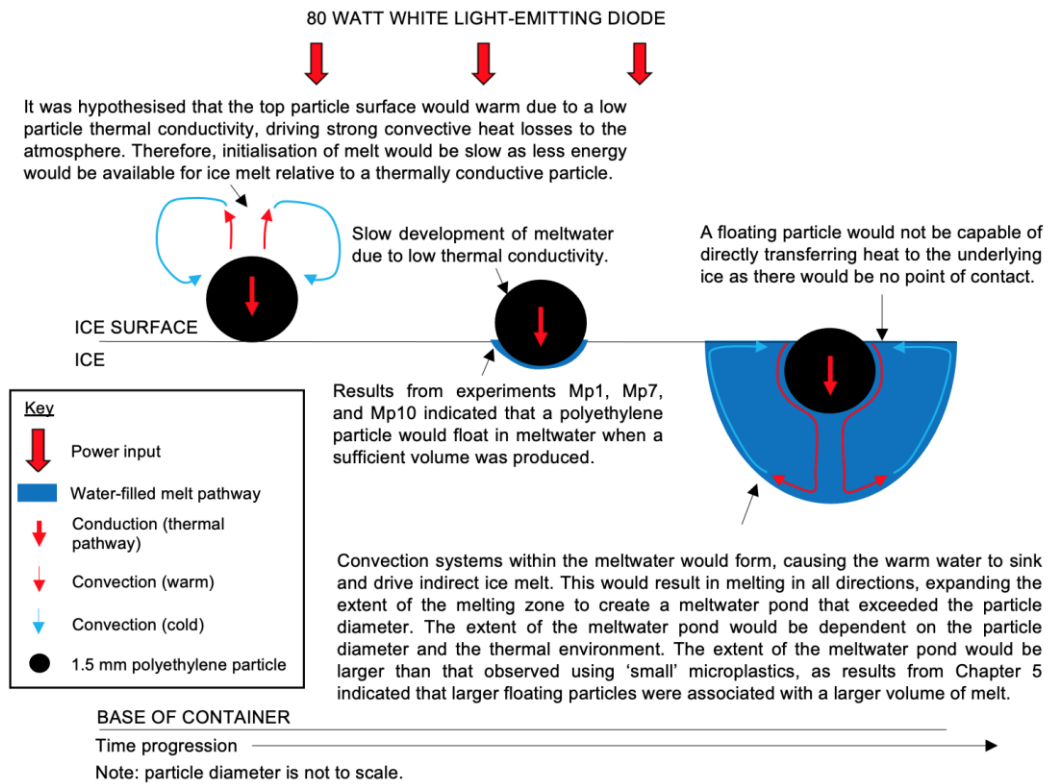


Figure 6.6. Schematic cross-sectional view of the hypothesised particle-ice interaction in experiment Mp8.

6.2.1. Results and interpretation

Particle-induced ice melt started within the first 30 minutes of the experiment, resulting in the formation of a circular surface meltwater pond. The Mp8 particle floated in the surface meltwater, with drainage events lowering the meltwater level.

6.2.2. Surface meltwater

Heat transfer into the ice created a circular surface meltwater pond, agreeing with the hypothesised outcome. This had a greater meltwater depth relative to previous experiments, likely due to drainage events (Figure 6.7). This was a similar process as that observed in Mp7, although this was to be expected as experiment Mp8 was conducted on the same ice block as Mp7; therefore, it experienced the same hydrological systems within the ice (e.g. the vein network). The meltwater pond was narrower at the bottom (approximately 3 mm), suggesting that the particle did not remain at the base of the drained melt pond for long. Instead, continued ice melt and drainage of surface melt into the

hollow resulted in an upwards movement of meltwater level and, subsequently, the particle to the ice surface.

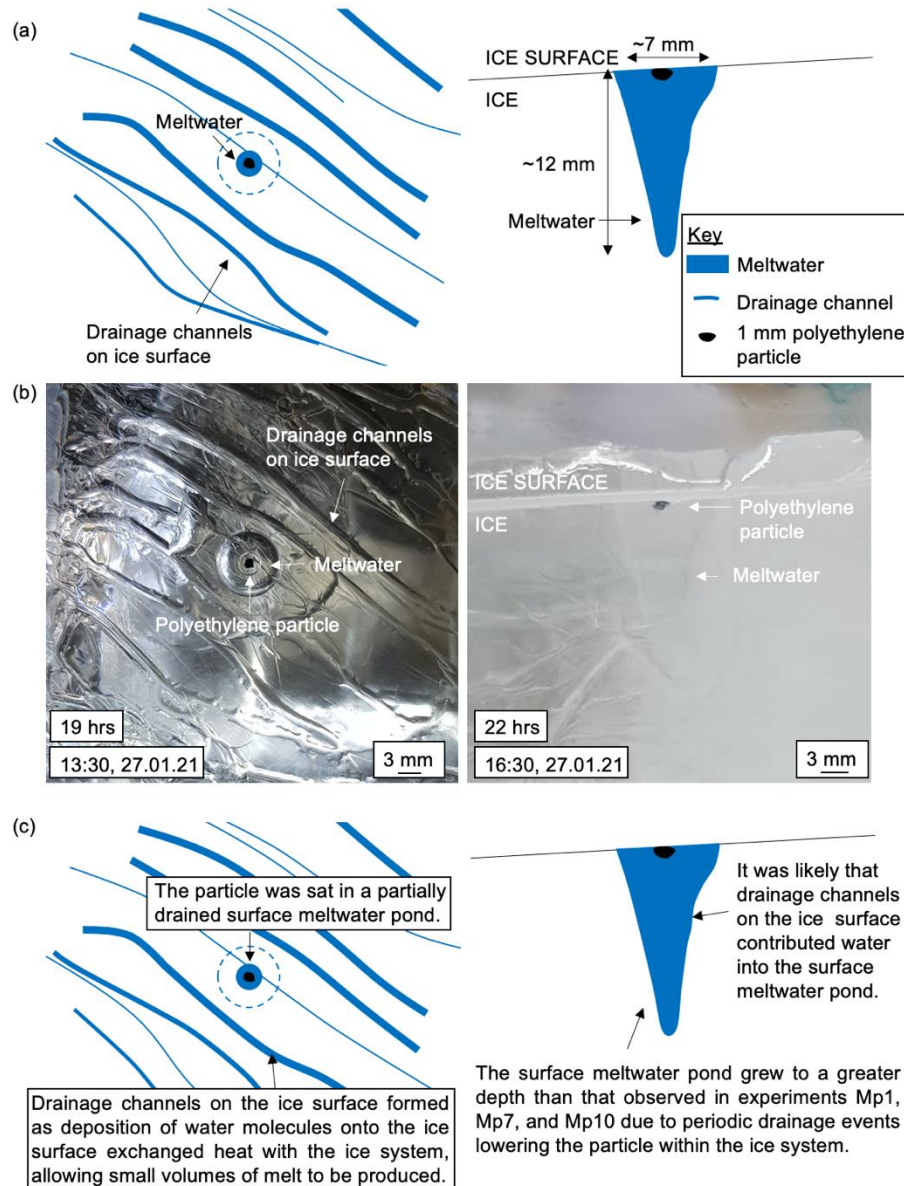


Figure 6.7. Images showing surface melting morphology in experiment Mp8, with a plan-view (left) and cross-sectional view (right). (a) observational line diagram, (b) photograph and (c) interpretation of the features.

A particle from a previous experiment (Mp7) was present within a drained channel on the ice surface at the start of the Mp8 experiment. The drained Mp7 melt pathway filled with water throughout the experiment duration, despite not being subjected to illumination. It was deduced that this was caused by surface meltwater drainage into the Mp7 drained channel, likely from Mp8 particle-induced ice melt. The presence of drainage channels and coarse vein network within the ice suggested that experiment Mp8 was conducted close to the

unstable thermal environment; however, this was not at PMP as the ice was stable in the solid state before the illumination was turned on. Therefore, melting was a result of: (1) particle-ice heat transfer, and (2) heat from vapour deposition onto the ice surface creating small-scale melt processes on the ice surface due to the proximity to PMP.

6.2.3. Summary

Results from experiment Mp8 compared well with those using smaller microplastic particles. Although the melt pond reached a greater depth, this was not simply a result of particle-induced ice melt as drainage processes were involved. Therefore, many of the hypothesised processes could not be confirmed (e.g. if a larger plastic particle was associated with a greater extent of ice melt).

This experiment was repeated in experiment Mp12. This was conducted on a different ice block to Mp8 and so did not experience the same hydrological conditions. Despite this, a very similar process occurred (i.e. a lowering of surface meltwater resulted in a downwards movement of approximately 17 mm by the floating particle into the ice). However, the morphology of the melt pathway was more comparable to experiment V21 than Mp7 and Mp8 as no re-filling events occurred; instead, the particle periodically moved downwards as it remained floating in the meltwater, creating an undulating morphology (as described in Chapter 5). It was noted that the container was leaking meltwater, and this facilitated drainage events.

6.3. Mp2: a large polyethylene surface particle

Mp2 investigated the behaviour of a large (approximately 5x2 mm) microplastic particle (Figure 6.8). This had an angular and thin (<1 mm) morphology. The hypothesis for experiment Mp2 is shown in Figure 6.9.

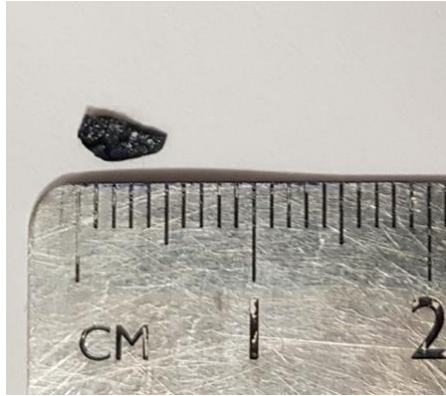


Figure 6.8. Plan-view photograph of the 5 mm Mp2 microplastic particle.

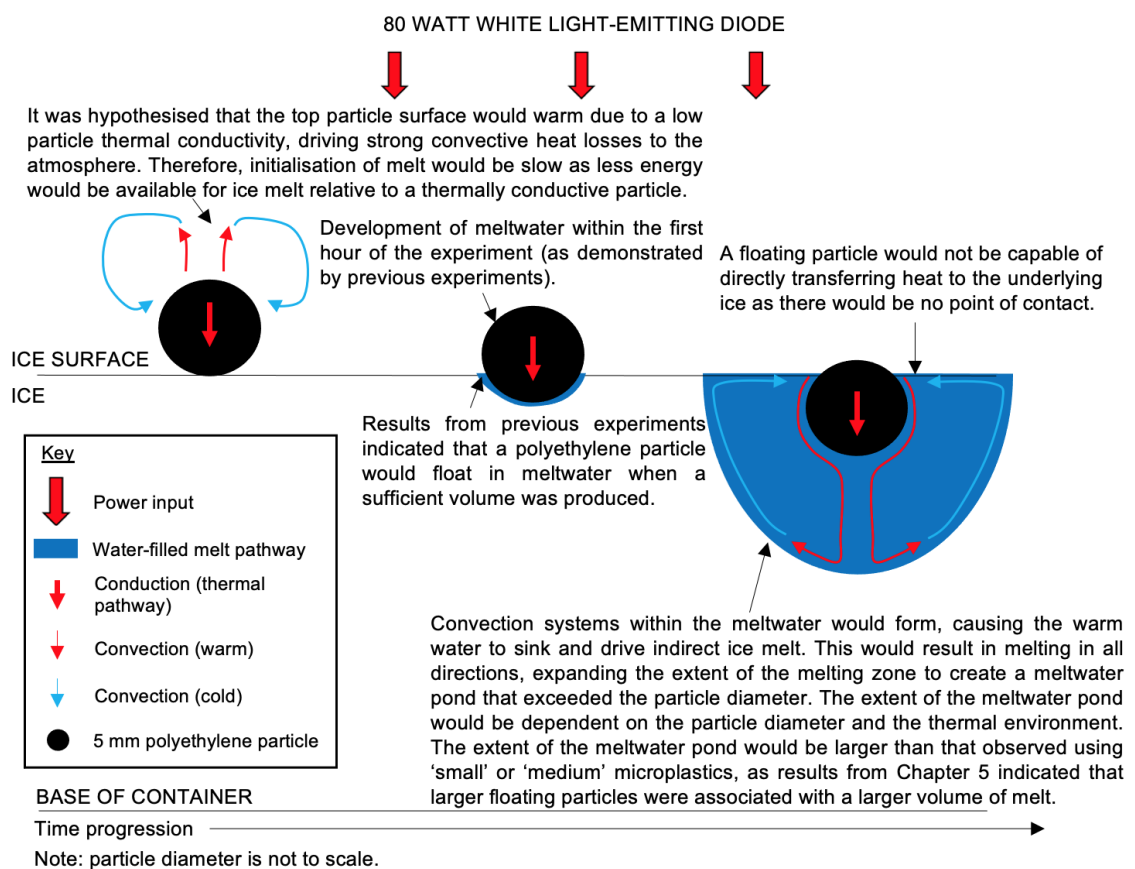


Figure 6.9. Schematic cross-sectional view of the hypothesised particle-ice interaction in experiment Mp2.

6.3.1. Results and interpretation

Similar to all previous microplastic experiments, ice melt began immediately after particle placement to create a meltwater pond. The Mp2 particle floated in meltwater, first observed within 25 minutes of the experiment start. The rapid initiation of floating behaviour may have been a result of the thin particle morphology (i.e. <1 mm), allowing fast heat conduction through the particle's

short thermal pathway to the underlying ice. Similar to previous experiments (e.g. Mp1), the floating behaviour facilitated lateral movement of the Mp2 particle by approximately 55 mm within 17 hours and created a channel of meltwater. However, this movement caused the particle to move to a region with no illumination. Lateral movement ceased when this occurred, and resumed when the cover was removed (thus, exposing the Mp2 particle to the illumination). This indicated that the particle heating effect was the driver of lateral movement across the ice surface by melting the proximal ice and driving convection.

The surface meltwater pond initially matched the morphology and size of the particle in the early development of surface melt (indicating conduction-driven melting). This evolved into a spherical meltwater pond extending approximately 1-2 mm from the particle extent (indicating convection-driven melting), until lateral movement of the particle created an elongated meltwater pond with a maximum dimension of approximately 65 mm in length, 20 mm in width and 1 mm in depth. However, there was also a deeper area of melt near the particle itself (approximately 3-4 mm depth). This was comparable to meltwater observed in experiment Mp1, although to a greater extent.

6.3.2. Summary

Experiment Mp2 demonstrated the role of particle heating in lateral migration of a low density particle across an ice surface. This moved laterally by approximately 55 mm until it was no longer able to absorb radiation, removing the particle heating effect. When absorption resumed (due to removal of a cover above the particle), lateral movement also resumed to cause a 65 mm migration across the ice surface. This had an influence on the morphology of the surface meltwater.

This experiment was repeated in two future experiments (Mp9 and Mp14). These both demonstrated the same buoyant behaviour as observed in previous experiments. However, both experiments were associated with a greater volume of ice melt compared to experiments investigating smaller particles, suggesting a relationship between microplastic size category and area of ice

melt. For example, the Mp9 and Mp14 particles created a meltwater pond with a width and depth of 30 mm and 27 mm, and 23 mm and 18 mm, respectively (although Mp9 also experienced drainage processes).

Experiment Mp9 and Mp14 showed a similar developmental progression of surface meltwater, where initial meltwater had a similar morphology to that of the particle (in this case, broadly triangular) until evolution into a circular melt pond was observed. These results indicated that the initial melt morphology was controlled by conduction of heat from the particle into the ice system as the particle surface was in contact with the ice. However, meltwater convection became the dominant heat transfer mechanism once conduction ceased as soon as the particle surface was no longer in contact with the ice (i.e. floating behaviour), favouring a circular melt morphology. Additionally, the migration of low density particles across an ice surface has been a common process in previous experiments; this was also observed in experiments Mp9 and Mp14 where lateral movements of approximately 30 mm and 25 mm, respectively, created elongated areas of surface melt (Figure 6.10). Lateral movement in Mp14 was rapid, with the particle moving to a new location on the ice block within each time-lapse image (e.g. within a five minute period) in the first three hours of the experiment.

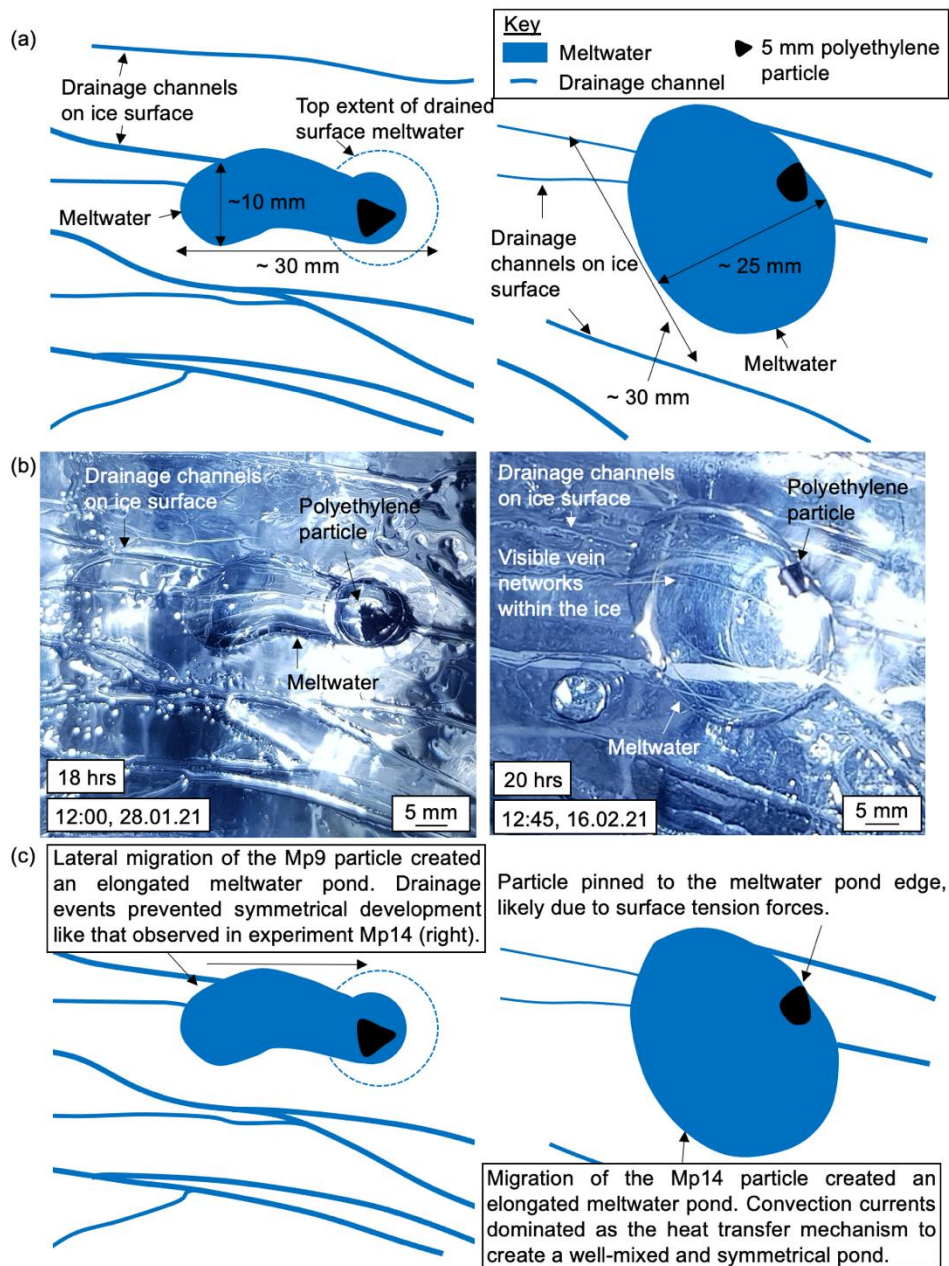


Figure 6.10. Cross-sectional images of elongated melt ponds in experiment Mp9 (left) and Mp14 (right). (a) observational line diagram, (b) photograph and (c) interpretation of the features.

Similar to experiments Mp7, Mp8, and Mp12, drainage events occurred within experiment Mp9 and lowered the particle to a depth of approximately 17 mm into the ice. This remained floating in an asymmetrical meltwater pond throughout (Figure 6.11). Multiple drainage events resulted in a fluctuation in the depth of the Mp9 particle within the ice, and likely contributed to the asymmetrical morphology of the meltwater pond. However, a refilling of the partially drained channel resulted in the upwards movement of the Mp9 particle

to reach the ice surface and facilitated further lateral movement in the final stages of the experiment. This demonstrates the dynamic nature of microplastic particle-ice interaction.

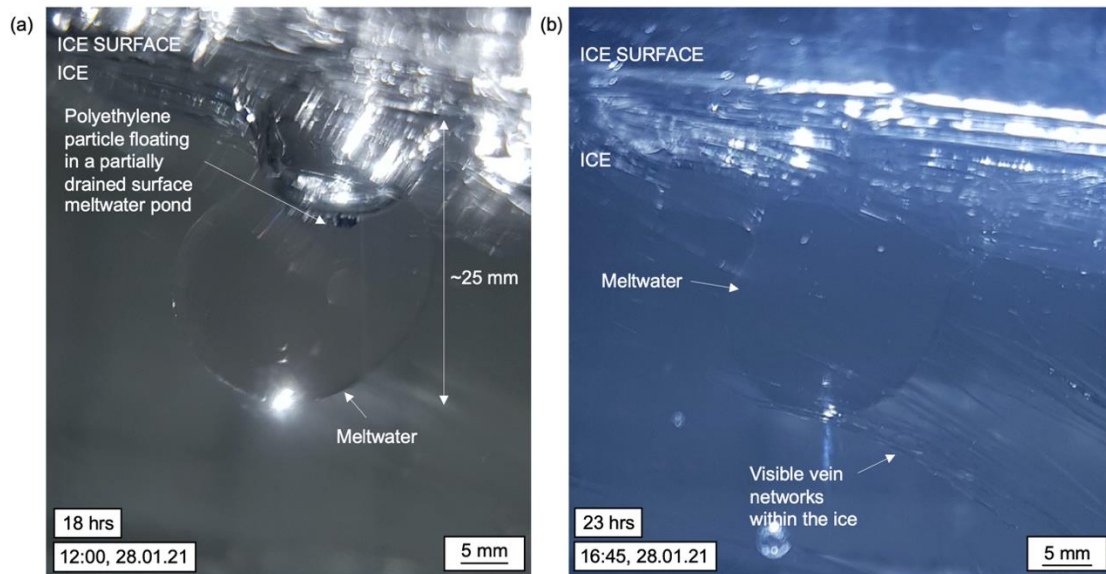


Figure 6.11. Cross-sectional photographs comparing a partially drained meltwater pond and re-filled drained meltwater pond in experiment Mp9, with (a)-(b) denoting a three hour difference.

6.4. Mp4: a large polypropylene surface particle

Experiment Mp4 investigated the behaviour of a large (5 mm) polypropylene particle. In addition to considering subtle differences in density (e.g. 890-920 kg m³ compared to 910-940 kg m³ of polyethylene), the experiment also considered the effect of particle morphology as the polypropylene particles were perfectly spherical, whilst polyethylene particles ranged in morphology from roughly spherical to angular (e.g. Mp9). The hypothesis for experiment Mp4 is shown in Figure 6.12.

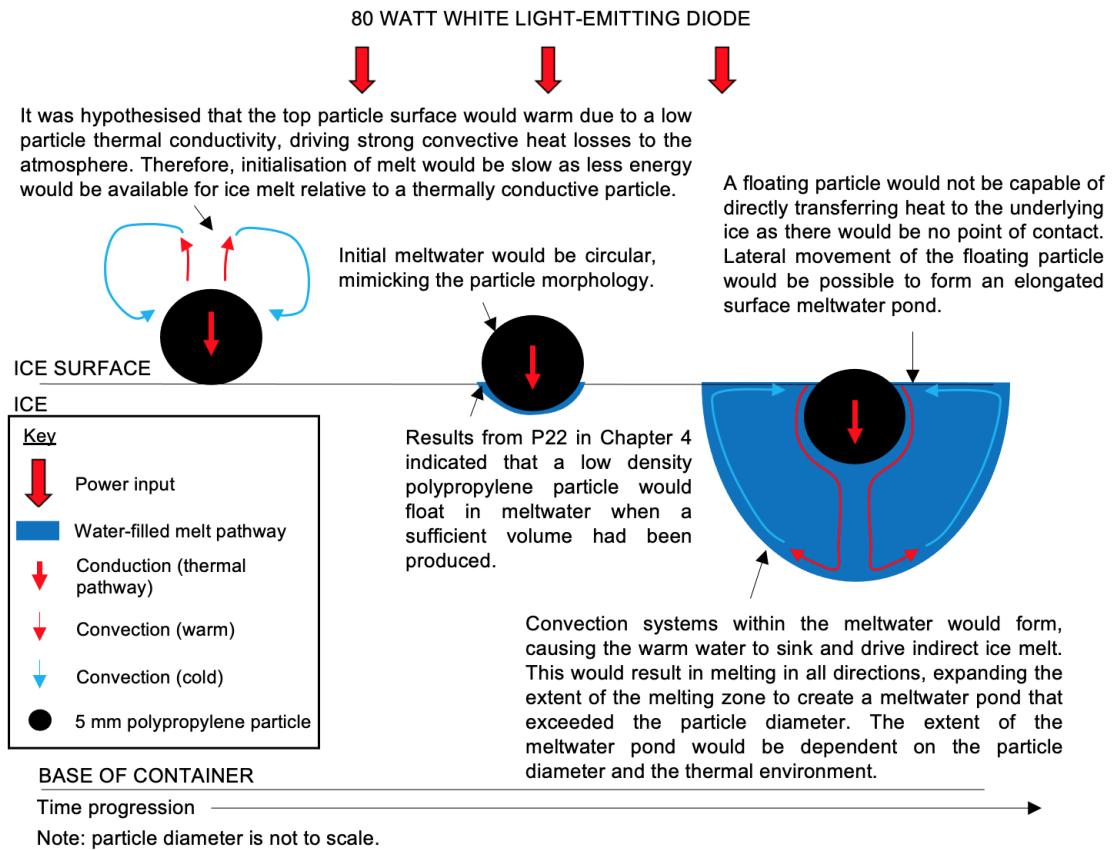


Figure 6.12. Schematic cross-sectional view of the hypothesised particle-ice interaction in experiment Mp4.

6.4.1. Results and interpretation

A surface meltwater pond formed immediately after surface placement. The initial morphology was spherical, matching the particle shape. This reached a maximum width and depth of approximately 7 mm and 4 mm, respectively (Figure 6.13). Therefore, the Mp4 particle did not generate sufficient meltwater to become fully submerged or buoyant. Although melting and refreezing processes settled into a state of equilibrium within four hours of the experiment start, drainage events after 32 hours caused a fluctuation of meltwater level (e.g. a lowering of approximately 2-3 mm). However, as the Mp4 polypropylene particle was not floating, this drainage event had little effect on the overall position of the particle within the ice.

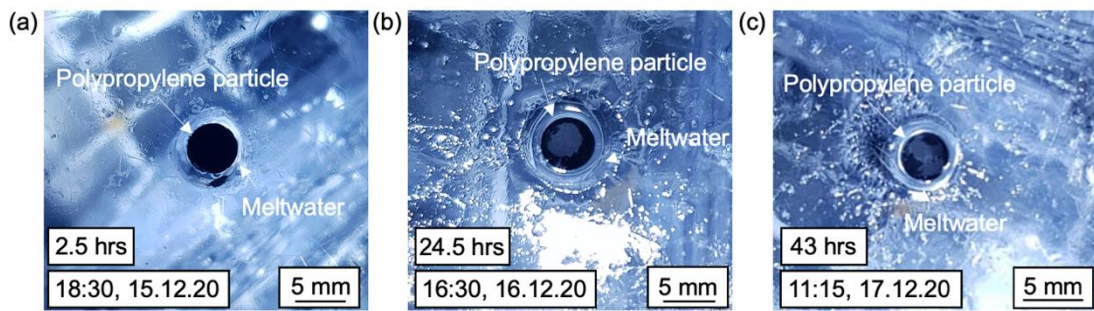


Figure 6.13. Plan-view photographs of meltwater progression in experiment Mp4, with (a)-(c) denoting a 41 hour time difference.

Limited production of meltwater relative to previous experiments (e.g. investigating polyethylene particles) was suggested to be a combination of factors: firstly, the particle in a previous experiment (Mp3) experienced a stable (cold) thermal environment due to low freezer temperatures. As Mp4 was conducted immediately after Mp3 without any freezer temperature modification, the reduced particle-ice interaction was likely a result of cold freezer temperatures (also recorded in the proxy ice temperatures), in addition to drainage processes in the latter stages of the experiment. Therefore, although the particle was transferring heat into the ice to cause ice melt, this was limited by conduction of energy away from the particle before the ice temperature could be raised to PMP by particle heat exchange. Secondly, the 5 mm polypropylene particle had a longer thermal pathway than a polyethylene particle (e.g. a width of approximately 1 mm). The longer thermal pathway may limit heat transfer to water and ice; instead, convective heat losses to the atmosphere drive heating of air. However, as melting could occur (albeit limited), it was deduced that the particle was within a stable (cool) thermal environment.

6.4.2. Summary

Experiment Mp4 did not provide detailed information of the behaviour of a large polypropylene particle interaction with ice as it was conducted within a stable (cool) thermal environment and showed limited particle-ice interaction. However, this indicated that a low density, low thermal conductivity, and low albedo spherical polypropylene particle was capable of melting ice despite melt-limiting conditions (as defined in previous experiments, e.g. cold temperatures,

drainage processes). This also suggested a role of particle morphology, and consequently, the length of the thermal pathway, in dictating the extent of melt.

Two repeat experiments were conducted to assess the behaviour of a large spherical microplastic as particle-ice interaction was limited in Mp4. Both repeat experiments (Mp5 and Mp11) experienced contrasting behaviour to Mp4; the Mp5 particle generated a large amount of meltwater (200x110 mm with a depth of approximately 19 mm), whilst Mp11 moved downwards into the ice through a lowering of meltwater by drainage events. Both experiments were complex and provided useful insights into the behaviour of low density particle-ice interaction and demonstrated that a 5 mm polypropylene particle was buoyant in the meltwater (i.e. floating behaviour began within one and two hours in experiment Mp5 and Mp11, respectively).

Firstly, Mp5 demonstrated the capability of a particle with a low thermal conductivity, density, and albedo to efficiently melt ice. Similar to many volcanic particles, the Mp5 particle created a proximal surface meltwater pond and a shallow surface meltwater pond. The proximal meltwater pond morphology was dependent on lateral movement of the particle (Figure 6.14). A shallow (4-5 mm) meltwater pond also extended across the entire ice surface (e.g. 200 mm).

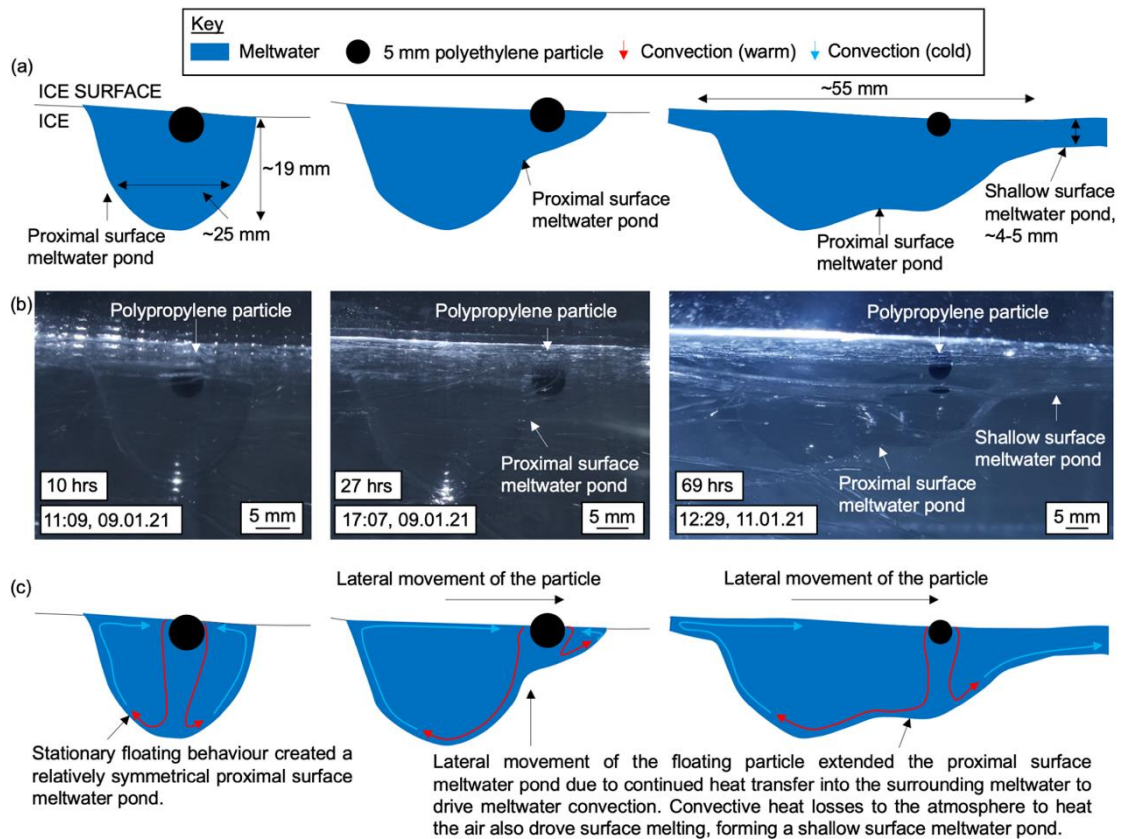


Figure 6.14. Cross-sectional images showing the development of a proximal surface meltwater pond over three time frames in experiment Mp5. (a) observational line diagram, (b) photograph and (c) interpretation of the features.

Experiment Mp5 also indicated the extent to which the advection of heat can trigger further ice melt. Melting was not restricted to the proximity of the particle as meltwater was observed across the ice surface, down the side of the ice block, and at the ice base (Figure 6.15). Bulk melting of ice due to an unstable thermal environment was discounted as other ice blocks stored within the freezer remained stable in the solid state, and so it was deduced that freezer temperatures allowed stable ice. Instead, the large volume of surface melt (created by air heating by the top surface of the particle) likely drained between the ice and container, resulting in the advection of heat along this trajectory to melt the proximal ice. This accumulated at the ice base, further driving ice melt to create a basal meltwater pond. Therefore, a forced convection system was established with the movement of warmer meltwater through gravity causing increased ice melt.

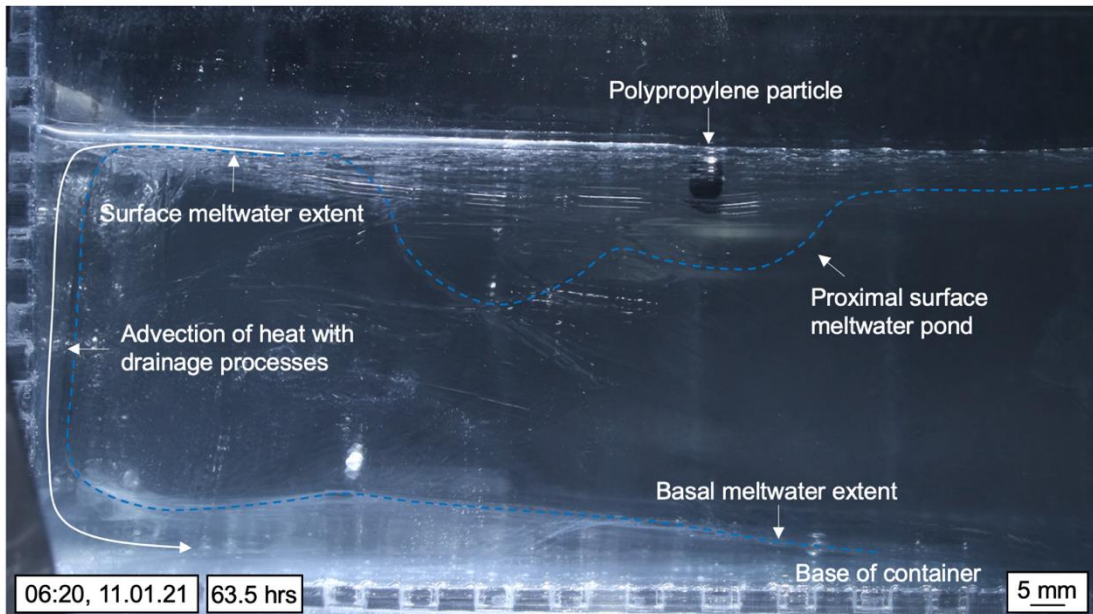


Figure 6.15. Cross-sectional photograph indicating melting associated with the advection of heat in experiment Mp5.

A combination of extensive lateral movement and frequent drainage events resulted in a complex interaction between the low density particle and ice in experiment Mp11 (Figure 6.16). Lateral particle movement was observed during initial drainage processes, extending the width of the lowered meltwater pond. The continued production of meltwater indicated that the particle was actively transferring heat into the ice to cause ice melt throughout the experiment duration.

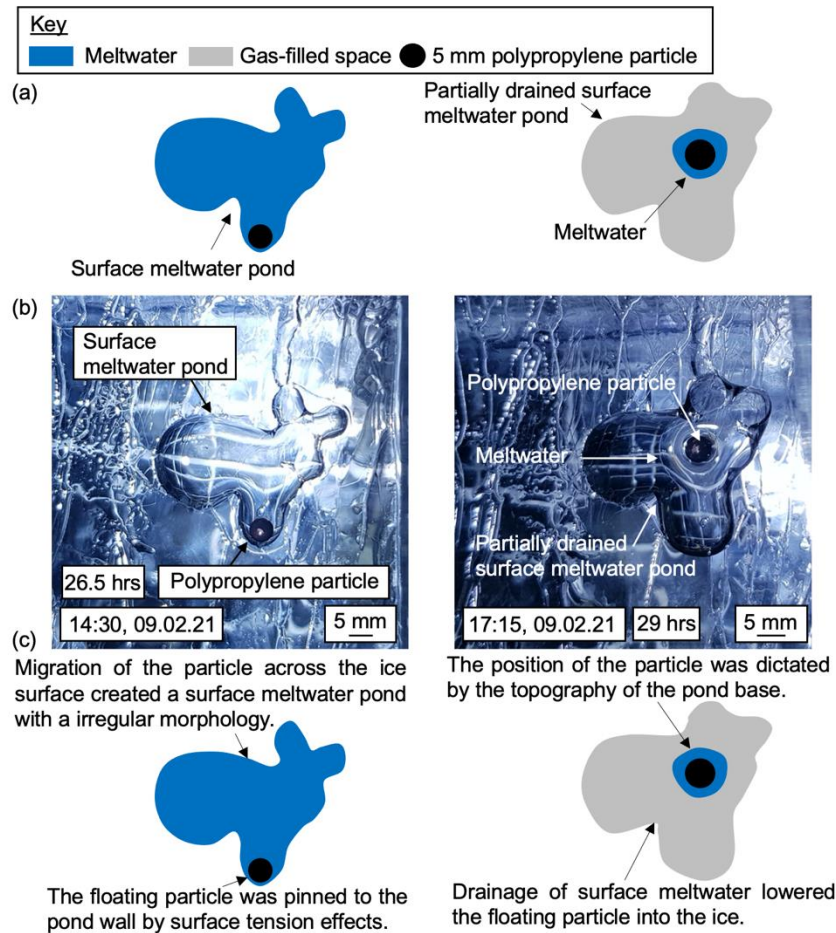


Figure 6.16. Plan-view images of irregular melt surface in a full and partially drained meltwater pond in experiment Mp11. (a) observational line diagram, (b) photograph and (c) interpretation of the features.

Although small-scale drainage events were continuous throughout, a large-scale drainage event occurred approximately 28 hours into the experiment, resulting in full drainage of meltwater within the meltwater pond. This lasted approximately nine hours and caused the particle to move downwards with the draining meltwater to a depth of approximately 38 mm. This large-scale drainage event was associated with a loss of meltwater from the ice container, and so it was no longer a closed system. The end of this drainage event was identified when downwards movement of the particle ceased and the development of a new meltwater pond at the base of the previously drained meltwater pond was observed. This grew to a maximum width and depth of approximately 19 mm and 25 mm, respectively; the addition of meltwater into the drained meltwater pond from particle-ice interaction allowed the particle to move upwards by approximately 16 mm as it floated in the meltwater produced

(Figure 6.17). This demonstrated that at this stage, the rate of ice melt exceeded the rate of drainage.

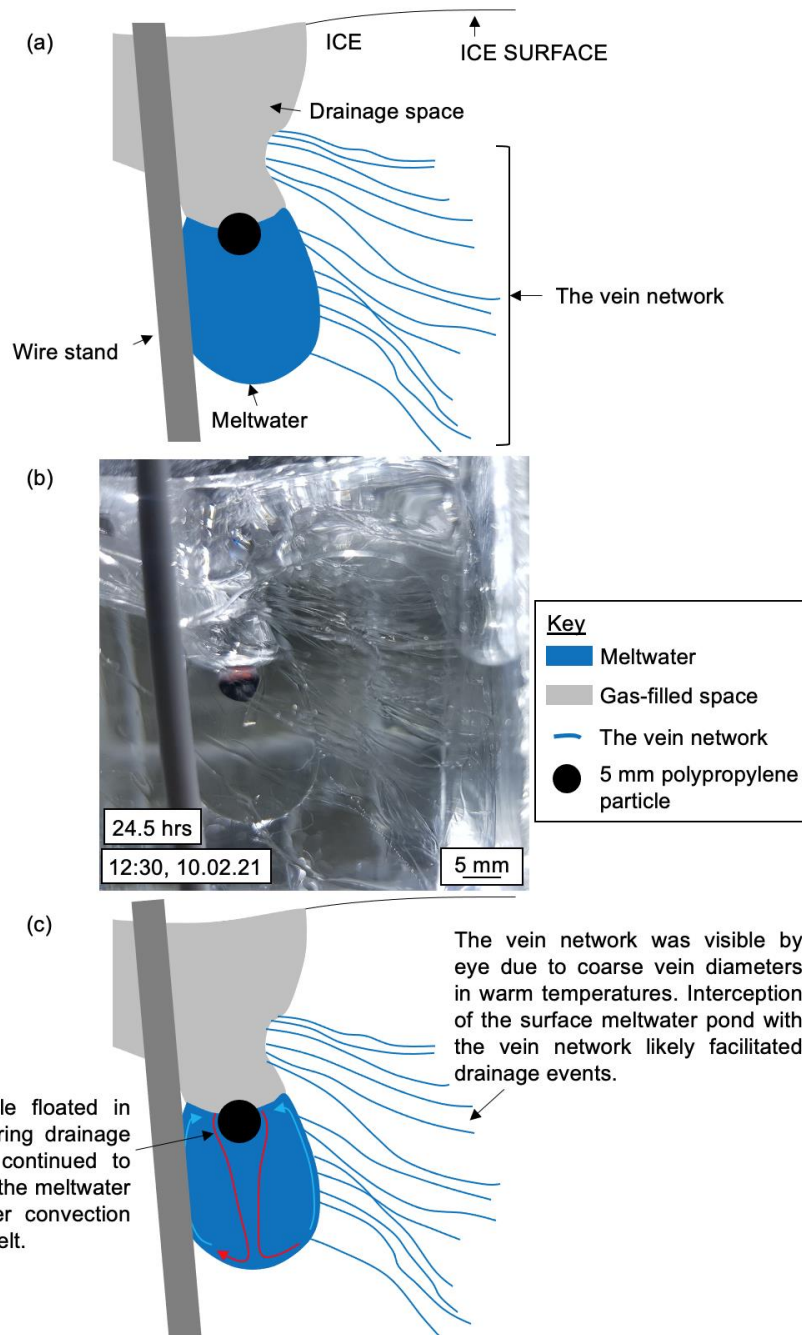


Figure 6.17. Cross-sectional images showing the development of a new meltwater pond at the base of the drained meltwater pond in experiment Mp11. (a) observational line diagram, (b) photograph and (c) interpretation of the features.

A second large-scale drainage event occurred approximately 60 hours into the experiment. This lasted approximately three hours and cause the Mp11 particle to lower to a depth of approximately 40 mm within the ice. The particle

remained at this depth for the remainder of the experiment and continued to transfer heat into the ice system to create a meltwater pond at the base of the partially drained melt pathway.

Icicles extruding from the leak point on the container were present; it is likely that these 'plugged' the container, and then were overwhelmed (Figure 6.18). The formation of these icicles from leaking meltwater also confirms that ice melt was caused by particle-ice interaction, as water refroze once sufficiently far from the particle-heat influence. It was deduced that the Mp11 particle experienced a stable (warm) thermal environment.

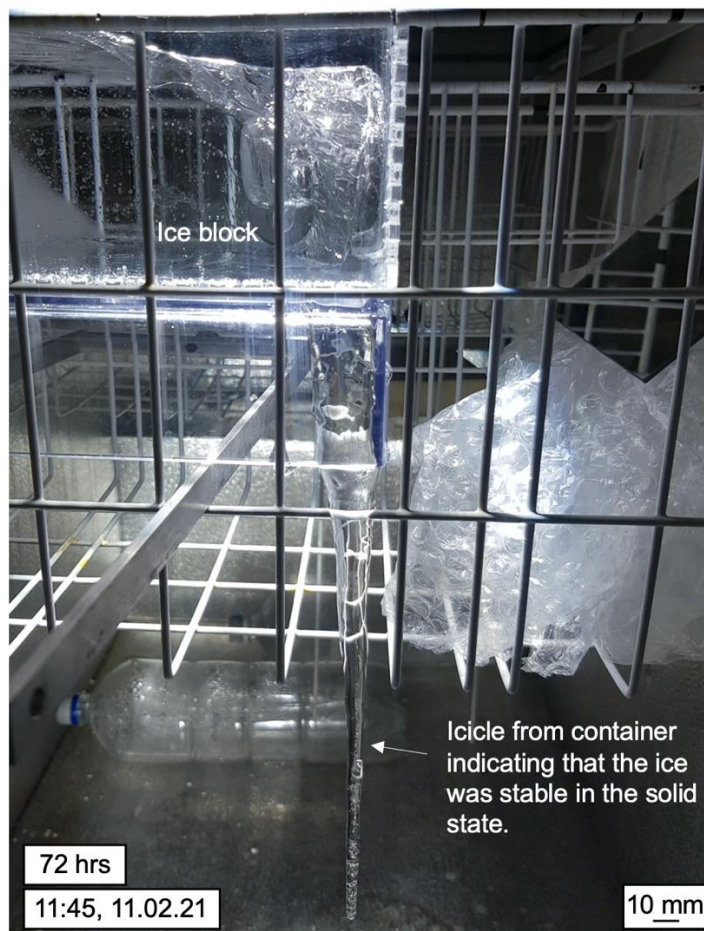


Figure 6.18. Cross-sectional photograph of icicles extruding from the Mp11 ice block.

Experiments Mp4, Mp5, and Mp11 demonstrated the complexity associated with low density particle-induced ice melt. Unlike those with a high density, refilling of meltwater within drained channels can result in the upwards migration of the low density particle (also observed in experiments Mp7, Mp8, and Mp9). Consistent with results from the polyethylene experiments, the

buoyant nature of polypropylene facilitated extensive and rapid lateral movement of a microplastic particle, consequently creating a complex network of melt channels on or within the ice.

6.5. Mp6: embedded microplastic particles

Experiment Mp6 investigated the behaviour of many large microplastics embedded within the ice (e.g. more than 30). These were polyethylene particles with diameters in the 'large' category. The hypothesis for experiment Mp6 is shown in Figure 6.19.

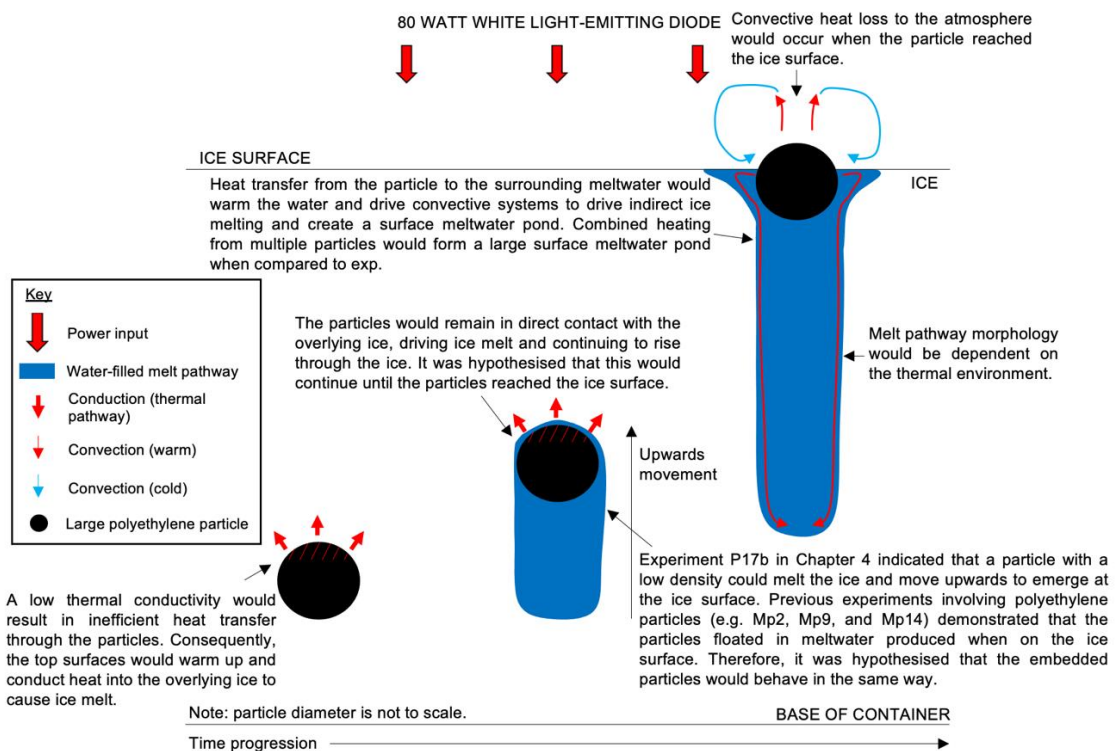


Figure 6.19. Schematic cross-sectional view of the hypothesised particle-ice interaction for experiment Mp6.

6.5.1. Results and interpretation

Ice melt was first observed within 30 minutes of the experiment start. This was identified as spherical areas of meltwater surrounding particles within the ice. A mixture of behaviour was observed, where four polyethylene particles moved upwards through the ice, and others remained at the ice base. Therefore, the latter behaviour was dominant. Upwards moving particles had mean velocities of $3.71 \times 10^{-7} \text{ m s}^{-1}$, $5.06 \times 10^{-7} \text{ m s}^{-1}$, $6.34 \times 10^{-7} \text{ m s}^{-1}$ and $8.21 \times 10^{-7} \text{ m s}^{-1}$. In some instances, particles were able to move upwards through the ice, but an

expanding basal meltwater pond reached the base of the particle melt pathway and led to small drainage events and prevented further particle movement. Additionally, it was noted that one microplastic particle moved through the ice to reach the ice surface with a high mean velocity of $8.21 \times 10^{-7} \text{ m s}^{-1}$. This behaviour was a result of the particle moving 45 mm to the ice surface within a single time-lapse image frame (i.e. five minutes). The particle was approximately 4x3 mm in size, with a width of <1 mm (and was, therefore, very thin). It was likely that the particle intercepted the water-filled vein network to move upwards to the ice surface within the five-minute period.

6.5.2. Melt pathway

The presence of multiple upwards moving particles created multiple melt pathways. These initially encased the particle in a spherical area of melt and became elongated when the particle started moving upwards through the ice. Particle movement was typically along an inclined trajectory (thought to be a result of the irregular morphology of the particle causing irregular heating patterns and possible intersection with the vein network); therefore, the melt pathways were also inclined (Figure 6.20). The presence of multiple melt pathways within the ice facilitated rapid movement of particles when intercepting another melt pathway. For example, a microplastic moved upwards by approximately 26 mm within a time-lapse frame (i.e. five minutes) as it intercepted an open melt pathway. No refreezing of the melt pathways was evident and so it was deduced that the Mp6 particles experienced a stable (warm) thermal environment.

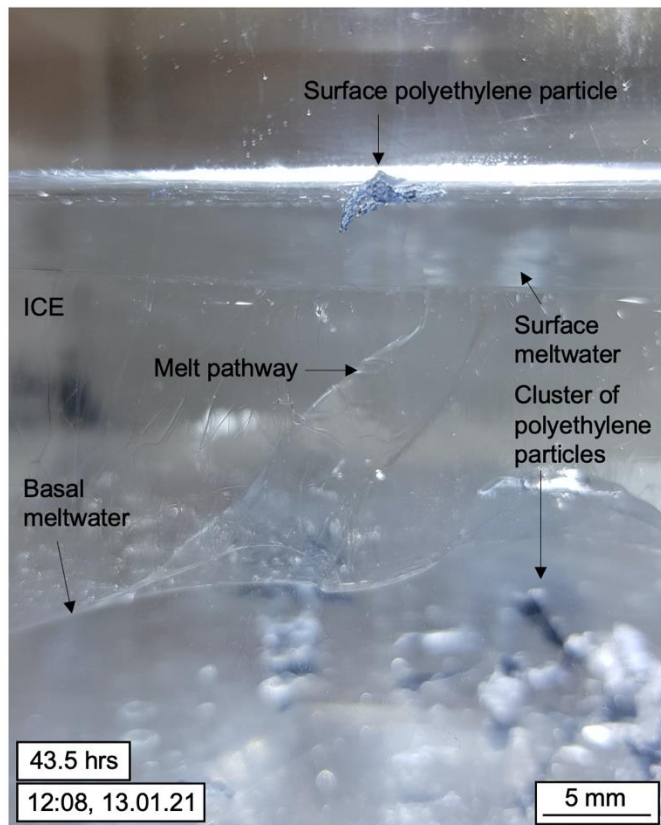


Figure 6.20. Cross-sectional photograph of inclined melt pathway in experiment Mp6.

6.5.3. Surface meltwater pond

Once at the ice surface, the microplastic particles continued to transfer heat into the ice to create a surface meltwater pond. This had the additional heating component by heating of the air from the particle top surface, likely extending the width of the surface meltwater. Lateral movement of the surface particles extended the surface meltwater width. Maximum dimensions reached across the full extent of the ice block (i.e. approximately 200 mm), inwards by approximately 130 mm, and had a maximum depth of approximately 14 mm.

6.5.4. Basal meltwater pond

Most particles did not move upwards through the ice block, suggesting that many previous floating particles were held at the surface by surface tension (facilitated by an 'intermediate' density close to the value of water). Instead, these transferred heat into the ice to induce melting and create individual melt ponds encasing the particles. These combined to form a basal meltwater pond within approximately five hours after the experiment start (Figure 6.21). This was connected to the surface meltwater pond at the left container edge 50

hours into the experiment. Approximately 8 mm of ice remained between the surface and basal meltwater pond; it was hypothesised that if the experiment had continued, the ice would have continued to melt until the entire area was melted. This demonstrated the strong particle-heating effect of multiple microplastic particles within a closed ice system.

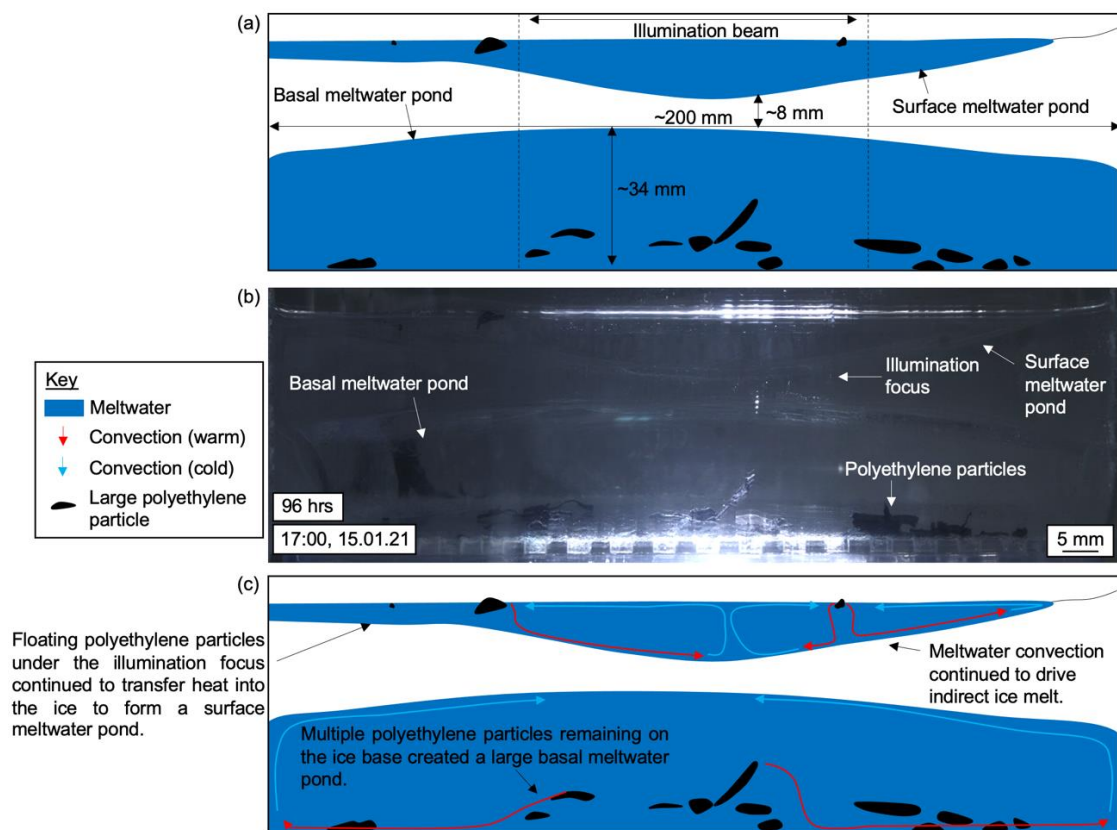


Figure 6.21. Cross-sectional images of the basal and surface meltwater pond in experiment Mp6. (a) observational line diagram, (b) photograph and (c) interpretation of the features.

6.5.5. Summary

Experiment Mp6 showed multiple microplastic behavioural modes that resulted in four microplastic particles moving to the ice surface to create a surface meltwater pond, and most microplastics remaining at the ice base to create a basal meltwater pond. The presence of multiple particles within the ice system resulted in a great extent of ice melt. This eventually resulted in the surface and basal meltwater ponds growing and nearly combining to form one large region of melt.

Two repeat experiments (Mp13 and Mp18) were conducted to confirm findings from experiment Mp6. These also assessed a range of microplastic sizes (e.g. spanning the medium and large categories). Similar to experiment Mp6, the dominant behaviour in both Mp13 and Mp18 was microplastics moving to the ice base and remaining in a basal meltwater pond. Mp13 saw two microplastics move up to the ice surface (with particle velocities of $1.90 \times 10^{-7} \text{ m s}^{-1}$ and $2.20 \times 10^{-7} \text{ m s}^{-1}$), whilst Mp18 saw three microplastics move upwards through the ice (with particle velocities of $6.36 \times 10^{-7} \text{ m s}^{-1}$, $9.19 \times 10^{-7} \text{ m s}^{-1}$ and $2.00 \times 10^{-6} \text{ m s}^{-1}$). A rapid movement occurring within a single time-lapse frame was also observed for both microplastics in experiment Mp13, where both particles moved 51 mm and 47 mm within five minutes. This rapid movement occurred on the same trajectory within the ice system; this could suggest that both microplastics intercepted the vein network within the ice.

Similar to experiment Mp6, experiment Mp13 demonstrated that initial melt was spherical in morphology and encased individual particles (Figure 6.22). These eventually combined to form a large volume of basal melt. It was noted that some drainage processes had occurred as gas bubbles were present at the top of most melt regions. This may have prevented upwards movement of the particles as many of the particles were at the top of a basal meltwater pond (i.e. they were floating). Multiple basal meltwater ponds were identified in the following locations, although it was noted that all basal meltwater was connected, except for basal pond (1):

- (1) Extending across the entire horizontal extent of the ice block with a height of approximately 15 mm. This contained a cluster of microplastics.
- (2) On the left-hand side of the ice block, with a width of approximately 75 mm and height of approximately 10 mm. This contained <10 microplastic particles.
- (3) On the right-hand side of the ice block, with a width of approximately 130 mm and height of approximately 5 mm. Does not appear to contain any microplastic particles.
- (4) Central pond in the focus of the beam with many plastics within. Drainage appears to have occurred due to the presence of gas spaces at the top of the meltwater pond. Therefore, drainage processes likely

prohibited upwards movement of some microplastic particles (in the same way as experiment Mp6).

The upwards motion of microplastics created a surface meltwater pond once the particles reached the ice surface. This extended the entire horizontal extent of the ice block, inwards by approximately 10 mm, and had a depth of approximately 3 mm. This was likely due to heating of air by convective heat loss by the particle.

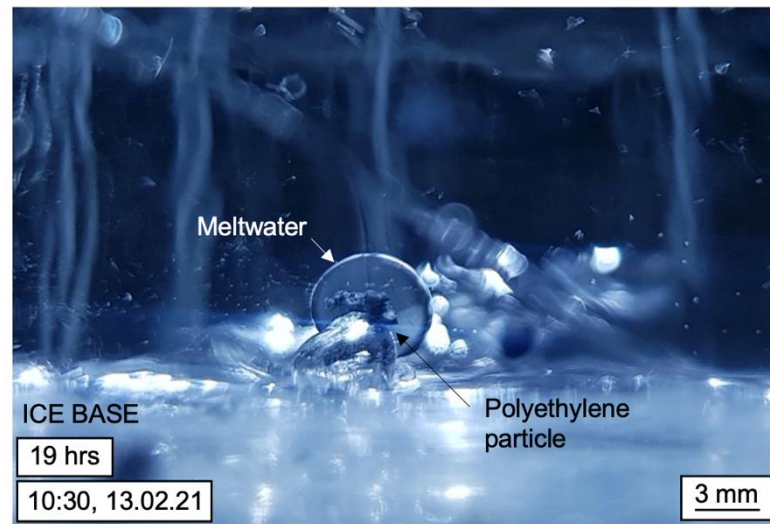


Figure 6.22. Cross-sectional photograph of meltwater surrounding an embedded microplastic particle in experiment Mp13.

Mp18 differed from Mp6 and Mp13 as two microplastic types were assessed: polyethylene and polypropylene. The polypropylene particle demonstrated rapid upwards movement (starting within one hour), as it melted the ice and floated in meltwater produced. This moved upwards with a particle velocity of $2.00 \times 10^{-6} \text{ m s}^{-1}$ to reach the ice surface within six hours and created a melt pathway with a width similar to the particle diameter (e.g. 5-6 mm). No refreezing processes were observed and so it was deduced that the particle was operating within a stable (warm) thermal environment. A drainage event lowered the particle into the ice (Figure 6.23), although the particle melted upwards again to reach the ice surface within a further three hours. In addition to a proximal surface meltwater pond, a shallow surface meltwater pond formed with a width and depth of approximately 180 mm and 10 mm, respectively. The pond width was likely formed by heating of the air through convective heat losses to the atmosphere, facilitated by the stable (warm) thermal environment.

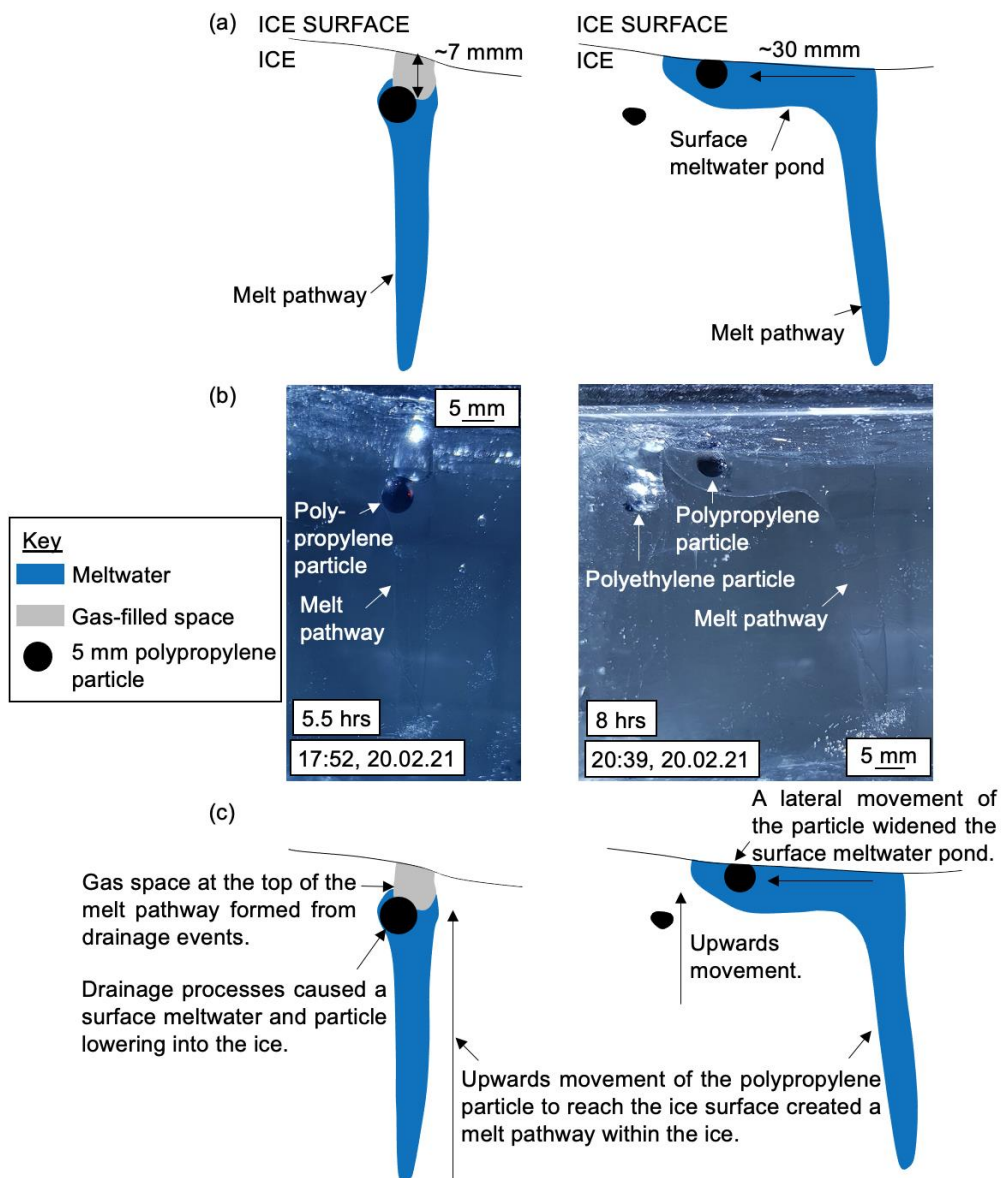


Figure 6.23. Cross-sectional images of the melt pathway and proximal surface meltwater pond associated with the polypropylene particle in experiment Mp18, where left is indicating drainage immediately after reaching the surface, and right is showing the development of surface meltwater with lateral movement. (a) observational line diagram, (b) photograph and (c) interpretation of the features.

Multiple polyethylene microplastics also moved upwards through the ice. Similar to experiment P17b (Chapter 4), these had a partially drained melt pathway that followed the particle movement (Figure 6.24). Mean particle velocities were calculated at $6.36 \times 10^{-7} \text{ m s}^{-1}$ and $9.19 \times 10^{-7} \text{ m s}^{-1}$; however, only one of the polyethylene particles reached the ice surface, as the other 'stalled' in the ice within a gas space that encased the entire particle (with a similar morphology to the meltwater pockets observed in experiment Mp13). The experiment ended

prior to this reaching the ice surface. This feature was observed in multiple instances where embedded microplastics, that initially moved upwards through the ice, were located at the base of a gas space formed by drainage processes.

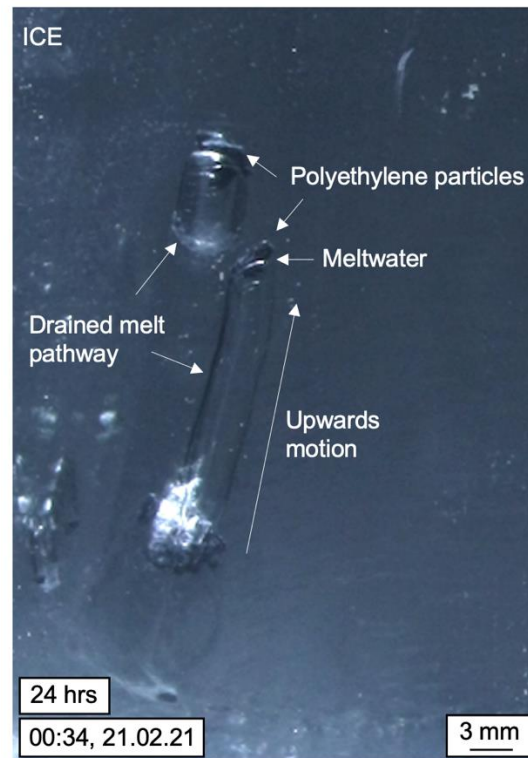


Figure 6.24. Cross-sectional photograph of polyethylene particles moving upwards through the ice in experiment Mp18.

Experiments assessing the behaviour of embedded polyethylene particles demonstrated multiple behavioural modes. The buoyant behaviour (and, therefore, upwards motion of particles through the ice) facilitated the development of a surface meltwater pond, whilst the non-buoyant behaviour (and, therefore, particles settling on the base of the ice) created a basal meltwater pond in the three experiments. These two behavioural modes were a result of the intermediate polyethylene density (i.e. a close value to water). Although results of polypropylene material were limited to one experiment, a polypropylene particle had a dominant floating effect compared to the polyethylene particles, suggesting that subtle changes in density can have large impacts on the behaviour of microplastics within ice. Additionally, all experiments experienced drainage events that prohibited upwards motion. The

vein network likely facilitated these drainage events and, therefore, the hydrological state of the ice block had a control on the particle behaviour.

6.6. Mp15: a scattering of small surface microplastics

Experiment Mp15 investigated the behaviour of a scattering of small (<1 mm) microplastics on an ice surface (Figure 6.25). These were placed on the ice surface using a 1 mm sieve to achieve a random distribution of particles in the focus of the illumination beam. The hypothesis for experiment Mp15 is shown in Figure 6.26.

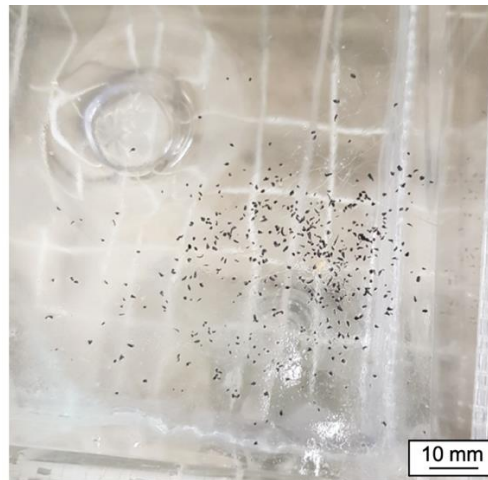


Figure 6.25. Plan-view photograph of the small microplastic particles in experiment Mp15.

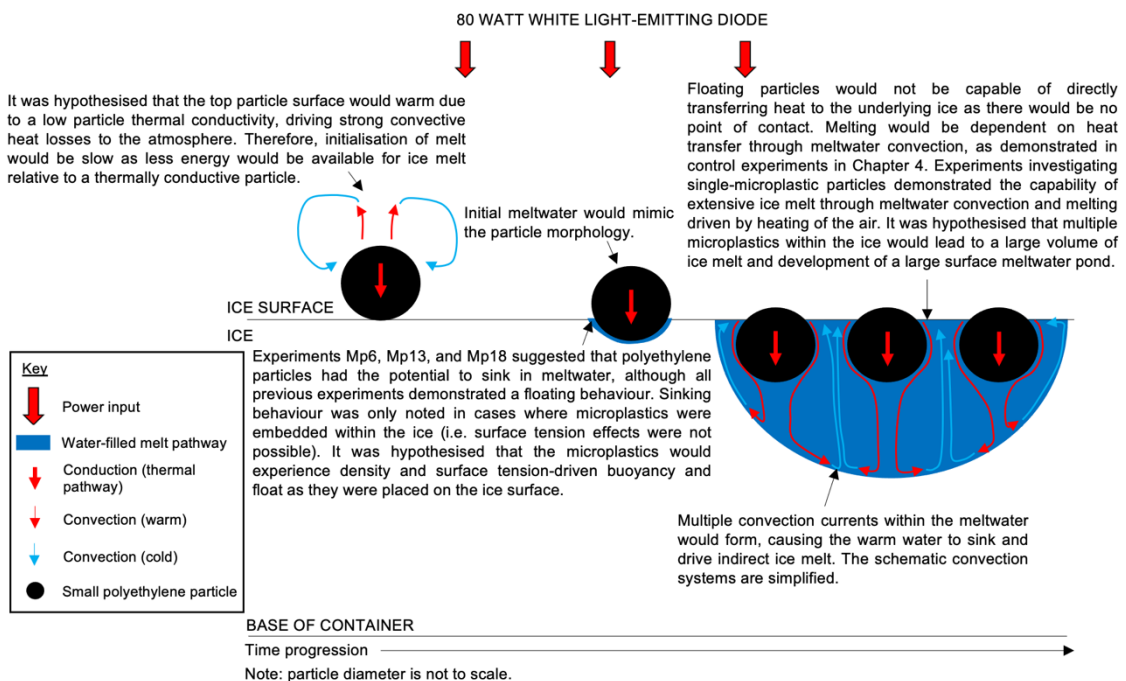


Figure 6.26. Schematic cross-sectional view of the hypothesised particle-ice interaction for experiment Mp15.

6.6.1. Results and interpretation

An immediate melting of the ice surface was observed, where several individual meltwater ponds formed. This scarred the ice surface in a similar way to experiments V33 and V34 (Chapter 5) and formed multiple channels.

Microplastic particles accumulated in the channels of meltwater (e.g. low topography regions), which exaggerated ice melt. However, many microplastics also moved downwards to the ice base (although, still less numerous than those floating in surface melt, e.g. >10). This did not support the hypothesised outcome and results from previous experiments involving placement on the ice surface. A variety of downwards particle velocities were observed (Table 6.2, Figure 6.27).

Table 6.2. The variability of microplastic particle velocities in experiment Mp15 with associated code in Figure 6.27.

Code and approximate size (mm)	Particle velocity (m s^{-1})
a, 0.1	1.02×10^{-6}
b, 0.5	9.77×10^{-7}
c, 1 x 1.5	1.25×10^{-6}
d, 0.5 x 1	1.22×10^{-6}

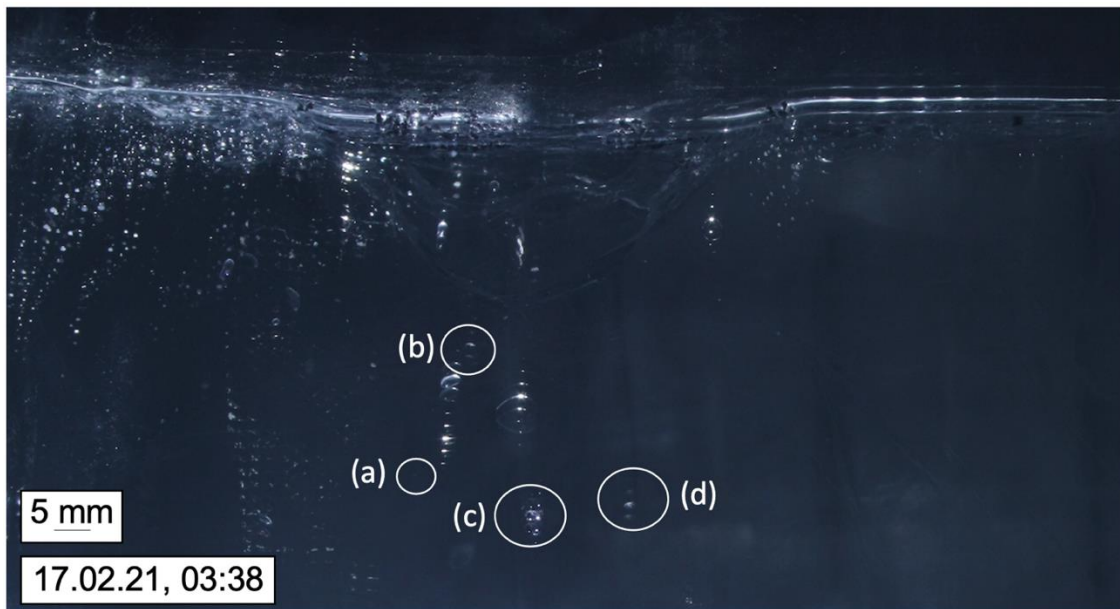


Figure 6.27. Cross-sectional photograph indicating the four microplastic particles described in Table 6.2.

6.6.2. Melt pathway

Microplastic particle descent through the ice formed multiple melt pathways within the ice (approximately 2-3 mm in diameter). These were wider than the particle, suggesting convection-driven ice melt, similar to observations in Chapter 4 (Section 4.3), and Chapter 5. Vertical and angular morphologies were observed (Figure 6.28).

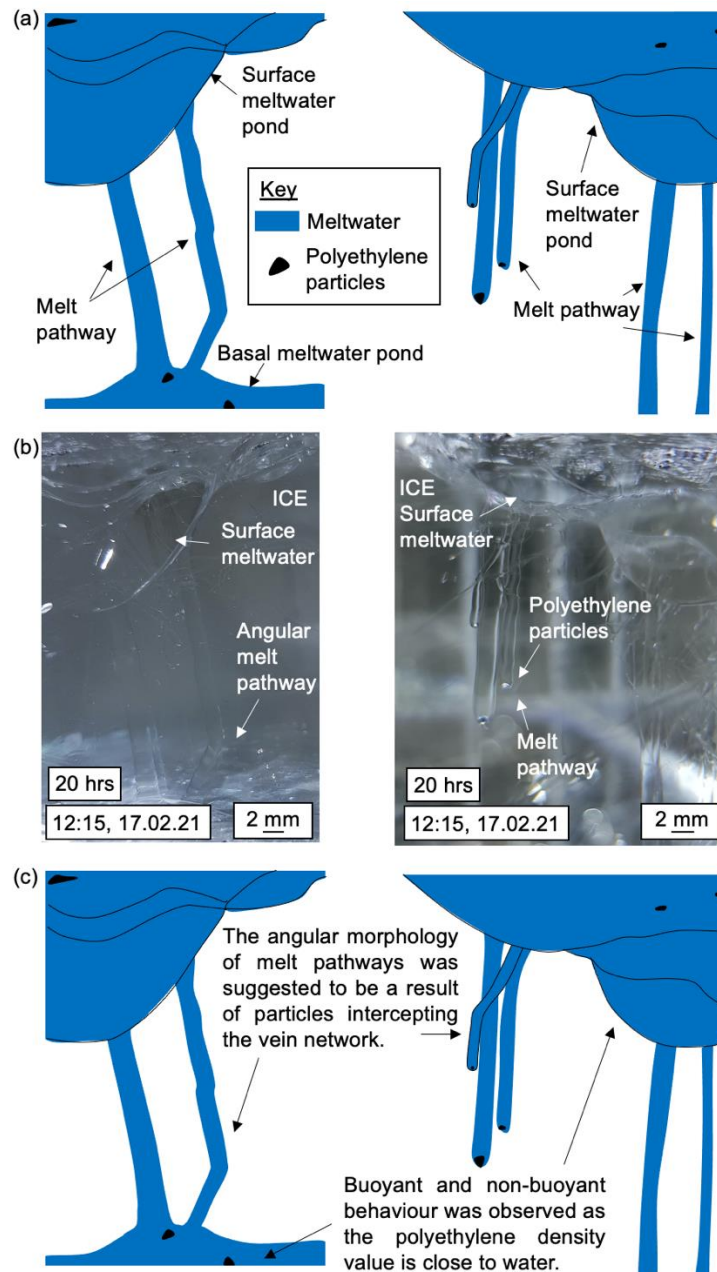


Figure 6.28. Cross-sectional images of the varied morphology of multiple melt pathways within the ice in experiment Mp15. (a) observational line diagram, (b) photograph and (c) interpretation of the features.

6.6.3. Proximal surface meltwater pond

Many microplastics transferred heat into melting the ice and floated in meltwater produced. These accumulated in surface meltwater to create a localised meltwater pond with a maximum depth of approximately 30 mm, although this was undulating due to the nature of combining multiple proximal meltwater ponds (Figure 6.29). Many of the microplastics clustered together in the meltwater, forming areas of a localised large absorption surface.

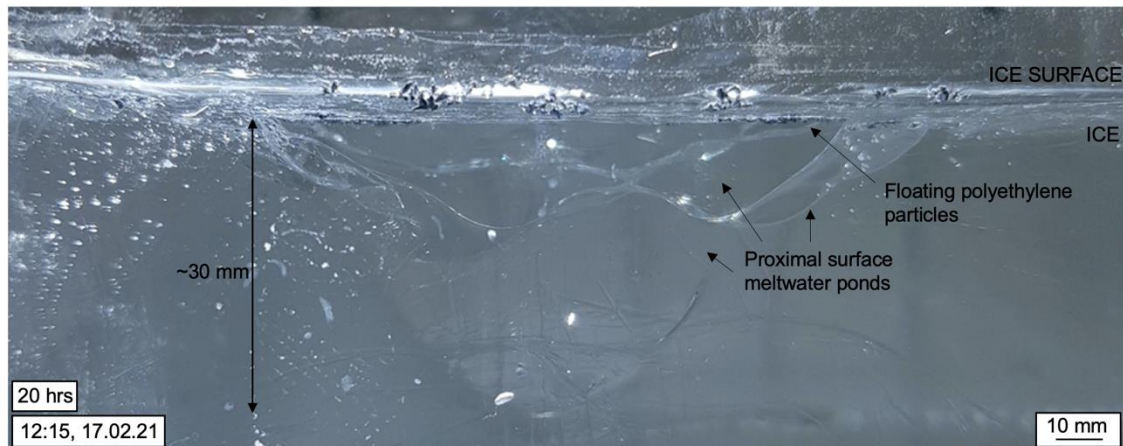


Figure 6.29. Cross-sectional images of the proximal surface meltwater pond in experiment Mp15.

6.6.4. Shallow surface meltwater pond

Surface microplastics initially melted the ice to form individual meltwater ponds, resulting in the development of a 'scarred' ice surface, where localised channels of meltwater formed. In addition to the formation of a deeper area of melt (i.e. the proximal surface meltwater pond), a larger region of surface melt developed when melt from individual microplastic particles combined. This reached approximately 115 mm across the ice block and approximately 70 mm inwards, with an average depth of approximately 1-2 mm.

6.6.5. Basal meltwater pond

Downwards movement of microplastics to the ice base formed a basal meltwater pond with a width of approximately 110 mm. This was undulating in nature (with a maximum height of approximately 6 mm and an average height of approximately 2 mm) and was connected to the surface meltwater by multiple melt pathways.

6.6.6. Summary

Results from experiment Mp15 did not support the hypothesised outcome, as buoyant and non-buoyant behaviour was observed. Although downwards movement had been observed in previous experiments, this was limited to three experiments involving embedded particles. Mp15 involved surface placement of particles and so the downwards movement of microplastics in this experiment contradicted previous results. The floating of particles observed in previous experiments investigating polyethylene microplastics was likely facilitated by surface tension effects due to the close density value to water. This intermediate density facilitated complex particle-particle interaction observed in experiment Mp15 (e.g. multiple modes of behaviours).

Experiment Mp16 was conducted as a repeat experiment to confirm results. However, particles were smaller than those investigated in experiment Mp15 (e.g. <0.5 mm), although still within the 'small' category. Results from experiment Mp16 were consistent with Mp15 as multiple behavioural modes were identified, allowing the development of an extensive surface meltwater pond, multiple melt pathways, and a basal meltwater pond. These had similar morphologies to those observed in experiment Mp15 (e.g. an undulating surface meltwater pond due to the combination of many individual meltwater ponds). The downwards movement of many microplastic particles was observed with varying particle velocities (Table 6.3, Figure 6.30).

Table 6.3. The variability of microplastic particle velocities in experiment Mp16 with associated code in Figure 6.30.

Code and approximate size (mm)	Particle velocity (m s ⁻¹)
a, 0.1	7.79 x 10 ⁻⁷
b, 0.1	7.55 x 10 ⁻⁷
c, 0.1	1.18 x 10 ⁻⁶
d, 0.1	1.27 x 10 ⁻⁶
e, 0.3	9.14 x 10 ⁻⁷

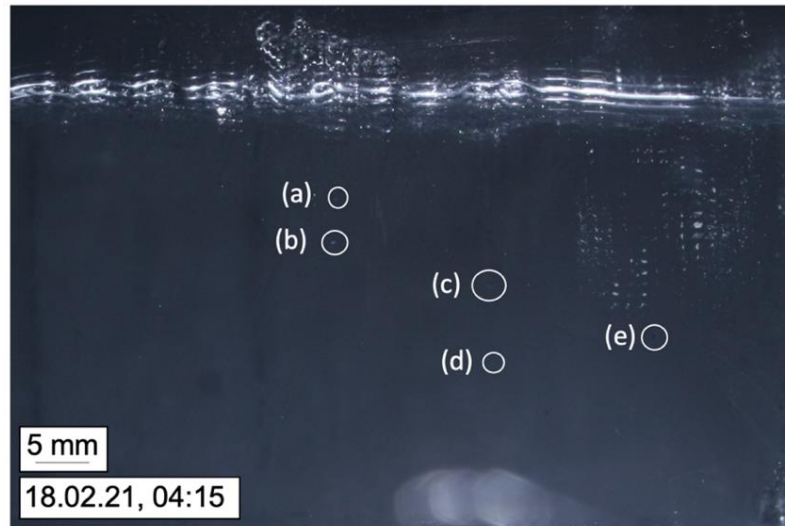


Figure 6.30. Cross-sectional photograph indicating the five microplastic particles described in Table 6.3.

In contrast to experiment Mp15, a greater number of downwards moving particles were observed, resulting in the development of an extensive network of melt pathways within the ice (Figure 6.31). These were smaller in diameter than those observed in experiment Mp15, likely reflecting the smaller particle diameters used in experiment Mp16. This strongly supported previous findings that particle diameter is a key control on the morphology of melt. Varying particle trajectories were also observed: for example, particle (a) moved downwards along a vertical trajectory, whilst particle (b) alternated the direction of downwards movement in three instances. This indicated particle interaction with the vein network within the ice. Particle-particle interaction was also observed, as particle (c) intercepted the melt pathway created by particle (d), facilitating rapid downwards movement (e.g. 25 mm in an hour period).

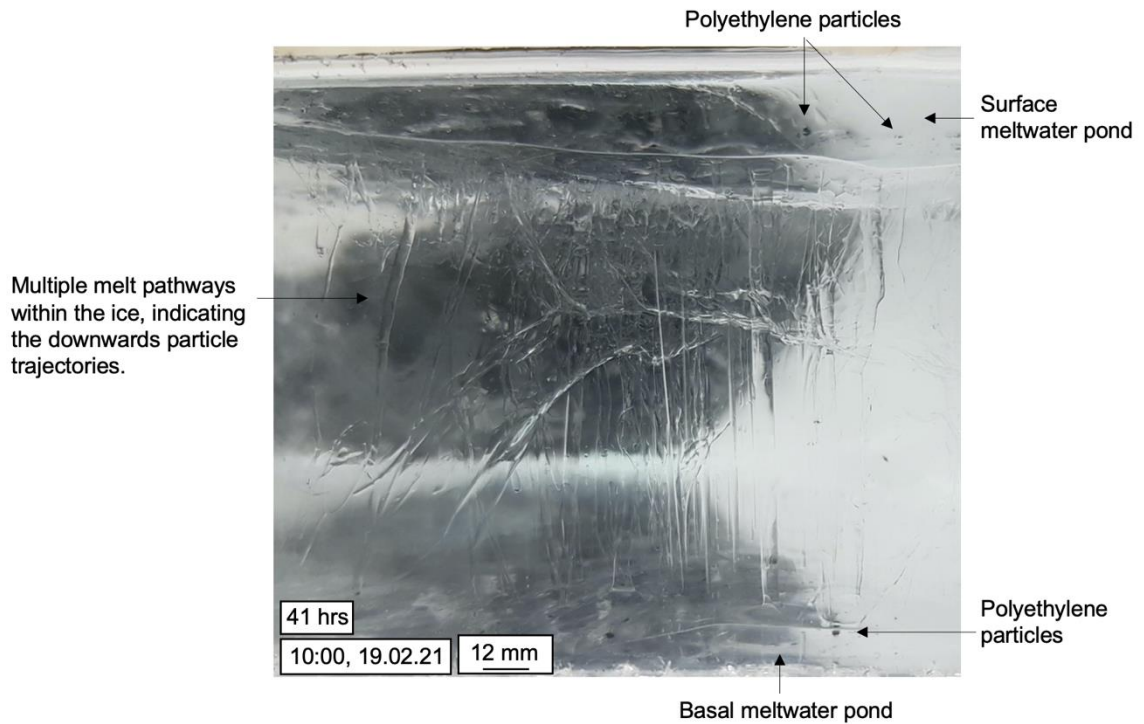


Figure 6.31. Cross-sectional photograph of melt pathway network within the ice in experiment Mp16.

6.7. Mp17: a scattering of small surface microplastics upon opaque ice

Experiment Mp17 assessed the behaviour of a scattering of small (<1 mm) microplastics on an opaque ice surface (Figure 6.32) to investigate the role of bubbles within the ice on microplastic-ice interaction. The hypothesis for experiment Mp17 is shown in Figure 6.33.

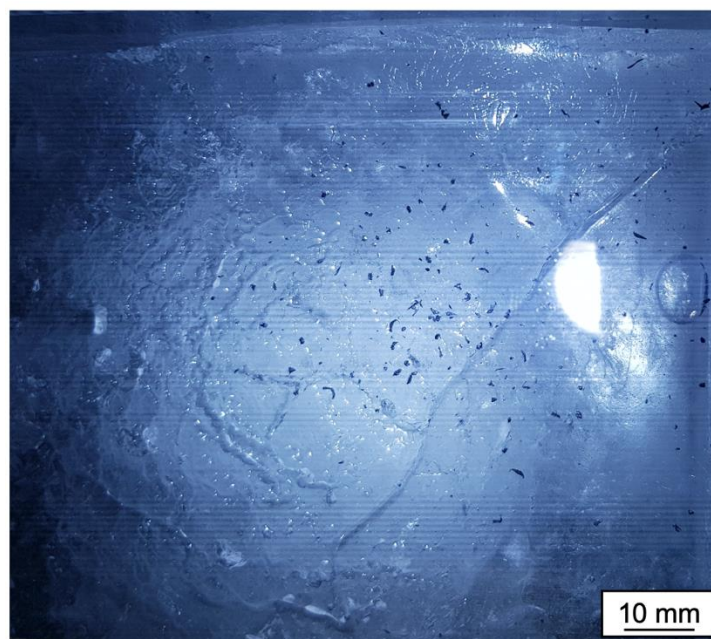


Figure 6.32. Plan-view photograph of the small microplastic particles in experiment Mp17.

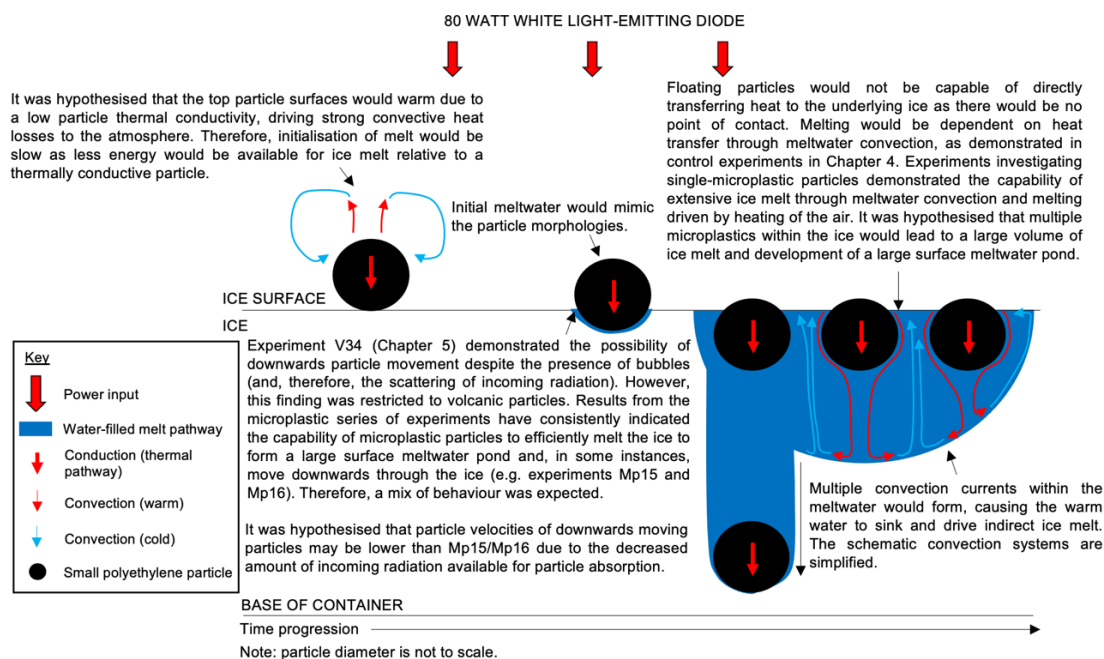


Figure 6.33. Schematic cross-sectional view of the hypothesised particle-ice interaction for experiment Mp17.

6.7.1. Results and interpretation

Results were strongly consistent with experiments Mp15 and Mp16, where initial melt was in the form of individual surface meltwater ponds that eventually combined to create a larger area of melt. A combination of floating and sinking microplastic particles were observed, both of which started immediately after the illumination source was turned on. Lateral movement of the floating particles was observed throughout the experiment, resulting in the extension of surface meltwater. Additionally, a variety of particle velocities for downwards moving particles were calculated (Table 6.4, Figure 6.34), with values comparing well with results from experiments Mp15 and Mp16.

Table 6.4. The variability of microplastic particle velocities in experiment Mp17 with associated code in Figure 6.34.

Code and approximate size (mm)	Particle velocity (m s ⁻¹)
a, <0.1	8.51 x 10 ⁻⁷
b, <0.1 x 0.7	1.21 x 10 ⁻⁶
c, 0.1	7.34 x 10 ⁻⁷
d, 0.5	6.90 x 10 ⁻⁷
e, 0.2	1.04 x 10 ⁻⁶
f, 0.5	8.62 x 10 ⁻⁷
g, 0.1 x 0.5	7.78 x 10 ⁻⁷

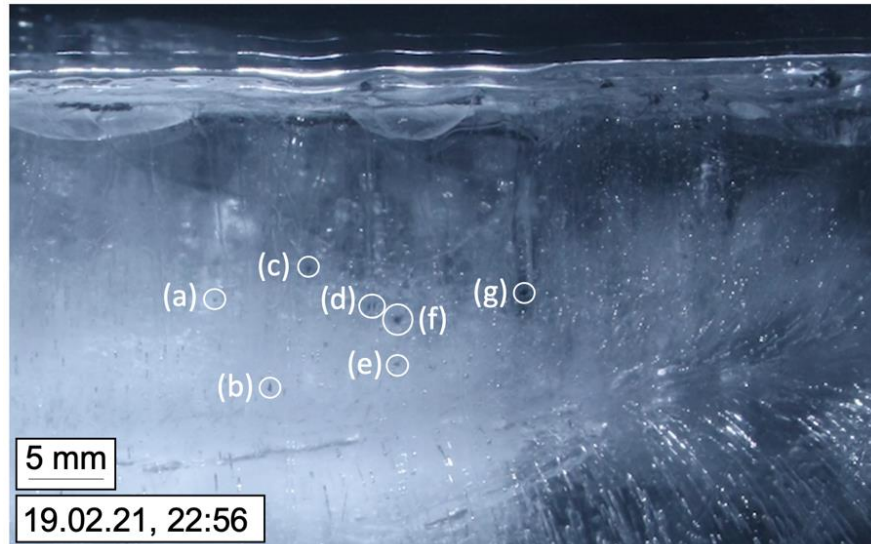


Figure 6.34. Cross-sectional photograph indicating the five microplastic particles described in Table 6.4.

6.7.2. Melt pathway

The downwards movement of microplastic particles created multiple melt pathways within the ice system. As observed in experiments Mp15 and Mp16, the pathways had a similar width to the particle diameters (approximately 1 mm). These remained connected to surface melt for the experiment duration and so it was deduced that the particles experienced a stable (warm) thermal environment.

6.7.3. Proximal surface meltwater pond

Many floating microplastic particles clustered together, creating a deep area of melt. This was approximately 85 mm in width with a depth of approximately 23 mm. The proximal surface meltwater pond had a similar morphology to that observed in experiment Mp15, where a central area of greater depth was surrounded by an undulating surface (representing the individual melt ponds that formed in the first hours of the experiment). Lateral movement of the cluster of microplastics extended the proximal surface meltwater pond, confirming that floating particles were responsible for the deeper melt.

6.7.4. Shallow surface meltwater pond

Individual melt ponds created a 'scarred' ice surface, consistent with results from experiments Mp15 and Mp16. This indicates that the presence of bubbles

within the ice did not have an influence on surface particle-ice interaction. Additionally, the particles initially arranged themselves in depressions and channels that formed on the ice surface. In some instances, this resulted in a linear feature of microplastic particles. A shallow area of surface meltwater developed alongside the proximal surface meltwater pond; this extended across the entirety of the ice block, inwards by approximately 90 mm, and had an average depth of approximately 2 mm (with the greatest depth of approximately 6 mm observed at the left extent of the ice block).

6.7.5. Basal meltwater pond

A basal meltwater pond developed in experiment Mp17. However, unlike previous experiments, this had a height of approximately 3 mm and did not form because of particle-ice interaction at the ice base (although, this likely contributed to the meltwater volume). Instead, meltwater likely drained down to the ice base to create the basal meltwater pond (informed by previous results).

6.7.6. Summary

The behaviour of microplastic particles within experiment Mp17 compared well with experiments Mp15 and Mp16, despite the use of an opaque ice block. This saw multiple behavioural modes (e.g. floating particles and sinking particles), and the development of an extensive area of surface melt. In contrast with previous experiments, the basal meltwater pond was small and developed across the entire extent of the basal ice. Although experiment Mp17 provided an insight into the behaviour of microplastics within an opaque ice system, the central focus of illumination (and, therefore, highest concentration of particles) was on the most transparent section of the ice. Therefore, it would be useful to conduct a repeat experiment on a more opaque ice block.

A repeat experiment (Mp19) confirmed these findings. This was conducted on a more opaque ice block, but results were predominantly consistent with those from experiments Mp15, Mp16, and Mp17. This showed the development of a surface meltwater pond from floating particles, and the downwards movement of particles. As in all other experiments involving a scattering of multiple

particles, the surface meltwater from individual particle meltwater ponds initially scarred the ice surface. However, in other experiments this eventually combined to form large volumes of meltwater, whilst experiment Mp19 retained a scarred surface for the experiment duration (Figure 6.35). As cross-sectional imaging of the ice was challenging due to the opaque nature, only a small number of downwards moving particles were identified. These moved through the ice with particle velocities of $4.97 \times 10^{-7} \text{ m s}^{-1}$, $5.97 \times 10^{-7} \text{ m s}^{-1}$, and $6.39 \times 10^{-7} \text{ m s}^{-1}$.

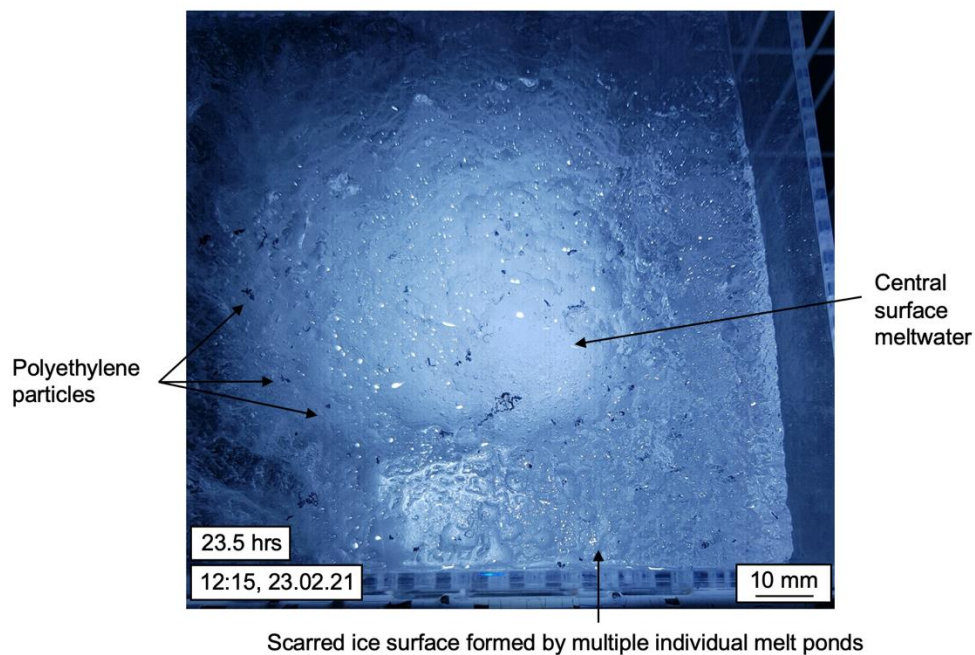


Figure 6.35. Plan-view photograph of the surface meltwater and scarred surface in experiment Mp19.

6.8. Conclusions

Multiple behavioural modes were observed when investigating microplastic particle-ice interaction (i.e. floating and sinking behaviour), although floating was the dominant behaviour. This was attributed to low particle densities, as described in Chapter 4, and surface tension effects holding intermediate density particles (e.g. polyethylene) at the ice surface. A low particle density also facilitated an upwards movement of embedded particles (e.g. experiments Mp6 and Mp13). A scarred ice surface was created in experiments with multiple microplastic particles, similar to those observed when investigating multiple volcanic particles in Chapter 5.

The floating behaviour of the microplastic particles facilitated the development of a surface meltwater pond. This varied in morphology and volume depending on the number of particles, the morphology of the particle, and the thermal environment. For example, a greater number of absorbing surfaces within the ice resulted in a greater volume of associated ice melt. Additionally, it was noted that elongate microplastic particles (e.g. approximately 1 mm wide, associated with the polyethylene particles) were faster at initiating ice melt, compared to spherical particles with a 5 mm diameter (e.g. polypropylene). Logically, a larger surface meltwater pond was associated with a warmer thermal environment; however, this was also typically associated with drainage events due to a wider vein network.

The irregular surface meltwater pond morphology provided an insight into the heat transfer mechanisms that initiated melting. For example, the initial morphology of the meltwater pond typically matched the microplastic particle shape (suggesting conduction-driven melting). This developed into a circular morphology through the establishment of meltwater convection. However, lateral movement of particles within surface meltwater was common. This modified the surface meltwater morphology to create an elongated pond (e.g. experiments Mp9, Mp11, Mp14, etc.). This increased the meltwater volume in a stable (warm) thermal environment and indicated the likelihood of redistribution of particles on the ice surface. Additionally, a wider meltwater pond was associated with a scattering of microplastics due to accumulation of particles.

7. Discussion

Experimental work presented in Chapters 4, 5, and 6 was designed to improve understanding of the physical processes associated with particle-ice interaction. Many micro-scale processes were observed through time-lapse imagery and in-person analysis of the experimental system. Chapter 7 will highlight key findings from experimental work and provide discussion of the processes identified, comparing these processes to the natural system and literature. The three overarching themes that have formed the structure of the thesis (i.e. the role of particle properties, the behaviour of volcanic particles, and the behaviour of microplastic particles) will be briefly summarised (Figure 7.1). Limitations to experimental design and implications for results have been considered throughout the presentation of results and the subsequent discussion.

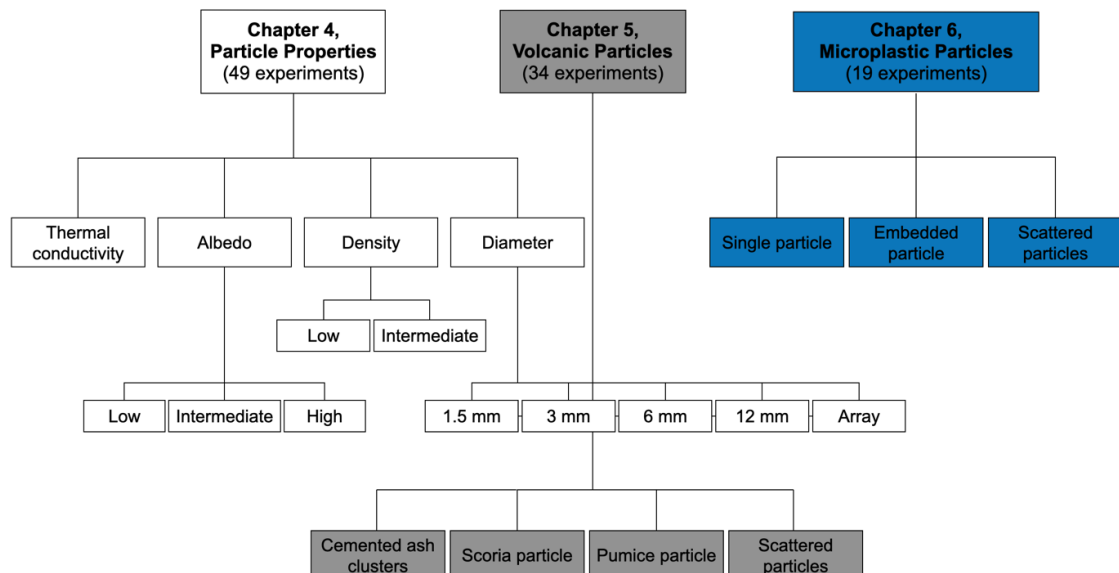


Figure 7.1. Hierarchy of the themes investigated in the experimental Chapters 4, 5, and 6. The ‘thermal conductivity’ theme was embedded throughout the thesis.

Chapter 4 sought to determine the role of particle properties in influencing particle-ice interaction, predominantly on an individual particle scale. This described a series of control experiments that mapped the influence of particle thermal conductivity, albedo, density, and diameter on ice melt (Table 7.1) as a systematic review of these properties is lacking in the published literature. Chapter 4 revealed a range of complexities associated with particle-ice interaction and formed the basis of interpretation for Chapter 5 and Chapter 6

(Figure 7.2). Therefore, many findings from Chapter 4 can be applied to specific particles within the natural system.

Table 7.1. Summary of key findings for properties investigated experimentally in Chapter 4.

Particle property	Summary
Thermal conductivity	<ul style="list-style-type: none"> • Important in initialisation of melt as thermal conductivity dictates the strength of convective heat losses from the particle to the atmosphere. • Controls the heat transfer mechanism. For example, thermally conductive particles can directly melt underlying ice at the particle base, whilst thermally insulating particles can indirectly melt ice through convection of air or water (driven from the absorbing top particle surface).
Albedo	<ul style="list-style-type: none"> • Influences the rate of particle motion within ice (used as a proxy for ice melting rate). • Results compare well with results from Hobbs (2014) that lower albedo particles produce increased ice ablation relative to higher albedo particles. However, little differences between a low and intermediate albedo particle were observed; for example, average particle velocities had approximately 4.0% difference between velocities ($1.84 \times 10^{-6} \text{ m s}^{-1}$ and $1.76 \times 10^{-6} \text{ m s}^{-1}$ for 0.12 and 0.50 albedo particles, respectively). However, the number of experiments using an intermediate albedo particle was limited to four within a stable (warm) thermal environment, likely contributing to a higher velocity than a low albedo particle used in experiments across a range of thermal environments. • A high albedo (0.60) brass particle had an average particle velocity approximately one order of magnitude slower than a low albedo (0.12) brass particle of the same size, e.g. $\sim 10^{-7} \text{ m s}^{-1}$ compared to $\sim 10^{-6} \text{ m s}^{-1}$, respectively.
Density	<ul style="list-style-type: none"> • Becomes important when sufficient volumes of meltwater have been produced to facilitate either floating or sinking behaviour. Therefore, important when considering changes in heat transfer mechanisms between a surface and embedded particle. • Can act as a particle sorting mechanism as a high density enables movement of particles into the ice, and a low density allows redistribution and runoff of particles when floating in meltwater.
Diameter	<ul style="list-style-type: none"> • Controls the thermal pathway length through a spherical particle and how heat is transferred into the ice. • Smaller particles are unable to melt the ice to the same extent as a larger particle at cooler temperatures, despite a shorter thermal pathway and efficient heat transfer. This is proposed to be due to larger particles retaining a convective component of heat transfer at lower temperatures. This effect is observed with thermally conductive particles as the effects of a long thermal pathway are masked with particles with a low thermal conductivity. • Has a control on the particle sphere of influence, i.e. larger particles are associated with a larger meltwater volume, although this is proportionate to the particle size. This compares well with suggestions by Bazhev (1975).

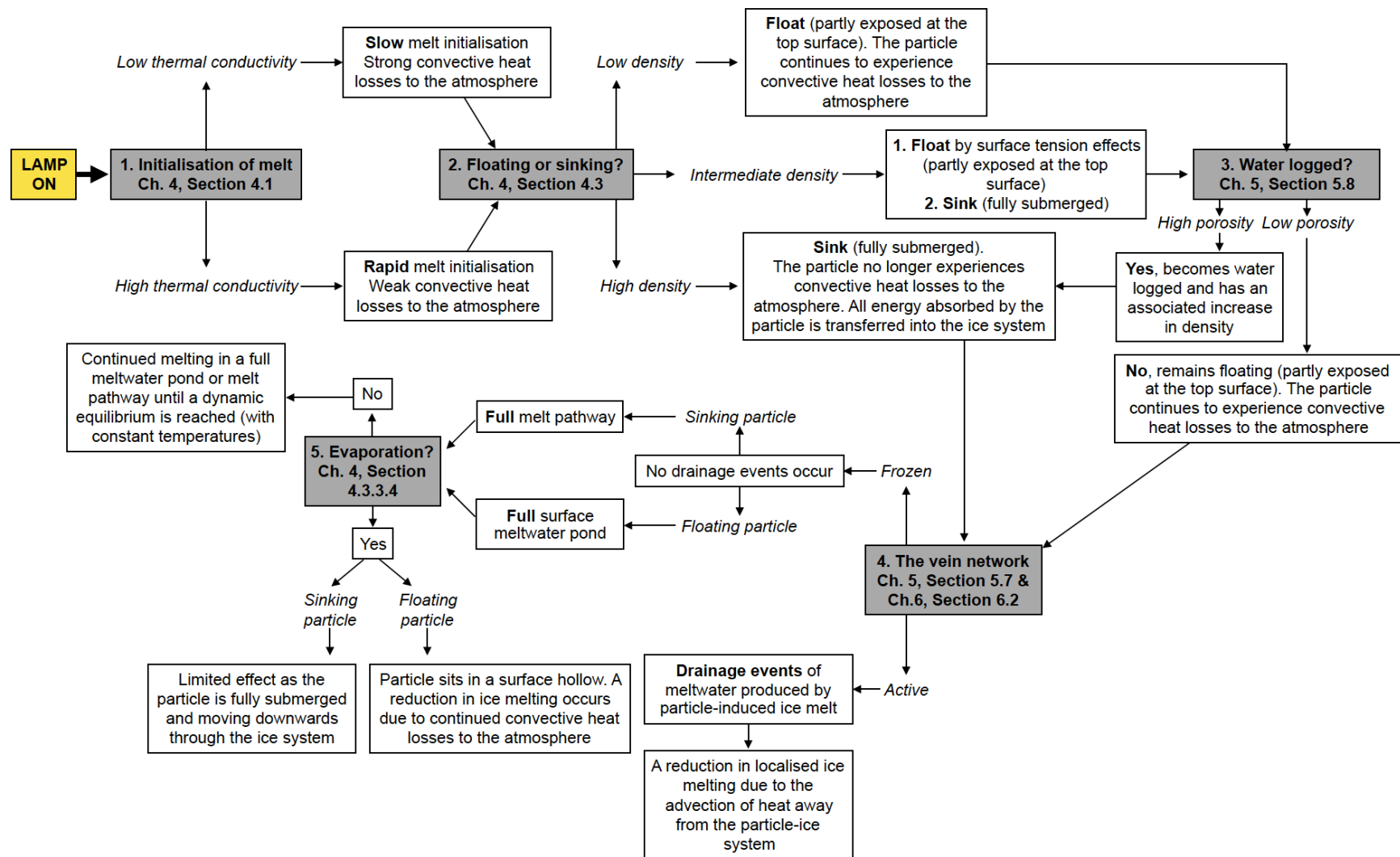


Figure 7.2. Flow diagram of some of the main the processes associated with particle-ice interaction for a particle initially placed on an ice surface, identified in experimental work.

A systematic assessment of the ice-particle behaviour of illuminated volcanic particles on and within ice was conducted (Chapter 5) as few studies had systematically investigated this in a controlled environment (e.g. Hobbs, 2014; Dragosics et al., 2016, Chapter 2). Experimental results from Chapter 5 supported existing knowledge in the literature as a wide range of behaviours and processes were noted, reflecting the variability of particle properties associated with volcanic material in the natural system (Möller et al., 2016). Experimental work improved understanding of micro-processes associated with volcanic particle-ice interaction. Some findings are noted here:

- (1) The melt pathway width exceeded the particle diameter, contrasting with results from thermally conductive particles (e.g. control metal particles used in Chapter 4).
- (2) Volcanic particles experienced loss of fine-grained material (e.g. <0.5 mm) from the particle surface, introducing absorbing surfaces into the ice and facilitating an increased volume of melting.
- (3) Particle fragmentation at the particle base was observed with all volcanic particles following saturation.
- (4) Smaller volcanic particles (e.g. < 3 mm) were associated with higher particle velocities relative to larger particles (e.g. > 6 mm). This contrasted with results for thermally conductive particles.

These experimental results demonstrate that volcanic particles can effectively melt ice in dirty ice conditions to float in surface meltwater ponds or melt downwards into the ice (e.g. particle velocities within the range of 7.03×10^{-7} – $1.40 \times 10^{-6} \text{ m s}^{-1}$). This contrasts with literature considering thick debris-covered ice conditions, where volcanic particles are typically viewed as ‘insulating’ (Kirkbride and Dugmore, 2003) and there has been no mention of downwards moving particles. However, general results are consistent with the limited number of fieldwork studies considering dirty ice/snow conditions, e.g. Brock et al. (2007) observed a 97% increase in ablation under a discontinuous layer of volcanic material relative to bare snow. Additionally, research in this thesis suggests that effective ice melt is likely exacerbated by the fact that a single volcanic particle is rarely a ‘single’ particle (e.g. through the addition of fine-

grained particles (< 0.5 mm) from the particle surface, and volcanic particle fragmentation within ice).

Research into the behaviour of microplastic particles within the cryosphere is at an early stage, with much of the published literature focusing on quantifying volumes and types of microplastics found (e.g. Ambrosini et al., 2019; Bergmann et al., 2019; Cabrera et al., 2020; Kelly et al., 2020; Stefánsson et al., 2021; Zhang et al., 2021). As such, experimental work in Chapter 6 provided new insights into microplastic-ice interaction. This work demonstrated the ability of embedded plastics to move upwards through ice to re-emerge at the ice surface, the likelihood of redistribution of particles on the ice surface, and the importance of surface tension in influencing particle behaviour. These processes are all important to consider when studying contamination of freshwater supply and movement of microplastics within the environment.

7.1. The melting processes

Laboratory experiments of particle-ice interaction provided an insight into the melting process via detailed observations. Results distinguished two key stages in particle-induced ice melt when considering dense particles: the initialisation of melt (i.e. surface behaviour) and melting within the englacial environment (i.e. sub-surface behaviour). The latter confirmed suggestions discussed by Evatt et al. (2016) where englacial warming due to solar absorption by buried particles was possible and evolves understanding of particle-induced ablation in dirty ice conditions (i.e. occurring on and within ice).

7.1.1. Initialisation of particle-induced ice melt

The initialisation of melting refers to the first stage in the melt process. This was largely dependent on: (1) the particle albedo, as this determined the amount of energy absorbed by the particle (for example, a high albedo (0.60) particle initiated melting within approximately 9 hours on average, whilst melting by a low albedo (0.12) particle was within the first five minutes), and (2) the particle thermal conductivity, as this dictated the extent of energy absorbed that could interact with the ice to cause ice melt. These findings were generally in

accordance with processes described in the literature (e.g. Kayastha et al., 2000). However, the role of albedo was less important than hypothesised, as melt was induced by particles with low, intermediate, and high albedos (Chapter 4 and Chapter 5), with only a 4.3% difference between average particle velocities of a LA (0.12) and IA (0.50) particle. Therefore, it was deduced that a particle would be capable of inducing ice melt unless it was a perfect reflector (i.e. an albedo of 1 and could not absorb any incoming solar radiation) or could not conduct heat sufficiently (a function of particle diameter and thermal conductivity). Although these findings agreed with the literature, additional complexities associated with particles moving into the ice were observed in experimental results.

7.1.2. Melting in the supraglacial and englacial environment

Aside from a limited number of experiments (Hobbs, 2014; Evatt et al., 2016; Hénot et al., 2021), the behaviour of embedded particles within ice (i.e. in the englacial environment) has not been investigated in the literature and is rarely considered an important environment for ablation. However, a key finding of experimental work in this thesis is an observed behavioural change once a particle became fully embedded within ice and submerged in meltwater (Table 7.2) to increase the particle-induced ice melt rate.

Once within the englacial environment, all heat absorbed by a particle is transferred into the ice, although the extent of subsequent ice melt is controlled by the thermal environment. In conditions that allow ice melt, experimental work showed that the englacial environment facilitates an increase in the rate of particle-ice interaction due to the removal of convective heat losses to the atmosphere (e.g. experiment P14 showed the IA brass particle velocity increased from 0 m s^{-1} for 70 hours to $2.36 \times 10^{-6} \text{ m s}^{-1}$ once convective heat losses to the atmosphere were removed, Chapter 4). As the particle density dictated if a particle would float (e.g. pumice, microplastics) or become submerged (e.g. scoria, iron-based meteorites) in meltwater following the initialisation of melt (Figure 7.2), it was noted that the particle density was a controlling property involved in this stage of the melting process, despite this

attracting little attention in the existing literature (e.g. with the exception of Hobbs, 2014).

The ice surface, analogous to the supraglacial environment, was a 'melt-limiting' environment relative to the englacial environment, particularly in the case with melt-limiting particle properties (e.g. low thermal conductivity and high albedo). For example, a surface particle may be unable to induce ice melt whilst a submerged particle of the same type may induce melting at the same temperatures within the same period. This process is exacerbated with cooler temperatures as more energy input is required to raise the proximal ice to 0°C to induce ice melt. The implication of this in the natural system is that it may be possible for particle-induced ice melt to occur within the photic zone of the englacial environment, to produce meltwater that causes ice mass loss through runoff, despite surface conditions suggesting little ice melt is possible. Therefore, the englacial environment must also be considered when predicting future changes to global ice mass and runoff patterns.

Table 7.2. Summary of key processes associated with a combination of particle properties and the shift in behaviour from a surface particle to a submerged particle. ¹Evatt et al. (2016), ²Labus and Labus (2018), and ³Opeil et al. (2012).

Particle properties	Example particle	Supraglacial environment	Englacial environment
<ul style="list-style-type: none"> • High thermal conductivity • High density 	Iron and stony-iron meteorites ¹ , igneous rocks, sedimentary rocks ² , metamorphic rocks ² , rocks with high quartz content (e.g. quartzite, sandstone) ²	Fast initialisation of melt through direct melting of ice.	Weak convection of meltwater to create a narrow melt pathway that mimics the particle diameter.
<ul style="list-style-type: none"> • Low thermal conductivity • High density 	Volcanic particles (e.g. wet scoria, wet pumice), typically fine-grained sedimentary rocks (e.g. claystone and siltstone) ¹ , stony meteorites ³	Slow initialisation of melt due to strong convective heat losses to the atmosphere.	Strong convection of meltwater to create a melt pathway approximately double the particle diameter.
<ul style="list-style-type: none"> • Low thermal conductivity • Intermediate density 	Microplastics (e.g. Delrin®, polyethylene) Volcanic particles (depending on the vesicularity of particles)	Susceptible to external influence, e.g. surface tension effects.	Possibility of full submergence of the particle in meltwater dependent on surface tension effects. Strong convection of meltwater to create a melt pathway approximately double the particle diameter.
<ul style="list-style-type: none"> • High thermal conductivity • Low density 	No suggested examples	Production of a large surface meltwater pond. Floating particle and lateral movement can extend this.	Possibility of the particle becoming fully embedded in the englacial environment following an accumulation season. This was not considered experimentally.
<ul style="list-style-type: none"> • Low thermal conductivity • Low density 	Volcanic particles (e.g. dry pumice), microplastic particles (e.g. polypropylene, polystyrene, etc.)	Ice melt to produce a surface meltwater pond. The extent of meltwater is dependent on the thermal regime and ice temperatures. Any runoff of meltwater will likely prevent further ice melt as melting is dependent on convection currents within the meltwater.	Saturation of porous particles (e.g. pumice) leading to an increase in density and full submergence of the particle in meltwater. Strong convection of meltwater to create a melt pathway approximately double the particle diameter. Burial of low-density particles within ice from the accumulation season; this may lead to an upwards movement of low-density particles able to absorb incoming solar radiation during the ablation season.

The differences in behaviour associated with particles within a supraglacial and englacial environment highlight simplifications and limitations of some assumptions involved in modelling debris-covered and dirty ice. For example, a common assumption is that particle properties are constant spatially and temporally during the modelled ice ablation period (e.g. Nakawo and Young, 1981). However, experimental work in this study demonstrates that the relative impact of each property varies depending on the glacial environment. For example, thermal conductivity has an important role in the supraglacial environment, whilst particle density has an important role in determining movement to the englacial environment. Additionally, temporal changes to particle properties are likely: for example, saturation of pore spaces can lead to an increase in particle density (e.g. observed in Chapter 5) and particle thermal conductivity (Juen et al., 2013). Additionally, the movement of particles into the englacial system is not taken into consideration within ablation models, and the englacial environment has been shown to be crucial in particle-ice interaction.

7.1.3. Thermal environment

Much of the cryosphere exists within a sensitive threshold of temperatures, where the ice is close to the phase transition of melting, i.e. the pressure melting point, PMP (Colombo et al., 2019). Experiments in this thesis investigated the sensitivities of the thermal state of the ice in the proximity to foreign particles (defined in experimental work as the thermal environment, Figures 7.3 and 7.4). The thermal state ultimately controls the extent of ice that can be warmed into the unstable state in response to heat transfer from a particle into ice. The following key findings were noted.

- (1) At PMP, particle-induced ice melt occurs if there is illumination (e.g. solar radiation).
- (2) At cold temperatures, or with no illumination (analogous to night conditions), there is no particle-induced ice melt.
- (3) Between the PMP and cold states there is a stable equilibrium melt pond or melt pathway created by particle-induced ice melt with a volume that scales with temperature. For example, average basal meltwater extent was a factor of approximately 4 and 1.3 wider and higher, respectively, in a stable (warm) thermal environment compared to stable (cool)

environment. Additionally, average surface meltwater extent was a factor of approximately 3 and 2.6 wider and deeper, respectively, in a stable (warm) thermal environment compared to stable (cool) environment.

Note that these comparisons are between particles of the same type and morphology.

- (4) Refreezing processes only occur with moving particles (e.g. teardrop morphology) between PMP and cold states, whilst stationary particles achieve an equilibrium with their surroundings (as above).
- (5) Drainage from melt ponds may modify the described thermal processes by the advection of water and energy (e.g. advection of heat through draining meltwater in experiment P13 reduced the IA particle velocity from $1.46 \times 10^{-6} \text{ m s}^{-1}$ to 0 m s^{-1}).
- (6) The thermal environment experienced by particles is partly dependent on particle properties.

The implications of diurnal cycles on the findings discussed above are that in the natural environment, fluctuations in particle behaviour (and, therefore, the volume of meltwater) would occur in response to temperature fluctuations. This would be represented by a fluctuation between particle-induced ice melt and no melting (i.e. points (1) and (2) above), rather than the development of a stable equilibrium system (as described in point (3) above).

7.1.3.1. Particle-ice equilibrium

The findings of this study support those of Reznichenko et al. (2010), who noted that particles that were not subjected to diurnal cycles could establish a steady-state conduction and equilibrium (e.g. with a stable meltwater volume). This was not achieved when diurnal cycling occurred (Reznichenko et al., 2010). Although temperature cycling processes (e.g. diurnal cycles) that occur in the natural system were not considered experimentally in work presented in this thesis, results indicated that the time-taken for equilibrium systems to establish ranged 3-23 hours, taking nine hours on average. As the average value is on a shorter time-frame than the ablating component of diurnal cycles (i.e. approximately 12 hours), it is possible for an equilibrium between particle and ice to be achieved in the natural environment when considering individual and

small (e.g. <12 mm) particles. However, it is likely that the presence of temperature cycling would end equilibrium systems once established (e.g. moving into a stable (cold) environment as observed in many experiments in this thesis, analogous to night conditions). This confirms discussion in the literature that dirty ice conditions facilitate thermal equilibrium on a faster timescale than conditions with particle layering due to the small heat capacity of individual/widely dispersed particles (Nicholson and Benn, 2006). This is important as many ablation models assume a state of thermal equilibrium (Nakawo and Young, 1981; Rana et al, 1997; Kayastha et al., 2000; Han et al., 2006; Nicholson and Benn, 2006, etc.).

7.1.3.2. Deviations from PMP

Results of this study additionally demonstrate that the assumption in dirty ice modelling that the ice is at PMP (i.e. 0°C or classed as in the unstable thermal environment as defined in this thesis) generalises the behaviour of particle-ice interaction (Section 2.3.4, Chapter 2). Including this assumption in models will likely lead to an overestimation of predicted melting of glaciers as experimental work presented in this thesis has indicated large shifts in particle-ice behaviour through subtle changes in temperature (in stable (warm), stable (cool), and stable (cold) thermal environments). For example, brass, cemented ash clusters, scoria, and Delrin® particle velocities (used as a proxy for ice melt rate) within a stable (warm) thermal environment were on average a factor of 1.29, 9.74, 1.74, and 2.50 higher, respectively, than those conducted within a stable (cool) thermal environment. Therefore, subtle changes in the temperature can modify the outcome of particle-ice interaction and so it is suggested that dirty ice models should consider these processes and deviations from the ice PMP to give an accurate prediction of melt and better understanding of dirty ice response to climate change.

7.1.3.3. Refreezing of meltwater

Refreezing of meltwater in the proximity of a particle was observed in many experiments, contrasting with a common assumption involved in debris-covered and dirty ice models (e.g. Evatt et al., 2015). These models generally assume

that meltwater leaves a debris layer immediately after being produced (e.g. through run-off) and does not have an impact on energy exchange processes through phase changes (e.g. evaporation or refreezing). However, studies have demonstrated that this assumption can lead to an overestimation of modelled ablation (e.g. Rounce et al., 2015). The importance of this was confirmed in experimental work in this thesis as refreezing processes were a common observation in many experiments and would likely occur in natural systems due to natural temperature cycles (e.g. diurnal cycling). This highlights the need to quantify the effect of refreezing processes when modelling ablation arising from particle-ice interaction as it is a common process involved in dirty ice conditions.

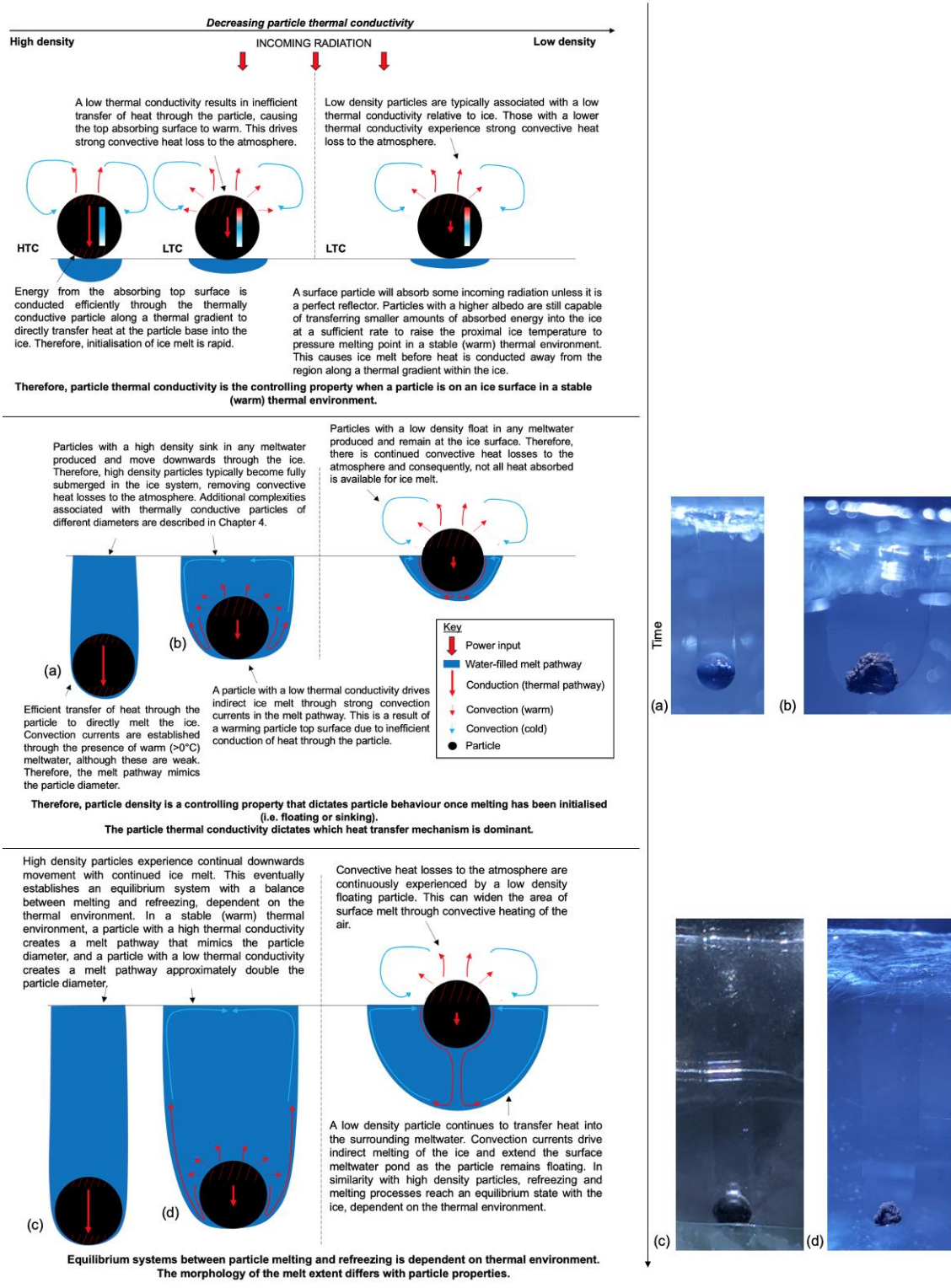


Figure 7.3. The association between particle properties and a stable (warm) thermal environment, where HTC is 'high thermal conductivity' and LTC is 'low thermal conductivity'. Conduction of heat away from the particle proximity through the ice is not considered in this figure as this does not prevent particle-induced ice melt in the particle proximity.

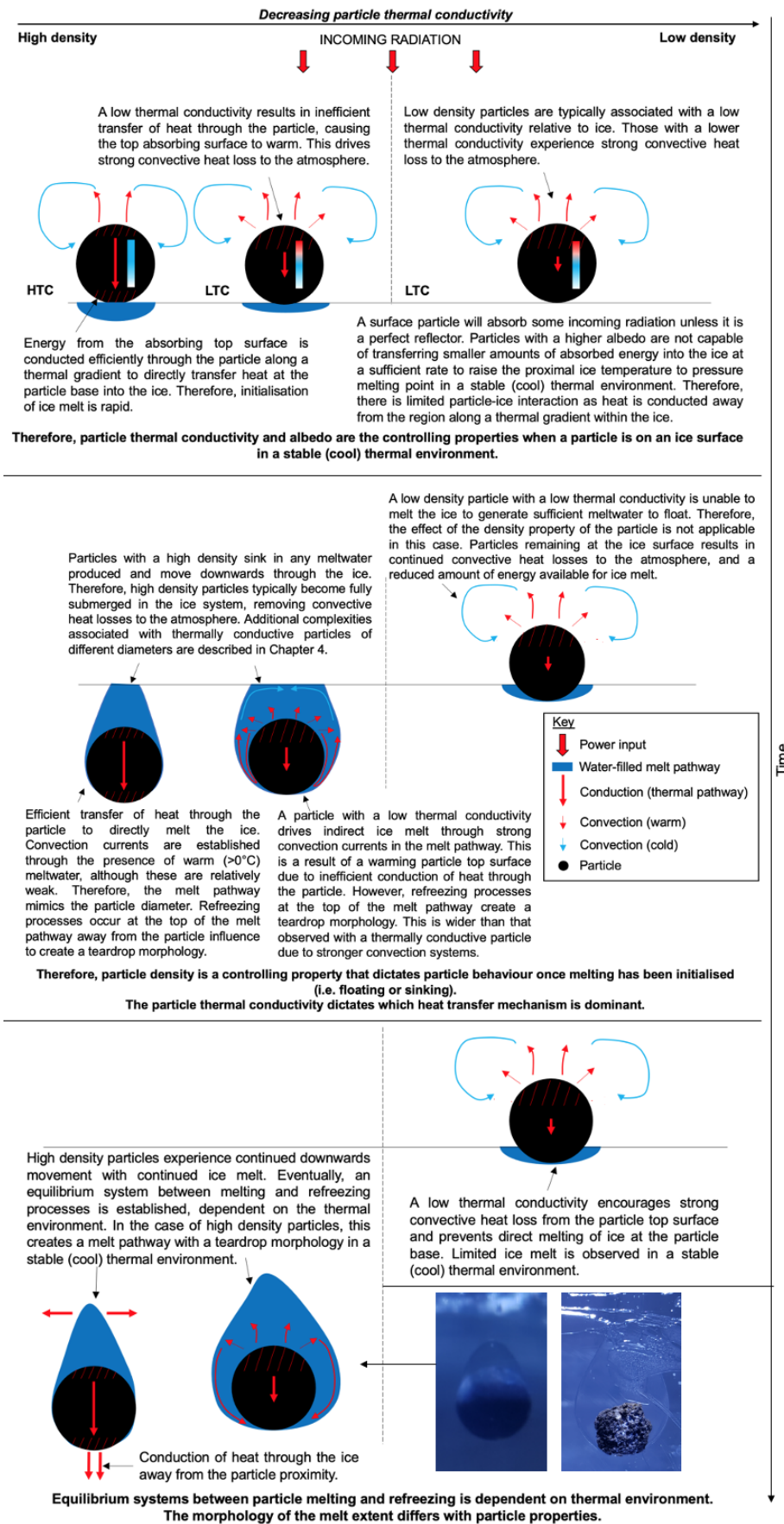


Figure 7.4. The association between particle properties and a stable (cool) thermal environment, where HTC is ‘high thermal conductivity’ and LTC is ‘low thermal conductivity’.

7.2. Other ablation processes

7.2.1. Sublimation

Although sublimation is not considered a major contributor to ablation of glaciers on Earth, it is a process that is experienced in many regions. For example, in the Dry Valleys (Fountain et al., 2006) and blue ice areas (Bintanja, 1999) in Antarctica, and in many tropical glaciers confined to high altitudes (e.g. 5000 m or higher), as these regions are associated with optimal sublimation conditions (warm surface, dry air, and strong winds, Harvey et al., 2001). Therefore, sublimation as a process cannot be overlooked when considering glacier ablation. Prior studies have also indicated the importance of sublimation in the formation of 'zenn stones' in the environment (e.g. Hobbs, 2014; Taberlet and Plihon, 2021). This occurs with a combination of ice surface lowering and the blockage of ice surface water molecule escape by a surface particle to form an ice pedestal on which the particle sits. Experimental results presented in this thesis (e.g. experiment M24, Appendix 6, and experiment P1a, Chapter 4) supported this general process of pedestal formation. In particular, results supported key findings by Hobbs (2014) and Taberlet and Plihon (2021) where it was noted that particle properties did not appear to have an influence on the sublimation process. In the case of the experimental work in this thesis, pedestal formation occurred under the most 'efficient' ablating particle (e.g. a low albedo and high thermal conductivity), indicating that particle properties had little influence in strong sublimating conditions.

Insights gained from Chapter 4 demonstrated that, in addition to causing a surface lowering, sublimation conditions were also associated with an ice surface cooling (e.g. experiment P1a in Chapter 4, Section 4.1.1). It is generally agreed that optimal sublimation conditions in the natural system typically involve strong winds (Stigter et al., 2018) as this removes the capability for water deposition processes to offset sublimation processes; this is similar to conditions in experiment P1a and method development experiments presented in this thesis as the experimental design included a fan to circulate air within the freezer (e.g. Figure 4.2 in Chapter 4). It is common in windy environments for the sublimation rate to exceed the deposition rate, demonstrating the role of forced convection on ablation (Dundas and Byrne, 2009). When considering

this as a balance of heat transfer processes, this preferentially drives ice surface cooling as the rate of heat removed through sublimation will exceed the rate of heat gained through deposition. This effect was revealed in this study, where experiments without a glass cover over the ice demonstrated that sublimation conditions could hinder melting processes that would otherwise occur from particle-ice interaction. This was likely due to sublimation cooling encouraging a strong thermal gradient in the ice that conducts heat away from the particle prior to heat transfer raising the ice temperature to PMP.

7.2.2. Evaporation

A small number of experiments in this study suggested the role of evaporation processes in controlling the melt process. It was noted that a surface meltwater pond formed if the atmospheric relative humidity was high (e.g. assumed to be 100%) in the closed controlled experimental system. However, a particle of the same type (e.g. 6 mm brass particle) sat in an empty hollow when the atmospheric relative humidity was low (e.g. 37% as observed in experiment P15). These findings can be upscaled to the natural system: for example, the latter conditions can be encouraged by wind reducing relative humidity in the proximity of the particle. Therefore, secondary experimental insights confirm the well-established fact that wind across ice surfaces in the natural environment has an influence on particle-ice interaction (Ohno et al., 1992). This is also of particular importance when considering ablation on glaciers and ice sheets in arid environments as this encourages evaporation processes.

7.3. Ice structure and hydrology

The vein network within ice can exist below 0°C (Price, 2007); therefore, this has a dominant impact on particle-ice interaction and can facilitate multiple processes within ice, as listed here.

- (1) Particles can utilise the vein network within ice to move along pre-existing weaknesses through the ice. Therefore, the vein network is a key control on the direction of particle movement. This process is more 'active' in stable (warm) thermal environments due to the growth of the vein network with warmer temperatures (Price, 2007).

- (2) The vein network can cross-cut meltwater production zones (termed 'melt pathways' in experimental work in this thesis), leading to drainage events and melt pathway morphology changes. This was confirmed in all themes of experimental work (e.g. experiment P13 in Chapter 4, experiment V12 in Chapter 5, and experiment Mp12 in Chapter 6).
- (3) The vein network can facilitate widespread rapid movement (e.g. 45 mm within a single time-lapse frame (a period of five minutes) observed in experiment Mp6) of any particle smaller than the vein diameter, as observed in embedded microplastic experiments (Chapter 6). This was observed in multiple instances for microplastic particles < 5 mm in diameter, and it is suggested that this process would be exacerbated with warmer ice due to a widening of the vein network.
- (4) An increase in drainage events is associated with relatively warm thermal environments. This is suggested to be due to active vein networks enabling the drainage of meltwater due to the formation of hydrological connections between the veins and the particle-ice system. These form more readily in warmer temperatures (e.g. experiment V21, Chapter 5).

7.3.1. Modifying the internal ice structure

Experimental work in this study demonstrated that refreezing of meltwater from changes to the thermal environment and drainage events can modify the englacial structure of the ice (e.g. by creating small-scale bubble trails (e.g. approximately 1 mm in size) or gas-spaces). Drainage events were closely related to the ice structure and the vein network, agreeing with findings from Benn et al., (2012) where it was noted that the englacial structure had a key control on supraglacial lake drainage and surface ablation rates. Drainage processes typically modify the optical properties of the ice by introducing gas spaces and, consequently, produces interfaces with strong refractive index contrasts. Drainage from a closed melt pathway in experimental work in this study were small-scale (e.g. <30 mm) features analogous to 'englacial voids', described by Benn et al., (2012), which are susceptible to collapse and can initiate the formation of a supraglacial lake. Therefore, the englacial environment can play a crucial role in both supraglacial lake formation and drainage (Benn et al., 2012). Additionally, the coupling of supraglacial and

englacial processes will likely encourage ablation and downwasting processes; the coupling of these two environments is likely to be exacerbated with particle-ice interaction due to dense particles moving into the englacial system and linking the supraglacial and englacial environment by the formation of small-scale channels, as demonstrated in experimental work in this study.

7.3.2. Particle-particle interaction

Experimental work in this study provided an insight into the behaviour of particle-particle interaction (e.g. experiments P3 and P13, Chapter 4). This demonstrated the possibility of hydrological connections forming between particles. This noted that small-scale ice hydrology can override particle behaviour through the advection of heat away from a particle-ice system (for example, the advection of heat away from an intermediate albedo particle in experiment P13 reduced particle movement from an average of $1.46 \times 10^{-6} \text{ m s}^{-1}$ to 0 m s^{-1}). This provided insights into questions raised by Fountain et al. (2004), where the possibility of connections between particle-induced ice ablation features was posed (e.g. cryoconite holes). Particles often interact in nature (Fountain et al., 2004), and so it is likely that hydrological connections form between englacial and supraglacial debris. This is likely to result in some debris becoming stranded within the ice (e.g. as demonstrated by experiment P13b, Chapter 4) and other debris being washed out, highlighting an additional complexity associated with particle-ice interaction and the fate of foreign particles in ice systems.

7.4. Sorting mechanisms of particles within ice

The interpretation of a systematic series of particle-ice experiments with particles of various properties (e.g. particle thermal conductivity, albedo, diameter, and density), previously lacking in the literature, improved understanding of how individual properties influence the behaviour of particle-ice interaction. This indicated several modes of sorting processes of particles within ice, largely dependent on the particle properties (Figure 7.5).

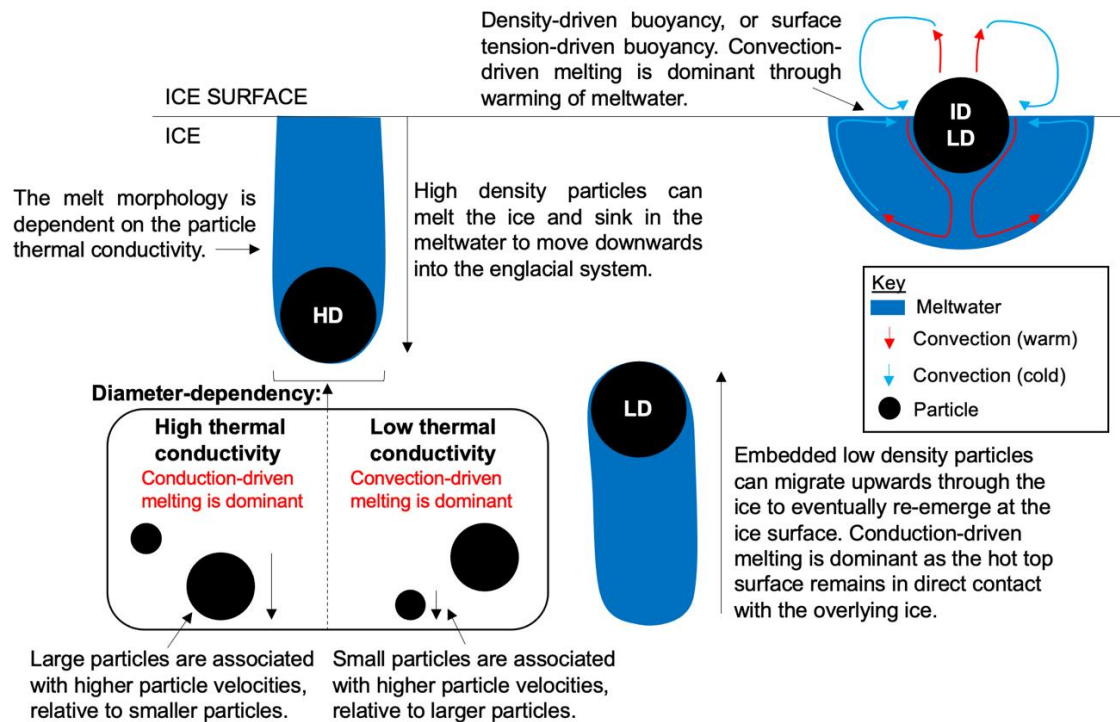


Figure 7.5. Summary diagram of sorting mechanisms of particles within ice, where: HD is high density, ID is intermediate density, and LD is low density. Spherical particles are depicted for simplicity.

7.4.1. Sorting of dense particles

The fundamental behaviour of dense particles observed in 65 experiments in this study compared well with the results of Hobbs (2014), Evatt et al. (2016), Hénot et al. (2021), and Taberlet and Plihon (2021), where it was demonstrated that surface particles can sink into ice if sufficiently dense (e.g. iron-based meteorites, volcanic particles such as scoria, igneous particles such as granite, dense plastics, etc.). Experimental work in Chapters 4 and 5 provided detailed insights into the mechanism of sinking particles. This indicated that some downwards movement of particles was possible across the entire range of particle properties investigated (e.g. high and low thermal conductivity, high and low albedo, and varying diameters, although the latter had associated complexities), suggesting that particle density is the dominant control on this behaviour. This process is important when considering possible meteorite-loss mechanisms within ice (Section 7.6.1), and the movement, and subsequent fate, of particles within an ice system (e.g. stratification of particles within the englacial environment). Additionally, in many cases, the process of sinking particles can contribute to the development of cryoconite holes (Section 7.6.2)

and a weathering crust (Section 7.6.3) due to differential ablation across an ice surface. Cryoconite holes, and other features formed by differential ablation and sinking particles, have a key control on the overall albedo of an ice system, which is strongly linked to the energy balance of the ice.

Experimental work in this thesis found that thermally conductive particles had a diameter-dependency to particle behaviour (Chapter 4). This behaviour is hypothesised to be a result of the particle area and distribution of heat transfer. Generally, heat transfer within an isothermal sphere is a function of the particle area ($4\pi r^2$ where r is radius; Holman, 2010). In the case of this experimental work, this property would mean that embedded smaller particles (e.g. < 3 mm) efficiently conduct heat absorbed by incoming radiation into the surrounding ice due to a short thermal pathway, whilst larger particles (e.g. > 6 mm) experience a warming top surface due to a long thermal pathway, driving strong convection processes (Figure 7.6). This difference in heat transfer was evident when all particles were embedded within the ice, and at cooler temperatures.

Experiments have demonstrated that the relationship between a particle and the melting behaviour is sensitive; therefore, it is suggested that in cooler environments, the absence of meltwater convection processes in the case of smaller (e.g. < 3 mm) particles can cause an embedded small particle to stall within the ice. However, it is important to note that the described processes occur with very subtle changes in temperature and heat transfer mechanisms. Thus, it has been identified by experimental work that subtle changes in temperatures around the PMP can result in large changes in behaviour. Therefore, there is a need to consider the effect of subtle temperature changes when attempting to model the behaviour or fate of particles on or within ice.

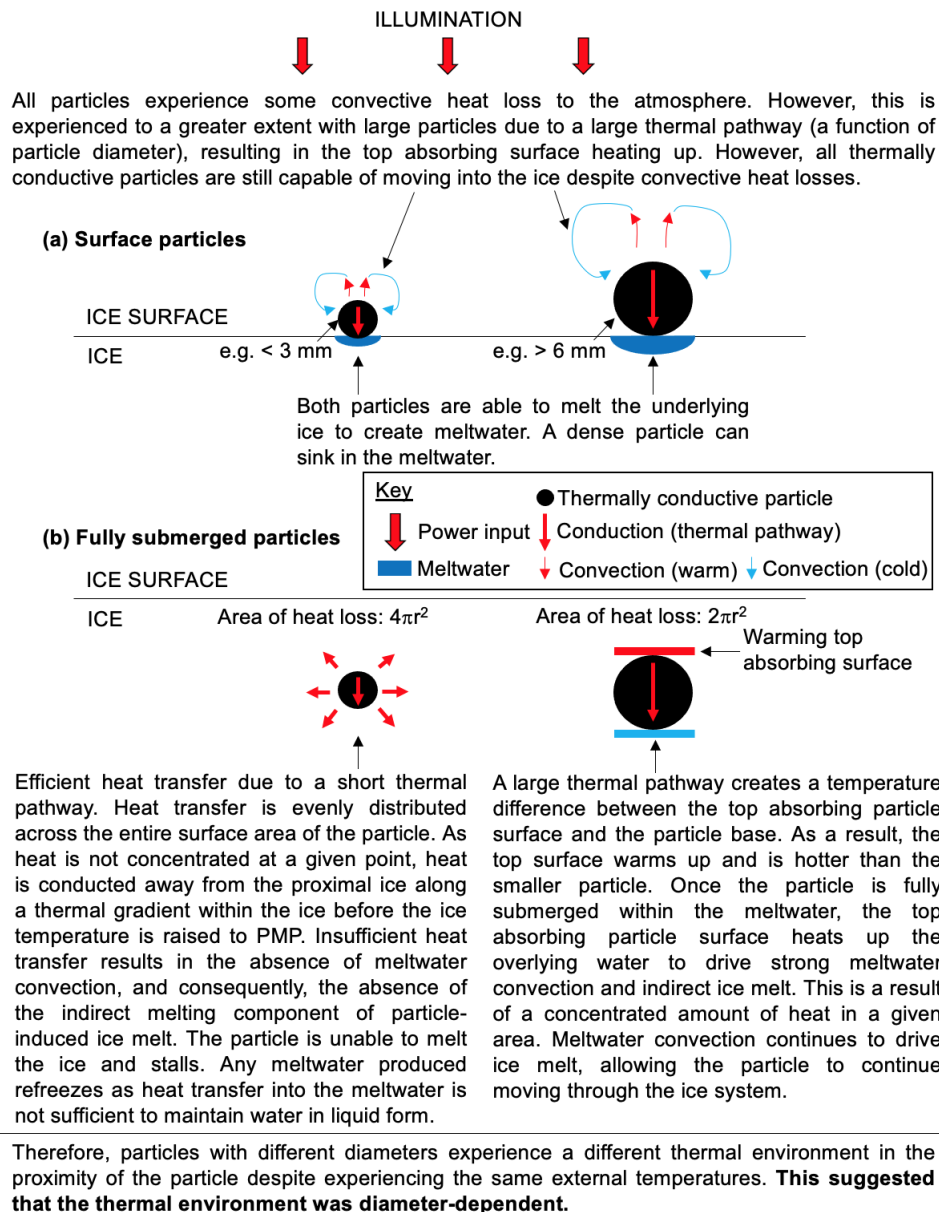


Figure 7.6. Working hypothesis for heat transfer mechanisms of particles of different sizes, showing the difference in heat transfer between (a) surface particles and (b) embedded particles. Meltwater is not included in panel (b) for simplicity.

Conversely, particles with relatively low thermal conductivities demonstrated the opposite behaviour, where smaller particles (e.g. $< 3\text{ mm}$) were associated with a higher particle velocity (used as a proxy for ice melt rate) relative to larger particles (e.g. $> 6\text{ mm}$). All particles with a low thermal conductivity experienced strong convective heat losses from the warm top absorbing particle surface, regardless of the particle diameter, and so the effect of reduced convective heat losses from the top surface on ice melt observed with thermally conductive particles was likely masked.

7.4.2. Sorting of buoyant particles

The density of a particle was another constraint on particle movement within ice. Low-density particles were confined to the ice surface (or close to the surface), whilst high density particles were able to move downwards through the ice. However, findings also demonstrated the capability of embedded low-density particles (e.g. microplastics) to melt the ice and move upwards to re-emerge at the ice surface. Experimental observations of this process added an additional mechanism to hypotheses used to explain the presence of a dark band of ice (with an albedo 0.12 lower than surrounding ice) that extends from 65°N to 70°N on the Greenland Ice Sheet (Wientjes et al., 2011; Tedesco et al., 2016). This region has been darkening since 1996, and Tedesco et al. (2016) suggested that this could, in part, be a result of ice ablation re-exposing underlying dirty ice conditions (e.g. cryoconite containing local dust particles with mainly quartz, feldspar, and plagioclase minerals, and algae; Wientjes et al., 2011).

In the natural system, the upwards migration of low-density embedded particles to reach an ice surface (Figure 7.7) could contribute to the darkening of ice regions, like that described on the Greenland ice sheet. It is suggested that this could cause previously buried particles (e.g. during an accumulation season) could become exposed on the ice surface. However, it is important to note that experimental conditions differed from the natural environment (i.e. experiments used visible illumination only, optically transparent ice, and an absence of diurnal cycles). In reality, the introduction of infrared radiation interaction with ice would likely encourage this process (e.g. as the ice would also be melting independently of particles), whilst the presence of bubbles within the ice may hinder the process. For example, drainage processes observed in experiment Mp6 prevented further upwards migration of low-density particles due to removal of the medium that facilitated movement. Additionally, overlying bubbles may shield the embedded particle from incoming solar radiation (although, control experiments investigating behaviours of particles within opaque ice systems indicated very similar behaviours to those within an optically transparent ice system, e.g. P48, V34, Mp17, and Mp19). Overall, the

capability of upwards particle migration in the photic zone (i.e. the uppermost surface of ice) has been demonstrated by experimental work in this study; this has not previously been acknowledged in the literature. Therefore, it is suggested that there are two processes of ice darkening, in addition to deposition of new particles: (1) re-exposure of buried particle by ablation as described by Tedesco et al. (2016), and (2) upwards migration of low-density particles, as demonstrated in this thesis. The implication of this is a continued reduction of ice albedo, independent of particle deposition on an ice surface, as particles migrate from the englacial to the supraglacial environment. This process, previously unmentioned in the literature, could contribute to the positive ice-albedo feedback that has been noted to be responsible for accelerated glacial recession (Yue et al., 2020)

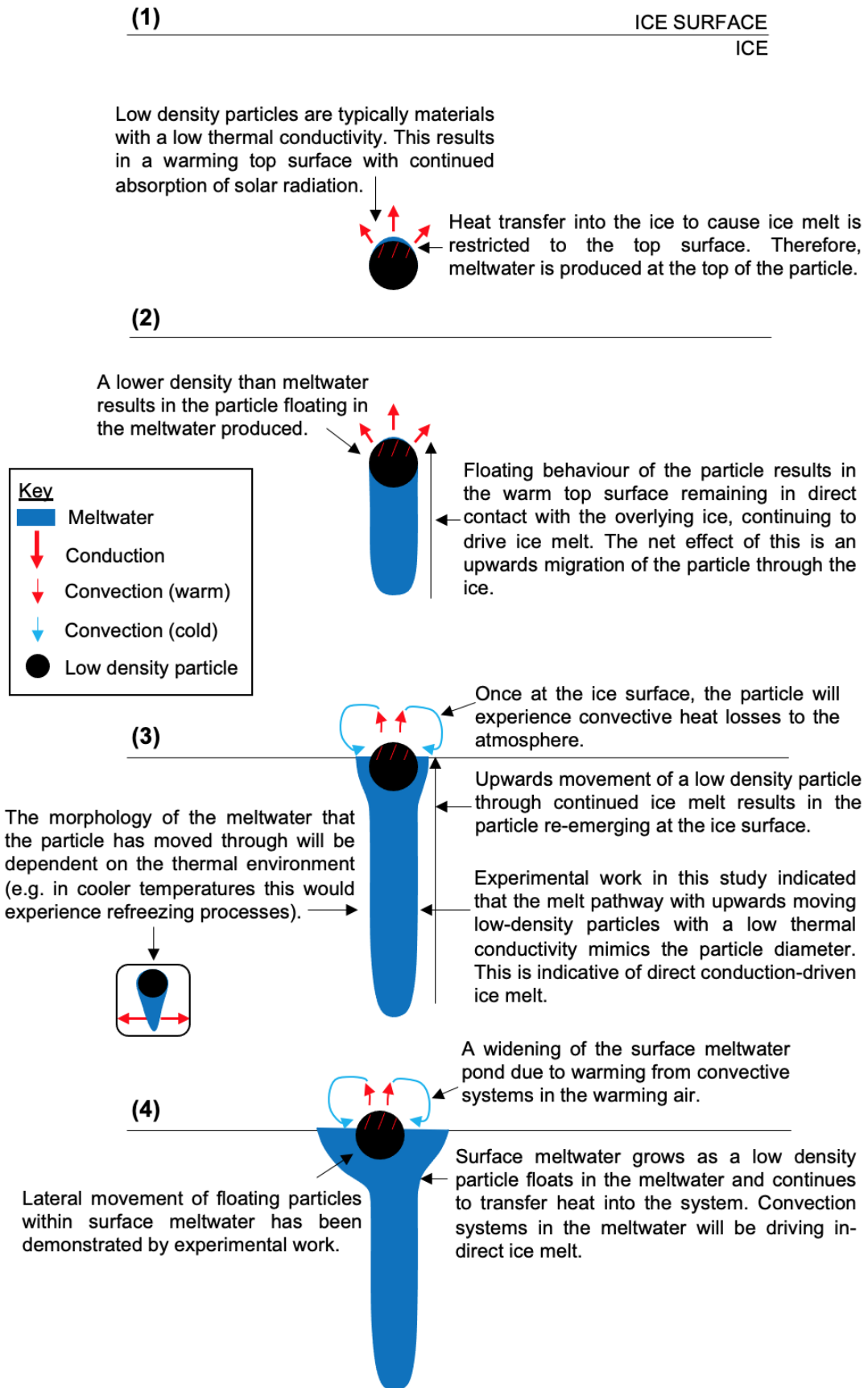


Figure 7.7. The process of re-emerging particles within the ice system, with 1-4 denoting progression through time. Spherical particle used for simplicity.

7.5. Redistribution processes on an ice surface

The current study found that low density particles (e.g. microplastics and pumice particles) and fine-grained (e.g. <0.5 mm) volcanic material remained on the ice surface after melting the ice. These typically formed and floated within surface meltwater ponds, the size of which depended on the temperature of the system. This was a dynamic process as particle movement was observed in almost all experiments with the development of surface meltwater, largely attributed to convection currents in the meltwater (driven by particle heating), and surface tension causing a clustering of particles. This self-assembly of particle clusters is largely due to attractive capillary forces between the floating particles (Vassileva et al., 2005; Danov and Kralchevsky, 2010; Lee, 2018) and a reduction in the surface area as driven by surface tension forces (Burton, 1924). This floating regime is applicable to anthropogenic contamination within the cryosphere due to the small size and low density nature of many anthropogenic particles (e.g. microplastic particles).

The process of redistribution and aggregation of particles is consistent with results described by Dragosics et al. (2016), who noted that fine-grained particles (e.g. < 0.5 mm) were susceptible to redistribution and aggregation processes, largely due to the low friction coefficient of particles used. However, experimental work in this thesis demonstrated that this was also common with larger particles (e.g. > 5 mm) and highlighted the importance of surface-tension effects in this process, particularly when considering particles with a density similar to that of water. For example, a 1.5 mm scoria particle was held at the water surface despite control experiments indicating downwards movement with the removal of surface tension.

It was suggested by Dragosics et al. (2016) that coarser-grained material (e.g. > 0.5 mm in the case of Dragosics et al., 2016) on an ice surface had a strong influence on the general albedo of the surface as these particles typically remained stationary on the ice surface. However, experimental work in this study noted that the aggregation of fine-grained (e.g. < 0.1 mm) low albedo material floating within surface meltwater results in a transfer of low albedo absorbing surfaces across an ice surface, allowing for an increased volume of

ice melt. This process was controlled by the particle density, again highlighting the importance of particle density as a property in controlling the behaviour of particle-ice interaction in dirty ice conditions.

Redistribution processes were particularly important when considering microplastic particles within the cryosphere. Redistribution is typically associated with low-density particles that are susceptible to accumulation processes by surface tension forces, and redistribution processes through the movement of meltwater. This could suggest that microplastics would remain within the meltwater produced and likely follow drainage patterns over the ice surface, and/or enter the englacial regime (i.e. entering the vein network, as demonstrated by experiment Mp13, Chapter 6). Additionally, microplastic particles typically attach themselves to the edges of ponds through surface tension effects. These redistribution processes are a particular area of interest when considering the possibility of microplastic contamination in downstream areas of glaciers and the fate of microplastics within the cryosphere. These findings are an example of how a systematic assessment of the role of particle properties in influencing ice melt can aid prediction of movement of particles within an ice system.

7.6. Application to the natural environment

7.6.1. Meteorite loss mechanisms

A difference between behaviours of iron-based and stony meteorite interaction with ice has been noted (Evatt et al., 2016), confirmed by a lack of iron-based meteorites recovered from Antarctica (e.g. 0.7%) relative to other locations (e.g. 5.5%, Folco et al., 2002; Evatt et al. 2016). Evatt et al. (2016) hypothesised that this is controlled by particle thermal conductivity, where a thermally conductive particle, such as iron-based meteorites, can melt downwards into the ice to be 'lost' from the supraglacial system to the englacial system. This was based on the premise that the rate of downwards movement of iron-based meteorite particles exceeded the rate of upwards movement through ice flow. Evatt et al. (2016) investigated this in four laboratory experiments and demonstrated downwards movement of an iron-based and stony meteorite (approximately

15x10 mm in size). Particle velocities determined by Evatt et al. (2016) were broadly comparable with results using thermally conductive particles with similar diameters (e.g. 12 mm and 8 mm) in this thesis: for example, an average particle velocity of $6.67 \times 10^{-7} \text{ m s}^{-1}$ for an iron-based meteorite (Evatt et al., 2016), and $1.36 \times 10^{-6} \text{ m s}^{-1}$ and $1.05 \times 10^{-6} \text{ m s}^{-1}$ for brass and chrome steel particles, respectively. The average values from the experimental work in this thesis were a factor of 1.5-2 higher than values from Evatt et al. (2016), which may reflect: (1) differences between the laboratory techniques used (e.g. different illumination sources such as an Oriel Solar Simulator arc lamp compared to an LED lamp, embedded versus surface initial particle position, etc. in Evatt et al. (2016) and this study, respectively), (2) the difference in number of experiments conducted using these materials (e.g. four in Evatt et al. (2016) and nine experiments involving 12 mm particles in experiments in this thesis), and (3) differences in particle diameters, the effect of which is discussed in Section 7.4.1. Additionally, the brass particles used in experimental work in this thesis had a thermal conductivity value a factor of 5 higher than the iron-based meteorites used by Evatt et al. (2016). However, the thermal conductivity of the chrome steel particle was comparable to the iron-based meteorite, for example, $\sim 30 \text{ W m}^{-1} \text{ K}^{-1}$ relative to $\sim 25 \text{ W m}^{-1} \text{ K}^{-1}$, respectively (Opeil et al., 2010; Evatt et al., 2016).

The chondrite meteorite sample (i.e. with a low thermal conductivity) assessed by Evatt et al. (2016) had an average particle velocity of $4.17 \times 10^{-7} \text{ m s}^{-1}$. This was lower than the particle velocities obtained from experimental work in this study: comparable material with a low thermal conductivity (e.g. 12 mm cemented ash clusters and scoria particles) had average particle velocities of $7.03 \times 10^{-7} \text{ m s}^{-1}$ and $1.21 \times 10^{-6} \text{ m s}^{-1}$, respectively, and so were a factor of 1.7-2.9 higher than results presented in Evatt et al. (2016) However, the chondrite meteorite used by Evatt et al. (2016) had a higher thermal conductivity value of $1.5 \text{ W m}^{-1} \text{ K}^{-1}$ when compared to the cemented ash clusters (e.g. $0.3 \text{ W m}^{-1} \text{ K}^{-1}$) and scoria particles (e.g. $0.1 \text{ W m}^{-1} \text{ K}^{-1}$) used in this study.

The application of experimental results in Chapter 4 suggests that there is a difference in behaviour of iron-based meteorites with different diameters, in

addition to a difference between meteorite types as described above. Evatt et al. (2016) concluded that the general downwards movement of iron-based meteorites would likely exceed upwelling from the flow of ice into meteorite stranding zones, resulting in meteorite loss. This was developed further to consider meteorite diameter, and Evatt et al. (2016) suggested that downwards movement of large (defined as > 22 cm) meteorites may exceed upwelling of ice, but downwards movement of small meteorites may not exceed upwelling of ice. However, experiments in this thesis highlight complexities associated with this and suggest that a threshold of behaviours lie within particles with smaller diameter values (e.g. < 22 cm) than that investigated by Evatt et al. (2016). Within a diameter range of 1.5-12 mm investigated in this thesis, results suggested that it is possible that meteorites larger than 6 mm are lost more readily from the surface environment than meteorites smaller than 6 mm, due to the processes discussed in Figure 7.6.

Although different size categories were assessed in Evatt et al. (2016) and this thesis, general processes discussed can be compared. Evatt et al. (2016) suggested that larger meteorites are found more readily at ice surfaces due to a long thermal pathway and, consequently, inefficient heat transfer. It was suggested that smaller meteorites (< 22 cm) can transfer heat to the underlying ice more efficiently due to a short thermal pathway. However, findings presented in Chapter 4 in this thesis indicate that efficient heat transfer may not necessarily be associated with high downwards particle velocities (required for offsetting upwards ice flow). Instead, less efficient heat transfer (e.g. as a result of a long thermal pathway associated with large particles) may encourage higher downwards particle velocities due to a warming top surface driving strong convection systems within meltwater to further drive ice melt. The threshold between these described behaviours is noted as between 3 and 6 mm in this thesis. Although the findings presented in this thesis develop on work described by Evatt et al. (2016), it is clear that there are many complexities involved. Therefore, there is a need to further investigate the working hypotheses of particle diameter influence on particle behaviour described in this thesis using a larger range of particle sizes, and further work would be required to precisely quantify the threshold between these behaviours.

Comparisons between experimental work presented in this thesis and those conducted by Evatt et al. (2016) demonstrate that the particle velocities are useful as a comparison tool. These evolved insights may also be useful when developing search campaigns for meteorites in the cryosphere, as a better understanding of some of the complexities involved in meteorite loss mechanisms has been provided. This is useful for study of the solar system and when using information of meteorites as a proxy for the internal composition of Earth (e.g. iron-based meteorites can provide an insight into the composition of the Earth's core; Ni et al., 2020).

7.6.2. Cryoconite holes

Many of the features observed in experimental work were similar to cryoconite holes in the natural system. It is common for these to be water-filled, and for particles to remain at the base of the hole throughout development. The particles may heat the water within the hole which will enlarge the hole diameter (Fountain et al., 2004). This concept is reinforced by results presented in this thesis (e.g. convection systems were shown to extend the region of melt from the particle dimensions by double the particle width when investigating volcanic particles or plastics) and is dependent on particle properties. Cryoconite holes are commonly areas with high biodiversity due to microbial habitats that form in the basal sediments (Cook et al., 2016) and are found in many cryospheric settings (e.g. glaciers, ice sheets, and sea ice, Podgorny and Grendfell, 1996).

Several field experiments have been conducted to investigate the effect of cryoconite holes on the melt of ice. Cryoconite holes have been examined in the Arctic (Gerdel and Drouet, 1960; Gribbon, 1979; Säwström et al., 2002; Takeuchi, 2002), Antarctica (Paige, 1968; Fountain et al., 2004; Bagshaw et al., 2013), Himalaya (Takeuchi et al., 2001a; Takeuchi, 2002) and other regions such as the Japan Alps (Kohshima et al., 1994) and Patagonia glaciers (Takeuchi et al., 2001b). Studies investigated: (a) the structural features of the holes (e.g. depth, diameter, presence of ice lids, etc.); (b) the hydrological features of the holes (e.g. subglacial drainage networks), and (c) the surface albedo.

This thesis built upon processes described in the literature (e.g. structural features) and provided insights into the formation of cryoconite holes. Experimental results demonstrated the dynamic nature of the processes that occur within cryoconite holes (i.e. sinking particles to create a cylindrical hole, drainage events, etc.) and were consistent with formation processes described in the literature: for example, particles absorb solar radiation and melt downwards into the underlying ice at a higher rate than the remaining ice surface to create a hole on the ice surface (Takeuchi et al., 2018). Therefore, the dense nature of the particles involved facilitates the formation of this feature. Experimental work indicated that a scattered configuration of particles will likely accumulate together to form cylindrical holes (e.g. experiments V33, V34, Mp15, Mp16, Mp17, and Mp19). Therefore, dirty ice conditions act as an environment for cryoconite hole formation. The likelihood of dense surface particles to create holes of this type, as consistently demonstrated by experimental work, suggests that the presence of surface particles can increase the capability of temporary meltwater storage on an ice surface in sediment holes. As such, cryoconite formation and preservation is crucial when considering meltwater contribution to regions downstream of glaciers.

Experimental work presented in this thesis also provided understanding of the formation of ice lids within the cryoconite systems, and processes that dictated the morphology of the holes. The variability of cryoconite hole morphology (e.g. 5-145 cm range in diameter, 4-45 cm range in depth, with ice lids > 36 cm thick) that has been observed in Antarctica (e.g. Fountain et al., 2004; Bagshaw et al., 2013) was also observed in experimental work in this thesis, albeit on a smaller scale (e.g. 6-20 mm in diameter and >80 mm in depth). This was largely attributed to differences in particle type and, consequently, to differences in properties of the particles (Chapters 4 and 5). Gerdel and Drouet (1960) suggested that the convection of heated water was a crucial mechanism in enlarging the holes. This concept was developed in this thesis, where a clear criterion for the morphology of cryoconite holes was determined, dependent on particle thermal conductivity: for example, dense particles with a low thermal conductivity (e.g. scoria particles with a thermal conductivity of $0.2 \text{ W m}^{-1} \text{ K}^{-1}$ as shown in this thesis) could create wide areas of melt due to strong convection-

driven melting, whilst dense particles with a high thermal conductivity could create holes with narrow diameters.

The formation of ice lids was observed in many experiments in the stable (cool) thermal environment. However, this differed to the morphology of cryoconite ice lids described in the literature (Figure 7.8) because a teardrop morphology developed, rather than a flat ice lid. The teardrop form was likely a result of being a density-driven feature (i.e. due to particle movement) in a refreezing environment, associated with high particle velocities (e.g. 10^{-6} m s^{-1}), whilst experimental results (e.g. experiment V12) showed a spherical morphology formed in the case of slower moving (e.g. $1.68 \times 10^{-7} \text{ m s}^{-1}$) particles. Therefore, it is suggested that the morphology of ice lids may vary depending on the velocity of downwards moving particles. Experimental work in this thesis was restricted to depths of approximately 60-80 mm, and so the development of cryoconite holes in regimes deeper than this were not investigated experimentally. Additionally, particles in this experimental work were subjected to constant radiation and, therefore, the effect of diurnal cycling was not considered. It is likely that this could also contribute to differences in ice lid morphology described in the literature and that observed in experimental work in this study due to the removal of convection processes with the removal of particle-absorption of solar radiation at night. After solar heating and convection is re-activated, convection processes may be isolated from the ice lid by an air gap, as shown in Figure 7.8. However, it is suggested that a narrowing of the meltwater extent, as observed in experimental work in this study, would occur if refreezing of the meltwater occurred on a faster timescale than diurnal cycling.

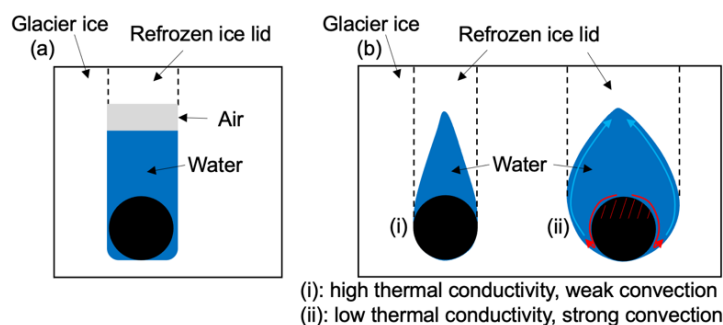


Figure 7.8. Cross-sectional comparison of cryoconite hole morphology described in (a) the literature (e.g. Fountain et al., 2004) and (b) in experimental work in this thesis. Individual particles are considered in (b) for simplicity, but features can be applied to a group of particles.

7.6.3. Weathering crusts

Features that formed on ice following the scattering of surface particles in experimental work (e.g. volcanic and microplastic particles) were similar to descriptions of weathering crusts in the literature. This is a common feature in the ablation zone of glaciers (e.g. Bazhev, 1975), and refers to an uppermost ice surface (e.g. < 2 m) that develops after interaction with incoming shortwave radiation to form a porous, low-density 'rotting' layer of ice (Cook et al., 2016; Stevens et al., 2018). This is typically fragmented from a coarsening of the vein network, also observed in this study (e.g. experiment Mp7) and associated with the formation of cryoconite holes. It has been suggested that the state of the weathering crust is of equal importance on ice surface albedo as the role of direct melting from light absorbing particles on an ice surface (although the two are ultimately interlinked), and the state of this uppermost surface drives the variability in albedo in natural systems, e.g. the western Greenland Ice Sheet (Tedstone et al., 2020).

Experiments investigating a scattering of surface particles (size range 0.1-4 mm) provided information on the evolution of weathering crusts observed in nature. It is suggested that the presence of widely dispersed particles (i.e. in dirty ice conditions) can encourage the development of a 'rotting' ice surface, through increased interaction with incoming solar radiation. Components of a conceptual model discussed by Cooper et al. (2018) were confirmed in experimental work in this thesis, where the relationship between cryoconite hole development and weathering crusts was noted facilitated by downwards moving particles. However, experimental work also suggested several other particle processes beyond cryoconite hole development due to the dynamic nature of particle-ice interaction: for example, a clustering of particles in meltwater through capillary action, redistribution of particles across the ice surface, dynamic drainage processes, and advection of water, heat, and particles into the vein network (Figure 7.9). Results also noted that the evolution of a scarred ice surface was rapid (e.g. < 1 hour) after the introduction of a scattering of surface particles. Therefore, it is suggested that the presence of widely dispersed surface particles encourage the development of a weathering crust

environment within natural diurnal cycles due to the fast initiation of melt observed in experiments presented in this thesis.

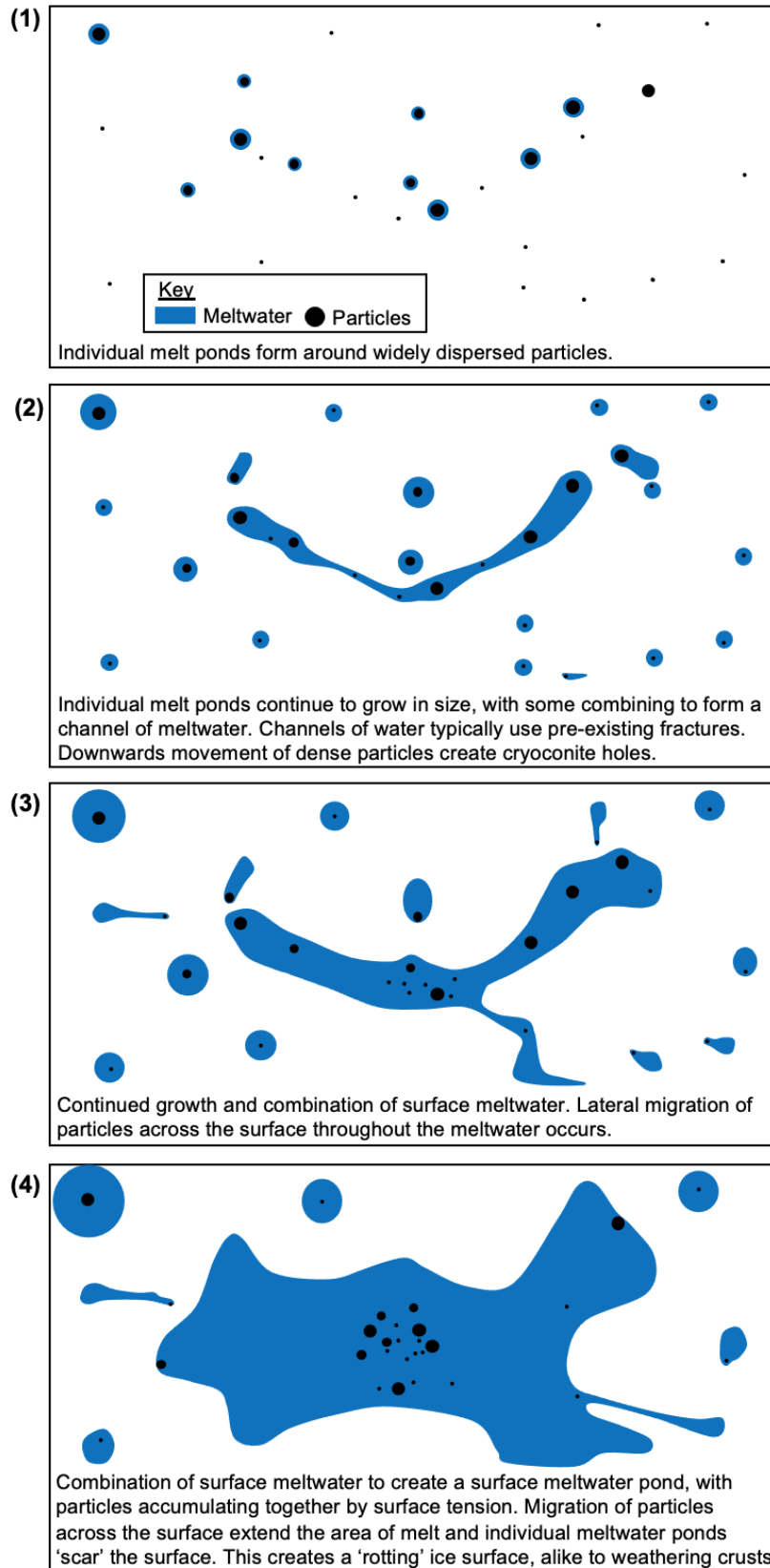


Figure 7.9. Plan view of the simplified evolution of surface meltwater in dirty ice conditions, informed by experimental work in Chapters 5 and 6, with 1-4 denoting progression through time.

Weathering crusts are typically in a 'rotting' and unstable state (Stevens et al., 2018). Therefore, there is much possibility for redistribution of particles within the coarse vein network (as identified in Chapter 6); a particle may enter and move through the vein network if the particle diameter is smaller than the vein diameter. As the vein network is typically larger in warm conditions (Price, 2007), it is logical to suggest that particle movement within the vein network will increase with increasing temperatures. Additionally, the porous ice may facilitate 'washing away' of particles within the weathering crust system. However, experimental work in Chapter 5 showed that this can also encourage melting within the photic zone of the englacial regime due to a lowering of floating particles into the ice system by drainage events. In the case of experimental work in this thesis, these processes were considered in the top 80 mm of ice.

7.6.4. Microplastic particle contamination within ice

The emerging research into microplastic contamination within ice has focused on assessing the sources and transportation mechanisms of microplastic particles (Bergmann et al., 2019), in addition to attempting to quantify the composition of particles found (Kanhai et al., 2020). Although an understanding of the characteristics of microplastic particles found in remote regions is being developed, the behaviour of these particles within the cryosphere is poorly understood. Experimental work in Chapter 4 and Chapter 6 provided a new insight into the behaviour of these particles within the cryosphere.

7.6.4.1. The behaviour of microplastic particles in meltwater

Many microplastic particles have a low density relative to water – a property that also facilitates widespread transportation around the globe (Evangelidou et al., 2020). Following absorption of radiation and heat transfer into the local area to cause ice melt, the low-density property of microplastic particles results in many particles floating in meltwater. This is either through density-driven buoyancy or surface tension-driven buoyancy due to comparable density values with water making the particles susceptible to surface tension effects.

7.6.4.2. Microplastic particle movement within ice

Redistribution (discussed in Section 7.5) of microplastic particles is common once meltwater has been produced. This is facilitated by the small size of the particles, demonstrated in experimental work, where polypropylene and polyethylene particles of varying sizes (e.g. approximately 0.1-5 mm) and morphologies (e.g. spherical and irregular) were susceptible to movement within the meltwater. Therefore, the likelihood of microplastics entering downstream fluvial systems is high. Results also demonstrated the re-emergence of particles at the ice surface due to upwards movement (discussed in Section 7.4.2).

Experimental work (Chapter 6) showed that particle transportation through the vein network is possible, particularly in warmer temperatures, as the vein network diameter may exceed the diameter of the microplastic particles (e.g. a thin microplastic particle approximately 4x3 mm, with a width of <1 mm moved through veins in experiment Mp6). This compared well with the literature, where it was noted that the vein network could provide a transport mechanism for impurities within ice (Mader, 1992; Rempel, 2005). Therefore, it is likely that the vein network will be an important feature when investigating microplastic contamination in ice and should be considered in future work.

7.6.4.3. Microplastic particle aggregation

Aggregation of microplastic particles in meltwater was observed when a scattering of particles was considered. Experimental work indicated that this configuration was more likely to create a large surface meltwater pond relative to when considering individual particles. For example, aggregated small (<1 mm) polyethylene microplastics created an average surface meltwater pond extent approximately 3.7x and 17.5x wider and deeper, respectively, than a surface meltwater pond created by an individual particle of the same type. This observed effect compares well with the literature, where it is noted that particle aggregation is likely to contribute to the positive feedback associated with snow/ice albedo (e.g. through an increased volume of meltwater, or accumulation of low albedo particles in a region). The implication of this finding is that it is likely that microplastic contamination within the cryosphere will

contribute to the positive ice-albedo effect in the cases where microplastics are not washed off an ice surface and may exacerbate glacial retreat (Yue et al., 2020).

7.6.4.4. Microplastic particle morphology

Experimental work in Chapter 6 demonstrated that the particle morphology dictates the subsequent morphology of initial surface meltwater. This provided unique insights into the heat transfer mechanisms associated with microplastic particle-ice interaction, whereby it was noted that conduction-driven ice melt was dominant in the first instance, until heating of water enabled meltwater convection processes and subsequent modification to the meltwater morphology (i.e. to a spherical pond). This indicates the evolution of conduction-driven melt to convection-driven melt associated with many microplastic particles. Additionally, the particle morphology dictates the thermal pathway length within the particle. It was noted that a spherical, large microplastic particle was associated with a lower volume of ice melt compared to a thin microplastic particle; this was likely due to a longer thermal pathway associated with the spherical particle, and subsequent increased convective heat loss to the atmosphere. Therefore, it is suggested that smaller microplastic particles are capable of melting ice to a greater extent than larger microplastic particles; this finding is most applicable in a 'melt-limiting' regime (e.g. cooler temperatures). This is consistent with findings associated with volcanic particles in Chapter 5 (i.e. a higher particle velocity was associated with a smaller volcanic particle (e.g. < 3 mm) relative to a larger volcanic particle (e.g. > 6 mm), attributed to the low thermal conductivity of the particles. It is suggested that processes associated with particles with a low thermal conductivity can be applied to the behaviour of microplastics.

Results in this thesis contribute new knowledge to the field of microplastic particle contamination within the environment. These findings demonstrate the importance of future research to understand how the ice state may change with future microplastic contamination (e.g. contribution to the positive ice albedo effect through particle aggregation) and to predict the fate of microplastic particles within the cryosphere and possible entry into marine systems.

7.7. Fragmentation of volcanic particles within ice

Chapter 6 revealed the process of volcanic particle fragmentation within ice. Particle fragmentation was observed in at least one instance with all volcanic materials used (e.g. cemented ash clusters, scoria, and pumice). Interestingly, fragmentation processes occurred in all cases of pumice particles, suggesting that it was a common process associated with cold pumice interaction with ice. Discussion of this process will, therefore, predominantly focus on the application to pumice particles, although the working hypotheses described are suggested to be applicable to cemented ash clusters and scoria particles.

Pumice particles are vesicular by definition, with a subsequent low particle density that facilitates floating behaviour within water. Therefore, the general behaviour observed in this study supported the consensus that pumice particles typically initially float in water. However, the role of pumice saturation is crucial when considering the behaviour of porous particles (Whitham and Sparks, 1986; Hobbs, 2014). Whilst this concept has been previously studied, this has predominantly been restricted to consideration of pumice saturation in sedimentary environments or water systems (Whitham and Sparks, 1986; Manville et al., 1998; Manville et al., 2002). This thesis, in combination with work by Juen et al., (2013) and Hobbs (2014), considered the saturation of pumices within the cryosphere.

Experimental work in Chapter 5 evolved findings from previous work to demonstrate additional complexities associated with pumice saturation. It was proposed that saturation indirectly facilitated subsequent fragmentation of the porous particles (Figure 7.10). Once particle-induced ice melt was initiated, meltwater likely immediately percolated through the pores within the pumice particles through capillary action, as is common for porous material (e.g. water influx is at its highest in the first five minutes of submergence, Whitham and Sparks, 1986; Vella and Huppert, 2007). The base of the pumice particle was in direct contact with the ice and facilitated direct conduction of heat in the ice away from the point of contact, resulting in meltwater freezing at the pumice base. Freezing processes caused meltwater to expand within particle pore spaces, driving fracturing at the particle base through freeze-thaw action and

subsequent fragmentation of the volcanic particles. Fragmentation of the pumice particles was first observed following the development of a meltwater pond and subsequent floating behaviour of the pumice particle (e.g. on average 11 hours following particle placement). Therefore, it is suggested that the pumice fragments dropped off the particle base once the ice within the particle had melted.

This process occurred more readily with pumice particles due to the higher porosity relative to the scoria particles and cemented ash clusters. The process can be up-scaled to natural glacial environments, where it is likely that freeze-thaw action within a porous material would occur as a consequence of diurnal cycling of temperatures, in addition to small-scale refreezing encouraged by a thermal gradient at the pumice base directly in contact with the ice, as described above. The fragmentation of volcanic particles observed in our experimental work would likely occur in cryospheric environments and act as a contributor of additional particles (and, therefore, additional absorbing surfaces) into an ice system, potentially facilitating increased ice melt.

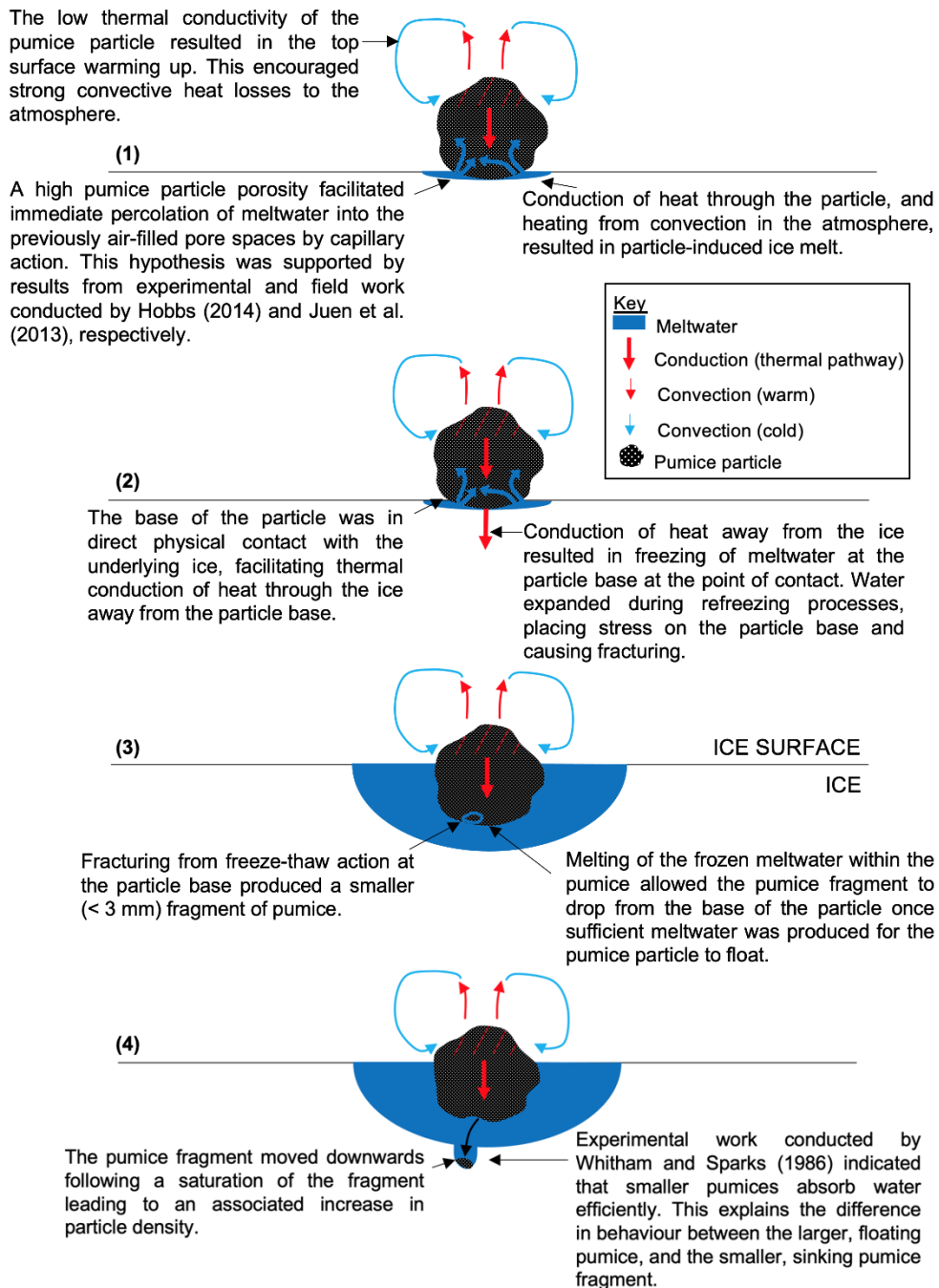


Figure 7.10. Cross-sectional schematic diagram of the working hypothesis for pumice fragmentation within the ice system, with 1-4 denoting progression through time.

In natural environments, pumice particles can float in water on a timescale of months-years (Whitham and Sparks, 1986; Fauria et al., 2017). Whitham and Sparks (1986) and Manville et al. (1998) noted that the pumice size had an influence on the percolation of water into the pore spaces, in addition to the connectiveness of the pore spaces (Manga et al., 2018). For example, smaller pumices were associated with a higher rate of saturation and subsequent associated density change; the experimental work for this study supported this

finding as the small fragments of pumice, broken off at the particle base, moved downwards through the ice, indicating a higher density than water (although, this was to be expected due to the saturation processes associated with freeze-thaw fragmentation). Experimental work conducted by Manville et al. (1998) demonstrated that pumices in the size range 1-2 mm experienced full saturation immediately and, therefore, sank in water immediately after deposition. Experimental work in Chapter 5 was in accordance with these results, with observed downwards moving pumice fragments in the size range of 0.5-2 mm.

The pumice particles initially placed on the ice surface did not experience sufficient density change during the experimental time-period to facilitate downwards movement. This was consistent with the general behaviour of pumices described in the literature, i.e. it can take years before full saturation of a pumice particle (Whitham and Sparks, 1986). In most cases, this was likely due to the large particle size (e.g. > 2 mm) resulting in a slow absorption of water (Whitham and Sparks, 1986). Additionally, it is possible that trapped gases within the pumice can keep a pumice particle afloat (Fauria et al., 2017). This is due to the saturation process likely being a 'two-step process': the first being a high influx of water in the first instance (e.g. five minutes, Whitham and Sparks, 1986) by capillary action, also trapping gases within the pore spaces (Fauria et al., 2017); and the second being a slower absorption of water and slow gas diffusion out of the pore spaces. This second phase would enable pumices to eventually sink if the first phase did not cause sinking behaviour (e.g. as observed within the size range 1-2 mm by Manville et al. (1998), and 0.5-2 mm in experimental work in this thesis). Therefore, it is suggested that the larger pumices (e.g. < 2 mm) in our experimental work had trapped gases within the pumice, preventing sinking behaviour on the time-scale of experimental work (e.g. < 64 hours).

In the case of the smaller particles (e.g. 1.5 mm) placed on the ice surface (i.e. not those formed by particle fragmentation), these could remain at the ice surface despite a possible full saturation due to surface tension effects; experiments involving dense 1.5 mm scoria particles demonstrated surface tension induced buoyancy and supported this interpretation. Conversely, the

small fragments of pumice particles broken from the originally placed particle were able to move downwards through the ice as these fragmented at the particle base and, therefore, were already submerged within the meltwater. These would not experience surface tension effects retaining the pumice at the water surface.

The implications of these findings are that saturation of a pumice particle can facilitate multiple modes of melting within an ice system (e.g. the surface particle and embedded particle), further evolving findings by Hobbs (2014), who also considered pumice saturation within an ice system. However, results contrasted with the behaviour of water-logged pumices described by Hobbs (2014), as the pumices in Hobbs' experiments settled on the base of a meltwater pond (previously created by the floating pumice) but were not capable of further embedding within the ice. The fragmented pumice particles in experiments presented in this thesis became fully embedded within the ice and sank to depths of 60-80 mm. The differences between these results may be due to the contrast in pumice sizes: for example, Hobbs (2014) used pumices approximately 13 mm in diameter, whilst the fragmented pumices that experienced downwards movement in the experimental work presented here were < 3 mm. Experiments described in this thesis suggest that when considering particles with a low thermal conductivity, smaller particles were most efficient at melting the ice. This demonstrates the need to consider particle diameter when predicting the behaviour of particle-ice interaction.

7.8. Modelling dirty ice behaviour

Comparisons of the particle velocities calculated from the simple melt model described in Chapter 3 (Section 3.5.2) with observed behaviour can provide an insight into some of the uncertainties associated with modelling dirty ice behaviour. Although simplified relative to many energy balance models, this has similarities with the general energy balance models developed for modelling dirty ice (e.g. Fyffe et al., 2014; Chapter 2).

There is some variability between the modelled and observed particle velocities presented in this thesis (Table 7.3 and Figures 9.1, 9.2, and 9.3, Appendix 18).

Deviations from the modelled calculations are likely to be due to the simplicity of assumptions (as described in Chapter 3) compared with a very complex system (as demonstrated in Chapters 4, 5, and 6). For example, there was a reduced variation in the modelled particle velocities (e.g. all within a 10^{-7} m s⁻¹ magnitude) compared to observed results (ranging from 10^{-8} to 10^{-6} m s⁻¹ magnitudes) – this likely represents the additional complex processes involved in particle-ice interaction that were not captured within the simple melt model (e.g. role of internal ice structure, sensitivity of particles to temperature, etc.). The assumption that the ice was at PMP was deemed most crucial when looking at the error associated with the simple melt model, as experimental work consistently demonstrated that subtle temperature changes were responsible for large shifts in particle behaviours. Evidence for this was the varied particle velocities observed in differing thermal environments (for example, average particle velocities for stable (warm) were a factor of 1.29-9.74 higher than stable (cool) depending on particle type). Deviations from the PMP were estimated in experimental work through the categories of stable (cold), stable (cool), stable (warm), and unstable; however, further work is required to build the bridge from this experimental categorisation to allow consideration of deviations from PMP in models.

Table 7.3. Comparison of modelled and observed particle velocity. Modelled particle velocities were calculated using the simple melt model described in Chapter 3.

Particle type		Modelled particle velocity (m s ⁻¹)	Average observed particle velocity (m s ⁻¹)			
Chrome steel	LA	8.63×10^{-7}	1.05×10^{-6}			
	HA	4.22×10^{-7}	8.46×10^{-8}			
Brass	LA	8.63×10^{-7}	1.5 mm	3 mm	6 mm	12 mm
			8.32×10^{-7}	9.85×10^{-7}	1.84×10^{-6}	1.36×10^{-6}
	IA	4.90×10^{-7}	1.76×10^{-6}			
	HA	3.92×10^{-7}	2.39×10^{-7}			
Delrin		8.63×10^{-7}	3.78×10^{-7}			
Polypropylene		8.63×10^{-7}	1.41×10^{-6}			
Polyethylene		8.04×10^{-7}	7.95×10^{-7}			
Polystyrene		8.63×10^{-7}	2.20×10^{-6}			
Cemented ash cluster		6.96×10^{-7}	3 mm	6 mm	12 mm	
			1.01×10^{-6}	1.40×10^{-6}	7.03×10^{-7}	
Scoria		8.43×10^{-7}	3 mm	6 mm	12 mm	
			1.04×10^{-6}	7.86×10^{-7}	1.21×10^{-6}	
Pumice		6.08×10^{-7}	-			

The observed particle interaction with the vein network likely facilitated a higher particle velocity than modelled (e.g. downwards movement from additional processes to ice melt) as the importance of the ice hydrological system has been consistently demonstrated as a control on particle-ice interaction. Detailed comparisons of modelled versus observed behaviour can be found in Appendix 18.

Experimental results presented here have demonstrated the complexities associated with a dirty ice environment, even in a partially controlled laboratory setting. The findings in this study are, therefore, useful for addressing some assumptions used when modelling dirty ice environments, as noted below:

- (1) The presence of surface meltwater associated with low density particle-ice interaction, and refreezing processes of meltwater produced by downwards moving particles, contradicts a common assumption of debris-covered and dirty ice modelling described in the literature. Pooling of meltwater is disregarded in many models and assumes immediate run-off. Therefore, phase changes associated with evaporation or refreezing are not considered in the ablation process, typically leading to an overestimation of modelled ablation.
- (2) Cold temperatures reduced the particle-ice interaction and particle velocity. This was because the ice was not at PMP and not all heat transferred caused ice melt due to the conduction of heat along a thermal gradient in the ice. However, conduction of heat away from the particle proximity through the ice is not considered in dirty ice modelling, and the ice is assumed to be at PMP.
- (3) Advection of heat from drainage events or particle-particle interaction reduced the particle velocity relative to the modelled output (e.g. in experiment P13 the IA particle velocity was reduced by 22% relative to the modelled output, with a 78% reduction when compared to the average recorded IA brass velocity without drainage events). This demonstrates the complexity involved and challenges the assumption that all heat absorbed by the particles is transferred into melting the ice.

- (4) The ice structure can influence the orientation and velocity of particle movement throughout the ice, as discussed in the application of the simple melt model to observed results above.
- (5) The englacial environment as a platform for particle-ice interaction is rarely considered in modelling ablation of dirty ice; however, experimental work in this study has demonstrated that it is an optimal environment for ablation.
- (6) The relative importance of particle properties, and the absolute value of particle properties (e.g. density and thermal conductivity), can change during active particle-ice interaction (for example, absorption of water into pore spaces in volcanic material). However, many modelling techniques assume particles with temporally and spatially constant properties.

The processes described in (2) is of particular importance: englacial heat conduction through the ice away from the debris/ice interface is commonly omitted as a parameter in DEB modelling (e.g. Nawako and Young, 1986; Han et al., 2006). However, it has been noted that this process is important when considering colder regions. This may result in reduced ablation in reality when compared to estimates from modelled outputs that do not consider englacial conduction (Reid and Brock, 2010; Nicholson and Benn, 2013). Experimental results demonstrated a dependency on the thermal environment in the proximity of the particle; this considers the balance of heat conduction away from the particle (i.e. resulting in refreezing processes) and heat transfer from the particle into the ice (i.e. resulting in melting processes). Often, this was described as a sensitive balance where large behavioural changes in particle-induced ice melt occurred in response to subtle changes in ice temperatures. These results have confirmed the need for consideration of this component.

This discussion considers the complexity associated with dirty ice conditions, whilst many models are predominantly first-order. Simplifications in modelling techniques may ultimately result in inaccuracies in modelled dirty ice ablation; however, if the behaviour of particle-ice interaction in dirty ice conditions can be predicted and understood more accurately, then modelling of dirty ice might

provide a better understanding of glacier response to climate change. These findings provide a foundation for reducing the knowledge gaps involved in modelling dirty ice conditions.

7.9. Future research

7.9.1. Microplastic particle contamination in the cryosphere

Experimental work in Chapter 6 provided a new insight into microplastic particles interaction with ice. However, the properties investigated were limited when considering the large range of properties associated with microplastic particles. For example, microplastic particles have a wide range of colours, morphologies, and diameters (Allen et al., 2019; Stefánsson et al., 2021). Therefore, it would be useful to conduct future research to map the behaviour of the properties of microplastic particles (e.g. considering a range of particle albedos), in addition to considering how these durable particles may behave when part of a debris layer. This is crucial when considering the impact of microplastic contamination of the cryosphere as this is a critical freshwater resource (Cabrera et al., 2020; von Friesen et al., 2020).

7.9.2. The behaviour of embedded particles

When considering meteorite loss mechanisms within ice, Evatt et al. (2016) suggested that large meteorites (e.g. > 22 cm) would emerge at an ice surface as downwards particle velocity would not exceed upward ice transport. However, experimental work in this study demonstrated that within the subcategory of 'small' particle size (e.g. < 22 cm), there are discrepancies in behaviours: for example, larger particles (e.g. > 6 mm) are less sensitive to subtle changes in temperature and, therefore, are more likely to sink to a greater ice depth than smaller particles (e.g. < 3 mm). This demonstrates additional complexities to theories described by Evatt et al. (2016) and demonstrates the need to further improve understanding of the behaviour of embedded particles. This is important for field campaigns that search for meteorites on ice sheets; improving the understanding of thermally conductive particles within ice may facilitate the finding of a greater number of iron-based meteorites. This, in turn, would drive understanding of the early solar system

and the composition of planetary bodies, because iron-based meteorites likely represent material originated from the core of its parent planet body (Ni et al., 2020).

Experimental work in Chapters 4 and 6 showed that embedded low-density particles can migrate upwards through ice to reach an ice surface. It would be useful to assess this process in future studies to improve our understanding of movement within an ice system with additional complexities (e.g. opaque ice, movement over a longer distance than considered in this experimental work, the effect of the presence of other particles on englacial particle movement, etc.).

7.9.3. Sublimation cooling offsetting melting processes

Experimental work in Chapters 3 and 4 demonstrated that sublimation cooling of an ice surface could offset particle-induced ice melt under insolation. However, this was not a focus of this study (rather, a secondary result of the experimental design process and early experimental work). Therefore, it would be useful to investigate this process through further research to improve understanding between the relationship of sublimation processes and surface particles to complement work conducted by Hobbs (2014) and Taberlet and Plihon (2021).

7.9.4. Modelling dirty ice

The experimental work within this thesis provides insights into assumptions involved in dirty ice modelling. Therefore, there is scope for building the bridge between the results presented in this thesis and the dirty ice models – and this should lead to improved forecasting of the durability of ice on Earth and other planets.

8. Conclusions

This thesis aimed to improve understanding of particle-ice interaction in dirty ice conditions under insolation. Many studies agree that debris insulation reduces glacier sensitivity to climate change. However, the thickness required to achieve these insulating properties differs between debris type (Chapter 2) and is not always experienced on a glacial surface. Instead, a sparse distribution of particles (i.e. dirty ice) is common and this is thought to accelerate glacier ablation. A review of the literature (Chapter 2) demonstrated the following knowledge gaps in dirty ice science that this thesis aimed to address: (1) the role of particle properties on influencing particle-ice interaction (Chapter 4), (2) the behaviour of volcanic particles in dirty ice conditions (Chapter 5), and (3) the behaviour of microplastic particle-ice interaction (Chapter 6). Analysis across these three themes aimed to improve understanding of processes involved in dirty ice conditions that may contribute to the global accelerating trend of glacier mass loss.

Laboratory experiments were designed to investigate particle-ice processes in a partially controlled environment analogous to dirty ice conditions (Chapter 3). This experimental approach was developed solely for the intent of addressing the knowledge gaps noted in Chapter 2 and has proved to be a useful method of isolating particle-ice interaction on the individual particle scale and when considering a scattering of surface particles. Cross-sectional imaging of ice is a pioneering and useful technique that was critical for providing information about the behaviour of the dirty ice system under insolation. The calculation of particle velocities, used as a key tool for interpretation of processes within this thesis, also allowed valuable comparisons of data from experimental studies in the literature (e.g. Evatt et al., 2016).

This study has confirmed that dirty ice conditions can modify the thermodynamic behaviour of the upper surface and englacial environment of an ice body relative to clean ice to encourage ablation. The systematic review of particle properties described in Chapter 4 helped to create a knowledge bank of individual particle properties and the importance of each respective property in

terms of inducing ice ablation. There is a need for future work to develop this systematic understanding to use as a tool to map the fate of particles within the cryosphere and to predict the particle-induced ablation in dirty ice conditions. Chapter 5 evolved the understanding of the processes associated with volcanic particle-ice interaction (e.g. the role of convective heat transfer arising from a low thermal conductivity) in dirty ice conditions and demonstrated the likelihood of particle fragmentation once within the ice/water system; the latter has not previously been recognised in dirty ice science. Experimental work in Chapter 6 established the fundamental behaviour of microplastic particles within the cryosphere, not previously investigated in the literature, and, thus, contributed new knowledge to our understanding of microplastic contamination within the environment.

In summary, results (Chapters 4-6) demonstrated the effectiveness of particles inducing ice melt under insolation through a range of complex processes. The wider implications of this study on our understanding of dirty ice processes are as follows:

- 1) Particle thermal conductivity is an important particle property in influencing the melt initialisation process. Particle density is crucial in determining if a particle experiences a supraglacial or englacial environment. Therefore, particle density is argued to be of comparable importance to particle thermal conductivity and albedo. It is suggested that particle density should be considered when predicting the behaviour (and, therefore, influence on ablation) and fate of dispersed particles in ice.
- 2) The englacial environment can experience significant ablation due to particle-ice interaction. This appears to be to a greater degree than the supraglacial environment due to convective heat losses to the atmosphere for particles in the supraglacial regime, although the englacial environment is often overlooked in ablation modelling. Therefore, both ablation environments should be considered in ablation modelling to accurately estimate ice mass loss and run-off patterns in dirty ice conditions.

- 3) Subtle changes in temperatures can result in large behavioural changes of particles. The extent of behavioural change is dependent on the particle properties. This is important when considering assumptions (e.g. deviations from the pressure melting point, PMP) used in debris-covered and dirty ice models. It is suggested that temperature deviations from PMP should be quantified in ablation modelling to better forecast how particle-induced ice melt will contribute to glacial ablation.
- 4) The internal ice structure has a significant influence on the behaviour of particles by facilitating drainage events through the vein network, enabling rapid movement of small particles (i.e. microplastic particles smaller than the diameter of channels in the vein network) through the ice and influencing the orientation of downwards particle trajectories. This effect is exacerbated in warmer temperatures due to a widening of the vein network. Therefore, it is possible for microplastic particles and other small particles to move within the vein network, encouraging englacial melting within the photic zone, and allowing a pathway for microplastics to move through ice and enter downstream fluvial or marine systems.
- 5) Particle properties can act as a sorting mechanism for particles within ice. This has implications for meteorite search campaigns in Antarctica and Greenland as an improved understanding of the transport of particles within ice may help with the search for iron-based meteorites, and the fate of microplastic particles following deposition on an ice surface.
- 6) Upwards migration of embedded low density particles can result in re-exposure of material at the ice surface and may contribute to a lowering of ice surface albedo, increased surface ice ablation, and, subsequently, to the ice-albedo positive feedback.
- 7) A particle with a low thermal conductivity (e.g. a volcanic particle) within the englacial environment drives melting through indirect meltwater convection from a warm particle top surface, resulting in a wide region of melt. A particle with a high thermal conductivity (e.g. an iron-based meteorite) within the englacial environment drives

melting directly at the particle base from heat conduction through the particle, resulting in a narrow region of melt. This improves our understanding of the morphology of melting channels and cryoconite holes, as we may be able to better predict the morphology of features created by particles depending on the properties of a particle. This also improves understanding of the fate of particles moving within an ice system, and possible stratification of particles within ice.

- 8) The loss of fine-grained material from volcanic particle surfaces and freeze-thaw fragmentation of porous material increases the effectiveness of volcanic particles to melt the ice in dirty ice conditions. This contrasts with the insulating behaviour when considered in volcanic debris-covered ice environments. This means that multiple melting regions are likely following dispersed volcanic particle deposition (e.g. denser particles moving into the englacial environment, and less dense particles remaining at the ice surface). High rates of ablation may be induced by volcanic material due to the possibility of additional absorbing surfaces being introduced into the ice system.
- 9) Microplastic particles can effectively induce ice ablation. A variety of behavioural modes (e.g. downwards moving particles, floating particles with lateral movement, etc.) are possible due to particle density being close to that of water and other highly varied particle properties (e.g. albedo and morphology).
- 10) Surface tension forces are a key control on the movement of low density or intermediate density particles within an ice system. This effect can, therefore, influence the fate of low and intermediate density particles (e.g. microplastics) within the cryosphere by: (1) encouraging aggregation of floating fine-grained material to create a concentrated area of a low albedo surfaces, and (2) retain intermediate density particles at an ice surface despite a higher density than water to contribute to surface melting. An improved understanding of these forces in influencing particle position within the ice system is beneficial when assessing the fate of microplastics, and other low/intermediate density particles, within the cryosphere.

Taken overall, this thesis offers new and important insights in an area that has quickly become a human imperative. Offering a unique contribution in its own right, as well as supporting further research in this area, it plays a part in helping to understand glacier ablation, which is a critical aspect of the global climate challenge.

9. Appendices

Appendix 1: Summary of key light absorbing particles.

Appendix 2: Supplementary table of reviewed published fieldwork studies.

Appendix 3: Supplementary table of reviewed published laboratory studies.

Appendix 4: Supplementary table of reviewed published modelling studies.

Appendix 5: Supplementary table of method development experiments to create optically transparent ice blocks.

Appendix 6: Supplementary table of method development experiments to determine the appropriate artificial radiation source.

Appendix 7: Example of workflow of a standard experimental procedure.

Appendix 8: Temperature data of experimental work conducted in Chapter 4.

Appendix 9: Key findings of experimental work investigating the role of particle thermal conductivity on particle-ice interaction.

Appendix 10: Key findings of experimental work investigating the role of particle albedo on particle-ice interaction.

Appendix 11: Key findings of experimental work investigating the role of particle density on particle-ice interaction.

Appendix 12: Summary of behaviour observed in experiment P21.

Appendix 13: Key findings of experimental work investigating the role of particle diameter on particle-ice interaction.

Appendix 14: Temperature data of experimental work conducted in Chapter 5.

Appendix 15: Key findings of experimental work investigating volcanic particle-ice interaction.

Appendix 16: Temperature data of experimental work conducted in Chapter 6.

Appendix 17: Key findings of experimental work investigating microplastic particle-ice interaction.

Appendix 18: A comparison of modelled and observed particle velocities.

Appendix 19: Glossary of key terms.

9.1. Appendix 1: Summary of key light absorbing particles.

Table 9.1. A summary of the key characteristics of ice surface particles that can influence ice ablation rates. *PCDs = pyroclastic density currents.

Particle	Formation	Composition	Transportation	Interaction with ice	Likely increased presence on ice in the future?
Black carbon	Anthropogenic (e.g. fossil fuel combustion) and natural (e.g. wildfires) sources.	Carbonaceous particles, with a chain structure of volatile organic compounds around a carbon core (micrometre scale).	Atmospheric transport due to small size of the particle.	Reduces surface albedo of ice and increases the ablation rate of ice. This is a strong absorber of solar radiation (and wavelength independent).	Yes (due to increased frequency of wildfires, emissions from boats, and melting of ice exposing buried particles).
Brown carbon	Anthropogenic (e.g. biomass burning) and natural (e.g. biogenic aerosols) sources.	Carbonaceous particles with a large (nanometre scale) carbon core. Many species, but all are organic. Compositional changes can occur through transport (e.g. bleaching).	Atmospheric transport due to small size of the particle.	Reduces surface albedo of ice and increases ablation rate of ice, although the extent of this varies due to a range of particle compositions and properties. Wavelength dependence absorption of solar radiation, with absorption predominantly in the shorter wavelengths (e.g. blue and ultraviolet).	Yes (due to increased frequency of peatland fires in high latitudes).
Dust	Natural (e.g. arid and semi-arid areas) and anthropogenic (e.g. land use) sources.	Soil-derived particles (micrometre scale) of varying composition (reflecting the source conditions).	Atmospheric transport due to small size of the particle.	Reduces surface albedo of ice and increases the ablation rate of ice. Absorption predominantly in the visible region. Absorption is not as strong as other particles.	Yes (due to deforestation, wind erosion and increased frequency of dust storms).

Particle		Formation	Composition	Transportation	Interaction with ice	Likely increased presence on ice in the future?
Cryoconite		Aggregation of surface dust to form larger units containing microorganisms.	85-95% dust plus organic matter. Composition is dependent on the dust, which is dependent on the source location.	Atmospheric transport due to small size of the particle.	Aggregation of material leads to localised regions of decreased albedo and the formation of holes on the ice surface. Continued darkening of sediments from consolidation events.	Yes (due to increased dust deposition).
Rock debris		Natural source (e.g. scree slopes and glacier deposits).	Highly varied as reliant on the local factors (e.g. geology).	Gravity-driven transportation (e.g. rockfall from scree slopes)	This depends on the thickness of the deposit. Thinner layers will increase ablation, whilst thicker layers will preserve the ice.	
Volcanic particles	Airfall	Natural source (volcanic eruptions).	Highly varied (e.g. silica content, pore spaces, etc). Therefore, the thermal and optical properties vary considerably.	Atmospheric transportation of smaller particles. These can settle on the ice as thick layers (typically near the eruption site) or as a scattering of particles.	This depends on the thickness of the deposit. Thinner layers will increase ablation, whilst thicker layers will preserve the ice.	No (due to no expected increase in eruption frequency, although possible re-exposure of buried particles from melting glaciers).
	PCDs*		Mixtures of volcanic debris and gases; therefore, the composition is highly varied, and the thermal properties vary.	Gravity-driven transportation.		
Meteorites		Natural source (formation in space).	Composition varies depending on the type of meteorite. Three classes: chondrites (stony class), carbonaceous chondrites	From meteorite fall events. Concentrated in meteorite stranding zones on ice sheets.	Variable interaction with ice due to range of composition and properties. Stony meteorites remain on the	No (due to no expected increase in fall frequency).

Particle	Formation	Composition	Transportation	Interaction with ice	Likely increased presence on ice in the future?
		(stony class), and iron meteorites.		ice surface, whilst iron meteorites sink into ice.	
Microplastics	Anthropogenic sources (e.g. road traffic emissions, beauty products, plastic fibres from clothing).	< 5 mm plastic particles with a varied composition (the most common found in ice systems are polyethylene, polypropylene, and polyamide). Therefore, the thermal and optical properties vary considerably.	Atmospheric transport due to small size of the particle.	Unknown.	Yes (due to the fact that microplastics can persist in the environment for long periods, and the annual waste production of microplastics is expected to increase).

9.2. Appendix 2: Supplementary table of reviewed published fieldwork studies.

Table 9.2. Comparison of results from fieldwork experiments, where ¹cited in Kirkbride and Dugmore, (2003) ²cited in Fujii (1977), ³Kayastha et al (2000) and ⁴cited in Fyffe et al. (2020). Climate classification is from Peel et al. (2007), where ^a: tropical, ^b: arid, ^c: temperate, ^d: cold, and ^e: polar.

Study	Location and climate	Debris type and characteristics	Substrate/type of cover	Duration of study	Key outcomes
Swithinbank, 1949	Vatnajökull, Iceland)	Debris dirt cones comprised from volcanic ash from the 1947 Hekla eruption. These extended from ~1-3 m in height (averaging at 2 m from the surrounding ice).	Ice/Natural	-	<ul style="list-style-type: none"> Thick layers of debris protected the underlying ice from ablation to form dirt cones. Thin layers of debris on the extent of the dirt cones accelerated ice melt. Debris thickness, radiation absorbance coefficient, and conductivity were the primary controls on ice ablation.
Lister, 1953 ¹	Breidamerkurjökull, Iceland	Tephra	Ice	-	<ul style="list-style-type: none"> Critical thickness 0.4-0.7 cm.
Östrem, 1959	Isfallsglaciaren, Sweden	Rock (sand and gravel) with various grain sizes and layer thicknesses (0-30 cm).	Ice/Artificial. Plots approximately 2 m ² .	26 days, 10 July-5 August 1956.	<ul style="list-style-type: none"> The upper sand layer (9 °C) was +4°C higher than the ambient air temperature (5.4 °C). Distribution of heat energy varied with grain sizes and thickness of debris layer. Increased melting of ice under thin debris layers relative to bare ice and decreased melting of ice under thick debris layers relative to bare ice. Effective and critical thicknesses measured at 0.5 cm and 1 cm, respectively.
Loomis, 1970 ^{2,4}	Kaskawulsh Glacier, Alaska	Rock	Ice	-	<ul style="list-style-type: none"> Development of effective thickness (e.g. 1 cm) and critical thickness (e.g. 5 cm) values. Thin layers increased ablation by 129% relative to bare ice ablation.
Moribayashi, 1972 ²	Japanese Central Alps	-	Snow	-	<ul style="list-style-type: none"> Similar effective and critical thickness values as those observed by Östrem (1959) of approximately 0.5 cm and 1.5 cm, respectively.
Small and Clark, 1974 ^{1,4}	Glacier de Tsidjiore Neuve, Switzerland	Light grey gneiss with a variety of grain sizes, and highly fractured dark schists.	Ice	-	<ul style="list-style-type: none"> Ablation increased by 121.9-172.3% under debris layers 1 cm relative to bare ice. Ablation increased by 117.3% under debris layers 2-3 cm relative to bare ice.

Study	Location and climate	Debris type and characteristics	Substrate/type of cover	Duration of study	Key outcomes
					<ul style="list-style-type: none"> Effective and critical thicknesses were measured at 1 cm and 3 cm, respectively.
Bazhev, 1975	Medvezhiy glacier, Pamir mountains, Tajikistan	Coal dust particles with 0.2-0.5 mm diameters. Manual dusting of particles using 12.5, 25, and 50 g of coal dust per 1 m ² .	Snow/firn and ice/Artificial. Four 2x2 m plots.	Three experimental series, each 3-4 days, 25 August-6 September 1965.	<ul style="list-style-type: none"> Ablation of snow/firn covered surfaces was higher than ice covered surfaces. Dusting of particles resulted in the formation of a 'melt crust' as the particles sunk into the ice. The maximum ice melt was experienced with coal dust at a density of 5 g/m² due to the optimum zone of particle radius and zone of heat effect (e.g. highest proportion of the glacier that experienced the heat effect of coal dust).
Fujii, 1977	Rikha Samba Glacier, Nepal	Black phyllite sand	Snow/Artificial. Nine plots with a debris thickness 0.5-8 cm.	4 hours 35 minutes, August 1974.	<ul style="list-style-type: none"> Confirmation of 'Östrem' curve, where thick layers of debris protected the ice from ablation and thin layers of debris accelerated ice melt. Noted that additional experimental field work studies were required to understand the role of particle properties (e.g. particle size, albedo mechanism of debris formation, and heat transfer mechanisms).
Higuchi and Nagoshi, 1977	Tsurugizawa, Tateyama Mountain range, Central Japan	Mineral dust (quartz and feldspar), with diameter ranges of ~4-10µm.	Snow/Natural	-	<ul style="list-style-type: none"> Albedo of snow decreases with increasing particulate matter concentration. Increasing concentration of particulate matter within the surface snow was observed throughout the ablation season (June-October) due to concentration in the surface snow layer after snow melt. This resulted in a decrease of snow albedo throughout the ablation season.
		Sand	Snow/Artificial. Thicknesses of 0.1, 0.2, 0.3, 0.5, 1, 2 and 5 cm.		<ul style="list-style-type: none"> Demonstrated effective and critical thickness values of 0.5 cm and 2 cm, respectively, for sand grained particles.
Driedger, 1981	South Cascade Glacier, USA.	Tephra (specifically ash), with a focus on thin ash deposits (from Mount. St.	Snow (firn)/ Eight artificial plots (bare	8 days, 18 -26 August 1980.	<ul style="list-style-type: none"> Deposition of ash onto the snow resulted in the ash absorbing water. This had an albedo of 0.16.

Study	Location and climate	Debris type and characteristics	Substrate/type of cover	Duration of study	Key outcomes
	Maritime climate with heavy annual ppt. (up to 4.5 m)	Helens eruption). 91% of the particles were 0.25 – 1 mm in diameter, with 55% greater than 0.5 mm.	snow, 0.075, 0.2, 0.5, 1, 1.5, 2, 3 cm), and one natural plot with 0.025 cm of debris.		<ul style="list-style-type: none"> Effective thickness (0.3 cm) and critical thickness (2 cm) values were determined. Ash layers with the effective thickness increased ice melt by approximately 90% (relative to bare ice). Suggested the need for more research into the 'effective thickness' values (e.g. 0.2-0.5 mm) to provide clarity on this part of the Östrem curve.
Nakawo and Young, 1982	Peyto Glacier, Canada	Ottawa sand (dried). This is medium grained silica sand with an average grain diameter of 0.4 mm.	/Six artificial plots with debris layer thickness ranging 1-10 cm.	2 days, 20-22 August 1979	<ul style="list-style-type: none"> Surface irregularities developed during the experiment due to differential ablation. Saturation of debris layers was observed. This appeared to be uniform in most plots, aside from one instance where only the basal particles were saturated.
Khan, 1989	Barpu Glacier, Karakoram Himalaya, Pakistan.	Rock (disintegration of local metamorphic and igneous rocks) with a variety of grain sizes from clay grade to boulders > 4m.	Ice/Natural occurring. 37 ablation stakes in facet (slope angle approximately 45°)	18 days over three 6-day periods, May-July. Short periods were selected to mitigate against natural modification to debris thicknesses with time.	<ul style="list-style-type: none"> All facets were surrounded by two stakes near the top edge and two stakes near the bottom edge. This ablation stake network demonstrated that there was increased ablation at the top of the facet relative to the bottom. Facet ablation predominantly relied on incoming radiation as ablation rate between facets was due to the slope aspect. These represented almost bare ice surfaces. However, although horizontal surfaces received the greatest amount of radiation, the lowest amount of ablation was experienced in these regions due to the presence of debris layers insulating the ice (see below). Uneven rates of ablation associated with varying debris thicknesses, where greater ablation rates were observed under areas of thinner debris thicknesses. Critical thickness values were measured at 3 cm. The effective thickness was measured at 1 cm, where there was a 63% increase in ablation. Areas of uncertainty were associated with thin layers (e.g. ~2 cm) of debris. 20% of the area experienced thicknesses up to 3 cm, 55% had debris thicknesses 3-15cm, and
			Ice/Natural occurring. 45 ablation stakes in flat study. Natural range of 0-30 cm thick over the ablation stake network.		

Study	Location and climate	Debris type and characteristics	Substrate/type of cover	Duration of study	Key outcomes
					25% had debris thickness 16-70 cm. Therefore, 80% of the field area experienced reduced ablation.
Mattson et al., 1993	Rakhiot Glacier, Western Himalayas, Pakistan	Rock from Pleistocene lateral moraines. A range of grain sizes from silts, sands, and gravels to cobbles and boulders.	Ice/Artificial (12 plots) and naturally occurring (ten sites). Layer thicknesses varying 0-40 cm.	47 days, 22 June-8 August 1986.	<ul style="list-style-type: none"> • Consistent trend of increased ablation beneath thinner layers, where an effective thickness was measured at 1 cm. Decreased ablation was observed under layers thicker than this, with a critical thickness measured at 3 cm. • Extending the Östrem curve from this study estimated that ablation would stop in instances where debris thicknesses exceeded 100 cm.
Syverson and Mickelson, 1995 ¹	Burroughs Glacier, Alaska, USA	Rock	Ice	-	<ul style="list-style-type: none"> • Effective and critical thicknesses were measured at 0.7 cm and 2 cm, respectively.
Rana et al., 1997 ³	Lirung Glacier	Debris. The mean albedo of debris surface: 0.1	Ice/Natural	-	<ul style="list-style-type: none"> • Effective thickness measured at 2.6 cm, whilst critical thickness was measured at 9 cm.
Adhikary et al., 2000	Lirung Glacier, Nepal. ^c	Dust, specifically black soil containing organic matter, albedo: 0.08 (dry) and 0.06 (wet), bulk density: 450 kg m ⁻³ , particle size: 0.35 ≥ φ > 0.15 mm.	Ice/Artificial. Ten plots, eight on a flat surface, two on a 25° sloping surface.	9 hours, 28, 29 and 30 May 1996.	<ul style="list-style-type: none"> • Effective thickness was measured at 0.02 cm, whilst critical thickness was measured at 0.13 cm. Maximum ablation was five times greater than bare ice. This demonstrated that the maximum ablation under dust particles was achieved at much thinner layers than previous experiments and provided an insight into the behaviour of 'dirty ice' states. • Reduction of ice albedo to 0.15-0.22 with the presence of dust particles (compared to 0.39 of bare ice). • Modification of ablation patterns due to migration of dust particles with meltwater. This allowed the reduced albedo surface to be translated to adjacent bare ice surfaces. • Comparisons with previous work suggested that dust particles behaved differently on ice surfaces compared to snow. A 1.4 x higher concentration of particles was required for maximum ablation to

Study	Location and climate	Debris type and characteristics	Substrate/type of cover	Duration of study	Key outcomes
					be achieved on an ice surface relative to snow (e.g. 0.112 kg m ⁻² compared to 0.08 kg m ⁻²).
Kayastha et al., 2000	Khumbu Glacier, Nepal	Angular, loosely packed wet cobbles of light-coloured granitic rocks up to 3 cm in size.	Ice/Artificial. Six plots with debris thicknesses ranging from 2-40 cm, one plot of bare ice.	11 days, 21 May-1 June 1999.	<ul style="list-style-type: none"> Effective and critical thickness demonstrated at 0.3 cm and 5 cm, respectively. Ablation ceased under debris thicknesses larger than 1 m. Thermal conductivity and albedo are the main debris properties that control heat transfer from a particle to ice surface.
Takeuchi et al., 2000	Khumbu Glacier, Nepal	Debris	Ice/Natural. Varying debris thicknesses ranging 2-40 cm.	Ten days, 22 May-1 June Ablation rates were measured four times a day.	<ul style="list-style-type: none"> Inverse correlation between ablation rates and albedo of ice surface. Direct comparisons between thermodynamic response of debris-covered ice and debris-free ice within the same region demonstrated that ice covered with a debris layer of 10 cm experienced 40% less melt relative to a bare ice surface with the same low albedo. This was suggested to be a result of the insulating effects of the debris where heat was not conducted through the layer.
Unpublished data ¹	Giggjokull, Iceland	Tephra fallout from the 1947 Hekla eruption (first phase – dark andesitic tephra, second phase – light dacitic tephra).	Ice/Artificial	Ten days.	<ul style="list-style-type: none"> Effective and critical thicknesses were measured at 0.2 and 0.55 cm, respectively. Determined that the lower critical thickness value compared to previous studies was due to the lower thermal conductivity of porous tephra relative to sedimentary rock debris.
Brock et al., 2007	Villarrica volcano, Chile. ^c	Tephra (predominantly lapilli, with some ash). Andesitic-basaltic composition, with a silica content of approximately 53-56%. Loosely compacted and well sorted tephra cover. Porous lapilli, compacted ash.	Snow/Artificial. Tephra thicknesses 5, 10, 20, 30, 40, 50, and 90 mm (seven plots), a discontinuous layer of tephra (eighth plot), 'natural' snow containing trace concentrations	165 days, 82 in 2004 and 83 in 2005.	<ul style="list-style-type: none"> A 97% increase in snow ablation was observed underneath the discontinuous layer of tephra (0.1 kg m⁻²). The effective and critical thicknesses occurred before the tephra layer was continuous, contrasting to previous studies looking at tephra. This most correlated with results from Adhikary et al. (2000) where dust was investigated. This suggested that maximum ablation was under 'dirty ice' conditions, rather than 'debris-covered ice' conditions. The low critical thickness value was suggested to be due to the low thermal conductivity of the porous material (e.g. 0.35 W

Study	Location and climate	Debris type and characteristics	Substrate/type of cover	Duration of study	Key outcomes
			of tephra, dust, etc., (ninth plot), clean snow (tenth plot).		<p>$m^{-1} K^{-1}$), agreeing with suggestions by Kirkbride and Dugmore, 2003 (unpublished data).</p> <ul style="list-style-type: none"> Reduction in snow albedo from ~0.55 to ~0.1. Noted that there were large changes in the thicknesses of the tephra layer throughout the measurement period.
Mihalcea et al., 2008	Miage Glacier, Italy	Debris from deglaciated rock walls, and moraines	Ice/Natural.	June and July 2005, summer 2006.	<ul style="list-style-type: none"> Surface temperature was primarily controlled by thickness of debris layers. Supraglacial debris evolution is dynamic over short periods (e.g. less than a decade).
Richardson and Brook, 2010	Summit Plateau ice field, Mt. Ruapehu, New Zealand	Tephra (from the 2007 Mt. Ruapehu eruption). This deposited tephra of variable thickness: < 2 m diameter ballistic blocks and ash-lapilli deposits of various thicknesses onto the summit plateau ice field.	Ice/Natural. 12 stakes were emplaced into the ice through tephra with a thickness range of 0-40 cm.	16 days, 17 January to 2 February 2008.	<ul style="list-style-type: none"> Effective and critical thickness values were measured at 7 cm and 12 cm, respectively. Ablation was close to zero underneath debris layers of approximately 50 cm. Previous studies investigating tephra layers demonstrated smaller effective/critical thicknesses than those reported in this study (< 1 cm). It was proposed that geothermal contribution to melt may have been occurring at this field site.
Yang et al., 2010	24K Glacier, southeast Tibetan Plateau	Dark-grey coarse sandy debris	Ice/Natural. 14 ablation stakes were emplaced from the upper glacier margins to the glacier terminus.	October 2007-September 2008. Results were collected from stakes on three days (July 19, August 18, September 4).	<ul style="list-style-type: none"> Similar trend that debris thickness impacted the ablation of ice (strong ablation observed with thicknesses 0-4 cm, with effective thickness observed at 1 cm thick). Presence of debris also modified the ablation gradient in the ablation zone (e.g. maximum mass loss was observed in the middle segment rather than the terminus due to a shift to a negative mass balance in the thick debris-covered areas at the terminus).
Brook and Paine, 2011	Fox Glacier, New Zealand. ^c	Ice-cored moraine deposits	Ice/Natural. 21 stakes within continuous layers of varying debris thickness (0-36 cm).	11 days	<ul style="list-style-type: none"> Effective and critical thickness values were calculated at 2 cm and 3 cm, respectively. Agreement with many previous studies. Suggested that difference between previous results were predominantly due to the climate (e.g. maritime climate).

Study	Location and climate	Debris type and characteristics	Substrate/type of cover	Duration of study	Key outcomes
Juen et al., 2013	Vernagtferner, Austria. ^c	Three lithologies were investigate: (1) mica schist, (2) black, basaltic tephra from Mount Etna (Italy), (3) grey, trachytic pumice from Sete Cidades volcano (Azores, Portugal). Grain sizes were in the sand and gravel fraction, dependent on lithology (1-2 to 30-50 mm thick). Sieving techniques were used to ensure consistent grain sizes per plot.	Ice/Artificial. Ten plots with debris thicknesses 2.5-18 cm. Plots of different lithology were placed next to one another to allow direct comparisons of different rock type experiencing the same meteorological conditions.	Ablation (summer) season 2010). Twice daily measurements were taken during 11 days of the measurement period (25 June-1 July, 5-10 July 2010).	<ul style="list-style-type: none"> • This study demonstrated that the lithology, grain size, porosity, and moisture content have a influence on sub-debris ice melt. • Redistribution of particles formed ice cones in the volcanic plots. It was suggested that this process did not occur in the mica schist plots as these were bigger (1x1 m compared to 50x50 cm). • Direct comparison between mica schist and tephra of the same layer thicknesses demonstrated that tephra particles were more insulating. This was suggested to be due to the lower thermal conductivity because of increased porosity. • Pumice was observed as the most insulating material. This was suggested to be due to a high albedo and a high porosity, although the albedo property was deduced as the determining factor. Direct comparisons between white (high albedo) and black (low albedo) volcanic material showed a melt increase of 1.75 by the high albedo material, despite a slightly higher porosity. • The sand fraction of mica schist demonstrated a higher ablation compared to the gravel fraction of the same material, with the same layer thickness. This general trend was also observed with fine versus coarse pumice. • Higher moisture content within a porous material resulted in a higher thermal conductivity.
Meinander et al., 2013	Sodankylä, Finland	Black carbon and brown carbon.	Natural	April 2009	<ul style="list-style-type: none"> • Albedo measurements of a snowpack (in the 290-550 nm wavelengths) demonstrated albedo values of 0.5-0.7. This was lower than values of clean snow in the literature (e.g. 0.97-0.99). It was suggested that low albedo values were due to large snow grain sizes, meltwater surrounding snow grains, and the presence of impurities.

Study	Location and climate	Debris type and characteristics	Substrate/type of cover	Duration of study	Key outcomes
					<ul style="list-style-type: none"> Black carbon concentrations were measured at 87 ppb, whilst brown carbon concentrations were measured at 2984 ppb during albedo measurements from snow samples.
Hobbs, 2014	Sollipulli Caldera, Chile	Volcanic particles (specifically scoria) Basaltic-andesitic in composition. Solid rock densities were around 2600 kg m ⁻³ with porosities varying from 54 – 65%. Dominant grainsize is in the ash-lapilli grade (although some volcanic bombs were present). The albedo of the particles ranged from 0.09-0.14 in the dry samples, and 0.05-0.07 in the wet samples.	<p>Snow/Artificial (four experimental plots separated into 7-12 areas of thicknesses ranging 0.3-10 cm, a natural and artificial control, and a discontinuous layer.</p> <p>Ice/Artificial (one plot with a thickness range of 0.3-2 cm, a discontinuous layer, and a natural control.</p> <p>Natural (observation of six dirt cones)</p>	25 days (February – March 2011)	<ul style="list-style-type: none"> Critical thickness values were within the range of 0.36-0.48 cm. Thicker patches of debris were least affected by glacial dynamics and external factors. Exposure of snow surfaces or redistribution of debris in the thinner layers of debris was observed. Topographic irregularities also developed under the thinner layers (e.g. <1.5 cm). Redistribution within discontinuous patches of debris resulted in the concentration of particles to form a continuous layer. Prior to this, ablation was enhanced under discontinuous layers. The critical thickness was below 0.3 cm. This was deduced with reference to the natural control that was naturally dirty. This demonstrated enhanced ablation, whilst none of the continuous layers enhanced ablation. This compared well with findings from Brock et al. (2007). Slightly reduced ablation on the ice surface compared to the snow surfaces. This demonstrated the capability of dirt cones to combine with one another. An increase in dirt cone height was observed with time (due to surface lowering in the proximal region). Height increases ranged from ~25-140 cm. This was a function of debris thickness.

Study	Location and climate	Debris type and characteristics	Substrate/type of cover	Duration of study	Key outcomes
Meinander et al., 2014	Sodankylä, Finland	Black carbon particles.	Snow/Artificial (a plot containing 1465 ppb BC, and a reference plot).	Four days (April 2013)	<ul style="list-style-type: none"> • Demonstrated a correlation between snow density and black carbon content. The addition of impurities decreased the snow density of melting snow relative to a reference plot. This was observed in instances with and without precipitation events. • It was suggested that density differences between naturally melting clean snow versus dirty snow was due to the light absorbing properties of the particles leading to increased melt and, consequently, increased air pockets surrounding the particles. This increased melting process would also create larger grain sizes, resulting in lower water retention capacity. It was also suggested that BC particles reduced adhesion between water and snow grains, again, reducing the water retention capacity of the snowpack.
Dragosics et al., 2016	Finnish Meteorological Institute (FMI) in Helsinki, Finland. ^e	Tephra (ash from the 2010 Eyjafjallajökull eruption). Two grain sizes (1 ϕ and 3.5 ϕ , therefore, 0.5 mm and 0.1 mm) were investigated. The bulk density was 2.57 and 2.46 g cm ⁻³ , respectively. Blocky-shaped particles with angular (involving clusters of clasts comprised of smaller ash particles) or stepped surfaces.	Snow and ice/Artificial	17 days	<ul style="list-style-type: none"> • Combination of laboratory and fieldwork experiments, with a similar focus to Juen et al. (2013) as the influence of grain size on particle-induced ice ablation was assessed. • Grain sizes behave differently in terms of critical/effective thickness values and redistribution. The smaller grain sizes slipped off the ice surface. It was proposed that this was because the smaller grain sized material had smoother surfaces in this instance. • Volcanic particles with a 0.5 mm grain size had an effective thickness of 0.1 cm, whilst a volcanic particle with a 0.1 mm grain size had an effective thickness of 0.1-0.2 cm. • Volcanic particles with a 0.5 mm grain size had a critical thickness of 0.9-1.5 cm, and a volcanic particle with a 0.1 mm grain size had a critical thickness of 1.3 cm.

Study	Location and climate	Debris type and characteristics	Substrate/type of cover	Duration of study	Key outcomes
Möller et al., 2016	Svínafellsjökull, Iceland	Tephra from Grímsvötn volcano. Bulk density of the tephra was 850 kg m ⁻³ and grain size was below 5 mm.	Ice/Artificial plots on a flat surface (12 experimental plots with tephra thicknesses ranging from 0.5-10 cm, one bare plot).	13 days of daily measurements (May 2013)	<ul style="list-style-type: none"> • Effective thicknesses ranged from 0.1-0.2 cm (with a ~25% increase in ice ablation relative to bare ice), whilst a critical thickness was met at 1 cm. A continued decrease in ablation was observed in thicknesses above this value. The maximum thickness investigated (e.g. 10 cm) demonstrated an 80% reduction in ablation relative to bare ice. • Surface roughness has an influence on ablation under thin layers of tephra. This can impact the albedo and thermal conductivity effect of the tephra due to distribution of bare-ice outcrops. It was proposed that the same material and thickness of tephra could experience different ablation patterns in instances where the surface roughness varied. • It was observed that the increased ablation under thin layers was to a lesser extent when there were higher levels of precipitation. It was suggested that pore spaces and water content may lead to the variation in tephra ablation rates, also proposed by Juen et al. (2013). However, this suggested the opposite effect than Juen et al. (2013): a reduction in melt with increasing precipitation and, therefore, water content. It may be that the observed pattern was due to other meteorological features associated with precipitation (e.g. cloud cover). This was not discussed in the paper.
Khan et al., 2017	Woodfjorden and Mine 7, Svalbard	Coal dust (black carbon particles)	Snow/Natural	-	<ul style="list-style-type: none"> • Dark coal dust deposits were visually observed near an active mine. This was associated with a reduction in the albedo by 84% (in the visible region, 400 nm-500 nm). • A remote site was also monitored (Woodfjorden). This allowed long-range transported particles to be quantified. This demonstrated a low

Study	Location and climate	Debris type and characteristics	Substrate/type of cover	Duration of study	Key outcomes
					<p>concentration of particles (e.g. 1.1 ng g⁻¹) compared to the mine site (see below).</p> <ul style="list-style-type: none"> • There were higher concentrations of BC next to the mine (e.g. 345 ng g⁻¹) compared to upwind (4.7 ng g⁻¹) and downwind (87-345 ng g⁻¹). Large variations in particle size (e.g. tenths to tens of microns) depending on proximity to the mine were also observed. This was the first observation of BC deposition on snow following this pattern, and confirmed hypotheses that larger BC particles fall out close to the source. This demonstrates a similar behaviour to tephra fallout.
Möller et al., 2018	Tungnaárjökull, Iceland	Tephra from Eyjafjallajökull and Grímsvötn. Bulk density of Eyjafjallajökull tephra: 1276 kg m ⁻³ . Bulk density of Grímsvötn tephra: 791 kg m ⁻³ .	Snow/Artificial (six tephra plots of variable thickness (~0.15, ~0.85 and ~8 cm) for two tephra types from Eyjafjallajökull and Grímsvötn. The bulk density was 1276 kg m ⁻³ and 791 kg m ⁻³ , respectively. One reference site with no tephra).	122 days, although reliable measurements were restricted to a 50-day period (May-September 2015).	<ul style="list-style-type: none"> • Thicknesses within the ablation plots were chosen from results from Möller et al. (2016) as these approximately matched the effective and critical thickness values from the previous study. • Snow surface lowering of 2.25 m at a reference site (no tephra), whilst a snow surface lowering of between 2.21 and 2.97 m was observed at the tephra plots. Lowering rates became comparable throughout the measurement period (e.g. late July) due to disintegration of the tephra plots altering the behaviour of particle-induced ablation/preservation. • Ablation was slightly increased under the Grímsvötn material compared to the Eyjafjallajökull material. • Snow surface lowering was observed under the thickest layer of Eyjafjallajökull material (e.g. 8 cm), despite previous research suggesting that full insulation processes begin at these thicknesses. It was suggested that this was due to the different substrate (e.g. snow rather than ice), suggesting that the substrate also has an influence on ablation patterns under tephra

Study	Location and climate	Debris type and characteristics	Substrate/type of cover	Duration of study	Key outcomes
					<p>layers. Only a very slight insulation effect was observed under the thicker Grímsvötn material.</p> <ul style="list-style-type: none"> • A pattern between precipitation events and ablation patterns was also identified. These contrasted with Möller et al. (2016) and demonstrated higher ablation rates in wet conditions. Therefore, It was suggested that the critical thickness for wet tephra was higher than that for dry tephra. • In the latter phases of the experiment (e.g. August onwards), redistribution of particles from ablation processes exposed bare-ice or snow surfaces, modifying the response of the ice to the tephra layer.

9.3. Appendix 3: Supplementary table of reviewed published laboratory studies.

Table 9.3. Comparison of results from laboratory experiments.

Study	Aims of study and particles considered	Experimental set-up	Key findings
Reznichenko et al., 2010	<p>To examine the effect of different thicknesses of sand* debris on ice melt. *Well-sorted medium grey-wacke river sand (high permeability).</p>	<ul style="list-style-type: none"> • 35 L of water frozen into an ice block. No mention of state of ice used; therefore, this was assumed to be opaque. • Combination of warm white electric bulb and incandescent bulb to access both shortwave (0.35-0.75 μm) and longwave radiation to induce ice ablation. • Bare ice and debris-covered ice (1, 5, 9, and 13 cm thicknesses). Vertical strings emplaced within the ice to measure surface changes every 12 hours. 	<ul style="list-style-type: none"> • Under continuous radiation, there are initial differences in the melt rates of ice under different thicknesses of sand (e.g. ice melt is delayed by ~12 hours under a 13 cm layer). However, once conduction reaches a steady-state, the melt rates become comparable for all layer thicknesses. This was reached within 60 hours for the 13 cm thick layer. • A 1 cm layer of debris increased ablation by ~10% relative to bare ice. 5, 9, and 13 cm thick layers reduced ablation relative to bare ice.
	<p>To assess the influence of diurnal cycles of radiation on ice ablation under a sand debris cover.</p>	<ul style="list-style-type: none"> • Three series of experiments: continuous radiation, diurnal cycling of radiation, and diurnal cycling of radiation with simulated precipitation events. • Diurnal cycles were assessed by alternating the exposure of ice to radiation and a cooling environment (using a freezer) for equal time periods. • To simulate rainfall, 10 mm of water was sprayed onto the ice over a period of one hour during exposure to radiation. 	<ul style="list-style-type: none"> • Under a diurnal cycle of radiation, melt rates for sand layers >5 cm remained lower than that for bare ice and 1 cm layer. This was suggested to be because the debris layer did not reach a steady-state heat flux. • It was suggested that ablation rates of debris-covered ice would vary with durations of diurnal cycle. Therefore, the large variability observed within fieldwork generated critical thicknesses was likely strongly controlled by variations in diurnal cycles.
	<p>To assess the influence of heat transfer via rainfall under a high permeable (sand) and low permeable (rock avalanche*) debris layer. *Poorly-sorted rock-avalanche deposit of coarse grains embedded in very fine grained material (low permeability).</p>		<ul style="list-style-type: none"> • A higher melting rate was observed under the permeable debris layer within the experiments involving precipitation events. This was suggested to be due to the advection of heat from the warm debris to the ice. • Ablation did not occur under the low permeable debris layer due to time-delays in advecting heat to the ice surface lasting longer than the ablation cycle.

Study	Aims of study and particles considered	Experimental set-up	Key findings
Hadley and Kirchstetter, 2012	To assess how black carbon particles can influence the albedo of snow in a laboratory setting, considering the effect of snow grain growth and positive feedbacks associated with these processes.	<ul style="list-style-type: none"> • Freezing of water droplets using liquid nitrogen within an insulated chamber to create spherical snow grains. Three snow grain sizes (optical effective radius of 55, 65 and 110 μm) were investigated. • Black carbon particles were added by spraying an aqueous suspension of particles. Five concentrations of black carbon (0, 110, 450, 860 and 1680 ppb) were investigated. • A spectrometer was used to measure the albedo of each snowpack in the wavelength region 0.39-0.95 μm. 	<ul style="list-style-type: none"> • An increase in the black carbon content causes a decrease in snow albedo (e.g. -0.05). This effect was observed to a greater extent in the visible region of the electromagnetic spectrum, with the near-infrared effect being masked by ice absorption in this region also. • Albedo decrease associated with black carbon content is experienced to a greater extent with large snow grains (e.g. 110 μm), suggesting that ageing of snow can cause an amplification of black carbon influence. • The overall albedo change was identified as being a function of (1) albedo change of snow with age, (2) albedo change of snow with black carbon impurities, and (3) albedo change because of the positive feedback of black carbon perturbation when the snow grains grow to a radius of 110 μm.
Hobbs, 2014	<p>To investigate how the physical properties of volcanic particles impact melting of ice, with the focus on the albedo, thermal conductivity, and bulk density. This was investigated with reference to (a) single particle melting* and (b) vertical surface melting (to replicate caldera walls). *Black ball bearing, white ball bearing, scoria (dry and wet), and pumice (dry and wet).</p> <p>To investigate how the physical properties of volcanic particles impact sublimation of ice. This was investigated with reference to (a) single particle sublimation* and (b) layer particle sublimation**.</p>	<ul style="list-style-type: none"> • Magnetic stirrer to disrupt >300 ml deionised water to form an optically transparent ice block. Preferential freezing encouraged using side insulation. • One filtered incandescent bulb to simulate the wavelength range of 0.35-1.034 μm to induce ice ablation. A water filter removed wavelength bands that are naturally absorbed by the atmosphere. • Unchanged environment and under a variety of air temperatures (to assess the influence of varying air temperatures on the quantity of meltwater produced). • Mass loss was calculated, and 3D models of the ice surface were created. 	<ul style="list-style-type: none"> • The presence of a surface particle enhances melting when the ice is subjected to radiation. • Thermal conductivity has a bigger effect on ablation than albedo, both in terms of amount of meltwater produced and time taken to initiate melting. Thermally conductive particles moved downwards through the ice and became embedded. • Melting is sensitive to small temperature variations. <hr/> <ul style="list-style-type: none"> • The presence of surface particles prevented sublimation processes directly beneath the particle and formed ice pedestals below. • The morphology and size of the pedestals varied (e.g. vertical morphology beneath the ball

Study	Aims of study and particles considered	Experimental set-up	Key findings
	<p><i>*Black ball bearing, white ball bearing, scoria, and pumice.</i> <i>**5 mm layer of Ballotini beads (>60 μm-1.5 mm size) and airfall deposits (1.7- 2.0 mm).</i></p>	<ul style="list-style-type: none"> • Sublimation experiments were conducted in temperatures that would not allow melting of the ice. 	<p>bearings, and inclined morphology beneath the white ball bearings).</p> <ul style="list-style-type: none"> • Albedo does not have an impact on sublimation. • Increasing permeability of a particle will result in increasing rates of sublimation. • Layers of particles appear to inhibit sublimation rates, although the physical properties of these particles do not seem to have a significant influence.
Dragosics et al., 2016	<p>To investigate the influence of volcanic ash (specifically from the 2010 Eyjafjallajökull eruption), on ice and snow melt using both field and laboratory experiments. This considered grain sizes and layer thicknesses*. <i>*Negligible, 1 mm, 3 mm and 9-13 mm) of the same grain size (0.5 mm diameter).</i></p>	<ul style="list-style-type: none"> • 200 ml of water frozen into an ice block. No mention of state of ice used; therefore, this was assumed to be opaque. • Relied on laboratory temperatures of +24°C to induce ice ablation. • Basal drainage holes in the ice containers to allow drained meltwater volumes to be quantified. • Monitoring of additional external factors. 	<ul style="list-style-type: none"> • Coarse grains have a bigger effect on the albedo of an ice body because the fine-grained particles can be easily washed off and redistributed. • Ice covered by thicker ash layers (e.g. 9-13 mm) takes longer to start melting in both a laboratory and outdoor setting, whilst thinner ash layers (e.g. up to 1 mm thick) cause enhanced melting.
Evatt et al., 2016	<p>To determine the role of thermal conductivity in the burial of meteorites* using a controlled laboratory experiment combined with a mathematical model. <i>*Two 15 x 10 mm spherical meteorites (ordinary chondrite and achondritic iron).</i></p>	<ul style="list-style-type: none"> • Slow freezing (2-3 days) of 8 L water to create an optically transparent ice (-1°C). • Specialist Oriel solar simulating arc lamp to mimic solar radiation over a wavelength range of 0.25-2.5 μm (the closest artificial replica of natural radiation) to induce ice ablation. This was 1 cm above the ice surface. • Monitoring of additional external factors. • Time-lapse imagery to capture ice response to meteorites over a 3-hour period. 	<ul style="list-style-type: none"> • Iron meteorites sink at a faster rate and to a deeper depth than stony meteorites due to a more efficient conduction of solar energy. • Meteorites with a sufficiently high thermal conductivity can become trapped within the ice as the downward movement offsets the removal of overlying ice through ablation.
Hénot et al., 2021	<p>To assess the formation of glacier tables using artificial cylinders* in a controlled setting.</p>	<ul style="list-style-type: none"> • Clear ice laid over Styrofoam to prevent basal melting. • Cylindrical caps of five materials with thermal conductivity values spanning two magnitudes placed on the ice surface. 	<ul style="list-style-type: none"> • The behaviour of the five cylindrical caps varied due to the different thermal conductivity values of the materials. • The extruded polystyrene cylinder did not ablate the ice and, therefore, formed a table

Study	Aims of study and particles considered	Experimental set-up	Key findings
	<p><i>*Extruded polystyrene, rigid polyvinyl chloride, plaster, cement, and granite.</i></p>	<ul style="list-style-type: none"> Time-lapse imaging every 8 minutes to monitor changes to the height of the ice surface and if ablation occurred from surface particles over an eight hour period. 	<p>underneath as the rest of the ice surface melting from air temperatures above the ice pressure melting point.</p> <ul style="list-style-type: none"> The polyvinyl chloride cylinder ablated the ice to some degree, but this did not exceed the melting of the remaining ice surface. Therefore, a table formed underneath the cap. The granite cylinder ablated the ice at a high rate and moved downwards into the ice. A table did not form underneath the particle. A linear evolution of the vertical position of the cylindrical caps was observed, suggesting that a steady state system was reached within minutes. Results were compared with an analytical heat conduction model that estimated the critical rock size for glacial tables to form at 10-20 cm, agreeing with field results.
<p>Taberlet and Plihon, 2021</p>	<p>To investigate the formation of zen stones in a controlled setting.</p>	<ul style="list-style-type: none"> Purified and degassed water in rectangular plastic containers (15 cm x 15 cm, depth of 5 cm) placed in a lyophilizer. Infrared radiation from vacuum chamber walls (at room temperature) provided energy for sublimation. Temperatures of -45°C to favour sublimation over melting. Metal disks placed on ice surface. These were polished to prevent absorption of infrared radiation. Time-lapse imaging every 5 minutes. 	<ul style="list-style-type: none"> Formation of zen stones was primarily controlled by differential sublimation of the ice. It was proposed that this was result of the stone providing shade and driving differential sublimation rates. The presence of a depression surrounding the pedestal was noted; it was suggested that this was a result of the stone emitting far infrared radiation that increased sublimation in the proximity. The thermal properties of the metal disks did not influence the behaviour of zen stone formation.

9.4. Appendix 4: Supplementary table of reviewed published modelling studies.

Table 9.4. Comparison of results from modelling experiments.

Study	Model type	Assumptions	Key outcomes
Drake, 1981	Energy balance model (EBM)	<ul style="list-style-type: none"> • Uniform layer. • Spherical particles. 	<ul style="list-style-type: none"> • Agreement with the literature where thick layers hinder melting and thin layers increase melting. • Modelled output curves compared well with the Östrem curve. • Agreed well with in-situ observations in Scheffervi, Quebec snowpack, where a melting duration was observed as 14 days. In-situ observations noted that the presence of a single layer of dust particles reduced the melting period by four days. The modelled output agreed with this and calculated an increased melting rate, associated with a subsequent overall reduction of 4.5 days in the melting duration.
Nakawo and Young, 1981	Energy balance model (EBM)	<ul style="list-style-type: none"> • Uniform layer. • Linear temperature gradient within the debris layer (e.g. a state of thermal equilibrium). • Heat conduction into the ice beneath is neglected. 	<ul style="list-style-type: none"> • General EBM equation: $M = S + L + H + LE + P + G$ (M= energy available for melt, S= net solar shortwave radiation, L= net longwave radiation, H= sensible heat transfer, LE= latent heat transfer, P=heat flux due to precipitation, G= conductive heat flux below the surface). • Fairly good agreement between the modelled output and observations at Peyto Glacier, Canada. • Differences between modelled output and observations were attributed to error in the measurement of surface temperature (as this was limited to twice a day), the assumption of a steady state temperature profile which may not be the case, and the lack of consideration of advection as an influencer of heat exchange and an ice surface. • Surface temperature can estimate the thermal properties of a debris layer. • Requirement of a large amount of input data (e.g. wind velocity, air temperature, surface temperature, relative humidity, etc.). • Overestimation of melt rates at night and underestimation of melt rates during the day due to the assumption of a linear temperature gradient within the debris layer.
Bozhinskiy et al., 1986	Energy balance model (EBM)	<ul style="list-style-type: none"> • Homogenous composition of debris cover. 	<ul style="list-style-type: none"> • Perfect agreement between modelled output and observations at Djankuat Glacier, North Caucasus. • Complexities of evolving debris with time.

Study	Model type	Assumptions	Key outcomes
Rana et al, 1997	EBM from Nakawo and Young (1981) in combination with a precipitation-runoff model	<ul style="list-style-type: none"> • Meltwater leaves the debris layer instantaneously. • Precipitation is a function of altitude. • Stored heat in the debris layer is constant. • Linear temperature gradient within the debris layer (e.g. a state of thermal equilibrium). 	<ul style="list-style-type: none"> • Incorporates equations to consider debris properties (e.g. porosity, density, specific heat, heat conductivity, and albedo). • Fair agreement between simulated daily runoff in the Lirung basin, Nepal using meteorological data and thermal resistance of the debris layer (calculated from surface temperature observations from remote sensing techniques). • Modelling three scenarios (i.e. debris-free, no melting under debris, and modelled ablation under debris) showed that simulating run-off when including the melting that was associated with debris-cover agreed with the observed runoff. This indicated that the debris-covered components of glaciers need to be included when simulating run-off in a given region. • Identifies that the relationship between the ablation rate and surface temperature is non-linear. It was suggested that this was the cause of the 30% underestimation of melt at the beginning and end of the ablation period. • Improving knowledge and observations of the distribution of surface temperatures across a debris layer would address uncertainties within this modelling approach.
Kayastha et al., 2000	Degree-day methods	<ul style="list-style-type: none"> • The amount of snow/ice melt is proportional to the sum of daily mean temperatures above melting point. 	<ul style="list-style-type: none"> • A comparison of different modelling techniques to estimate ablation rates under debris layers. • An energy balance model was used to assess ablation in bare ice conditions relative to a debris layer of 10 cm. This experienced overestimation of melting in both cases. It was suggested overestimation was a result of uncertainty in the parameterisation of the energy balance equations and the simplification of the processes through including assumptions. • The positive-degree-day factor (PDD) was a successful predictor of ablation on Khumbu Glacier, Nepal.
	Energy balance model (EBM)	<ul style="list-style-type: none"> • Linear temperature gradient within the debris layer (e.g. a state of thermal equilibrium). • Saturated vapour pressure at the debris surface. 	

Study	Model type	Assumptions	Key outcomes
Hansen and Nazarenko, 2003	Climate model (Goddard Institute for Space Studies climate model)	-	<ul style="list-style-type: none"> • Modelling to assess the impact of soot climate forcing, rather than ablation modelling (as described previously). • The modelling climate simulation indicated that soot contamination and associated decrease in albedo contributed to one quarter of the observed warming in the period 1880-2000. • Uncertainties due to sparse accurate soot content and snow albedo measurements. Improved links between the role of snow albedo and melting ice in climate change are required.
Han et al., 2006	Energy balance model (EBM)	<ul style="list-style-type: none"> • Heat conduction into the ice beneath is neglected. • Heat flow through the debris layer is dominated by conduction. • Linear temperature gradient within the debris layer (e.g. a state of thermal equilibrium). 	<ul style="list-style-type: none"> • Modelled ablation under a thick debris covered and compared with a case study site (e.g. Koxkar glacier, China). Modelled output and observations compared fairly well. • Discrepancies between modelled output and observations were likely due to the complex relationship between debris temperatures and heat flux
Nicholson and Benn, 2006	Energy balance model (EBM)	<ul style="list-style-type: none"> • Linear temperature gradient within the debris layer (e.g. a state of thermal equilibrium). • Heat delivered by precipitation to the surface energy balance was omitted. • Ice temperature is at 0°C. • All conductive heat flux within the ice is used for melt. 	<ul style="list-style-type: none"> • Sub-debris melt rate can be calculated using the following equation: $M = \frac{Q_m}{\rho_i L_f}$, where Q_m= downward energy flux at base of debris layer, ρ_i = ice density, and L_f = latent heat of fusion. • Conductive heat flux was calculated from the debris layer thermal conductivity, a steady-state surface and ice temperatures, and debris thickness. • Many previous studies assessed debris thicknesses up to 10 cm, but many glaciers can have debris-layers much thicker than this. Thick debris layers exacerbate the problem of including assumptions of a linear temperature gradient within a debris-layer due to thermal disequilibrium, demonstrating the importance for including an appropriate time interval for analysis. Therefore, 24 hours was chosen as the minimal interval as it was noted that equilibrium (i.e. a linear temperature gradient) could not be established on timescales shorter than this. This was referred to as the 'diurnally averaged melt model'.

Study	Model type	Assumptions	Key outcomes
			<ul style="list-style-type: none"> • EBM: $Q_s + Q_l + Q_h + Q_e + Q_c = 0$, where Q_s = net shortwave radiation flux, Q_l = net longwave radiation flux, Q_h = net sensible heat flux, Q_e = net latent heat flux, Q_c = conductive heat flux into the debris. • The debris surface temperature influences the values of variables in the above equation, aside from Q_s. Therefore, this is a crucial component to EBM models. However, an accurate way of calculating this has not yet been fully developed. Instead, this can be estimated from meteorological variables. • Comparisons of modelled output with fieldwork observations (e.g. Ghiacciaio del Belvedere and Larsbreen) compared well (e.g. within 5% of measured value) in instances where the moisture content of the debris layer was known, demonstrating agreement with modelling and observations when specific properties about the debris layer are known. • Overestimation of melting in modelled output between observed values was suggested to be due to the assumption that the ice is at 0°C and temperature gradients within the ice were not considered. • A modelled Östrem curve was generated, although this was missing the 'rising limb' associated with high melt rates under thin layers. This may be due to the time-constraints of the model (i.e. ~24 hours), as thin layers of debris may reach a thermal equilibrium faster than this period. Thin layers of debris also likely extend the duration of melting in a given day. Therefore, this time-step was not appropriate for dirty ice modelling. Instead, shorter timescale of melt calculation should be considered. • A small amount of surface debris was still considered as a continuous layer of uniform thickness in this model; therefore, it did not consider dirty ice conditions – the reality of many glaciers. Therefore, the model used by Nicholson and Benn (2006) is applicable to most debris-covered glaciers, but not those in dirty ice conditions.
Brock et al., 2007	Energy balance model (EBM)	<ul style="list-style-type: none"> • Air temperature at 0°C. 	<ul style="list-style-type: none"> • Combined fieldwork results (e.g. observations of meteorological, surface temperature and ablation measurements) with energy balance modelling. • Modelled output and observations compared well, although there was some melt overestimation, suggested to be due to the model assumption that air temperature did not drop below 0°C.

Study	Model type	Assumptions	Key outcomes
Richardson and Brook, 2010	Degree-day methods	<ul style="list-style-type: none"> PDD assumes the amount of snow/ice melt is proportional to the sum of mean daily temperatures above the melting point. Simplification of complex factors associated with ablation. 	<ul style="list-style-type: none"> The formation of a 'weathering crust' also likely contributed to uncertainties, as it was observed that melt closely compared in the conditions where higher wind speeds removed the weathering crust. Simple positive-degree-day (PDD) approach (similar to Kayastha et al., 2000) from observations of air temperature. This was used in combination with fieldwork assessing ablation over 12 ablation plots in Summit Plateau ice field, Mt Ruapehu. Positive-degree-day-factor (k) links PDD to ablation: $k = \frac{\sum a}{PDD}$, where $\sum a$ is total ablation over the same period as used for the PDD calculations. Good comparison of positive-degree-day-factor (k) with the literature (e.g. bare ice = 7.8 mm d⁻¹ °C⁻¹ and 10 cm volcanic particles = 6.0 mm d⁻¹ °C⁻¹). It was noted that this considers meteorological conditions and debris properties, whilst the PDD only considers meteorological conditions.
Reid and Brock, 2010	Debris energy-balance model (DEB)	<ul style="list-style-type: none"> There is no accumulation (i.e. negative melt rates calculated) because all meltwater runs off immediately without pooling and refreezing. Ice/debris interface remains at melting point (therefore, only considers the ablation season). 	<ul style="list-style-type: none"> DEB evolved from EBM where a non-linear debris temperature gradient is considered. Therefore, this considered the flux of subsurface heat conduction into debris-free ice and snow. The effectiveness of this is tested by comparing hourly debris surface temperatures and melt rates to observed data collected over three ablation seasons (2005, 2006, and 2007). This suggested that non-linear temperature gradients occur when a layer is warming or cooling, but linear temperature profiles during the warmest and coldest times of the day. DEB is driven by meteorological variables (i.e. incoming shortwave radiation, reflected shortwave radiation, downwelling longwave radiation, upwelling longwave radiation, air temperature at 2.16 m height, wind speed at 2.16 m height, relative humidity of air at 2.16 m height, relative humidity at debris surface). Debris surface temperature estimated by considering heat fluxes at air/debris interface. It is assumed to change on every time-step to a temperature that allows the sum of heat fluxes at a debris surface to equal 0. Melt rates at the debris/ice interface estimated by calculating heat conduction through the debris layer.

Study	Model type	Assumptions	Key outcomes
			<ul style="list-style-type: none"> • Agreement of an approximate 3-4 hour lag between the maximum temperature at the bottom of the layer reaching the maximum surface temperature. • A 3 hour lag between modelled debris temperature and observed temperature was suggested to be a result of varying debris properties that affected thermal diffusivity. • Shortwave, longwave, conductive, and sensible heat fluxes were determined as the most important fluxes (e.g. when removed the model output did not fit surface temperatures). Precipitation heat fluxes had minimal impact, providing a justification for previous modelling techniques where heat flux from precipitation was considered negligible and, therefore, was omitted (e.g. Nicholson and Benn, 2006). • Predicted values of hourly debris surface temperature and internal temperature compared well with measured values of rock (Miage glacier) and volcanic material (Villarrica volcano, Chile). • Success of a DEB model in estimating the mean daily melt rates under varied debris thicknesses (e.g. to produce a modelled Östrem curve). However, overestimation of the melt rate under layers < 15 cm were observed. • Modelled melt rate is very sensitive to thermal conductivity, as demonstrated when making small changes to input value (e.g. default of 0.35 to 0.1) for volcanic material better matched observations. • Defined a 'patchiness' parameter to assess the ratio of exposed ice to debris-covered ice in dirty ice conditions. Modelled melt rates when including this parameter matched Östrem curves. • Noted that downwards conduction into ice should be included when considering colder regions.
Yang et al., 2010	Degree-day methods	<ul style="list-style-type: none"> • PDD assumes the amount of snow/ice melt is proportional to the sum of mean daily temperatures above the melting point. 	<ul style="list-style-type: none"> • Degree-day method of modelling in the Tibetan Plateau region, considering bare ice and thick debris (>65 cm) conditions. • Daily ablation was calculated with the following equation: $M(H,t) = DDF(H) T(H,t) S(H)$, where M= total ablation (m³ water equivalent), T= daily mean air temperature, S= surface area, H= altitude, t= day, and DDF= degree-day factor.

Study	Model type	Assumptions	Key outcomes
		<ul style="list-style-type: none"> Simplification of complex factors associated with ablation. 	<ul style="list-style-type: none"> Total ablation would increase by 36% if the 24K glacier was debris-free but would decrease by 59% if covered by thick debris. Results and observations demonstrated that thick debris cover insulated the lower regions of glaciers in this area and protected against otherwise ablating conditions. Degree-day model is a simplification of complex processes; however, this allows a calculation of ablation under a debris layer without considering the debris thermal properties.
Benn et al., 2012	Debris energy-balance model (DEB)	<ul style="list-style-type: none"> The energy flux through a debris layer is entirely conduction-based from energy exchanges at the upper and lower surfaces. Sublimation is not considered. 	<ul style="list-style-type: none"> Theoretical mass balance modelling of the Ngozumpa Glacier, Himalaya. Evolution of a heat flux through a debris layer is a function of debris temperature and debris-layer properties (e.g. density, specific heat capacity, and thermal conductivity). Method required large volume of meteorological data and information regarding the debris properties. Surface energy balance can be estimated from 24-hours of meteorological data using equations described in Nicholson and Benn (2006) when substantial meteorological data is missing. Conductive heat flux determines the surface melt under a debris layer. Successful replication of the modelled Östrem curve (e.g. increased melt rate under thin layers, and exponential decrease in melt rate under thick layers, relative to clean ice). An inverted ablation gradient on the lower parts of the glacier were noted. This was a result of thick debris layers insulating the ice, offsetting the warmer temperatures at lower elevations. Ablation gradient is very sensitive on debris properties (e.g. layer thickness, thermal conductivity, and albedo), which are not well known in this study. Sublimation processes are not included in the ablation modelling, although it was noted that this likely had an influence at higher elevations. Many assumptions used in energy-balance equations means that only a general picture of ablation under debris-covered glaciers can be given. However, it is successful in giving a broad picture that may inform fieldwork approaches.

Study	Model type	Assumptions	Key outcomes
Brook and Paine, 2011	Degree-day methods	<ul style="list-style-type: none"> • PDD assumes the amount of snow/ice melt is proportional to the sum of mean daily temperatures above the melting point. • Simplification of complex factors associated with ablation. 	<ul style="list-style-type: none"> • Degree-day method from air temperature data, calculated by dividing ablation by the sum of positive air temperatures. • The DDF calculated for bare ice compared well with other studies (e.g. 5.1 mm d⁻¹ °C⁻¹). • A low DDF for thick debris layers compared to other studies (e.g. 3.5 d⁻¹ °C⁻¹ compared to 15.6 d⁻¹ °C⁻¹, 14.0 d⁻¹ °C⁻¹, 3.5 d⁻¹ °C⁻¹, and 5.5 d⁻¹ °C⁻¹, Kayastha et al., 2000). It was suggested that this was due to a low incoming solar radiation Fox Glacier, New Zealand compared to Himalayan glaciers.
Reid et al., 2012	Distributed glacier melt model (point model). EBMs for snow, bare-ice, and debris-covered ice.	<ul style="list-style-type: none"> • Debris cover distribution does not change over a yearly period. 	<ul style="list-style-type: none"> • Digital elevation model (DEM) to inform surface cover (e.g. debris-covered, 0-50 cm or bare ice). A bare ice energy balance model was used to calculate ablation in bare ice conditions, whilst the DEB used in Reid and Brock (2010) was used in cases of debris-cover. • Information of the debris properties were required in the DEB model (e.g. debris albedo, thermal conductivity, density, specific heat capacity, emissivity, and aerodynamic roughness length). Aerodynamic roughness length was noted as a complex property when considering discontinuous layers of debris, and so was assumed spatially constant. However, it was noted that further research investigating spatial changes associated with discontinuous layer is needed to improve the accuracy of this variable in future ice ablation modelling. • Dirty ice conditions were not considered in this model (e.g. bare ice in between patches of debris with fine-grained material), despite an acknowledgement that this would impact the albedo of the assumed 'bare' ice. • Debris albedo was used as a constant (0.13). • The modelled ablation curve agrees well with the general shape of the Östrem curve and suggest that the presence of a 6 cm debris-cover on Haut Glacier d'Arolla, Switzerland, could reduce glacier run-off by 7%. • This study highlights the need to consider spatial variability of surface cover on a glacier in ablation modelling.

Study	Model type	Assumptions	Key outcomes
Nicholson and Benn, 2013	Review of properties included in EBMs		<ul style="list-style-type: none"> • It was noted that future work should focus on improving understanding of how thin, sparse debris cover and downwards moving particles contributes to the heterogenous debris/ice surface. • Linear gradients are applicable approximation of the debris layer temperature gradient when considering longer time frames (e.g. 24 hours). However, instantaneous energy fluxes within a debris layer are not associated with a linear temperature gradient. • Includes a consideration of debris properties within energy balance models. • Key properties of the debris layer are effective thermal conductivity, surface albedo, and debris thickness. Sensitives to debris thickness is most apparent when modelling < ~0.5 m thick layers. • The consideration of the englacial heat flux is crucial when considering colder environments or ablation modelling over long timescales. However, this is not included in ablation models.
Lejeune et al., 2013	Crocus-DEB models	<ul style="list-style-type: none"> • A debris layer can be considered a snow layer in the Crocus snowpack model if assigned debris properties. • Debris properties remain constant during the modelled period. • There is no water content in the debris layer. Therefore, there are no associated phase changes. 	<ul style="list-style-type: none"> • Development of the Crocus model (snowpack model) allowed consideration of debris-covered glaciers, and when the debris cover is overlain with snow. • The debris layer was inserted as stacks of snow layers but assigned debris properties to distinguish between debris and snow (e.g. a vertical layering of ice, debris, and a snowpack). • The distinguishing property between ice/snowpack and debris is the temperature. Therefore, the debris stacks were assigned a given thickness, density, thermal conductivity, and specific heat capacity. • Generally, good agreement between simulations and observations. • Discrepancies between the modelled output and observations were attributed to the phase changes that occurred within the debris layer that were not considered in the model inputs. • The consideration of the temperature profile in the Crocus-DEB model was beneficial when compared to standard DEB models (that usually assume the ice below the debris layer is at melting point), as it allows the Crocus-DEB model to be utilised during time frames outside of the ablation period.
Fyffe et al., 2014	DEB model for debris-covered ice Clean-ice model	<ul style="list-style-type: none"> • Evaporation and condensation did not occur within the debris. 	<ul style="list-style-type: none"> • Use of a combination of pre-existing models to accurately estimate ablation across an entire glacial surface, considering different surface conditions.

Study	Model type	Assumptions	Key outcomes
	Dirty-ice model	<ul style="list-style-type: none"> • Does not consider refreezing of meltwater within debris. • Ice temperature is at 0°C. • Conduction of heat into the ice/snow was not considered. • Penetration of shortwave radiation into ice/snow was not considered. • Constant debris properties with time. 	<ul style="list-style-type: none"> • Remote sensing techniques (e.g. an orthorectified aerial photograph of Miage glacier) was used to identify surface cover: debris-covered ice, dirty ice, or clean ice. These were defined as continuous debris, discontinuous debris, and no debris. • Three models were implemented: DEB model for debris-covered ice, clean-ice model with dirty ice parameters for dirty ice, and clean ice model with clean ice parameters for clean ice. The energy balance equations for assessing ablation under debris-covered ice were those derived by Reid and Brock (2010). Standard energy balance equations used to calculate melt rates for dirty ice. • An hourly time-step was used in the melt models. This generated hourly meteorological data at Miage glacier (incoming shortwave and longwave radiation, air temperature, wind speed, relative humidity, and total rainfall). • 9% underestimation of debris-covered ice ablation (i.e. DEB model) when compared to ablation stake data. Uncertainty was greatest when considering ablation stakes that were monitoring ablation for short time periods (i.e. <1 week). Removal of this data resulted in a 5% underestimation of debris-covered ice ablation. There was no relationship with error and debris thickness. Instead, it was likely that error was associated with a change in debris properties with time; this was not considered in the modelled output. • Melting under thicker layers was initiated over a longer timescale than thinner layers. Therefore, melting began later in the day. • Overall, good comparison of modelled ablation and observed ablation at Miage glacier. This provided insights into the regions of the glacier that were associated with the highest melt rates, e.g. highest melt rates and variability on the mid-part of the glacier due to a mixture of surface types. • Typically, a debris-covered glacier is assumed to have a reverse ablation gradient due to debris usually found on the lower parts of a glacier. This study demonstrated that the reality is typically more complex.
Evatt et al., 2015	Debris energy-balance model (DEB)	<ul style="list-style-type: none"> • Spatially uniform and continuous debris layer. 	<ul style="list-style-type: none"> • Assessment of ablation under a dry porous debris layer by incorporating debris-layer airflow into a DEB. Therefore, this considers the energy exchange between moving air and ice and the energy available for evaporation.

Study	Model type	Assumptions	Key outcomes
		<ul style="list-style-type: none"> • Ice temperature is at 0°C. • Meltwater that is not evaporated does not pool and does not influence the energy exchange process. 	<ul style="list-style-type: none"> • A patchy debris cover was also considered. However, this was still assumed to have a layer of a single grain thickness. • Melt rates with debris layers generated the standard shape of the Östrem curve and compared well with field observations by Nicholson and Benn (2006). It was determined that the insulation effects of thick debris layers were the driver of the Östrem curve shape.
Rounce et al., 2015	Debris energy-balance model (DEB)		<ul style="list-style-type: none"> • DEB modelling used in combination with fieldwork results to assess ablation of Imja–Lhotse Shar Glacier, Nepal. This study used three models to assess the common assumption that the latent heat flux is zero. • The debris thermal conductivity, albedo, and roughness were noted as the key properties that influenced the EBM. • Assuming that the latent heat flux is zero overestimated ablation. • Modelled the well-established fact that ablation is typically enhanced under thin layers and hindered under thick layers. • Models showed a sensitivity to thermal conductivity values and highlighted the importance of accurately measuring or estimating the thermal conductivity of the debris layer. • The modelled ablation was compared to observed ablation; this generally agreed with ablation stake measurements, with the exception of a site where the debris properties were not known. This was noted as one of the key problems in DEBs. • It was noted that further work should focus on investigating the effect of water content in a debris layer on particle thermal conductivity and incorporating this effect into the modelling methods.
Carenzo et al., 2016	Degree-day methods (enhanced temperature index), DETI	<ul style="list-style-type: none"> • PDD assumes the amount of snow/ice melt is proportional to the sum of mean daily temperatures above the melting point. 	<ul style="list-style-type: none"> • Development of a debris temperature index model (DETI) to combine temperature index (i.e. degree day method) and DEB models. Accounted for debris thickness in the simple temperature index model. Therefore, this requires estimates of spatial variations in debris thicknesses on a given glacier for future application. • This demonstrated a comparable modelled ablation relative to DEB models alone, with the benefit of a reduced number of input parameters.

Study	Model type	Assumptions	Key outcomes
Möller et al., 2016	Combination of methods (e.g. degree-day methods, EBM)	<ul style="list-style-type: none"> • Varied assumptions based on the model type (see above examples). 	<ul style="list-style-type: none"> • The DETI model simulated the part of the Ostrem curve under thick debris layers well but had associated uncertainties with ablation under thin layers. • A combination of modelling techniques was applied to compare with observations on Grímsvötn volcano, Iceland: <ul style="list-style-type: none"> ○ Temperature index model (i.e. degree-day method) ○ Temperature/net shortwave radiation-index model ○ EDM • Model (2) has not been used in this context before. • Model (1) was a function of daily average air temperatures. This was described as a function of debris thickness. • Model (2) was a function of daily average air temperatures and net shortwave radiation (i.e. considering albedo and measured global radiation). These were described as a function of debris thickness. • Model (3) was based on DEB models that assessed the debris temperature and heat flux through the debris layer. This took into consideration the thermal conductivity of the debris (i.e. volcanic material) and considered the latent heat of fusion and ice density to calculate the ice ablation under the debris layer. • Debris thicknesses from 0-100 mm were considered. • The three models all showed an increase in accuracy with increasing debris thickness. Therefore, uncertainties were most limited to thin debris layers. • Models (1) and (2) yielded more accurate results relative to model (3). • Model (2) yielded the most accurate results when considering thin (e.g. < 10 mm) debris layers (although this was still limited). This suggested that in these conditions, it is useful to consider the albedo and shortwave radiation component as these are dominant processes associated with thin debris layers.
Shaw et al., 2016	DEB		<ul style="list-style-type: none"> • Used the DEB model developed in Fyffe et al. (2014). • The model overestimated melt for thinner layers and underestimated melt for thicker layers. • Thinner layers were more sensitive to air temperatures. • It was noted that future work should focus on improving incorporation of spatial and temporal variations in debris thickness.

Study	Model type	Assumptions	Key outcomes
Steiner et al., 2018	Review of processes ignored in ablation models		<ul style="list-style-type: none"> • This study assessed the relative importance of turbulent fluxes in debris-covered ice melt. • Accurate estimates of surface temperature, wind speed, and roughness are crucial in understanding the role of turbulent fluxes on ice melt. • Turbulent fluxes reduce the energy available for melt by 17% and so should be considered in ablation models.

9.5. Appendix 5: Supplementary table of method development experiments to create optically transparent ice blocks.

Table 9.5. A summary of method development experiments focusing on creating optically transparent ice blocks. These were placed in an upright freezer operating at temperatures between -10°C and -20°C.

Experiment	Date	Description	Results and outcomes
M1	12.07.18-16.07.18	<ul style="list-style-type: none"> Deionised water. 	The ice had a fractured surface with a highly opaque central mass.
M2	16.07.18-20.07.18	<ul style="list-style-type: none"> Deionised water. Insulation on one side of the container (bubble wrap). 	The ice had a fractured surface with a highly opaque central mass.
M3	23.07.18-27.07.18	<ul style="list-style-type: none"> Deionised water. Insulation on sides and top (bubble wrap). Magnetic stirrer placed in the far corner of the insulated side of the container so that it froze last. 	The ice was reasonably transparent, with one side slightly opaque (this was the last area to freeze). This had a lumpy surface caused by expansion of water as it froze.
M4	10.08.18-14.08.18	<ul style="list-style-type: none"> Deionised water. 	The ice had a fractured surface with a highly opaque central mass. There were many air bubbles throughout, although the ice was transparent near the bottom of the ice block.
M5	14.08.18-15.08.18	<ul style="list-style-type: none"> Tap water. 	The ice had a fractured surface with a highly opaque central mass. Key outcome: no clear difference between an ice block made from deionised water compared to tap water.
M6	14.08.18-16.08.18	<ul style="list-style-type: none"> Deionised water. Insulation on one side of the container (bubble wrap). 	The ice had a fractured surface with a highly opaque central mass. This extended halfway through the ice block; the bottom half was almost entirely transparent and free of air bubbles.
M7	15.08.18-16.08.18	<ul style="list-style-type: none"> Deionised water. 	Entirely opaque throughout the ice block. Air bubbles extended upwards in vertical trails and were present throughout the entire extent of the block.
M8	15.08.18-20.08.18	<ul style="list-style-type: none"> Deionised water. Insulation on one side (bubble wrap) and top (foam, 19.5 cm x 23 cm). 	The central opaque mass present in previous ice blocks did not form. Instead, the ice had air bubbles extending upwards in vertical trails. Aside from these bubble trails, the ice was optically transparent. Key outcome: side insulation was successful in reducing the opacity of the ice block.

Experiment	Date	Description	Results and outcomes
M9	16.08.18- 28.08.18	<ul style="list-style-type: none"> • Deionised water. • Insulation on one side and top (bubble wrap). 	<p>The ice had a fractured surface with a highly opaque central mass. Vertical trails of bubbles were also observed in the ice. This ice block was less transparent than that created in M8, suggesting that the use of foam roof insulation may be more effective than bubble wrap.</p> <p>Key outcome: foam will be used as roof insulation in future experiments.</p>
M10	20.08.18- 30.08.18	<ul style="list-style-type: none"> • Deionised water. • Magnetic stirrer (x 8). • No insulation. 	<p>This created an optically transparent ice block apart from a concentrated area of bubbles in a localised point around the stirrer.</p> <p>Key outcome: magnetic stirrer is the dominant technique in creating optically transparent ice.</p>
M11	28.08.18- 30.08.18	<ul style="list-style-type: none"> • Deionised water. • Insulation on one side and top (bubble wrap, double thickness to that in M9). 	<p>Vertical trails of air bubbles extended upwards through the top half of the ice block. The bottom half of the ice block was entirely optically transparent.</p> <p>Key outcome: confirmed importance of the magnetic stirrer.</p>
M12	30.08.18- 03.09.18	<ul style="list-style-type: none"> • Deionised water. • Development on M10 by combining techniques from all experiments: <ul style="list-style-type: none"> • Insulation on one side (bubble wrap) and top (foam, 19.5 cm x 23 cm). • Magnetic stirrer (x 8). 	<p>The ice had an undulating surface with many air bubbles surrounding the magnetic stirrer. The ice was optically transparent away from the proximity of the stirrer.</p>
M13	03.09.18- 07.09.18	<ul style="list-style-type: none"> • Deionised water. • Insulation on one side (bubble wrap) and top (foam, 19.5 cm x 23 cm). • Magnetic stirrer (x 6). 	<p>The ice block was optically transparent except for the area surrounding the stirrer.</p>
M14	03.09.18- 05.09.18	<ul style="list-style-type: none"> • Deionised water. • Insulation on one side and top (wool). 	<p>Air bubbles were present throughout the top two thirds of the ice block. These appeared to point in the direction of freezing. The presence of air bubbles suggested that the ice was continuing to form 'top-down' as gases were trapped within the ice, and so wool insulation was not sufficient.</p> <p>Key outcome: foam insulation was confirmed as the most efficient material for roof insulation.</p>
M15	10.09.18- 19.09.18	<ul style="list-style-type: none"> • Deionised water. 	<p>This created an optically transparent ice block, apart from air bubbles in the proximity of the magnetic stirrer. Roof</p>

Experiment	Date	Description	Results and outcomes
		<ul style="list-style-type: none"> Insulation on one side (bubble wrap) and top (foam, 28 cm x 38 cm). Magnetic stirrer (x 8). 	insulation was larger than that in previous experiments; this was successful in preventing rapid top-down freezing, although this slowed freezing substantially as it extended across the entire freezer diameter and blocked convection of air. Future experiments will assess a smaller foam board that extends past the container but does not block air convection in the freezer.
M16	21.09.18-26.09.18	<ul style="list-style-type: none"> Deionised water. Insulation on one side (bubble wrap) and top (foam, 28 cm x 28 cm). Roof insulation was covered with a weight so that it acted as a seal. This was moved to allow a small (~2 cm) gap when the ice was halfway frozen to speed up the freezing process. Magnetic stirrer (x 10 at start, reduced throughout the experiment to reflect the decrease in water volume). 	<p>This created an optically transparent ice block, apart from a very small region of air bubbles concentrated around the magnetic stirrer. This was over a smaller region than that in M15.</p> <p>Key outcome: ‘middle’ size foam insulation will be used as roof insulation. Tap water will be used in all future experiments as previous method development experiments have indicated no differences between tap or deionised water.</p>

9.6. Appendix 6: Supplementary table of method development experiments to determine the appropriate artificial radiation source.

Table 9.6. A summary of the method development experiments focusing on designing the experimental set-up and determining the artificial radiation source.

Experiment	Date	Description	Results and outcomes
M17	24.09.18- 25.09.18	<ul style="list-style-type: none"> • Halogen illumination. • Horizontal water filter to try to remove the infrared radiation (mimicking water vapour in the Earth's atmosphere). • Black brass nut particle placed on the ice after being cooled in the freezer. 	<p>The particle moved downwards from the ice surface into the ice. All activity occurred overnight, and so changes could not be monitored.</p> <p>Key outcome: a time-lapse camera would be set up to monitor future experiments when in-person observation was not possible.</p>
M18	03.10.18- 05.10.18	<ul style="list-style-type: none"> • Halogen illumination. • No water filter to determine the effectiveness of the water filter at removing infrared radiation from the halogen bulb. • Black brass nut particle (same ice block as M17 and so this experiment started with the particle embedded within the ice). 	<p>All ice melted due to ice interaction with infrared radiation. However, this experiment did not represent a natural Earth environment as much of the infrared radiation from the halogen illumination would be absorbed by water vapour in the Earth's atmosphere (and would, therefore, be unavailable for ice interaction). Therefore, this was not a suitable set-up for future experiments.</p> <p>Key outcome: a water filter will be used in subsequent experiments to mimic water-vapour absorption of infrared radiation in the Earth's atmosphere.</p>
M19	22.10.18- 24.10.18	<ul style="list-style-type: none"> • Halogen illumination. • 8 mm black ball bearing (cooled). • Horizontal water filter directly below the radiation source. • Periscope system to image the cross-sectional view of the ice in time-lapse images. 	<p>The radiation source was close to the water filter and deformed the plastic container that held the water, so it was determined that the halogen bulb had to be sufficiently far from the water filter in future experiments. Time-lapse images showed that there was optical distortion of the ice as a result of the cylindrical containers and so future experiments will be conducted in cuboid containers. Aside from this distortion, the set-up of time-lapse imagery was successful with a clear view of the ice cross-section.</p> <p>Key outcome: maintaining a sufficient distance between the halogen bulb and the water filter and using cuboid containers will be important for future experiments.</p>
M20	02.11.18- 05.11.18	<ul style="list-style-type: none"> • Halogen illumination. • 8 mm black ball bearing (same ice as that used in M19). 	<p>Most of the ice block had melted, with any remaining ice floating on the meltwater. The particle had dropped through the meltwater and was sat on the bottom of the container. However, it was determined</p>

Experiment	Date	Description	Results and outcomes
			that melting was from radiation-ice interaction, rather than particle-ice interaction. Additionally, the glass door of the freezer above the ice block was warm and so may have also been warming up the local area. Key outcome: to use a vertical water filter and mirror to direct the beam of radiation to reduce additional heating of the system.
M21	07.11.18-09.11.18	<ul style="list-style-type: none"> • Halogen illumination. • Vertical water filter with mirror to direct radiation beam. • No ice block used as this experiment was to determine whether a vertical water filter would result in heating of the freezer glass door. 	The freezer glass door was not hot and so there was no additional source of radiation to the system. Key outcome: confirmed the use of a vertical water filter in subsequent experiments.
M22	09.11.18-12.11.18	<ul style="list-style-type: none"> • Halogen illumination. • 8 mm black ball bearing. This was not cooled prior to placement as it prevented the particle rolling on the ice surface and away from the centre focus of the radiation beam. • Vertical water filter with mirror to direct radiation beam. 	The ice block melted independently of the particle (observed through drainage channels on the ice surface away from the particle and water pathways between grain boundaries). Key outcome: the freezer temperature was adjusted/decreased.
M23	12.11.18-13.11.18	<ul style="list-style-type: none"> • Halogen illumination. • All subsequent experiments now use a cuboid container following the optical distortion found in the time-lapse images in experiment M19. • Optically-transparent ice without a particle was left for 24 hours with the radiation source on to determine whether the freezer temperature was in a stable regime. 	The ice did not melt and so was stable at the freezer temperatures and heat input from the radiation source. Key outcome: confirmed successful set-up and freezer temperature.
M24	13.11.18-23.11.18	<ul style="list-style-type: none"> • Halogen illumination. • 8 mm black ball bearing (room temperature). • Vertical water filter with mirror to direct radiation beam. 	No particle-ice interaction on 15.11.18 and so the particle was removed from the ice surface. Freezer temperatures were increased, and the ice was left under the radiation for 24 hours to assess whether the new thermal regime was stable. The ice had not melted on 16.11.18, although the vein structure was visible

Experiment	Date	Description	Results and outcomes
		<ul style="list-style-type: none"> Freezer temperature modifications throughout the experiment (to higher temperatures). 	<p>through the presence of meltwater at the grain boundaries. The particle was placed on the surface again on 16.11.18, although this did not melt the ice. On 23.11.18, it was noted that the particle was protecting the underlying ice against sublimation as it sat on a small pedestal. Modifications to the freezer temperature did not result in particle-ice melt despite the ice block being close to its melting point. It was, therefore, suggested that the lack of particle-induced ice melt may be a result of the light power (rather than the ice temperature) and possible sublimation cooling effects.</p> <p>Key outcome: to use a fan in subsequent experiments to disrupt the thermal stratification in the freezer. Sublimation cooling will be investigated in subsequent experiments. An LED will be used in experiments M29-M31 as the halogen bulb had a relatively low power density.</p>
M25	27.11.18-29.11.18	<ul style="list-style-type: none"> Halogen illumination. 8 mm black ball bearing (room temperature). Vertical water filter with mirror to direct radiation beam. 	<p>The ice surface remained frozen despite a significant portion of the block melting. The particle was fully submerged in the ice, although the melt pathway was frozen at the ice surface despite freezer temperatures being above pressure melting point. This demonstrated that there was an active freezing surface in an environment above 0 °C. This highlighted the importance of sublimation in the experimental design and so subsequent experiments investigated the extent of the influence of sublimation-cooling of the ice surface.</p> <p>Key outcome: confirmed sublimation cooling processes.</p>
M26	29.11.18-05.12.18	<ul style="list-style-type: none"> Halogen illumination. Same ice block as that used in M25, although this was covered to prevent sublimation. Vertical water filter with mirror to direct radiation beam. Sealed bottles containing water to act as a control and determine whether water was stable in the solid state under the current thermal regime. One uncovered container containing ice to act as a control and determine whether 	<p>All ice in sealed containers had melted to form liquid water, suggesting that the freezer temperatures were above melting point. However, the unsealed container had a frozen surface (~2-5 mm thick), suggesting that sublimation cooling may have been keeping the surface solid.</p> <p>Key outcome: confirmed sublimation cooling processes.</p>

Experiment	Date	Description	Results and outcomes
		sublimation cooling was occurring in the current thermal regime.	
M27	05.12.18-18.12.18	<ul style="list-style-type: none"> • Halogen illumination. • New optically transparent ice block. • Sealed bottles containing water to act as a control and determine whether water was stable in the solid state during the experiment. • Covered with a clear glass cover on 11.12.18 to assess the role of sublimation. 	On 11.12.18, meltwater was observed under the ice surface. This continued to melt after being covered with the glass cover, although melting was a slow process. After the ice block was covered, a wet ice surface developed with vein structures visible. The water in the control sealed containers remained in liquid form throughout the experiment.
M28	18.12.18-07.01.19	<ul style="list-style-type: none"> • Comparison of an uncovered ice block with a covered ice block to assess the role of sublimation in affecting the state of the ice. 	The uncovered ice block had a 'dry' upper surface with slight veining visible. Approximately $\frac{1}{4}$ of the ice volume had melted. The covered ice block had a 'wet' upper surface with well-developed vein structures. Approximately $\frac{1}{2}$ of the ice had melted.
M29	09.01.19	<ul style="list-style-type: none"> • LED illumination. • Vertical water filter with mirror to direct radiation beam. 	The water filter did not warm up (suggesting that it was not absorbing much infrared radiation from the LED bulb). It may not be required in future experiments.
M30	11.01.19-14.01.19	<ul style="list-style-type: none"> • LED illumination. • 8 mm black ball bearing (cooled) before being placed on the ice. • Vertical water filter with mirror to direct radiation beam. • Covered ice block to prevent sublimation cooling. 	Successful coupling between the particle and the ice; the particle melted the ice and sank down to the ice base. The particle continued to couple heat into the ice when on the ice base and created a basal meltwater pond (approximately 9 mm in height). There was no observed melting of the ice aside from that in the proximity of the particle.
M31		<ul style="list-style-type: none"> • LED illumination directly overhead. • Covered ice block to prevent sublimation cooling. 	No obvious signs of melting even without the water filter. Therefore, the ice does not interact with an LED illumination source. Key outcome: a water filter is not required when using LED illumination.

9.7. Appendix 7: Example of workflow of a standard experimental procedure.

Date/time: _____ **Experiment code:** _____

Objective:

Ice condition:

Illumination:

- (1) Take a note of particle characteristics.

	Notes
Material:	
Diameter:	
Colour:	

- (2) Take freezer temperature and relative humidity readings.

	Temperature (°C)	Relative Humidity (%)
Current:		
Maximum:		
Minimum:		

- (3) Place ice block on central shelf in chest freezer on top of the thermocouple. Ensure this is visible in the periscope mirror system and is underneath the radiation source.

- (4) Take reading of ice temperature from thermocouple (°C): _____

- (5) Make indent on ice block surface for particle and place particle on ice surface. Ensure it is in the centre of the radiation beam.

- (6) Cover with glass tray to prevent sublimation cooling of the ice surface.

- (7) Cover any sections of the ice block that have previously been used with a mirror to prevent particle-particle interaction.

- (8) Set up time-lapse imagery camera and ensure focus is on particle. Turn illumination onto full power and turn on camera timer for imaging every five minutes.

9.8. Appendix 8: Temperature data of experimental work conducted in Chapter 4.

Table 9.7. Average temperature values for experimental work in Chapter 4.

Experiment	Freezer temperature (°C)			Proxy ice temperature (°C)
	Current	Maximum	Minimum	
P1a	-1.2	0.0	-3.5	-0.3
P1b	-1.9	-0.3	-3.5	-0.5
P2a/b	-0.9	0.8	-5.9	0.0
P3	-0.9	0.3	-1.9	-0.3
P4	-1.1	0.6	-2.4	1.3
P5	-0.7	1.4	-2.6	-0.3
P6	0.1	0.6	-3.4	-0.3
P7	-1.1	0.4	-3.1	-0.4
P8	-0.1	4.1	-1.7	0.1
P9	-0.4	1.2	-1.8	-0.1
P10	-2.0	0.8	-3.7	-0.8
P11a	-0.5	0.3	-1.5	-0.8
P11b	6.5	6.6	-1.5	2.2
P12	-0.1	1.3	-2.4	-0.4
P13	0.1	0.9	-1.6	0.0
P14	-0.2	1.2	-2.2	0.0
P15	-1.5	0.8	-5.9	-0.6
P16	-1.6	0.8	-5.9	-0.5
P17b	0.5	1.0	-1.3	0.5
P18	-0.8	2.8	-3.2	-0.2
P19	-0.8	0.4	-2.8	-0.5
P20	-0.5	0.7	-2.9	-0.5
P21	-0.7	0.3	-2.1	-0.7
P22	0.0	1.3	-1.4	-0.2
P23a	-0.7	0.4	-2.4	-1.2
P23b	-0.1	0.8	-1.5	-0.2
P24	0.3	1.0	-1.5	-0.4
P25a	-1.2	1.9	-2.9	-1.4
P25b	-0.1	1.3	-2.5	-0.6
P26a	-0.3	0.3	-2.5	-0.6
P26b	-0.2	0.5	-2.2	-0.5
P27	-0.2	1.4	-2.6	0.4
P28	-0.4	1.9	-2.6	-0.2
P29	0.3	1.6	-2.4	-0.2
P30	0.2	1.4	-1.5	0.4
P31	0.1	1.4	-1.4	-0.2
P32	0.3	1.7	-0.9	-0.1
P33	-0.2	1.2	-1.2	-0.2
P34	-0.1	1.2	-0.9	-0.2
P35	0.9	1.1	-0.5	0.0
P36	0.2	1.5	-0.9	-0.1
P37	0.4	1.6	-0.7	-0.1
P38	0.5	1.3	-0.7	0.9
P39	0.4	1.3	-0.8	0.1
P40	0.6	1.8	-0.9	-0.2
P41	1.2	2.3	-0.6	0.3
P42	0.8	2.1	-0.9	0.2
P43	0.2	3.1	-0.8	-0.7
P44	-0.3	2.1	-1.5	-0.1
P45	-0.4	1.4	-2.0	-0.2

Experiment	Freezer temperature (°C)			Proxy ice temperature (°C)
	Current	Maximum	Minimum	
P46	0.1	1.7	-1.5	0.3
P47	-0.3	2.1	-1.2	0.0
P48	0.4	1.4	-1.2	0.0
P49	0.2	1.7	-1.5	-0.2

9.9. Appendix 9: Key findings of experimental work investigating the role of particle thermal conductivity on particle-ice interaction.

Table 9.8. Key findings from the thermal conductivity series of experiments (e.g. P1-P9, P48-P49).

Experiment	Description	Particle velocity (m s ⁻¹)	Particle movement duration	Experiment duration	Key findings
P1a	Single 8 mm chrome steel particle with a high thermal conductivity, high density, and low albedo	-	20 m	41 h 43 m	<ul style="list-style-type: none"> • Sublimation cooling of the ice surface prevented particle-ice interaction. • Differential rates of sublimation formed a topographic high underneath the particle.
P1b	Single 8 mm chrome steel particle with a high thermal conductivity, high density, and low albedo	7.19 x 10 ⁻⁷	23 h 28 m	66 h 51 m	<ul style="list-style-type: none"> • Removal of sublimation cooling (but otherwise with the same conditions as experiment P1a) facilitated particle-induced ice melt. • A high-density particle could melt the ice to move downwards through the ice. This created a melt pathway (i.e. trail of meltwater). • Fluctuations in the rate of particle-induced ice melt and orientation of particle movement were due to subtle temperature changes and interaction with the vein network, respectively.
P2a	Single 8 mm chrome steel particle with a high thermal conductivity, high density, and low albedo	-	-	169 h 9 m	<ul style="list-style-type: none"> • A stable (cold) thermal environment prevented particle-ice interaction.
P2b	Single 8 mm chrome steel particle with a high thermal conductivity, high density, and low albedo	-	-	144 h 7 m	<ul style="list-style-type: none"> • Confirmed key findings from experiment P1b (e.g. a dense, thermally conductive particle with a low albedo would melt downwards through the ice, the particle trajectory was influenced by the vein network). • Demonstrated the possibility of drainage from the melt pathway.
P3	Single 6 mm brass particle with a high thermal conductivity, high density, and low albedo	2.35 x 10 ⁻⁶	7 h 20 m	25 h 4 m	<ul style="list-style-type: none"> • A higher particle velocity was associated with a smaller particle with a higher thermal conductivity (e.g. compared to particle used in experiments P1b and P2b).

					<ul style="list-style-type: none"> • Drainage processes relied on the internal structure of the ice (e.g. the vein network). • Multiple particles formed a hydrological connection within ice to create a greater volume of meltwater compared to previous experiments.
P4	Single 6 mm brass particle with a high thermal conductivity, high density, and low albedo	-	-	66 h 23 m	<ul style="list-style-type: none"> • A staggered progression of ice melt was observed. This was due to subtle changes in temperature.
P5	Single 6 mm brass particle with a high thermal conductivity, high density, and low albedo	1.03×10^{-6}	17 h	20 h 44 m	<ul style="list-style-type: none"> • Steady downwards movement with refreezing processes to create gas bubbles within the ice (i.e. modifying the optical properties of the ice).
P6	Single 6 mm brass particle with a high thermal conductivity, high density, and low albedo	1.87×10^{-6}	11 h 45 m	24 h 10 m	<ul style="list-style-type: none"> • Demonstrated the dynamic nature of melt pathways and drainage events. • Suggested an increase in particle movement once fully submerged. It was deduced that this was due to the removal of convective heat losses to the atmosphere once submerged.
P7	Single 6 mm brass particle with a high thermal conductivity, high density, and low albedo	1.32×10^{-6}	17 h 37 m	20 h 14 m	<ul style="list-style-type: none"> • Confirmed results from experiment P6. • Drainage events modified the internal structure of the ice.
P8	Comparison of two 6 mm brass particles with a high thermal conductivity, high density, and low albedo	-	29 h 5 m ~27 h	29 h 8 m	<ul style="list-style-type: none"> • A difference between two particles of the same type within the same ice system was observed. This was due to one particle stalling with the ice system after becoming fully submerged. This was due to particle sensitives to subtle changes to temperature when near the stable (cold) boundary of the thermal range, and the particle interaction with the vein network.
P9	Comparison of two 6 mm brass particles with a high thermal conductivity, high density, and low albedo	-	-	23 h 20 m	<ul style="list-style-type: none"> • Confirmed results from experiment P8 (i.e. that there was a difference between two particles of the same type). This was due to interaction with the vein network (identified by inclined particle trajectory associated with a higher particle velocity).
P48	Single 6 mm brass particle with a high thermal conductivity, high density, and low albedo on opaque ice	1.75×10^{-6}	9 h	24 h 44 m	<ul style="list-style-type: none"> • Particle-ice interaction with a high density and thermally conductive particle within an opaque ice system was comparable with optically transparent ice system.

P49	Cold single 6 mm brass particle with a high thermal conductivity, high density, and low albedo	2.07×10^{-6}	6 h 35 m	22 h 26 m	<ul style="list-style-type: none"> No apparent difference between the initialisation of ice melt from a pre-cooled particle and a particle of the same type placed on the ice surface at room temperature.
-----	--	-----------------------	----------	-----------	---

9.10. Appendix 10: Key findings of experimental work investigating the role of particle albedo on particle-ice interaction.

Table 9.9. Summary of key findings from the albedo series of experiments (e.g. P10-P14).

Experiment	Description	Particle velocity (m s ⁻¹)	Particle movement duration	Experiment duration	Key findings
P10	Single particle with a high albedo, high density, and high thermal conductivity	8.46×10^{-8}	42 h 40 m	66 h	<ul style="list-style-type: none"> A high albedo particle can absorb incoming radiation and transfer energy into the ice to cause ice melt. Movement was limited to a depth of approximately 13 mm, contrasting to previous results using LA particles.
P11a	Single particle with a high albedo, high density, and high thermal conductivity	-	3 h 20 m	170 h 58 m	<ul style="list-style-type: none"> Cold temperatures prevented particle-ice interaction.
P11b	A direct comparison of three particles with a high, intermediate, and low albedo, and a high density and high thermal conductivity	IA: 2.32×10^{-6} LA: 3.63×10^{-6}	HA: 19 h 16 m IA: 7 h 40 m LA: 3 h 45 m	24 h 10 m	<ul style="list-style-type: none"> Particle properties will dictate the behaviour of particle-induced melt until the ice reaches its PMP and begins to melt independently. Low albedo particles are most efficient at melting the ice.
P12a	A direct comparison of three particles with a high, intermediate, and low albedo, and a high density and high thermal conductivity	-	-	46 h 55 m	<ul style="list-style-type: none"> Cold temperatures prevented particle-ice interaction.
P12b	A direct comparison of three particles with a high, intermediate, and low albedo, and a high density and high thermal conductivity	HA: 2.39×10^{-7} IA: 1.94×10^{-6} LA: 2.29×10^{-6}	HA: 51 h IA: 9 h 10 m LA: 7 h 45 m	62 h 50 m	<ul style="list-style-type: none"> Changes in temperature can influence particle-ice interaction, confirming previous findings that the thermal environment dictates particle-induced ice melt.

Experiment	Description	Particle velocity (m s ⁻¹)	Particle movement duration	Experiment duration	Key findings
P13	A direct comparison of three particles with a high, intermediate, and low albedo, and a high density and high thermal conductivity	IA (phase one): 1.46 x 10 ⁻⁶ IA (total): 3.81 x 10 ⁻⁷ LA: 1.68 x 10 ⁻⁶	IA: 54 h LA: 12 h 15 m	66 h 16 m	<ul style="list-style-type: none"> Small scale hydrology can override influence from particle properties in determining particle-ice interaction.
P14	Single particle with an intermediate albedo, high density, and high thermal conductivity	2.40 x 10 ⁻⁶	7 h 16 m	92 h	<ul style="list-style-type: none"> There is a difference in heat transfer mechanism of surface particles and embedded particles.

9.11. Appendix 11. Key findings of experimental work investigating the role of particle density on particle-ice interaction.

Table 9.10. Key findings from the density series of experiments (P15-P22).

Experiment	Description	Particle velocity (m s ⁻¹)	Particle movement duration	Experiment duration	Key findings
P15	Single polystyrene particle with a low albedo, low density, and low thermal conductivity	-	-	146 h	<ul style="list-style-type: none"> • A low density particle will float in meltwater when a sufficient volume has been produced to create a surface meltwater pond. Therefore, the top surface of the particle will remain exposed to the atmosphere and experience convective heat loss. • A particle with a low density and low thermal conductivity is highly sensitive to subtle changes in the temperature, especially if the thermal environment is near the stable (cold) threshold.
P16	Single polystyrene particle with a low albedo, low density, and low thermal conductivity with an oblique heating angle	-	-	47 h 1m	<ul style="list-style-type: none"> • Limited ice melt with a particle of this type in a stable (cool) thermal environment. • No apparent difference between heating angles.
P17a	Embedded single polystyrene particle with a low albedo, low density, and low thermal conductivity	-	-	48 h 43 m	<ul style="list-style-type: none"> • Cold temperatures limited particle-ice interaction.
P17b	Embedded single polystyrene particle with a low albedo, low density, and low thermal conductivity	2.20 x 10 ⁻⁶	8 h 5 m	28 h 29 m	<ul style="list-style-type: none"> • An embedded particle with a low density can melt the ice to move upwards to the ice surface. Therefore, re-exposure of low density particle to the ice surface.
P18	Single polyoxymethylene (Delrin®) particle with a low albedo, intermediate density, and low thermal conductivity	-	-	63 h 6 m	<ul style="list-style-type: none"> • Slow initialisation of melt due to a low particle thermal conductivity and strong convective heat losses to the atmosphere when on the ice surface.

Experiment	Description	Particle velocity (m s ⁻¹)	Particle movement duration	Experiment duration	Key findings
					<ul style="list-style-type: none"> • A particle with an intermediate density (i.e. slightly higher than that of water, Chapter 3) will sink in meltwater. • A sinking particle with a low thermal conductivity created a melt pathway approximately double the particle diameter (differing from results involving thermally conductive particles).
P19	Single polyoxymethylene (Delrin®) particle with a low albedo, intermediate density, and low thermal conductivity	4.72 x 10 ⁻⁷	-	63 h 37 m	<ul style="list-style-type: none"> • The behaviour of a particle with an intermediate density (i.e. that close to water) can be held at the water surface due to surface tension effects. • Convection systems leading to indirect ice melt was the dominant form of ice melt with a floating particle.
P20	Single polyoxymethylene (Delrin®) particle with a low albedo, intermediate density, and low thermal conductivity	-	34 h 55 m	43 h 21 m	<ul style="list-style-type: none"> • Confirmed results from experiment P18. • Advection of heat through drainage events can melt the ice away from the proximity of a particle.
P21	Single polyoxymethylene (Delrin®) particle with a low albedo, intermediate density, and low thermal conductivity	Active particle movement: 1.89 x 10 ⁻⁷	-	529 h	<ul style="list-style-type: none"> • Confirmed the interpretation of experiments P18 and P19 that the fundamental behaviour of a particle with an intermediate density is to sink in the meltwater produced. • Confirmed the interpretation of experiment P14 that a surface particle is more sensitive to subtleties in thermal environment (relative to an embedded particle), identified by staggered particle movement. • Indirect melting has a dominant role in particle-induced ice melt. • Possibility of a positive feedback process to drives ice melt. • Drainage of meltwater can remove heat from the system and prevent melting.
P22	Single polypropylene particle with a low albedo, low density, and low thermal conductivity	8.18 x 10 ⁻⁷	-	47 h 55 m	<ul style="list-style-type: none"> • A low-density particle will float in meltwater to create a surface meltwater pond.

9.12. Appendix 12: Summary of behaviour observed in experiment P21.

Table 9.11. General behaviour observed in experiment P21(i)-P21(v).

Phase	Start hour	Duration	Particle movement	General behaviour
P21 (i)	0	15 hours and 21 minutes	3.3 mm	Downwards movement was restricted to a two-hour period. The extent of meltwater was not visible in the images, although in-person observations noted that a small meltwater pond was surrounding the particle by approximately 0.5 mm.
P21 (ii)	94	51 hours, following an 81-hour gap in time-lapse images.	3.6 mm to a depth of 7.1 mm	<p>The particle top surface was exposed to the atmosphere throughout. Upwards particle movement occurred during a six-hour period, coinciding with a reduction of meltwater volume (similar to that observed in experiment P18). Therefore, the particle could not maintain a stable meltwater pond as refreezing processes exceeded melting. Experiments P18, P19 and P20 demonstrated that a particle of this type was able to sufficiently melt the ice to reach the ice base, and so it was determined that this behaviour was thermal environment dependent. A lateral movement of approximately 10 mm and periodic drainage events were observed.</p> <p>To assess the role of meltwater convection in triggering ice melt, a drop of water was pipetted onto the particle into two instances. This triggered particle movement in both cases (e.g. to a depth of approximately 1.6 and 1.1 mm) over a short period (e.g. < three hours), but refreezing processes and drainage of meltwater prohibited any significant melt. The particle top surface remained exposed to the atmosphere in both instances due to partial drainage events. The heat loss at the particle surface to the atmosphere removed energy available for ice melt, and drainage of meltwater resulted in the removal of a medium for heat transfer from the particle edges into the meltwater (to drive ice melt). Therefore, this could suggest that the P21 particle experienced a stable (cold) thermal environment in this phase, in the same way as that observed in experiment P14 (i).</p>
P21 (iii)	166	68 hours following a 20-hour gap in time-lapse images.	0.9 mm to a depth of 8 mm.	Meltwater fluctuations were observed (e.g. a lowering of 4 mm below the original meltwater surface level). This was indicative of a drainage environment and supported processes that occurred in the P21 (ii) phase of the experiment. Fluctuations in the refractive indices of interfaces within the time-lapse images and in-person observations confirmed this interpretation. An upwards movement of the particle was also observed (although this was minimal at <1 mm), indicating refreezing processes.
P21 (iv)	267	68 hours following a 29-hour gap in time-lapse images.	1.2 mm to a depth of 9 mm.	Movement was staggered and predominantly relied on external processes (e.g. refreezing events over a six hour period, and two drainage events). The top particle surface remained exposed to the atmosphere due to a partially drained meltwater pond. Drainage processes were particularly evident in hours 313-323 with meltwater fluctuations in the same way as P21 (iii). This was associated with lateral movement of the particle, resulting in minor changes to the particle depth (e.g. <1 mm). Drainage of meltwater caused the particle to sit in an empty hollow; this was frozen at the particle base to the underlying ice 24 hours into this phase (as noted by in-person observations), suggesting that there were instances with no active

				particle-ice interaction. This would be due to the heat loss from the hot absorbing top surface to the atmosphere and slow heat conduction through the particle (due to the relatively low thermal conductivity).
P21 (v)	460	69 hours following a 123-hour gap in time-lapse images.	22 mm to a depth of 34 mm. This then moved to the ice base, although this was not captured in time-lapse images.	<p>Continued downwards movement by approximately 1.5 mm between P21 (iv) and P21 (v) indicated that active ice melt was possible. Therefore, the P21 particle became fully submerged in meltwater. A fluctuation of downwards and upwards movement was observed in the first four hours of this phase, and upwards movement by approximately 1.1 mm coincided with a reduction of meltwater extent by approximately 4 mm. This suggested that subtle fluctuations in temperature and drainage events may have prohibited a dynamic equilibrium being established between refreezing and melting processes, and the resulting behaviour shifted periodically.</p> <p>A permanent change of behaviour occurred from hour 494, where the particle moved downwards through the ice with a particle velocity of $1.89 \times 10^{-7} \text{ m s}^{-1}$. The trigger of downwards movement appeared to be associated with a rotational movement of the particle and led to the development of a large meltwater pathway that extended up to the ice surface with a diameter of approximately 20 mm. This compared well with observations from P18 and P20. A narrowing of the melt pathway was noted, indicating refreezing processes during particle movement. This eventually closed at the ice surface due to full freezing of the melt pathway. This suggested that the particle experienced a stable (cool) thermal environment. When on the ice base, the particle created a basal meltwater pond approximately 70 mm in length and 13 mm in height.</p>

9.13. Appendix 13: Key findings of experimental work investigating the role of particle diameter on particle-ice interaction.

Table 9.12. Key findings from the diameter series of experiments (P23b-P47)

Experiment	Description	Particle velocity (m s ⁻¹)		Particle movement duration	Experiment duration	Key findings
P23a	Comparison between an 8 mm chrome steel particle and a 6 mm brass particle	-		-	66 h 22 m	<ul style="list-style-type: none"> Cold temperatures limited particle-ice interaction.
P23b	Comparison between an 8 mm chrome steel particle and a 6 mm brass particle	6 mm:	1.69 x 10 ⁻⁶	12 h 45 m	26 h 28 m	<ul style="list-style-type: none"> Particles with different diameters appeared to experience different thermal environments; this affected the particle movement within the ice.
		8 mm:	1.41 x 10 ⁻⁶	15 h 5 m		
P24	Comparison between an 8 mm chrome steel particle and a 6 mm brass particle	6 mm:	2.96 x 10 ⁻⁶	6 h 45 m	65 h 47 m	<ul style="list-style-type: none"> Confirmed findings from experiment P23b.
		8 mm:	1.01 x 10 ⁻⁶	7 h 25 m		
P25a	Single 12 mm brass particle with a high thermal conductivity, high density, and low albedo	-		-	42 hr 38 m	<ul style="list-style-type: none"> A stable (cold) thermal environment prevented particle-induced ice melt.
P25b	Single 12 mm brass particle with a high thermal conductivity, high density, and low albedo	1.32 x 10 ⁻⁶		12 h 10 m	73 h 13 m	<ul style="list-style-type: none"> A 12 mm particle behaved in a similar way to a 6 mm particle of the same type. Confirmed that the lack of movement observed in experiment P25a was a result of a stable (cold) thermal environment.
P26a	Single 12 mm brass particle with a high thermal conductivity, high density, and low albedo	-		-	47 h 1 m	<ul style="list-style-type: none"> A stable (cold) thermal environment prevented particle-induced ice melt.
P26b	Single 12 mm brass particle with a high thermal conductivity, high density, and low albedo	7.05 x 10 ⁻⁷		16 h	62 h 56 m	<ul style="list-style-type: none"> Confirmed results from experiment P25b. A dynamic equilibrium system was established between melting and refreezing processes, resulting in the formation of a melt pathway with a constant height throughout particle movement.

Experiment	Description	Particle velocity (m s ⁻¹)	Particle movement duration	Experiment duration	Key findings
P27	Single 12 mm brass particle with a high thermal conductivity, high density, and low albedo	3.10 x 10 ⁻⁶	5 h 50 m	16 h 59 m	<ul style="list-style-type: none"> Confirmed results from experiment P25b and P26b. A higher particle velocity was associated with a warmer thermal environment.
P28	Single 3 mm brass particle with a high thermal conductivity, high density, and low albedo	1.26 x 10 ⁻⁶	10 h 10 m	43 h 20 m	<ul style="list-style-type: none"> The 3 mm particle stalled within the ice after experiencing a shift in behaviour once becoming embedded.
P29	Single 1.5 mm brass particle with a high thermal conductivity, high density, and low albedo	1.59 x 10 ⁻⁷	33 h 5 m	53 h 56 m	<ul style="list-style-type: none"> A slower particle velocity was observed with a 1.5 mm particle. The 1.5 mm particle stalled within the ice after experiencing a shift in behaviour once becoming embedded, in the same way as the 3 mm particle in experiment P28.
P30	Single 1.5 mm brass particle with a high thermal conductivity, high density, and low albedo	-	-	47 h 59 m	<ul style="list-style-type: none"> Confirmed results from experiment P29.
P31	Single 12 mm brass particle with a high thermal conductivity, high density, and low albedo	1.12 x 10 ⁻⁶	15 h	25 h 52 m	<ul style="list-style-type: none"> Confirmed results from experiment P25b, P26b and P27. Establishment of a dynamic equilibrium system between melting and refreezing processes in the same way as experiment P26b.
P32	Single 1.5 mm brass particle with a high thermal conductivity, high density, and low albedo	-	1 h 5 m	46 h 2 m	<ul style="list-style-type: none"> Confirmed results from experiment P29 and P30. Bubbles within the ice did not have an impact on the limited 1.5 mm particle-ice interaction.
P33	Single 1.5 mm brass particle with a high thermal conductivity, high density, and low albedo	-	-	46 h 41 m	<ul style="list-style-type: none"> Confirmed results from experiment P29, P30 and P33. The Black 2.0 paint on the particle did not have an impact on the limited 1.5 mm particle-ice interaction.
P34	Single 3 mm brass particle with a high	-	-	67 h 40 m	<ul style="list-style-type: none"> Confirmed results from experiment P28 that indicated that a 3 mm thermally conductive

Experiment	Description	Particle velocity (m s ⁻¹)		Particle movement duration	Experiment duration	Key findings
	thermal conductivity, high density, and low albedo					particle was not capable of melting the ice to sufficient move to the ice base. This contrasted with results from experiments investigating 6 mm and 12 mm thermally conductive particles.
P35	Single 12 mm brass particle with a high thermal conductivity, high density, and low albedo	8.73 x 10 ⁻⁷		19 h 15 m	32 h 45 m	<ul style="list-style-type: none"> Confirmed results from experiment P25b, P26b, P27 and P31. Establishment of a dynamic equilibrium system between melting and refreezing processes in the same way as experiment P26b and P31.
P36	Multiple 3 mm particles in a 3 x 3 particle array	9.16 x 10 ⁻⁸		18 h 12 m	120 h 15 m	<ul style="list-style-type: none"> A 3 x 3 mm particle array appeared to act as single particles and were not able to transfer heat to sufficiently melt the ice to reach the ice base. The thermal environment diameter-dependency may only be applicable to submerged particles as surface particles behaved in a similar manner.
P37	Direct comparison of four particle diameters (1.5 mm, 3 mm, 6 mm, and 12 mm)	3 mm:	4.15 x 10 ⁻⁷	17 h 10 m	44 h 29 m	<ul style="list-style-type: none"> The smallest particle (1.5 mm) was trapped at the ice surface, the middle-sized particle (3 mm) stalled when became embedded within the ice, and the largest particles (6 mm and 12 mm) melted the ice sufficiently to move to the ice base. Demonstrated that the thermal environment may be diameter dependent. This would act as a sorting mechanism within ice.
		6 mm:	1.06 x 10 ⁻⁶	15 h 35 m		
		12 mm:	9.03 x 10 ⁻⁷	18 h 15 m		
P38	Multiple 3 mm particles in a 3 x 3 particle array	9.16 x 10 ⁻⁸		4 h	66 h 41 m	<ul style="list-style-type: none"> Confirmed results from experiment P36. A 3 x 3 mm particle array appeared to act as individual particles and were not able to transfer heat to sufficiently melt the ice.
P39	Multiple 3 mm particles in a 5 x 3 particle array	-		1 h 30 m	67 h 5 m	<ul style="list-style-type: none"> Confirmed results from experiment P38.

Experiment	Description	Particle velocity (m s ⁻¹)		Particle movement duration	Experiment duration	Key findings
P40	Multiple 3 mm particles in a 4 x 3 particle array	-		21 h 27 m	21h 17 m	<ul style="list-style-type: none"> Confirmed results from experiment P38 and P39.
P41	Direct comparison of four particle diameters (1.5 mm, 3 mm, 6 mm, and 12 mm)	1.5 mm:	6.47×10^{-7}	2 h 35 m	20 h 59 m	<ul style="list-style-type: none"> Possibility of particle-particle interaction as the 3 mm, 6 mm, and 12 mm particles moved downwards through the ice as a unit.
		3 mm:	8.32×10^{-7}	18 h 25 m		
		6 mm:	8.55×10^{-7}	18 h		
		12 mm:	9.05×10^{-7}	16 h 50 m		
P42	Multiple 3 mm particles in a 9 x 3 particle array			4 h	66 h 56 m	<ul style="list-style-type: none"> Confirmed results from experiment P38, P39 and P40.
P43	Multiple 3 mm particles in a 16 x 3 particle array	Phase 1: 8.93×10^{-7} Phase 2: 7.48×10^{-7} Entire: 5.92×10^{-7}		22 h 45 m	44 h 34 m	<ul style="list-style-type: none"> Demonstrated the ability of a group of smaller particles to act as a single larger unit to sufficiently melt the ice to the ice base. Highlighted complexities with the clustering of particles within ice.
P44	Direct comparison of four particle diameters (1.5 mm, 3 mm, 6 mm, and 12 mm)	1.5 mm:	1.09×10^{-6}	17 h 30 m	23 h 41m	<ul style="list-style-type: none"> Contrasted with results from P37 and P41 and all four particles were able to sufficiently melt the ice to reach the ice base. A variable thermal environment demonstrated different behaviours by particles of different sizes at a given temperature, confirming interpretation that the thermal environment is diameter dependent.
		3 mm:	1.37×10^{-6}	14 h 15 m		
		6 mm:	1.61×10^{-6}	12 h 5 m		
		12 mm:	1.60×10^{-6}	12 h 10 m		
P45	Single 3 mm brass particle with a high thermal conductivity, high density, and low albedo	5.04×10^{-7}		7 h 10 m	26 h 50 m	<ul style="list-style-type: none"> Confirmed results from experiments P28 and P34 that a 3 mm particle could not melt the ice sufficiently to move to the ice base. These findings suggested that a small particle (i.e. < 6 mm) was less efficient at inducing ice melt relative to large particles (e.g. > 6 mm).
P46	Single 1.5 mm brass particle with a high thermal conductivity, high density, and low albedo	-		8 h 10 m	21h 1m	<ul style="list-style-type: none"> Results contrasted with previous experiments of this type (e.g. P29, P20, P32 and P33) as the 1.5 mm particle moved downwards to the ice base. Particle-ice interaction is ultimately controlled by the thermal environment.
P47		1.5 mm:	7.68×10^{-7}	18 h 27 m	19 h 40 m	

Experiment	Description	Particle velocity (m s ⁻¹)		Particle movement duration	Experiment duration	Key findings
	Direct comparison of four particle diameters (1.5 mm, 3 mm, 6 mm, and 12 mm)	3 mm:	1.53 x 10 ⁻⁶	9 h 14 m		<ul style="list-style-type: none"> • Contrasted with results from experiments P37 and P41 and all four particles were able to sufficiently melt the ice to reach the ice base. Compared well with results from experiment P44. • Behaviour was a result of the ice temperature approaching PMP.
		6 mm:	1.26 x 10 ⁻⁶	11 h 16 m		
		12 mm:	1.72 x 10 ⁻⁶	8 h 15 m		

9.14. Appendix 14: Temperature data of experimental work conducted in Chapter 5.

Table 9.13. Average temperature values for experimental work in Chapter 5.

Experiment	Freezer temperature (°C)			Proxy ice temperature (°C)
	Current	Maximum	Minimum	
V1	0.5	1.1	-1.0	-0.1
V2	0.3	1.6	-1.3	-0.3
V3	-0.2	1.2	-1.3	-0.5
V4	0.1	1	-1.0	-0.1
V5	0.4	2.6	-0.9	-0.2
V6a	-0.8	0.4	-2.4	-0.6
V6b	-0.2	0.6	-1.6	-0.3
V7	-0.7	0.7	-2.2	-0.4
V8	-0.8	0.4	-2.1	-0.5
V9	0.1	1.1	-1.1	0.1
V10	-0.1	1.5	-1.7	0.1
V11	-0.3	1.7	-1.4	-0.2
V12	-0.3	1.2	-1.8	-0.6
V13	0.4	1.4	-1.2	-0.4
V14	0.6	1.7	-0.2	0.2
V15	0.3	1.7	-0.4	0.3
V16	-0.3	0.9	-0.9	-0.8
V17	-0.1	1.0	-0.8	-0.2
V18	0.1	1.6	-0.9	-0.1
V19	0.2	1.6	-1.3	-
V20	0.0	1.7	-1.9	0.3
V21	0.2	2.3	-1.1	0.2
V22	0.2	1.1	-2.2	0.2
V23	0.2	1.6	-0.4	0.3
V24	0.2	1.4	-0.8	0.2
V25	0.1	1.6	-0.8	0.2
V26	0.4	1.8	-1.1	-0.2
V27	0.1	1.1	-0.6	0.3
V28	0.0	3.2	-0.7	0.3
V29	0.3	1.5	-0.5	0.4
V30	0.2	2.2	-0.5	0.4
V31	-0.5	0.2	-1.6	-0.3
V32	-0.1	1.0	-1.0	0.2
V33	-0.1	1.7	-1.0	0.6
V34	0.0	1.7	-1.0	0.6

9.15. Appendix 15: Key findings of experimental work investigating volcanic particle-ice interaction.

Table 9.14. Key findings from the volcanic particle series of experiments (V1-V34).

Experiment	Description	Particle velocity (m s ⁻¹)	Particle movement duration	Experiment duration	Key findings
V1	Cemented ash (Eyjafjallajökull), 6 mm	1.13 x 10 ⁻⁶	15 h 40 m	44 h 19 m	<ul style="list-style-type: none"> • A high density resulted in downwards movement of the particle. • Particle velocity was higher than that observed by the plastics in Chapter 4. • The melt pathway was approximately double the diameter of the particle. • The V1 cluster lost fine-grained particles that floated in meltwater and created a surface meltwater pond away from the proximity of the V1 cluster.
V2	Cemented ash (Eyjafjallajökull), 12 mm	7.57 x 10 ⁻⁷	22 h 5 m	66 h 31 m	<ul style="list-style-type: none"> • Confirmed results in experiment V1 of the creation of a wider melt pathway and the presence of floating fine-grained material maintaining surface meltwater. • A 12 mm volcanic cluster had a lower particle velocity than a 6 mm cluster of the same type.
V3	Cemented ash (Eyjafjallajökull), 3 mm	1.01 x 10 ⁻⁶	22 h 17 m	53 h 42 m	<ul style="list-style-type: none"> • A 3 mm volcanic cluster had a comparable particle velocity to a 6 mm cluster. • The diameter-dependency of the thermal environment identified in Chapter 4 did not appear to apply to thermally insulating volcanic clusters due to the cluster driving strong convection systems.
V4	Cemented ash (Eyjafjallajökull), 6 mm	2.71 x 10 ⁻⁶	18 h 12 m	66 h 21 m	<ul style="list-style-type: none"> • Confirmed results from experiment V1. • Irregular melt pathway morphology due to rotation of the cluster and irregular heating from irregular morphology of cluster.
V5	Cemented ash (Eyjafjallajökull), 12 mm	9.06 x 10 ⁻⁷	27 h 35 m	66 h 12 m	<ul style="list-style-type: none"> • Confirmed results from experiment V2.

Experiment	Description	Particle velocity (m s ⁻¹)	Particle movement duration	Experiment duration	Key findings
V6b	Cemented ash (Eyjafjallajökull), 12 mm	4.46 x 10 ⁻⁷	36 h 9 m	207 h 53 m	<ul style="list-style-type: none"> Cemented ash clusters can disintegrate to form smaller clusters of volcanic material. Smaller cemented ash clusters have a higher rate of ice melt and downwards movement than larger clusters. Disintegration of material was likely due to freeze-thaw mechanisms.
		5.21 x 10 ⁻⁷	30 h 56 m		
V7	Cemented ash (Eyjafjallajökull), 6 mm	1.92 x 10 ⁻⁷	86 h 38 m	94 h 47 m	<ul style="list-style-type: none"> Confirmed results from V6b, where disintegration of the cemented ash cluster into smaller ash clusters resulted in a higher rate of downwards movement.
		2.01 x 10 ⁻⁷	82 h 57 m		
V9	Basaltic-andesitic scoria (Volcán Sollipulli), 6 mm	6.70 x 10 ⁻⁷	7 h 3 m available data	65 h 22 m	<ul style="list-style-type: none"> Similar behaviour to volcanic cluster: (1) melt pathway width exceeding the particle diameter and (2) scoria particles are capable of 'shedding' fine-grained (<0.1 mm) particles to the ice system to create a surface meltwater pond away from the proximity of the V9 particle.
V10	Basaltic-andesitic scoria (Volcán Sollipulli), 6 mm	8.71 x 10 ⁻⁷	20 h 25 m	22 h 44 m	<ul style="list-style-type: none"> Confirmed results from experiment V9.
V11	Basaltic-andesitic scoria (Volcán Sollipulli), 12 mm	5.77 x 10 ⁻⁷	28 h 24 m	44 h 54 m	<ul style="list-style-type: none"> The scoria particle shed a smaller fragment (e.g. mm scale) that moved downwards through the ice. This differed from the loss of fine-grained material observed in previous experiments.
V12	Basaltic-andesitic scoria (Volcán Sollipulli), 12 mm	1.68 x 10 ⁻⁷	95 h 47m	112 h 46 m	<ul style="list-style-type: none"> Indicated that the particle velocity influenced the morphology of a melt pathway (e.g. a low velocity was associated with an almost spherical melt pathway, whilst a high velocity was associated with a teardrop morphology, in a stable (cool) thermal environment. Drainage processes prevented further downwards movement due to the advection of heat away from the particle-ice interface.

Experiment	Description	Particle velocity (m s ⁻¹)	Particle movement duration	Experiment duration	Key findings
V13	Basaltic-andesitic scoria (Volcán Sollipulli), 6 mm	4.15 x 10 ⁻⁷	50 h 12 m	50 h 41 m	<ul style="list-style-type: none"> • Provided an insight to a variable thermal environment (e.g. a negative shift across the thermal range reducing particle activity, and a subsequent positive shift across the thermal range facilitating continued particle-ice interaction).
V14	Basaltic-andesitic scoria (Volcán Sollipulli), 6 mm	9.15 x 10 ⁻⁷	21 h 33 m	60 h 24 m	<ul style="list-style-type: none"> • Confirmed results from experiment V9 and V10. • Demonstrated the capability of a volcanic particle to generate a large volume of meltwater due to the introduction of fine-grained particles into the ice system.
V15	Basaltic-andesitic scoria (Volcán Sollipulli), 3 mm	1.01 x 10 ⁻⁶	17 h 48 m	26 h 24 m	<ul style="list-style-type: none"> • Suggested a higher particle velocity associated with a smaller volcanic particle (e.g. 3 mm) relative to larger volcanic particles (e.g. 6- and 12- mm).
V16	Basaltic-andesitic scoria (Volcán Sollipulli), 3 mm	6.30 x 10 ⁻⁷	28 h 13 m available data	118 h 30 m	<ul style="list-style-type: none"> • Confirmed findings in experiment V12 that melt pathway morphology was dependent on particle velocity.
V17	Basaltic-andesitic scoria (Volcán Sollipulli), 3 mm	1.20 x 10 ⁻⁶	16 h 24 m	22 h 56 m	<ul style="list-style-type: none"> • Confirmed results from experiment V15.
V18	Basaltic-andesitic scoria (Volcán Sollipulli), 1.5 mm	-	26 h 37 m	26 h 37 m	<ul style="list-style-type: none"> • A 1.5 mm was held at the meltwater surface despite having a higher density than water. This was due to surface tension effects. • Surface pond geometry was controlled by the pre-existing ice structure (e.g. melting along 'weaker' areas of the ice).
V19	Basaltic-andesitic scoria (Volcán Sollipulli), 3 mm	1.31 x 10 ⁻⁶	16 h 44 m	65 h 52 m	<ul style="list-style-type: none"> • Confirmed results from experiment V15 and V17, and preliminary suggestions from experiment V3, that smaller thermally insulating particles (e.g. 3 mm) have a higher particle velocity than larger particles (e.g. 6- and 12 mm). This indicated the opposite finding for thermally conductive particles (as described in Chapter 4).

Experiment	Description	Particle velocity (m s ⁻¹)	Particle movement duration	Experiment duration	Key findings
V20	Basaltic-andesitic scoria (Volcán Sollipulli), 1,5 mm	-	23 h 1 m	23 h 1 m	<ul style="list-style-type: none"> Confirmed results from experiment V18 that surface tension can retain a 1.5 mm particle at the water surface. Lateral movement of the floating particle also dictated the morphology of the surface meltwater.
V21	Basaltic-andesitic scoria (Volcán Sollipulli), 1.5 mm	-	42 h 56 m	46 h 22 m	<ul style="list-style-type: none"> Confirmed results from experiment V18 and V20 where a 1.5 mm volcanic particle floated at the surface. The floating particle produced a complex melt pathway morphology due to periodic drainage events. These were controlled by vein network intersection with the melt pathway. This modified the optical properties and internal structure of the ice.
V22	Basaltic-andesitic scoria (Volcán Sollipulli), 6 mm	1.06×10^{-6}	17 h 13 m	20 h 31 m	<ul style="list-style-type: none"> Confirmed results from experiment V9, V10, and V14.
V23	Basaltic-andesitic scoria (Volcán Sollipulli), 12 mm	1.06×10^{-6}	19 h 35 m	23 h 1 m	<ul style="list-style-type: none"> Confirmed the behaviour of a 12 mm particle as comparable to that of a 6 mm particle.
V24	Basaltic-andesitic scoria (Volcán Sollipulli), 12 mm	1.52×10^{-6}	12 h 24 m	21 h 47 m	<ul style="list-style-type: none"> Confirmed results from experiment V11, V12, and V23.
V25	Rhyolitic pumice (Mount St. Helens), 6 mm	Fragment: 7.66×10^{-7}	22 h 7 m	48 h 47 m	<ul style="list-style-type: none"> The 6 mm pumice particle floated in the meltwater produced to create a 'proximal surface meltwater pond'. The higher albedo surface did not appear to have a great impact on the volume of meltwater produced as this was significant and comparable to volumes generated by the lower albedo particles. Fragmentation of the V25 particle to create a small (approx. 0.5-1mm) fragment that moved downwards through the ice was observed. Loss of fine-grained material observed to create a 'shallow surface meltwater pond' as seen in experiments V1-V24.

Experiment	Description	Particle velocity (m s ⁻¹)	Particle movement duration	Experiment duration	Key findings
V26	Rhyolitic pumice (Mount St. Helens), 3 mm	Fragment (0.5 mm): 3.94 x 10 ⁻⁷	45 h 47 m	63 h 54 m	<ul style="list-style-type: none"> A 3 mm pumice particle exhibited similar behaviour to a 6 mm pumice particle (e.g. floated in meltwater to create a proximal meltwater pond, experienced loss of fine-grained material to create a shallow surface meltwater pond and fragmented to create a small fragment that moved downwards through the ice).
V27	Rhyolitic pumice (Mount St. Helens), 12 mm	Fragment (2 mm x 1 mm): 6.52 x 10 ⁻⁷ (< 0.5 mm): 5.55 x 10 ⁻⁷	23 h 1 m	23 h 1 m	<ul style="list-style-type: none"> A 12 mm pumice particle exhibited similar behaviour to a 3- and 6- mm pumice particle.
V28	Rhyolitic pumice (Mount St. Helens), 1.5 mm	-	25 h 18 m	25 h 18 m	<ul style="list-style-type: none"> A 1.5 mm pumice particle placed on the ice surface floated in the meltwater. This contrasted to the behaviour of fragments of particles of similar sizes.
V29	Rhyolitic pumice (Mount St. Helens), 3 mm	Fragment (0.5 mm): 4.29 x 10 ⁻⁷	20 h 4 m	20 h 4 m	<ul style="list-style-type: none"> Confirmed results from experiment V26. Surface morphology of the ice surface acted as a control on the development of the surface meltwater pond.
V30	Rhyolitic pumice (Mount St. Helens), 6 mm	Fragment: 2.35 x 10 ⁻⁷	25 h 58 m	25 h 58 m	<ul style="list-style-type: none"> Confirmed results from experiment V25.
V31	Rhyolitic pumice (Mount St. Helens), 12 mm	-	24 h 54 m	24 h 54 m	<ul style="list-style-type: none"> Confirmed results from experiment V27. The larger particle (i.e. 12 mm) created the proximal surface meltwater pond, whilst loss of fine-grained (e.g. <0.1 mm) material from the particle surface created the shallow surface meltwater pond.
V32	Rhyolitic pumice (Mount St. Helens), 1.5 mm	-	24 h 10 m	24 h 10 m	<ul style="list-style-type: none"> Confirmed results from experiment V28. Smaller particles were associated with smaller proximal surface meltwater ponds.
V33	Basaltic-andesitic scoria (Volcán Sollipulli), scattering	Varied (from 7.94 x 10 ⁻⁷ -1.96 x 10 ⁻⁶)	19 h 50 m	19 h 50 m	<ul style="list-style-type: none"> Behaviours observed across the entire experimental series were observed in experiment V33.

Experiment	Description	Particle velocity (m s ⁻¹)	Particle movement duration	Experiment duration	Key findings
					<ul style="list-style-type: none"> • Demonstrated the likelihood of a variety of behaviours occurring within a natural system. • Clusters of fine-grained were most efficient at inducing ice melt. • In the case of single particles, finer grained material (e.g. <1 mm) experienced higher particle velocities than larger particles (e.g. > 3 mm). This compared well with results from this series that the smaller particles were more efficient at inducing ice melt.
V34	Basaltic-andesitic scoria (Volcán Sollipulli), scattering	2.38 x 10 ⁻⁶	24 h 49 m	24 h 49 m	<ul style="list-style-type: none"> • Results from experiments using opaque ice and optically-transparent ice were comparable and very similar particle behaviours and features were observed. • Opaque ice appeared to encourage drainage events.

9.16. Appendix 16: Temperature data of experimental work conducted in Chapter 6.

Table 9.15. Average temperature values for experimental work in Chapter 6.

Experiment	Freezer temperature (°C)			Proxy ice temperature (°C)
	Current	Maximum	Minimum	
Mp1	-0.1	1.1	-1.2	0.4
Mp2	-0.2	0.7	-1.1	0.2
Mp3	-0.3	0.8	-1.3	0.1
Mp4	-0.6	0.4	-1.4	-0.2
Mp5	0.5	1.4	-2.7	0.2
Mp6	-0.4	1.4	-2.5	0.1
Mp7	-0.3	0.9	-2.0	0.2
Mp8	0.0	1.1	-1.6	0.4
Mp9	-0.3	1.0	-1.4	0.5
Mp10	-0.2	1.1	-1.5	0.1
Mp11	-0.2	1.0	-1.3	-0.1
Mp12	-0.1	1.1	-1.2	0.0
Mp13	0.0	1.7	-1.5	0.2
Mp14	-0.2	2.2	-1.3	-0.2
Mp15	0.0	1.1	-1.5	0.1
Mp16	-0.1	1.8	-1.1	-0.6
Mp17	0.0	2.0	-1.1	-0.7
Mp18	0.4	1.5	-1.1	-0.1
Mp19	0.1	1.1	-1.2	0.5

9.17. Appendix 17: Key findings of experimental work investigating microplastic particle-ice interaction.

Table 9.16. Key findings from the microplastic particle series of experiments (Mp1-Mp19), where PE is polyethylene and PP is polypropylene.

Experiment	Description	Particle velocity (m s ⁻¹)	Experiment duration	Key findings
Mp1	PE (small), single surface	-	21 h 27 m	<ul style="list-style-type: none"> The polyethylene microplastic particle was buoyant in meltwater produced. Despite a low thermal conductivity, heat transfer to the ice system was sufficient to cause ice melt. Migration of the particle across the ice surface was observed, demonstrating the possibility of redistribution processes.
Mp2	PE (large), single surface	-	25 h 23 m	<ul style="list-style-type: none"> A large microplastic behaved in a similar way to a small microplastic. The initial meltwater matched the morphology of the particle, suggesting that initial melting was conduction driven. This evolved into a circular area of melt after meltwater convection driven melting was established. Lateral movement of the floating particle extended the area of melting.
Mp3		-		<ul style="list-style-type: none"> No particle-ice interaction due to a stable (cold) thermal environment.
Mp4	PP (large), single surface	-	43 h 14 m	<ul style="list-style-type: none"> A state of equilibrium was reached approximately 4 hours into the experiment. The spherical large microplastic saw reduced ice-melt due to a longer thermal pathway (relative to the thin polyethylene particles), encouraging strong convective heat loss to the atmosphere. Microplastic particle-ice interaction is reduced under cold temperatures.
Mp5	PP (large), single surface	-	63 h 45 m	<ul style="list-style-type: none"> Contrasting results to that from experiment Mp4 due to a warmer thermal environment. Indicated the importance of melting by the advection of heat due to melting of ice from drainage processes. Strong convective heat loss may have driven heat transfer, and consequently, ice melting over a wider area due to air heating by the top surface of the particle.

Mp6	PE (large), multiple embedded	3.71 x 10 ⁻⁷ 5.06 x 10 ⁻⁷ 6.34 x 10 ⁻⁷ 8.21 x 10 ⁻⁷	96 h 4 m	<ul style="list-style-type: none"> • Embedded particles melted the surrounding ice to form spherical areas of melt encasing the particles. • Four low-density particles moved upwards through the ice to emerge at the ice surface. These created individual melt pathways within the ice. • Drainage events prohibited upwards movement of some particles. • Possibility of small microplastics intercepting the vein network within the ice to move upwards over a 45 mm distance within a five minute period.
Mp7	PE (small), single surface	-	23 h 49 m	<ul style="list-style-type: none"> • Confirmed results from experiment Mp1. • Periodic drainage events resulted in a low density particle moving downwards within an ice body as it remained floating on the draining meltwater. • Confirmed interpretation in Chapter 4 that drainage events were dynamic.
Mp8	PE (medium), single surface	-	22 h 27 m	<ul style="list-style-type: none"> • Similar behaviour to that of 'small' microplastic particles (e.g. experiment Mp1, Mp7, and Mp10).
Mp9	PE (large), single surface	-	23 h 21 m	<ul style="list-style-type: none"> • Confirmed results from experiment Mp2. • Multiple drainage events resulted in a fluctuation of depth of the polyethylene particle as it followed the meltwater surface depth fluctuations.
Mp10	PE (small), single surface	-	44 h 39 m	<ul style="list-style-type: none"> • Confirmed results from experiment Mp1 and Mp7.
Mp11	PP (large), single surface	-	72 h 8 m	<ul style="list-style-type: none"> • Additional processes such as migration across a meltwater pond and drainage events created a complex surface meltwater pond. • Subsequent refilling of surface meltwater after drainage events by continued particle-induced ice melt resulted in upwards movement of a low density particle.
Mp12	PE (medium), single surface	-	23 h 50 m	<ul style="list-style-type: none"> • Confirmed results from experiment Mp8. • Drainage processes occurred (facilitated by a leaking container), resulting in the same downwards moving process as observed by experiment Mp7 as the polyethylene particle movement followed the surface lowering of meltwater.

Mp13	PE (medium), multiple embedded	1.90 x 10 ⁻⁷ 2.20 x 10 ⁻⁷		62 h 55 m	<ul style="list-style-type: none"> Confirmed results from experiment Mp6. Two microplastics moved upwards to the ice surface.
Mp14	PE (large), single surface	-		21 h 57 m	<ul style="list-style-type: none"> Confirmed results from experiment Mp2 and Mp9.
Mp15	PE (small), scattering surface	9.77 x 10 ⁻⁷ 1.02 x 10 ⁻⁶ 1.22 x 10 ⁻⁶ 1.25 x 10 ⁻⁶		20 h 15 m	<ul style="list-style-type: none"> Initial 'scarring' of the ice surface with a scattering of particles was observed. This evolved into a surface meltwater pond. Varied behaviour of floating and sinking particles. Sinking particles created a melt pathway wider than the particle, indicating convection-driven melting. Clustering of floating microplastic particles by capillary forces.
Mp16	PE (small), scattering surface	0.1 mm:	7.55 x 10 ⁻⁷ 7.79 x 10 ⁻⁷ 1.18 x 10 ⁻⁶ 1.27 x 10 ⁻⁶	4 h 22 m	<ul style="list-style-type: none"> Confirmed results from experiment Mp15 that multiple behavioural modes were possible with microplastic particles. A greater number of downwards moving particles were observed in experiment Mp16 compared to experiment Mp15. Alternating particle trajectory during descent through the ice was indicative of vein network interception.
		0.3 mm:	9.14 x 10 ⁻⁷		
Mp17	PE (small), scattering surface, opaque ice	<0.1 mm	1.21 x 10 ⁻⁶	22 h 42 m	<ul style="list-style-type: none"> Results compared well with experiment Mp15 and Mp16, despite an opaque ice system.
		0.1 mm	8.51 x 10 ⁻⁷ 7.34 x 10 ⁻⁷		
		0.2 mm	1.04 x 10 ⁻⁶		
		0.5 mm	6.90 x 10 ⁻⁷ 8.62 x 10 ⁻⁷		
Mp18	PE and PP (medium and large), multiple embedded	PE	6.39 x 10 ⁻⁷ 9.19 x 10 ⁻⁷	22 h 42 m	<ul style="list-style-type: none"> Confirmed results from experiment Mp6 and Mp13. Three microplastics moved upwards to the ice surface. Indication of microplastic interception of the vein network. Polypropylene particle moved upwards to reach the ice surface at a higher rate than the polyethylene particles.
		PP	2.00 x 10 ⁻⁶		
Mp19	PE (small), scattering surface, opaque ice	4.97 x 10 ⁻⁷ 5.97 x 10 ⁻⁷ 6.39 x 10 ⁻⁷		22 h 21 m	<ul style="list-style-type: none"> Confirmed results from experiment Mp17 that multiple behavioural modes of microplastic particle-interaction with ice was possible within an opaque ice system.

9.18. Appendix 18: A comparison of modelled and observed particle velocities.

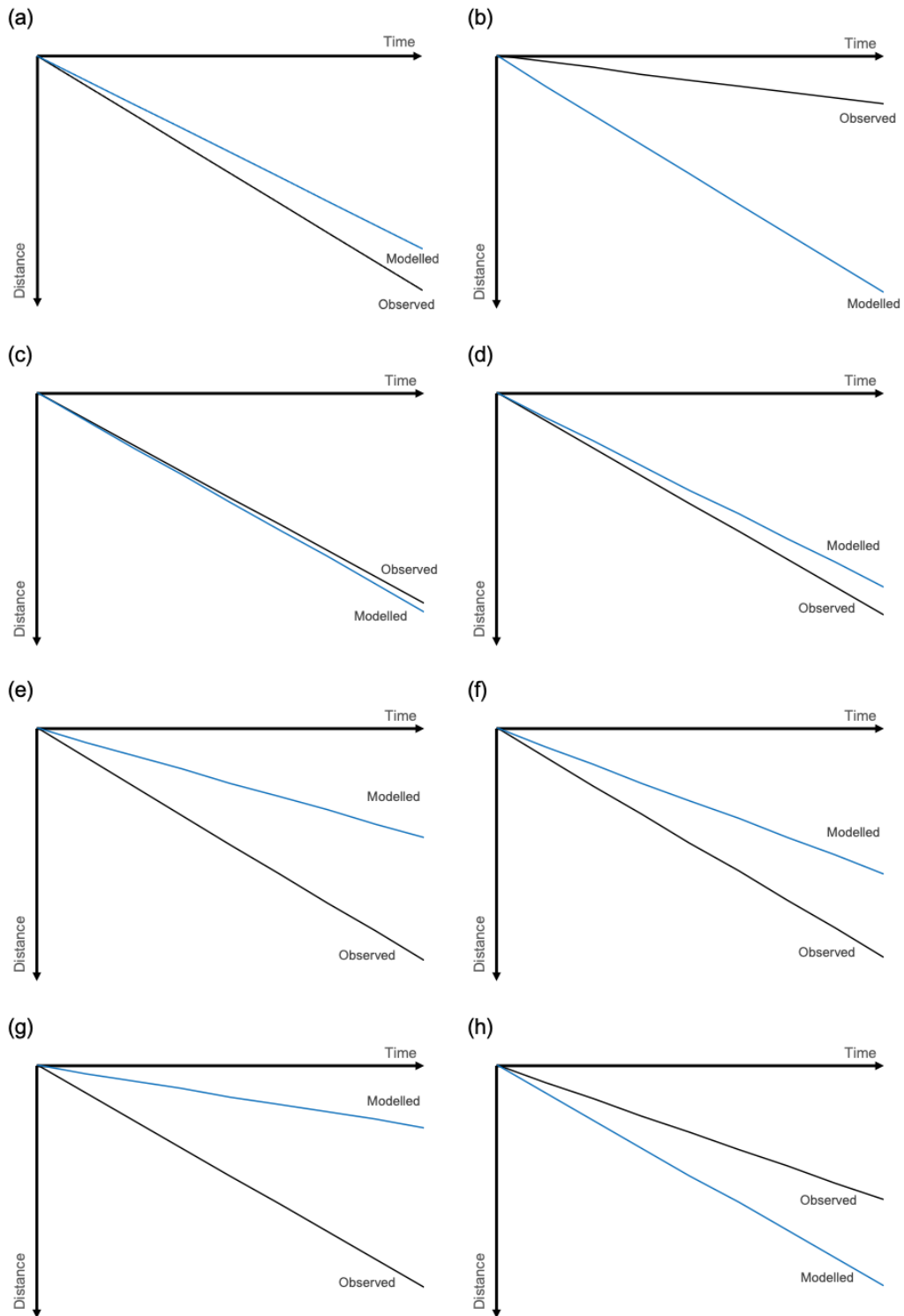


Figure 9.1. Comparison of modelled and observed particle velocities of metal particles. (a) low albedo 8 mm chrome steel, (b) high albedo 8 mm chrome steel, (c) low albedo 1.5 mm brass, (d) low albedo 3 mm brass, (e) low albedo 6 mm brass, (f) low albedo 12 mm brass, (g) intermediate albedo 6 mm brass, and (h) high albedo 6 mm brass particles. Data from Table 7.4, Chapter 7.

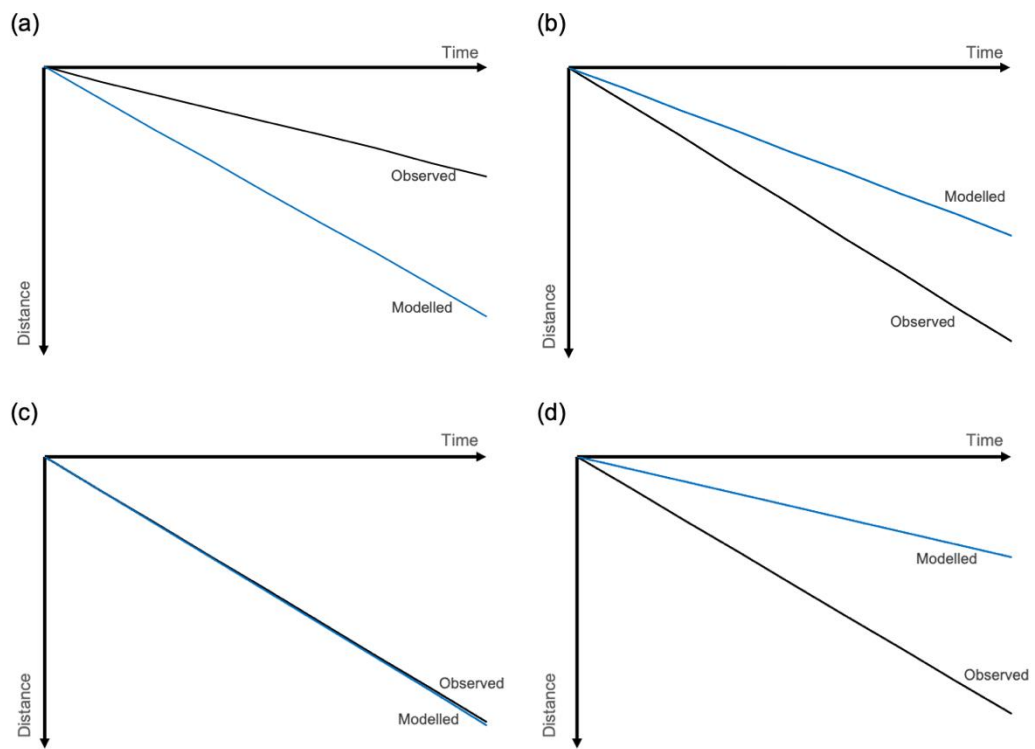


Figure 9.2. Comparison of modelled and observed particle velocities of plastic particles. (a) Delrin®, (b) polypropylene, (c) polyethylene, and (d) polystyrene. Data from Table 7.4, Chapter 7.

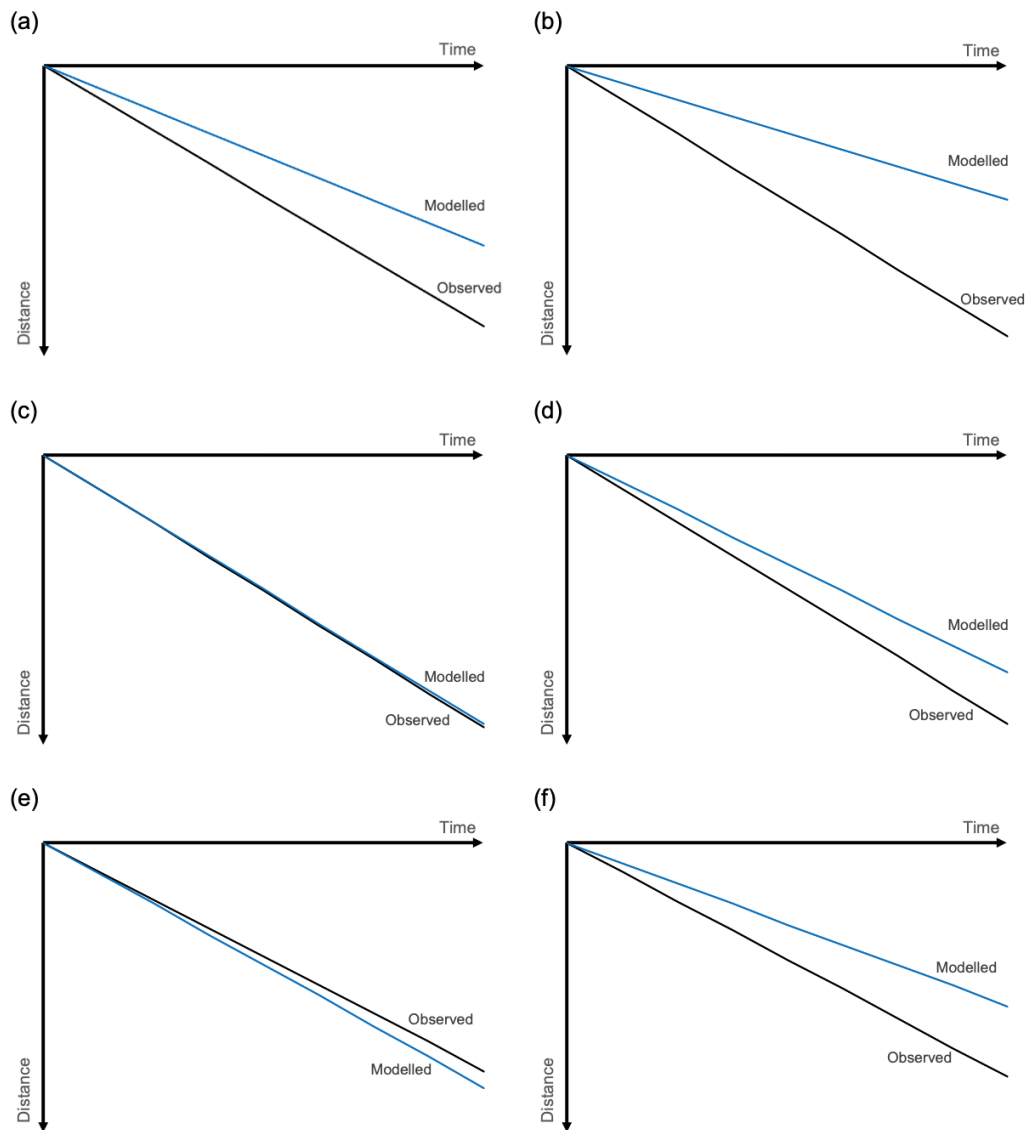


Figure 9.3. Comparison of modelled and observed particle velocities of volcanic particles. (a) 3 mm cemented ash cluster, (b) 6 mm cemented ash cluster, (c) 12 mm cemented ash cluster, (d) 3 mm scoria, (e) 6 mm scoria, and (f) 12 mm scoria particles. Data from Table 7.4, Chapter 7.

9.19. Appendix 19: Glossary of key terms

Ablation	Removal of ice mass
Accumulation	Addition of ice mass
Advection	Heat transfer through the physical movement of a fluid
Condensation	A phase change from gaseous water to liquid water
Conduction	Heat transfer through vibrations of neighbouring atoms
Convection	Heat transfer through the movement of heated fluid (typically driven by density movement along a thermal gradient)
Cryosphere	Any component of the natural system that retains a frozen state of water
Debris covered ice	Ice with a continuous layer of debris on its surface
Deposition	A phase change from gaseous water to solid water
Dirty ice	Ice with a discontinuous layer of debris on its surface
Evaporation	A phase change from liquid water to gaseous water
Freezing	A phase change from liquid water to solid water
Glacier	Ice bodies that have originated from an accumulation of snowfall, compacted to form flowing ice
Ice cap	A < 50,000 km ² mass of ice that covers the topography
Icefield	A < 50,000 km ² mass of ice (although typically smaller than an ice cap) in which the landscape peaks extrude from under the ice
Ice sheet	A > 50,000 km ² mass of ice that covers a landscape in which large-scale movement is independent of bed topography
Melting	A phase change from solid water to liquid water
Melt pathway	A pathway of liquid water created as a dense particle melts the ice and moved downwards in the meltwater
Mountain glacier	Glaciers that develop in mountainous regions (typically from an icefield), bound by topography
Östrem curve	A standardized curve of enhanced ice ablation under thin particle layers and reduced ice ablation under thick particle layers, relative to bare ice
Outlet glacier	Channelled ice that moves from the interior of an ice sheet or ice cap
Pressure melting point (PMP)	The temperature at which ice melts at a given pressure
Proximal surface meltwater pond	The deep zone of meltwater produced by a floating particle
Radiation	Emission of heat energy by an object
Shallow surface meltwater pond	The large extent of shallow melt on the ice surface produced by a floating particle
Sphere of influence	The zone of particle-heating

Sublimation	A phase change from solid water to gaseous water
Thermal environment	Classification of the thermal state of the ice in the proximity of a particle
Thermal range	The range of thermal environments of the ice experienced in the proximity of a particle, from stable (cold), stable (cool), stable (warm), and unstable
Thermal regime	A glaciers internal temperature structure

10. References

- ABRAM, N., GATTUSO, J.-P., PRAKASH, A., CHENG, L., CHIDICHIMO, M. P., CRATE, S., ENOMOTO, H., GARSCHAGEN, M., GRUBER, N., HARPER, S., HOLLAND, E., KUDELA, R. M., RICE, J., STEFFEN, K. & VON SCHUCKMANN, K. 2019. Framing and Context of the Report. *In: PÖRTNER, H.-O., ROBERTS, D. C., MASSON-DELMOTTE, V., ZHAI, P., TIGNOR, M., POLOCZANSKA, E., MINTENBECK, K., ALEGRIA, A., NICOLAI, M., OKEM, A., PETZOLD, J., RAMA, B. & WEYER, N. M. (eds.) IPCC Special Report on the Ocean and Cryosphere in a Changing Climate*. In Press.
- ADHIKARY, S., NAKAWO, M., SEKO, K. & SHAKYA, B. 2000. Dust influence on the melting process of glacier ice: experimental results from Lirung Glacier, Nepal Himalayas. *In: NAKAWO, M., RAYMOND, C. F. & FOUNTAIN, A. (eds.) Debris-Covered Glaciers*. Oxfordshire: IAHS Press.
- ALEXANDER, D. T. L., CROZIER, P. A. & ANDERSON, J. R. 2008. Brown Carbon Spheres in East Asian Outflow and Their Optical Properties. *Science*, 321 (5890), 833-836, DOI:10.1126/science.1155296.
- ALLEN, M. R., DUBE, O. P., SOLECKI, W., ARAGÓN-DURAND, F., CRAMER, W., HUMPHREYS, S., KAINUMA, M., KALA, J., MAHOWALD, N., MULUGETTA, Y., PEREZ, R., WAIRIU, M. & ZICKFELD, K. 2018. Framing and Context. *In: MASSON-DELMOTTE, V., ZHAI, P., PÖRTNER, H.-O., ROBERTS, D. C., SKEA, J., SHUKLA, P. R., PIRANI, A., MOUFOUMA-OKIA, W., PÉAN, C., PIDCOCK, R., CONNORS, S., MATTHEWS, J. B. R., CHEN, Y., ZHOU, X., GOMIS, M. I., LONNOY, E., MAYCOCK, T., TIGNOR, M. & WATERFIELD, T. (eds.) Global Warming of 1.5°C. An IPCC Special Report on the impacts of global warming of 1.5°C above pre-industrial levels and related global greenhouse gas emission pathways, in the context of strengthening the global response to the threat of climate change, sustainable development, and efforts to eradicate poverty*. In Press.
- ALLEN, S., ALLEN, D., PHOENIX, V. R., LE ROUX, G., DURÁNTÉZ JIMÉNEZ, P., SIMONNEAU, A., BINET, S. & GALOP, D. 2019. Atmospheric transport and deposition of microplastics in a remote mountain catchment. *Nature Geoscience*, 12, 339-344, <https://doi.org/10.1038/s41561-019-0335-5>.
- AMBROSINI, R., AZZONI, R. S., PITTINO, F., DIOLAUTI, G., FRANZETTI, A. & PAROLINI, M. 2019. First evidence of microplastic contamination in the supraglacial debris of an alpine glacier. *Environ Pollut*, 253, 297-301, DOI: 10.1016/j.envpol.2019.07.005.
- ANDREASSEN, L. M., VAN DEN BROEKE, M. R., GIESEN, R. H. & OERLEMANS, J. 2008. A 5 year record of surface energy and mass balance from the ablation zone of Storbreven, Norway. *Journal of Glaciology*, 54 (185), 245-258, doi:10.3189/002214308784886199.
- ANESIO, A. M., LUTZ, S., CHRISMAS, N. A. M. & BENNING, L. G. 2017. The microbiome of glaciers and ice sheets. *NPJ Biofilms Microbiomes*, 3:10, DOI:10.1038/s41522-017-0019-0.
- ASKEBJER, P., BARWICK, S. W., BERGSTRÖM, L., BOUCHTA, A., CARIUS, S., DALBERG, E., ENGEL, K., ERLANDSSON, B., GOOBAR, A., GRAY, L., HALLGREN, A., HALZEN, F., HEUKENKAMP, H., HULTH, P. O., HUNDERTMARK, S., JACOBSEN, J., KARLE, A., KANDHADAI, V., LIUBARSKY, I., LOWDER, D., MILLER, T., MOCK, P., MORSE, R. M., PORRATA, R., PRICE, P. B., RICHARDS, A., RUBINSTEIN, H., SCHNEIDER, E., SPIERING, C., STREICHER, O., SUN, Q., THON, T., TILAV, S., WISCHNEWSKI, R., WALCK, C. & YODH, G. B. 1997. Optical properties of deep ice at the South Pole: absorption. *Applied Optics*, 36 (18), 4168-4180.
- BAGSHAW, E. A., TRANTER, M., FOUNTAIN, A. G., WELCH, K. A., BASAGIC, H. & LYONS, W. B. 2007. Biogeochemical evolution of cryoconite holes on Canada Glacier, Taylor Valley, Antarctica. *Journal of Geophysical Research*, 112 (G4), doi:10.1029/2007JG000442
- BAGSHAW, E. A., TRANTER, M., FOUNTAIN, A. G., WELCH, K. A. & BASAGIC, H. J. 2013. Do Cryoconite Holes Have the Potential to be Significant Sources of C, N, and P to Downstream Depauperate Ecosystems of Taylor Valley, Antarctica? *Arctic, Antarctic, and Alpine Research*, 45(4), 440-454, DOI: 10.1657/1938-4246-45.4.440.
- BARR, I. D., LYNCH, C. M., MULLAN, D., DE SIENA, L. & SPAGNOLO, M. 2018. Volcanic impacts on modern glaciers: A global synthesis. *Earth-Science Reviews*, 182, 186-203, <https://doi.org/10.1016/j.earscirev.2018.04.008>.

- BARRIE, I. A. 1985. Atmospheric particles: their physical and chemical characteristics, and deposition processes relevant to the chemical composition of glaciers. *Annals of Glaciology*, 7, 100-108.
- BAZHEV, A. B. 1975. Artificial augmentation of snow melting in a firn basin of a mountain glacier with the aim of increasing runoff. *Snow and Ice Symposium*, 211-218.
- BEER, E., EISENMAN, I. & WAGNER, T. J. W. 2020. Polar Amplification Due to Enhanced Heat Flux Across the Halocline. *Geophysical Research Letters*, 47 (4), doi: e2019GL086706.
- BENN, D. & EVANS, D. J. A. 2014. *Glaciers and Glaciation*, Routledge.
- BENN, D. I., BOLCH, T., HANDS, K., GULLEY, J., LUCKMAN, A., NICHOLSON, L. I., QUINCEY, D., THOMPSON, S., TOUMI, R. & WISEMAN, S. 2012. Response of debris-covered glaciers in the Mount Everest region to recent warming, and implications for outburst flood hazards. *Earth-Science Reviews*, 114 (1-2), 156-174, <https://doi.org/10.1016/j.earscirev.2012.03.008>.
- BERGMANN, M., MÜTZEL, S., PRIMPKE, S., TEKMAN, M. B., TRACHSEL, J. & GERDTS, G. 2019. White and wonderful? Microplastics prevail in snow from the Alps to the Arctic. *Science Advances*, 5 (8), doi: eaax1157
- BERGSTROM, R. W., PILEWSKIE, P., RUSSELL, P. B., REDEMANN, J., BOND, T. C., QUINN, P. K. & SIERAU, B. 2007. Spectral absorption properties of atmospheric aerosols. *Atmospheric Chemistry and Physics*, 7(23), 5937-5943, <https://doi.org/10.5194/acp-7-5937-2007>.
- BINTANJA, R. 1999. On the glaciological, meteorological, and climatological significance of Antarctic blue ice areas. *Reviews of Geophysics*, 37(3), 337-359, <https://doi.org/10.1029/1999RG900007>.
- BOGGILD, C. E., BRANDT, R. E., BROWN, K. J. & WARREN, S. G. 2010. The ablation zone in northeast Greenland: ice types, albedos and impurities. *Journal of Glaciology*, 56(195), 101-113, DOI:10.3189/002214310791190776.
- BOWEN, M. & VINCENT, R. F. 2021. An Assessment of the spatial extent of polar dust using satellite thermal data. *Scientific Reports*, 11 (901), <https://doi.org/10.1038/s41598-020-79825-7>.
- BOX, J. E., FETTWEIS, X., STROEVE, J. C., TEDESCO, M., HALL, D. K. & STEFFEN, K. 2012. Greenland ice sheet albedo feedback: thermodynamics and atmospheric drivers. *The Cryosphere*, 6, 821-839, <https://doi.org/10.5194/tc-6-821-2012>.
- BOZHINSKY, A. N., KRASS, M. S. & POPOVNIN, V. V. 1986. Role of Debris Cover in the Thermal Physics of Glaciers. *Journal of Glaciology*, 32, 255-266, DOI:10.3189/S0022143000015598.
- BRANDT, R. E., WARREN, S. G. & CLARKE, A. D. 2011. A controlled snowmaking experiment testing the relation between black carbon content and reduction of snow albedo. *Journal of Geophysical Research*, 116 (D8), D08109, doi:10.1029/2010JD015330.
- BROCK, B. W., RIVERA, A., CASASSA, G., BOWN, F. & ACUÑA, C. 2007. The surface energy balance of an active ice-covered volcano: Villarrica Volcano, southern Chile. *Annals of Glaciology*, 45, 104-114, DOI:10.3189/172756407782282372.
- BROOK, M. S. & PAINE, S. 2011. Ablation of ice-cored moraine in a humid, maritime climate: fox glacier, new zealand. *Geografiska Annaler: Series A, Physical Geography*, 94, 339-349, <https://doi.org/10.1111/j.1468-0459.2011.00442.x>.
- BURTON, E. 1924. Surface Tension and Fine Particles. *Nature*, 114, 502.
- CABRERA, M., VALENCIA, B. G., LUCAS-SOLIS, O., CALERO, J. L., MAISINCHO, L., CONICELLI, B., MASSAINE MOULATLET, G. & CAPPARELLI, M. V. 2020. A new method for microplastic sampling and isolation in mountain glaciers: A case study of one antisana glacier, Ecuadorian Andes. *Case Studies in Chemical and Environmental Engineering*, 2, <https://doi.org/10.1016/j.cscee.2020.100051>
- CARENZO, M., PELLICCIOTTI, F., MABILLARD, J., REID, T. & BROCK, B. W. 2016. An enhanced temperature index model for debris-covered glaciers accounting for thickness effect. *Adv Water Resour*, 94, 457-469, <https://doi.org/10.1016/j.advwatres.2016.05.001>.
- CARTE, A. E. 1961. Air Bubbles in Ice. *Proceedings of the Physical Society*, 77, 757-768.
- CAWLEY, M. F., MCGLYNN, D. & MOONEY, P. A. 2006. Measurement of the temperature of density maximum of water solutions using a convective flow technique. *International Journal of Heat and Mass Transfer*, 49, 1763-1772, <https://doi.org/10.1016/j.ijheatmasstransfer.2005.11.018>.

- CHAPLIN, M. 2022. *Water Absorption Spectrum* [Online] Available: https://water.lsbu.ac.uk/water/water_vibrational_spectrum.html [Accessed: 04.02.22].
- CHUNG, C. E., RAMANATHAN, V. & DECREMER, D. 2012. Observationally constrained estimates of carbonaceous aerosol radiative forcing. *Proc Natl Acad Sci U S A*, 109(29), 11624-11629, <https://doi.org/10.1073/pnas.1203707109>.
- CHURCH, J. A., CLARK, P. U., CAZENAVE, A., GREGORY, J. M., JEVREJEVA, S., LEVERMANN, A., MERRIFIELD, M. A., MILNE, G. A., NEREM, R. S., NUNN, P. D., PAYNE, A. J., PFEFFER, W. T., STAMMER, D. & UNNIKRISSHANN, A. S. 2013. Sea Level Change. In: STOCKER, T. F., QIN, D., PLATTNER, G.-K., TIGNOR, M., ALLEN, S. K., BOSCHUNG, J., NAUELS, A., XIA, Y., BEX, V. & MIDGLEY, P. M. (eds.) *Climate Change 2013: The Physical Science Basis. Contribution of Working Group I to the Fifth Assessment Report of the Intergovernmental Panel on Climate Change*. Cambridge, United Kingdom: Cambridge University Press.
- COOK, J. M., HODSON, A. J. & IRVINE-FYNN, T. D. 2016. Supraglacial weathering crust dynamics inferred from cryoconite hole hydrology. *Hydrological Processes*, 30(3), 433-446, <https://doi.org/10.1002/hyp.10602>.
- COOPER, M. G., SMITH, L. C., RENNERMALM, A. K., MIÈGE, C., PITCHER, L. H., RYAN, J. C., YANG, K. & COOLEY, S. W. 2018. Meltwater storage in low-density near-surface bare ice in the Greenland ice sheet ablation zone. *The Cryosphere*, 12, 955-970, <https://doi.org/10.5194/tc-12-955-2018>.
- COSSART, E., BRAUCHER, R., FORT, M., BOURLÈS, D. L. & CARCAILLET, J. 2008. Slope instability in relation to glacial debuitressing in alpine areas (Upper Durance catchment, southeastern France): Evidence from field data and ¹⁰Be cosmic ray exposure ages. *Geomorphology*, 95, 3-26, DOI:10.1016/j.geomorph.2006.12.022.
- CUBASH, U., WUEBBLES, D., CHEN, D., FACCHINI, M.C., FRAME, D., MAHOWALD, N. & WINTHER, J.-G. 2013. Introduction. In: STOCKER, T. F., QIN, D., PLATTNER, G.-K., TIGNOR, M., ALLEN, S. K., BOSCHUNG, J., NAUELS, A., XIA, Y., BEX, V. & MIDGLEY, P. M. (eds.) *Climate Change 2013: The Physical Science Basis. Contribution of Working Group I to the Fifth Assessment Report of the Intergovernmental Panel on Climate Change*. Cambridge, United Kingdom: Cambridge University Press.
- CUFFEY, K. M. & PATERSON, W. S. B. 2010. *Physics of Glaciers*, Elsevier Science & Technology.
- DANOV, K. D. & KRALCHEVSKY, P. A. 2010. Capillary forces between particles at a liquid interface: General theoretical approach and interactions between capillary multipoles. *Advances in Colloid and Interface Science*, 154(1-2), 91-103, DOI:10.1016/j.cis.2010.01.010.
- DELISLE, G., FRANCHI, I., ROSSI, A. & WIELER, R. 1993. Meteorite finds by EUROMET near Frontier Mountain, North Victoria Land, Antarctica. *Meteorites*, 28(1), 126-129, <https://doi.org/10.1111/j.1945-5100.1993.tb00257.x>.
- DENTENER, F. J., CARMICHAEL, G. R., ZHANG, Y., LELIEVELD, J. & CRUTZEN, P. J. 1996. Role of mineral aerosol as a reactive surface in the global troposphere. *Journal of Geophysical Research*, 101, 22869-22889, <https://doi.org/10.1029/96JD01818>.
- DOHERTY, S. J., GRENFELL, T. C., FORSSSTRÖM, S., HEGG, D. L., BRANDT, R. E. & WARREN, S. G. 2013. Observed vertical redistribution of black carbon and other insoluble light-absorbing particles in melting snow. *Journal of Geophysical Research: Atmospheres*, 118, 5553-5569, <https://doi.org/10.1002/jgrd.50235>.
- DOHERTY, S. J., WARREN, S. G., GRENFELL, T. C., CLARKE, A. D. & BRANDT, R. E. 2010. Light-absorbing impurities in Arctic snow. *Atmospheric Chemistry and Physics*, 10(23), 11647-11680, <https://doi.org/10.5194/acp-10-11647-2010>.
- DRAGOSICS, M., MEINANDER, O., JÓNSDÓTTÍR, T., DÜRIG, T., DE LEEUW, G., PÁLSSON, F., DAGSSON-WALDHAUSEROVÁ, P. & THORSTEINSSON, T. 2016. Insulation effects of Icelandic dust and volcanic ash on snow and ice. *Arabian Journal of Geosciences*, 9, 126.
- DRAKE, J. J. 1981. The Effects of Surface Dust on Snowmelt Rates. *Arctic and Alpine Research*, 13 (2), 219-223.

- DRIEDGER, C. L. 1981. Effect of ash thickness on snow ablation. *In*: MULLINEAUX, D. R. (ed.) *The 1980 eruptions of Mount St. Helens, Washington. US. Geological Survey Professional Paper 1250*. Washington: US Government Printing Office.
- DU, Z., XIAO, C., LIU, Y., YANG, J. & LI, C. 2017. Natural vs. anthropogenic sources supply aeolian dust to the Miaoergou Glacier: Evidence from Sr–Pb isotopes in the eastern Tianshan ice core. *Quaternary International*, 430(B), 60-70, <https://doi.org/10.1016/j.quaint.2015.11.069>.
- DUMONT, M., BRUN, E., PICARD, G., MICHOU, M., LIBOIS, Q., PETIT, J.-R., GEYER, M., MORIN, S. & JOSSE, B. 2014. Contribution of light-absorbing impurities in snow to Greenland's darkening since 2009. *Nature Geoscience*, 7, 509-512, <https://doi.org/10.1038/ngeo2180>.
- DUNDAS, C. M. & BYRNE, S. 2009. Modeling sublimation of ice exposed by new impacts in the martian mid-latitudes. *Icarus*, 206, 716-728, DOI:10.1016/j.icarus.2009.09.007.
- DYURGEROV, M. B. & MEIER, M. F. 2005. Glaciers and the changing Earth System: a 2004 snapshot. *In*: RESEARCH, I. O. A. A. A. (ed.). Colorado: University of Colorado.
- EISENBERG, D. & KAUZMANN, W. 1969. *The Structure and Properties of Water*. London: Oxford University Press.
- EVANGELIOU, N., GRYTHE, H., KLIMONT, Z., HEYES, C., ECKHARDT, S., LOPEZ-APARICIO, S. & STOHL, A. 2020. Atmospheric transport is a major pathway of microplastics to remote regions. *Nature Communications*, 11, 3381.
- EVATT, G. W., ABRAHAMS, I. D., HEIL, M., MAYER, C., KINGSLAKE, J., MITCHELL, S. L., FOWLER, A. C. & CLARK, C. D. 2015. Glacial melt under a porous debris layer. *Journal of Glaciology*, 61(229), 825-836, DOI:10.3189/2105JoG14J235.
- EVATT, G. W., COUGHLAN, M. J., JOY, K. H., SMEDLEY, A. R., CONNOLLY, P. J. & ABRAHAMS, I. D. 2016. A potential hidden layer of meteorites below the ice surface of Antarctica. *Nat Commun*, 7, 10679, DOI:10.1038/ncomms10679.
- FAURIA, K. E., MANGA, M. & WEI, Z. 2017. Trapped bubbles keep pumice afloat and gas diffusion makes pumice sink. *Earth and Planetary Science Letters*, 460, 50-59, <https://doi.org/10.1016/j.epsl.2016.11.055>.
- FINNEY, J. 2015. *Water: A Very Short Introduction*. Oxford: Oxford University Press.
- FOLCO, L., CAPRA, A., CHIAPPIN, M., FREZZOTTI, M., MELLINI, M. & TANACCO, I. E. 2002. The Frontier Mountain meteorite trap (Antarctica). *Meteoritics & Planetary Science*, 37, 209-228, <https://doi.org/10.1111/j.1945-5100.2002.tb01105.x>.
- FORMENTI, P. 2003. Chemical composition of mineral dust aerosol during the Saharan Dust Experiment (SHADE) airborne campaign in the Cape Verde region, September 2000. *Journal of Geophysical Research*, 108(D18), <https://doi.org/10.1029/2002JD002648>.
- FOUNTAIN, A.G., TRANTER, M., NYLEN, T. H., LEWIS, K. J. & MUELLER, D. R. 2004. Evolution of cryoconite holes and their contribution to meltwater runoff from glaciers in the McMurdo Dry Valleys, Antarctica, *Journal of Glaciology*, 50(168), 35-45, DOI:10.3189/172756504781830312.
- FOUNTAIN, A.G., NYLEN, T. H., MACCLUNE, K. L. & DANA, . L. 2006. Glacier mass balances (1993-2001), Taylor Valley, McMurdo Dry Valleys, Antarctica, *Journal of Glaciology*, 52(178), 451-462, DOI:10.3189/172756506781828511.
- FUJII, Y. 1977. Field Experiment on Glacier Ablation under a Layer of Debris Cover. *Journal of the Japanese Society of Snow and Ice*, 39, 20-21.
- FYFFE, C. L., REID, T. D., BROCK, B. W., KIRKBRIDE, M. P., DIOLAIUTI, G., SMIRAGLIA, C. & DIOTRI, F. 2014. A distributed energy-balance melt model of an alpine debris-covered glacier. *Journal of Glaciology*, 60(221), 587-602. DOI:10.3189/2104JoG13J148.
- FYFFE, C. L., WOODGET, A. S., KIRKBRIDE, M. P., DELINE, P., WESTOBY, M. J. & BROCK, B. W. 2020. Processes at the margins of supraglacial debris cover: Quantifying dirty ice ablation and debris redistribution. *Earth Surface Processes and Landforms*, 45, 2272-2290, <https://doi.org/10.1002/esp.4879>.
- GERDEL, R. W. & DROUET, F. 1960. The Cryoconite of the Thule Area, Greenland. *Transactions of the American Microscopical Society*, 79 (3), 256-272, <https://doi.org/10.2307/3223732>.
- GOLLEDGE, N. R., KELLER, E. D., GOMEZ, N., NAUGHTEN, K. A., BERNALES, J., TRUSEL, L. D. & EDWARDS, T. L. 2019. Global environmental consequences of twenty-first-century ice-sheet melt. *Nature*, 566, 65-72, DOI:10.1038/s41586-019-0889-9.
- GRAHAM, A. L. & ANNEXSTAD, J. O. 1989. Antarctic meteorites. *Antarctic Science*, 1, 3-14.

- GRENFELL, T. C. & PEROVICH, D. K. 1981. Radiation absorption coefficients of polycrystalline ice from 400–1400 nm. *Journal of Geophysical Research*, 86, 7447-7450, <https://doi.org/10.1029/JC086iC08p07447>.
- GRIBBON, P.W.F. 1979. Cryoconite holes on Sermikavsak, West Greenland. *Journal of Glaciology*, 22(86), 177-181, DOI:10.3189/S0022143000014167.
- HAACK, H., SCHUTT, J., MEIBOM, A. & HARVEY, R. P. 2007. Results from the Greenland Search for Meteorites expedition. *Meteoritics & Planetary Science*, 42, 1727-1733, <https://doi.org/10.1111/j.1945-5100.2007.tb00533.x>.
- HADLEY, O. L. & KIRCHSTETTER, T. W. 2012. Black-carbon reduction of snow albedo. *Nature Climate Change*, 2, 437-440, <https://doi.org/10.1038/nclimate1433>.
- HALL, M. H. P. & FAGRE, D. B. 2003. Modeled Climate-Induced Glacier Change in Glacier National Park, 1850–2100. *BioScience*, 52(2), 131-140, [https://doi.org/10.1641/0006-3568\(2003\)053\[0131:MCIGCI\]2.0.CO;2](https://doi.org/10.1641/0006-3568(2003)053[0131:MCIGCI]2.0.CO;2).
- HAMBREY, M. J. & GLASSER, N. F. 2012. Discriminating glacier thermal and dynamic regimes in the sedimentary record. *Sedimentary Geology*, 251-252, 1-33, <https://doi.org/10.1016/j.sedgeo.2012.01.008>.
- HAN, H., YONGJING, D. & SHIYIN, L. 2006. A simple model to estimate ice ablation under a thick debris layer. *Journal of Glaciology*, 52(179), 528-536, DOI:10.3189/172756506781828395.
- HANSEN, J. & NAZARENKO, L. 2004. Soot climate forcing via snow and ice albedos. *PNAS*, 101(2), 424-428, <https://doi.org/10.1073/pnas.2237157100>.
- HARVEY, R. 2003. The Origin and Significance of Antarctic Meteorites. *Geochemistry*, 63, 93-147, <https://doi.org/10.1078/0009-2819-00031>.
- HE, Y. D., & PRICE, P. B. 1998. Remote sensing of dust in deep ice at the South Pole, *Journal of Geophysical Research*. 103, 17041-17056, <https://doi.org/10.1029/98JD01643>.
- HÉNOT, M., PLIHON, N. & TABERLET, N. 2021. Onset of Glacier Tables. *Phys Rev Lett*, 127, 108501.
- HERREID, S. & PELLICCIOTTI, F. 2020. The state of rock debris covering Earth's glaciers. *Nature Geoscience*, 13, 621-627, <https://doi.org/10.1038/s41561-020-0615-0>.
- HEWITT, K. 2005. The Karakoram Anomaly? Glacier Expansion and the 'Elevation Effect,' Karakoram Himalaya. *Mountain Research and Development*, 25, 332-340, 9, [https://doi.org/10.1659/0276-4741\(2005\)025\[0332:TKAGEA\]2.0.CO;2](https://doi.org/10.1659/0276-4741(2005)025[0332:TKAGEA]2.0.CO;2).
- HIGUCHI & NAGOSHI 1977. Effect of particulate matter in surface snow layers on the albedo of perennial snow patches. *Isotopes and Impurities in Snow and Ice*. Grenoble: IAHS Press.
- HOBBS, L. 2014. *The role of cold supraglacial volcanic deposits in influencing glacial ablation*. Doctor of Philosophy, Lancaster University.
- HOLMAN, J. P. 2010. *Heat Transfer*, New York, McGraw Hill.
- HUO, D., BISHOP, M. P. & BUSH, A. B. G. 2021. Understanding Complex Debris-Covered Glaciers: Concepts, Issues, and Research Directions. *Frontiers in Earth Science*, 9, <https://doi.org/10.3389/feart.2021.652279>.
- IMMERZEEL, W. W., VAN BEEK, L. P. H. & BIERKENS, M. F. P. 2010. Climate Change Will Affect the Asian Water Towers. *Science Reports*, 328(5984), 1382-1385, DOI: [10.1126/science.1183188](https://doi.org/10.1126/science.1183188).
- IPCC 2019. Summary for Policy Makers. In: PORTNER, H.-O., ROBERTS, D. C., MASSON-DELMOTTE, V., ZHAI, P., TIGNOR, M., POLOCZANSKA, E., MINTENBECK, K., ALEGRIA, A., NICOLAI, M., OKEM, A., PETZOLD, J., RAMA, B. & WEYER, N. M. (eds.) *IPCC Special Report on the Ocean and Cryosphere in a Changing Climate*. In Press.
- IQBAL, M. 1983. *An introduction to solar radiation*, Ontario, Academic Press Canada.
- IRVINE-FYNN, T. D. L., HODSON, A. J., MOORMAN, B. J., VATNE, G. & HUBBARD, A. L. 2011. Polythermal glacier hydrology: a review, *Reviews of Geophysics*, 49, <https://doi.org/10.1029/2010RG000350>.
- JAMES, M. R. 1998. *Electric charge within volcanic plumes on Earth and Io*. Doctor of Philosophy, Lancaster University.
- JUEN, M., MAYER, C., LAMBRECHT, A., HAN, H. & LIU, S. 2014. Impact of varying debris cover thickness on ablation: a case study for Koxkar Glacier in the Tien Shan. *The Cryosphere*, 8, 377-386, <https://doi.org/10.5194/tc-8-377-2014>.
- JUEN, M., MAYER, C., LAMBRECHT, A., WIRBEL, A. & KUEPPERS, U. 2013. Thermal properties of a supraglacial debris layer with respect to lithology and grain size.

- Geografiska Annaler: Series A, Physical Geography*, 95, 197-209, <https://doi.org/10.1111/geoa.12011>.
- KANHAI, D. K., GARDFELDT, K., KRUMPEN, T., THOMPSON, R. C. & O'CONNOR, I. 2020. Microplastics in sea ice and seawater beneath ice floes from the Arctic Ocean. *Sci Rep*, 10, 5004, DOI:10.1038/s41598-020-61948-6.
- KASER, G., GROSSHAUSER, M. & MARZEION, B. 2010. Contribution potential of glaciers to water availability in different climate regimes. *PNAS*, 104(47), 20223-20227, <https://doi.org/10.1073/pnas.1008162107>.
- KAYASTHA, R. B., TAKEUCHI, Y., NAKAWO, M. & AGETA, Y. 2000. Practical prediction of ice melting beneath various thickness of debris cover on Khumbu Glacier, Nepal, using a positive degree-day factor. In: NAKAWO, M., RAYMOND, C. F. & FOUNTAIN, A. (eds.) *Debris Covered Glaciers*. Oxfordshire: IAHS Press.
- KEEGAN, K. M., ALBERT, M. R., MCCONNELL, J. R. & BAKER, I. 2014. Climate change and forest fires synergistically drive widespread melt events of the Greenland Ice Sheet. *Proc Natl Acad Sci U S A*, 111, 7964-7, DOI:10.1073/pnas.1405397111.
- KELLY, A., LANNUZEL, D., RODEMANN, T., MEINERS, K. M. & AUMAN, H. J. 2020. Microplastic contamination in east Antarctic sea ice. *Marine Pollution Bulletin*, 154, 111130, DOI:10.1016/j.marpolbul.2020.111130.
- KHAN, M. I. 1989. *Ablation on Barpu glacier, Karakoram Himalaya, Pakistan a study of melt processes on a faceted, debris-covered ice surface*. Masters of Arts, Wilfrid Laurier University.
- KHAN, A. L., DIERSSEN, H., SCHWARZ, J. P., SCHMITT, C., CHLUS, A., HERMANSON, M., PAINTER, T. H. & MCKNIGHT, D. M. 2017. Impacts of coal dust from an active mine on the spectral reflectance of Arctic surface snow in Svalbard, Norway. *Journal of Geophysical Research: Atmospheres*, 122, 1767-1778, <https://doi.org/10.1002/2016JD025757>.
- KIRCHSTETTER, T. W., NOVAKOV, T. & HOBBS, P. V. 2004. Evidence that the spectral dependence of light absorption by aerosols is affected by organic carbon. *Journal of Geophysical Research*, 109, <https://doi.org/10.1029/2004JD004999>.
- KIRKBRIDE, M. P. & DUGMORE, A. J. 2003. Glaciological response to distal tephra fallout from the 1947 eruption of Hekla, south Iceland. *Journal of Glaciology*, 49, 420-428, DOI:10.3189/172756503781830575.
- KLUG, C. & CASHMAN, K. V. 1996. Permeability development in vesiculating magmas: implications for fragmentation. *Bulletin of Volcanology*, 58, 87-100, <https://doi.org/10.1007/s004450050128>.
- KNUTTI, R., FLUCKIGER, J., STOCKER, T. F. & TIMMERMANN, A. 2004. Strong hemispheric coupling of glacial climate through freshwater discharge and ocean circulation. *Nature*, 430, 851-856, <https://doi.org/10.1038/nature02786>.
- KOHSHIMA, S., YOSHIMURA, Y., SEKO, K. & OHATA, T. 1994. Albedo reduction by biotic impurities on a perennial snow patch in the Japan alps. *Snow and ice covers: interactions with the atmosphere and ecosystems*. Proc. symposia, Yokohama.
- LABUS, M. & LABUS, K. 2018. Thermal conductivity and diffusivity of fine-grained sedimentary rocks. *Journal of Thermal Analysis and Calorimetry*, 132, 1669-1676, <https://doi.org/10.1007/s10973-018-7090-5>.
- LANGHAM, E. J. 1984. Network geometry of veins in polycrystalline ice, *Canadian Journal of Earth Sciences*, 11, 1274-1279.
- LAU, W. K. M., KIM, M.-K., KIM, K.-M. & LEE, W.-S. 2010. Enhanced surface warming and accelerated snow melt in the Himalayas and Tibetan Plateau induced by absorbing aerosols. *Environmental Research Letters*, 5(2), DOI:10.1088/1748-9326/5/2/025204.
- LEE, J. 2018. The Static Profile for a Floating Particle, *Colloids and Interfaces*, 2(2), 18, DOI: 10.3390/colloids2020018
- LEHMAN, S. J. & KEIGWIN, L. D. 1992. Sudden changes in North Atlantic circulation during the last deglaciation. *Nature*, 356, 757-762, <https://doi.org/10.1038/356757a0>.
- LEJEUNE, Y., BERTRAND, J.-M., WAGNON, P. & MORIN, S. 2013. A physically based model of the year-round surface energy and mass balance of debris-covered glaciers. *Journal of Glaciology*, 59(214), 327-344, DOI:10.3189/2013JoG12J149.
- LIU, K. N. 2002. Chapter 3 – Absorption and Scattering of Solar Radiation in the Atmosphere. *International Geophysics*, 84, 65-115.
- MADER, H. M. 1992. The thermal behaviour of the water-vein system in polycrystalline ice. *Journal of Glaciology*, 38(130), 359-374, DOI:10.3189/S002214300002240.

- MAHOWALD, N., ALBANI, S., KOK, J. F., ENGELSTAEDER, S., SCANZA, R., WARD, D. S. & FLANNER, M. G. 2014. The size distribution of desert dust aerosols and its impact on the Earth system. *Aeolian Research*, 15, 53-71, <https://doi.org/10.1016/j.aeolia.2013.09.002>.
- MANGA, M., FAURIA, K. E., LIN, C., MITCHELL, S. J., JONES, M., CONWAY, C. E., DEGRUYTER, W., HOSSEINI, B., CAREY, R., CAHALAN, R., HOUGHTON, B. F., WHITE, J. D. L., JUTZELER, M., SOULE, S. A. & TANI, K. 2018. The pumice raft-forming 2012 Havre submarine eruption was effusive. *Earth and Planetary Science Letters*, 489, 49-58, <https://doi.org/10.1016/j.epsl.2018.02.025>.
- MANVILLE, V., WHITE, J. D. L., HOUGHTON, B. F. & WILSON, C. J. N. 1998. The saturation behaviour of pumice and some sedimentological implications. *Sedimentary Geology*, 119, 5-16, [https://doi.org/10.1016/S0037-0738\(98\)00057-8](https://doi.org/10.1016/S0037-0738(98)00057-8).
- MANVILLE, V., HODGSON, K. A., HOUGHTON, B. F., KEYS, J. R. & WHITE, J. D. L. 2000. Tephra, snow and water: complex sedimentary responses at an active snow-capped stratovolcano, Ruapehu, New Zealand. *Bulletin of Volcanology*, 62, 278-293, <https://doi.org/10.1007/s004450000096>.
- MARSHALL, S. J. 2011. *The Cryosphere*, Princeton University Press.
- MARZEION, B., COGLEY, G. J., RICHTER, K. & PARKES, D. 2014. Attribution of global glacier mass loss to anthropogenic and natural causes. *Science Reports*, 345(6199), 919-921, DOI:10.1126/science.1254702.
- MATTSON, L. E., GARDNER, J. S. & YOUNG, G. J. 1993. Ablation on Debris Covered Glaciers: an Example from the Rakhiot Glacier, Punjab, Himalaya. In: YOUNG, G. J. (ed.) *Snow and Glacier Hydrology*. IAHS Press.
- MAURELLIS, A. & TENNYSON, J. 2003. The climatic effects of water vapour. *Physics World*.
- MEINANDER, O., KAZADZIS, S., AROLA, A., RIIHELÄ, A., RÄISÄNEN, P., KIVI, R., KONTU, A., KOUZNETSOV, R., SOFIEV, M., SVENSSON, J., SUOKANERVA, H., AALTONEN, V., MANNINEN, T., ROUJEAN, J.-L. & HAUTECOEUR, O. 2013. Spectral albedo of seasonal snow during intensive melt period at Sodankylä, beyond the Arctic Circle. *Atmospheric Chemistry and Physics*, 13, 3793-3810, <https://doi.org/10.5194/acp-13-3793-2013>.
- MEINANDER, O., KONTU, A., VIRKKULA, A., AROLA, A., BACKMAN, L., DAGSSON-WALDHAUSEROVÁ, P., JÄRVINEN, O., MANNINEN, T., SVENSSON, J., DE LEEUW, G. & LEPPÄRANTA. 2014. Brief communication: Light-absorbing impurities can reduce the density of melting snow. *The Cryosphere*, 8, 991-995, <https://doi.org/10.5194/tc-8-991-2014>.
- MELONI, D., DI SARRA, A. & MONTELEONE, F. 2006. Aerosol optical properties at Lampedusa (Central Mediterranean). 2. Determination of single scattering albedo at two wavelengths for different aerosol types. *Atmospheric Chemistry and Physics*, 6(3), 715-727, <https://doi.org/10.5194/acp-6-715-2006>.
- MENG, S., GREENLEE, L. F., SHEN, Y. R. & WANG, E. 2015. Basic science of water: Challenges and current status towards a molecular picture. *Nano Research*, 8, 3085-3110, <https://doi.org/10.1007/s12274-015-0822-y>.
- MEYER, K. W., ACIEGO, S. & KOORNNEEF, J. M. 2017. Radiogenic isotopic compositions of low concentration dust and aerosol from the GISP2 ice core. *Chemical Geology*, 472, 31-43, <https://doi.org/10.1016/j.chemgeo.2017.09.021>.
- MIHALCEA, C., BROCK, B. W., DIOLAIUTI, G., D'AGATA, C., CITTERIO, M., KIRKBRIDE, M. P., CUTLER, M. E. J. & SMIRAGLIA, C. 2008. Using ASTER satellite and ground-based surface temperature measurements to derive supraglacial debris cover and thickness patterns on Miage Glacier (Mont Blanc Massif, Italy). *Cold Regions Science and Technology*, 52(3), 341-354, <https://doi.org/10.1016/j.coldregions.2007.03.004>.
- MING, J., CACHIER, H., XIAO, C., QIN, D., KANG, S., HOU, S. & XU, J. 2008. Black carbon record based on a shallow Himalayan ice core and its climatic implications. *Atmospheric Chemistry and Physics*, 8, 1343-1352, <https://doi.org/10.5194/acp-8-1343-2008>.
- MÖLLER, R., MÖLLER, M., KUKLA, P. A. & SCHNEIDER, C. 2016. Impact of supraglacial deposits of tephra from Grímsvötn volcano, Iceland, on glacier ablation. *Journal of Glaciology*, 62(235), 933-943, DOI:10.1017/jog.2016.82.
- MÖLLER, R., MÖLLER, M., KUKLA, P. A. & SCHNEIDER, C. 2018. Modulation of glacier ablation by tephra coverage from Eyjafjallajökull and Grímsvötn volcanoes, Iceland: an

- automated field experiment. *Earth System Science Data*, 10, 53-60, <https://doi.org/10.5194/essd-10-53-2018>.
- MORGANA, S., GHIGLIOTTI, L., ESTEVEZ-CALVAR, N., STIFANESE, R., WIECKZOREK, A., DOYLE, T., CHRISTIANSEN, J. S., FAIMALI, M. & GARAVENTA, F. 2018. Microplastics in the Arctic: A case study with sub-surface water and fish samples off Northeast Greenland. *Environmental Pollution*, 242(B), 1078-1086, <https://doi.org/10.1016/j.envpol.2018.08.001>.
- MUNARI, C., INFANTINI, V., SCOPONI, M., RASTELLI, E., CORINALDESI, C. & MISTRI, M. 2017. Microplastics in the sediments of Terra Nova Bay (Ross Sea, Antarctica). *Marine Pollution Bulletin*, 122(1-2), 161-165, <https://doi.org/10.1016/j.marpolbul.2017.06.039>.
- MUSCHITIELLO, F., PAUSATA, F. S. R., LEA, J. M., MAIR, D. W. F. & WOHLFARTH, B. 2017. Enhanced ice sheet melting driven by volcanic eruptions during the last deglaciation. *Nat Commun*, 8, 1020, <https://doi.org/10.1038/s41467-017-01273-1>.
- MYHRE, G., SAMSET, B. H., SCHULZ, M., BALKANSKI, Y., BAUER, S., BERNTSEN, T. K., BIAN, H., BELLOUIN, N., CHIN, M., DIEHL, T., EASTER, R. C., FEICHTER, J., GHAN, S. J., HAUGLUSTAINE, D., IVERSEN, T., KINNE, S., KIRKEVÅG, A., LAMARQUE, J.-F., LIN, G., LIU, X., LUND, M. T., LUO, G., MA, X., VAN NOIJE, T., PENNER, J. E., RASCH, P. J., RUIZ, A., SELAND, Ø., SKEIE, R. B., STIER, P., TAKEMURA, T., TSIGARIDIS, K., WANG, P., WANG, Z., XU, L., YU, H., YU, F., YOON, J.-H., ZHANG, K., ZHANG, H., and ZHOU, C. 2013. Radiative forcing of the direct aerosol effect from AeroCom Phase II simulations, *Atmos. Chem. Phys.*, 13, 1853–1877, <https://doi.org/10.5194/acp-13-1853-2013>.
- NAGATA, T. 1978. Possible mechanism of concentration of meteorites within the meteorite ice field in Antarctica. *National Institute of Polar Research*, 70-92.
- NAKAWO, M. & YOUNG, G. J. 1981. Field experiments to determine the effect of a debris layer on ablation of glacier ice. *Annals of Glaciology*, 2, 85-91, DOI:10.3189/172756481794352432.
- NAKAWO, M. & YOUNG, G. J. 1982. Estimate of Glacier Ablation under a Debris Layer from Surface Temperatures and Meteorological Variables. *Journal of Glaciology*, 28(98), 29-34, DOI:10.3189/S002214300001176X.
- NASA. 2009. *Incoming Sunlight* [Online]. NASA. Available: <https://earthobservatory.nasa.gov/features/EnergyBalance/page2.php> [Accessed 28.03.21 2021].
- NEUMANN, B., VAFEIDIS, A. T., ZIMMERMANN, J. & NICHOLLS, R. J. 2015. Future coastal population growth and exposure to sea-level rise and coastal flooding--a global assessment. *PLoS One*, 10, e0118571.
- NI, P., CHABOT, N. L., RYAN, C. J. & SHAHAR, A. 2020. Heavy iron isotope composition of iron meteorites explained by core crystallization. *Nature Geoscience*, 13, 611-615, DOI:10.1038/s41561-020-0617-y.
- NICHOLSON, L. & BENN, D. I. 2006. Calculating ice melt beneath a debris layer using meteorological data. *Journal of Glaciology*, 52(178), 463-470, DOI:10.3189/172756506781828584.
- NICHOLSON, L. & BENN, D. I. 2013. Properties of natural supraglacial debris in relation to modelling sub-debris ice ablation. *Earth Surface Processes and Landforms*, 38, 490-501, <https://doi.org/10.1002/esp.3299>.
- NICHOLSON, L., WIRBEL, A., MAYER, C. & LAMBRECHT, A. 2021. The Challenge of Non-Stationary Feedbacks in Modeling the Response of Debris-Covered Glaciers to Climate Forcing. *Frontiers in Earth Science*, 9, DOI:10.3389/feart.2021.662695.
- NIELD, J. M., CHIVERRELL, R. C., DARBY, S. E., LEYLAND, J., VIRCAVS, L. H. & JACOBS, B. 2013. Complex spatial feedbacks of tephra redistribution, ice melt and surface roughness modulate ablation on tephra covered glaciers. *Earth Surface Processes and Landforms*, 38, 95-102, <https://doi.org/10.1002/esp.3352>.
- NSIDC. 2020a. *All about glaciers* [Online]. Available: <https://nsidc.org/cryosphere/glaciers/questions/what.html> [Accessed 27.10.20].
- NSIDC. 2020b. *Cryosphere glossary* [Online]. Available: <https://nsidc.org/cryosphere/glossary/term/albedo> [Accessed 23.11.20].
- NYE, J. F. 1989. The geometry of water veins and nodes in polycrystalline ice. *Journal of Glaciology*, 35(119), 17-22, DOI:10.3189/002214389793701437.

- OBBARD, R. W. 2018. Microplastics in Polar Regions: The role of long range transport. *Current Opinion in Environmental Science & Health*, 1, 24-29. <https://doi.org/10.1016/j.coesh.2017.10.004>.
- OHNO, H., OHATA, T., & HIGUCHI, K. 1992. The influence of humidity on the ablation of continental-type glaciers. *Annals of Glaciology*, 16, 107-114, DOI:10.3189/1992AoG16-1-107-114.
- OKAJIMA, H., ANDO, M. & HAMAGUCHI, H.-O. 2018. Formation of “Nano-Ice” and Density Maximum Anomaly of Water. *Bulletin of the Chemical Society of Japan*, 91, 991-997, <https://doi.org/10.1246/bcsj.20180052>.
- OPEIL, C. P., CONSOLMAGNO, G. J. & BRITT, D. T. 2010. The thermal conductivity of meteorites: New measurements and analysis. *Icarus*, 208(1), 449-454, <https://doi.org/10.1016/j.icarus.2010.01.021>.
- OPEIL, C. P., CONSOLMAGNO, G. J., SAFARIK, D. J. & BRITT, D. T. 2012. Stony meteorite thermal properties and their relationship with meteorite chemical and physical states. *Meteoritics & Planetary Science*, 47, 319-329, <https://doi.org/10.1111/j.1945-5100.2012.01331.x>.
- OPPENHEIMER, M., GLAVOVIC, B. C., HINKEL, J., VAN DE WAL, R., MAGNAN, A. K., ABD-ELGAWAD, A., CAI, R., CIFUENTES-JARA, M., DECONTO, R. M., GHOSH, T., HAY, J., ISLA, F., MARZEION, B., MEYSSIGNAC, B. & SEBESVARI, Z. 2019. Sea Level Rise and Implications for Low-Lying Islands, Coasts and Communities. In: PÖRTNER, H.-O., ROBERTS, D. C., MASSON-DELMOTTE, V., ZHAI, P., TIGNOR, M., POLOCZANSKA, E., MINTENBECK, K., ALEGRIA, A., NICOLAI, M., OKEM, A., PETZOLD, J., RAMA, B. & WEYER, N. M. (eds.) *IPCC Special Report on the Ocean and Cryosphere in a Changing Climate*. In Press.
- ÖSTREM, G. 1959. Ice Melting under a Thin Layer of Moraine, and the Existence of Ice Cores in Moraine Ridges. *Geografiska Annaler*, 41, 228-230, <https://doi.org/10.1080/20014422.1959.11907953>.
- PARISH, T. R. & BROMWICH, D. H. 1987. The surface wind field over the Antarctic ice sheets. *Nature*, 328, 51-54, <https://doi.org/10.1038/328051a0>.
- PATTI, A. & ACIERNO, D. 2020. Thermal Conductivity of Polypropylene-Based Materials. *Polypropylene - Polymerization and Characterization of Mechanical and Thermal Properties*.
- PEEL, M. C., FINLAYSON, B. L. & MCMAHON, T. A. 2007. Updated world map of the Köppen-Geiger climate classification. *Hydrology and Earth System Sciences*, 11, 1633-1644, <https://doi.org/10.5194/hess-11-1633-2007>.
- PODGORNY, I. A. & GRENFELL, T. C. 1996. Absorption of solar energy in a cryoconite hole. *Geophysical Research Letters*, 23(18), 2465-2468, <https://doi.org/10.1029/96GL02229>.
- POPE, R. M. & FRY, E. S. 1997. Absorption spectrum (380–700 nm) of pure water. II. Integrating cavity measurements. *Applied Optics*, 36, 8710-8723.
- PRENTICE, I. C., BAINES, P. G., SCHOLZE, M., WOOSTER, M. J., CORNELL, S., PRENTICE, I. C., HOUSE, J. & DOWNY, C. 2012. Fundamentals of climate change science. *Understanding the Earth System*.
- PRICE, P. B. 2007. Microbial life in glacial ice and implications for a cold origin of life. *FEMS Microbiol Ecol*, 59(2), 217-31, <https://doi.org/10.1111/j.1574-6941.2006.00234.x>.
- PRITCHARD, H. D. 2019. Asia's shrinking glaciers protect large populations from drought stress. *Nature*, 569, 649-654, <https://doi.org/10.1038/s41586-019-1240-1>.
- RACOVITEANU, A. E., NICHOLSON, L., GLASSER, N. F., MILES, E., HARRISON, S. & REYNOLDS, J. M. 2021. Debris-covered glacier systems and associated glacial lake outburst flood hazards: challenges and prospects. *Journal of the Geological Society*, 179(3), <https://doi.org/10.1144/jsg2021-084>.
- RAM, M. & GAYLEY, R. I. 1991. Long-range transport of volcanic ash to Greenland Ice Sheet. *Nature*, 349, 401-404, <https://doi.org/10.1038/349401a0>.
- RANA, B., NAKAWO, M., FUKUSHIMA, Y. & AGETA, Y. 1997. Application of a conceptual precipitation-runoff model (HYCYMODEL) in a debris-covered glacierized basin in the Langtang Valley, Nepal Himalaya. *Annals of Glaciology*, 25, 226-231, DOI:10.3189/S0260305500014087.
- REID, T. D. & BROCK, B. W. 2010. An energy-balance model for debris-covered glaciers including heat conduction through the debris layer. *Journal of Glaciology*, 56, 903-916, DOI:10.3189/002214310794457218.

- REID, T. D., CARENZO, M., PELLICCIOTTI, F. & BROCK, B. W. 2012. Including debris cover effects in a distributed model of glacier ablation. *Journal of Geophysical Research: Atmospheres*, 117, D18105, DOI:10.1029/2012JD017795.
- REMPEL, A. 2005. Englacial phase changes and intergranular flow above subglacial lakes, *Annals of Glaciology*, 40, 191-194, DOI:10.3189/172756405781813564.
- REZNICHENKO, N., DAVIES, T., SHULMEISTER, J. & MCSAVENEY, M. 2010. Effects of debris on ice-surface melting rates: an experimental study. *Journal of Glaciology*, 56(197), 384-394, DOI:10.3189/002214310792447725.
- RICHARDSON, J. N. & BROOK, M. S. 2010. Ablation of debris-covered ice: some effects of the 25 September 2007 Mt Ruapehu eruption. *Journal of the Royal Society of New Zealand*, 40, 45-55, <https://doi.org/10.1080/03036758.2010.494714>.
- RICHARDSON, S. D. & REYNOLDS, J. M. 2000. An overview of glacial hazards in the Himalayas. *Quaternary International*, 65/66, 31-47, [https://doi.org/10.1016/S1040-6182\(99\)00035-X](https://doi.org/10.1016/S1040-6182(99)00035-X).
- ROUNCE, D. R., QUINCEY, D. J., & MCKINNEY, D. C. 2015. Debris-covered glacier energy balance model for Imja–Lhotse Shar Glacier in the Everest region of Nepal. *The Cryosphere*, 9, 2295-2310, <https://doi.org/10.5194/tc-9-2295-2015>.
- SAKAI, A., NAKAWO, M. & FUJITA, K. 2002. Distribution Characteristics and Energy Balance of Ice Cliffs on Debris-covered Glaciers, Nepal Himalaya. *Arctic, Antarctic, and Alpine Research*, 34, 12-19, <https://doi.org/10.1080/15230430.2002.12003463>.
- SALEH, R. 2020. From Measurements to Models: Toward Accurate Representation of Brown Carbon in Climate Calculations. *Current Pollution Reports*, 6, 90-104, <https://doi.org/10.1007/s40726-020-00139-3>.
- SÄWSTRÖM, C., MUMFORD, P., MARSHALL, W., HODSON, A. & LAYBOURN-PARRY, J. 2002. The microbial communities and primary productivity of cryoconite holes in an Arctic glacial (Svalbard 79°N). *Polar Biology*, 25, 591-596, <https://doi.org/10.1007/s00300-002-0388-5>.
- SCHEPANSKI, K. 2018. Transport of Mineral Dust and Its Impact on Climate. *Geosciences*, 8(5), DOI:10.3390/geosciences8050151.
- SCHERLER, D., WULF, H. & GORELICK, N. 2018. Global Assessment of Supraglacial Debris-Cover Extents. *Geophysical Research Letters*, 45, 11798-11805, <https://doi.org/10.1029/2018GL080158>.
- SCHEWE, J., HEINKE, J., GERTEN, D., HADDELAND, I., ARNELL, N. W., CLARK, D. B., DANKERS, R., EISNER, S., FEKETE, B. M., COLON-GONZALEZ, F. J., GOSLING, S. N., KIM, H., LIU, X., MASAKI, Y., PORTMANN, F. T., SATOH, Y., STACKE, T., TANG, Q., WADA, Y., WISSER, D., ALBRECHT, T., FRIELER, K., PIONTEK, F., WARSZAWSKI, L. & KABAT, P. 2014. Multimodel assessment of water scarcity under climate change. *PNAS*, 111(9), 3245-3250, <https://doi.org/10.1073/pnas.1222460110>.
- SCHNEIDER, T., O'GORMAN, P. A. & LEVINE, X. J. 2010. Water Vapor and the Dynamics of Climate Changes. *Reviews of Geophysics*, 48, <https://doi.org/10.1029/2009RG000302>.
- SHAW, T. E., BROCK, B. W., FYFFE, C.L., PELLICCIOTTI, F., RUTTER, N. & DIOTRI, F. 2016. Air temperature distribution and energy-balance modelling of a debris-covered glacier. *Journal of Glaciology*, 62(231), 185-198, DOI:10.1017/jog.2016.31.
- SHEN, Z., ZHANG, Q., CAO, J., ZHANG, L., LEI, Y., HUANG, Y., HUANG, R. J., GAO, J., ZHAO, Z., ZHU, C., YIN, X., ZHENG, C., XU, H. & LIU, S. 2017. Optical properties and possible sources of brown carbon in PM 2.5 over Xi'an, China. *Atmospheric Environment*, 150, 322-330, <https://doi.org/10.1016/j.atmosenv.2016.11.024>.
- SHUKLA, J. B., VERMA, M. & MISRA, A. K. 2017. Effect of global warming on sea level rise: A modeling study. *Ecological Complexity*, 32(A), 99-110, <https://doi.org/10.1016/j.ecocom.2017.10.007>.
- SOLOMINA, O., HAEBERLI, W., KULL, C. & WILES, G. 2008. Historical and Holocene glacier-climate variations: General concepts and overview. *Global and Planetary Change*, 60(1-2), 1-9, <https://doi.org/10.1016/j.gloplacha.2007.02.001>.
- STEFÁNSSON, H., PETERNELL, M., KONRAD-SCHMOLKE, M., HANNESDÓTTIR, H., ÁSBJÖRNSSON, E. J. & STURKELL, E. 2021. Microplastics in Glaciers: First Results from the Vatnajökull Ice Cap. *Sustainability*, 13, 4183, <https://doi.org/10.3390/su13084183>.
- STEINER, J. F., LITT, M., STIGTER, E. E., SHEA, J., BIERKENS, M. F. P. & IMMERZEEL, W. W. 2018. The Importance of Turbulent Fluxes in the Surface Energy Balance of a

- Debris-Covered Glacier in the Himalayas. *Frontiers in Earth Science*, 6 (144), DOI:10.3389/feart.2018.00144.
- STIBAL, M., SABACKA, M. & KASTOVSKA, K. 2006. Microbial communities on glacier surfaces in Svalbard: impact of physical and chemical properties on abundance and structure of cyanobacteria and algae. *Microb Ecol*, 52, 644-54, <https://doi.org/10.1007/s00248-006-9083-3>.
- STIGTER, E. E., LITT, M., STEINER, J. F., BONEKAMP, P. N. J., SHEA, J. M., BIERKENS, M. F. P. & IMMERZEEL, W. W. 2018. The Importance of Snow Sublimation on a Himalayan Glacier. *Frontiers in Earth Science*, 6: 108, DOI:10.3389/feart.2018.00108.
- SVENSSON, J., STRÖM, J., KIVEKÄS, N., DKHAR, N. B., TAYAL, S., SHARMA, V. P., JUTILA, A., BACKMAN, J., VIRKKULA, A., RUPPEL, M., HYVÄRINEN, A., KONTU, A., HANNULA, H. R., LEPPÄRANTA, M., HOODA, R. K., KORHOLA, A., ASMI, E. & LIHAVAINEN, H. 2018. Light-absorption of dust and elemental carbon in snow in the Indian Himalayas and the Finnish Arctic. *Atmos. Meas. Tech.*, 11, 1403-1416, <https://doi.org/10.5194/amt-11-1403-2018>.
- SWITHINBANK, C. 1950. The Origin of Dirt Cones on Glaciers. *Journal of Glaciology*, 1, 461-465.
- TABERLET, N. & PLIHON, N. 2021. Sublimation-driven morphogenesis of Zen stones on ice surfaces. *PNAS*, 118 (40), DOI:e2109107118
- TAKEUCHI, Y., KAYASTHA, R. B. & NAKAWO, M. 2000. Characteristics of ablation and heat balance in debris-free and debris-covered areas on Khumbu Glacier, Nepal Himalayas, in the pre-monsoon season. In: NAKAWO, M., RAYMOND, C. F. & FOUNTAIN, A. (eds.) *Debris Covered Glaciers*. Oxfordshire: IAHS Press.
- TAKEUCHI, N., KOHSHIMA, S. & SEKO, K. 2001a. Structure, Formation, and Darkening Process of Albedo-reducing Material (Cryoconite) on a Himalayan Glacier: A Granular Algal Mat Growing on the Glacier. *Arctic, Antarctic, and Alpine Research*, 33(2), 115-122, <https://doi.org/10.1080/15230430.2001.12003413>.
- TAKEUCHI, N., KOHSHIMA, S., SHIRAIWA, T. & KUBOTA, K. 2001b. Characteristics of cryoconite (surface dust on glaciers) and surface albedo of a Patagonian glacier, Tyndall Glacier, Southern Patagonia Icefield. *Bulletin of Glaciological Research*, 18, 65-59.
- TAKEUCHI, N. 2002. Optical characteristics of cryoconite (surface dust) on glaciers: the relationship between light absorbency and the property of organic matter contained in the cryoconite. *Annals of Glaciology*, 34, 409-414, DOI:10.3189/172756402781817743.
- TAKEUCHI, N., ISHIDA, Y. & LI, Z. 2011. Microscopic analyses of insoluble particles in an ice core of Ürümqi Glacier No. 1: Quantification of mineral and organic particles. *Journal of Earth Science*, 22, 431-440, <https://doi.org/10.1007/s12583-011-0197-2>.
- TAKEUCHI, N., SAKAKI, R., UETAKE, J., NAGATSUKA, N., SHIMADA, R., NIWANO, M. & AOKI, T. 2018. Temporal variations of cryoconite holes and cryoconite coverage on the ablation ice surface of Qaanaaq Glacier in northwest Greenland, *Annals of Glaciology*, 59(77), 21-30, DOI:10.1017/ago.2018.19.
- TANAKA, H. 1998. Simple Physical Explanation of the Unusual Thermodynamic Behavior of Liquid Water. *Physical Review Letters*, 80, 5750-5753, <https://doi.org/10.1103/PhysRevLett.80.5750>.
- TANAKA, H., GIRARD, G., DAVIS, R., PEUTO, A. & BIGNELL, N. 2001. Recommended table for the density of water between 0°C and 40°C based on recent experimental reports. *Metrologia*, 38, 301-309.
- TAWFIK, M., TONNELIER, X. & SANSOM, C. 2018. Light source selection for a solar simulator for thermal applications: A review. *Renewable and Sustainable Energy Reviews*, 90, 802-813, <https://doi.org/10.1016/j.rser.2018.03.059>.
- TEDESCO, M., DOHERTY, S., FETTWEIS, X., ALEXANDER, P., JEYARATNAM, J. & STROEVE, J. 2016. The darkening of the Greenland ice sheet: trends, drivers, and projections (1981–2100). *The Cryosphere*, 10, 477-496, <https://doi.org/10.5194/tc-10-477-2016>.
- TEDSTONE, A. J., COOK, J. M., WILLIAMSON, C. J., HOFER, S., MCCUTCHEON, J., IRVINE-FYNN, T., GRIBBIN, T. & TRANTER, M. 2020. Algal growth and weathering crust state drive variability in western Greenland Ice Sheet ice albedo. *The Cryosphere*, 14, 521-538, <https://doi.org/10.5194/tc-14-521-2020>.
- TENNYSON, J., BERNATH, P. F., BROWN, L. R., CAMPARGUE, A., CSÁSZÁR, A. G., DAUMONT, L., GAMACHE, R. R., HODGES, J. T., NAUMENKO, O. V., POLYANSKY,

- O. L., ROTHMAN, L. S., VANDAELE, A. C. & ZOBOV, N. F. 2014. A database of water transitions from experiment and theory (IUPAC Technical Report). *Pure and Applied Chemistry*, 86, 71-83, <https://doi.org/10.1515/iupac.86.0001>.
- THAYYEN, R. J. & GERGAN, J. T. 2010. Role of glaciers in watershed hydrology: a preliminary study of a "Himalayan catchment". *The Cryosphere*, 4, 115-128, <https://doi.org/10.5194/tc-4-115-2010>.
- TRENBERTH, K. E. 2014. Earth's Energy Balance. *Reference Module in Earth Systems and Environmental Sciences*, 859-870.
- VAN DEN BROEKE, M. R., SMEETS, P., ETTEMA, J., VAN DER VEEN, C., VAN DE WAL, R. & OERLEMANS, J. 2008. Partitioning of melt energy and meltwater fluxes in the ablation zone of the west Greenland ice sheet. *The Cryosphere*, 2, 179-189, <https://doi.org/10.5194/tc-2-179-2008>.
- VASSILEVA, N. D., VAN DEN ENDE, D., MUGELE, F. & MELLEMA, J. 2005. Capillary Forces between Spherical Particles Floating at a Liquid-Liquid Interface, *Langmuir*, 21, 11190-11200, DOI:10.1021/la051186o.
- VAUGHAN, D. G., COMISO, J. C., ALLISON, I., CARRASCO, J., KASER, G., KWOK, R., MOTE, P., MURRAY, T., PAUL, F., REN, J., RIGNOT, E., SOLOMINA, O., STEFFEN, K. & ZHANG, T. 2013. Observations: Cryosphere. In: STOCKER, T. F., QIN, D., PLATTNER, G.-K., TIGNOR, M., ALLEN, S. K., BOSCHUNG, J., NAUELS, A., XIA, Y., BEX, V. & MIDGLEY, P. M. (eds.) *Climate Change 2013: The Physical Science Basis. Contribution of Working Group I to the Fifth Assessment Report of the Intergovernmental Panel on Climate Change*. Cambridge, UK: Cambridge University Press.
- VELLA, D. & HUPPERT, H. E. 2007. The waterlogging of floating objects. *Journal of Fluid Mechanics*, 585, 245-254, DOI:10.1017/S002211200700715X.
- VINCENT, C., KAPPENBERGER, C., VALLA, F., BAUDER, A., FUNK, M. & LE MEUR, E. 2004. Ice ablation as evidence of climate change in the Alps over the 20th century. *Journal of Geophysical Research*, 109, D10104, DOI:10.1029/2003JD003857.
- VON FRIESEN, L. W., GRANBERG, M. E., PAVLOVA, O., MAGNUSSON, K., HASSELLOV, M. & GABRIELSEN, G. W. 2020. Summer sea ice melt and wastewater are important local sources of microlitter to Svalbard waters. *Environment International*, 139, 105511, <https://doi.org/10.1016/j.envint.2020.105511>.
- WANG, X., XU, B. & MING, J. 2014. An Overview of the Studies on Black Carbon and Mineral Dust Deposition in Snow and Ice Cores in East Asia. *Journal of Meteorological Research*, 28, 354-370, <https://doi.org/10.1007/s13351-014-4005-7>.
- WARREN, S. G. 1982. Optical Properties of Snow. *Reviews of Geophysics and Space Physics*, 20, 67-89, <https://doi.org/10.1029/RG020i001p00067>.
- WARREN, S. G. & BRANDT, R. E. 2008. Optical constants of ice from the ultraviolet to the microwave: A revised compilation. *Journal of Geophysical Research*, 113, D14220, DOI:10.1029/2007JD009744.
- WARREN, S. G., BRANDT, R. E. & GRENFELL, T. C. 2006. Visible and near-ultraviolet absorption spectrum of ice from transmission of solar radiation into snow. *Applied Optics*, 45, 5320-5334, <https://doi.org/10.1364/AO.45.005320>.
- WHELAN, P. M. & HODGSON, M. J. 1989. *Essential Principles of Physics*, Great Britain, Hazell Watson & Viney Ltd.
- WHITHAM, A. G. & SPARKS, R. S. J. 1986. Pumice. *Bulletin of Volcanology*, 48, 209-223, <https://doi.org/10.1007/BF01087675>.
- WIJNTJES, I. G. M., VAN DE WAL, R. S. W., REICHAERT, G. J., SLUIJS, A. & OERLEMANS, J. 2011. Dust from the dark region in the western ablation zone of the Greenland ice sheet, *The Cryosphere*, 5, 589-601, <https://doi.org/10.5194/tc-5-589-2011>.
- WU, G., WAN, X., RAM, K., LI, P., LIU, B., YIN, Y., FU, P., LOEWEN, M., GAO, S., KANG, S., KAWAMURA, K., WANG, Y. & CONG, Z. 2020. Light absorption, fluorescence properties and sources of brown carbon aerosols in the Southeast Tibetan Plateau. *Environmental Pollution*, 257, 113616, <https://doi.org/10.1016/j.envpol.2019.113616>.
- WU, G.-M., CONG, Z.-Y., KANG, S.-C., KAWAMURA, K., FU, P.-Q., ZHANG, Y.-L., WAN, X., GAO, S.-P. & LIU, B. 2016. Brown carbon in the cryosphere: Current knowledge and perspective. *Advances in Climate Change Research*, 7(1-2), 82-89, <https://doi.org/10.1016/j.accre.2016.06.002>.
- XIE, F., LIU, S., WU, K., ZHU, Y., GAO, Y., QI, M., DUAN, S., SAIFULLAH, M. & TAHIR, A. A. 2020. Upward Expansion of Supra-Glacial Debris Cover in the Hunza Valley,

- Karakoram, During 1990 ~ 2019. *Frontiers in Earth Science*, 8:308, DOI:10.3389/feart.2020.00308
- YANG, W., TANDONG, Y., BAIQING, X. & HANG, Z. 2010. Influence of supraglacial debris on summer ablation and mass balance in the 24k Glacier, southeast Tibetan Plateau. *Geografiska Annaler*, 92A(3): 353-360, <https://doi.org/10.1111/j.1468-0459.2010.00400.x>.
- YUE, X., LI, Z., ZHAO, J., FAN, J., TAKEUCHI, N. & WANG, L. 2020. Variation in albedo and its relationship with surface dust at Urumqi Glacier No. 1 in Tien Shan, China, *Frontiers in Earth Science*, 8:110, DOI:10.3389/feart.2020.00110.
- ZARSKY, J. D., STIBAL, M., HODSON, A., SATTLER, B., SCHOSTAG, M., HANSEN, L. H., JACOBSEN, C. S. & PSENNER, R. 2013. Large cryoconite aggregates on a Svalbard glacier support a diverse microbial community including ammonia-oxidizing archaea. *Environmental Research Letters*, 8 (3), DOI:10.1088/1748-9326/8/3/035044.
- ZHANG, T., XIAO, C., COLGAN, W., QIN, X., DU, W., SUN, W., LIU, Y. & DING, M. 2013. Observed and modelled ice temperature and velocity along the main flowline of East Rongbuk Glacier, Qomolangma (Mount Everest), Himalaya, *Journal of Glaciology*, 59(215), 438-448, DOI:10.3189/2013JoG12J202.
- ZHANG, Y., GAO, T., KANG, S., ALLEN, S., LUO, X. & ALLEN, D. 2021. Microplastics in glaciers of the Tibetan Plateau: Evidence for the long-range transport of microplastics. *Science of the Total Environment*, 758, 143634, <https://doi.org/10.1016/j.scitotenv.2020.143634>.
- ZHEN, W. & SHIYIN, L. 2012. Imaging the Debris Internal Structure and Estimating the Effect of Debris Layer on Ablation of Glacier Ice. *Journal Geological Society of India*, 80, 825-835, <https://doi.org/10.1007/s12594-012-0211-z>.